Power System Dynamics and Stability

Da Xie, Yanchi Zhang, Dongdong Li, Chenghong Gu, Ignacio Hernando-Gil, Nan Zhao

Published in Journals: Electricity, Electronics,
Energies and Processes

Topic Reprint

Power System Dynamics and Stability

Edited by
Da Xie, Yanchi Zhang, Dongdong Li, Chenghong Gu,
Ignacio Hernando-Gil and Nan Zhao

mdpi.com/topics

MDPI

Power System Dynamics and Stability

Power System Dynamics and Stability

Editors

Da Xie
Yanchi Zhang
Dongdong Li
Chenghong Gu
Ignacio Hernando-Gil
Nan Zhao

MDPI

Basel • Beijing • Wuhan • Barcelona • Belgrade • Novi Sad • Cluj • Manchester

Editors

Da Xie
Shanghai Jiao Tong University
Shanghai
China

Yanchi Zhang
Shanghai Dianji University
Shanghai
China

Dongdong Li
Shanghai University of Electric Power
Shanghai
China

Chenghong Gu
University of Bath
Bath
UK

Ignacio Hernando-Gil
ESTIA Institute of Technology
Bidart
France

Nan Zhao
Lancaster University
Lancaster
UK

Editorial Office
MDPI AG
Grosspeteranlage 5
4052 Basel, Switzerland

This is a reprint of articles from the Topic published online in the open access journals *Electricity* (ISSN 2673-4826), *Electronics* (ISSN 2079-9292), *Energies* (ISSN 1996-1073), and *Processes* (ISSN 2227-9717) (available at: https://www.mdpi.com/topics/V3X52QM64H).

For citation purposes, cite each article independently as indicated on the article page online and as indicated below:

Lastname, A.A.; Lastname, B.B. Article Title. *Journal Name* **Year**, *Volume Number*, Page Range.

ISBN 978-3-7258-2163-1 (Hbk)
ISBN 978-3-7258-2164-8 (PDF)
doi.org/10.3390/books978-3-7258-2164-8

Contents

electronics

MDPI

Article

Improved Repetitive Control for an LCL-Type Grid-Tied Inverter with Frequency Adaptive Capability in Microgrids

Hongwei Zhang [1], Qiangsong Zhao [1,*], Shuanghong Wang [1] and Xuebin Yue [2]

[1] School of Electronic and Information, Zhongyuan University of Technology, Zhengzhou 451191, China; zhanghongwei@zut.edu.cn (H.Z.)
[2] Department of Electronic and Computer Engineering, Ritsumeikan University, Kusatsu 525-8577, Japan
* Correspondence: zhaoqiangsong@zut.edu.cn

Abstract: Repetitive control (RC), which can track any periodic signal with a known integer period with zero steady-state error, is widely used for current control of grid-tied inverters in microgrids. However, the inherent one fundamental period time delay, leads to poor dynamic performance. Furthermore, the performance of conventional RC (CRC) will degrade when operating at a high variation grid frequency. Therefore, this paper proposes a frequency adaptive improved RC (FA-IRC) for grid-tied inverters. The improved RC (IRC) consists of a repetitive controller with a modified internal model filter, plus a proportional controller. In comparison to the CRC, the IRC has a good dynamic response, because it provides a higher gain and a wider bandwidth at the resonant frequency. Moreover, to achieve the frequency adaptability of the IRC, a fractional delay, based on a finite impulse response (FIR) filter, is built into the IRC system, to ensure that the resonant frequency of the IRC is approximately equal to the actual grid frequency and harmonic frequency. Stability analysis and characteristic analysis of the FA-IRC system are reported in this paper. Simulations are conducted, to demonstrate the validity of the proposed method.

Keywords: repetitive control; grid-tied inverter; FIR filter

Citation: Zhang, H.; Zhao, Q.; Wang, S.; Yue, X. Improved Repetitive Control for an LCL-Type Grid-Tied Inverter with Frequency Adaptive Capability in Microgrids. *Electronics* **2023**, *12*, 1736. https://doi.org/10.3390/electronics12071736

Academic Editors: Da Xie, Yanchi Zhang, Dongdong Li, Chenghong Gu, Ignacio Hernando-Gil and Nan Zhao

Received: 1 March 2023
Revised: 3 April 2023
Accepted: 3 April 2023
Published: 5 April 2023

1. Introduction

Distributed power generation technologies using intermittent renewable energy sources, are an important means of solving energy problems and have therefore received extensive research [1,2]. As an important hub for energy conversion, the grid-tied inverter in the microgrid directly affects the stable and safe operation of the entire electrical energy system. Therefore, research on current harmonic suppression strategies for grid-tied inverters has received considerable attention [3].

Repetitive control (RC), based on the internal model principle (IMP), is widely used in inverter control, due to its advantage of high control accuracy, and it is particularly good at suppressing periodic disturbances, such as dead zones and periodic distortions in the output waveform, caused by non-linear rectifier loads or grid harmonics [4–7]. However, it has one fundamental period time delay. Furthermore, a repetitive controller can be equivalent to the sum of a negatively scaled term, an integral term, and a set of resonant controllers [8]. However, the negative proportional term will result in a slow transient response. To this end, researchers have proposed two methods to enhance the dynamic response of RC systems, one is to enable the system to have a higher RC gain and to increase the error convergence rate, by applying accurate phase compensation to the RC [9,10]. The other is to combine RC with a feedback control with fast dynamic response, typically in cascade or parallel, with a proportional or proportional-integral control, to form a composite control [11,12]. In [12], a proportional integral multi resonant-type RC (PIMR-RC), combining a repetitive controller and a proportional item, was proposed for control of grid-tied inverters, to enhance the transient response. This method has the benefit of a clearer design concept and improved low-frequency harmonic suppression performance.

The digital representation of the CRC is given by the formula $G_{CRC} = Q(z)z^{-N}/(1 - Q(z)z^{-N})$, where N is the order of RC and represents the proportion of the sampling frequency to the fundamental frequency. $Q(z)$ is typically a constant less than 1 or a zero-phase low-pass filter, to ensure a safe stability margin. In [13], a robust RC, based on a modified $Q(z)$ filter, was proposed, to obtain the performance improvement at the fundamental frequency. By utilizing this approach, it is possible to achieve a higher gain and a wider control bandwidth at the fundamental frequency, without the need for extensive computational resources. The wider bandwidth, implies that grid frequency variation in a small range (such as ± 0.2 Hz) does not significantly impact performance, which is suitable for control of the active power filter [14].

However, the N value in RC is usually rounded up or down when the grid frequency varies in a large range in distributed power generation systems. Consequently, the control gain of each harmonic will decline as the resonant frequency of the RC deviates from harmonic frequencies, resulting in harmonic suppression performance degrading and the total harmonic distortion (THD) increasing.

There are four main methods used to improve the frequency adaptation of RC: variable sampling frequency RC [15,16], bandwidth RC [17,18], higher-order RC (HORC) [19], and fractional-order RC (FORC) [20–23]. A scheme proposed in [15] ensures an integer RC order by changing the sampling rate, but real time changing of the sampling frequency increases the complexity of the controller implementation. In [16], a spatial RC based on the phase angle information of the grid voltage was proposed, which enables a guaranteed constant number of samples per cycle. It achieves a fixed number of samples per cycle, but the price paid is the inherent problem with the variable sampling method. Ref. [18] proposed a multi-bandwidth RC to resist the grid frequency variation in a grid-tied inverter. It sets each resonant bandwidth individually, and is implemented as a linear phase finite impulse response (FIR) filter, but the realization of the internal model filter is still complex. Using the HORC system, multi-cycle errors are accumulated. Compared to CRC, HORC can reduce interference at intermediate frequencies or against changes in the frequency of periodic signals [24]. However, on the other hand, this makes the system design more complex and computationally burdensome.

For frequency adaptability of the RC, the fractional-order RC (FORC) has been presented in many studies, which uses the fractional delay (FD) filter to approach the fractional order. The FORC with fractional delay Lagrange-interpolation-based FIR filter, has been proposed in a variety of applications [25–27]. In addition, in [28], a Thiran infinite impulse response (IIR) filter was proposed, to approximate the FD to enhance the frequency adaptability of CRC. Generally, the IIR filter has a full amplitude gain of one and requires only phase design, but it has poles, and the overall stability must be considered when designing the system, whereas with the FIR filter, stability issues do not need to be considered and it can be used directly. Nevertheless, the above fractional-order repetitive control using the FIR filter is CRC-based.

Therefore, this paper proposes a frequency adaptive improved RC (FA-IRC), to enhance the performance of a grid-tied inverter at grid frequency fluctuations. The control strategy is based on a novel improved repetitive control. The proposed IRC effectively increases the RC gain and resonance bandwidth at frequencies of interest, by introducing a positive proportional gain and a modified internal model filter repetitive controller, which speeds up the dynamic response time. Moreover, to further improve the frequency adaptation capability, the Lagrange interpolating-polynomial-based FIR filter is used to approximate the fractional part of the order of the IRC. Therefore, the proposed FA-IRC not only offers better dynamic performance, but also a lower THD when the grid frequency fluctuates.

The remainder of this article is organized as follows. An LCL-type grid-tied inverter system is introduced in Section 2. In Section 3, characteristics of the CRC, the PIMR-RC, and the proposed IRC are demonstrated. In Section 4, the FA-IRC with the FIR filter is established. The realization of fractional delay using an FIR filter is given. Moreover, a stability analysis and characteristic analysis of the FA-IRC system are performed. Section 5

discusses the simulation results that demonstrate the theoretical analysis's validity. Finally, conclusions are drawn in Section 6.

2. Grid-Tied Inverter System Modeling

Grid-tied inverters are widely used in microgrid distributed power generation systems. To prevent excessive harmonics, some filter topologies are proposed for grid-tied inverters. LCL filters have been used in place of L filters, to smooth the injected current with higher attenuation and reduction in size and weight of the components [29,30]. The impedance of the LLCL filter is almost zero at the switching frequency and therefore attenuates harmonic currents around the switching frequency [31]. The LLCL filter configuration simplifies the current control structure into single-loop current control, without extra damping loops. Nevertheless, extra control techniques are required to achieve active harmonic elimination.

Figure 1 shows an LCL-type single-phase grid-tied inverter control system [20]. In fact, the stability of a grid-tied inverter depends on the ratio of the grid impedance to the inverter impedance [32]. The stability of the internal current control loop of the individual inverter itself, in this paper, is related to the inherent LCL-filter resonance peak. To suppress the resonance peak of the LCL filter, a passive damping resistance R_d is employed. In Figure 1, PWM is an acronym for pulse width modulation, which is a commonly used control technique in power electronics, automatic control, and communication fields. It adjusts the width of the control signal's pulse, to control circuits or devices. ZOH stands for zero-order holder, which is a method for converting analog signals to digital signals. The phase-locked loop (PLL) is used to generate a signal whose phase is locked to the phase of the grid voltage at the point of common coupling (PCC). u_{inv} represents the output voltage of the inverter bridge, L_g represents the grid equivalent inductance, i_{ref} represents the tracked reference current, i_g represents the grid current, and u_g represents the grid voltage.

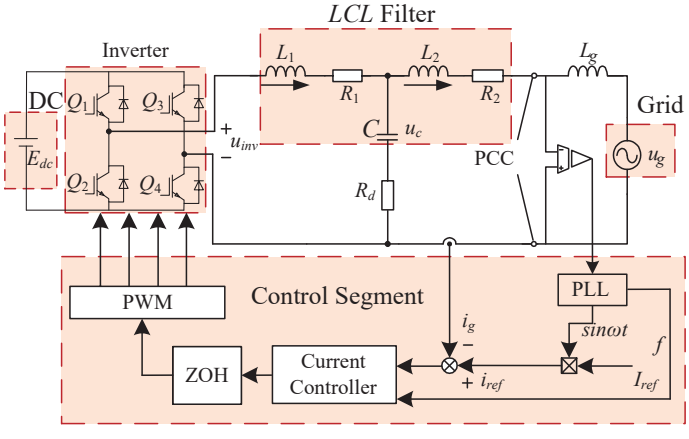

Figure 1. Model structure diagram of a single-phase LCL-type grid-tied inverter.

The equivalent resistance is ignored, and the transfer function from the input voltage u_{inv} to the grid current i_g is

$$G_{LCL}(s) = \frac{1 + R_d C s}{L_1 L_2 C s^3 + (L_1 + L_2) R_d C s^2 + (L_1 + L_2) s}. \quad (1)$$

The plant consists of a combination of inverter switches and the LCL filter, where the gain of the inverter switches is considered to be unity and the phase as zero degrees.

Therefore, the LCL filter is considered as the plant. The system parameters are given in Table 1. According to Table 1 and (1), it can be written in discretization as

$$P(z) = \frac{0.006802z^2 + 0.004736z - 0.002647}{z^3 - 1.991z^2 + 1.472z - 0.4803}. \tag{2}$$

Table 1. System parameters.

Parameters	Symbols	Value	Parameters	Symbols	Value
DC-link voltage	E_{dc}	380 V	L_1 equivalent resistance	R_1	0.48 Ω
Fundamental frequency	f_g	50 Hz	Grid-side inductor	L_2	2.5 mH
Sampling frequency	f_s	10 kHz	L_2 equivalent resistance	R_2	0.32 Ω
Switching frequency	f_{sw}	10 kHz	Output filter capacitance	C	10 μF
Inverter-side inductor	L_1	3 mH	Passive damping resistor	R_d	10 Ω
RMS value of grid voltage	u_g	220 V	Switching dead time	-	3 μs

3. Improved RC

3.1. CRC

The block diagram of CRC is shown in Figure 2, it can be written as:

$$G_{CRC}(z) = \frac{Q(z)z^{-N}}{1 - Q(z)z^{-N}}. \tag{3}$$

where $Q(z)$ and N are terms used in digital signal processing, with $Q(z)$ being an internal filter or a constant, and N representing the number of samples taken per cycle, with respect to the sampling frequency f_s and the grid fundamental frequency f_g. The transfer function of CRC in (3), can be derived as follows in the s-domain [8]:

$$\begin{aligned} G_{CRC}(s) = \frac{Qe^{-sT_0}}{1 - Qe^{-sT_0}} &= -\frac{1}{2} + \frac{1}{T_0 s + T_0\omega_c} + \frac{2}{T_0}\sum_{n=1}^{\infty} \frac{s + \omega_c}{s^2 + 2\omega_c s + \omega_c^2 + \left(\frac{2\pi n}{T_0}\right)^2} \\ &\approx -\frac{1}{2} + \frac{1}{T_0 s + T_0\omega_c} + \frac{2}{T_0}\sum_{n=1}^{\infty} \frac{s}{s^2 + 2\omega_c s + (n\omega_0)^2}, \end{aligned} \tag{4}$$

where $T_0 = 1/f_g = 2\pi/\omega_0$ is the fundamental period of the reference signal, ω_0 is the fundamental angular frequency, ω_c is the resonant bandwidth, and $\omega_c = -\ln Q/T_0$. It is clearly possible to see that the amplitude of $G_{CRC}(z)$ is nearly infinite at angular frequency $n\omega_0$, indicating that CRC can achieve zero steady-state error tracking for periodic signals.

However, it can be seen from Figure 2 and (3), that the internal mode of CRC can be decomposed into a positive feedback link and a delayed link. The former is used to accumulate signal, which acts as an integrator for periodic signals. The latter, however, is used to delay the output of the signal by one cycle, leading to a deteriorating influence on system performance. Moreover, the equivalent negative proportional term in (4), will result in a slow transient response. Hence, a PIMR-RC with CRC combined with a proportional gain, is proposed, in order to address this issue. The block diagram of the PIMR-RC system is shown in Figure 3 [12].

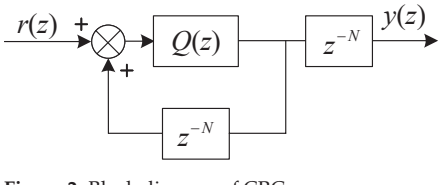

Figure 2. Block diagram of CRC.

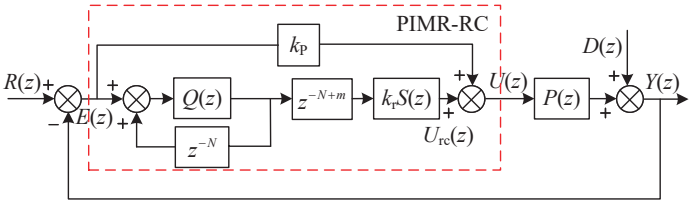

Figure 3. Block diagram of the PIMR-RC system.

In Figure 3, k_r is the CRC gain, k_p is the proportional gain, z^m is the phase-lead compensator for the system delay caused by the plant and controller. $S(z)$ is a low-pass filter that maintains system stability. $P(z)$ is the plant, and $D(z)$ is the disturbance. The transfer function from $Y(z)$ to $R(z)$ can be written as

$$\begin{aligned} G_0(z) &= \frac{\left(k_p + \frac{Q(z)z^{-N}}{1-Q(z)z^{-N}} z^m k_r S(z)\right) P(z)}{1 + \left(\left(k_p + \frac{Q(z)z^{-N}}{1-Q(z)z^{-N}} z^m k_r S(z)\right) P(z)\right)} \\ &= \frac{1 - Q(z)z^{-N}}{1 - Q(z)z^{-N}\left(1 + k_p P(z)\right) + P(z)Q(z)z^{-N} z^m k_r S(z)} \\ &= \frac{1 - Q(z)z^{-N}}{1 - Q(z)z^{-N} + Q(z)z^{-N} z^m k_r S(z) P_0(z)} \\ &\approx 1 - Q(z)z^{-N} \\ &\qquad if \quad z^m k_r S(z) P_0(z) = 1. \end{aligned} \tag{5}$$

When $z^m k_r S(z) P_0(z) = 1$, the symbol of approximate equality in the above equation is valid, which is an advantageous frequency property for the RC design. In (5), $P_0(z) = P(z)/(1 + k_p P(z))$ provides CRC with a new plant [12]. In fact, k_p can make the frequency response of $P_0(z)$ close to 0 dB, and a suitably large enough k_p can produce a larger range of k_r, which can improve the dynamic response.

3.2. The Proposed IRC

The proposed modified RC is shown in Figure 4, and the transfer function can be written as

$$\begin{aligned} G(z) &= \frac{Q(z)\left(2 - Q(z)z^{-N}\right)}{1 - Q(z)(2 - Q(z)z^{-N})z^{-N}} z^{-N} \\ &= \frac{Q_1(z)z^{-N}}{1 - Q_1(z)z^{-N}}, \end{aligned} \tag{6}$$

where $Q_1(z) = Q(z)\left(2 - Q(z)z^{-N}\right)$ is the modified internal model filter.

Figures 5 and 6 show the frequency characteristics of the modified RC and CRC, when $Q(z) = 0.99$. As can be seen, at resonant frequencies, the modified RC has a greater gain than the CRC. Compared to CRC, the modified RC provides nearly twice the gain at 50 Hz and 100 Hz. Meanwhile, the resonant bandwidth of the modified RC is wider than CRC. Therefore, the modified RC has better harmonic rejection performance and the ability to resist frequency shifts.

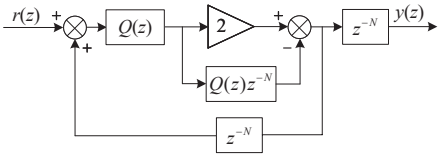

Figure 4. Block diagram of the proposed modified RC.

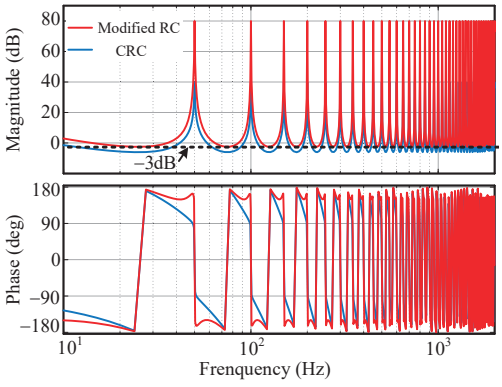

Figure 5. Bode diagram of modified RC and CRC.

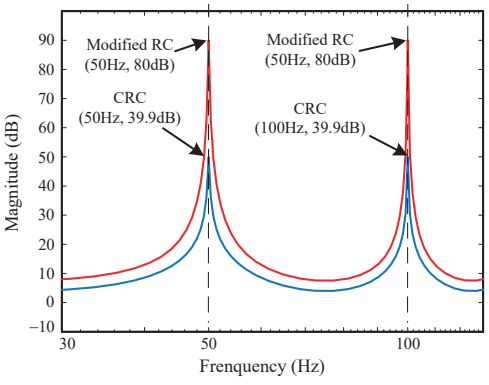

Figure 6. Magnitude response of modified RC and CRC.

In reference to the PIMR-RC, the IRC is comprised of a modified RC and a proportional controller, as shown in Figure 7. The transfer function of the system can be written as [14]

$$\begin{aligned} G_1(z) &= \frac{\left(k_p + \frac{Q_1(z)z^{-N}}{1-Q_1(z)z^{-N}} z^m k_r S(z)\right) P(z)}{1 + \left(\left(k_p + \frac{Q_1(z)z^{-N}}{1-Q_1(z)z^{-N}} z^m k_r S(z)\right) P(z)\right)} \\ &= \frac{1 - Q_1(z)z^{-N}}{1 - Q_1(z)z^{-N}\left(1 + k_p P(z)\right) + P(z)Q_1(z)z^{-N}z^m k_r S(z)} \\ &= \frac{1 - Q_1(z)z^{-N}}{1 - Q_1(z)z^{-N} + Q_1(z)z^{-N}z^m k_r S(z)P_0(z)} \\ &\approx 1 - Q_1(z)z^{-N} = G_0(z)^2 \\ &\quad if \quad z^m k_r S(z) P_0(z) = 1, \end{aligned} \tag{7}$$

where $P_0(z) = P(z)/(1 + k_p P(z))$. By comparing (5) and (7), it is clear that G_1 is the square of the function G_0 in (5), so the amplitude of IRC with the modified $Q(z)$ filter structure, changes significantly. In fact, higher gain means a better harmonic rejection performance in this control system. However, the gain of the IRC also drops off severely when the grid fluctuates. Therefore, we need to ensure that its resonant frequency follows the grid frequency.

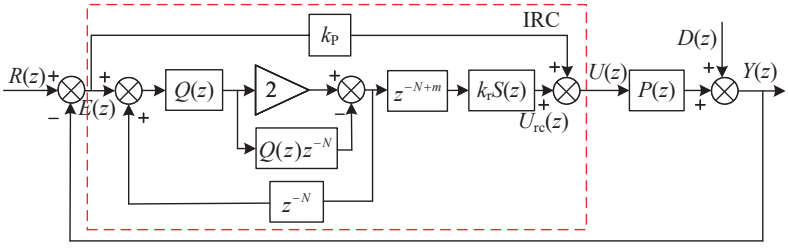

Figure 7. Block diagram of the proposed IRC system.

4. The Proposed Frequency Adaptive IRC

The grid frequency in the distributed power generation system may fluctuate [33], and $N = f_s/f_0$ may be a fraction. The values of N at different grid frequencies, when f_s = 10 kHz, are shown in Table 2.

Table 2. The corresponding RC delay, N, when the grid frequency changes.

Frequency (Hz)	49.5	49.6	49.7	49.8	49.9	50	50.1	50.2	50.3	50.4	50.5
N	202	201.6	201.2	200.8	200.4	200	199.6	199.2	198.8	198.4	198

In this case, it is possible to divide N into an integer N_i and a fraction D, as follows

$$z^{-N} = z^{-N_i} \times z^{-D}, N = N_i + D. \tag{8}$$

4.1. Fractional Delay FIR Filter

The FIR filter approximates the fractional delay, using the following expression [34]

$$z^{-D} \approx H(z) = \sum_{n=0}^{M} h(n) z^{-n}, \tag{9}$$

where M represents the filter order and $h(n)$ represents the polynomial coefficient.

The coefficient $h(n)$, can be determined by the Lagrangian interpolation method, and is calculated as follows [34]

$$h(n) = \prod_{k=0, k\neq n}^{M} \frac{D-k}{n-k}, n = 0, 1, 2, \ldots, M. \tag{10}$$

Coefficients for the Lagrange FD filter, with orders M = 1, 2, and 3, are given in Table 3 [35].

Table 3. Coefficients of the Lagrange FD filter.

	$M = 1$	$M = 2$	$M = 3$
$h(0)$	$1 - D$	$(D-1)(D-2)/2$	$-(D-1)(D-2)(D-3)/6$
$h(1)$	D	$-D(D-2)$	$D(D-2)(D-3)/2$
$h(2)$		$D(D-1)/2$	$-D(D-1)(D-3)/2$
$h(3)$			$D(D-1)(D-2)/6$

The best interpolation is achieved, when the interpolation point D, is close to the center of the sampled data, namely $D \approx M/2$. In addition, a larger M can achieve higher accuracy, but the computational effort becomes larger. In this article, a third-order FIR filter is used. For example, when f_s = 10 kHz, if f_0 changes to 49.6 Hz, then N = 201.6, $z^{-201.6}$ can be expressed as $z^{-200}z^{-1.6}$. According to Table 3,

$$z^{-1.6} = h(0)z^0 + h(1)z^{-1} + h(2)z^{-2} + h(3)z^{-3} = -0.056 + 0.448z^{-1} + 0.672z^{-2} - 0.064z^{-3}, \tag{11}$$

and

$$z^{-201.6} = z^{-201} \times (-0.056 + 0.448z^{-1} + 0.672z^{-2} - 0.064z^{-3}). \tag{12}$$

To obtain a high accuracy, the value of D is selected to be between 1.2 and 1.8 when the grid frequency varies. The frequency responses of FD filters based on Lagrangian interpolation, are shown in Figure 8 for different fractions of D, from 1.2 to 1.8, with order $M = 3$. The magnitude response of the FIR filter is close to one within the passband of the FD filter, which makes it possible to design repetitive controllers without considering the effect of the FIR on the system's amplitude and frequency performance. In addition, its high frequency attenuation is more conducive to system stability. More importantly, the coefficients in the FD filter consume relatively little computational effort, so it is relatively simple to use Lagrangian interpolation to create an FD filter [36].

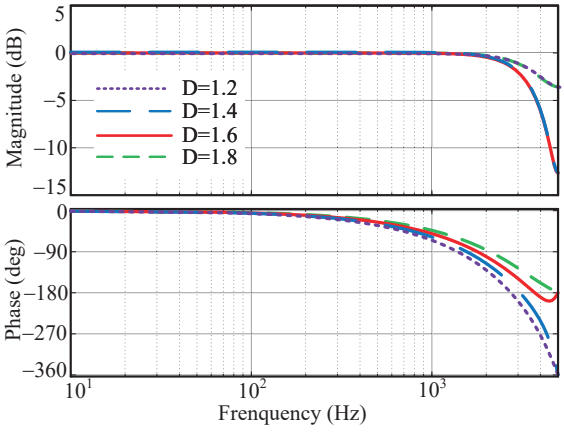

Figure 8. Frequency responses of Lagrange-interpolation-based FD filters.

4.2. Stability Analysis of FA-IRC System

The structure diagram of the FA-IRC-based inverter control system is shown in Figure 9, where $z^{-N} = z^{-N_i} \times z^{-D}$ is the delay unit of FA-IRC. z^{-D} is the fractional delay based on the FIR filter. The transfer function from i_{ref} and u_g to $E(z)$ is

$$E(z) = \frac{i_{ref}(z) - u_g(z)}{1 + G_{FO-IRC}P(z)}, \tag{13}$$

where

$$\begin{aligned} G_{FA\text{-}IRC} &= k_p + \frac{Q_1(z)z^{-N}}{1 - Q_1(z)z^{-N}} z^m k_r S(z) \\ &= k_p + G_2(z). \end{aligned} \tag{14}$$

From (13) and (14), this system has the following characteristic polynomial:

$$1 + [G_2(z) + k_p]P(z) = [1 + k_p P(z)][1 + G_2(z)P_0(z)]. \tag{15}$$

Thus, there are two stability conditions for the FA-IRC system:

(1) The roots of $1 + k_p P(z) = 0$ within the unit circle.
(2) $1 + G_2(z)P_0(z) \neq 0$.

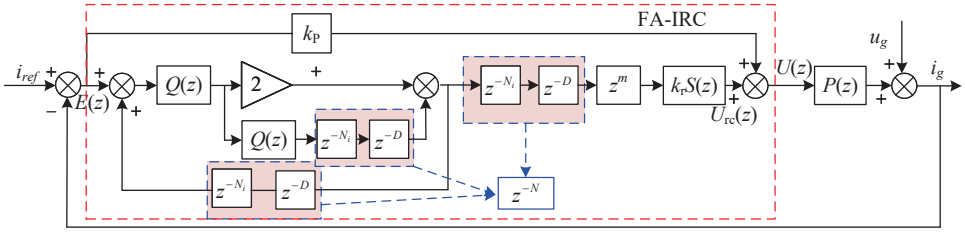

Figure 9. Block diagram of the FA-IRC system.

Obviously, the stability condition (1) is only related to the scale factor k_p, and is therefore easier to satisfy. It means that the pole of $P_0(z)$ should lie within the unit circle. Figure 10 shows the distribution of the dominant poles of $P_0(z)$ with different k_p. As can be seen, the stability condition (1) is satisfied when k_p changes from 6 to 30.

Substitute (14) into condition (2),

$$\begin{aligned} |1 - Q_1(z)z^{-N} + Q_1(z)z^{-N}z^m k_r S(z)P_0(z))| \neq 0, \\ \forall z = e^{j\omega T}, 0 < \omega < \frac{\pi}{T}, \end{aligned} \tag{16}$$

Expression (16) can be guaranteed if [12]

$$\begin{aligned} |Q_1(z)z^{-N}(1 - z^m k_r S(z)P_0(z))| < 1, \\ \forall z = e^{j\omega T}, 0 < \omega < \frac{\pi}{T}. \end{aligned} \tag{17}$$

If the frequency of reference signal i_{ref} and disturbance u_g approach $\omega_l = 2\pi l/N$, with $l = 0, 1, 2, \ldots, L$ ($L = N/2$ for even N and $L = (N-1)/2$ for odd N), then $z^N = 1$ [22]. Then, we have

$$|Q_1(z)(1 - z^m k_r S(z)P_0(z))| < 1, z = e^{j\omega T}. \tag{18}$$

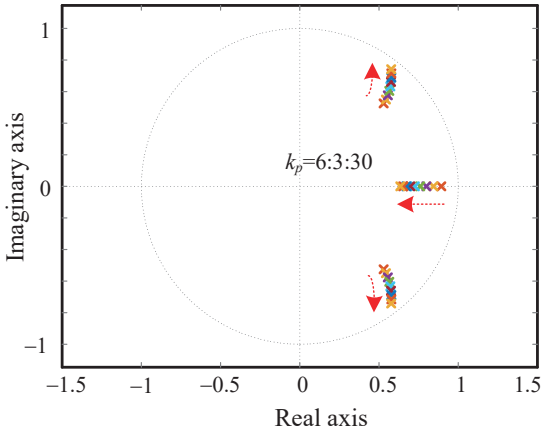

Figure 10. Distribution of the dominant poles of P_0(z) with different k_p.

The Bode diagram of $Q_1(z)$ with $Q(z) = 0.99$ and $Q(z) = 0.25z + 0.5 + 0.25z^{-1}$, is shown in Figure 11. It is obvious that the magnitude characteristic of $Q_1(z)$ is greater than 0, then (18) can be written as

$$|(1 - z^m k_r S(z)P_0(z))| < \frac{1}{Q_1(z)}, z = e^{j\omega T}. \tag{19}$$

Let $N_s(\omega)$, $N_{P_0}(\omega)$, and $N_{Q_1}(\omega)$ represent the magnitude characteristics of $S(z)$, $P_0(z)$, and $Q_1(z)$, respectively, and $\theta_s(\omega)$, $\theta_{p_0}(\omega)$, and $\theta_{Q_1}(\omega)$ represent their phase characteristics. They can be written as follows

$$\begin{aligned} P_0\left(e^{j\omega T_s}\right) &= N_{P_0}\left(e^{j\omega T_s}\right)\exp\left[j\theta_{P_0}\left(e^{j\omega T_s}\right)\right], \\ S\left(e^{j\omega T_s}\right) &= N_s\left(e^{j\omega T_s}\right)\exp\left[j\theta_s\left(e^{j\omega T_s}\right)\right], \\ Q_1(z)\left(e^{j\omega T_s}\right) &= N_{Q_1}\left(e^{j\omega T_s}\right)\exp\left[j\theta_{Q_1}\left(e^{j\omega T_s}\right)\right]. \end{aligned} \tag{20}$$

Then, (20) can be written as

$$\begin{aligned} &\left|1 - k_r N_S\left(e^{j\omega}\right) N_{P_0}\left(e^{j\omega}\right) e^{-j\left[\theta_S\left(e^{j\omega}\right)+\theta_{P_0}\left(e^{j\omega}\right)+m\omega\right]}\right| \\ &\qquad < \frac{1}{N_{Q_1}\left(e^{j\omega}\right) e^{-j\theta_{Q_1}\left(e^{j\omega}\right)}}. \end{aligned} \tag{21}$$

According to Euler's formula, since $k_r > 0$, $N_s(\omega)$, $N_{P_0}(\omega)$, and $N_{Q_1}(\omega)$ are also greater than 0. In order to maintain stability, the following conditions must be met

$$\left|\theta_s(\omega) + \theta_{p_0}(\omega) + m\omega T_s - \theta_{Q_1}(\omega)\right| < 90^\circ, \tag{22}$$

$$0 < k_r < \min \frac{2\cos\left[\theta_s(\omega) + \theta_{p_0}(\omega) + m\omega T_s - \theta_{Q_1}(\omega)\right]}{N_{Q_1}(\omega) N_s(\omega) N_{p_0}(\omega)}. \tag{23}$$

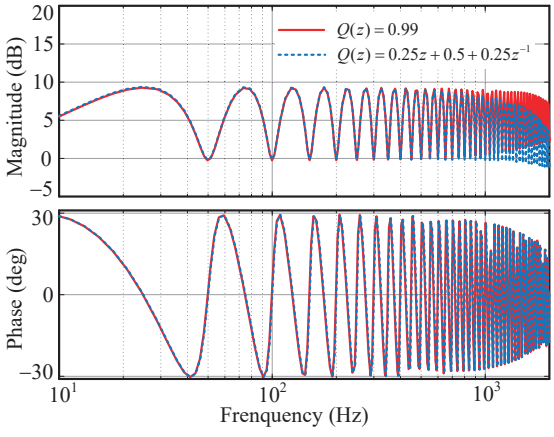

Figure 11. Bode diagram of $Q_1(z)$ with $Q(z) = 0.99$, and $Q(z) = 0.25z + 0.5 + 0.25z^{-1}$.

4.3. Characteristic Analysis

The Bode diagrams of the IRC and the FA-IRC under different N are shown in Figure 12. These show that, as the frequency increases, the deviation of the resonant frequency of the ideal IRC from the actual grid frequency and harmonic frequency, becomes larger. As a result, the reference signal tracking and harmonic rejection performance of the IRC degrades when the grid frequency fluctuates. Figure 13 describes the magnitude response around the fundamental frequency. It indicates that the amplitude of IRC is 79.8 dB at 50 Hz, whereas the amplitude of IRC decreases to 52 dB at 49.6 Hz and 50.4 Hz. While the FA-IRC's resonant frequency can follow the actual frequency of the grid, it still has a large gain at 49.6 Hz and 50.4 Hz. This means that the FA-IRC can effectively eliminate harmonics when the grid frequency varies.

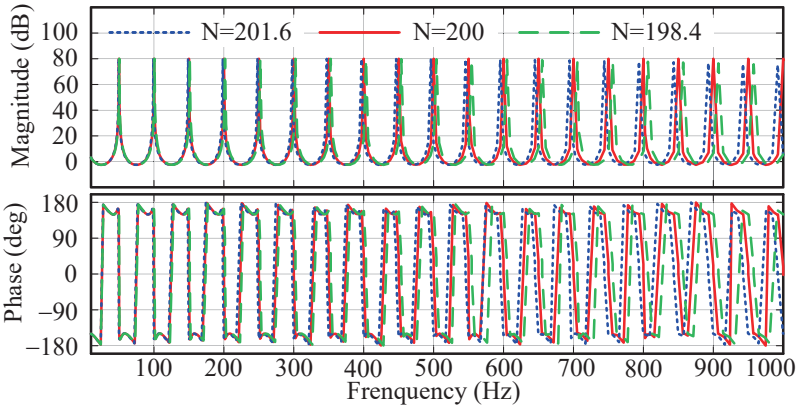

Figure 12. Bode diagrams of IRC (N = 200) and FA-IRC (N = 198.4 and 201.6).

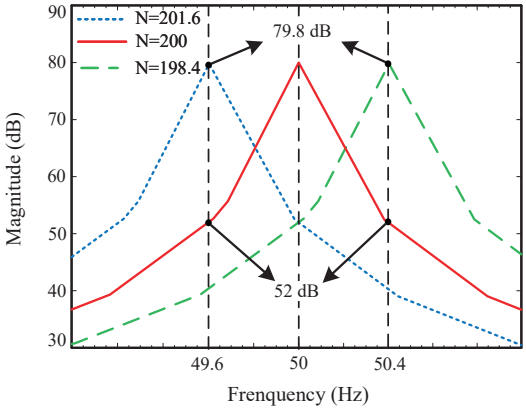

Figure 13. Magnitude characteristics of IRC (N = 200) and FA-IRC (N = 198.4 and 201.6) at the fundamental frequency.

5. Simulation Verification

In order to verify the performance of the proposed FA-IRC, a single-phase inverter control system based on this method was built using MATLAB/Simulink. The parameters of this system are shown in Table 1. According to [12] and the analysis above, the parameters of FA-IRC were selected as follows: k_p = 18, k_r = 5, m = 8, $Q(z) = 0.25z + 0.5 + 0.25z^{-1}$, and the fourth-order Butterworth low-pass filter $S(z)$, with cutoff frequency 1 kHz, is as follows

$$S(z) = \frac{0.028z^4 + 0.053z^3 + 0.071z^2 + 0.053z + 0.028}{z^4 - 2.206z^3 + 2.148z^2 - 1.159z + 0.279}. \quad (24)$$

For verifying the current tracking performance and the dynamic performance of the proposed FA-IRC, experimental results are compared with the CRC plus a proportional controller system (PIMR-RC system). In the PIMR-RC system, all control parameters remain fixed.

5.1. Steady State Response

The steady-state response is examined under a reference current of 20 A amplitude. When f_g is 50 Hz, the simulation results of the injected current i_g, and grid voltage u_g, under PIMR-RC are shown in Figure 14. The THD value of i_g is 0.60%. In addition, the THD

value of FA-IRC is 0.67% when f_g is 50 Hz, as can be obtained from Figure 15. Clearly, both control systems are effective in suppressing harmonics when f_g is 50 Hz.

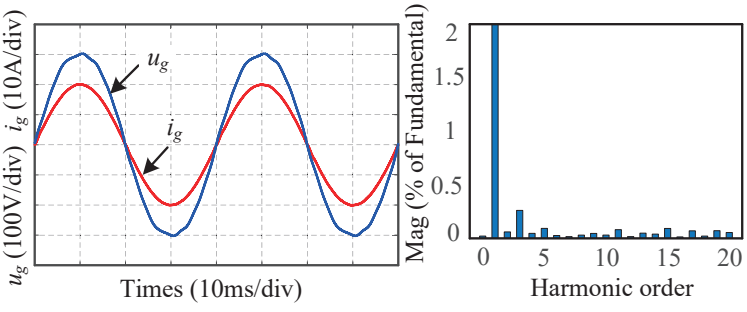

Figure 14. Output waveforms of the PIMR-RC system and spectrum analysis of the output current when f_g = 50 Hz.

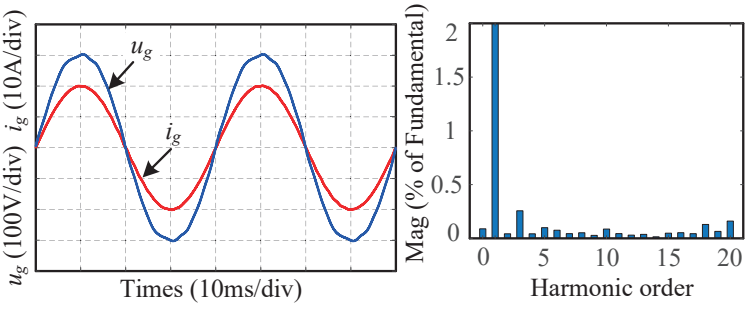

Figure 15. Output waveforms of the FA-IRC system and spectrum analysis of the output current when f_g = 50 Hz.

When f_g is set at 49.6 Hz, PIMR-RC still takes the order of RC as 200, and the THD of i_g increases to 1.70%, as shown in Figure 16. However, the THD value of i_g under FA-IRC is 0.59%, as shown in Figure 17. The reason why this is the case, is that the resonant frequencies of FA-IRC are very close to the actual grid frequency and harmonic frequencies. Figures 18 and 19 show similar results, to demonstrate the effectiveness of FA-IRC when the grid frequency is set at 50.4 Hz. The figures indicate that the THD of i_g, with FA-IRC based on the FIR filter, is 0.70%, while it is 1.73% for i_g with IRC.

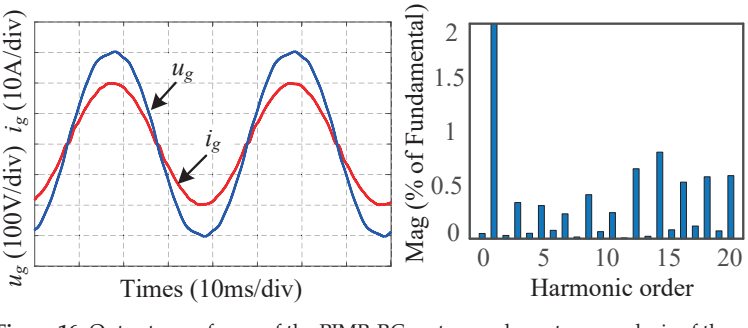

Figure 16. Output waveforms of the PIMR-RC system and spectrum analysis of the output current when f_g = 49.6 Hz.

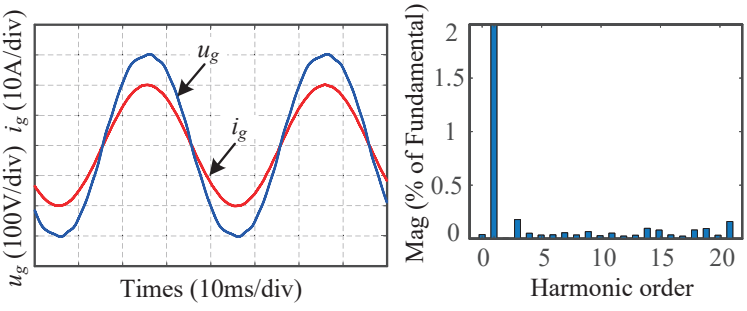

Figure 17. Output waveforms of the FA-IRC system and spectrum analysis of the output current when f_g = 49.6 Hz.

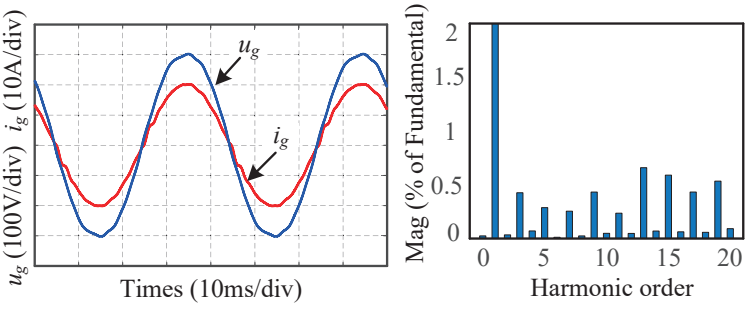

Figure 18. Output waveforms of the PIMR-RC system and spectrum analysis of the output current when f_g = 50.4 Hz.

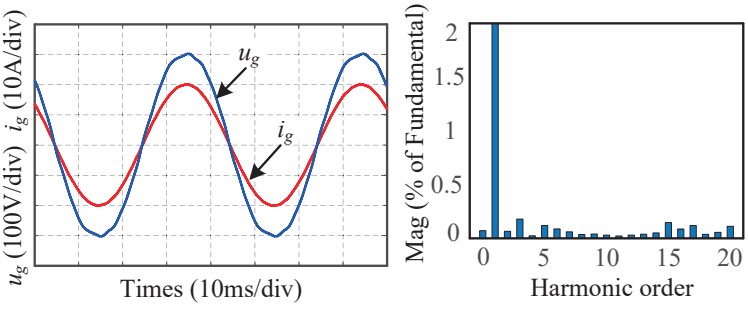

Figure 19. Output waveforms of the FA-IRC system and spectrum analysis of the output current when f_g = 50.4 Hz.

In fact, the use of Thiran-based IIR fractional delay filter during grid frequency fluctuations has been proposed in many studies of frequency adaptation [20,28]. In order to validate the frequency adaptation of the proposed scheme, a frequency adaptive IRC, based on a second-order IIR filter, has been built. In addition, to verify the harmonic rejection capability of the RC, a quasi-proportional resonant (QPR) control system is added for comparison [37]. The parameters are selected as follows: $k_p = 8$, $k_r = 4$, and $\omega_c = 5$ rad/s. The THD results of different control systems at different grid frequencies are summarized in Table 4. Table 4 indicates that the QPR control system is not affected by frequency variations, however, it has a higher THD compared to the RC based control system. In addition, it shows that the CRC and IRC systems are impacted by frequency changes to some extent. However, the proposed FA-IRC, and frequency adaptive IRC based on the IIR filter, maintain low THD values, due to their frequency adaptability.

Table 4. THD results of different control systems under various fundamental frequencies.

Fundamental Frequency (Hz)	THD Results of Different Control Systems (%)				
f_g	QPR	CRC	IRC	IRC with IIR	Proposed FA-IRC
49.6	4.19	1.70	2.36	0.62	0.59
49.7	4.19	1.52	1.51	0.67	0.66
49.8	3.97	1.22	0.99	0.72	0.59
49.9	3.96	0.80	0.75	0.67	0.68
50	3.91	0.60	0.67	0.67	0.67
50.1	3.98	0.91	0.84	0.64	0.67
50.2	3.87	1.43	1.59	0.64	0.66
50.3	3.80	1.69	2.17	0.68	0.61
50.4	3.93	1.73	2.40	0.62	0.70

5.2. Transient Response

To verify the dynamic performance of the proposed FA-IRC, the transient response of reference current amplitude changes is illustrated. Figures 20 and 21 give the transient waveforms and current error when the amplitude of i_{ref} drops from 20 A to 10 A, at different frequencies. The FA-IRC system can reach stability within 80 ms. Compared to the PIMR-RC system, the convergence rate of the FA-IRC system, with the same large gain, is equally fast. Furthermore, the current error of the FA-IRC system is approximately 0.04 A at grid frequencies of 49.6 Hz and 50.4 Hz, however, the current error of the PIMR-RC system is 0.2 A. Therefore, the proposed method can achieve good current tracking performance and dynamic performance when the grid frequency changes.

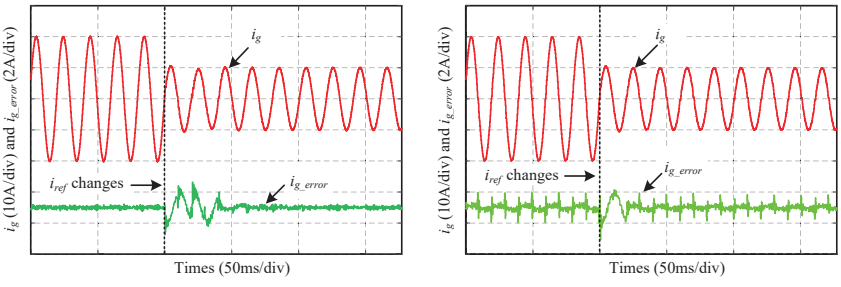

Figure 20. Transient waveforms and current errors of different control systems when reference current changes, with grid frequency $f_g = 49.6$ Hz. (**a**) FA-IRC system. (**b**) PIMR-RC system.

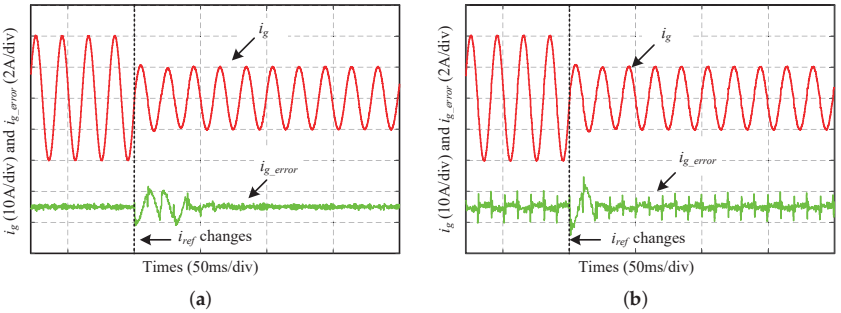

Figure 21. Transient waveforms and current errors of different control systems when reference current changes, with grid frequency $f_g = 50.4$ Hz. (**a**) FA-IRC system. (**b**) PIMR-RC system.

6. Conclusions

This paper proposes an FA-IRC with a fixed sampling rate, to reject the harmonic components in the injected current of grid-tied inverters when grid frequency varies. The control strategy is based on a novel improved repetitive control. The improved repetitive control, with a modified internal model $Q(z)$ filter and a positive proportional gain, has a higher gain and bandwidth at resonant frequencies. Therefore, it has good dynamic performance. Moreover, to achieve frequency adaptive capability, a fractional-order delay, based on a polynomial Lagrange interpolating FIR filter, is built into the system. The FA-IRC system can output high quality current when the grid fundamental frequency varies within ± 0.4 Hz, because it makes the resonant frequency of the IRC approximate the actual grid frequency and harmonic frequency. Simulation results demonstrate that the FA-IRC is effective at resisting variations in grid frequency.

It is worth mentioning that, for the control methods of the grid-tied inverters considered in this paper, grid voltage magnitude fluctuations and grid impedance variations, which are common in distributed generation systems, are not taken into account. The impedance analysis method is an important tool for the stability of grid-tied inverter–grid interaction systems. It conveniently implements the modeling of the frequency characteristics of the grid-tied inverter system, and effectively simplifies the complexity of the grid-tied inverter system impedance stability analysis during grid changes. In addition, the inverter–grid system can be kept stable with reasonable grid voltage feedforward values. These cases should be considered in future work.

Author Contributions: Conceptualization, H.Z. and Q.Z.; methodology, H.Z.; investigation, H.Z., Q.Z., S.W. and X.Y.; writing—original draft preparation, H.Z.; writing—review and editing, H.Z., Q.Z., S.W. and X.Y.; supervision, H.Z. All authors have read and agreed to the published version of the manuscript.

Funding: This work was supported in part by the National Natural Science Foundation of China, under grant 61973157 and 62073297, in part by the Natural Science Foundation of Henan Province, under grant 232300421239, in part by the Science and Technology Innovation Team of Colleges and Universities in Henan Province, under grant 22IRTSTHN015, and in part by the Incubation Program for Young Master Supervisor of Zhongyuan University of Technology, under grant D202213.

Data Availability Statement: All data generated or analysed during this study are included in this published article.

Conflicts of Interest: The authors declare no conflict of interest.

Abbreviations

The following abbreviations are used in this manuscript:

IRC	Improved repetitive control
RC	Repetitive control
CRC	Conventional repetitive control
HORC	Higher-order repetitive control
FA-IRC	Frequency adaptive improved repetitive control
FD	Fractional delay
FIR	Finite impulse response
IIR	Infinite impulse response
PIMR-RC	Proportional integral multi resonant-type repetitive control
IMP	Internal model principle
THD	Total harmonic distortion
PWM	Pulse width modulation
ZOH	Zero-order holder
PLL	Phase-locked loop
PCC	Point of common coupling
QPR	Quasi-proportional resonant

References

1. Abdullah, M.A.; Muttaqi, K.M.; Agalgaonkar, A.P. Sustainable energy system design with distributed renewable resources considering economic, environmental and uncertainty aspects. *Renew. Energy* **2015**, *78*, 165–172. [CrossRef]
2. Seifi, K.; Moallem, M. Synchronization and control of a single-phase grid-tied inverter under harmonic distortion. *Electronics* **2023**, *12*, 860. [CrossRef]
3. Yang, Y.; Zhou, K.; Blaabjerg, F. Current harmonics from single-phase grid-connected inverters—Examination and suppression. *IEEE J. Emerg. Sel. Top. Power Electron.* **2015**, *4*, 221–233. [CrossRef]
4. Lunardi, A.; Conde, E.; Assis, J.; Meegahapola, L. Repetitive predictive control for current control of grid-connected inverter under distorted voltage conditions. *IEEE Access* **2022**, *10*, 16931–16941. [CrossRef]
5. Peng, F.; Xie, W.; Yan, J. State feedback and deadbeat predictive repetitive control of three-phase Z-source inverter. *Electronics* **2023**, *12*, 1005. [CrossRef]
6. Ramos, G.A.; Costa-Castelló, R. Comparison of different repetitive control architectures: Synthesis and comparison. application to VSI converters. *Electronics* **2018**, *7*, 446. [CrossRef]
7. Jiang, S.; Cao, D.; Li, Y.; Liu, J.; Peng, F.Z. Low-THD, fast-transient, and cost-effective synchronous-frame repetitive controller for three-phase UPS inverters. *IEEE Trans. Power Electron.* **2012**, *27*, 2994–3005. [CrossRef]
8. Yang, Y.; Zhou, K.; Cheng, M.; Zhang, B. Phase compensation multiresonant control of CVCF PWM converters. *IEEE Trans. Power Electron.* **2012**, *28*, 3923–3930. [CrossRef]
9. Zhao, Q.; Ye, Y. Fractional phase lead compensation RC for an inverter: Analysis, design, and verification. *IEEE Trans. Ind. Electron.* **2016**, *64*, 3127–3136. [CrossRef]
10. Chen, S.; Zhao, Q.; Ye, Y.; Qu, B. Using IIR filter in fractional order phase lead compensation PIMR-RC for grid-tied inverters. *IEEE Trans. Ind. Electron.* 2022, *in press*. [CrossRef]
11. Wang, Y.; Darwish, A.; Holliday, D.; Williams, B.W. Plug-in repetitive control strategy for high-order wide-output range impedance-source converters. *IEEE Trans. Power Electron.* **2016**, *32*, 6510–6522. [CrossRef]
12. Zhao, Q.; Ye, Y. A PIMR-type repetitive control for a grid-tied inverter: Structure, analysis, and design. *IEEE Trans. Power Electron.* **2017**, *33*, 2730–2739. [CrossRef]
13. Kim, B.S.; Tsao, T.C. Robust repetitive controller design with improved performance. In Proceedings of the 2001 American Control Conference, Arlington, VA, USA, 25–27 June 2001; pp. 2027–2032.
14. Pandove, G.; Singh, M. Robust repetitive control design for a three-phase four wire shunt active power filter. *IEEE Trans. Ind. Informat.* **2018**, *15*, 2810–2818. [CrossRef]
15. Kurniawan, E.; Cao, Z.; Man, Z. Design of robust repetitive control with time-varying sampling periods. *IEEE Trans. Ind. Electron.* **2014**, *61*, 2834–2841. [CrossRef]
16. Kolluri, S.; Gorla, N.B.Y.; Sapkota, R.; Panda, S.K. A new control architecture with spatial comb filter and spatial repetitive controller for circulating current harmonics elimination in a droop-regulated modular multilevel converter for wind farm application. *IEEE Trans. Power Electron.* **2019**, *34*, 10509–10523. [CrossRef]
17. Song, Y.; Nian, H. Sinusoidal output current implementation of DFIG using repetitive control under a generalized harmonic power grid with frequency deviation. *IEEE Trans. Power Electron.* **2015**, *30*, 6751–6762. [CrossRef]
18. Zhu, M.; Ye, Y.; Xiong, Y.; Zhao, Q. Multibandwidth repetitive control resisting frequency variation in grid-tied inverters. *IEEE J. Emerg. Sel. Top. Power Electron.* **2021**, *10*, 446–454. [CrossRef]
19. Lu, W.; Wang, W.; Zhou, K.; Fan, Q. General high-order selective harmonic repetitive control for PWM converters. *IEEE J. Emerg. Sel. Top. Power Electron.* **2022**, *10*, 1178–1191. [CrossRef]
20. Zhao, Q.; Zhang, H.; Gao, Y.; Chen, S.; Wang, Y. Novel fractional-order repetitive controller based on Thiran IIR filter for grid-connected inverters. *IEEE Access* **2022**, *10*, 82015–82024. [CrossRef]
21. Escobar, G.; Hernandez-Gomez, M.; Valdez-Fernandez, A.A.; Lopez-Sanchez, M.J.; Catzin-Contreras, G.A. Implementation of a $6n \pm 1$ repetitive controller subject to fractional delays. *IEEE Trans. Ind. Electron.* **2015**, *62*, 444–452. [CrossRef]
22. Yang, Y.; Zhou, K.; Wang, H.; Blaabjerg, F.; Wang, D.; Zhang, B. Frequency adaptive selective harmonic control for grid-connected inverters. *IEEE Trans. Power Electron.* **2015**, *30*, 3912–3924. [CrossRef]
23. Zhao, Q.; Chen, S.; Wen, S.; Qu, B.; Ye, Y. A frequency adaptive PIMR-type repetitive control for a grid-tied inverter. *IEEE Access* **2018**, *6*, 65418–65428. [CrossRef]
24. Jamil, M.; Waris, A.; Gilani, S.O.; Khawaja, B.A.; Khan, M.N.; Raza, A. Design of robust higher-order repetitive controller using phase lead compensator. *IEEE Access* **2020**, *8*, 30603–30614. [CrossRef]
25. Chen, Y.; Zhou, K.; Tang, C.; Shu, Y.; Yang, Y. Fractional-order multiperiodic odd-harmonic repetitive control of programmable AC power sources. *IEEE Trans. Power Electron.* **2022**, *37*, 7751–7758. [CrossRef]
26. Chen, D.; Zhang, J.; Qian, Z. An Improved repetitive control scheme for grid-connected inverter with frequency-adaptive capability. *IEEE Trans. Ind. Electron.* **2013**, *60*, 814–823. [CrossRef]
27. Zou, Z.X.; Zhou, K.; Wang, Z.; Cheng, M. Frequency-adaptive fractional-order repetitive control of shunt active power filters. *IEEE Trans. Ind. Electron.* **2015**, *62*, 1659–1668. [CrossRef]
28. Ye, J.; Liu, L.; Xu, J.; Shen, A. Frequency adaptive proportional-repetitive control for grid-connected inverters. *IEEE Trans. Ind. Electron.* **2021**, *68*, 7965–7974. [CrossRef]

29. Jalili, K.; Bernet, S. Design of LCL filters of active-front-end two-level voltage-source converters. *IEEE Trans. Ind. Electron.* **2009**, *56*, 1674–1689. [CrossRef]
30. Zhang, Z.; Ding, W. Improved active disturbance rejection control strategy for LCL-type grid-connected inverters based on the backstepping method. *Electronics* **2022**, *11*, 2237. [CrossRef]
31. Wang, X.; Zhuang, R.; Cai, J. Theoretical analysis of a fractional-order LLCL filter for grid-tied inverters. *Fractal Fract.* **2023**, *7*, 135. [CrossRef]
32. Cespedes, M.; Sun, J. Adaptive Control of Grid-Connected Inverters Based on Online Grid Impedance Measurements. *IEEE Trans. Sustain. Energy* **2014**, *5*, 516–523. [CrossRef]
33. *IEEE Standard 1547.2-2008*; IEEE Application Guide for IEEE Std 1547, IEEE Standard for Interconnecting Distributed Resources with Electric Power Systems. IEEE: New York, NY, USA, 2009.
34. Laakso, T.I.; Valimaki, V.; Karjalainen, M.; Laine, U.K. Splitting the unit delay [FIR/all pass filters design]. *IEEE Signal Process. Mag.* **1996**, *13*, 1996. [CrossRef]
35. Xie, C.; Zhao, X.; Savaghebi, M.; Meng, L.; Guerrero, J.M.; Vasquez, J.C. Multirate fractional-order repetitive control of shunt active power filter suitable for microgrid applications. *IEEE J. Emerg. Sel. Top. Power Electron.* **2017**, *5*, 809–819. [CrossRef]
36. Kwan, H.K.; Jiang, A. FIR, allpass, and IIR variable fractional delay digital filter design. *IEEE Trans. Circuits Syst. I Reg. Pap.* **2009**, *56*, 2064–2074. [CrossRef]
37. Zmood, D.N.; Holmes, D.G. Stationary frame current regulation of PWM inverters with zero steady-state error. *IEEE Trans. Circuits Syst. I Reg. Pap.* **2003**, *18*, 814–822. [CrossRef]

processes

MDPI

Article

Circuit Breaker Fault Diagnosis Method Based on Coil Current Time Sequence Phase Trajectory Characteristics

Yaqi Chen [1], Qiong Li [1,*], Yang Zou [2], Guohua Long [2], Nianping Yan [2] and Ruixiang Fan [2]

[1] School of Information Engineering, Nanchang Hangkong University, Nanchang 330063, China; 2104086100005@stu.nchu.edu.cn
[2] Institute of Electric Power Research, State Grid Jiangxi Electric Power Company, Nanchang 330096, China; dky_zhouy@jx.sgcc.com.cn (Y.Z.)
* Correspondence: powerdsp339@163.com

Abstract: The traditional circuit breaker fault diagnosis method suffers from insufficient feature information extraction and is easily affected by abnormal signal acquisition. To address this, this paper introduces the phase space reconstruction algorithm to reconstruct the current signal for fault diagnosis based on phase trajectory features. The proposed method uses a first-order forward differencing method and mutual information method to process abnormal data and select the parameters of the reconstruction, then extract overall and local inflection point features to construct a fault feature set. The support vector machine algorithm-based model is trained and tested using actual samples, and the results show that the proposed method can adaptively sample anomalous signals, exhibit strong robustness, and significantly improve the accuracy of fault classification.

Keywords: circuit breaker; breaking coil current signal; phase space reconstruction; first-order forward differencing; phase trajectory

Citation: Chen, Y.; Li, Q.; Zou, Y.; Long, G.; Yan, N.; Fan, R. Circuit Breaker Fault Diagnosis Method Based on Coil Current Time Sequence Phase Trajectory Characteristics. *Processes* **2023**, *11*, 1241. https://doi.org/10.3390/pr11041241

Academic Editor: Hsin-Jang Shieh

Received: 13 March 2023
Revised: 11 April 2023
Accepted: 14 April 2023
Published: 17 April 2023

1. Introduction

The circuit breaker is a critical device that plays a vital role in controlling and protecting the power system. During its operation, the current timing signal of the breaking coil reflects the operating characteristics of the electromagnetic coil and contains rich information about the operating mechanism, thus characterizing the operating status of the circuit breaker operating mechanism [1,2], extracting the relevant characteristics of the current signal and analyzing and judging it can timely evaluate the operating status of the circuit breaker operating structure and accurately identify the type of fault, providing a technical basis for realizing condition maintenance and improving the stability and reliability of the power system [3,4].

The effectiveness of fault feature extraction for the circuit breaker is critical to the performance of the fault classification model. At present, scholars at home and abroad have conducted a lot of research on the fault feature extraction of high-voltage circuit breaker coil current signals, mainly focusing on signal time-frequency domain analysis. In Reference [5], a time-domain model based on spline interpolation combined with multiscale linear fitting was used to extract features from circuit breaker breaking coil currents, which provided a basis for subsequent circuit breaker fault state analysis. References [6,7] optimized the extraction of multiple feature vectors in the coil current time domain by principal component analysis and relief optimization methods to achieve accurate fault state assessment and improve the diagnosis efficiency. Reference [8] proposed the use of ensemble empirical modal decomposition and wavelet analysis to filter the current signal, combined with the time-domain polarization method for waveform feature extraction, which can effectively improve the feature extraction accuracy and fault diagnosis accuracy.

The time-frequency domain methods mentioned above are based on the linear characteristics of the signal system for analysis. Since the coil current signal generated by

the circuit breaker has nonlinear and non-smooth characteristics, only partial and limited information can be obtained from the perspective of this single variable with low accuracy, so the above linear analysis methods have their limitations, and it is difficult to accurately portray the nonlinear characteristics of the coil current signal. Therefore, for the single-variable time series of the circuit breaker coil current signal, another method needs to be introduced that can obtain more information from the high-dimensional space containing dynamic changes.

Currently, the technical method of extracting characteristic parameters in chaotic systems for evaluation and analysis of time-varying nonlinear and nonstationary systems is gaining more and more attention from scholars and is widely used in the field of fault diagnosis. For example, the phase space reconstruction technique is applied for signal characterization. In Reference [9], the phase space reconstruction method is applied for voltage gap detection and feature parameter localization identification, and the accurate detection of gaps can be performed even when the voltage signal is disturbed. Reference [10] transforms the sampling points in the one-dimensional time-series segments to the two-dimensional phase space based on the phase space reconstruction technique and calculates the similarity degree between the time-series segments based on the distribution of discrete points in the obtained two-dimensional phase space, which effectively realizes the real-time diagnosis of the signal fault state. Reference [11] used the phase space reconstruction technique to process the arc current signal, extracted the geometric features and attribute features of the phase plane attractor as the features to discriminate the arc fault, and characterized the change law of randomness and chaos before and after the occurrence of the arc fault. In References [12–14], phase space reconstruction was performed on the mechanical vibration signal of a high-voltage circuit breaker. The morphological features, attribute features, and image edge features of phase space trajectory were extracted as feature covariates for fault diagnosis, and good diagnostic results were achieved.

In the phase space reconstruction, the above literature did not consider the phenomenon of abnormal sampling points in the process of monitoring signal acquisition, resulting in the phase space reconstruction may occur at the sampling abnormalities, which cannot correctly describe the original signal structure dynamic state; at the same time, the above literature mainly focuses on the overall characteristics of the phase space trajectory, ignoring the differences in the local characteristics of different fault phase trajectories, which makes it difficult to ensure the diagnosis accuracy of different fault. It is difficult to ensure the accuracy of diagnosis for different fault types.

Therefore, this paper adopts phase space reconstruction technology to study the feature extraction of high-voltage circuit breaker coil current signal, study the influence of signal abnormal data on the phase space reconstruction effect, introduce the abnormal data processing method based on the first-order forward difference algorithm for signal processing, and then determine the reconstruction parameter delay time τ based on the two-dimensional phase space, and carry out phase space reconstruction to obtain the corresponding phase trajectory; secondly, in order to realize the full utilization of phase trajectory, in order to make full use of the phase trajectory information and enhance the differentiation of fault types, the overall features and local features of the phase trajectory are extracted to build a comprehensive fault feature set, which is used to establish a support vector machine fault classification model to achieve accurate diagnosis of different faults in circuit breakers. The experimental results demonstrate that the proposed method for fault diagnosis, which extracts phase trajectory features from signals with abnormal data, achieves an error rate of less than 1.1%. Furthermore, the average error in different fault feature extractions is less than 1.368% even under high noise levels. The accuracy rate for diagnosing different faults using this approach reaches 98.67%, representing a significant improvement over other diagnostic algorithms.

2. Coil Current Temporal Sequence Phase Space Reconstruction and Reconstruction Parameter Determination

In this section, the chaotic characteristics of circuit breaker coil currents are explored, and a novel approach based on phase space reconstruction and adaptive parameter determination is proposed. Specifically, the first-order forward difference method is introduced to determine appropriate adaptive reconstruction parameters for phase space reconstruction, and the resulting trajectories of coil currents in two-dimensional phase space effectively capture the system's nonlinear dynamic behavior.

2.1. Chaotic Characteristics of Breaker Coil Current Signal

In this paper, the HP550B2 high-voltage circuit breaker is used as the research object, as shown in Figure 1a for its solenoid mechanism to split-close the solenoid structure model. In the process of splitting and closing, the current applied to the coil causes the core of the solenoid to move upward, the spring is released to drive the mechanical parts to move after triggering the closing the button, and any abnormality in the process will affect the change of current in the coil. The equivalent circuit of the solenoid coil is shown in Figure 1b, where U_S is the circuit power supply, R_S is the power supply internal resistance, R_L is the coil and wiring equivalent resistance, and the circuit inductance L varies with the position of the closing the button. The coil is energized when the coil circuit receives a break-open command, where the variable inductance L is related to the air gap of the solenoid core. The closing coil current waveform is shown in Figure 1c. From the above analysis, it can be seen that during the closing process of the circuit breaker, the core mechanism, the closing decoupling close, the closing coil body, and other changes, which subsequently cause changes in the coil current time T_1, T_3, and T_5 and the corresponding current I_1, I_3, and I_5, which provides information for identification of faults in the circuit breaker operating mechanism such as core jamming and coil short circuit between turns.

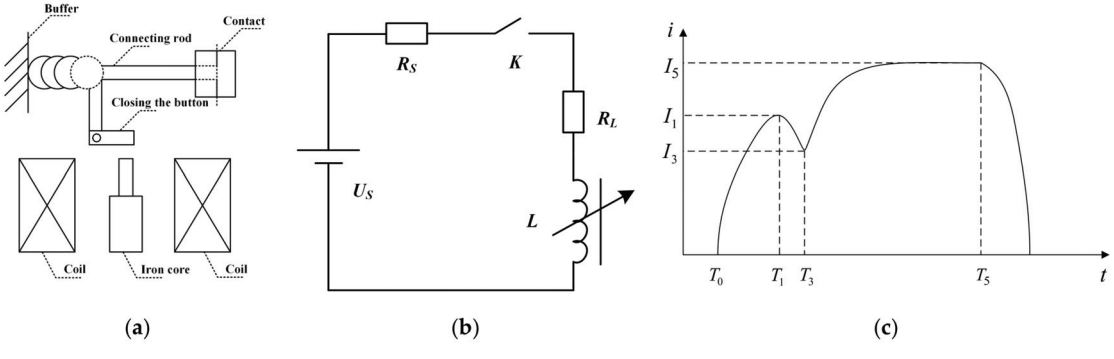

Figure 1. Model of HP550B2 breaking solenoid with coil equivalent circuit diagram and its closing current waveform: (**a**) split-close solenoid model; (**b**) coil solenoid equivalent circuit diagram; (**c**) coil current waveform.

The phase space reconstruction technique used in this paper is to reconstruct the one-dimensional chaotic time series into the high-dimensional phase space to extract and recover the original laws of the dynamical system. Therefore, prior to the application of this method, it is necessary to ascertain whether the high-voltage circuit breaker coil current signal exhibits chaotic characteristics. Only if this is the case can we analyze the signal using the phase space reconstruction technique.

According to chaos theory, a positive maximum Lyapunov exponent [15] can indicate that the signal has chaotic properties [16]. In this paper, we use the wolf method [17] to calculate the maximum Lyapunov exponent of the normal state during the closing process, where the initial point $X(t_0)$ is taken in the reconstruction space, and its distance from the nearest neighbor $X_0(t_0)$ is set to L_0. The time evolution of these two points is tracked until

their spacing exceeds a specified value $\varepsilon > 0$ at the moment t_1, $L' = |X(t_1) - X_0(t_1)| > \varepsilon$, Keep $X(t_1)$ and find another point $X_1(t_1)$ adjacent to $X(t_1)$ such that $L_1 = |X(t_1) - X_1(t_1)| < \varepsilon$ and the angle with it is as small as possible. Continue the above process until $X(t)$ reaches the end of the time series, at which time the total number of iterations of the tracking evolution process is M. The maximum Lyapunov exponent is:

$$\lambda_i = \frac{1}{t_M - t_0} \sum_{i=0}^{M} \ln \frac{L'_i}{L_i} \tag{1}$$

where t_0 and t_M are the initial and end moments; $L'_i = |X(t_i) - X(t_{i-1})|$; $L_i = |X(t_i) - Xi(t_i)|$.

In order to better analyze the chaotic characteristics of the circuit breaker coil current, take the same operating state of the continuous action test cycle for combined analysis, such as Figure 2a for the normal state of 10 cycles of successive current signals. Among them, Figure 2b shows the Lyapunov exponent spectrum in the normal state, and the maximum Lyapunov calculated by the mean value using the Wolf method is 1.2507 > 0. The calculation results of the current signals in five states are shown in Table 1, and the maximum Lyapunov exponent is greater than 0, indicating that the circuit breaker coil current signal has chaotic characteristics, and the phase space reconstruction technique can be used for subsequent analysis.

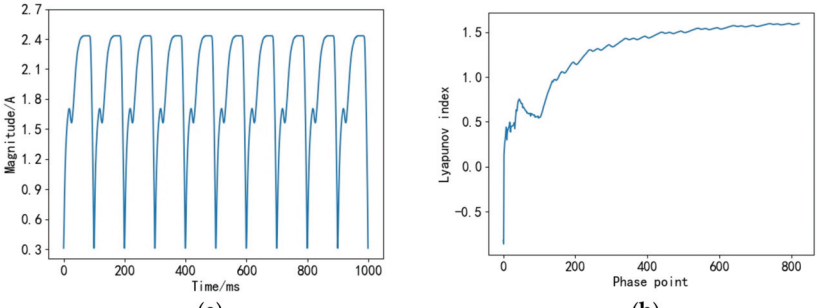

Figure 2. Normal state multi-cycle current signal with corresponding Lyapunov exponential spectrum: (**a**) multi-cycle current signal; (**b**) Lyapunov index spectrum.

Table 1. Maximum Lyapunov index for different fault states.

Failure Status	Normal	Core Jamming	Large Empty Travel of Iron Core	Short Circuit between Turns	Supply Voltage Too Low
Maximum Lyapunov index	1.2507	1.206	1.129	1.371	1.119

2.2. Phase Space Reconstruction of Coil Current Signal

According to Takens' theorem [18], for a given current time series of length N with $x(t) = \{x_1, x_2, x_3, \ldots, x_N\}$, with delay time τ and embedding dimension m, the reconstructed phase space can be expressed as:

$$X = \begin{bmatrix} X_1 \\ X_2 \\ \vdots \\ X_K \end{bmatrix} = \begin{bmatrix} x_1 & x_{1+\tau} & \cdots & x_{1+(m-1)\tau} \\ x_2 & x_{2+\tau} & \cdots & x_{2+(m-1)\tau} \\ \vdots & \vdots & \ddots & \vdots \\ x_K & x_{K+\tau} & \cdots & x_{K+(m-1)\tau} \end{bmatrix} \tag{2}$$

where $K = n - (m-1)\tau$. These K points in the phase space together constitute the current signal time-series phase trajectory.

From Takens' theorem, it is clear that the choice of τ and m in phase space reconstruction determines whether the reconstructed phase space can accurately reflect the characteristic information of the time series.

Figures 3 and 4 show the variation of the phase trajectory diagram of the coil current time series with different delay time variations when the embedding dimension $m = 2$, where the variable $x(t)$ is the horizontal axis, and the delay variable $x(t + \tau)$ with $x(t)$ is the vertical axis. Figure 3 shows the phase space reconstruction trajectory of the current signal time series in the normal state at the delay time $\tau = 9$. At this time, there is an obvious correspondence between the key points of the time-domain waveform of the coil current signal and the characteristic points of the phase space reconstruction trajectory: the T1 and T3 key points correspond to the trajectory inlet point A, and the T5 key point corresponds to the prominent point B at the top right of the trajectory; as in Figure 4a,b, respectively, the delay time $\tau = 3$ and 15 of the phase space reconstruction trajectories with delay time $\tau = 3$ and 15, respectively. As can be seen from the figure, when the delay time τ is too small, the phase trajectory transformation point A is compressed on the inner trap closed trajectory, and the phase trajectory transformation point B is compressed around the right vertex of the trajectory curve transformation complex; the delay time τ is too large, which will lead to the phase trajectory dispersion and make the component of the phase trajectory feature point A is stretched. Therefore, too large or too small a time delay will result in the current signal in the phase space not being obvious, making the subsequent feature extraction analysis difficult, and a suitable delay time needs to be selected to reconstruct a phase space that can correctly restore the initial signal dynamics information.

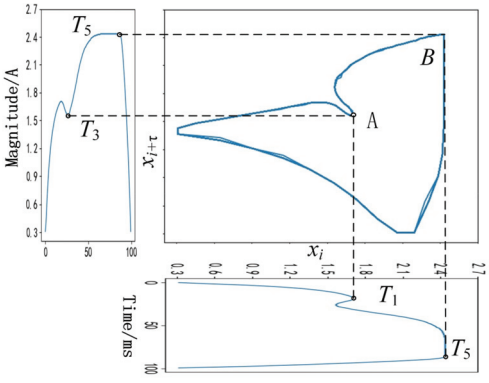

Figure 3. Phase trajectory at delay time $\tau = 9$ with the characteristics corresponding to the critical point of the current signal.

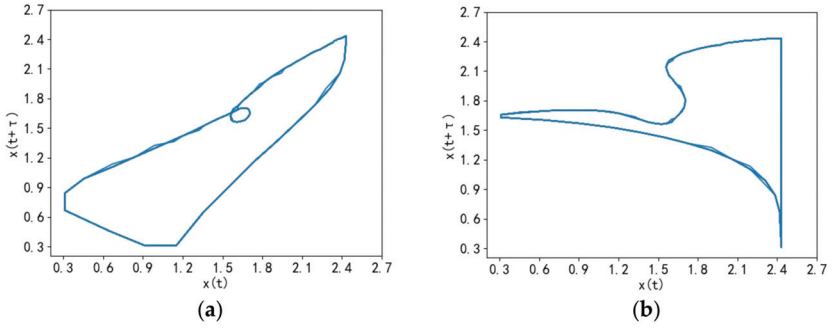

Figure 4. Phase trajectory with delay time $\tau = 3$, 15: (**a**) $\tau = 3$; (**b**) $\tau = 15$.

In addition, since the current signal collected during the actual circuit breaker breaking and closing process has abnormal sampling points in addition to noise, it will likewise have an impact on the selection of reconstruction parameters and subsequent feature extraction.

The acquisition process of the circuit breaker coil current signal is highly susceptible to the actual working conditions, and the acquired signal often appears abnormal. The abnormal data of the signal without considering noise are divided into two categories: one is missing data, and the other is data fluctuation over the limit. The abnormal signal with missing data cannot be reconstructed in phase space and thus cannot obtain the phase trajectory; the current signal with abnormal data fluctuation is shown in Figure 5a. Anomalous fluctuations in data points occurred in the T_1–T_3 segment of Cycles 3, 4, and 7 and in the vicinity of the T_5 characteristic point of Cycles 5 and 6, and the abnormal acquisition in actual working condition basically occurs near the more complex T_1–T_3 section and T_5 time-domain feature points, which is manifested as abnormal fluctuation in itself or the nearby data points, according to which the reconstructed phase trajectory is shown in Figure 5b, corresponding to T_1, T_3, and T_5. The trajectory features of key points are mingled around the phase trajectory corresponding to the abnormal data, which directly affects the extraction accuracy of the subsequent phase trajectory feature points.

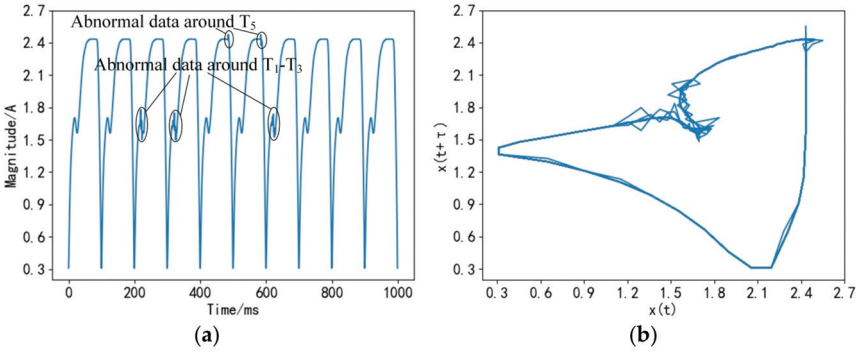

Figure 5. Current signals containing data fluctuation anomalies and corresponding reconstructed phase trajectory: (**a**) current signal; (**b**) reconstructed phase trajectory.

2.3. Adaptive Determination of Phase Space Reconfiguration Parameters

To solve the above problems, this paper proposes an adaptive processing method for the current signal based on the first-order forward differencing algorithm for anomalous data, and then uses the mutual information method to select a suitable delay time τ, so as to realize the adaptive determination of the phase space reconstruction parameters and lay the foundation for the subsequent feature extraction based on the phase trajectory.

2.3.1. Signal Anomaly Data Processing Based on First-Order Forward Differencing

For the lack of current signal data, it is only necessary to check whether the sampling point data are continuous and complete the data; for the signal abnormality in which the signal data fluctuation exceeds the limit described in Section 2.2, the continuous action of the current signal is to collect the abnormal fluctuation exceeding the limit. The differential value of the current signal time series reflects the fluctuation of the signal, and the frequency histogram distribution of the first-order positive differential absolute value of the current signal measuring point containing abnormal fluctuation data is analyzed, as shown in Figure 6.

From the figure, it is found that the frequency of the absolute value of the difference in the interval of 0~0.2 is close to 800, while the frequency of the place where the absolute value of the difference is after 1.0 is low, so the data corresponding to the part of the absolute value of the difference are relatively large and more likely to be abnormal overrun

data. Therefore, based on the above analysis, the first-order forward differencing method is introduced for abnormal data processing of the current signal.

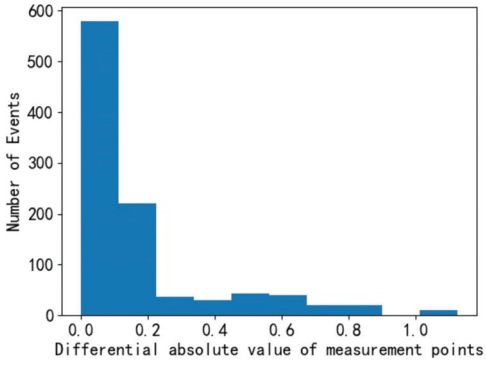

Figure 6. Frequency histogram distribution of the absolute value of the first-order forward difference.

For the anomalous data of the current signal, the specific process of filling in the missing data and rejecting the anomalous fluctuation data based on the first-order forward differencing method is as follows.

(1) Firstly, detecting the anomalous missing values of the signal and completing them by linear interpolation.
(2) Secondly, detection of abnormal overrun values based on the first-order forward difference algorithm: the first-order forward difference $\{x_i\}$ is calculated sequentially for the current signal time series Δx_i, where $\Delta x_i = x_{i+1} - x_i$, $i = 1, 2, \ldots, N-1$. Then, the threshold λ for judging abnormal overrun data is determined according to the frequency distribution of the absolute value of the difference, and the maximum number of signal abnormal segment data is recorded as n. The number of adjacent consecutive abnormal points in front of x_{i+1} is recorded as e_i, and k is cycled sequentially from 1 to $N-1$. The initial situation $e_i = 0$, $i = 0, 1, \ldots, N-1$, and the rules for judging the abnormal overrun data are shown in Figure 7.
(3) Finally, remove the detected abnormal out-of-range points and perform linear interpolation to complete them.

2.3.2. Determination of Delay Time

Since too small a τ will lead to the compression of the reconstructed phase space signal features and too large a τ will lead to the dispersion of the reconstructed phase space signal where no effective features can be obtained, a suitable value of τ must be selected to allow the features to be expressed more effectively. For the circuit breaker coil current signal time series in this paper, the mutual information method [19] is selected to obtain the delay time. The time series of the current signal is $x(t)$, and the time series $x(t+\tau)$ via the delay time τ. The mutual information method for selecting the delay time τ is the time corresponding to the first minimal value point of the mutual information function of the general dependence between successive points of the time series as the delay time, where the mutual information function is calculated as:

$$MI(x(t), x(t+\tau)) = \sum_{i=1}^{N} \sum_{j=1}^{N_\tau} P(i,j) \lg\left(\frac{P(i,j)}{P(i)P(j)}\right) \quad (3)$$

where N_τ is the length of the time series after the delay, $P(i)$ is the probability that the value of $x(t)$ is i, $P(j)$ is the probability that the value of $x(t+\tau)$ is j, and $P(i, j)$ is the joint probability that the value of $x(t)$ is i and the value of $x(t+\tau)$ is j.

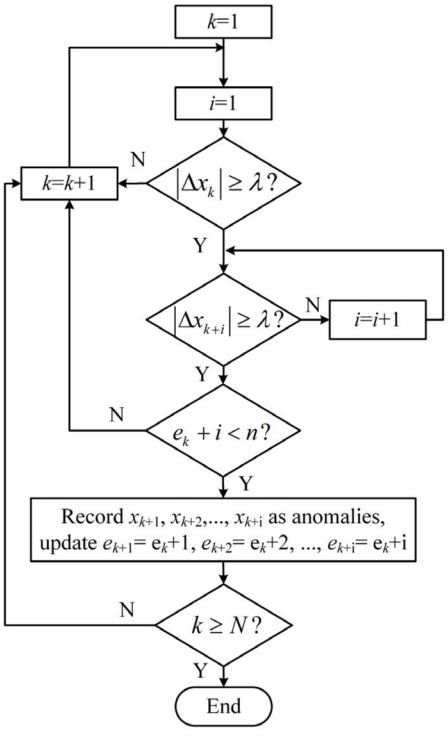

Figure 7. Abnormal overrun data detection.

Take the time series of the circuit breaker coil current with normal signal acquisition as $x(t)$, the time series of the coil current with abnormal acquisition (with abnormal data) as $x'(t)$, and the time series of the coil current after abnormal data processing as $x''(t)$ to calculate the mutual information function of the three, and the correlation change curve between mutual information function and τ is shown in Figure 8.

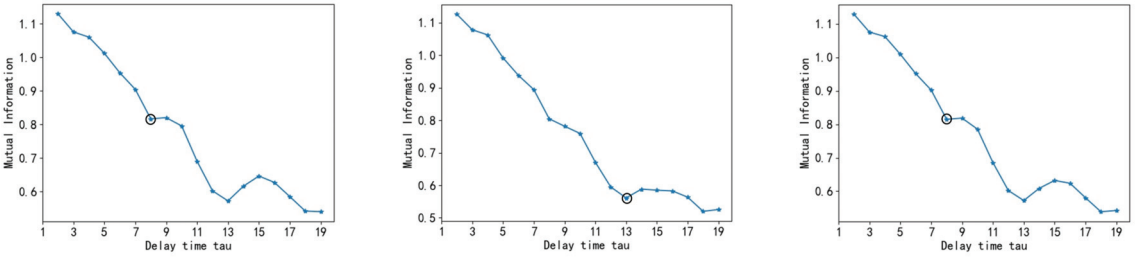

Figure 8. Mutual information function curve: (**a**) normal; (**b**) contains abnormal data; (**c**) after abnormal data processing.

According to the delay time selection principle of the mutual information method, when the signal is normal without abnormal data, the first local minima of the mutual information function is the point of $\tau = 8$; when the signal has abnormal data, the first local minima of mutual information function is the point of $\tau = 13$; when the signal has abnormal data but after the process of Section 2.3.1, the first local minima of mutual information function is the point of $\tau = 8$. It can be seen that after the signal anomaly data processing based on the first-order forward difference, the first local minima of the current timing

mutual information function originally affected by the anomaly data are the same as when the signal is normal without the anomaly data, and the optimal delay time τ is chosen to be the same.

Based on the optimal delay time selected by the above mutual information method and the selected embedding dimension $m = 2$, the phase trajectories in two-dimensional phase space are shown in Figure 9.

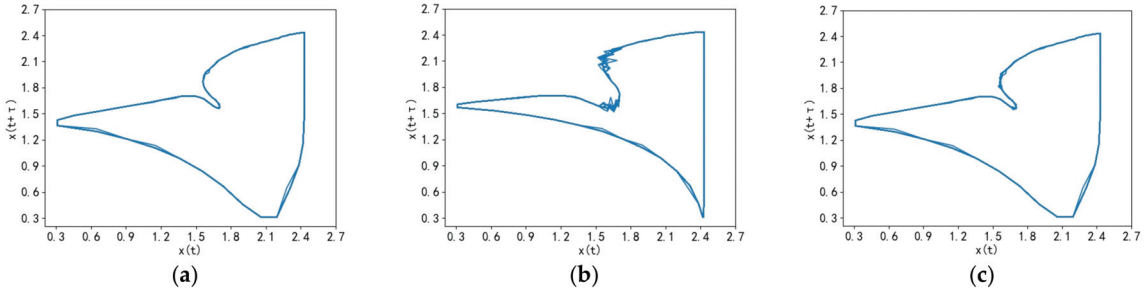

Figure 9. Phase trajectory comparison chart: (**a**) normal; (**b**) contains abnormal data; (**c**) after abnormal data processing.

The phase trajectories in Figure 9a have an obvious distribution of phase trajectory points A and B in the trapped angle and the right vertex, and the trajectories are uniformly distributed in the phase space as a whole; in Figure 9b, the trajectory trajectories have expanded in the trapped angle, the phase trajectory feature points A are mixed around the phase trajectories corresponding to the anomalous data and the feature components are stretched, and the overall state is diffuse; in Figure 9c, the overall shape of the phase trajectories and the distribution of local trajectory transformation points are basically the same as in Figure 9a.

It can be seen that the presence of anomalous data affects the selection of delay time for phase space reconstruction, resulting in large differences in the overall and local morphology of the reconstructed phase trajectory between the signal with normal acquisition and the signal with anomalous data, which further makes the subsequent phase trajectory analysis and feature extraction difficult, while the introduction of the first-order forward difference-based anomalous data processing method can adapt to the anomalous changes of the signal, and the reconstructed phase trajectory can still maintain stable morphological features when the signal contains anomalous data, thus avoiding the impact of the signal anomalous data on the subsequent signal analysis.

3. Extraction of Feature Parameters for Current Timing Phase Trajectories

The previously proposed phase space reconstruction method is utilized to extract the phase space trajectories of circuit breaker coil currents in different fault states, and their global and local characteristics are obtained. The global features consist of attribute features, such as association dimension D, and morphological features, including origin moments E. Meanwhile, the local features are represented by the amplitudes M_1, M_3, and M_5 of T_1, T_3, and T_5 in the phase space. Analysis of feature distribution reveals that the overall trajectory features cannot fully capture the differences among different fault types. Therefore, combining both global and local features is necessary to achieve a more precise fault diagnosis.

3.1. Phase Space Trajectory of Current Signal

According to the phase space reconstruction method described above, the 10-cycle current time series $x(t)$ of normal and four different faults are taken for phase space reconstruction analysis to obtain the phase trajectory plane diagram. Among them, the

single-cycle current signals in different states and the corresponding multi-cycle phase trajectory plots are shown in Figure 10a–f.

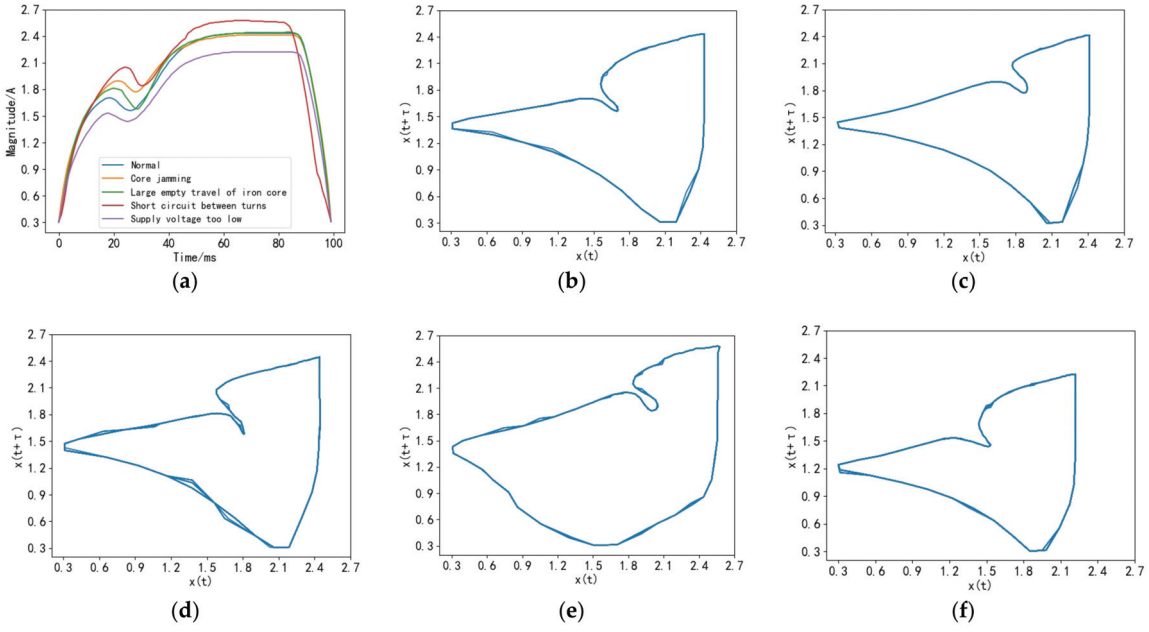

Figure 10. Current signals in different states and corresponding multi-period phase planes: (**a**) comparison of time-domain waveforms of current signals under different states; (**b**) normal state phase trajectory; (**c**) core card astringent phase track; (**d**) core empty travel large phase trajectory; (**e**) inter-turn short-circuit phase trajectory; (**f**) supply voltage too low phase track.

Combined with Figure 10a–d, the overall difference between current signal waveforms of core jamming and the large core air travel fault state compared with the normal state is small, while the amplitude and time in local T_1 and T_3 key points have different degrees of rise and delay, which is reflected in the consistency of the overall shape of the corresponding phase trajectory and the offset of local trajectory shift point A in the direction of origin. The diagram of the core empty travel large fault around A point shows that the trajectories are compressed together, making them more susceptible to abnormal data. Combined with Figure 10a,b,e,f, the inter-turn short-circuit supply voltage is too low a fault state compared to the normal state of the overall difference in the current signal waveform, while in the local T_1, T_3, and T_5, the key points have obvious amplitude changes, corresponding to the difference in the overall shape of the corresponding phase trajectory and local key points A and B in the direction of the origin of the obvious offset.

The attractor phase trajectories of the fault current signals in the above figures after phase space reconstruction have different degrees of differences in the overall and local characteristics, and the overall and local characteristics of the phase trajectories can be used to quantitatively characterize their trajectory characteristics and more intuitively and effectively analyze the potential differences before and after the occurrence of the fault.

3.2. Overall Characteristics and Distribution of Attractor Trajectories in Phase Space

(1) Property characteristics of phase trajectories

The correlation dimension reflects the sensitivity to the inhomogeneity of the system attractor and can quantitatively characterize the complexity of the dynamic structure of the attractor [20]. The correlation dimension is used to analyze the attribute of the system

attractor, extract the correlation dimension of the attractor trajectory in normal and different fault states, and analyze the change law of the attribute characteristic quantity, so as to better characterize the system chaotic characteristics of the coil current when different states occur. The calculation process of the correlation dimension is as follows:

Calculate the Euclidean distance d_{ij} of any two phase points in phase space:

$$d_{ij} = \left\| X_i - X_j \right\| \tag{4}$$

The critical distance variable d is set, and the associated integral $N_m(d)$ is defined as the proportion of all vectors less than d:

$$N_m(d) = \frac{1}{K(K-1)} \sum_{i,j=1}^{K} \theta(d - d_{ij}) \tag{5}$$

where K is the number of state points constituting the phase space trajectory, $i \neq j$, $\theta(d - d_{ij}) = \begin{cases} 0, & d - d_{ij} \geq 0 \\ 1, & d - d_{ij} < 0 \end{cases}$.

Determine the association dimension D:

$$D = \lim_{d \to 0} \frac{\ln N_m(d)}{\ln d} \tag{6}$$

(2) Morphological characteristics of phase trajectories

From the above phase plane diagram, it can be seen that the trajectory of the current signal phase plane attractor as a whole deviates from the origin. In the fault state, the attractor distribution changes, and it is close to or deviates from the origin, so the distance and each state point in the phase plane to the origin is extracted. This is called the origin moment, which can reflect the distribution characteristics of the phase point in the phase space to some extent. The specific expressions are:

$$E = \sum_{i=1}^{K} \sqrt{x_i^2 + x_{i+\tau}^2} \tag{7}$$

where $(x_i, x_{i+\tau})$ are the coordinates of the two-dimensional phase plane state points.

Figure 11 shows the distribution of the overall characteristic correlation dimension D and the origin moment E of the phase trajectory for each of the 10 cycles of the current signal in the normal state and the four fault states: the correlation dimension for the normal state fluctuates in the range of 0.48, while the correlation dimension for all four fault states exceeds 0.51, i.e., it is more than 6.25% higher than the normal state, which indicates that the unevenness of the system itself increases after the occurrence of a fault increases, and among them, the correlation dimensions of core jamming, large core air travel, and short circuit between turns, and low supply voltage all fluctuate in the range around 0.52 and 0.56, respectively, which indicates that different fault types will have similar unevenness changes. The normal state origin moment characteristics are distributed in the range of 870~880, while the characteristics of core jamming and large core air travel are all distributed between 880 and 900, with less than 2% change from the normal state and insignificant or even no difference in distribution, but the inter-turn short-circuit and low supply voltage origin moment characteristics are distributed between 910~920 and 790~800, respectively, with a 5% increase and a decrease of about 9%. The analysis of the above results shows that the different types of faults determine the degree of difference of the overall phase trajectory morphology distribution compared with the normal state, and the indicators of core jamming and large core air travel fault states are relatively close to each other, indicating that the phase trajectory morphology of some fault types is similar. Therefore, only the overall phase trajectory characteristics cannot effectively classify and identify each fault state.

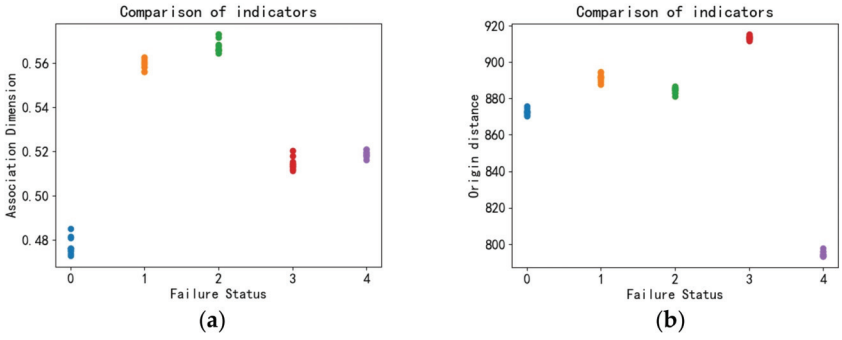

Figure 11. Overall characteristics of different fault phase trajectories *D*, *E* distribution: (**a**) association dimension *D*; (**b**) origin moment *E*.

3.3. Local Characteristics and Distribution of Attractor Trajectories in Phase Space

Under the premise that the overall characteristics of the phase plane attractor are analyzed in the previous section, further local characteristics of the system attractor are further analyzed in order to improve the variability of the trajectory characteristics of the faulty phase. As the trajectory transition point shown in Figure 3 of Section 2.2, the state coordinates of the two trajectory transition points of the attractor in the normal and fault states are extracted, which are the state coordinates x_i and $x_{i+\tau}$ of the trajectory transition inlet point A and the state coordinates xi of the trajectory transition protrusion point B, which are noted as the amplitudes M_1, M_3, and M_5 of T_1, T_3, and T_5 in the phase space, respectively.

Figure 12 shows the distribution of the phase trajectory local characteristics M_1, M_3, and M_5 for each of the 10 cycles of the current signal in the normal state and the four fault states; the amplitude M_1 under the T_1 phase space in the normal state fluctuates in the range of 5.5~5.75, while the M_1 of the four fault states has different degrees of change relative to this range, in which the M_1 of core jamming, large core empty travel, and inter-turn short circuit, respectively. The T_1 value of low supply voltage is reduced by about 11%, while the M_1 indexes of core jamming and large core empty travel faults are relatively close to each other; the amplitude of M_3 under the T_3 phase space in the normal state is distributed between 5.15 and 5.3, and the M_3 value distribution of large core empty travel faults has no obvious change relative to the normal state, while other faults have more obvious changes. Meanwhile, the M_3 value distribution of core jamming and inter-turn short circuit are 5.8~6.3 and 6.1~6.4, respectively, with overlapping parts; the M_5 value distribution under T_5 phase space in the normal state is around 8.1~8.15, and the M_5 values of core jamming and inter-turn short circuit are in 8.0~8.1 and 8.5~8.6, respectively, with more obvious differences.

From the above data analysis, it can be concluded that the local features indexes have different degrees of change when different faults occur, which is corresponding to the change of key points of the time-domain model, and the differentiation of fault states can be improved by combining the three local features. Therefore, since the overall features of the trajectory have the defect of incomplete description in the differentiation of fault types, combining these local features with the overall features mentioned above can maximize the differentiation of different fault type features, which can effectively improve the accuracy of subsequent fault identification.

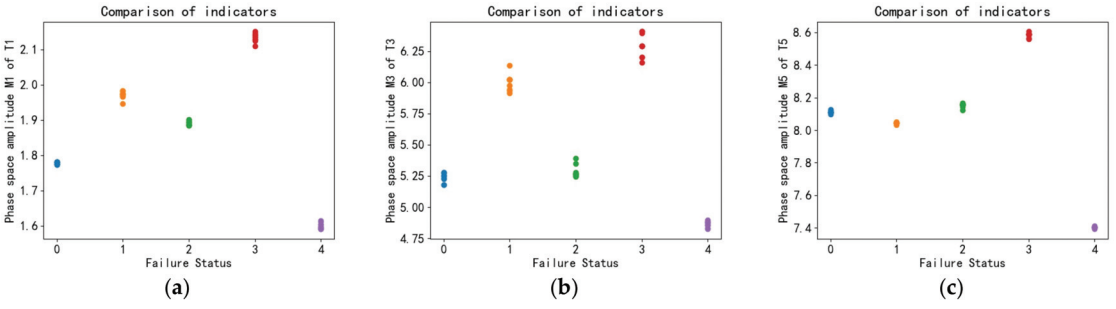

Figure 12. Distribution of local features M_1, M_3 and M_5 for different fault phase trajectories: (**a**) amplitude M_1 under T_1 phase space; (**b**) amplitude M_3 under T_3 phase space; (**c**) amplitude M_5 under T5 phase space.

4. Circuit Breaker Fault Diagnosis Process Based on Current Timing Phase Trajectory Feature and Support Vector Machine

The support vector machine [21] (SVM) can use the kernel function to map the feature vectors of the samples to the high-dimensional space and construct the hyperplane in the high-dimensional space to classify the sample feature vectors, which is more suitable for the small sample classification application of coil current signal phase trajectory characteristics. The key to the performance of the SVM model is to select the appropriate penalty parameter C and kernel function parameter g [22,23], to train with the feature parameters of the training samples and the corresponding fault labels, to find the optimal parameters C and g, and then to obtain the optimal classification model.

As shown in Figure 13, the process of circuit breaker fault identification based on current timing phase trajectory characteristics and support vector machine in this paper is as follows:

(1) Use the anomaly data processing method based on the first-order forward difference algorithm to process the coil current signal with anomaly data, determine the optimal phase space reconstruction parameters on the basis of the processed signal, and carry out phase space reconstruction with these parameters.

(2) Obtain the phase space trajectories of the coil current signals under different fault states, extract the overall features and local features of each phase trajectory, and constitute the sample set of phase trajectory fault features [D,E,M_1,M_3,M_5].

(3) The fault feature sample set is configured as the training set and the test set, the training set is input to the support vector machine model for training, and the model parameters are optimized to establish the fault diagnosis model based on phase trajectory fault feature-SVM. Finally, the test set is used to test the adaptive fault diagnosis performance of this model.

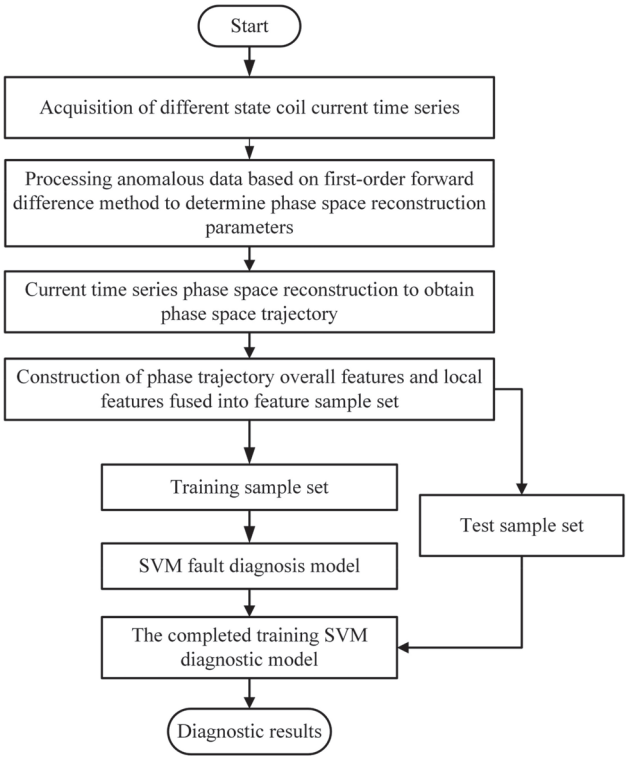

Figure 13. Overall fault identification process.

5. Test Results and Analysis

In this paper, the HP550B2 high-voltage circuit breaker is used for testing experiments, simulating five states of normal closing, core jamming, large core air travel, and low power supply voltage for inter-turn short circuit in the closing process; 40 groups of each of the above five state current signals are collected using current sensors, 25 groups are taken as training samples, and the remaining 15 groups are used as test samples. Firstly, the adaptiveness and robustness of the diagnostic model in fault feature extraction are verified and analyzed by introducing abnormal data and noise, and then the diagnostic performance of the model based on different algorithms and different feature indicators are compared.

5.1. Adaptation Analysis of Phase Trajectory Feature Extraction

To analyze the adaptability of feature extraction in the case of acquisition signal with abnormal data, the signal without abnormal data in the acquisition process is noted as I, the signal with abnormal data introduced is I_{error}, and the average error is:

$$\frac{1}{n}\sum_{i=1}^{n}\frac{|X_{iI_{\text{error}}} - X_{iI}|}{X_{iI}} \times 100\% \tag{8}$$

where X_{iI} is the i-th fault feature indicator of the signal without abnormal data, $X_{iI\text{error}}$ is the i-th fault feature indicator of the signal with abnormal data, n is the number of phase trajectory feature indicators, and the same feature indicators of different fault states have been normalized. Table 2 describes some of the results of extracting phase trajectory feature indicators for signals with and without abnormal data in each fault state of the circuit breaker. Based on the table of results, it is apparent that the average error range for extracting all state trajectory features falls between 0.702% and 1.064%. Furthermore, even

for the core air travel large fault feature extraction, which is highly susceptible to abnormal data, the average error rate is just 1.064%. These findings demonstrate that the proposed method of phase space reconstruction based on the first-order forward difference algorithm can effectively extract phase trajectory features from signals containing abnormal data, with an error rate of less than 1.1%, and the feature indicator values of signals containing abnormal data are obtained more accurately, indicating that the method can be adaptive to the extraction of signal features containing abnormal data. It shows that the method is adaptive to the extraction of signal features of anomalous data.

Table 2. Selected results of extracted phase trajectory characteristic indexes.

Failure Status	Signal	Phase Trajectory Characteristic Index X_i					Average Error %
		D	E	M_1	M_3	M_5	
Normal	I	0.819	0.938	0.841	0.820	0.938	1.047
	I_{error}	0.832	0.947	0.828	0.825	0.943	
Core jamming	I	0.978	0.965	0.915	0.938	0.925	0.938
	I_{error}	0.975	0.971	0.922	0.957	0.934	
Large empty travel of iron core	I	0.985	0.965	0.863	0.815	0.955	1.064
	I_{error}	0.994	0.960	0.886	0.819	0.948	
Short circuit between turns	I	0.891	0.981	0.990	0.993	1	0.702
	I_{error}	0.897	0.997	0.993	1	0.998	
Supply voltage too low	I	0.917	0.873	0.735	0.745	0.867	1.040
	I_{error}	0.909	0.865	0.744	0.757	0.862	

5.2. Robustness Analysis of Phase Trajectory Feature Extraction under Noise

However, the signals collected in real operating situations are usually accompanied by noise in addition to the anomalous data mentioned in this paper, which affects the performance of the diagnostic model. For example, Figure 14 shows different state current waveforms with 40 dB noise, and the algorithm model needs more stable feature extraction capability in the case that the current waveforms contain different levels of noise. Therefore, to test the robustness of the algorithm model proposed in this paper, different proportions of noise are added to the initial coil current signal with signal-to-noise ratios of 40 dB, 35 dB, 30 dB, 25 dB, and 20 dB, respectively, and further tested at the phase trajectory feature extraction based on different fault state current signals, and the test results are shown in Table 3, where the average error is calculated as described in Section 5.1 (where $X_{ilerror}$ is the noise containing signal).

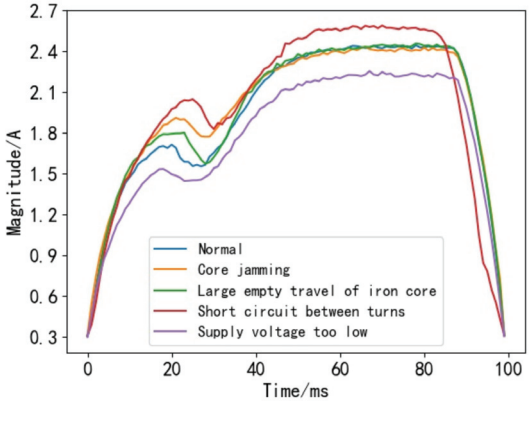

Figure 14. Current waveform with noise.

Table 3. Average error of phase trajectory feature extraction under different levels of noise.

Failure Status	Signal-to-Noise Ratio/dB				
	40	**35**	**30**	**25**	**20**
Normal	1.085	1.098	1.126	1.143	1.245
Core jamming	0.942	0.997	1.054	1.108	1.238
Large empty travel of iron core	1.075	1.104	1.118	1.134	1.368
Short circuit between turns	0.756	0.802	0.992	1.022	1.101
Supply voltage too low	1.062	1.078	1.093	1.125	1.340

From the data in the table, it can be seen that the average error of phase trajectory feature extraction increases with the increase in noise severity (i.e., the signal-to-noise ratio decreases) for the current signals of different fault states, but the range of change is small, and even in the case of only a 20 dB signal-to-noise ratio, the highest average error in each state is 1.101% to 1.368%, which shows the good robustness of phase trajectory feature extraction of the method in this paper under different degrees of noise environment.

5.3. Comparison of Different Algorithmic Models

The fault feature set [D,E,M_1,M_3,M_5] is constructed after the phase trajectory fault features of the circuit breaker current signal are extracted; the training set is input to the SVM model for training; the cross-validation method is used to obtain the model parameters C = 3.24 and g = 1.52, respectively; and the test set is input to the constructed SVM model for fault diagnosis test, and the accuracy of fault diagnosis is 98.67%.

In order to further verify the superiority of the algorithm model of this paper, the algorithm of this paper is compared with other commonly used machine learning classification algorithms, and the input features are compared with the time-domain current signal features and the phase trajectory features proposed in this paper for fault identification accuracy comparison. The algorithm aspect compares the performance of k-nearest neighbor [24] (KNN) and back propagation neural network [25] (BPNN, using the network seeking method to determine neurons and genetic algorithm to determine weights and bias parameters [26]) to identify faults under the same training samples and test samples, respectively. When the time-domain current signal features are set to the feature set [T_1,T_3,T_5,I_1,I_3,I_5] constructed from the time-domain features in Section 2.1, the training and test sample configurations are the same as the phase trajectory feature samples. The test comparison results are shown in Table 4.

Table 4. Accuracy of different classification models and input features.

Classifier	Input Features	Accuracy Rate/%
KNN	Time-domain current signal characteristics	73.33
	Phase trajectory characteristics	78.66
BPNN	Time-domain current signal characteristics	88.00
	Phase trajectory characteristics	93.33
SVM	Time-domain current signal characteristics	94.67
	Phase trajectory characteristics	98.67

From the analysis of the results in the above table, when phase trajectory features are used as input instead of time-domain current signal features, the diagnostic accuracy of the three classifiers is improved by 5.33%, 5.33%, and 4%, respectively. Therefore, using phase trajectory features as input can improve the accuracy of identifying circuit breaker faults. The accuracy rates of the three classifiers are 78.66%, 93.33%, and 98.67% when using phase trajectory features as input, with SVM having significantly higher accuracy rates than other algorithms.

6. Conclusions

This paper studies the distribution trajectory of the circuit breaker opening and closing coil current signal in the phase space, and establishes a circuit breaker fault diagnosis model based on coil current phase trajectory characteristics-SVM. Five different fault states of high-voltage circuit breakers were simulated for diagnostic testing, and the following conclusions were drawn:

(1) The preprocessing method employed, based on the first-order forward difference method, can adaptively eliminate anomalous data, resulting in an accurate reconstruction of phase trajectory characteristics of the coil current signal.
(2) Incorporating local phase trajectory characteristics enables maximum differentiation of different fault states, effectively solving the challenge of classifying similar phase trajectory patterns between certain faults, such as core jamming and large core air travel.
(3) Experimental verification confirms that the proposed fault diagnosis model has strong robustness in feature extraction against interference, with an average error of approximately 1% when the signal-to-noise ratio of noise is between 20 and 40 dB. Furthermore, utilizing phase trajectory features and SVM algorithm models results in significantly improved fault identification accuracy compared to the traditional diagnosis model based on time-frequency domain feature classification algorithms.

However, due to the large number of models of circuit breakers and their operating mechanisms and various types of faults, this study was conducted under common faults that can be simulated. For some faults that are difficult to simulate and cause irreversible damage to the circuit breakers, this method needs to be further validated due to the lack of sample data.

Author Contributions: Conceptualization, Y.C. and Q.L.; Data curation, Y.C.; Investigation, G.L.; Methodology, Y.C. and Q.L.; Project administration, R.F.; Resources, Q.L.; Software, Q.L.; Supervision, Y.Z.; Validation, Y.C.; Visualization, N.Y.; Writing—original draft, Y.C.; Writing—review and editing, Q.L. All authors have read and agreed to the published version of the manuscript.

Funding: This research was funded by State Grid Jiangxi Electric Power Co. Project, grant number 52182023000L and The APC was funded by National Natural Science Foundation of China, grant number 52267008.

Institutional Review Board Statement: Not applicable.

Informed Consent Statement: Not applicable.

Data Availability Statement: Not applicable.

Conflicts of Interest: The authors declare no conflict of interest.

References

1. Lu, H.; Ilihamu, Y.; Liu, P.; Zhang, P.; Li, Z.; Kari, T. High Voltage Circuit Breaker Fault Diagnosis Based on GWO-SVM. *Comb. Mach. Tools Autom. Mach. Technol.* **2022**, 103–107. [CrossRef]
2. Peng, Z.; Wang, S.; Yi, L.; Liu, Q.; Chen, X.; Liang, M.; Chu, F.; Cao, C.; Yan, H.; Liu, D. Research on fault diagnosis of high voltage circuit breaker breaking and closing coil based on SVM principal component analysis. *High Volt. Appl.* **2019**, *55*, 39–46. [CrossRef]
3. Pang, X.; Gan, Y.; Long, Y.; Xiu, S. Research on the diagnosis technology of SF_6 circuit breaker interrupter defect based on gas decomposition products. *J. Electr. Mach. Control* **2020**, *24*, 122–130. [CrossRef]
4. Hu, J.; Zhang, W.; Cao, D.; Wen, Y.; Rong, Y. Research on the health condition of power system based on fuzzy theory. *Power Syst. Prot. Control* **2016**, *44*, 61–66.
5. Yang, W.; Ke, Y.; Zhu, S.; Li, B.; Chen, Z.; Zhao, C.; Song, D.; Yang, H. High voltage circuit breaker spring mechanism condition detection based on spline interpolation and linear fit analysis. *High Volt. Appl.* **2017**, *53*, 147–153. [CrossRef]
6. Fan, H.; Li, X.; Su, H.; Chen, L.; Shi, Z. Research on circuit breaker fault diagnosis method based on principal component analysis-support vector machine optimization model. *High Volt. Appl.* **2020**, *56*, 143–151. [CrossRef]
7. Zhang, H.; Zhao, L.; Jing, W.; Yang, W.; Jiang, H.; Zhu, L.; Rong, Q.; Fu, R. Condition evaluation of circuit breaker operating mechanism based on Relief eigenvolume optimization and SOM network. *High Volt. Appl.* **2017**, *53*, 240–246. [CrossRef]

8. Sun, Y.; Zhang, W.; Zhang, Y.; Li, S.; Liu, X. Extraction of high voltage circuit breaker breaking coil current signal features and fault discrimination method. *High Volt. Appl.* **2015**, *51*, 134–139. [CrossRef]
9. Wang, N.; Ma, Z.; Jia, Q.; Dong, H. Voltage gap detection and feature parameter identification based on phase space reconstruction. *Chin. J. Electr. Eng.* **2017**, *37*, 5220–5227. [CrossRef]
10. Wu, X.; Dong, Y.; Hou, Z.; Cheng, W. Extraction of event-based time series segments based on phase space reconstruction. *Vib. Shock.* **2020**, *39*, 39–47. [CrossRef]
11. Cui, R.; Li, Z.; Tong, D. Aero-arc fault detection based on phase space reconstruction and PCA. *Chin. J. Electr. Eng.* **2021**, *41*, 5054–5065. [CrossRef]
12. Li, Z.; Wei, L.; Han, D.; Teng, W. Research on mechanical fault diagnosis of high-voltage circuit breaker based on phase space reconstruction. *Power Syst. Prot. Control* **2018**, *46*, 129–135.
13. Xia, X.; Lu, Y.; Su, Y.; Yang, J. Mechanical fault diagnosis of high-voltage circuit breaker based on phase space reconstruction and improved GSA-SVM. *Electr. Power* **2021**, *54*, 169–176.
14. Sheng, J.; Yin, X.; Deng, W.; Yuan, H.; Yang, A.; Wang, X.; Rong, M. Extraction of edge features of circuit breaker vibration signal based on phase space reconstruction technique. *High Volt. Appl.* **2022**, *58*, 27–36. [CrossRef]
15. Lorenz, E.N. Deterministic Nonperiodic Flow. *J. Atmos. Sci.* **1963**, *20*, 130–141. [CrossRef]
16. Ruan, J.; Yang, Q.; Huang, D.; Zhuang, Z. Chaotic attractor morphology characteristics of mechanical vibration signal of high voltage circuit breaker. *Power Autom. Equip.* **2020**, *40*, 187–193. [CrossRef]
17. Wolf, A.; Swift, J.B.; Swinney, H.L.; Vastano, J.A. Determining Lyapunov Exponents from a Time Series. *Phys. D Nonlinear Phenom.* **1985**, *16*, 285–317. [CrossRef]
18. Takens, F. Detecting Strange Attractors in Turbulence. In *Dynamical Systems and Turbulence, Warwick 1980*; Rand, D., Young, L.-S., Eds.; Lecture Notes in Mathematics; Springer: Berlin/Heidelberg, Germany, 1981; Volume 898, pp. 366–381. ISBN 978-3-540-11171-9.
19. Albers, D.J.; Hripcsak, G. Estimation of Time-Delayed Mutual Information and Bias for Irregularly and Sparsely Sampled Time-Series. *Chaos Solitons Fractals* **2012**, *45*, 853–860. [CrossRef]
20. Liu, Y.; He, H.; Xiao, J. Characterization of the correlation dimension of the dynamic pressure at the outlet of a centrifugal compressor. *J. Aerodyn.* **2021**, *36*, 300–309. [CrossRef]
21. Cortes, C.; Vapnik, V. Support-Vector Networks. *Mach. Learn.* **1995**, *20*, 273–297. [CrossRef]
22. Jannah, N.; Hadjiloucas, S. A Comparison between ECG Beat Classifiers Using Multiclass SVM and SIMCA with Time Domain PCA Feature Reduction. In Proceedings of the 2017 UKSim-AMSS 19th International Conference on Computer Modelling & Simulation (UKSim), Cambridge, UK, 5–7 April 2017; IEEE: Piscataway, NJ, USA; pp. 126–131.
23. Li, Y.; Zhang, R.; Guo, Y.; Huan, P.; Zhang, M. Nonlinear Soft Fault Diagnosis of Analog Circuits Based on RCCA-SVM. *IEEE Access* **2020**, *8*, 60951–60963. [CrossRef]
24. Li, B.; Qi, W.; Yang, Z.; Chen, C.; Gui, Y.; Ren, Z.; Yao, Y.; Wang, H.; Tu, S. High voltage circuit breaker fault diagnosis based on multi-feature selection method. *High Volt. Appl.* **2020**, *56*, 218–224. [CrossRef]
25. Rumelhart, D.E.; Hinton, G.E.; Williams, R.J. Learning Representations by Back-Propagating Errors. *Nature* **1986**, *323*, 533–536. [CrossRef]
26. Yan, R.; Lin, C.; Song, W.; Gao, S.; Zhong, L.; Zhang, W. High Voltage Circuit Breaker Fault Diagnosis Based on EEMD and Convolutional Neural Network. *High Volt. Appl.* **2022**, *58*, 213–220. [CrossRef]

energies

MDPI

Review

Review of RoCoF Estimation Techniques for Low-Inertia Power Systems

Xiaoyu Deng [1], Ruo Mo [1], Pengliang Wang [1], Junru Chen [1], Dongliang Nan [2] and Muyang Liu [1,*]

[1] School of Electrical Engineering, Xinjiang University, Urumqi 830046, China; xyd@stu.xju.edu.cn (X.D.)
[2] Electric Power Research Institute, State Grid Xinjiang Electric Power Co., Ltd., Urumqi 830011, China
* Correspondence: muyang.liu@xju.edu.cn; Tel.: +86-13677352908

Abstract: As the traditional generation is gradually replaced by inverter-based resources, a lack of rotational inertia is now a common issue of modern power systems, which leads to an increasingly larger rate of change of frequency (RoCoF) following contingencies and may result in frequency collapse. As a crucial index of the frequency security and stability of power systems, the accurate estimation of the RoCoF can be a foundation for the development of advanced operations and control techniques of the future power system. This paper firstly analyzes the role of the RoCoF in typical blackouts occurring in recent years and discusses the physical and numerical nature of the RoCoF; then, by introducing the frequency spatial distribution of the power system, the paper discusses the concept of the "center" RoCoF that can present the frequency security and stability of the entire system. The estimation and prediction techniques of the maximal power system RoCoF following a contingency and the existing real-time tracking techniques of the power system RoCoF are comprehensively reviewed. Finally, the open questions and related research topics of the RoCoF estimation are discussed.

Keywords: frequency stability; rate of change of frequency (RoCoF); power system stability; phasor measurement unit (PMU)

Citation: Deng, X.; Mo, R.; Wang, P.; Chen, J.; Nan, D.; Liu, M. Review of RoCoF Estimation Techniques for Low-Inertia Power Systems. *Energies* **2023**, *16*, 3708. https://doi.org/10.3390/en16093708

Academic Editor: Abu-Siada Ahmed

Received: 23 February 2023
Revised: 14 April 2023
Accepted: 24 April 2023
Published: 26 April 2023

1. Introduction

1.1. Motivation and Background

With the goal to decrease carbon emissions, inverter-based resources (IBRs) including wind and solar generation and energy storage systems play increasingly important roles in modern power systems around the world [1,2]. With the increasingly high penetration of IBRs, a lack of rotational inertia gradually becomes a common issue for power systems [3,4]. One of the significant results is the decreasing frequency stability of power systems. The operating frequency of low-inertia IBR-leading systems is vulnerable to any disturbance; the rate of change of frequency (RoCoF) will rapidly increase following a contingency, which leads to large frequency deviations and even the cascading failure of the system [5–7].

Severe blackouts occurring in recent years are typical extreme results for unexpected large RoCoFs following a contingency, e.g., the "8.9" blackout in Britain in 2019 [8]. In this context, the maximal RoCoF during the frequency evaluation of a power system has become a key index to indicate the frequency security of power systems [9,10], which can be used to evaluate the security margin for the potential risk to trigger the unexpected frequency protections that can lead to the cascading failure of the system. In modern power systems, the node frequency is obtained by local measurement; the corresponding RoCoF, therefore, is also local [11,12]. For an interconnected large power system, the long electrical distances among the nodes and the uneven inertia distribution lead to complicated spatial features of dynamic frequency. It means that the local RoCoF can be improper for use as the index of the frequency security of the entire system, as it can be at a significantly different level [13]. In this context, it is important to find a "center" RoCoF that can present the stability and security features of the entire system.

With a clear definition of the power system RoCoF that indicates the frequency security of the entire power system, newly developed artificial intelligence (AI) techniques have been applied to predict the maximal RoCoF following the potential contingencies of a system based on historical operating datum [14,15].

Meanwhile, faced with increasing frequency security and stability challenges for power systems, modern control strategies of IBRs have been developed to provide inertia and frequency support to the grid. To achieve the fast frequency response, RoCoF tends to be used as one of the input signals for these modern control techniques, e.g., virtual inertia control [16,17]. Moreover, RoCoF can feed to the newly developed protections, e.g., RoCoF relay [18,19]. Therefore, to ensure the smooth operating of the modern controllers and protections fed by the RoCoF signal, accurate real-time RoCoF tracking is crucial. Considering the mathematical nature of RoCoF, namely, a rate of change of a time-variant variable, RoCoF cannot be directly measured but needs to be computed by the internal algorithm of measuring devices for the real-time variables of AC systems. The most common measurement device that allows to track the RoCoF is the synchrophasor [20]. The accuracy and robustness against the measurement noise of the obtained RoCoF highly depend on the estimation techniques. At present, discrete Fourier transform (DFT) is still the most widely used phasor estimation technique [21–23]. However, the accuracy of this technique is still questionable, especially when phase jump issues occur [24,25]. To further increase the accuracy and reliability of RoCoF tracking, correlation phasor algorithms have been developed in recent years, which can be roughly divided into the following three categories: DFT-based methods, Kalman filter techniques, and other methods.

1.2. Contribution

This paper aims to provide a comprehensive review of RoCoF estimation techniques for power systems including related concepts and estimation techniques. The specific contributions of the paper are the following:

(i) Discussion on the role of the RoCoF in power system cascading failure and understanding the power system RoCoF;
(ii) Review the estimation and prediction techniques of the maximal RoCoF following a contingency;
(iii) Review the different methods of RoCoF real-time tracking techniques with a discussion on the advantages and disadvantages as well as the further development of existing methods.

1.3. Oriagnization

The rest of this paper is organized as follows. Section 2 discusses the typical blackouts occurring in recent years, explains the physical and numerical characteristics of power system RoCoF, and introduces the concept of "center" RoCoF. In Section 3, the estimation and prediction techniques of the maximal RoCoF following a contingency are reviewed, and a power system with zero rotational inertia is discussed in depth. Section 4 reviews the existing RoCoF real-time tracking techniques. The conclusions and related future research topics are provided in Section 5.

2. Frequency Stability of the Low-Inertia Power System

This section firstly discusses the typical blackouts in recent years that resulted from a lack of inertia and especially analyzes the features of the RoCoF during the dynamic evaluation of the blackouts, and then explains the "role" of the inertia and RoCoF in modern power systems. On this basis, the concept of "center" RoCoF is introduced. Table 1 lists the nomenclature of parameters in Section 2.

Table 1. Section 2 nomenclature.

Variable	Description
H_{eq}, H_G, H_V	Equivalent inertia constant of the power system, synchronous generator and IBRs
f^0, f_{CoI}, f	Normal frequency, frequency of center of inertia, and inner frequency of the sources
ΔP_G	The change of the output power from the generations providing the frequency support to the system
ΔP_L	The unbalanced active power caused by the contingency
D	The damping factor of the power system
S	The rated power
N_G, N_V	The number of synchronous machines and IBRs
$\mathbf{f}_B$	The vector consisting of the node frequency of the power system
$\mathbf{f}_G$	The vector consisting of the equivalent speed of the generation set
$\mathbf{A}$	The parameter matrix of the power system
$\overline{\mathbf{Y}}$	The admittance matrix of the power system
$\mathbf{h}$	Normalized inertia constants with dimension $m \times 1$
$\mathbf{1}_{n\times 1}, \mathbf{I}_m$	Identity matrix with dimension $n \times 1$ and unit matrix with dimension $m \times m$

2.1. Typical Blackouts in Low-Inertia Systems

The rotational inertia level of the power system continuously decreases alongside the adjustment of the energy composition structure of the power grid [3]. In recent years, frequency collapses caused by a lack of inertia have occurred in many countries, which largely increases attention to the frequency security and stability of modern power systems. Figure 1 summarizes the typical blackouts in low-inertia systems from recent years.

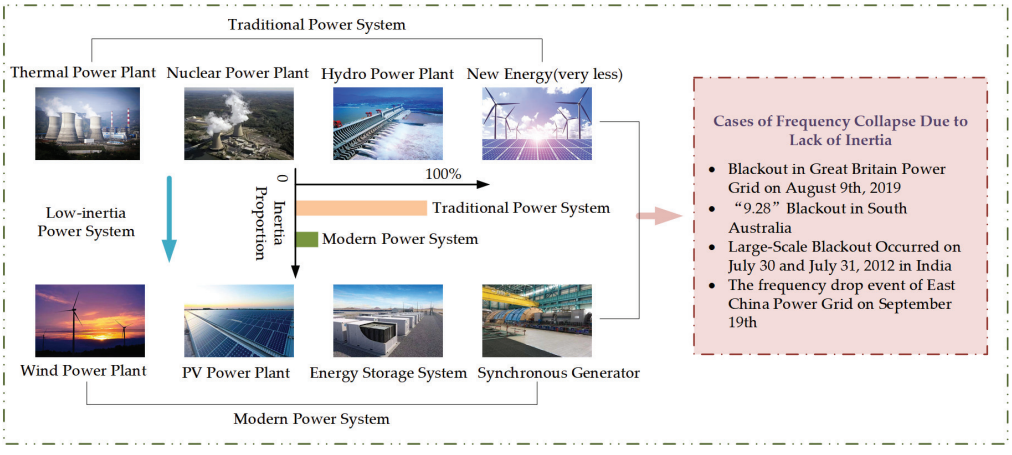

Figure 1. Frequency security problems of low-inertia systems.

The details for each blackout shown in Figure 1 are the following:

(i) British "8.9" blackout: At around 17:00 local time on 9 August 2019, due to a lightning strike, a single-phase grounding short-circuit fault occurred on a transmission line in the British power system and caused the successive disconnection of the Little Barford gas power station and Hornsea offshore wind plant as their frequency protections were triggered. The inertia of the British power system at that time was 210 GW·s [8], for the 30% wind penetration. The RoCoF of the British system was recorded at 500 ms and 0.135 Hz/s following the contingency [8], which is over the threshold of the RoCoF protection of the most distributed sources at 0.125 Hz/s [8,26] and thus led to the extra 345 MW power loss due to the cut-off of the distributed sources. As a result, an under-frequency load shedding (UFLS) of the system was triggered, and finally led to a large-scale power outage in England and Wales. The load loss was about 3.2% of the whole British system and about 1 million people were affected. During this incident, the unexpectedly

large RoCoF resulted in the unexpected trip of the generation units, and therefore, the occurrence of UFLS.

(ii) South Australia "9.28" blackout: On the afternoon of 28 September 2016, local time, a severe typhoon and storm hit South Australia and caused the break of six transmission lines. The voltage drop occurred six times within 2 min at the point of common coupling (PCC) of the wind farm at Davenport, which led to the large-scale cut-off of wind generations and resulted in the loss of the generation of 445 MW [27]. To maintain the frequency stability of the state system, there was about 850–900 MW of power imported by the Heywood tie line that went beyond its maximal capacity at 600 MW [28]. Finally, the state grid was isolated due to the trip of the Heywood tie line and thus the power supply of the entire state was interrupted for about 50 h. At the time of the accident, the wind and solar power penetration of the South Australia system was 48.36%, and the inertia of the system was 3000 MW·s, the lowest level in history. At the beginning of the accident, the RoCoF reached 6.1 Hz/s and the frequency nadir was 47 Hz, i.e., −3 Hz below the nominal value [27–29].

(iii) India "7.30" and "7.31" blackouts: On 30–31 July 2012, the largest power outage occurred in India since 2000, which affected 20 Indian states and more than 600 million residents. The normal frequency of the Indian power system is 49.5~50.2 Hz [30], which allows for relatively large frequency fluctuations compared with the other countries with strong power systems. On the day the blackout occurred, 47 transmission lines above 400 kV were out of work for maintenance, which further weakened the grid. At the beginning of this event, the 220 kV transmission line Gwalior–Malanpur I tripped, which led to a cascading failure including the disconnection between the western and northern India power systems. The northern India power system collapsed after 25 s of the disconnection. On the following day, the Rajasthan State generation unit tripped and was followed by the trip of the 220 kV Badod Modak line [30,31]. After 2 min, the disconnection of the western and eastern Indian power system occurred, which was followed by the collapse of the eastern and northern systems. The total installed capacity of the Indian power grid was 202,979 MW, and the renewable energy penetration rate of the system was 33.66% [31,32]. The typical low-inertia features resulted in a large RoCoF following the contingency and thus led to the above two cascading failures. Frequency deviations over 1.2 Hz were observed during the blackout [32].

According to the above discussion, a relatively low-inertia level and extremely high RoCoF was recorded during these events. Therefore, the following subsection discusses the "role" of inertia and RoCoF for modern power systems.

2.2. The "Role" of Inertia and RoCoF for Modern Power Systems

Power system frequency stability refers to the power system's ability to maintain a stable frequency following a large disturbance that leads to the unbalance between the power supply and load demand [3,33]. The collapse of the frequency stability observed in typical blackouts is discussed in the above subsection. For a power system that maintains the frequency stability following a contingency, its frequency evolution trajectory is shown in Figure 2, which can be divided into four stages [34,35]: inertia response, primary frequency control (PFC), secondary frequency control (SFC), and tertiary frequency control (TFC).

As we can see in Figure 2, at the first stage of the evolution, the frequency drops following the contingency. At this stage, the inertial response dominates the frequency dynamics by converting the kinetic energy into electrical energy to depress the frequency deviation from the normal value. The larger the inertia, the more the stored kinetic energy is, and therefore, the smaller the RoCoF is at this stage [2,36,37]. When the frequency is out of the dead band of the turbine governor (TG), the TG acts and the PFC is triggered. With the effect of PFC, the frequency starts to recover from the nadir. Note that the stages that are dominated by the inertial response and the PFC can be partly overlapped [34], as shown in the yellow area of Figure 2. There usually exists a quasi-steady status with obvious frequency deviations at the second stage of the frequency evolution due to the limited effect

of PFC. Since then, in the following SFC and TFC dominant stages, the frequency slowly recovers to the normal value with the RoCoF approaching zero.

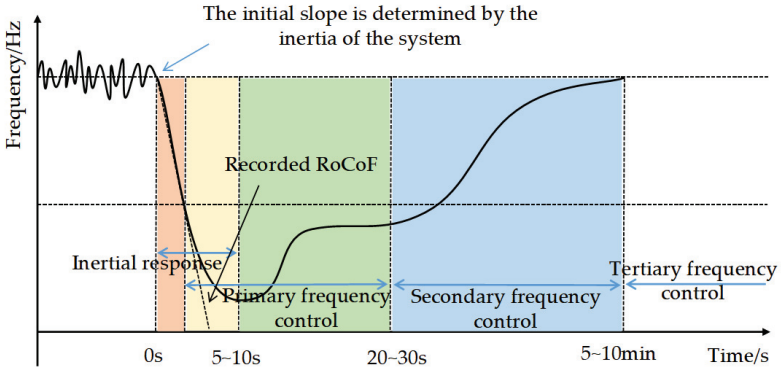

Figure 2. Typical frequency evolution of a power system.

According to the above discussion, the RoCoF estimation for the initial response and PFC-dominant stages is interesting. One can introduce the following equation to describe the relationship between the inertia and RoCoF [34,38]:

$$\frac{2H_{eq}}{f^0}\frac{df_{CoI}}{dt} = \Delta P_G(t) - \Delta P_L - D_{eq}\Delta f \tag{1}$$

where Δf is the frequency deviation from the normal frequency; H_{eq} can be computed by Equation (2):

$$H_{eq} = \frac{\sum_{i=1}^{N_G} H_{G,i}S_i + \sum_{j=1}^{N_V} H_{V,j}S_j}{\sum_{i=1}^{N_G} S_i + \sum_{j=1}^{N_V} S_j} \tag{2}$$

where $H_{G,i}$ is the equivalent inertia constant of the i-th synchronous generator; S_i is the rated power of the i-th synchronous generator; $H_{V,j}$ is the equivalent inertia constant of the j-th IBRs providing virtual inertia to the grid; S_j is the rated power of the j-th IBRs. Equation (2) indicates that the inertia of the grid mainly consists of two parts, namely the rotational inertia from synchronous generator and the virtual inertia from IBRs [34]. It is worth noting that $H_{V,j}$ is usually unknown and time-varying because it depends on the operating state and control method of the IBR. The relevant inertia estimation techniques for power systems with high penetrations of IBRs have therefore been developed in recent years [34,39,40], which can be the technical foundation to predict the critical value of the RoCoF of the power system.

With the developing interconnections between regional grids, the modern power system has an increasingly wider geographical distribution. The inertia level of different subsystems can be very different due to the uneven distributions of the synchronous generator with large inertia and the IBR that cannot provide inertia support. In this context, the frequency event occurring at different places within the power system may be followed by the frequency evaluation with very different features, including the RoCoF. Therefore, the distribution of the inertia, to some extent, shapes the temporal and spatial characteristics of the dynamic frequency.

2.3. Concept of "Center" RoCoF

2.3.1. Frequency of CoI and Its Estimation Method

The real-world power system constantly suffers from the disturbances of the stochastics of renewable power and load and can be attacked by unpredictable events such as a

tripped critical transmission line and unexpected loss of generation, which leads to the ever-changing frequency of the system [41]. The dynamic frequency at each node of the power system is under the impact of many factors [38,42], e.g., the local inertia level and distances from the disturbances, and therefore, can be different from each other. Professor F. Milano proposes the following frequency divider formula (FDF) to describe the spatial distribution of the power system frequency [43]:

$$\begin{cases} \mathbf{f}_B = \mathbf{1} + \mathbf{A}(\mathbf{f}_G - \mathbf{1}) \\ \mathbf{A} = -(\mathrm{Im}\{\overline{\mathbf{Y}}_{BB} + \overline{\mathbf{Y}}_{B0}\})^{-1}\mathrm{Im}\{\overline{\mathbf{Y}}_{BG}\} \end{cases} \tag{3}$$

where $\overline{\mathbf{Y}}_{BB}$ is the admittance matrix of power grid; $\overline{\mathbf{Y}}_{B0}$ is a diagonal matrix, which takes into account the internal impedances of synchronous generators at the generator buses; $\overline{\mathbf{Y}}_{BG}$ is the admittance matrix at the bus.

As FDF implies, the dynamic frequency at each node of the power system is different [43,44]. The concept of frequency of center of inertia (CoI) is proposed to present the "center" frequency (also abbreviated as system frequency in some reports and papers) of the power system [38,45–48]:

$$f_{CoI} = \frac{\sum_{i=1}^{N} H_{eq,i} f_i}{\sum_{i=1}^{N} H_{eq,i}} \tag{4}$$

where $H_{eq,i}$ and f_i are the inertia constant and the inner frequency of the i-th sources.

Reference [46] proposes the following expression to estimate the frequency of the CoI:

$$\begin{cases} f^*_{CoI} = \boldsymbol{\xi}^T \mathbf{f}_B + \boldsymbol{\alpha} \\ \boldsymbol{\xi}^T = -\mathbf{h}^T \mathrm{Im}\{\overline{\mathbf{Y}}^+_{BG}\}\mathrm{Im}\{\overline{\mathbf{Y}}_{BB} + \overline{\mathbf{Y}}_{B0}\} \\ \boldsymbol{\alpha} = 1 - \boldsymbol{\xi}^T \mathbf{1}_{n,1} \end{cases} \tag{5}$$

where $\overline{\mathbf{Y}}^+_{BG}$ is the left inverse of $\overline{\mathbf{Y}}_{BG}$, i.e., $\overline{\mathbf{Y}}^+_{BG}\overline{\mathbf{Y}}_{BG} = \mathbf{I}_m$; the i-th element of $\mathbf{h}$ is $h_i = H_i/H_T$ and $H_T = \sum_{j=1}^{m} H_j$.

2.3.2. RoCoF of the Frequency of CoI

With the concept of frequency of CoI, we can deduce the "center" RoCoF that can present the frequency security feature of the power system as the time derivative of the frequency of CoI. The threshold to trigger the RoCoF protection of the power system in some countries, such as Britain [49] and Denmark [49], has been set as a maximal value of the system RoCoF.

3. Estimation and Prediction of the Maximal RoCoF following a Contingency

According to the above discussion, the maximal RoCoF of the system discussed in this section is derived from the frequency of CoI following a contingency. This section discusses the estimation and prediction of the maximal RoCoF following a contingency. It is worth noting that the maximal RoCoF prediction techniques still need to be improved in accuracy and interpretability. Relevant solutions are provided in this section, mainly using the method of slope estimation. The magnitude of the maximal RoCoF highly depends on the contingency and the inertia level of the system, which is an important index to present the frequency security of the power system [49–51]. This section discusses the estimation of the maximal RoCoF following an already-occurred event and the prediction of the maximal RoCoF following a potential contingency of the system; the specific classification is shown in Figure 3. Table 2 lists the nomenclature of parameters in Section 3.

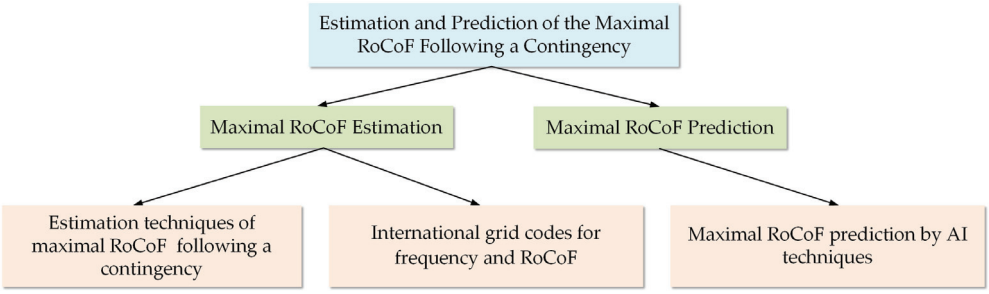

Figure 3. Taxonomy of offline RoCoF estimation techniques for power systems.

Table 2. Section 3 nomenclature.

Variable	Description
$\widetilde{f}$	Averaged system frequency
T	A short period following the contingency
$f(t_0), f(t_0+T)$	The pre-contingency frequency and the frequency of a short period T following the contingency
RoCoF_m^*	The approximated maximal RoCoF

3.1. Maximal RoCoF Estimation

The most commonly used estimation method of the maximal RoCoF is calculating the maximal RoCoF from the obtained trajectory of the dynamic frequency following an event. This method can provide the most accurate RoCoF to the Transmission System Operators (TSOs). The curve fitting technique used to analyze the maximal power system RoCoF is found in reference [52], where a fifth-order polynomial to mimic the frequency response of the power system is proposed and the "analytic" RoCoF function as the first-time derivative of the polynomial can be obtained. One can easily deduce the maximal RoCoF according to the obtained RoCoF function. Then, reference [53] assumes a polynomial to describe the dynamic frequency $\widetilde{f}$ of the power system:

$$\widetilde{f}(t) = k[1 + \sigma e^{-\varsigma\omega_n t}\sin(\omega_r t + \phi)] \tag{6}$$

where $k, \sigma, \varsigma, \omega_n, \omega_r$, and ϕ are unknown parameters of $\widetilde{f}$ and t is the time, these parameters need to be identified according to the dynamic behavior of the system. Following that work, reference [54] proposes an adaptive polynomial fitting technique to describe the dynamic frequency and also the RoCoF.

During the frequency evolution following a contingency, however, since the completed frequency trajectory is not available, the maximal RoCoF "saw" by the control and operation center (recorded as RoCoF_m^* in the remainder of the paper) of the system is usually the approximated value calculated by the data of the frequency obtained within a very short period following the contingency [35,52–54]:

$$\text{RoCoF}_m^* = \frac{f(t_0+T) - f(t_0)}{T} \tag{7}$$

where $f(t_0)$ is usually very close to the nominal value. The specific T for different grid codes is listed in Table 3.

Table 3. International grid codes for frequency and RoCoF.

Grid Code	T	Security Threshold (Normal Frequency)
IEEE [55]	N.A.	0.4 Hz/s (60 Hz)
Denmark [49,56]	500 ms	2 Hz/s (50 Hz)
Ireland [49,56]	200 ms	1 Hz/s (50 Hz)
UK [56]	500 ms	1 Hz/s (50 Hz)
Germany [49,56]	500 ms	2 Hz/s (50 Hz)
Australia [49]	N.A.	No standard for RoCoF (50 Hz)
USA [49,57]	N.A.	No standard for RoCoF (60 Hz)

Table 3 shows the typical approximated maximal RoCoF and their corresponding security thresholds from different grid codes [49,55–57]. As we can see in Table 3, the method to define the RoCoF_m^* and its security threshold for several European countries has been issued, while there is no specific rule in the IEEE standards to estimate RoCoF_m^* but a security threshold for the maximal RoCoF is provided. Australian and USA grid codes have not listed a clear requirement for RoCoF yet, but the related discussions become increasingly broad with the increasingly high penetration of the IBRs in these national grids.

The security threshold of a system RoCoF has to be small enough to protect the on-grid devices under extreme scenarios, while it also has to be large enough to avoid triggering unexpected cascading failures. Therefore, the RoCoF threshold in some countries, e.g., the UK and Ireland, has been modified with the developed online devices and increasingly high penetration of IBRs in recent years [49,56]. Ireland increased the RoCoF threshold from 0.5 Hz/s to 1 Hz/s in 2020 [49]. The new settings for RoCoF may be issued with the development and application of virtual inertia techniques.

3.2. Maximal RoCoF Prediction

With the rapid development of AI techniques in recent years, the applications of AI on the stability and security assessment of power systems have become a hot topic [2,14,15]. One of the typical applications of the AI algorithm on power system analysis is predicting the possible behavior of the system via training the proposed algorithm to learn from the historical operation datum. In this context, the AI algorithms that can predict the maximal RoCoF of the potential contingencies of the power system have been proposed.

Reference [14] utilizes a deep learning network based on stacked denoising auto encoders to predict the indexes of the frequency evolutions following the possible large disturbances including the maximal frequency deviation, maximal RoCoF, and quasi-steady-state frequency. Reference [15] proposes an online frequency security assessment method based on the multi-layer extreme learning machine (ML-ELM). In the process of unsupervised training, an automatic encoder algorithm and regularization coefficient are utilized to optimize layer by layer, which can accurately predict the maximal RoCoF with a relatively small computational burden.

Although AI techniques are supposed to have a wide application for power system analysis, in the current phase, the lack of interpretability raises a common doubt for their further development in the power system field [39]. A reliable and accurate maximal RoCoF prediction AI technique that can actually assist the TSO with satisfied interpretability may be still on the way.

3.3. Towards the Power System with Zero Rotational Inertia

To date, 100% renewable energy systems have been built and can operate safely and stably for a long time. For example, many countries have built or are close to building 100% renewable energy power systems, including hydro, wind, and solar power sources [1,3,58,59]. The hydropower included in renewable energy power systems can provide rotational inertia to the grid, and at the same time, these kinds of power systems are always equipped with synchronous compensators to improve the voltage stability of the power system, which

can also provide rotational inertia [1,3]. Therefore, the 100% renewable energy system can be regarded as a low-inertia power system rather than a zero rotational inertia system.

At present, Xinjiang, China, as the energy base of China, has built a typical ultra-high proportion new energy power system, including 100% new energy areas with only solar, wind power, and energy storage devices, but it has not reached the situation with zero rotational inertia, because there is still asynchronous motors existing in the load side, providing a small amount of inertia support. Theoretically speaking, if there is no asynchronous motor at all on the load side, then the system can be regarded as zero inertia, and since the load side is also 100% power electronic equipment, then this system no longer needs to maintain a 50/60 Hz nominal frequency, because all equipment is connected to the power system via power electronic converters, and even a pure DC system can be formed. However, this kind of system does not exist at present because most of the electrical equipment is designed to operate normally at the nominal frequency. Even if the power supply is 100% power electronization, the system still operates around the nominal frequency in order to satisfy the requirement of most power consumption devices. In this context, to avoid damaging the load-side electrical equipment, the frequency security and stability needs to be ensured by inertial support that depress the frequency fluctuations and extremely high RoCoF [3].

Based on the above discussion, it is necessary to use virtual inertia techniques to provide inertia support to suppress the drastic changes in frequency and RoCoF in all the real-world power systems now and in the near future [60,61]. Considering that virtual inertia is uncertain compared with the constant rotational inertia, because virtual inertia is a typical control technique of the power electronic converters, the effect of the control can be easily affected by the adjustable parameters and the state of the energy sources [60–62]. Therefore, it will become more challenging to set a reasonable RoCoF security threshold and potential RoCoF prediction techniques in the power system with virtual inertia as the main inertial support form due to the high uncertainty of the spatial and temporal distribution of the virtual inertia.

4. Real-Time RoCoF Tracking Techniques

According to the well-known frequency definition of AC power system given in IEEE Std. IEC/IEEE 60255-118-1 [63], the RoCoF can be presented as

$$\text{RoCoF} = \dot{f}(t) = \frac{1}{2\pi}\ddot{\vartheta}(t) = \frac{1}{2\pi}\ddot{\theta}(t) \tag{8}$$

where ϑ is the angular position of the signal $x(t) = X_m(t)\cos(\vartheta(t))$ [63]; θ is the phase difference between the angular position ϑ of the signal x(t) and the phase caused by the reference normal frequency. Equation (8) implies that the measurement device that can track the dynamic voltage/current phase at a node of the power system, namely the synchrophasor, can be used to track the real-time local RoCoF with a proper algorithm; however, RoCoF estimation techniques face great challenges in accuracy and robustness. This section provides a comprehensive review of the existing real-time RoCoF tracking algorithms of synchrophasors, which can be divided into three main categories: (i) DFT-based [64–76], (ii) Kalman filter techniques [77–92], and (iii) other methods [93–100]. The details for each category are provided in the subsection. The specifics are shown in Figure 4. Table 4 lists the nomenclature of parameters in Section 4.

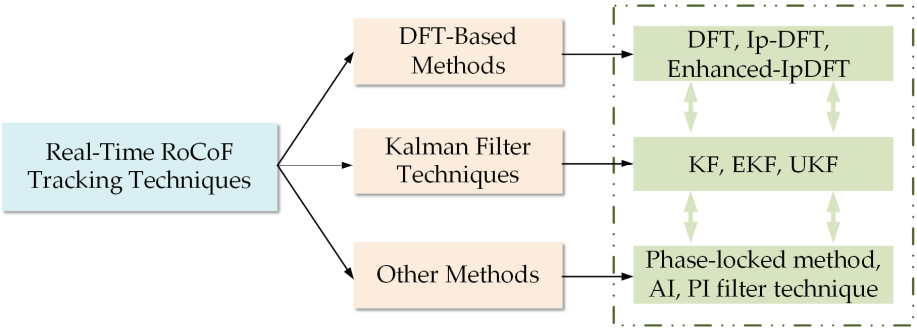

Figure 4. Taxonomy of real-time RoCoF tracking techniques.

Table 4. Section 4 nomenclature.

Variable	Description
V_m	The magnitude of the voltage waveforms
f	The signal frequency to be estimated
ϕ_V	The phase angle
T_s	The sampling interval
f_s	The sampling frequency
$\mathbf{x}$	The vector of state variables
$\mathbf{z}$	The vector of measurements
$\mathbf{u}$	The control vector
$\mathbf{A}$	The state transition matrix
$\mathbf{B}$	The control matrix
$\mathbf{H}$	The measurement matrix
$\mathbf{w}$	The column vector of process noise
$\mathbf{v}$	The column vector of measurement noise
$\hat{\square}$	Estimated values
$\square^-$	Predicted values
$\square^T$	Transposition of the matrix
$\mathbf{P}$	Covariance matrix
$\mathbf{Q}$	Covariance of process noise
$\mathbf{K}$	Kalman gain matrix
$\mathbf{R}$	Covariance of measurement noise
$L, \lambda, \alpha, \kappa, \beta$	Adjustable parameters of UKF algorithm
$\mathbf{f}, \mathbf{h}$	Vectors consisting of nonlinear state transition functions and measurement functions
$\mathbf{W}^{(m)}, \mathbf{W}^{(c)}$	Weights for the mean and covariance, respectively
K_p, K_i, T_f	PI filter parameters

4.1. DFT-Based Methods

DFT is the most basic and common signal processing method at present. The DFT method can be used to calculate the amplitude phase angle, frequency, and RoCoF of the input signals collected by synchrophasors [64–68]. The voltage/current waveform of the AC power system measured by the synchrophasor can be described as the following:

$$V(t) = V_m \cos(2\pi f t + \phi_V) \tag{9}$$

DFT refers to transforming a discrete time series with finite length into a signal in frequency domain, by sampling the signal at given intervals. For a periodic signal, N points are sampled in each T period, namely, $T = NT_s$. The voltage signal in the frequency domain obtained via DFT is given by

$$V(k) = \sum_{n=0}^{N-1} V(n) e^{-j\frac{2\pi}{N}nk}, k = 0, 1, 2 \ldots N-1 \tag{10}$$

where k is the frequency bin index, n is the sample index.

The dynamic frequency of the system can be estimated by finding the frequency bin index k that corresponds to the largest magnitude in the frequency domain (recorded as k_m). The highest frequency bin represents the fundamental waveform of the signal and its frequency can be the coarse estimation as follows [69]:

$$f_c = k_m \frac{f_s}{N} \tag{11}$$

Because of the spectral leakage and fence effect in sampling, DFT may introduce obvious errors for the processing of signals with relative rapid variations [69–71]. In this context, the improved DFT methods with higher accuracy and robustness against the sampling techniques are developed for real-time RoCoF tracking in the power system.

Reference [71] proposes a windowed DFT which allows the tracking of frequency deviation under various power system operation conditions and RoCoF and presents the satisfied accuracy defined by the IEEE standards.

The interpolated DFT (IpDFT) is another well-known technique, which estimates the synchrophasors by interpolating the DFT spectrum of the signal [72]. The windowed interpolation techniques are used to suppress the spectral leakage of DFT methods via introducing an appropriate window function for sampling. The interpolated DFT can be represented mathematically as follows:

$$V(k) = \sum_{n=0}^{N-1} V(n) e^{-j\frac{2\pi}{N}n(k+\Delta k)}, k = 0, 1, 2 \ldots N-1 \tag{12}$$

where Δk is the interpolation factor and the selection of Δk is related to the window function. In particular, the IpDFT applying windowing function to reduce the spectral leakage effects [66,72,73]. References [67,72,74,75] prove that with proper window function, the IpDFT can largely reduce the errors resulting from the spectral leakage. The Hanning window is better than the traditional rectangular window, with a reduced leakage and fluctuation for IpDFT.

Reference [72] proposes an enhanced IpDFT algorithm for synchronous phasor frequency estimation that computes RoCoF as the first-time derivative of the obtained frequency passing by a low-pass filter. The enhanced IpDFT algorithm combines three different methods to reduce the influence of errors caused by spectrum interference, including windowing, DFT interpolation, and iterative solution [76].

4.2. Kalman Filter Techniques

The Kalman filter technique is widely used in the field of the power system state estimation [77–79]. The real-time RoCoF tracking techniques based on the Kalman filter can effectively avoid the impact of harmonics and noise of the input signal fed into the synchrophasor through solving the optimal estimation problem of the continuous prediction–correction operation [78,80,81]. Kalman filter techniques require the establishment of appropriate state equations and measurement equations that can be solved iteratively; the basic formulas of the standard Kalman filter are shown in (13)–(15) [82,83].

The state/measurement equations of the Kalman filter are

$$\begin{cases} \mathbf{x}_k = \mathbf{A}\mathbf{x}_{k-1} + \mathbf{B}\mathbf{u}_{k-1} + \mathbf{w}_{k-1} \\ \mathbf{z}_k = \mathbf{H}\mathbf{x}_k + \mathbf{v}_k \end{cases} \tag{13}$$

where the subscript k represents the k-th iteration.

The prediction steps of the equations are

$$\begin{cases} \hat{\mathbf{x}}_k^- = \mathbf{A}\hat{\mathbf{x}}_{k-1} + \mathbf{B}\mathbf{u}_{k-1} \\ \mathbf{P}_k^- = \mathbf{A}\mathbf{P}_{k-1}\mathbf{A}^T + \mathbf{Q} \end{cases} \tag{14}$$

The update steps of the equations are

$$\begin{cases} \mathbf{K}_k = \mathbf{P}_k^- \mathbf{H}^T (\mathbf{H}\mathbf{P}_k^- \mathbf{H}^T + \mathbf{R})^{-1} \\ \hat{\mathbf{x}}_k = \hat{\mathbf{x}}_k^- + \mathbf{K}_k (\mathbf{z}_k - \mathbf{H}\hat{\mathbf{x}}_k^-) \\ \mathbf{P}_k = (\mathbf{I} - \mathbf{K}_k \mathbf{H}) \mathbf{P}_k^- \end{cases} \tag{15}$$

Reference [83] proposes a method based on the standard Kalman filter in solving the frequency and RoCoF as the state variables, the estimation error of the obtained RoCoF is below 0.1 Hz/s. Reference [84] uses the wavelet-based signal pre-processing technique to remove the noise of the frequency obtained through the wide-area measurement system and then estimates the corresponding RoCoF through a Kalman filter technique similar to the method proposed in [83]. Reference [82] proposes a method based on the Smoothed Taylor–Kalman filter (STKF) technique to track the RoCoF; this method is a linear system based on the Taylor series expansion and the Kalman filter. By using the backward filter based on the smoother, the accuracy of STKF on tracking the frequency and RoCoF is much improved compared with the classic Kalman filter.

References [24,25] show that phase jumps of the input signal resulting from faults can lead to an erroneous frequency and RoCoF estimation. To deal with this issue, the Extended Kalman filter (EKF) and Unscented Kalman filter (UKF) techniques are used for the frequency and RoCoF estimation of the power system. UKF always shows a higher accuracy and better numerical stability than EKF by introducing the unscented transformation (UT) technique to replace the linearization step of EKF [85]. The UKF, therefore, is the most advanced Kalman filter technique for the power system frequency and RoCoF estimation at present. The basic steps of the UKF algorithm are presented in Algorithm 1 [85–87].

From the basic equation of UKF shown in Algorithm 1, it can be found that UKF is consistent with the basic Kalman filter algorithm, including prediction step and update step; UKF, based on UT, abandons the traditional method of linearizing nonlinear functions, and uses UT to deal with the nonlinear transfer of mean and covariance, which becomes the UKF algorithm. It is worth noting that in the process of selecting sigma points, three parameters are very important [88,89]: α determines the distribution state of sigma points, usually $0 \leq \alpha \leq 1$; the specific value of κ depends on the situation, for the case of Gaussian distribution, when the state variable is univariate, $\kappa = 2$ is selected, and when it is multivariate, $\kappa = 3 - L$ is generally used to determine the value of κ; the parameter to be adjusted, β, can improve the accuracy of variance. For Gaussian distribution, $\beta = 2$ is the optimal value.

Reference [90] proposes an algorithm of interpolated DFT combined with UKF, which estimates the frequency and corresponding RoCoF in two steps: firstly, the frequency through the IDFT with the Hanning window is tracked; and then, the UKF method is used to observe the system state including RoCoF, and the accuracy meets all IEEE standards for RoCoF estimation. References [87,91,92] show that the computational complexity of the UKF increases dramatically with the larger system size and therefore may not suit the real-world power system.

Several methods to improve the computational efficiency and the numerical stability of the UKF have been developed, which broaden the applications of UKF on the system with high dimension and nonlinearity, including the real-world power system. Reference [87] points out that during the iterations of the UKF algorithm to solve the dynamic states of the power system, the estimation error covariance $\mathbf{P}$ with positive semi-definiteness may not exist. Therefore, the $\sqrt{\mathbf{P}}$ in the unscented transformation stage cannot be computed properly and the iteration would be terminated without an effective result. Reference [87] compares six different methods to cope with this issue, including the 'schol' algorithm, parameter optimization, modifying the covariance matrix (utilized in the step 3 and 6 in Algorithm 1), modifying the predicted covariance matrix (utilized in the step 3 in Algorithm 1), and using the square-root UKF (SR-UKF) form. The results show that the effect of the SR-UKF that introduces the guaranteed positive semi-definite estimation error covariance is the best at avoiding this numerical issue. In the implementation of SR-UKF,

$\sqrt{\mathbf{P}}$ is considered instead of $\mathbf{P}$ to avoid refactorizing $\mathbf{P}$ at each step, and therefore, effectively improves the computational efficiency and numerical stability of the UKF without the loss of any accuracy.

Algorithm 1: Unscented Kalman Filter

1. Compute the sigma points:
$\chi_{k-1} = [\hat{\mathbf{x}}_{k-1}, \hat{\mathbf{x}}_{k-1} + \mathbf{E}, \hat{\mathbf{x}}_{k-1} - \mathbf{E}]$
where $\mathbf{E} = \sqrt{(L+\lambda)\mathbf{P}_{k-1}}$
$\chi_k^- = \mathbf{f}(\chi_{k-1})$
2. Predict the state:
$\hat{\mathbf{x}}_k^- = \sum_{i=0}^{2L} \mathbf{W}_i^{(m)} \chi_{i,k}^-$
3. Predict the covariance:
$\mathbf{P}_k^- = \sum_{i=0}^{2L} \mathbf{W}_i^{(c)} [\chi_{i,k}^- - \hat{\mathbf{x}}_k^-][\chi_{i,k}^- - \hat{\mathbf{x}}_k^-]^T + \mathbf{Q}$
where $\begin{cases} \mathbf{W}_0^{(m)} = \lambda/(L+\lambda) \\ \mathbf{W}_0^{(c)} = \lambda/(L+\lambda) + (1-\alpha^2+\beta) \\ \mathbf{W}_i^{(m)} = \mathbf{W}_i^{(c)} = 1/2(L+\lambda) \end{cases}$
4. The propagated sigma points with measurement function:
$\mathbf{Z}_k^- = \mathbf{h}(\chi_{k-1})$
5. The predicted measurement:
$\hat{\mathbf{z}}_k^- = \sum_{i=0}^{2L} \mathbf{W}_i^{(m)} \mathbf{Z}_{i,k}^-$
6. Compute measurement covariance:
$\mathbf{P}_{\mathbf{z}_k\mathbf{z}_k} = \sum_{i=0}^{2L} \mathbf{W}_i^{(c)} [\mathbf{Z}_{i,k}^- - \hat{\mathbf{z}}_k^-][\mathbf{Z}_{i,k}^- - \hat{\mathbf{z}}_k^-]^T + \mathbf{R}$
7. Compute cross-covariance:
$\mathbf{P}_{\mathbf{x}_k\mathbf{z}_k} = \sum_{i=0}^{2L} \mathbf{W}_i^{(c)} [\chi_{i,k}^- - \hat{\mathbf{x}}_k^-][\mathbf{Z}_{i,k}^- - \hat{\mathbf{z}}_k^-]^T$
8. The Kalman Gain:
$\mathbf{K}_k = \mathbf{P}_{\mathbf{x}_k\mathbf{z}_k} \mathbf{P}^{-1}_{\mathbf{z}_k\mathbf{z}_k}$
9. Update the state:
$\hat{\mathbf{x}}_k = \hat{\mathbf{x}}_k + \mathbf{K}_k(\mathbf{z}_k - \hat{\mathbf{z}}_k^-)$
10. Update the covariance:
$\mathbf{P}_k = \mathbf{P}_k^- - \mathbf{K}_k \mathbf{P}_{\mathbf{z}_k\mathbf{z}_k} \mathbf{K}_k^T$

4.3. Other Methods

Reference [93] proposes an orthogonal phase-locked method for frequency estimation that is combined with gradient descent algorithm to model the system. This method tracks the rate of change of angular frequency through Equation (16):

$$\dot{\omega} = -\rho_2 A^2 \sin(2\psi) + 2\rho_2 A^2 u(t) \cos(2\psi) \tag{16}$$

where

$$\begin{cases} A = \sqrt{A_s^2 + A_c^2} \\ \psi = \phi + \tan^{-1}(\frac{A_c}{A_s}) \end{cases} \tag{17}$$

where ρ is the coefficient that the advised value is 0.5; $u(t)$ is the input signal; A_c and A_s obtain the optimal parameters through gradient descent algorithm. This orthogonal phase-locked method can accurately track the dynamic frequency and the corresponding RoCoF with high robustness against the measurement noise and harmonics. In reference [94], the power system frequency and RoCoF are obtained by computing the space vector (SV) in a reference frame that rotates at the rated angular frequency. Based on [94], reference [95] proposes a digital phase-locked loop to improve the accuracy of the SV-based RoCoF estimation algorithm, by constructing the instantaneous position of a rotating reference frame.

Reference [96] proposes a least square method based on polynomial curve fitting to improve the robustness of RoCoF calculation. Reference [97] designs an accurate RoCoF

estimation algorithm combining DFT and least squares method, which solves the inevitable RoCoF estimation error caused by noise and disturbance in the real frequency measurement through ingenious design. In addition, before using the algorithm, a median filter is designed and applied, and the window size of the algorithm is determined by analyzing the historical event data. Simulation results show that the accuracy of this method in frequency estimation is far less than that of the IEEE standard (the maximum frequency error is 0.005 Hz), and the online/offline RoCoF estimation is compared and analyzed with a time window of 0.3 s, with high accuracy. Reference [98] proposes the generalized Taylor weighted least squares (GTWLS) method to track the power system RoCoF. GTWLS is an extension of the classical Taylor weighted least squares method, which deduces the real-time RoCoF as a function of the real-time frequency deviation. To further improve the accuracy of the RoCoF estimation, reference [98] also suggests to combine the GTWLS with the IpDFT algorithm.

Reference [99] proposes an inflection point detector technique, which only uses the locally measured frequency to estimate the CoI RoCoF and does not mandate PMUs at all generator terminals. This method skillfully uses the second derivative of frequency to change the characteristics of its symbol. The local frequency curve intersects the CoI frequency curve around the inflection points of the former. By connecting the inflection points, we can obtain the approximate estimated value of the CoI frequency, so that the CoI RoCoF can be obtained, accordingly. Reference [100] proposes that the CoI frequency and RoCoF of the power system can be calculated more accurately by PMU data from multiple locations. Firstly, the equivalent inertia constant is obtained by the least squares method, and then the CoI frequency is calculated according to Equation (4), and the RoCoF is the first-time derivative of CoI frequency; the simulation results show that the error can be effectively reduced.

Reference [34] proposes a universal and lightweight PI filter technique; through the output RoCoP of the units, the internal angular frequency of the power supply can be estimated only by the deviation between the bus angular frequency measured by PMU and the rated angular frequency. Then, RoCoF can be obtained by using the first derivative of the internal angular frequency of the power supply output by the PI filter. The control block diagram of the PI filter is shown in Figure 5, and reference [34] suggests that the PI filter with parameters $K_p = 50$, $K_i = 1$, and $T_f = 0.0001$ can effectively track the local RoCoF for inertia estimation.

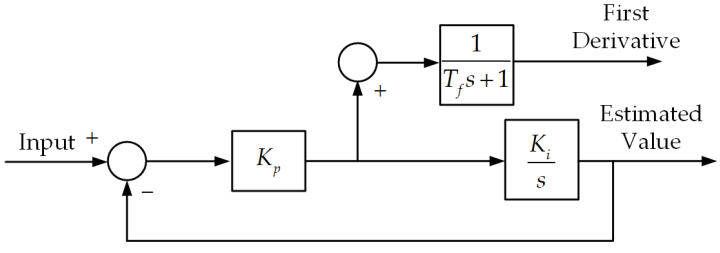

Figure 5. The control block diagram of the PI filter.

4.4. Discussions

Generally speaking, DFT is the most common signal processing method for the existing synchrophasors utilized in power systems. However, the accuracy of real-time RoCoF tracking with DFT can be very sensitive to the noise and sampling techniques. Improved DFT methods, e.g., IpDFT, can improve the accuracy of the frequency and RoCoF estimation. Kalman filter techniques are of great interest for the future development of the power system RoCoF estimation due to its high accuracy and robustness against noise and harmonics. Especially, the improved UKF technique has been proven to be feasible and reliable for the power system state estimation. The heavy computational burden, however, still limits the application of Kalman filter techniques on the real-time RoCoF tracking of the

real-world power system. The RoCoF estimation combining the DFT with the Kalman filter can further improve computational efficiency and accuracy. In addition to the above two kinds of techniques, new methods for phase lock, e.g., orthogonal phase-locked method and digital phase-locked loop, have also been developed to track power system frequency and RoCoF. In addition, new methods of combining the least squares method with other estimation techniques, such as the combination of DFT and least squares method, and GTWLS techniques, have made good progress in RoCoF estimation, are also considered to further improve the accuracy and robustness of the RoCoF estimation. In addition, the inflection point detector techniques and PI filter are also new methods that have been developed in recent years; the former skillfully uses the second derivative of frequency to change the characteristics of its symbol and realize the accurate estimation of RoCoF, while the latter can also realize the accurate estimation by choosing appropriate parameters.

5. Conclusions

In low-inertia power systems, the magnitude of the RoCoF can be a crucial index to present the frequency security and stability of the system. Meanwhile, real-time RoCoF tracking can be a key foundation for the development of advanced control and protection techniques in the low-inertia system. This paper discusses the basic concept and estimation techniques of power system RoCoFs. A comprehensive review on the estimation and prediction methods of maximal RoCoF following a contingency and the real-time RoCoF tracking techniques is provided. The review indicates that with the lack of inertia gradually becoming a common and increasingly more severe issue for power systems around the world, the research related to the analysis and estimation of the power system RoCoF can be increasingly more important. Several potential research topics in related fields are provided; the conclusions are as follows:

(i) Grid codes and standards for RoCoF: With the increasingly high penetration of IBRs and the diversified inertia support in the future power system including both the rotational and virtual inertia, the setting of security threshold for the RoCoF will be further studied in order to protect the in-grid devices and avoid potential cascading failure.

(ii) AI techniques for the RoCoF prediction of the power system: The wide application of synchrophasors that can record the dynamic frequency and corresponding RoCoF ensures the rich source of training datum for AI techniques to assess the frequency security and stability of power systems. According to the review, several studies have already been concerned with predicting the maximal RoCoF following the potential contingency of the system, and further research on AI techniques is needed in the future to solve the problem of poor robustness and interpretability of AI techniques. We can expect further development on this topic with the rapid development of AI techniques.

(iii) Real-time RoCoF tracking algorithm with increased accuracy and reliability: Although the existing real-time RoCoF tracking algorithms embedded into the synchrophasor perform a relatively satisfied accuracy, the errors can be induced due to reasons such as the phase jump following a fault. These errors may result in an unexcepted fatal issue for the power system if the obtained RoCoF is fed to the control or protection. Therefore, further research on RoCoF estimation is needed in the future, so as to further improve the accuracy and robustness of RoCoF estimation through the fusion of multiple algorithms.

Author Contributions: Conceptualization, X.D. and R.M.; methodology X.D. and M.L.; resources R.M., P.W. and D.N.; writing-original draft preparation X.D.; writing-review and editing X.D. and J.C.; supervision M.L. All authors have read and agreed to the published version of the manuscript.

Funding: This research was funded by [Science Foundation Project of Xinjiang Province and China Postdoctoral Science Foundation] grant number [2021D01C088 and 2021M702749].

Data Availability Statement: Not applicable.

Conflicts of Interest: The authors declare no conflict of interest.

References

1. Kroposki, B.; Johnson, B.; Zhang, Y.C.; Gevorgian, V.; Denholm, P.; Hodge, B.M.; Hannegan, B. Achieving a 100% Renewable Grid: Operating Electric Power Systems with Extremely High Levels of Variable Renewable Energy. *IEEE Power Energy Mag.* **2017**, *15*, 61–73. [CrossRef]
2. Liu, M.Y.; Chen, J.R.; Xie, Y.S.; Deng, X.Y.; Milano, F. Least Square Method for the Identification of Equivalent Inertia Constant. In Proceedings of the 2022 IEEE Power & Energy Society General Meeting (PESGM), Denver, CO, USA, 17–21 July 2022.
3. Milano, F.; Dörfler, F.; Hug, G.; Hill, D.J.; Verbič, G. Foundations and Challenges of Low-Inertia Systems (Invited Paper). In Proceedings of the 2018 Power Systems Computation Conference (PSCC), Dublin, Ireland, 11–15 June 2018.
4. Winter, W.; Elkington, K.; Bareux, G.; Kostevc, J. Pushing the Limits: Europe's New Grid: Innovative Tools to Combat Transmission Bottlenecks and Reduced Inertia. *IEEE Power Energy Mag.* **2015**, *13*, 60–74. [CrossRef]
5. Panda, R.K.; Mohapatra, A.; Srivastava, S.C. Application of Indirect Adaptive Control Philosophy for Inertia Estimation. In Proceedings of the 2019 IEEE PES GTD Grand International Conference and Exposition Asia (GTD Asia), Bangkok, Thailand, 19–23 March 2019.
6. Mo, R.; Deng, X.Y.; Liu, M.Y.; Chang, X.Q. Ambient-Measurement-Based Equivalent Inertia Constant Identification Via Tikhonov Regularization Algorithm. In Proceedings of the 2022 International Conference on Renewable Energies and Smart Technologies (REST), Tirana, Albania, 28–29 July 2022.
7. Nedd, M.; Browell, J.; Bell, K.; Booth, C. Containing a Credible Loss to Within Frequency Stability Limits in a Low-Inertia GB Power System. *IEEE Trans. Ind. Appl.* **2020**, *56*, 1031–1039. [CrossRef]
8. Pandey, A.; Kumar, S.; Mohire, S.; Pentayya, P.; Kazi, F. Dynamic Modeling and Cascade Failure Analysis of the Mumbai Grid Incident of October 12, 2020. *IEEE Access* **2022**, *10*, 43598–43610. [CrossRef]
9. Frigo, G.; Derviškadić, A.; Zuo, Y.H.; Paolone, M. PMU-Based ROCOF Measurements: Uncertainty Limits and Metrological Significance in Power System Applications. *IEEE Trans. Instrum. Meas.* **2019**, *68*, 3810–3822. [CrossRef]
10. Albu, M.; Dumitrescu, A.M.; Popovici, R. Rate of change of frequency—A power quality descriptor. In Proceedings of the 2014 16th International Conference on Harmonics and Quality of Power (ICHQP), Bucharest, Romania, 25–28 May 2014.
11. Milano, F.; Ortega, Á. A Method for Evaluating Frequency Regulation in an Electrical Grid-Part I: Theory. *IEEE Trans. Power Syst.* **2021**, *36*, 183–193. [CrossRef]
12. Ortega, Á.; Milano, F. A Method for Evaluating Frequency Regulation in an Electrical Grid-Part II: Applications to Non-Synchronous Devices. *IEEE Trans. Power Syst.* **2021**, *36*, 194–203. [CrossRef]
13. Zhao, J.B.; Mili, L.; Milano, F. Robust Frequency Divider for Power System Online Monitoring and Control. *Trans. Power Syst.* **2018**, *33*, 4414–4423. [CrossRef]
14. Zhao, R.Z.; Wen, Y.F.; Ye, X.; Tang, Q.; Li, W.Y.; Chen, Y.H.; Qu, X.B. Research on Frequency Indicators Evaluation of Disturbance Events Based on Improved Stacked Denoising Autoencoders. *Proc. CSEE* **2019**, *39*, 4081–4093.
15. Wen, Y.F.; Zhao, R.Z.; Xiao, Y.Q.; Liu, Z.B. Power system frequency stability assessment based on multi-layer extreme learning machine. *Autom. Electr. Power Syst.* **2019**, *43*, 133–143.
16. Hu, Y.L.; Wei, W.; Peng, Y.G.; Lei, J.Y. Fuzzy virtual inertia control for virtual synchronous generator. In Proceedings of the 35th Chinese Control Conference, Chengdu, China, 27–29 July 2016.
17. Maaruf, M.; Ferik, S.E.; Al-Ismail, F.S.; Khalid, M. Robust Optimal Virtual Inertia Control for Microgrid Frequency Regulation Considering High Renewable Energy Penetration. In Proceedings of the 1st IEEE International Conference on Renewable Energy Research and Applications, Istanbul, Turkey, 18–21 September 2022.
18. Gupta, P.; Bhatia, R.S.; Jain, D.K. Active ROCOF Relay for Islanding Detection. *IEEE Trans. Power Deliver.* **2017**, *32*, 420–429. [CrossRef]
19. Alam, M.R.; Begum, M.T.A.; Muttaqi, K.M. Assessing the Performance of ROCOF Relay for Anti-Islanding Protection of Distributed Generation Under Subcritical Region of Power Imbalance. *IEEE Trans. Ind. Appl.* **2019**, *55*, 5395–5405. [CrossRef]
20. *IEEE Std C37.118^{TM}.1-2011 (Revision of IEEE Std C37.118^{TM}-2005)*; IEEE Standard for Synchrophasor Measurements for Power Systems. IEEE Power & Energy Society: Piscataway, NJ, USA, 2011; pp. 1–61.
21. Wang, M.H.; Sun, Y.Z. A practical method to improve phasor and power measurement accuracy of DFT algorithm. *IEEE Trans. Power Deliver.* **2006**, *21*, 1054–1062. [CrossRef]
22. Yang, R.G.; Xue, H. A Novel Algorithm for Accurate Frequency Measurement Using Transformed Consecutive Points of DFT. *IEEE Trans. Power Syst.* **2008**, *23*, 1057–1062. [CrossRef]
23. Castello, P.; Liu, J.Q.; Muscas, C.; Pegoraro, P.A.; Ponci, F.; Monti, A. A Fast and Accurate PMU Algorithm for P+M Class Measurement of Synchrophasor and Frequency. *IEEE Trans. Instrum. Meas.* **2014**, *63*, 2837–2845. [CrossRef]
24. Wright, P.S.; Davis, P.N.; Johnstone, K.; Rietveld, G.; Roscoe, A.J. Field Measurement of Frequency and ROCOF in the Presence of Phase Steps. *IEEE Trans. Instrum. Meas.* **2019**, *68*, 1688–1695. [CrossRef]
25. Roscoe, A.J.; Dyśko, A.; Marshall, B.; Lee, M.; Kirkham, H.; Rietveld, G. The Case for Redefinition of Frequency and ROCOF to Account for AC Power System Phase Steps. In Proceedings of the 2017 IEEE International Workshop on Applied Measurements for Power Systems (AMPS), Liverpool, UK, 20–22 September 2017.
26. Li, T.; Li, Y.; Li, S.; Zhang, W. Research on Current-Limiting Control Strategy Suitable for Ground Faults in AC Microgrid. *IEEE J. Emerg. Sel. Top. Power* **2021**, *9*, 1736–1750. [CrossRef]

27. Masood, N.A.; Yan, R.F.; Saha, T.K. Cascading Contingencies in a Renewable Dominated Power System: Risk of Blackouts and Its Mitigation. In Proceedings of the 2018 IEEE Power & Energy Society General Meeting (PESGM), Portland, OR, USA, 5–10 August 2018.
28. Jamborsalamati, P.; Moghimi, M.; Hossain, M.J.; Taghizadeh, S.; Lu, J.; Konstantinou, G. A Framework for Evaluation of Power Grid Resilience Case Study: 2016 South Australian Blackout. In Proceedings of the 2018 IEEE International Conference on Environment and Electrical Engineering and 2018 IEEE Industrial and Commercial Power Systems Europe (EEEIC/I&CPS Europe), Palermo, Italy, 12–15 June 2018.
29. Yan, R.F.; Masood, N.A.; Saha, T.K.; Bai, F.F.; Gu, H.J. The Anatomy of the 2016 South Australia Blackout: A Catastrophic Event in a High Renewable Network. *IEEE Trans. Power Syst.* **2018**, *33*, 5374–5388. [CrossRef]
30. Lai, L.L.; Zhang, H.T.; Mishra, S.; Ramasubramanian, D.; Lai, C.S.; Xu, F.Y. Lessons learned from July 2012 Indian blackout. In Proceedings of the 9th IET International Conference on Advances in Power System Control, Operation and Management (APSCOM 2012), Hong Kong, China, 18–21 November 2012.
31. Rampurkar, V.; Pentayya, P.; Mangalvedekar, H.A.; Kazi, F. Cascading Failure Analysis for Indian Power Grid. *IEEE Trans. Smart Grid* **2016**, *7*, 1951–1960. [CrossRef]
32. Suresh, V.; Sutradhar, R.; Mandal, S.; Debnath, K. Near Miss of Blackout in Southern Part of North Eastern Grid of India. In Proceedings of the 2020 3rd International Conference on Energy, Power and Environment: Towards Clean Energy Technologies, Shillong, Meghalaya, India, 5–7 March 2021.
33. Hartono, J.; Pramana, P.A.A.; Kusuma, A.A.; Munir, B.S. Power System Inertia Estimation Based on Frequency Measurement. In Proceedings of the 2019 Asia Pacific Conference on Research in Industrial and Systems Engineering (APCoRISE), Depok, Indonesia, 18–19 April 2019.
34. Liu, M.Y.; Chen, J.R.; Milano, F. On-Line Inertia Estimation for Synchronous and Non-Synchronous Devices. *IEEE Trans. Power Syst.* **2021**, *36*, 2693–2701. [CrossRef]
35. Delkhosh, H.; Seifi, H. Power System Frequency Security Index Considering All Aspects of Frequency Profile. *IEEE Trans. Power Syst.* **2021**, *36*, 1656–1659. [CrossRef]
36. Sun, M.; Xie, G.W.; Chen, L.; Liu, Y.M.; Li, X.J.; Min, Y. Study on the Necessity and Role of Inertia in Power System Frequency Response. In Proceedings of the 2020 IEEE 4th Conference on Energy Internet and Energy System Integration (EI2), Wuhan, China, 30 October–1 November 2020.
37. Bevrani, H.; Golpîra, H.; Messina, A.R.; Hatziargyriou, N.; Milano, F.; Ise, T. Power system frequency control: An updated review of current solutions and new challenges. *Electr. Power Syst. Res.* **2021**, *194*, 107114. [CrossRef]
38. Kundur, P. *Power System Stability and Control*; McGraw-Hill: New York, NY, USA, 1994.
39. Tan, B.D.; Zhao, J.B.; Netto, M.; Krishnan, V.; Terzija, V.; Zhang, Y.C. Power System Inertia Estimation: Review of Methods and the Impacts of Converter-Interfaced Generations. *Int. J. Elec. Power* **2022**, *134*, 107362. [CrossRef]
40. Hatziargyriou, N.; Rahmann, C.; Canizares, C.; Hiskens, I.; Pourbeik, P.; Cutsem, T.V. Definition and Classification of Power System Stability–Revisited & Extended. *IEEE Trans. Power Syst.* **2021**, *36*, 3271–3281.
41. Wen, J.X.; Bu, S.Q.; Li, F.X.; Du, P.W. Risk assessment and mitigation on area-level RoCoF for operational planning. *Energy* **2021**, *228*, 120632. [CrossRef]
42. Zhao, J.B.; Tang, Y.; Terzija, V. Robust Online Estimation of Power System Center of Inertia Frequency. *IEEE Trans. Power Syst.* **2019**, *34*, 821–825. [CrossRef]
43. Milano, F.; Ortega, Á. Frequency divider. *IEEE Trans. Power Syst.* **2017**, *32*, 1493–1501.
44. Ortega, Á.; Milano, F. Frequency Participation Factors. *IEEE Trans. Power Syst.* **2018**, *33*, 5563–5571. [CrossRef]
45. Wen, J.X.; Bu, S.Q.; Zhou, B.W.; Chen, Q.Y.; Yang, H.K. A Fast-Algorithmic Probabilistic Evaluation on Regional Rate of Change of Frequency (RoCoF) for Operational Planning of High Renewable Penetrated Power Systems. *Energies* **2020**, *13*, 2780. [CrossRef]
46. Milano, F. Rotor Speed-Free Estimation of the Frequency of the Center of Inertia. *IEEE Trans. Power Syst.* **2018**, *33*, 1153–1155. [CrossRef]
47. Sauer, P.W.; Pai, M.A. *Power System Dynamics and Stability*; Prentice Hall: Upper Saddle River, NJ, USA, 1998.
48. Milano, F. *Power System Modelling and Scripting*; Springer: London, UK, 2010.
49. Bašakarad, T.; Holjevac, N.; Kuzle, I.; Ivanković, I.; Zovko, N. Rocof Importance in Electric Power Systems with High Renewables Share: A Simulation Case for Croatia. In Proceedings of the 12th Mediterranean Conference on Power Generation, Transmission, Distribution and Energy Conversion (MEDPOWER 2020), Online Conference, 9–12 November 2020.
50. Doheny, D.; Conlon, M. Investigation into the local nature of rate of change of frequency in electrical power systems. In Proceedings of the 2017 52nd International Universities Power Engineering Conference (UPEC), Heraklion, Greece, 28–31 August 2017.
51. Ghosh, R.; Tummuru, N.R.; Rajpurohit, B.S.; Monti, A. Virtual Inertia from Renewable Energy Sources: Mathematical Representation and Control Strategy. In Proceedings of the 2020 IEEE International Conference on Power Electronics, Smart Grid and Renewable Energy (PESGRE2020), Cochin, India, 2–4 January 2020.
52. Inoue, T.; Taniguchi, H.; Ikeguchi, Y.; Yoshida, K. Estimation of power system inertia constant and capacity of spinning-reserve support generators using measured frequency transients. *IEEE Trans. Power Syst.* **1997**, *12*, 136–143. [CrossRef]
53. Du, P.W.; Makarov, Y. Using Disturbance Data to Monitor Primary Frequency Response for Power System Interconnections. *IEEE Trans. Power Syst.* **2014**, *29*, 1431–1432. [CrossRef]

54. Phurailatpam, C.; Rather, Z.H.; Bahrani, B.; Doolla, S. Measurement-Based Estimation of Inertia in AC Microgrids. *IEEE Trans. Sustain. Energ.* **2020**, *11*, 1975–1984. [CrossRef]
55. *IEEE Std C37.118.1a™-2014 (Amendment to IEEE Std C37.118.1™-2011)*; IEEE Standard for Synchrophasor Measurements for Power Systems. IEEE Power & Energy Society: Piscataway, NJ, USA, 2014; pp. 1–25.
56. Bründlinger, R. *Grid Codes in Europe—Overview on the Current Requirements in European Codes and National Interconnection Standards*; AIT Austrian Institute of Technology: Vienna, Austria, 2019.
57. DGA Consulting. International Review of Frequency Control Adaptation. *Australian Energy Market Operator*, 14 October 2016.
58. Khalili, S.; Breyer, C. Review on 100% Renewable Energy System Analyses—A Bibliometric Perspective. *IEEE Access* **2022**, *10*, 125792–125834. [CrossRef]
59. Jacobson, M.Z.; Krauland, A.K.V.; Burton, Z.F.M.; Coughlin, S.J.; Jaeggli, C.; Nelli, D.; Nelson, A.J.H.; Shu, Y.B.; Smith, M.; Tan, C.; et al. Transitioning All Energy in 74 Metropolitan Areas, Including 30 Megacities, to 100% Clean and Renewable Wind, Water, and Sunlight (WWS). *Energies* **2020**, *13*, 4934. [CrossRef]
60. Roy, N.K.; Islam, S.; Podder, A.K.; Roy, T.K.; Muyyen, S.M. Virtual Inertia Support in Power Systems for High Penetration of Renewables—Overview of Categorization, Comparison, and Evaluation of Control Techniques. *IEEE Access* **2022**, *10*, 129190–129216. [CrossRef]
61. Zaid, S.A.; Bakeer, A.; Magdy, G.; Albalawi, H.; Kassem, A.M.; El-Shimy, M.E.; AbdelMeguid, H.; Manqarah, B. A New Intelligent Fractional-Order Load Frequency Control for Interconnected Modern Power Systems with Virtual Inertia Control. *Fractal Fract.* **2023**, *7*, 62. [CrossRef]
62. Wang, T.; Jin, M.X.; Li, Y.D.; Wang, J.M.; Wang, Z.P.; Huang, S.L. Adaptive Damping Control Scheme for Wind Grid-Connected Power Systems with Virtual Inertia Control. *IEEE Trans. Power Syst.* **2022**, *37*, 3902–3912. [CrossRef]
63. *IEC/IEEE 60255-118-1*; IEEE/IEC International Standard–Measuring Relays and Protection Equipment–Part 118-1: Synchrophasor for Power Systems–Measurements. IEEE: Piscataway, NJ, USA, 2018; pp. 1–78.
64. Sozanski, K.; Szczesniak, P. Advanced Control Algorithm for Three-Phase Shunt Active Power Filter Using Sliding DFT. *Energies* **2023**, *16*, 1453. [CrossRef]
65. Bertocco, M.; Frigo, G.; Narduzzi, C.; Muscas, C.; Pegoraro, P.A. Compressive Sensing of a Taylor–Fourier Multifrequency Model for Synchrophasor Estimation. *IEEE Trans. Instrum. Meas.* **2015**, *64*, 3274–3283. [CrossRef]
66. Grandke, T. Interpolation Algorithms for Discrete Fourier Transforms of Weighted Signals. *IEEE Trans. Instrum.* **1983**, *32*, 350–355. [CrossRef]
67. Belega, D.; Petri, D. Accuracy Analysis of the Multicycle Synchrophasor Estimator Provided by the Interpolated DFT Algorithm. *IEEE Trans. Instrum. Meas.* **2013**, *62*, 942–953. [CrossRef]
68. Li, Z.Q.; Zhang, W.F.; Zhuang, Z.Y.; Jin, T. A Novel Synchrophasor Estimation Based on Enhanced All-Phase DFT with Iterative Compensation and Its Implementation. *Energies* **2022**, *15*, 6964. [CrossRef]
69. Xu, C.J.; Zhou, L.Y.; Chen, C.; Zhang, Q.Y. A Low Computational Complexity Frequency Estimation Method with High Precision of Sinusoid Based on DFT. In Proceedings of the 2017 4th International Conference on Information Science and Control Engineering (ICISCE), Changsha, China, 21–23 July 2017.
70. Castello, P.; Ferrero, R.; Pegoraro, P.A.; Toscani, S. Space Vector Taylor–Fourier Models for Synchrophasor, Frequency, and ROCOF Measurements in Three-Phase Systems. *IEEE Trans. Instrum. Meas.* **2019**, *68*, 1313–1321. [CrossRef]
71. Petri, D.; Fontanelli, D.; Macii, D.; Belega, D. A DFT-based synchrophasor, frequency and ROCOF estimation algorithm. In Proceedings of the 2013 IEEE International Workshop on Applied Measurements for Power Systems (AMPS), Aachen, Germany, 25–27 September 2013.
72. Romano, P.; Paolone, M. Enhanced Interpolated-DFT for Synchrophasor Estimation in FPGAs: Theory, Implementation, and Validation of a PMU Prototype. *IEEE Trans. Instrum. Meas.* **2014**, *63*, 2824–2836. [CrossRef]
73. Jain, V.K.; Collins, W.L.; Davis, D.C. High-Accuracy Analog Measurements via Interpolated FFT. *IEEE Trans. Instrum. Meas.* **1979**, *28*, 113–122. [CrossRef]
74. Belega, D.; Macii, D.; Petri, D. Fast Synchrophasor Estimation by Means of Frequency-Domain and Time-Domain Algorithms. *IEEE Trans. Instrum. Meas.* **2014**, *63*, 388–401. [CrossRef]
75. Andria, G.; Savino, M.; Trotta, A. Windows and interpolation algorithms to improve electrical measurement accuracy. *IEEE Trans. Instrum. Meas.* **1989**, *38*, 856–863. [CrossRef]
76. Derviškadić, A.; Romano, P.; Paolone, M. Iterative-interpolated DFT for synchrophasor estimation in M-class compliant PMUs. In Proceedings of the 2017 IEEE Manchester PowerTech, Manchester, UK, 18–22 June 2017.
77. Wu, X.H.; Qian, Q.Q.; Bao, Y.Q. Demand Response Using Disturbance Estimation-Based Kalman Filtering for the Frequency Control. *Energies* **2022**, *15*, 9377. [CrossRef]
78. Namba, M.; Nishiwaki, T.; Yokokawa, S.; Ohtsuka, K.; Ueki, Y. Identification of Parameters for Power System Stability Analysis Using Kalman Filter. *IEEE Trans. Power Appar. Syst.* **1981**, *PER-1*, 37. [CrossRef]
79. Huang, C.H.; Lee, C.H.; Shih, K.J.; Wang, Y.J. Frequency Estimation of Distorted Power System Signals Using a Robust Algorithm. *IEEE Trans. Power Deliver.* **2008**, *23*, 41–51. [CrossRef]
80. Wu, C.C.; Magaña, M.E.; Cotilla-Sánchez, E. Dynamic Frequency and Amplitude Estimation for Three-Phase Unbalanced Power Systems Using the Unscented Kalman Filter. *IEEE Trans. Instrum. Meas.* **2019**, *68*, 3387–3395. [CrossRef]

81. Wan, W.K.; Feng, J.G.; Song, B.; Li, X.X. Huber-Based Robust Unscented Kalman Filter Distributed Drive Electric Vehicle State Observation. *Energies* **2021**, *14*, 750. [CrossRef]
82. Fontanelli, D.; Macii, D.; Petri, D. Dynamic synchrophasor estimation using Smoothed Kalman filtering. In Proceedings of the 2016 IEEE International Instrumentation and Measurement Technology Conference Proceedings, Taipei, Taiwan, 23–26 May 2016.
83. Gajjar, G.; Soman, S.A. Auto detection of power system events using wide area frequency measurements. In Proceedings of the 2014 Eighteenth National Power Systems Conference (NPSC), Guwahati, India, 18–20 December 2014.
84. Shaw, P.; Jena, K.M. A Novel Event Detection and Classification Scheme Using Wide-Area Frequency Measurements. *IEEE Trans. Smart Grid* **2021**, *12*, 2320–2330. [CrossRef]
85. Wilches-Bernal, F.; Wold, J.; Concepcion, R.; Budai, J. A Method for Correcting Frequency and RoCoF Estimates of Power System Signals with Phase Steps. In Proceedings of the 2019 North American Power Symposium (NAPS), Wichita, KS, USA, 13–15 October 2019.
86. Szabat, K.; Wróbel, K.; Dróżdż, K.; Janiszewski, D.; Pajchrowski, T.; Wójcik, A. A Fuzzy Unscented Kalman Filter in the Adaptive Control System of a Drive System with a Flexible Joint. *Energies* **2020**, *13*, 2056. [CrossRef]
87. Qi, J.J.; Sun, K.; Wang, J.H.; Liu, H. Dynamic State Estimation for Multi-Machine Power System by Unscented Kalman Filter with Enhanced Numerical Stability. *IEEE Trans. Smart Grid* **2018**, *9*, 1184–1196. [CrossRef]
88. Gao, C.; Sun, J. Dynamic State Estimation for Power System Based on M-UKF Algorithm. In Proceedings of the 2020 IEEE 4th Conference on Energy Internet and Energy System Integration (EI2), Wuhan, China, 30 October 2020–1 November 2020.
89. Zhao, H.Q.; Tian, B.Y. Robust Power System Forecasting-Aided State Estimation with Generalized Maximum Mixture Correntropy Unscented Kalman Filter. *IEEE Trans. Instrum. Meas.* **2022**, *71*, 9002610. [CrossRef]
90. Singh, A.K.; Pal, B.C. Rate of Change of Frequency Estimation for Power Systems Using Interpolated DFT and Kalman Filter. *IEEE Trans. Power Syst.* **2019**, *34*, 2509–2517. [CrossRef]
91. Ghahremani, E.; Kamwa, I. Online State Estimation of a Synchronous Generator Using Unscented Kalman Filter from Phasor Measurements Units. *IEEE Trans. Energy Conver.* **2011**, *26*, 1099–1108. [CrossRef]
92. Wang, S.B.; Gao, W.Z.; Meliopoulos, A.P.S. An Alternative Method for Power System Dynamic State Estimation Based on Unscented Transform. *IEEE Trans. Power Syst.* **2012**, *27*, 942–950. [CrossRef]
93. Karimi, H.; Karimi-Ghartemani, M.; Iravani, M.R. Estimation of frequency and its rate of change for applications in power systems. *IEEE Trans. Power Deliver.* **2004**, *19*, 472–480. [CrossRef]
94. Toscani, S.; Muscas, C.; Pegoraro, P.A. Design and Performance Prediction of Space Vector-Based PMU Algorithms. *IEEE Trans. Instrum. Meas.* **2017**, *66*, 394–404. [CrossRef]
95. Ferrero, R.; Pegoraro, P.A.; Toscani, S. A Space Vector Phase-Locked-Loop Approach to Synchrophasor, Frequency and Rocof Estimation. In Proceedings of the 2019 IEEE International Instrumentation and Measurement Technology Conference (I2MTC), Auckland, New Zealand, 20–23 May 2019.
96. Yao, W.X.; You, S.T.; Wang, W.K.; Deng, X.D.; Li, Y.C.; Zhan, L.W.; Liu, Y.L. A Fast Load Control System Based on Mobile Distribution-Level Phasor Measurement Unit. *IEEE Trans. Smart Grid* **2020**, *11*, 895–904. [CrossRef]
97. Yin, H.; Wu, Y.R.; Qiu, W.; Zeng, C.J.; You, S.T.; Tan, J.; Hoke, J.; Kruse, C.J.; Rockwell, B.W.; Kawamura, K.A.; et al. Precise ROCOF estimation algorithm for low inertia power grids. *Electr. Pow. Syst. Res.* **2022**, *209*, 107968. [CrossRef]
98. Belega, D.; Fontanelli, D.; Petri, D. Dynamic Phasor and Frequency Measurements by an Improved Taylor Weighted Least Squares Algorithm. *IEEE Trans. Instrum. Meas.* **2015**, *64*, 2165–2178. [CrossRef]
99. Sun, M.Y.; Liu, G.Y.; Popov, M.; Terzija, V. Azizi, S. Underfrequency Load Shedding Using Locally Estimated RoCoF of the Center of Inertia. *IEEE Trans. Power Syst.* **2021**, *36*, 4212–4222. [CrossRef]
100. You, S.T.; Li, H.Y.; Liu, S.Y.; Sun, K.Q.; Wang, W.K.; Liu, Y.L. Calculate Center-of-Inertia Frequency and System RoCoF Using PMU Data. In Proceedings of the 2021 IEEE Power & Energy Society General Meeting (PESGM), Washington, DC, USA, 26–29 July 2021.

electronics

MDPI

Article

A Gray-Box Stability Analysis Method of Grid-Connected Inverter Considering Synchronization Dynamics

Tianzhi Zheng [1], Fannie Kong [1], Guojin Li [1], Zhenmin Wang [2] and Yanming Chen [1,*]

[1] Guangxi Key Laboratory of Power System Optimization and Energy Technology, Guangxi University, Nanning 530004, China; 1602120421@st.gxu.edu.cn (T.Z.)
[2] School of Mechanical and Automotive Engineering, South China University of Technology, Guangzhou 510640, China
* Correspondence: yanmingchen@gxu.edu.cn

Abstract: The Grid-Connected Inverter (GCI) can be considered a gray box when circuit and controller parameters are missing due to intellectual property rights or parameter variations caused by aging, which poses an impediment to assessing the stability of the system. This paper presents a gray-box stability analysis method based on impedance identification of GCI considering the synchronization dynamics. The impedance frequency responses of GCI are measured by the frequency scanning method on the dq-frame. Meanwhile, the influence of synchronization dynamics and background harmonics is theoretically investigated. A vector fitting (VF) algorithm, co-designed with impedance identification, is then applied to generate polynomial transfer functions. Based on the obtained transfer functions, the stability of the GCI can be judged by the distance relationship between the prohibited area boundary and the center of the gershgorin-circle through the distance formula. Finally, the experiments of both RT-LAB and experimental prototypes are conducted to verify the feasibility of the proposed method.

Keywords: grid-connected inverter; stability criterion; weak grid; frequency scanning; vector fitting algorithm

Citation: Zheng, T.; Kong, F.; Li, G.; Wang, Z.; Chen, Y. A Gray-Box Stability Analysis Method of Grid-Connected Inverter Considering Synchronization Dynamics. *Electronics* **2023**, *12*, 2509. https://doi.org/10.3390/electronics12112509

Academic Editor: Fabio Corti

Received: 5 April 2023
Revised: 26 May 2023
Accepted: 30 May 2023
Published: 2 June 2023

1. Introduction

Grid-connected inverters (GCIs) are commonly used with renewable energy resources, power transmission systems to transmit power into the utility grid [1,2]. The ever-increasing penetration of GCI is radically changing the dynamic operations of traditional power systems. And thus, instability phenomena triggered by the GCI under different grid conditions have been increasingly reported [3,4].

To tackle the stability problems introduced by the GCI, the impedance-based stability analysis method is applied in [5,6]. In [7], an impedance analysis based on the dq coordinate frame is presented. Further studies are reported in [8,9], which reveals that the interactions between inverter and grid are characterized by the generalized Nyquist stability criterion (GNSC), and the multiple-input and multiple-output (MIMO) impedance matrix based on the dq-frame can be decomposed into four single-input-single-output (SISO) transfer functions for the stability judgment. Yet, the detailed parameters of the system are needed when implementing the transfer function-based method, which is usually a challenging task in practice, caused by the confidentiality of control parameters [10], and the variation for hardware parameters due to temperature fluctuation, and aging [11,12]. Therefore, the impedance identification to obtain the system dynamic response for the stability analysis of the GCI is increasing demanded [13].

In [14,15], a vector fitting (VF) algorithm combining impedance identification based on a frequency scanning method is proposed, and the stability of the system can be measured by the system's eigenvalues. Furthermore, the instability sources in the system, component, and parameter levels of the multiple-inverter-fed power systems can be identified

through VF and impedance frequency responses [16,17]. The VF algorithm was utilized to fit the impedance frequency response, from which the impedance transfer function was obtained. The control parameters are obtained by comparing with the actual control structure. Furthermore, the VF algorithm can be utilized for impedance remodeling in gray box systems [18] or reducing the model order of power cables [19]. In [18], a gray-box parameter identification method has been presented to identify the internal parameters of GCI. By adjusting the internal parameters of an inverter, the terminal output impedance can be reshaped to mitigate the oscillation issue that results from time-varying grid impedance. In [19], Prony analysis (PA) and VF are used to fit the frequency response and obtain the state space model of power cables, reducing the computational burden of power cable modeling and improving modeling and analysis efficiency. However, the identification of impedance by the aforementioned method does not consider the influence of perturbation, such as background harmonics, grid frequency deviation [20], and Phase Locked Loop (PLL) dynamics [21]. To improve the accuracy of the impedance measurement, more considerations, including grid harmonics, to improve the identification performances via twice-measurement can be found in [22], and the measurement method by the frequency selection principle has been investigated in [20,23]. During the impedance measurement, the voltage and current in the abc-frame need to be measured before being transformed into the dq-frame. The perturbation signals used for impedance measurement are usually designed in the dq-frame and then converted to the abc-frame. Therefore, PLL is typically used to track the system frequency online and estimate the synchronization phase angle for coordinate transformation. To reduce non-negligible phase errors caused by frequency deviation of the grid voltage, the PLL control bandwidth needs to be relatively high. However, controlling a PLL with an excessively high bandwidth may introduce undesired disturbances to impedance calculations [24,25]. And the errors of impedance identification increase with the bandwidth of PLL [21]. If a low-bandwidth PLL is employed, the tracking performance is poor under the circumstance of the time-varying frequency of grid voltage, which leads to non-negligible phase errors [26]. Hence, further research thinking about the impact of the synchronization dynamics on impedance identification should be carried out.

On the other side, the GNSC has been widely applied to the stability analysis of GCIs at the cost of complicated computation [27]. It is revealed that the GNSC is rigorous in mathematics, the eigenvalues of the impedance matrix of the MIMO systems need to be calculated at each frequency, which is a tedious process. Besides, the eigenvalue loci of MIMO systems exhibit implicit characteristics, which results in an unintuitive analysis process [28]. To facilitate the analysis, the non-diagonal elements are often neglected, which brings hidden problems to the stability analysis. In [27,29], there are two gershgorin circle bands around the diagonal elements loci when considering the non-diagonal elements, but it is still a cumbersome process on the premise of a reduced computation of the criterion. In [30,31], a G-Sum criterion has been presented, which is concisely compared to the GNSC, but it is highly conservative. In order to reduce the conservatism, the forbidden-region criterion has been proposed in [32], but the trouble still exists. In [33], the stability criterion expressions are derived by analyzing the distance between the center of gershgorin circle and the prohibited area in different cases, in which the computational procedure is relatively simple. However, four different cases need to be analyzed respectively, so that a cleaner approach is expected to evolve. For the moment, the balance between reduced computation and conservatism for the stability criterion is still an open issue.

To address the above challenges, this article presents an improved impedance calculation method, which makes it possible to accurately extract the phase difference in PLL during the frequency scanning, and the errors caused by synchronization dynamics are corrected. Besides, the frequencies of perturbations are selected to adapt background harmonics. Moreover, the distance relationship between the prohibited area and the gershgorin-circle in the complex field is divided into two different cases through the distance formula. Then, the stability of GCI can be judged. The proposed stability criterion has a much simpler computational procedure compared with the existing stability criterion.

Finally, based on the measured impedance and proposed stability criterion, the stability of the gray box GCI in different grid conditions can be analyzed.

The remainder of the paper proceeds as follows. Section 2 introduces the impedance measurement of the three-phase grid-connected inverter. The improved impedance calculation method and the proposed sufficient stability criterion and their corresponding simplified analysis are presented in Section 3. Section 4 investigates the proposed method by simulation and experiments. Finally, the conclusions are made in Section 5.

2. Impedance Measurement Three-Phase Grid-Connected Inverter

In order to simplify the analysis, an L-filtered GCI is used to discuss the proposed method. Figure 1 is the three-phase GCI and its control structure, which is based on PI controller in dq-frame. The U_{dc} is DC bus voltage, L_{inv} are filter inductors, U_g is grid voltage, and Z_g is equivalent grid impedance. I^*_{dq} is the reference value of the grid-connected current in the dq-frame, U_{abc}, I_{abc} is the grid-connected voltage and grid-connected current in the point of common coupling (PCC), respectively, I_{dq} is the grid-connected current in the dq-frame. θ is the grid synchronization angle from PLL, PI is the proportional-integral current controller.

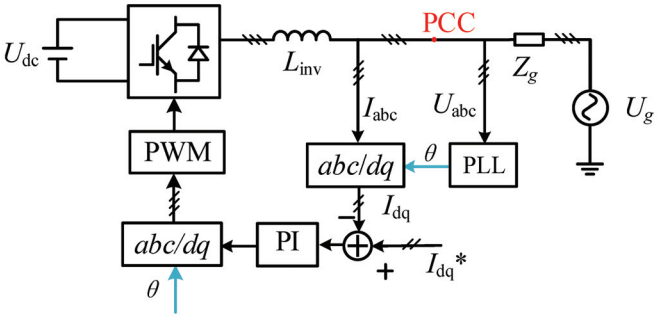

Figure 1. Three-phase grid-connected inverter and its control structure.

The impedance analysis method shows that the GCI system is stable when the ratio of the grid impedance and the output impedance of the GCI satisfies the GNSC. In a weak grid, grid impedance exhibits resistance inductance, its expression in the dq-frame is shown in Equation (1). Here, ω represents the grid synchronous angular velocity.

$$Z_g(s) = \begin{bmatrix} R_g + sL_g & -\omega L_g \\ \omega L_g & R_g + sL_g \end{bmatrix} \tag{1}$$

The ratio between the output impedance of the GCI and the grid impedance in the dq-frame, which can be expressed in terms of the return rate matrix. The rate matrix is denoted as Equation (2).

$$\mathbf{L}(s) = \begin{bmatrix} L_{dd}(s) & L_{dq}(s) \\ L_{qd}(s) & L_{qq}(s) \end{bmatrix}^T = \mathbf{Z}_g(s)\mathbf{Y}_{inv}(s) \tag{2}$$

In Equation (2), $L_{dd}(s)$, $L_{dq}(s)$, $L_{qd}(s)$, $L_{qq}(s)$ are the elements in the return rate matrix $\mathbf{L}(\mathbf{s})$. $\mathbf{Y}_{inv}(\mathbf{s})$ is the output conduction of the GCI. This can be measured by injecting voltage or current disturbances at the PCC (Point of Common Coupling). The perturbation response obtained in the abc-frame is then transformed into the dq-frame. Subsequently, the amplitude and phase of the disturbance response can be calculated using Fast Fourier

Transform (FFT). The mathematical model of the inverter voltage disturbance and current response can be expressed as

$$\begin{bmatrix} \Delta U_{\mathrm{d}} \\ \Delta U_{\mathrm{q}} \end{bmatrix} = \mathbf{Z}_{\mathrm{dq}} \begin{bmatrix} I_{\mathrm{d}} \\ \Delta I_{\mathrm{q}} \end{bmatrix} = \begin{bmatrix} Z_{\mathrm{dd}} & Z_{\mathrm{dq}} \\ Z_{\mathrm{qd}} & Z_{\mathrm{qq}} \end{bmatrix} \begin{bmatrix} \Delta I_{\mathrm{d}} \\ \Delta I_{\mathrm{q}} \end{bmatrix} \tag{3}$$

In Equation (3), Δ is the small disturbance of voltage and current at the equilibrium operating points. Z_{dd}, Z_{dq}, Z_{qd}, Z_{qq} are four unknown quantities to be measured, which represent the dq-axis impedance of the GCI and its cross-coupling impedance. In order to measure the four independent unknown quantities in Equation (3), two sets of linearly independent perturbations are injected into the system separately in the same frequency. The impedance model of the system in the dq-frame can be obtained as the following:

$$\mathbf{Z}_{\mathrm{dq}} = \begin{bmatrix} Z_{\mathrm{dd}} & Z_{\mathrm{dq}} \\ Z_{\mathrm{qd}} & Y_{\mathrm{qq}} \end{bmatrix} = \begin{bmatrix} U_{\mathrm{d1}} & U_{\mathrm{d2}} \\ U_{\mathrm{q1}} & U_{\mathrm{q2}} \end{bmatrix} \begin{bmatrix} I_{\mathrm{d1}} & I_{\mathrm{d2}} \\ I_{\mathrm{q1}} & I_{\mathrm{q2}} \end{bmatrix}^{-1} \tag{4}$$

In Equation (4), the subscript '1', '2' denotes it as two sets of linearly independent perturbations and their responses, U_{d}, U_{q}, I_{d}, I_{q} are the voltage and current in the dq-frame.

3. Theoretical Analysis

3.1. Impedance Measurement Error and Its Compensation Method

It is necessary to obtain the synchronous angle of the grid for disturbance injection and impedance calculation during impedance measurement. It is important to note that, the PLL for disturbance injection and impedance calculation is different from the PLL used in the control loop of the three-phase grid-connected inverter. Disturbance signals injected into the system and the system frequency variations affect the phase angle of the PLL, which in turn affects the calculation of impedance measurements. The GCI system exists in two different coordinate systems under the dq coordinate system in practice when the PLL dynamic is considered [30]. Considering the effect of the perturbation measurement signal injected into the GCI system on the phase angle of the PLL output during impedance measurement, the different dq-frame is represented as Figure 2.

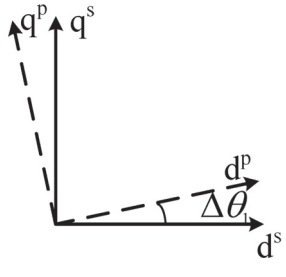

Figure 2. The dq-frames under PLL dynamics.

In Figure 2, the superscript 'p', 's' denotes the perturbation-voltage dq-frame and the PCC-voltage dq-frame, respectively. $\Delta\theta_1$ is the phase angle difference between the different dq-frames. The angular difference between different dq-frames has an impact on both the perturbation injection and impedance calculation processes, and the impact of PLL dynamics is smaller in the perturbation injection process; however, it has a greater impact on accuracy in the impedance calculation process [21]. The trigonometric function for conversion between different frames can be approximated as $\sin(\Delta\theta_1) \approx \Delta\theta_1$ and $\cos(\Delta\theta_1) \approx 1$. The Voltage components between different frames is expressed as

$$\begin{bmatrix} U_{d0}^{s} + U_{d}^{s} \\ U_{q0}^{s} + U_{q}^{s} \end{bmatrix} = \begin{bmatrix} \cos(\theta_1 + \Delta\theta_1) & \sin(\theta_1 + \Delta\theta_1) \\ -\sin(\theta_1 + \Delta\theta_1) & \cos(\theta_1 + \Delta\theta_1) \end{bmatrix} \begin{bmatrix} U_{d0}^{p} + U_{d}^{p} \\ U_{q0}^{p} + U_{q}^{p} \end{bmatrix} \tag{5}$$

In Equation (5), $U^s_{d0,q0}$ and $U^p_{d0,q0}$ are steady-state voltage components in each respective frame. $U^s_{d,q}$ and $U^p_{d,q}$ are minor disturbance voltages, θ_1 is phase angle in the perturbation-voltage dq-frame. Thus, the minor disturbance voltages between different frames is expressed as [30]

$$\begin{bmatrix} U^s_d \\ U^s_q \end{bmatrix} = \begin{bmatrix} \cos\theta_1 & \sin\theta_1 \\ -\sin\theta_1 & \cos\theta_1 \end{bmatrix} \begin{bmatrix} U^p_d \\ U^p_q \end{bmatrix} - \Delta\theta_1 \begin{bmatrix} \sin\theta_1 & -\cos\theta_1 \\ \cos\theta_1 & \sin\theta_1 \end{bmatrix} \begin{bmatrix} U^p_{d0} \\ U^p_{q0} \end{bmatrix} \tag{6}$$

The small signal transfer function of traditional PLL in the GCI can be represented as [26]

$$\begin{aligned} \Delta\theta(s) &= G_{\text{pll}}(s)U_{\text{q}} \\ G_{\text{pll}}(s) &= \frac{k_{\text{ppll}}s + k_{\text{ipll}}}{s^2 + U_{d0}k_{\text{ppll}}s + k_{\text{ipll}}} \end{aligned} \tag{7}$$

Therefore, the relationship of perturbation measurement signals in Equation (4) between different frames is

$$\begin{bmatrix} U^p_{\text{d1}} & U^p_{\text{d2}} \\ U^p_{\text{q1}} & U^p_{\text{q2}} \end{bmatrix} = \begin{bmatrix} 1 & U^s_{q0}G_{\text{pll}} \\ 0 & 1 - U^s_{d0}G_{\text{pll}} \end{bmatrix} \begin{bmatrix} U^s_{\text{d1}} & U^s_{\text{d2}} \\ U^s_{\text{q1}} & U^s_{\text{q2}} \end{bmatrix} \tag{8}$$

Similarly, the relationship between the current in the PCC-voltage dq-frame and that in the perturbation-voltage dq-frame can be simplified as

$$\begin{bmatrix} I^p_{\text{d1}} & I^p_{\text{d2}} \\ I^p_{\text{q1}} & I^p_{\text{q2}} \end{bmatrix} = \begin{bmatrix} I^s_{\text{d1}} & I^s_{\text{d2}} \\ I^s_{\text{q1}} & I^s_{\text{q2}} \end{bmatrix} + \begin{bmatrix} 0 & I^s_{q0}G_{\text{pll}} \\ 0 & -I^s_{d0}G_{\text{pll}} \end{bmatrix} \begin{bmatrix} U^s_{\text{d1}} & U^s_{\text{d2}} \\ U^s_{\text{q1}} & U^s_{\text{q2}} \end{bmatrix} \tag{9}$$

According to (8) and (9), the relationship between the measured impedance Z^p_{dq} and the actual impedance in PCC Z^s_{dq} is derived as

$$Z^p_{dq} = \begin{bmatrix} 1 & U^s_{q0}G_{\text{pll}} \\ 0 & 1 - U^s_{d0}G_{\text{pll}} \end{bmatrix} Z^s_{dq} + \begin{bmatrix} 1 & U^s_{q0}G_{\text{pll}} \\ 0 & 1 - U^s_{d0}G_{\text{pll}} \end{bmatrix} \begin{bmatrix} 0 & I^s_{q0}G_{\text{pll}} \\ 0 & -I^s_{d0}G_{\text{pll}} \end{bmatrix}^{-1} \tag{10}$$

The mismatch between the measured impedance and the actual impedance caused by the dynamic of the PLL can be mitigated when the term $U^s_{d0}G_{\text{pll}}$ and $I^s_{d0}G_{\text{pll}}$ are sufficiently small. From Equation (7), the terms $U^s_{d0}G_{\text{pll}}$ and $I^s_{d0}G_{\text{pll}}$ are equivalent to a low-pass filter. When the perturbation signal frequency is higher than the PLL bandwidth, it will be filtered, making it difficult to influence the measurement results. Yet, when the perturbation frequency is lower than the bandwidth of the phase-locked loop, the effect of the perturbation signal cannot be ignored. It is an effective way to attenuate the effect of disturbing signals on measurement results by reducing the PLL bandwidth when the frequency deviation in the grid has been ignored. If the bandwidth of the PLL is too low, there is a non-negligible angle difference $\Delta\theta_1$ when the system is subjected to harmonics and grid frequency deviation [26]. There is, thus, the impedance measurement error caused by synchronization dynamics, which cannot be completely ignored, even though the bandwidth of the PLL is designed suitably.

From the small signal model for PLL [31], the angle difference $\Delta\theta_1$ between the PLL output phase angle and the input voltage phase angle can be simplified as

$$\begin{aligned} \Delta\theta_1 &= U_q t f_{\text{pll}} \tfrac{1}{s} \\ t f_{\text{pll}} &= k_{\text{ppll}} + k_{\text{ipll}} \tfrac{1}{s} \end{aligned} \tag{11}$$

From (11), the angle difference $\Delta\theta_1$ can be extracted from PLL, and the voltage and current in the PCC-voltage dq-frame (for calculated actual impedance) can be acquired after the correction based on (8) and (9). The actual impedance of the GCI can be obtained consequently.

To calibrate the voltage and current in the perturbation-voltage dq-frame, it is crucial to accurately extract the phase differences $\Delta\theta_1$ when injecting the disturbed signal using the frequency scanning method. In this method, a single frequency excitation signal is injected at a time, and the resulting phase difference contains the corresponding frequency component. A phase extraction method is presented in Figure 3, taking into account both the filtering performance and the characteristics of the frequency scanning method. In this method, a second-order band-pass filter is utilized to extract the phase differences during impedance measurement. Its transfer function can be derived as follows:

$$G_{\mathrm{BPF}}(s) = \frac{\xi\omega_{\mathrm{n}}s}{s^2 + \xi\omega_{\mathrm{n}}s + \omega_{\mathrm{n}}^2} \tag{12}$$

In Equation (12), ω_{n} is the frequency of the disturbed signal in frequency scanning, and the ξ is chosen as 1.5.

In addition, the background harmonics of the inverter caused by the dead time and the background harmonics of the grid derived from nonlinear loads has the impact of impedance measurement [20,34]. Therefore, the frequencies of the injected perturbation signals must be carefully selected to minimize errors. Ideally, the frequencies of the perturbation signals should not overlap with the background harmonic frequencies (which are typically integral multiples of the fundamental frequency), and the signal should be sufficiently strong. By ensuring these conditions are met, the impedance can be accurately obtained.

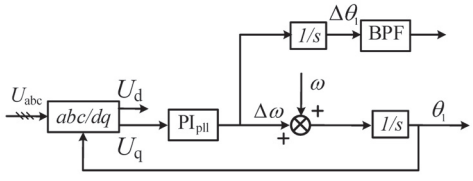

Figure 3. The improvement of PLL structure for impedance measurement.

3.2. Improved Stability Criteria Based on Gershgorin Circle Theorem

This paper considers the stability of GCI connected to the grid in weak grid conditions, but does not consider the situation when the grid is unstable ($\mathbf{Z}_{\mathrm{g}}(\mathbf{s})$ exists the unstable pole) or when the new energy-generating units are unstable ($\mathbf{Y}_{\mathrm{inv}}(\mathbf{s})$ exists the unstable pole). The GCI system is stable when the eigenvalue locus of the return rate matrix $\mathbf{L}(\mathbf{s})$ is unencircled $(-1, \mathrm{j}0)$. In GNSC, calculating system eigenvalues is a tedious process. The circle theorem uses the diagonal elements of the matrix to replace the eigenvalues of the system, ignoring the errors caused by the non-diagonal elements of the matrix, and estimates the range of the eigenvalues of the system by the diagonal and non-diagonal elements of the matrix. For the matrix of system $A = (a_{ij})$, the magnitude of the off-diagonal elements in row i is $r_i(A) = \sum_{i \neq j} |a_{ij}|$. All eigenvalues distribute in a gershgorin circle, with centers at the diagonal elements a_{ii} and radii $r_i(A)$. Thus, relationship between the eigenvalues of the return rate matrix $\mathbf{L}(\mathbf{s})$ and its four elements can be represented as follows:

$$\begin{cases} |\lambda_{\mathrm{i}}(s) - L_{\mathrm{dd}}(s)| < \left|L_{\mathrm{dq}}(s)\right| \\ \left|\lambda_{\mathrm{i}}(s) - L_{\mathrm{qq}}(s)\right| < \left|L_{\mathrm{qd}}(s)\right| \end{cases} \tag{13}$$

The forbidden region of the forbidden region based criterion (FRBC) is on display in Figure 4.

Eigenvalue trajectories of $\mathbf{L}(\mathbf{s})$ satisfy the GNSC when any frequency point of two gershgorin circles lies to the right of the parallel line $\mathrm{Re} = -1$ (all gershgorin circles are

not intersecting with the grey areas in Figure 4). Expressions for the stability of FRBC are as follows:

$$\begin{cases} \mathrm{Re}(L_{\mathrm{dd}}(s)) - \left|L_{\mathrm{dq}}(s)\right| > -1 \\ \mathrm{Re}(L_{\mathrm{qq}}(s)) - \left|L_{\mathrm{qd}}(s)\right| > -1 \end{cases} \tag{14}$$

From the foregoing, it is clear that the discussion on the diagonal elements L_{dd} and L_{qq} is basically the same. Thus, the proposed method is discussed using the element L_{dd} as an example.

In order to establish the exclusion zone, the stability margin parameters h ($0 < h < 1$) and p ($0 < p < \pi/2$) are introduced. The forbidden region of the proposed method is displayed in Figure 5.

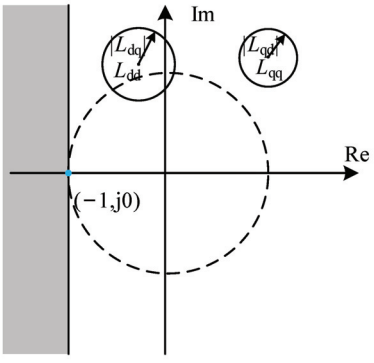

Figure 4. Forbidden region of FRBC.

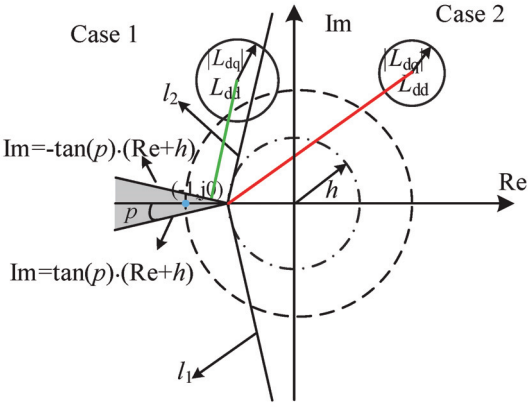

Figure 5. Forbidden region of proposed method.

In Figure 5, the complex field is divided into two cases (case1 and case2) by two straight lines (l_1 : $\mathrm{Im} = \tan(\pi/2 - p)(\mathrm{Re} + h)$ and l_2 : $\mathrm{Im} = -\tan(\pi/2 - p)(\mathrm{Re} + h)$), and the grey area is the forbidden region in the proposed method. When L_{dd} is located in case1, it is represented as follows:

$$\{L_{\mathrm{dd}} || \mathrm{Im}(L_{\mathrm{dd}}) | > \tan(\pi/2 - p) \cdot (\mathrm{Re}(L_{\mathrm{dd}}) + h)\} \cap \{L_{\mathrm{dd}} || \mathrm{Im}(L_{\mathrm{dd}}) | \geq -\tan(p) \cdot (\mathrm{Re} + h)\} \tag{15}$$

The distance between L_{dd} and the forbidden region is indicated in Figure 5 by a green line, and its equation is as follows:

$$D(s) = \frac{|\tan(p) \cdot \mathrm{Re}(L_{dd}) + \mathrm{Im}(L_{dd}) + \tan(p) \cdot h|}{\sqrt{(\tan(p))^2 + 1}} \tag{16}$$

When L_{dd} is located in case2, that is

$$\{L_{dd} || Im(L_{dd}) | \leq \tan(\pi/2 - p) \cdot (\mathrm{Re}(L_{dd}) + h)\} \tag{17}$$

The distance between L_{dd} and the forbidden region is indicated in Figure 5 by a red line, and the equation can be simplified as follows:

$$D(s) = \sqrt{(\mathrm{Re}(L_{dd}) + h)^2 + (\mathrm{Im}(L_{dd}))^2} \tag{18}$$

Then, the stability judgment can be obtained by comparing $D(s)$ and $\left|L_{dq}\right|$.

$$W(s) = D(s) - \left|L_{dq}\right| \tag{19}$$

When the stability criterion condition $W(s)$ is less than 0, the system is unstable. Apparently, the conservative condition is related to the stability margin parameters (h and p).

4. Results and Discussion

Based on the topology and the control block diagram shown in Figure 1. The impedance identification simulation model of the grid-connected inverter system is built, and the specific parameters of the model are shown in Table 1. Due to the lack of an adequate hardware platform, the proposed impedance measurement method is verified by RT-LAB. Using the RT-LAB real-time simulation platform from OPAL-RT Technologies, the GCI simulation model is built according to the system block diagram in Figure 1 and the parameters in Table 1, and the real-time simulation experimental setup is shown in Figure 6.

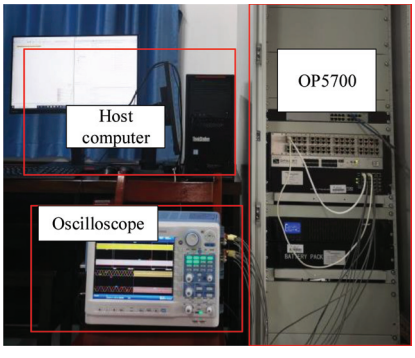

Figure 6. RT-LAB test platform.

The grid-connected inverter control and disturbance injection are implemented in the OP5700 real-time digital simulator, and the data obtained in the OP5700 are swept for impedance calculation in the Matlab software of the host computer.

Table 1. Main parameters of grid-connected inverter.

Parameter	Value	Parameter	Value
Switching frequency	15 kHz	Inductance of inverter output inductor	3 mH
Inverter input dc voltage	700 V	Grid voltage	220 V
Proportional gain of current controller	4	Integrator gain of current controller	2000
Proportional gain of inverter PLL	2.5	Integral gain of inverter PLL	50
D channel current reference	20 A	Line frequency	50 Hz

The discrete impedance data obtained are fitted with VF to obtain the analytical formula of the inverter output impedance for the stability analysis of the inverter in the subsequent section. The VF algorithm is a rational function approximation algorithm that can fit the discrete data obtained from impedance measurements to obtain the impedance transfer function of the GCI [13].

Based on the GCI model be built in the OP5700 real-time digital simulator, the voltage disturbance sources with amplitudes ranging from 5∼10% of PCC voltage are sequentially connected in series at the PCC. In addition, the bandwidth of the PLL in the impedance measurement needs to be high to track the frequency deviation, which is $k_{\mathrm{ppll}} = 0.5$ and $k_{\mathrm{ipll}} = 50$.

In Figure 7, it shows the impedance measurement results based on different measurement methods considering both the influence of the varying system frequencies, background harmonics and injected perturbations. The blue line and green dots indicate that the high bandwidth of the traditional method significantly influences the results of Z_{dq}, Z_{qd} and Z_{qq}. Nevertheless, the measured results match the analytical model to a large extent when the method proposed in this article is adopted, as shown by the red points. However, the dq coupling of the model utilized in this paper is relatively small, particularly within the low-frequency range. As a result, the perturbation voltage used for measuring Z_{dq} and Z_{qd} is unable to elicit a sufficient response across the cross axis, leading to significant discrepancies in Z_{dq} and Z_{qd} at low frequencies. Furthermore, the Z_{dq} and Z_{qd} of the model utilized in this paper is relatively small. Thus, it does not affect the stability judgment through the method proposed in this paper.

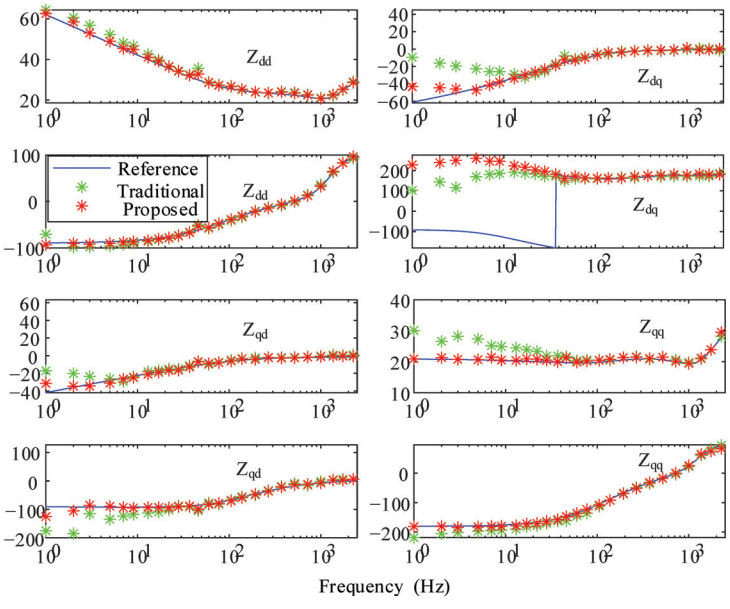

Figure 7. Impedance of GCI based on different measurement methods.

The VF algorithm is able to fit the frequency response of the discrete impedance series in the s-domain and derive a polynomial transfer function [15,16], and the polynomial transfer function can be shown as follows:

$$f(s) = \frac{\sum_{i=0}^{m} B_i s^i}{\sum_{i=0}^{m} A_i s^i} + Es \tag{20}$$

In Equation (20), m represents the order of the polynomial transfer function, E is nonzero when fitting the impedance model of the L-filtered GCI. During the VF fitting process, the impedance matrix based on the dq-frame, which is multiple-input and multiple-output (MIMO), can be broken down into four single-input and single-output (SISO) transfer functions. Before applying the VF algorithm to fit the discrete frequency response data, it is necessary to determine the order and initial poles of the function. Taking the fitting process of Z_{dd} as an example, the VF procedure can be explained in detail.

According to [35], the order of the model is an important parameter for VF, which can be chosen based on some information extracted from the system frequency response samples. In short, the number of initial poles in the VF algorithm can be quickly determined based on the resonance peaks found in the sample data, and one resonance peak corresponds to a conjugate pole pair. In addition, the frequency response of real poles is smooth. The major resonance peaks were detected using the Equation (21) when the frequency response samples Y(si) were obtained.

$$\left|y_{11}(s_{p-1})\right| < \left|y_{11}(s_p)\right| > \left|y_{11}(s_{p+1})\right| \tag{21}$$

According to [35] and Equation (21), the order of the transfer function about Z_{dd} can be selected as 3. However, increasing the order can reduce the fitting error, and in practice, selecting an order of 5 for the GCI results in a small enough fitting error [17].

After determining the initial poles, the frequency response data in Figure 7 were fitted to obtain a polynomial transfer function, as shown in Equation (20), and the coefficients of the fitted 5-order polynomial transfer functions about Z_{dd} are shown in Table 2. Similarly, we can use the same method to fit the data of Z_{dq}, Z_{qd} and Z_{qq}, as shown in Figure 8. Then, the return rate matrix can be obtained based on the fitting results and grid impedance. The curves of h1 and h2 (h1, h2 is the eigenvalue curves based on the stability criterion proposed in this article) under different SCRs are obtained in Figures 9 and 10.

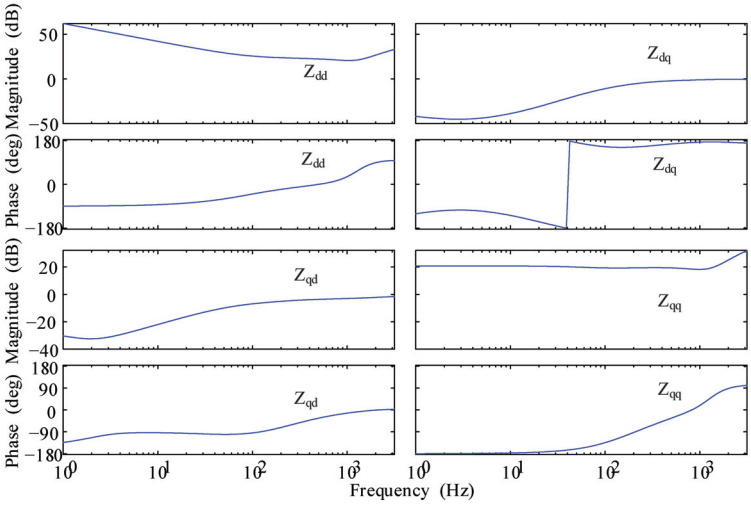

Figure 8. The results of fitting based on measured impedance.

Table 2. The coefficients of the fitted 5-order polynomial transfer functions (20) about Z_{dd}.

Parameter	Value	Parameter	Value
A_5	1	B_5	-15.979
A_4	3.3443×10^4	B_4	-1.1536×10^5
A_3	3.0308×10^8	B_3	3.6880×10^9
A_2	4.7661×10^{11}	B_2	9.16734×10^{12}
A_1	1.4220×10^{14}	B_1	5.9198×10^{15}
A_0	1.1474×10^5	B_0	1.1376×10^{18}
E	0.003		

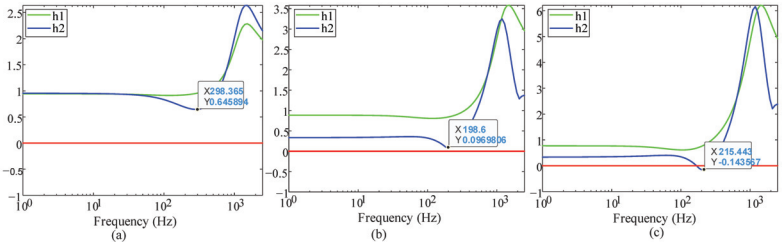

Figure 9. Curves with different SCRs based the GCI analytical model: (**a**) $SCR = 8$. (**b**) $SCR = 5$. (**c**) $SCR = 3.5$.

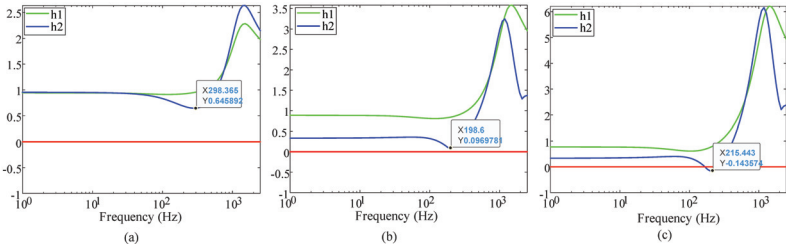

Figure 10. Curves with different SCRs based the measured model: (**a**) $SCR = 8$. (**b**) $SCR = 5$. (**c**) $SCR = 3.5$.

In Figures 9 and 10, the measurement error in Z_{dq} and Z_{qd} will not affect the stability judgment. According to the stability criterion proposed in this paper, when h1 or h2 is less than zero at any frequency, the system can be considered unstable. As shown, as the SCR drops to 3.5, the curve of h2 has two intersection points with the zero plane. Consequently, the GCI system is unstable. According to Figure 10, the frequency of the intersection of λ_2 with the unit circle less than 215 Hz.

To enhance the depiction of the instability phenomenon witnessed during the experiment, the Nyquist curves of the eigenvalue of the return rate matrix $\mathbf{L}(\mathbf{s})$ is introduced, as shown in Figure 11.

According to Figure 11, the characteristic value λ_2 of $\mathbf{L}(\mathbf{s})$ is surround the point $(-1,$ j0), the GCI system is unstable. And the frequency of the intersection of λ_2 with the unit circle is 173 s.

The experimental results of the GCI connected into a weak grid with different SCRs are based on the experimental platform in Figure 12.

Before the stability experiment, the dynamic experiment in Figure 13 was used to demonstrate the dynamic performance of the inverter system.

The experimental results under different SCRs are given in Figures 14 and 15. As shown, when the SCR decreases from 5 (shown in Figure 14) to 3.8 (shown in Figure 15), the system changes from a stable state to an unstable one.

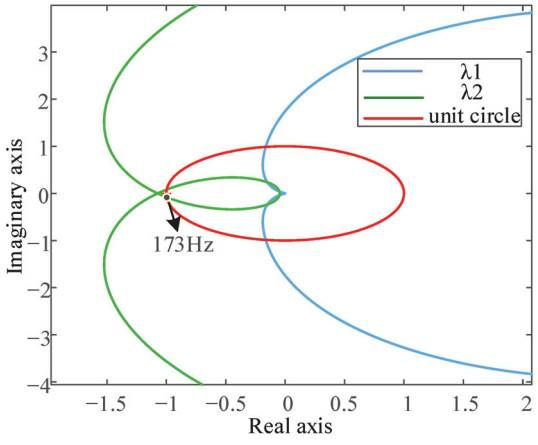

Figure 11. Nyquist curves of the characteristic values of $\mathbf{L}(\mathbf{s})$ in dq frame ($SCR = 3.5$).

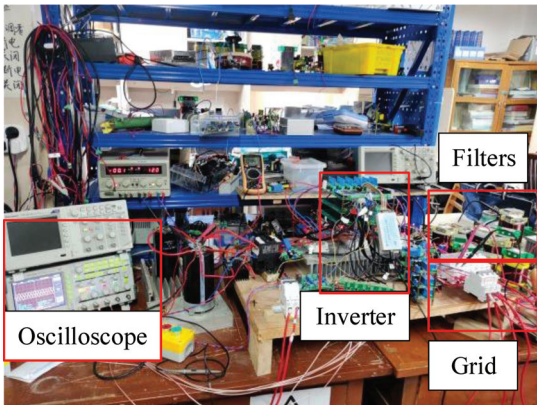

Figure 12. Experimental platform of grid-connected inverter.

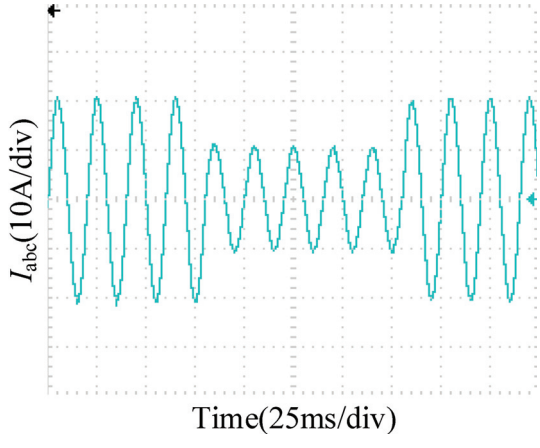

Figure 13. The dynamic experiment of a phase in GCI.

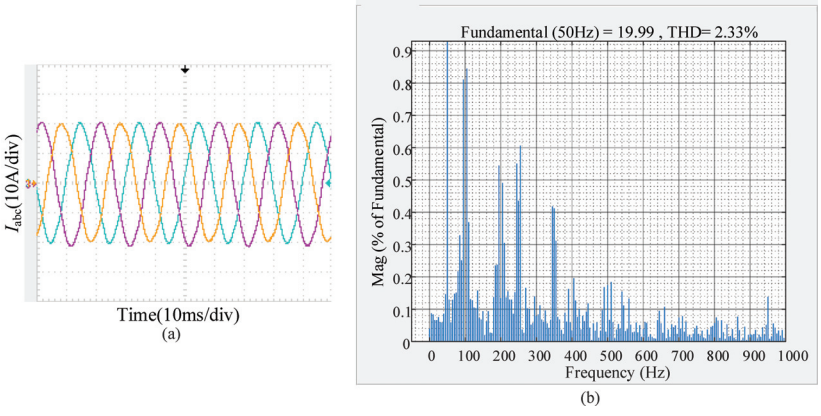

Figure 14. Experiment results of GCI with $SCR = 5$. (**a**) Output current waveforms of GCI; (**b**) THD of output current.

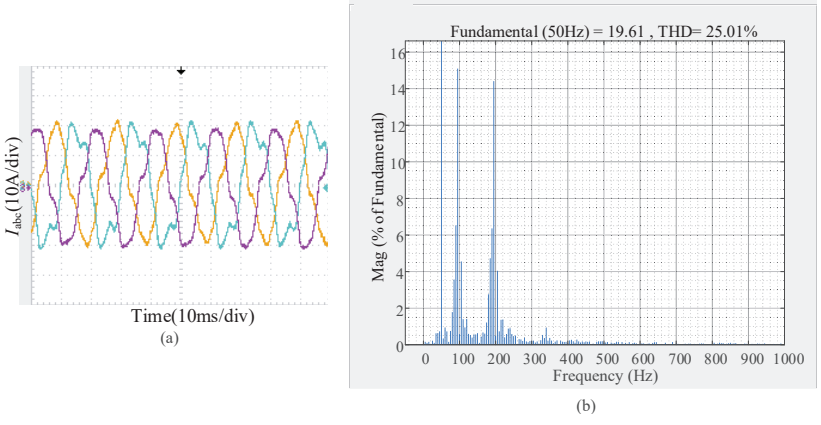

Figure 15. Experiment results of GCI with $SCR = 3.8$. (**a**) Output current waveforms of GCI; (**b**) THD of output current.

According to Figure 14a, the output current of the GCI is stable when $SCR = 5$. Yet, in Figure 15a, the output current of the GCI suffers from harmonic instability [2]. By importing data from an oscilloscope into matlab, THD analysis results of the grid-connected current are obtained, as shown in Figures 14b and 15b. According to Figure 15b, the frequency of harmonic instability is 195 Hz, and the coupling frequency is 95 Hz. In [2], the frequency of harmonic instability is almost consistent with the result of adding or subtracting the fundamental frequency at the frequency of the intersection of λ_2 with the unit circle. Therefore, the frequency of harmonic instability is 173 ± 50 Hz in the theoretical analysis. Clearly, discrepancies can be observed between the theoretical analysis results and the experimental findings. However, based on the aforementioned analysis, the proposed method remains feasible even when considering the errors between the actual circuit and the simulation model.

5. Conclusions

This paper has analyzed the impact of synchronization dynamics and background harmonics on impedance measurement. An improved impedance calculation method is proposed, incorporating a frequency selection principle for injected voltages during frequency scanning. This enables accurate identification of perturbations injected into the measurement system. The proposed method ensures a sufficient bandwidth for the PLL to

track grid frequency deviations and mitigates the influence of synchronization dynamics caused by perturbations. Consequently, the impedance can be accurately determined using this method.

To assess stability based on the measured impedance, a stability criterion based on the Gershgorin circle theorem is introduced. This criterion reduces the computational burden compared to existing methods. Simulation and experimental results of the GCI system validate the effectiveness of the proposed method.

Author Contributions: Conceptualization, T.Z. and Y.C.; methodology, T.Z. and Y.C.; software, T.Z.; validation, T.Z. and G.L.; formal analysis, G.L. and F.K.; investigation, T.Z., G.L., F.K. and Z.W.; resources, G.L., F.K. and Z.W.; data curation, F.K., Z.W. and Y.C.; writing—original draft preparation, T.Z. and Y.C.; writing—review and editing, G.L., F.K. and Z.W.; visualization, T.Z.; supervision, G.L., F.K. and Z.W.; project administration, G.L., F.K. and Z.W.; funding acquisition, G.L., F.K. and Z.W. All authors have read and agreed to the published version of the manuscript.

Funding: This work was supported by the Project supported by the Guangxi Natural Science Foundation no. 2021GXNSFAA220136 and the Guangdong Basic and Applied Basic Research Foundation (Guangdong-Guangxi Joint Foundation-Key Program) no. 2021B1515420006.

Data Availability Statement: The original contributions presented in the study are included in the article. Further inquiries can be directed to the corresponding author.

Conflicts of Interest: The authors declare no conflict of interest.

References

1. Zhao, E.; Han, Y.; Lin, X.; Yang, P.; Blaabjerg, F.; Zalhaf, A. Impedance characteristics investigation and oscillation stability analysis for two-stage PV inverter under weak grid condition. *Electr. Power Syst. Res.* **2022**, *209*, 108053. [CrossRef]
2. Tu, C.; Gao, J.; Fan, X.; Qi, G.; Fei, J. Stability Analysis of the Grid-Connected Inverter Considering the Asymmetric Positive-Feedback Loops Introduced by the PLL in Weak Grids. *IEEE Trans. Ind. Electron.* **2022**, *69*, 5793–5802. [CrossRef]
3. Gupta, B.; Sekhar, K. A Current Controller Gain Characterization of Weak Grid Coupled Solar Inverter Through Impedance Interaction Modeling. *IEEE Trans. Ind. Electron.* **2023**, *70*, 2520–2530. [CrossRef]
4. Fang, T.; Zhang, Y.; Shuheng, S.; Wu, H.; Liu, H.; Zhang, H. High-Bandwidth Grid-Connected Inverter to Enhance System Robustness Against Weak Grid. *IEEE Trans. Ind. Electron.* **2023**, *70*, 6993–7003. [CrossRef]
5. Cao, W.; Ma, Y.; Yang, Y.; Wang, F.; Tolbert, L.M. D–Q impedance based stability analysis and parameter design of three-phase inverter-based AC power systems. *IEEE Trans. Ind. Electron.* **2017**, *64*, 6017–6028. [CrossRef]
6. Wen, B.; Dong, D.; Boroyevich, D.; Burgos, R.; Mattavelli, P.; Shen, Z. Impedance-based analysis of grid-synchronization stability for three-phase paralleled converters. *IEEE Trans. Power Electron.* **2016**, *31*, 26–38. [CrossRef]
7. Wang, X.; Harnefors, L.; Blaabjerg, F. Unified impedance model of grid-connected voltage-source converters. *IEEE Trans. Power Electron.* **2018**, *33*, 1775–1787. [CrossRef]
8. Neshvad, S.; Chatzinotas, S.; Sachau, J. Wideband Identification of Power Network Parameters Using Pseudo-Random Binary Sequences on Power Inverters. *IEEE Trans. Smart Grid.* **2015**, *5*, 2293–2301. [CrossRef]
9. Wen, B.; Boroyevich, D.; Burgos, R.; Mattavelli, P.; Shen, Z. Small-signal stability analysis of three-phase AC systems in the presence of constant power loads based on measured d-q frame impedances. *IEEE Trans. Power Electron.* **2015**, *30*, 5952–5963. [CrossRef]
10. Valdivia, V.; Lazaro, A.; Burgos, A.; Zumel, P.; Fernandez, C.; Sanz, M. Black-box modeling of three-phase voltage source inverters for system-level analysis. *IEEE Trans. Power Electron.* **2012**, *59*, 3648–3662. [CrossRef]
11. Wu, T.-F.; Misra, M.; Jhang, Y.-Y.; Huang, Y.-H.; Lin, L.-C. Direct digital control of single-phase grid-connected inverters with LCL filter based on inductance estimation model. *IEEE Trans. Power Electron.* **2019**, *34*, 1851–1862. [CrossRef]
12. Zhou, W.; Wang, Y.; Chen, Z. Frequency and Temperature-Dependent Power Cable Modelling for Stability Analysis of Grid-Connected Inverter. In Proceedings of the 2018 IEEE 4th Southern Power Electronics Conference (SPEC), Singapore, 10–13 December 2018; pp. 1–8.
13. Zhou, W.; Raymundo, E.T.-O.; Göthner, F.; Beerten, J.; Zadeh, M.K.; Wang, Y.; Chen, Z. A Robust Circuit and Controller Parameters' Identification Method of Grid-Connected Voltage-Source Converters Using Vector Fitting Algorithm. *IEEE J. Emerg. Sel. Top. Power Electron.* **2022**, *10*, 2748–2763. [CrossRef]
14. Rygg, A.; Molinas, M. Apparent Impedance Analysis: A Small-Signal Method for Stability Analysis of Power Electronic-Based Systems. *IEEE J. Emerg. Sel. Top. Power Electron.* **2017**, *5*, 1474–1486. [CrossRef]
15. Bakhshizadeh, K.; Blaabjerg, F.; Hjerrild, J.; Kocewiak, L.; Bak, L. Improving the Impedance-Based Stability Criterion by Using the Vector Fitting Method. *IEEE Trans. Energy Convers.* **2018**, *33*, 1739–1747. [CrossRef]

16. Zhou, W.; Raymundo, E.T.-O.; Wang, Y.; Chen, Z. A Gray-Box Hierarchical Oscillatory Instability Source Identification Method of Multiple-Inverter-Fed Power Systems. *IEEE J. Emerg. Sel. Top. Power Electron.* **2021**, *9*, 3095–3113. [CrossRef]
17. Zhou W.; Wang Y.; Chen, Z. A gray-box parameters identification method of voltage source converter using vector fitting algorithm. In Proceedings of the 2019 10th International Conference on Power Electronics and ECCE Asia (ICPE 2019-ECCE Asia), Busan, Republic of Korea, 27–30 May 2019; pp. 2948–2955.
18. Zhou, W.; Wang, Y.; Cai, P.; Chen, Z. A Gray-Box Impedance Reshaping Method of Grid-Connected Inverter for Resonance Damping. In Proceedings of the 2019 10th International Conference on Power Electronics and ECCE Asia (ICPE 2019-ECCE Asia), Busan, Republic of Korea, 27–30 May 2019; pp. 2660–2667.
19. Zhou W.; Wang Y.; Chen, Z. Vector fitting-based reduced order modelling method for power cables. In Proceedings of the 15th IET International Conference on AC and DC Power Transmission (ACDC 2019), Coventry, UK, 5–7 February 2019; pp. 1–6.
20. Zhong, P.; Sun, J.; Tian, Z.; Huang, M.; Yu, P.; Zha, X. An Improved Impedance Measurement Method for Grid-Connected Inverter Systems Considering the Background Harmonics and Frequency Deviation. *IEEE J. Emerg. Sel. Top. Power Electron.* **2021**, *9*, 4236–4247. [CrossRef]
21. Shen, Z.; Jaksic, M.; Zhou, B.; Mattavelli, P.; Boroyevich, D.; Verhulst, J.; Belkhayat, M. Analysis of Phase Locked Loop (PLL) influence on DQ impedance measurement in three-phase AC systems. In Proceedings of the 2013 Twenty-Eighth Annual IEEE Applied Power Electronics Conference and Exposition (APEC), Long Beach, CA, USA, 17–21 March 2013; pp. 939–945.
22. Martin, D.; Nam, I.; Siegers, J.; Santi, E. Wide bandwidth three-phase impedance identification using existing power electronics inverter. In Proceedings of the 2013 Twenty-Eighth Annual IEEE Applied Power Electronics Conference and Exposition (APEC), Long Beach, CA, USA, 17–21 March 2013; pp. 334–341.
23. Cespedes, M.; Sun, J. Three-phase impedance measurement for system stability analysis. In Proceedings of the 2013 IEEE 14th Workshop on Control and Modeling for Power Electronics (COMPEL), Salt Lake City, UT, USA, 23–26 June 2013; pp. 1–6.
24. Roinila, T.; Vilkko, M.; Sun, J. Online Grid Impedance Measurement Using Discrete-Interval Binary Sequence Injection. *IEEE J. Emerg. Sel. Top. Power Electron.* **2014**, *2*, 985–993. [CrossRef]
25. Roinila, T.; Messo, T.; Luhtala, R.; Scharrenberg, R.; de Jong, E.C.W.; Fabian, A.; Sun, Y. Hardware-in-the-Loop Methods for Real-Time Frequency-Response Measurements of on-Board Power Distribution Systems. *IEEE Trans. Ind. Electron.* **2019**, *66*, 5769–5777. [CrossRef]
26. Gong, H.; Yang, D.; Wang, X. Impact Analysis and Mitigation of Synchronization Dynamics for DQ Impedance Measurement. *IEEE Trans. Power Electron.* **2019**, *34*, 8797–8807. [CrossRef]
27. Ren, Y.; Chen, L.; Min, Y.; Li, G.; Wang, L.; Zhang, Y. A Strictly Sufficient Stability Criterion for Grid-Connected Converters Based on Impedance Models and Gershgorin's Theorem. *IEEE Trans. Power Deliv.* **2020**, *35*, 1606–1609. [CrossRef]
28. Zeng, Z.; Zhao, J.; Liu, Z.; Mao, L.; Qu, K. Stability assessment for multiple grid-connected converters based on impedance-ratio matrix and Gershgorin's Theorem. *Int. J. Electr. Power Energy Syst.* **2022**, *138*, 107869.
29. Wen, B.; Boroyevich, D.; Mattavelli, P.; Shen, Z.; Burgos, R. Experimental verification of the Generalized Nyquist stability criterion for balanced three-phase ac systems in the presence of constant power loads. In Proceedings of the 2012 IEEE Energy Conversion Congress and Exposition (ECCE), Raleigh, NC, USA, 15–20 September 2012; pp. 3926–3933.
30. Wen, B.; Burgos, R.; Boroyevich, D.; Mattavelli, P.; Shen, Z. AC stability analysis and DQ frame impedance specifications in power-electronics-based distributed power systems. *IEEE J. Emerg. Sel. Top. Power Electron.* **2017**, *5*, 1455–1465.
31. Wen, B.; Boroyevich, D.; Burgos, R.; Mattavelli, P.; Shen, Z. Analysis of d-q small-signal impedance of grid-tied inverters. *IEEE Trans. Power Electron.* **2016**, *31*, 675–687. [CrossRef]
32. Jiang, K.; Zhang, C.; Ge, X. Low-frequency oscillation analysis of the train-grid system based on an improved forbidden-region criterion. *IEEE Trans. Ind. Appl.* **2018**, *54*, 5064–5073. [CrossRef]
33. Xu, H.; Wu, H.; Li, Z.; Yan, Q.; Blaabjerg, F. Gershgorin-Circle Based Low-Complexity Generalized Nyquist Stability Criterion for DFIG Driven Wind Turbines. *IEEE J. Emerg. Sel. Top. Circuits Syst.* **2022**, *12*, 29–40. [CrossRef]
34. Zhong, P.; Sun, J.; Li, Q.; Wang, Y.; Zha, X. Impedance Measurement of Grid-Tied Inverter With Deviate-Frequency Harmonic Current Injection. In Proceedings of the 2019 IEEE 4th International Future Energy Electronics Conference (IFEEC), Singapore, 25–28 November 2019; pp. 1–5.
35. Hu, Y.; Wu, W.; Zhang, B. A Fast Method to Identify the Order of Frequency-Dependent Network Equivalents. *IEEE Trans. Power Syst.* **2016**, *31*, 54–62. [CrossRef]

processes

MDPI

Article

Research on the Access Planning of SOP and ESS in Distribution Network Based on SOCP-SSGA

Yuxin Jia, Qiong Li *, Xu Liao, Linjun Liu and Jian Wu

School of Information Engineering, Nanchang Hangkong University, Nanchang 330063, China; 2104085400069@nchu.edu.cn (Y.J.); 2204085400068@stu.nchu.edu.cn (X.L.); 2204081100018@stu.nchu.edu.cn (L.L.); flywujian@nchu.edu.cn (J.W.)

* Correspondence: power-arm-lq@nchu.edu.cn

Abstract: This paper proposes a two-stage planning model for soft open point (SOP) and energy storage system (ESS) that considers the cost of faults in response to the current issue of SOP and ESS systems not considering the impact of SOP access on load transfer in the event of a fault in the distribution network. Firstly, considering the uncertainty of "PV-load", typical scenarios of PV and load are constructed based on the clustering algorithm. Secondly, aiming at the economic performance of the distribution network and the capacity of PV access, a two-stage optimization model is established for the joint integration of SOP and ESS into the distribution network (normal and fault operation) under typical scenarios. The model is solved by using the second-order cone programming algorithm and steady-state genetic algorithm (SOCP-SSGA). Stage one involves planning for the integration capacity and location of SOP and ESS into the distribution network under each scenario within a period based on SOCP with the goal of minimizing economic costs. In stage two, the PV access capacity of the distribution network is optimized using SSGA with the goal of enhancing the PV accommodation capability. Finally, verification and analysis are conducted on an improved IEEE33 node system. The results show that when the system optimizes access to a group of SOP and ESS, the total economic cost is reduced by RMB 61,729 compared to random access, and the accessible PV capacity is increased by 0.5278 MW. Moreover, optimizing access to two sets of SOP and ESS can further reduce the total economic cost by RMB 107,048 compared to the optimized access group and increase accessible PV capacity by 1.5751 MW. Therefore, the proposed plan for SOP and ESS planning in this paper can significantly reduce the economic cost of distribution networks, enhance the absorption capacity of distributed photovoltaics, improve the voltage level of power grid operation, and, thereby, improve the economic and reliability of distribution network operation.

Keywords: soft open point; energy storage; second-order cone planning; steady-state genetic algorithm; economic costs

Citation: Jia, Y.; Li, Q.; Liao, X.; Liu, L.; Wu, J. Research on the Access Planning of SOP and ESS in Distribution Network Based on SOCP-SSGA. *Processes* **2023**, *11*, 1844. https://doi.org/10.3390/pr11061844

Academic Editor: Ignacio Hernando-Gil

Received: 8 May 2023
Revised: 16 June 2023
Accepted: 17 June 2023
Published: 19 June 2023

1. Introduction

In recent years, with the continuous development and popularization of renewable energy, distributed photovoltaic power generation has become an important part of the distribution network. However, large-scale distributed photovoltaic access brings huge challenges to the distribution network, such as voltage instability, photovoltaic capacity limitation, and loss increase [1,2]. In order to solve these problems, SOP and ESS technologies have been widely applied in the distribution network [3,4]. Therefore, how to effectively plan the access of SOP and ESS to improve the reliability and economic benefits of the grid has become one of the hot spots of current research, and researchers at home and abroad have carried out a large number of studies on the access of SOP and ESS.

The literature [5] (2019) proved the feasibility and superiority of a flexible multistate switch in a power system by simulating and analyzing the mathematical model of a flexible multistate switch. The literature [6] (2019) expanded the functions and application scenarios

of SOP, analyzed the positive role of SOP in improving the system energy-consumption rate, reducing loss and improving power quality, etc., and verified that SOP can achieve good results in the distribution network. Reference [7] (2020) discusses the active power and reactive power coordination operating conditions and influence mechanism when flexible multistate switches are connected to an active distribution network. A dynamic optimal operation model and scheduling architecture for active and reactive power coordination between flexible multistate switches and active distribution networks under multitime periods are established, and a model-solving method for second-order cone programming and nonlinear programming is proposed. The literature [8] (2020) proposes a reliability evaluation method for a multiterminal interconnected distribution system based on a flexible multistate switch, discusses the influence of FMSS access strategy on the system operation mode and network structure, and provides theoretical support for the planning of flexible interconnected distribution system. The literature [9] (2021) establishes the power flow model of an active distribution network, considers the influence of flexible multistate switch access, takes the comprehensive operation cost of the distribution network as the objective function, builds the second-order cone programming model of flexible multistate switch location in the active distribution network, and optimizes and solves it to obtain the optimal SOP planning scheme. The literature [10] (2020), aiming at the SOP site-selection problem, considering the diversity of SOP operation modes, a dynamic coding strategy suitable for two-port SOP in an interconnected distribution network is proposed, and the improved genetic algorithm is used to solve the complex mixed integer nonlinear programming problem. The literature [11] (2017) established a double-layer programming model for SOP siting with constant capacity with the goal of optimizing multiple economic indicators and used a simulated annealing algorithm and cone programming algorithm to solve the problem.

In response to the problem of reduced stability of active distribution networks caused by a high proportion of new energy generation, document [12] (2023) established an ESS multiobjective optimization model and used nondominated sorting genetic algorithm II (NSGA-II) to solve it. By configuring ESS, the stability of the active distribution network is improved. The literature [13] (2020) proposes a distributed hybrid energy storage optimization method based on distribution-network zoning, which effectively improves the utilization efficiency of energy storage and the economy of the configuration scheme. The literature [14] (2020) proposes a data-driven uncertainty modeling method and establishes a distributionally robust optimization model to determine the optimal energy storage-system planning strategy in high photovoltaic penetration distribution systems. The literature [15] (2020) established a multiobjective model for solving the optimal capacity and power of distributed energy storage, taking into account the uncertainties of economics, technical standards, and distributed power generation. The literature [16] (2022) considers the coupling between planning and operation. They established a multiobjective optimization model of an energy storage system in an active distribution network and proposed an improved multiobjective particle-swarm optimization algorithm to solve the model. This approach aims to improve the robustness and economics of active distribution networks to address their vulnerabilities. The literature [17] (2020) solves the problem of energy storage site selection and capacity by constructing a hybrid probability optimization algorithm, which combines the discretization method with the multiobjective particle-swarm optimization (MOPSO) algorithm and the nondominating ranking genetic algorithm, which can better realize the voltage distribution and reduce the network loss.

In the above studies, the configuration of the power grid was optimized in the case of the access of SOP or ESS itself, and the joint planning of SOP and ESS was not considered to control the power grid. In practical-application scenarios, the joint planning of SOP and ESS could better realize the control and regulation of the power grid. To solve this problem, the literature [18] (2018) considered the coordinated operation relationship between SOP and ESS and studied the role of SOP and ESS in improving the operation economy of an active distribution network from the perspective of optimal configuration. In the literature [19]

(2021), a two-stage joint-interval optimization model of an intelligent soft switch and energy storage system of an active distribution network is established. Column and constraint generation algorithm is adopted to solve the model, so as to cope with the uncertainty of the output and load demand of the distributed power supply and effectively reduce the loss cost of the active distribution network. The literature [20] (2018) established a sequential optimization model for SOP and ESS, which was accurately solved using the primal–dual interior-point algorithm to reduce active distribution network losses. The literature [21] (2021) proposed SOP and ESS operating models in an active distribution network aiming at the optimization of operating cost, loss cost, and battery-degradation cost, converted a mixed-integer nonlinear programming model into a mixed-integer linear programming model and solved the model. The literature [22] (2022) established SOP and ESS two-layer programming models based on temporal and spatial characteristics. The minimum annual comprehensive operation cost of the distribution network and the minimum sum of network loss cost and voltage offset were taken as optimization objectives, and the planning scheme was determined by a community mining algorithm and improved load moment method. These research results provide some ideas and methods for SOP and ESS access in a distribution network.

The above research has the following shortcomings: (1) the transfer and support functions of SOP and ESS to loads during distribution network failures are not considered. Therefore, when the objective is to minimize the annual comprehensive cost of the distribution network, the cost of distribution network failures is usually not considered and the operating layer mainly calculates the distribution-network losses during normal operation. As a result, the adjustment potential of SOP in time and space is not fully utilized. (2) The reasonable planning of SOP and ESS plays an important role in improving the access of distributed photovoltaics, but it is also affected by the random fluctuations of distributed power sources and it is necessary to coordinate the planning of SOP, ESS, and distributed photovoltaics. Therefore, this paper considers the uncertainty of PV load and establishes a planning model with the goal of comprehensive economic cost and PV access capacity in the distribution network. The objective function takes into account not only the power loss during normal operation of the distribution network but also the benefits of SOP and ESS in supporting loads after faults occur and introduces a fault-cost index. A mixed-solving method based on SOCP-SSGA is used to solve the model and simulation verification is carried out in an improved IEEE33 node distribution network to analyze the economic and effective aspects of the planning model.

2. Flexible Distribution Network with SOP and ESS

2.1. SOP Basic Structure and Control Mode

The soft open point (SOP) is composed of high-power electronic components and has the characteristics of fast response speed, real-time continuous power control, and suitability for different scenarios. It can replace traditional tie switches and not only has the on/off function of traditional tie switches but also can transfer active power of feeders, improving the distribution of power flow in the distribution network [23]. In the event of a fault, SOP can provide some voltage support to improve feeder voltage levels, achieve uninterrupted power supply in nonfault areas, and, thereby, improve system operation safety. This paper uses a back-to-back voltage source converter (VSC) as the research model. SOP is mainly connected to the DC capacitor through the converter and plays a role in voltage support and smoothing DC voltage fluctuations. L is the filtering inductance and R is the equivalent resistance. The basic structure diagram of the back-to-back SOP is shown in Figure 1.

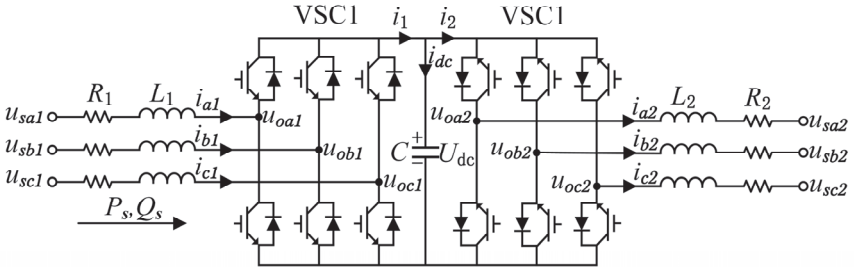

Figure 1. The basic structure of back-to-back SOP.

Take VSC1 as an example; where $u_{sa1}, u_{sb1}, u_{sc1}$ is the three-phase voltage at the AC side, i_{a1}, i_{b1}, i_{c1} is the three-phase current at the AC side, $u_{oa1}, u_{ob1}, u_{oc1}$ is the three-phase voltage at the AC side of VSC, U_{dc} is the voltage at the DC side of VSC, i_{dc} is the current at the DC side of VSC, and P_s, Q_s is the active and reactive power input at the AC side. SOP mainly adjusts the power flow between systems through amplitude-phase or vector-control mode, and vector control can overcome the shortcoming of no current protection in amplitude-phase control. There are four operation modes for VSC [24,25]: fixed DC voltage control, fixed AC voltage control, fixed active power control, and fixed reactive power control. Under normal conditions, one VSC in the SOP controls the power transmission, while the other VSC controls the DC voltage. When a fault occurs, the fault detection VSC is adjusted to the fixed AC voltage control, and the nonfault side VSC is used to control the fluctuation of DC voltage. For detailed mathematical models and commutation principles of SOP, please refer to references [26,27].

2.2. Energy Storage-System Model

Energy storage systems (ESS) can be charged during the day when there is sufficient sunlight and the load electricity consumption is less than the output electricity from photovoltaics. They can then discharge during periods of low output, such as rainy days or nighttime, to meet the demand of the load. ESS not only enhances the absorption level of photovoltaic power generation by the distribution network but also increases the load level of distribution transformers [28]. In a flexible distribution network, distributed energy storage is mainly electrochemical energy storage. The model is shown as follows:

When charging, the energy storage-system power can be expressed as follows:

$$E_{ESS}(t) = E_{ESS} \cdot (t - \Delta t) + P^{c}_{ESS}(t) \cdot \Delta t \cdot \eta_c \tag{1}$$

when discharging, the energy storage-system electricity can be expressed as follows:

$$E_{ESS}(t) = E_{ESS} \cdot (t - \Delta t) + \frac{P^{dis}_{ESS}(t) \cdot \Delta t}{\eta_d} \tag{2}$$

where $E_{ESS}(t)$ is the electricity stored in the energy storage system at time t, Δt is the time interval, $P^{c}_{ESS}(t)$ is the charging power of energy storage at time t, $P^{dis}_{ESS}(t)$ is the discharge power at time t, η_c is the charging efficiency, and η_d is the discharge efficiency.

3. Two-Stage Planning Model for SOP and ESS Access

The main purpose of this paper is to optimize the power flow of the distribution network by SOP and ESS, and to minimize the economic cost of the distribution network, and maximize the absorption capacity of the photovoltaic under the premise of safety and reliability. Therefore, the stage-one planning model in this paper integrated various scenarios and took the minimum economic cost within the cycle as the objective function to determine the site capacity of SOP and ESS, while the objective function of the stage-two optimize model was to improve the PV absorption capacity in the distribution network.

3.1. Stage-One Planning Model

3.1.1. Objective Function

The objective function of the stage-one planning model is to find the access capacity of SOP and ESS under the condition that the economic cost of the distribution network is minimal in the period, and the economic cost in this document consists of four parts, which are expressed as follows:

$$\min F = C_{INV} + C_{OPE} + C^s_{LOSS} + C^s_{Fault} \tag{3}$$

where F is the economic cost in the distribution network, C_{INV} is the investment cost of SOP and ESS, C_{OPE} is the operation and maintenance cost of SOP and ESS in the cycle, C^s_{LOSS} is the cost of power loss in the distribution network, and C^s_{Fault} is the loss cost in the event of a failure in the distribution network. The cost expressions are as follows:

1. SOP and ESS investment costs C_{INV}

$$C_{INV} = \frac{d(1+d)^{y_{SOP}}}{(1+d)^{y_{SOP}} - 1} \sum_{k=1}^{N_{SOP}} (C_{SOP} \cdot S_{SOP}) + \frac{d(1+d)^{y_{ESS}}}{(1+d)^{y_{ESS}} - 1} \sum_{k=1}^{N_{ESS}} (C_{ESS} \cdot S_{ESS}) \tag{4}$$

where d is the discount rate; y_{SOP}, y_{ESS} and y_{SOP} are the economic service life of SOP, ESS, and PV, N_{SOP} and N_{ESS} are the number of SOP and ESS to be installed, C_{SOP} and C_{ESS} are the unit-capacity investment costs corresponding to SOP and ESS, and S^s_{SOP} and S^s_{ESS} are the installed capacity of SOP and ESS.

2. SOP and ESS operation and maintenance costs C^s_{OPE}

$$C_{OPE} = \lambda_{ESS} \sum_{k=1}^{N_{ESS}} (C_{ESS} \cdot S_{ESS}) + \lambda_{SOP} \sum_{k=1}^{N_{SOP}} (C_{SOP} \cdot S_{SOP}) \tag{5}$$

where λ_{ESS} and λ_{SOP} are the operating and maintenance cost coefficients of SOP and ESS, respectively.

3. The cost of loss of electrical energy in the distribution network C^s_{LOSS}

$$C^s_{LOSS} = P_s \cdot \sum_{s=1}^{K} \left[\varphi \cdot \sum_{t=1}^{n} (R_{ij} \cdot {I^s_{ij,t}}^2 + P^{s,L,SOP}_{ij,t} + P^{s,L,ESS}_{ij,t}) \cdot \Delta t \right] \tag{6}$$

where φ is the economic cost coefficient of power loss in the distribution network, R_{ij} is the resistance value on the branch ij, ${I^s_{ij,t}}^2$ is the current value of the branch ij at a time t, $P^{s,L,SOP}_{ij,t}$ is the active power loss of the SOP installed on the branch, $P^{s,L,ESS}_{ij,t}$ is the active power loss of the ESS installed on the branch, Δt is the time interval, P_s is the probability corresponding to scenario s, and K is the number of clustered scenarios.

4. TCost of fault loss in the distribution network C^s_{fault}

$$C^s_{fault} = P_s \cdot \sum_{s=1}^{K} \left[C_E \cdot P^{s,L,LOAD}_t \cdot P_{fault} \right] \tag{7}$$

where C_E is the electricity price, $P^{s,L,LOAD}_t$ is the lost power of the load in the event of a line failure, and P_{fault} is the probability of line failure.

3.1.2. Constraints

1. SOP operation constraints

$$P^{SOP}_i + P^{SOP}_j + P^{SOP,L}_i + P^{SOP,L}_j = 0 \tag{8}$$

$$\begin{cases} P_i^{SOP,L} = A_i^{SOP}\sqrt{\left(P_i^{SOP}\right)^2 + \left(Q_i^{SOP}\right)^2} \\ P_j^{SOP,L} = A_j^{SOP}\sqrt{\left(P_j^{SOP}\right)^2 + \left(Q_j^{SOP}\right)^2} \end{cases} \tag{9}$$

$$\begin{cases} -\mu S_{i,j}^{SOP} \le Q_i^{SOP} \le \mu S_{i,j}^{SOP} \\ -\mu S_{i,j}^{SOP} \le Q_j^{SOP} \le \mu S_{i,j}^{SOP} \end{cases} \tag{10}$$

$$\begin{cases} \sqrt{\left(P_i^{SOP}\right)^2 + \left(Q_i^{SOP}\right)^2} \le S_i^{SOP} \\ \sqrt{\left(P_j^{SOP}\right)^2 + \left(Q_j^{SOP}\right)^2} \le S_j^{SOP} \end{cases} \tag{11}$$

where P_i^{SOP} and P_j^{SOP} are the active power transmitted by the flexible switch at nodes i and j, Q_i^{SOP} and Q_j^{SOP} are the reactive power transmitted by the flexible switch at nodes i and j, P_i^{SOP} and P_j^{SOP} are the loss of SOP, A_i^{SOP} and A_j^{SOP} are the loss coefficient of the flexible switch at nodes i and j, the value is 0.02, μ is the absolute value of the power factor angle sinusoid, and $S_{i,j}^{SOP}$ is the capacity of SOP between nodes.

2. ESS operating constraints

The injection of energy storage into the grid is defined as positive and the operational constraints are expressed as follows:

$$P_{i,t}^{ESS} = \begin{cases} \eta_{dic} \cdot P_{i,t}^{dis} \cdot P_{i,t}^{ESS} \ge 0 \\ \eta_c \cdot P_{i,t}^{c} \cdot P_{i,t}^{ESS} < 0 \end{cases} \tag{12}$$

$$Q_i^{ESS,\min} \le Q_{i,t}^{ESS} \le Q_i^{ESS,\max} \tag{13}$$

$$\sqrt{\left(P_{i,t}^{ESS}\right)^2 + \left(Q_{i,t}^{ESS}\right)^2} \le S_i^{ESS} \tag{14}$$

$$E_{i,t+1}^{ESS,\min} = E_{i,t}^{ESS} + P_{i,t}^{ESS}\Delta t \tag{15}$$

$$E_t^{ESS,\min} \le E_t^{ESS} \le E_t^{ESS,\max} \tag{16}$$

$$E_{N_T,i}^{ESS} = E_{0,i}^{ESS} \tag{17}$$

where $P_{i,t}^{c}$ and $P_{i,t}^{dis}$ are the charging power and discharge power of the energy storage at the t moment i node, η_c and η_{dic} are the charge and discharge efficiency of the energy storage reset, $E_{i,t}^{ESS}$ is the electricity stored by the energy storage device of the i node at the t moment, $Q_i^{ESS,\min}$ and $Q_i^{ESS,\max}$ are the upper and lower limits of the reactive power that the energy storage device can output on the i node, $E_t^{ESS,\min}$ and $E_t^{ESS,\max}$ are the upper and lower limits of the amount of energy that can be stored by the energy storage device, and S_i^{ESS} is the capacity of the energy storage device of the i node. The amount of electricity stored by the energy storage device in the time series is continuous and the cumulative calculation is carried out according to the power of charge and discharge, and the energy storage capacity at each moment needs to meet the requirements of the upper and lower limits, and the initial power and the final power need to remain equal in one operating cycle.

3. System operating power-flow constraint

$$\begin{cases} \sum\limits_{ij\in\Omega_i} \left(P_{ij,t} - r_{ij}I_{ij,t}^2\right) + P_{i,t} = \sum\limits_{jk\in\Psi_i} P_{jk,t} \\ \sum\limits_{ij\in\Omega_i} \left(Q_{ij,t} - x_{ij}I_{ij,t}^2\right) + Q_{i,t} = \sum\limits_{jk\in\Psi_i} Q_{jk,t} \end{cases} \tag{18}$$

$$\begin{cases} P_{i,t} = P_{i,t}^{PV} + P_{i,t}^{SOP} + P_{i,t}^{ESS} - P_{i,t}^{LOAD} \\ Q_{i,t} = Q_{i,t}^{SOP} + Q_{i,t}^{ESS} - Q_{i,t}^{LOAD} \end{cases} \tag{19}$$

$$U_{t,i}^2 - U_{t,j}^2 + (r_{ij}^2 + x_{ij}^2) I_{ij,t}^2 - 2(r_{ij} P_{ij,t} + x_{ij} Q_{ij,t}) = 0 \tag{20}$$

$$U_{t,i}^2 I_{ij,t}^2 = P_{ij,t}^2 + Q_{ij,t}^2 \tag{21}$$

where $P_{ij,t}$ and $Q_{ij,t}$ are the active and reactive power of the branch ij flowing from node i to node j at the t moment, r_{ij} and x_{ij} are the resistance and reactance of the branch ij, $I_{ij,t}$ is the current of the branch ij at the t moment, $U_{i,t}$ and $U_{j,t}$ are the voltage of nodes i and j at time t, $P_{i,t}$ and $Q_{i,t}$ are the active and reactive power flowing into node i at the t moment, $P_{i,t}^{PV}$, $P_{i,t}^{SOP}$, $P_{i,t}^{ESS}$ and $P_{i,t}^{LOAD}$ are the active power of PV, SOP, ESS, and LOAD at t moment, $Q_{i,t}^{SOP}$, $Q_{i,t}^{ESS}$ and $Q_{i,t}^{LOAD}$ are the reactive power of t moment SOP, ESS, and LOAD, Ω_i is the collection of the first node of the branch with node i as the end node, and Ψ_i is the collection of branch end nodes of the first end node.

3.2. Stage-Two Optimize the Model

3.2.1. Objective Function

The optimization model of stage two has the largest access to distributed photovoltaic capacity under various constraints of the distribution network and the objective function of the model can be expressed as follows:

$$F = \max S_{PV} \tag{22}$$

where S_{PV} is the photovoltaic capacity of the access system.

3.2.2. Constraints

In addition to the constraints of stage one, the following constraints must be met.

1. Distributed photovoltaic operating power constraints:

$$-\sqrt{{S_{PV}}^2 - {P_{PV,t}}^2} \le Q_{PV,t} \le \sqrt{{S_{PV}}^2 - {P_{PV,t}}^2} \tag{23}$$

where $P_{PV,t}^s$ is the active power of the access PV at the t moment and $Q_{PV,t}^s$ is the reactive power of the access PV at the t moment.

2. Distribution network safe operation constraints:

$$\begin{cases} U_{\min} \le U_j \le U_{\max} \\ |I_i| \le I_i^{\max} \end{cases} \tag{24}$$

where U_j is the voltage amplitude of the first node j, $U_{\min}$ is the minimum allowable value of voltage amplitude, and the maximum allowable value of $U_{\max}$ voltage amplitude; I_i is the current on branch i, and $I_i^{\max}$ is the maximum current that branch i is allowed to carry.

4. The Solution Method of the Model

The model constructed in this paper is a mixed-integer nonlinear programming model. The access location and capacity of SOP and ESS are determined at the first stage and the model is solved by second-order cone programming (SOCP). In the second stage, a steady-state genetic algorithm (SSGA) is used to calculate the distributed PV access capacity. In order to achieve an efficient solution, a hybrid algorithm of second-order cone programming and steady-state genetic algorithm (SOCP-SSGA) is proposed in this paper to solve the two-stage programming model.

4.1. Second-Order Cone Programming Algorithm and Transformation

SOCP is a mathematical programming on a convex cone in linear space, which has been widely used in power-system problems [29]. Based on the second-order cone programming algorithm, this paper transforms the objective function and constraints into the second-order cone model, which can transform the nonlinear equation into a linear expression [30].

Distribution network stage-one planning model (8), (20), (22), (23) with quadratic terms; replacing $I_{t,ij}^2$ with $I_{2,t,ij}$, and $U_{2,t,i}$ with $U_{2,t,i}^2$ yields expressions (25), (26), (27), (28):

$$C^{loss} = \varphi \cdot \sum_{t=1}^{n} (R_{ij} \cdot I_{2,t,ij} + P_{ij,t}^{L,SOP} + P_{ij,t}^{ESS}) \cdot \Delta t \tag{25}$$

$$\begin{cases} \sum\limits_{ij \in \Omega_i} (P_{ij,t} - r_{ij} I_{2,t,ij}) + P_{i,t} = \sum\limits_{jk \in \Psi_i} P_{jk,t} \\ \sum\limits_{ij \in \Omega_i} (Q_{ij,t} - x_{ij} I_{2,t,ij}) + Q_{i,t} = \sum\limits_{jk \in \Psi_i} Q_{jk,t} \end{cases} \tag{26}$$

$$U_{2,t,i} - U_{2,t,j} + (r_{ij}^2 + x_{ij}^2) I_{2,t,ij} - 2(r_{ij} P_{ij,t} + x_{ij} Q_{ij,t}) = 0 \tag{27}$$

$$U_{2,t,i} I_{2,t,ij} = P_{ij,t}^2 + Q_{ij,t}^2 \tag{28}$$

Convex relaxation of Equations (9), (11), (14) and (28) yields the following second-order conical constraint:

$$\begin{cases} \left\| [P_i^{SOP} \; Q_i^{SOP}]^{\mathrm{T}} \right\|_2 \le \frac{P_i^{SOP,L}}{A_i^{SOP}} \\ \left\| [P_j^{SOP} \; Q_j^{SOP}]^{\mathrm{T}} \right\|_2 \le \frac{P_j^{SOP,L}}{A_j^{SOP}} \end{cases} \tag{29}$$

$$\begin{cases} \left\| [P_i^{SOP} \; Q_i^{SOP}]^{\mathrm{T}} \right\|_2 \le S_i^{SOP} \\ \left\| [P_j^{SOP} \; Q_j^{SOP}]^{\mathrm{T}} \right\|_2 \le S_j^{SOP} \end{cases} \tag{30}$$

$$\left\| [P_{i,t}^{ESS} \; Q_{i,t}^{ESS}]^{\mathrm{T}} \right\|_2 \le S_i^{ESS} \tag{31}$$

$$\left\| [2P_{ij,t} \; 2Q_{ij,t} \; I_{2,t,ij} - U_{2,t,i}]^{\mathrm{T}} \right\|_2 \le I_{2,t,ij} + U_{2,t,i} \tag{32}$$

After the above cone transformation, the nonlinear expression in the stage-one programming model is converted into a linear or second-order cone expression.

4.2. Steady-State Genetic Algorithm

In this paper, the SSGA is used to solve the stage-two optimization model and the SSGA can effectively maintain population diversity because only a small number of individuals are updated in each generation so as to reduce the risk of falling into the local optimal solution, and the SSGA has the characteristics of fast convergence, high operation efficiency, and adaptation to large-scale datasets, and the execution steps are as follows:

1. Population initialization and coding: take the photovoltaic capacity as the population chromosome, set the decision variables upper bound ub and lower bound lb, determine the number of individuals, and generate initialized population $[x_1, x_{2,} \cdots x_n]^T$ after binary coding;
2. Calculate population-fitness value: the objective function in this paper is the maximum access capacity of the photovoltaic in a flexible distribution network and the objective function value F is used as the fitness value fit, and a set of fitness value $FitnV$ is generated after each generation of calculation, $FitnV = [fit_1, fit_{2,} \cdots fit_n]^T$;
3. Perform the selection operation: this operation is based on individual fitness to determine the individuals who carry out crossover and mutation; this paper uses roulette selection, individuals in the population are mapped to successive fragments

of the interval, and the length of the fragment in which each individual is located is proportional to its fitness, the corresponding individual is selected according to the fragment in which it falls, and the process is repeated until the required number of individuals is obtained;

4. Perform crossover and mutation operations: in this paper, two intersections are randomly set in two individuals, and some genes are exchanged according to the crossover probability, and binary mutation operators are used in this paper;
5. Set the number of iterations and repeat steps 2–4 above until the end of evolution to obtain the optimal capacity of a node connected to the PV.

4.3. SOCP-SSGA Solution Flow

By using SOCP-SSGA to solve the two-stage planning model, firstly, typical scenarios for photovoltaic and load are constructed. In the first stage, the SOCP algorithm is used to optimize the positions and capacities of SOP and ESS in all typical scenarios and the comprehensive installation locations and capacities of SOP and ESS under various typical scenarios are obtained. The location and capacity information are then transmitted to stage two. In the second stage, the distributed photovoltaic capacity in the distribution network is optimized based on the SSGA algorithm and the optimized PV capacity results are returned to stage one. Stage one continues to use the data transmitted from stage two to calculate the objective function value and this cycle continues until the minimum economic cost and optimal photovoltaic capacity are obtained. The process of using the SOCP-SSGA hybrid algorithm to solve the two-stage planning model is shown in Figure 2.

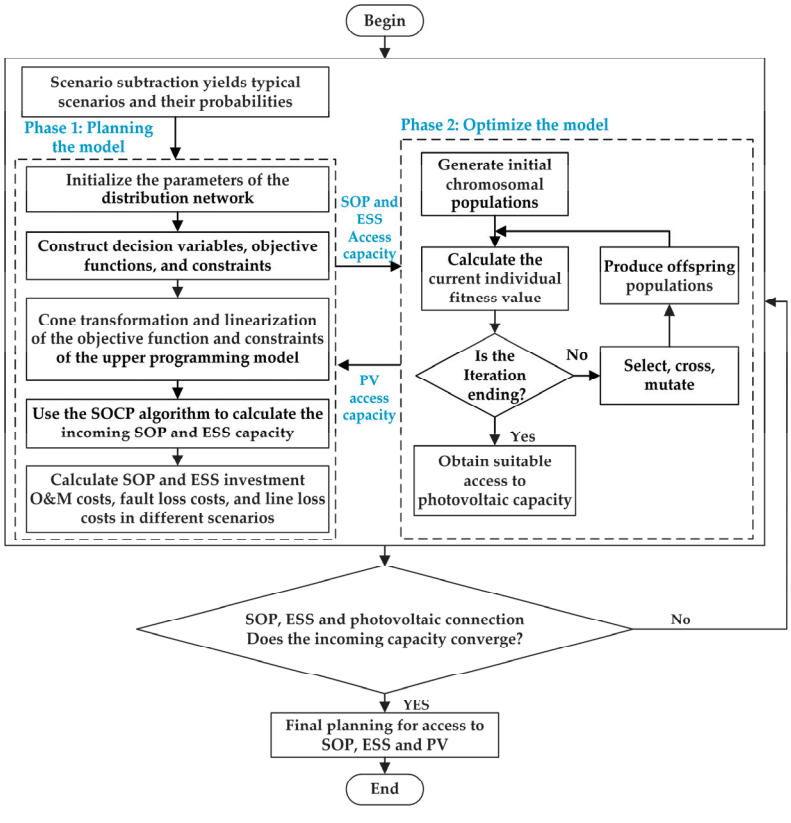

Figure 2. Two-stage programming-model solution flowchart.

5. Example Analysis

5.1. Optimization Schemes and Parameters

In this paper, the improved IEEE33 node is selected to analyze and verify the SOP and ESS access planning in the distribution network. The improved voltage level of the IEEE33 node is 12.66 KV, the total active load is 3175 KW, and the fault lines are between nodes 6 and 7 and between nodes 15 and 16. The system-structure diagram of the improved IEEE33 nodes is shown in Figure 3. According to the annual photovoltaic output and load power in a certain place in Jiangxi, the joint distribution scenario of five photovoltaic power-generation scenarios and five load scenarios was obtained by scene reduction, and the distribution of each scene is shown in Table 1 and Figure 4. In Figure 4, the 5 lines represent PV and load power changes throughout the day under 5 different scenarios. The initial PV units with 450 kVA, 500 kVA, 450 kVA, and 400 kVA capacities are connected to nodes 14, 22, 24, and 31, respectively. Considering that the installation of SOP is limited by geographic location, the installation location for SOP is selected at the connection switch. Additionally, one photovoltaic unit is planned to be installed at node 11. The optimization of SOP, ESS, and PV is conducted based on all typical scenarios, and, finally, the optimized results are validated under a specific scenario of photovoltaic (scenario 3) and load (scenario 1).

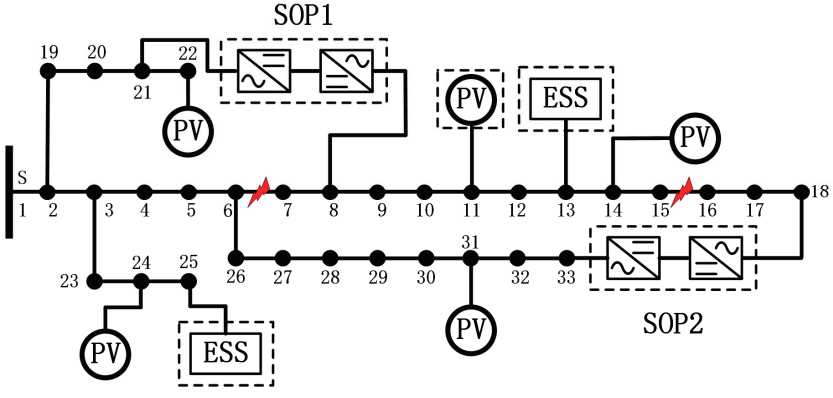

Figure 3. Improving the IEEE33 node distribution-network system.

Table 1. PV-load scenario probability.

P_{PV}	P_{LOAD}				
	Scenario 1	**Scenario 2**	**Scenario 3**	**Scenario 4**	**Scenario 5**
Scenario 1	0.0142	0.046	0.0417	0.0681	0.0412
Scenario 2	0.0473	0.0255	0.0563	0.0348	0.0384
Scenario 3	0.0771	0.0073	0.0181	0.0673	0.0219
Scenario 4	0.0693	0.0535	0.0084	0.0112	0.0049
Scenario 5	0.0182	0.0424	0.0629	0.0657	0.0581

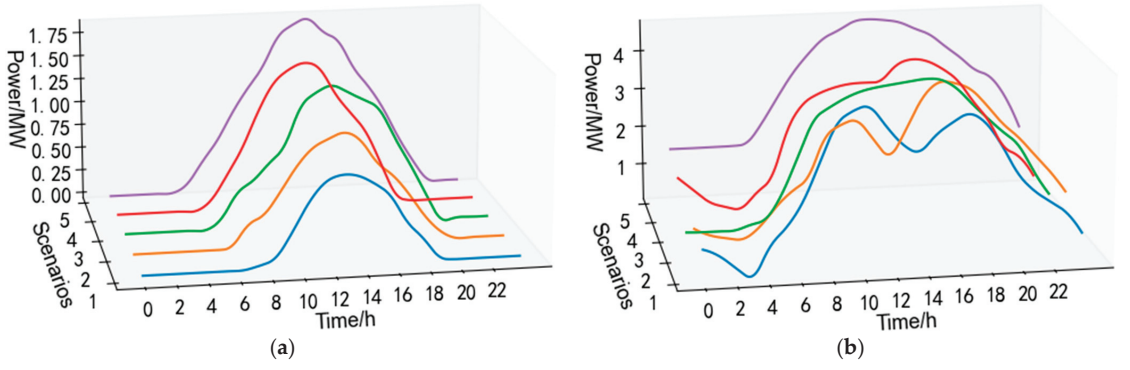

Figure 4. Photovoltaic and load scenarios with daily output curves: (**a**) photovoltaic; (**b**) load.

In this example, the four access comparison schemes are set as follows:

Scheme 1: Do not install any SOP and ESS;

Scheme 2: Install a set of SOP and ESS at random locations;

Scheme 3: The system optimizes access to one set of SOP and one set of ESS.

Scheme 4: The system optimizes access to two sets of SOP and two sets of ESS.

The four schemes are progressively advanced and compared with each other. Scheme 1 directly uses the SSGA algorithm to solve the access photovoltaic capacity. Scheme 2 randomly selects the installation positions of SOP and ESS to determine the installation capacity of each device. Scheme 3 and Scheme 4 use the SOCP-SSGA hybrid algorithm to optimize the installation of SOP, ESS, and PV, resulting in optimal economic cost and access to distributed photovoltaic capacity for each scenario in the distribution network cycle. Finally, draw the voltage diagram of each node and the running-state diagram of each device in a typical scenario (photovoltaic scenario 3 and load scenario 1). Table 2 shows the parameters in the distribution network system planning.

Table 2. Parameters in system planning.

Parameter	Numeric Value
SOP life/year	20
ESS life/year	9
PV life/year	25
SOP investment cost per unit capacity/(RMB/kVA)	1000
ESS investment cost per capacity/(RMB/kVA)	800
PV unit-capacity investment cost/(RMB/kVA)	2000
SOP, ESS, and PV operating maintenance factors	0.01
Cost factor for loss	0.08
electrovalence	0.6
Discount rate d	0.08
Converter loss factor	0.02
Probability of line failure	2.19%
Steady-state genetic algorithm population size	50
Number of steady-state genetic algorithm iterations	200

5.2. Comparative Analysis of Optimization Schemes

1. Scheme 1

No SOP and ESS were installed in the system and a photovoltaic unit was connected at node 11. The SSGA algorithm was used to optimize the photovoltaic access capacity and calculate the economic components. The optimized PV capacity and economic costs are shown in Tables 3 and 4, respectively. The voltage changes at each node throughout the day before and after the optimization of PV are shown in Figure 5a,b.

Table 3. PV capacity after optimization in Scheme 1.

Access Device	PV
Access Capacity (MW)	3.7865

Table 4. Economic cost after optimization of Scheme 1.

Economic Component	Fee (RMB 10,000)
Failure loss	7.8965
Electrical energy loss	4.3496
total	12.2461

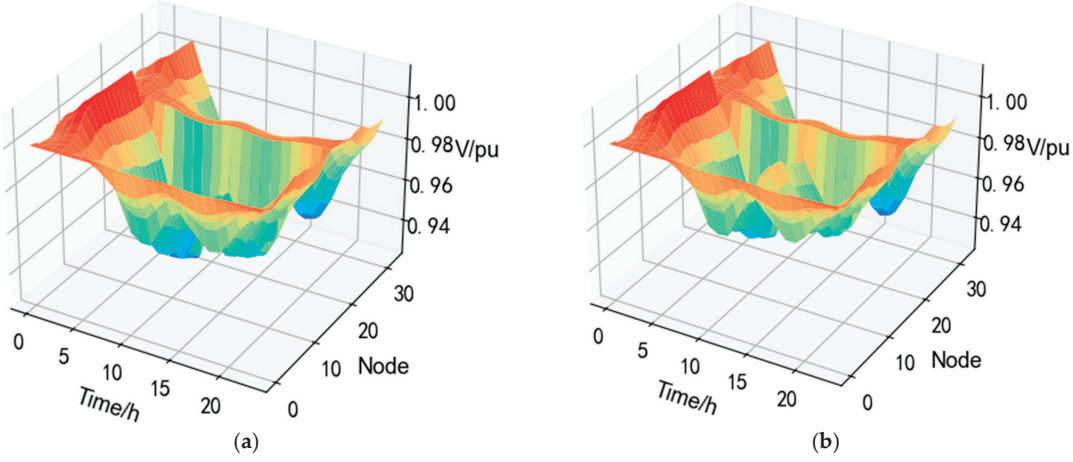

Figure 5. Voltage change chart of each node: (**a**) PV not connected; (**b**) Access PV.

As can be seen from Figure 5, PV access raises the voltage near the access node, but the overall voltage value is low.

2. Scheme 2

A set of SOP and ESS are installed at random locations. The random installation location of SOP is between nodes 12 and 22; the random access to ESS is node 15; and a group of photovoltaic units are connected at node 11, and the access capacity of each component is solved by the optimization algorithm optimization. The configuration and economic cost of each capacity after optimization are shown in Tables 5 and 6. The voltage changes at each node throughout the day before and after the optimization of PV are shown in Figure 6a,b. The active power output and reactive power compensation of the SOP during daily operation after optimization are shown in Figure 7a,b, and the daily operating energy of the ESS is shown in Figure 8.

Table 5. Optimized capacity configuration in Scheme 2.

Access Device	SOP	ESS	PV
Access Capacity (MW)	1.11939 × 2	0.92168	4.3254

Table 6. Optimized economic costs of Scheme 3.

Economic Component	Fee (RMB 10,000)
SOP investment	22.8025
SOP operation and maintenance	2.2388
ESS Investment	8.6144
ESS operation and maintenance	0.7373
Failure loss	5.6928
Electrical energy loss	4.7130
total	44.7988

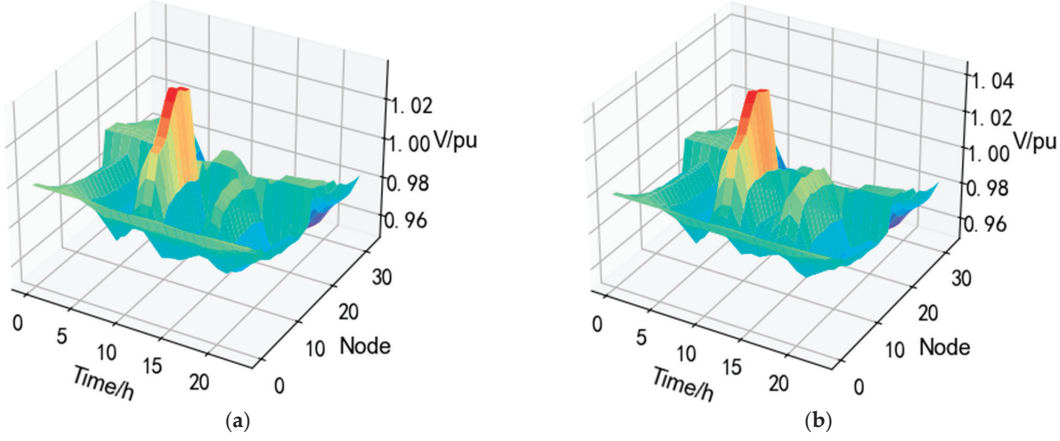

Figure 6. Voltage change chart of each node: (**a**) PV not connected; (**b**) Access PV.

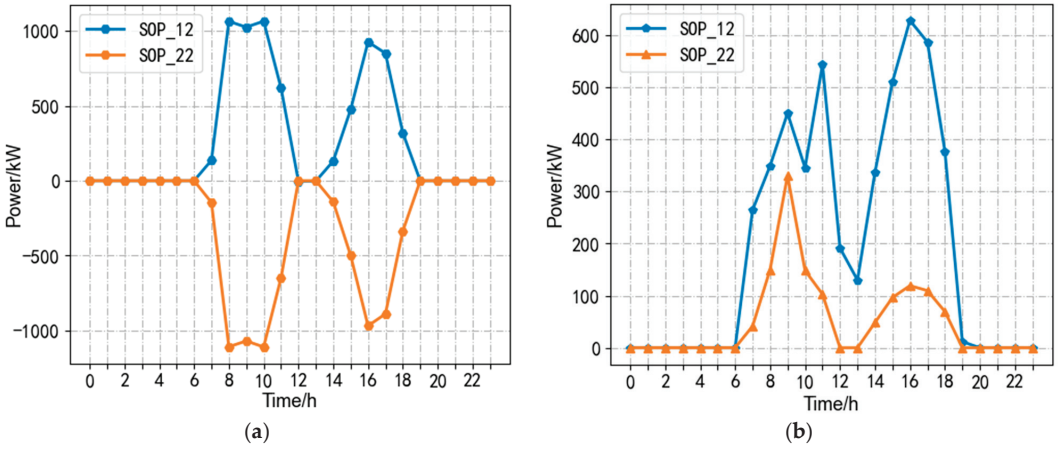

Figure 7. SOP running active and reactive power: (**a**) SOP active power; (**b**) SOP reactive power.

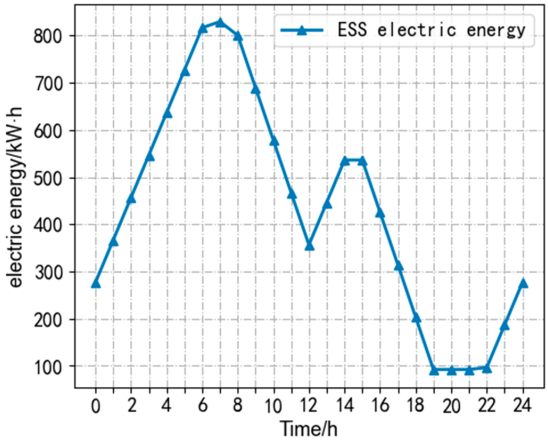

Figure 8. The operating power of ESS.

From Figure 6, it can be seen that the installation of SOP and ESS changes the voltage distribution at each node, while the installation of photovoltaic units raises the voltage at each node. From Figures 4 and 7, it can be seen that during the time periods of 6:00–11:00 and 14:00–19:00, when the system load is high, SOP provides reactive power compensation to balance the power distribution in the system. As can be seen from Figure 8, ESS will charge before the peak load, and supply power to the grid after the peak to balance the load burden. The charging power is low at 14:00 because the PV output power is high at this time and the load is lower than in the morning session, therefore, the demand for ESS power is correspondingly reduced.

3. Scheme 3

The system installed one set of SOP and ESS each and a set of photovoltaic units was installed at node 11. After optimization using the SOCP-SSGA algorithm, the optimal positions for SOP and ESS were determined to be between nodes 8 and 21 and at node 13, respectively. After optimization, the configuration and economic cost of each capacity are shown in Tables 7 and 8. The voltage changes at each node before and after PV optimization are shown in Figure 9a,b, respectively. The daily active power output and reactive power compensation of SOP after optimization are shown in Figure 10a,b, respectively, and the daily operation of ESS is shown in Figure 11.

Table 7. Optimized capacity configuration in Scheme 3.

Access Device	SOP	ESS	PV
Access Capacity (MW)	0.91479 × 2	1.07771	4.8532

Table 8. Economic cost after optimization of Scheme 3.

Economic Component	Fee (RMB 10,000)
SOP investment	18.6347
SOP operation and maintenance	1.8296
ESS Investment	10.0727
ESS operation and maintenance	0.8622
Failure loss	3.0117
Electrical energy loss	4.2150
total	38.6259

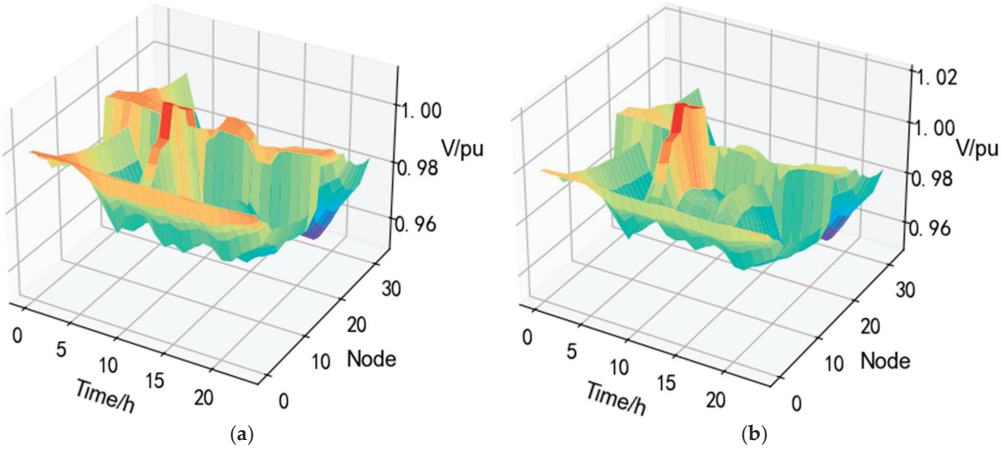

(**a**) (**b**)

Figure 9. Voltage change chart of each node: (**a**) PV not connected; (**b**) Access PV.

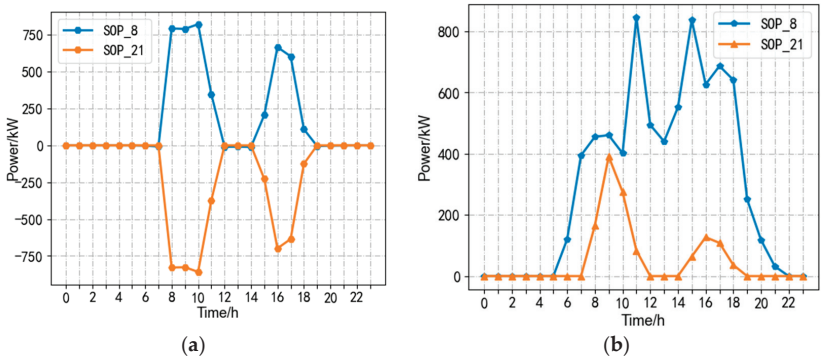

(**a**) (**b**)

Figure 10. SOP running active and reactive power: (**a**) SOP active power; (**b**) SOP reactive power.

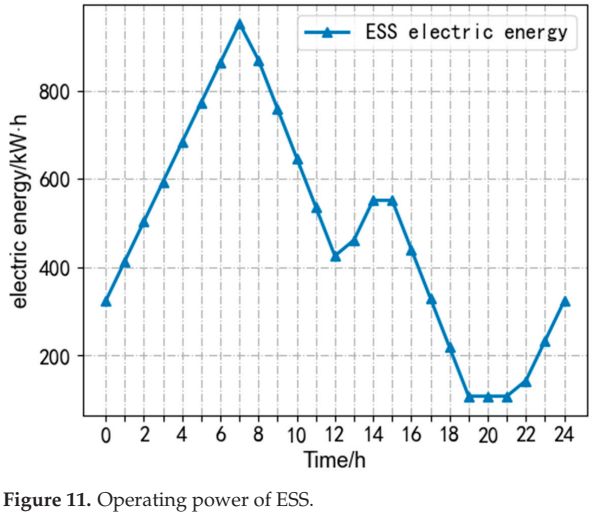

Figure 11. Operating power of ESS.

After SOCP-SSGA is used to optimize the position and capacity in Scheme 3, the operation trend of various system indicators is roughly the same as that in Scheme 2. Moreover, due to reasonable access of SOP and ESS, SOP can provide more accurate reactive power compensation for the system, and after PV is connected to the system, the system voltage fluctuation is small, and various economic indicators of the system are better after optimization.

4. Scheme 4

Two sets of SOP and ESS were installed in the system and one set of PV units was installed at node 11. Based on the optimized location in Scheme 3, the SOCP-SSGA algorithm was used for further optimization. The results showed that the new SOP access points were between nodes 18 and 33, while the ESS access point was at node 25. The optimized capacity configuration and economic cost are shown in Tables 9 and 10, respectively. The voltage changes over a day at each node before and after PV optimization are shown in Figure 12a,b, respectively. The active power output and reactive power compensation of the optimized SOP are shown in Figure 13a,b and the ESS operating power is shown in Figure 14.

Table 9. Optimized capacity configuration in Scheme 4.

Access Device	SOP1	SOP1	ESS1	ESS2	PV
Access Capacity (MW)	0.42591 × 2	0.28113 × 2	0.4264	0.3575	6.4283

Table 10. Economic cost after optimization of Scheme 4.

Economic Component	Fee (RMB 10,000)
SOP investment	14.4028
SOP operation and maintenance	1.4141
ESS Investment	7.3266
ESS operation and maintenance	0. 6271
Failure loss	2.3506
Electrical energy loss	1.8000
total	27.9211

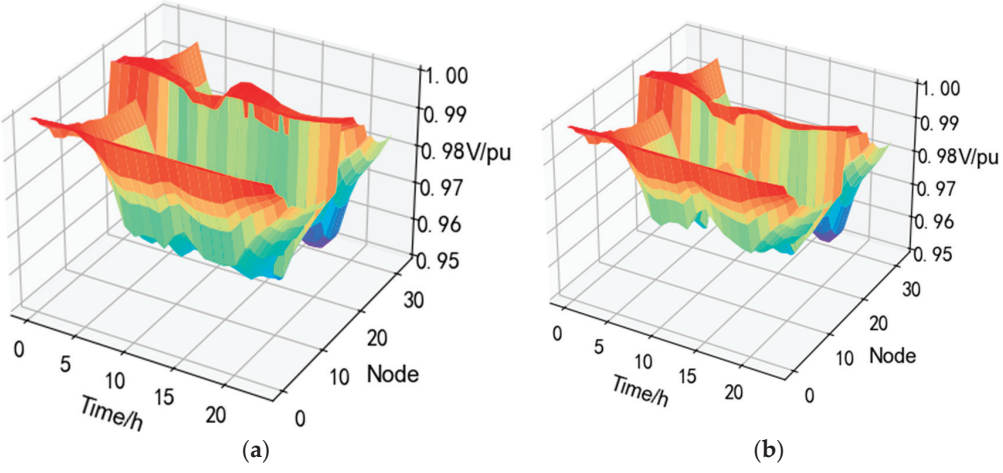

Figure 12. Voltage change chart of each node: (**a**) PV not connected; (**b**) Access PV.

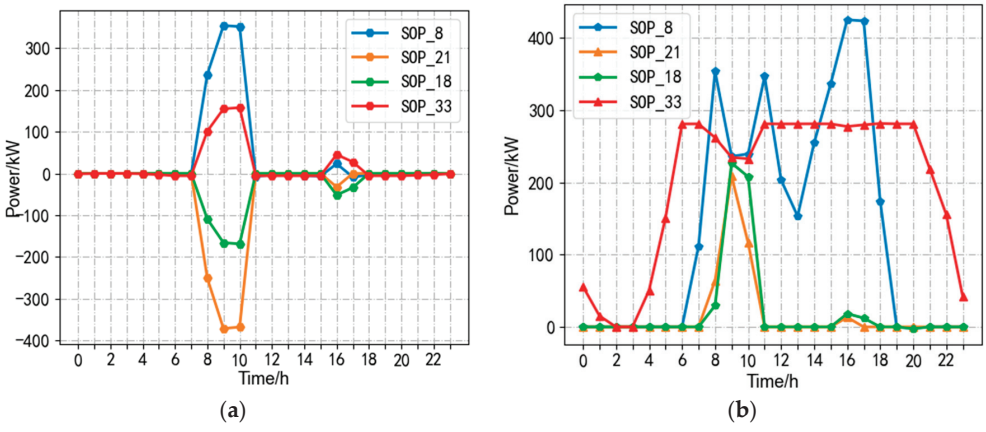

Figure 13. SOP running active and reactive power: (**a**) SOP active power; (**b**) SOP reactive power.

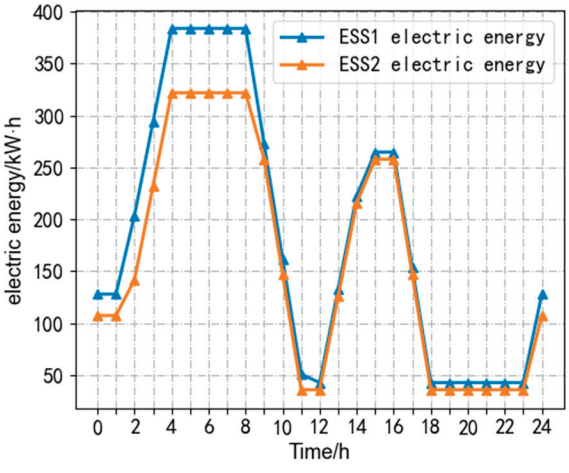

Figure 14. Operating power of ESS.

From Figure 12, it can be seen that as the number of SOP increases, Scheme 4 significantly improves the voltage quality of the distribution network, with voltage values at each node closer to the per-unit value. It can be observed from Figure 12 that the addition of SOP leads to a wider range of reactive power regulation time for Node 33. This is because the new PV is connected to a different feeder than Node 33, and Node 33 has a higher demand for load in the system. Therefore, SOP provides reactive power compensation to better utilize solar energy to regulate voltage and improve system stability.

From the ESS operating energy diagram in each scheme, it can be seen that the distribution network will store energy in the ESS during low load power, and as the load power increases, the ESS releases energy to balance the power load and improve power quality. With the increase of the number of ESS, the new ESS added will share the power system demand with the initial ESS so the installation capacity of the initial ESS can be appropriately reduced, and with the increase of the number of SOP, the regulating ability of the system by SOP becomes more prominent so the ESS access capacity can be further reduced. Similarly, with the increase in the number of SOP, adding a new SOP will reduce the initial SOP capacity, and multiple SOPs can cooperate to regulate the distribution-network system, and the voltage level is significantly improved.

Four schemes were compared and analyzed. In Scheme 1, the SOP and ESS are not connected to the system. When compared with this scheme, it was found that in Scheme 2, after the SOP and ESS were randomly connected, the PV capacity of the distribution network was increased from 3.7865 MW to 4.3254 MW, while the fault-loss cost decreased from RMB 78,965 to RMB 56,928. Therefore, it can be concluded that connecting the SOP and ESS significantly increases the PV access capacity and reduces the fault-loss cost.

In Scheme 3, the system optimizes access to a set of SOP and ESS and, compared with the random access of the Scheme 2 system, it can be found that the installation location and capacity of SOP and ESS after the optimization of Scheme 3 are better, mainly reflected in the fact that the system-failure loss cost after optimization is reduced from RMB 56,928 to RMB 30,117, the total economic cost is reduced from RMB 447,988 to RMB 386,259, and the PV capacity is increased from 4.3254 MW to 4.8532 MW.

With the increase in the number of Sops and ESS installed in Scheme 4, compared with the single access Sops and ESS in Scheme 3, the investment, operation, and maintenance cost of multiple Sops and ESS is lower than the investment and operation and maintenance cost of single access Sops and ESS. The fundamental reason is that multiple Sops and ESS can coordinate different locations of the distribution network, thus easing the adjustment pressure required for a single access. In addition, with the increase in the number of ESS and SOP access, the fault-loss cost and power-loss cost of the distribution network decreased significantly, the fault loss cost decreased from RMB 30,117 to RMB 23,506, and the power loss cost decreased from RMB 42,150 in the single optimized access to RMB 18,000. The PV access capacity increased from 4.3254 MW to 6.4283 MW and the access capacity was significantly improved.

5.3. Discussion

The results of the two-stage optimization model constructed in this article are influenced by several factors. Firstly, the type and severity of faults are important factors that affect the model results. Different types of faults may have different impacts on the load transfer after SOP access, which will directly affect the calculation results of the model. Secondly, the characteristics of the storage system also affect the model results. Different sizes, types, and technologies of ESS may have different performances, leading to differences in the model's solution results. In addition, market factors such as market competition, price changes, and policy changes are also important factors. With the continuous development of technology, the performance and cost of SOP, ESS, and PV may change, which may affect the model. Therefore, in future research, it is necessary to conduct experiments on the model under different fault scenarios, consider market factors, and test and analyze the specific characteristics of different SOPs, ESS, and PVs to better evaluate the reliability of the model.

6. Conclusions

In this paper, considering the uncertainty of distributed PV and load, the scenario reduction was carried out to form a typical PV-load output scenario, the location and capacity-planning model of two-stage SOP, ESS, and PV under multiple scenarios was established, and the SOCP-SSGA hybrid optimization algorithm was used to solve the problem. Simulation analysis and verification are carried out on the improved IEEE33-node distribution network, and the results of different access schemes are compared. The following conclusions are drawn:

(1) The SOP and ESS siting-capacity model proposed in this paper introduces fault-cost indexes under multiple scenarios into the planning objective function, which not only considers the network loss during normal operation of the distribution network but also considers the load-supporting role of SOP and ESS after faults, so as to further reduce the comprehensive operation cost of the distribution network.

(2) The SOCP-SSGA hybrid optimization algorithm was adopted to solve the problem. The planning model proposed in this paper integrated all typical scenarios and

calculated the access location and capacity of SOP and ESS. The application of this planning model makes the access scheme applicable to various scenarios so as to improve the accuracy and reliability of distribution-network planning and better meet the actual needs.

(3) The two-stage scale model proposed in this paper improves the maximum access capacity of distributed photovoltaics in the distribution network by fully exploring the regulating role of SOP and ESS and improves the economic benefits of the distribution network on the basis of ensuring the safe operation of the system, improves the flexibility and operation efficiency of the distribution network, and makes better use of the advantages of SOP and ESS.

Author Contributions: Conceptualization, Y.J. and Q.L.; methodology, Y.J. and Q.L.; validation, J.W.; Project administration, Q.L.; data curation, X.L. and L.L.; writing—original draft preparation, Y.J.; writing—review and editing, Q.L.; supervision, Y.J. and Q.L.; All authors have read and agreed to the published version of the manuscript.

Funding: This research was funded by the National Natural Science Foundation of China, grant number 52267008.

Institutional Review Board Statement: Not applicable.

Informed Consent Statement: Not applicable.

Data Availability Statement: Not applicable.

Conflicts of Interest: The authors declare no conflict of interest.

References

1. Lai, C.; Li, J.; Chen, B.; Huang, Y.; Wei, S. Review of Photovoltaic Power Output Prediction Technology. *Trans. China Electrotech. Soc.* **2019**, *34*, 1201–1217. [CrossRef]
2. Chai, Y.; Guo, L.; Wang, C.; Liu, Y.; Zhao, Z. Hierarchical Distributed Voltage Optimization Method for HV and MV Distribution Networks. *IEEE Trans. Smart Grid* **2020**, *11*, 968–980. [CrossRef]
3. Lin, X.; Li, Z.; Ye, Y.; Ma, X.; Wang, Z.; Xu, F.; Wang, C. Sizing method of flexible multi-state switches based on union-find set. *Electr. Power Autom. Equip.* **2020**, *40*, 1–8. [CrossRef]
4. Yang, W.; Tu, C.; Lan, Z.; Xiao, F.; Guo, Q.; Wang, X. Flexible interconnection strategy between DC microgrid and AC distribution grid based on energy storage flexible multi-state switch. *Electr. Power Autom. Equip.* **2021**, *41*, 254–260. [CrossRef]
5. Jia, G.; Chen, M.; Zhao, B.; Lu, Y.; Yang, Y. Application of Flexible Multi-State Switch in Intelligent Distribution Network. *Trans. China Electrotech. Soc.* **2019**, *34*, 1760–1768. [CrossRef]
6. Ji, H.; Wang, C.; Li, P.; Ding, F.; Wu, J. Robust operation of soft open points in active distribution networks with high penetration of photovoltaic integration. *IEEE Trans. Sustain. Energy* **2019**, *10*, 280–289. [CrossRef]
7. Peng, Y.; Mai, Z.; Ai, W.; Li, M.; Yan, H.; Dong, J. Active and Reactive Power Coordinated Dynamic Optimization for Active Distribution Network with Flexible Distribution Switch. *Autom. Electr. Power Syst.* **2020**, *44*, 54–61. [CrossRef]
8. Liu, W.; Huang, Y.; Yang, Y.; Liu, X. Reliability evaluation and analysis of multi-terminal interconnect power distribution system with flexible multi-state switch. *ET Gener. Transm. Distrib.* **2020**, *14*, 4746–4754. [CrossRef]
9. Li, Z.; Ye, Y.; Wang, Z.; Wu, Y.; Xu, H. Integrated Planning and Operation Evaluation of Micro-Distribution Network Based on Flexible Multi-State Switch Interconnection. *Trans. China Electrotech. Soc.* **2021**, *36*, 487–495+516. [CrossRef]
10. Ye, Y.; Ma, X.; Lin, X.; Li, Z.; Lu, Y.; Ding, C. Study on Site Selection of Soft Open Points Based on Dynamic GA Coding Strategy. *High Volt. Eng.* **2020**, *46*, 1171–1181. [CrossRef]
11. Wang, C.; Song, G.; Li, P.; Ji, H.; Zhao, J.; Wu, J. Optimal Configuration of Soft Open Point for Active Distribution Network Considering the Characteristics of Distributed Generation. *Proc. CSEE* **2017**, *37*, 1889–1897. [CrossRef]
12. Su, R.; He, G.; Su, S.; Duan, Y.; Cheng, J.; Chen, H.; Wang, K.; Zhang, C. Optimal placement and capacity sizing of energy storage systems via NSGA-II in active distribution network. *Front. Energy Res.* **2023**, *10*, 1073194. [CrossRef]
13. Liu, H.; Xu, L.; Hao, S.; Zhang, X.; Zhang, C. Optimization method of distributed hybrid energy storage based on distribution network partition. *Electr. Power Autom. Equip.* **2020**, *40*, 137–145. [CrossRef]
14. Lu, Z.; Xu, X.; Yan, Z. Data-driven stochastic programming for energy storage system planning in high PV-penetrated distribution network. *Int. J. Electr. Power Energy Syst.* **2020**, *123*, 106326. [CrossRef]
15. Rasoul, G.; Mojtaba, M.; Yang, F.; Evan, G.; Lu, J. Multi-objective energy storage capacity optimization considering Microgrid generation uncertainties. *Int. J. Electr. Power Energy Syst.* **2020**, *119*, 105908. [CrossRef]
16. Yan, Q.; Dong, X.; Mu, J.; Ma, Y. Optimal configuration of energy storage in an active distribution network based on improved multi-objective particle swarm optimization. *Power Syst. Prot. Control* **2022**, *50*, 11–19. [CrossRef]

17. Ahmad, A.; Sirjani, R. Optimal Allocation of Energy Storage System in Transmission System Considering Wind Power. In Proceedings of the 2020 7th International Conference on Electrical and Electronics Engineering (ICEEE), Antalya, Turkey, 14–16 April 2020. [CrossRef]
18. Bai, L.; Jiang, T.; Li, F.; Chen, H.; Li, X. Distributed energy storage planning in soft open point based active distribution networks incorporating network reconfiguration and DG reactive power capability. *Appl. Energy* **2018**, *210*, 1082–1091. [CrossRef]
19. Sun, C.; Li, J.; Yuan, K.; Song, G.; Ji, J.; Li, P. Two-stage Optimization Method of Soft Open Point and Energy Storage System in Distribution Network Based on Interval Optimization. *High Volt. Eng.* **2021**, *47*, 45–54. [CrossRef]
20. Yao, C.; Zhou, C.; Yu, J.; Xu, K.; Li, P.; Song, G. A Sequential Optimization Method for Soft Open Point Integrated with Energy Storage in Active Distribution Networks. *Energy Procedia* **2018**, *145*, 528–533. [CrossRef]
21. Wang, J.; Zhou, N.; Tao, A.; Wang, Q. Optimal Operation of Soft Open Points-Based Energy Storage in Active Distribution Networks by Considering the Battery Lifetime. *Front. Energy Res.* **2021**, *10*, 633401. [CrossRef]
22. Huang, Z.; Chen, Y.; Mao, Z.; Sun, J.; Cha, X. Joint Access Planning of Soft Open Point and Distributed Energy Storage System. *Autom. Electr. Power Syst.* **2022**, *46*, 29–37.
23. Su., M.; Huo, Q.; Wei, T.; Guo, X. Flexible Multi-State Switch Application Scenario Analysis. In Proceedings of the 2019 14th IEEE Conference on Industrial Electronics and Applications (ICIEA), Xi'an, China, 19–21 June 2019. [CrossRef]
24. Wang, C.; Sun, C.; Li, P.; Xing, F.; Yu, Y. SNOP- based Operation Optimization and Analysis of Distribution Networks. *Autom. Electr. Power Syst.* **2015**, *39*, 82–87.
25. Li, P.; Ji, H.; Wang, C.; Zhao, J.; Song, G.; Ding, F.; Wu, J. Coordinated Control Method of Voltage and Reactive Power for Active Distribution Networks Based on Soft Open Point. *IEEE Trans. Sustain. Energy* **2017**, *8*, 1430–1442. [CrossRef]
26. Su, M.; Wei, T.; Huo, Q.; Guo, X. Research on Feeder Interconnect Flexible Multi-State Switch. In Proceedings of the 2019 IEEE Innovative Smart Grid Technologies—Asia (ISGT Asia), Chengdu, China, 21–24 May 2019. [CrossRef]
27. Yu, C.; Zhang, G.; Peng, B.; Xie, R.; Shen, C.; Xu, K. Feeder Power Flow Control Strategy for Flexible Multi-state Switch with Joint Access to the Distributed Generation. In Proceedings of the 2020 5th Asia Conference on Power and Electrical Engineering (ACPEE), Chengdu, China, 4–7 June 2020. [CrossRef]
28. Wu, S.; Li, Q.; Liu, J.; Zhou, Q.; Wang, C. Bi-level Optimal Configuration for Combined Cooling Heating and Power Multi-microgrids Based on Energy Storage Station Service. *Power Syst. Technol.* **2021**, *45*, 3822–3832. [CrossRef]
29. Huang, C.; Li, F.; Ding, T.; Jin, Z.; Ma, X. Second-Order Cone Programming-Based Optimal Control Strategy for Wind Energy Conversion Systems Over Complete Operating Regions. *IEEE Trans. Sustain. Energy* **2015**, *6*, 263–271. [CrossRef]
30. Sun, Y.; Zhang, B.; Ge, L.; Denis, S.; Wang, J.; Xu, Z. Day-ahead optimization schedule for gas-electric integrated energy system based on second-order cone programming. *CSEE J. Power Energy Syst.* **2020**, *6*, 142–151. [CrossRef]

electronics

MDPI

Article

Novel Heuristic Optimization Technique to Solve Economic Load Dispatch and Economic Emission Load Dispatch Problems

Nagendra Singh [1,*], Tulika Chakrabarti [2], Prasun Chakrabarti [3], Martin Margala [4], Amit Gupta [5], S. Phani Praveen [6], Sivaneasan Bala Krishnan [7] and Bhuvan Unhelkar [8]

[1] Department of Electrical Engineering, Trinity College of Engineering and Technology, Karimnagar 505001, Telangana, India
[2] Department of Chemistry, Sir Padampat Singhania University, Udaipur 313601, Rajasthan, India; tulika.chakrabarti@spsu.ac.in
[3] Department of Computer Science and Engineering, ITM SLS Baroda University, Vadodara 391510, Gujarat, India; drprasun.cse@gmail.com
[4] School of Computing and Informatics, University of Louisiana, Lafayette, LA 70504, USA; martin.margala@louisiana.edu
[5] Department of ECE, Nalla Malla Reddy Engineering College Hyderabad, Hyderabad 500088, Telangana, India; amitgupta.ece@nmrec.edu.in
[6] Department of Computer Science and Engineering, Prasad V. Potluri Siddhartha Institute of Technology, Vijayawada 520007, Andhra Pradesh, India; sppraveen@pvpsiddhartha.ac.in
[7] Engineering Cluster, Singapore Institute of Technology, Singapore 138683, Singapore; sivaneasan@singaporetech.edu.sg
[8] College of Business, University of South Florida, Tampa, FL 33620, USA; bunhelkar@usf.edu
* Correspondence: nsingh007@rediffmail.com

Citation: Singh, N.; Chakrabarti, T.; Chakrabarti, P.; Margala, M.; Gupta, A.; Praveen, S.P.; Krishnan, S.B.; Unhelkar, B. Novel Heuristic Optimization Technique to Solve Economic Load Dispatch and Economic Emission Load Dispatch Problems. *Electronics* **2023**, *12*, 2921. https://doi.org/10.3390/electronics12132921

Academic Editors: Ignacio Hernando-Gil, Da Xie, Yanchi Zhang, Dongdong Li, Chenghong Gu and Nan Zhao

Received: 25 May 2023
Revised: 21 June 2023
Accepted: 26 June 2023
Published: 3 July 2023

Abstract: The fundamental objective of economic load dispatch is to operate the available generating units such that the needed load demand satisfies the lowest generation cost and also complies with the various constraints. With proper power system operation planning using optimized generation limits, it is possible to reduce the cost of power generation. To fulfill the needs of such objectives, proper planning and economic load dispatch can help to plan the operation of the electrical power system. To optimize the economic load dispatch problems, various classical and new evolutionary optimization approaches have been used in research articles. Classical optimization techniques are outdated due to many limitations and are also unable to provide a global solution to the ELD problem. This work uses a new variant of particle swarm optimization techniques called modified particle swarm optimization, which is effective and efficient at finding optimum solutions for single as well as multi-objective economic load dispatch problems. The proposed MPSO is used to solve single and multi-objective problems. This work considers constraints like power balance and power generation limits. The proposed techniques are tested for three different case studies of ELD and EELD problems. (1) The first case is tested using the data of 13 generating unit systems along with the valve point loading effect; (2) the second case is tested using 15 generating unit systems along with the ramp rate limits; and (3) the third case is tested using the economic emission dispatch (EELD) as a multi-objective problem for 6 generating unit systems. The outcomes of the suggested procedures are contrasted with those of alternative optimization methods. The results show that the suggested strategy is efficient and produces superior optimization outcomes than existing optimization techniques.

Keywords: economic load dispatch (ELD); economic emission load dispatch (EELD); optimization technique; modified novel particle swarm optimization (MPSO); electrical power generation cost; environmental emission

1. Introduction

Since fuel resources (coal) are limited but the demand for electrical power is increasing, part of this research is to find the best solution to reduce the cost of power generation and

reduce emissions so that the global warming problem also reduces. The above-discussed issues are the main motivation for considering this topic in our work [1].

The primary objective of the proposed study is to identify the ideal producing point where the power production system will function and fuel costs may be reduced. If the generating stations operate at the optimum generation point, the generation cost should be minimal for any particular load demand. The second motive is to reduce emissions; if the burning of fuel definitely reduces, the emission of toxic gases also decreases, reducing the pollution level [2,3].

Various classical approaches are listed for finding the optimum solution to the ELD problem, such as linear programming (LP) [3], pattern search PS [4], quadratic programming (QP) [5], etc. Classical methods have many drawbacks, like the LP and QP methods, which need linear mathematical objectives. Pattern search methods are sensitive to changes in the parameters, and the DS (direct search) method's performance for large data is not good.

The objective of the ELD problem is to maintain the generating output power according to the load demand and reduce the cost of power generation [1]. ELD problems are also associated with constraints like power demand, generation limits, line losses, etc. Due to the presence of such constraints, economic load dispatch is a nonlinear computation problem. So, the optimization of such a problem requires efficient evolutionary techniques [2].

Some classical and heuristic methods are not effective for solving nonlinear optimization problems because they have many limitations and take a long time to compute. Most of the modern heuristic techniques are more effective and provide the best solution to the problem [6]. Heuristic optimizations techniques are the newest optimization techniques, as explained in various articles, and are very efficient, simple, and fast at computation. Such techniques effectively optimize the ELD data within seconds and cannot deviate in the direction of a local solution [7].

The latest optimization techniques have many features; they can optimize big data and provide a global solution without deviation from the constraints. These methods are unaffected by initial conditions or changes in the variables [8]. Optimization is the task of finding the most suitable solution to a problem. The optimization process starts randomly to find the solution of the objective function (constraints are also defined) in the search space within the defined limits and with a number of agents, or swarms, and finally finds the solution to the problem, which is the global optimum solution, by exploring as small a set of solutions as possible [9].

The proposed work considered a modified PSO (MPSO), which is the latest variant of particle swarm optimization and is very effective for single objective (ELD) and multi-objective (EELD) problems. This is a new variant of the PSO that has an attraction factor that helps the particle move in the direction of a solution; it controls the movement of particles in such a way that they cannot deviate from the search area.

Other variants of the PSO need to update the velocity and position of the particle continuously until they can find a solution to the problem. This work proposes a new modified PSO, where the velocity of the particles is controlled by the attraction factor in such a way that they cannot stop during the iteration process; hence, there is no need to update the velocity of the particles; only the position of the particles is required to be updated. That is the big advantage of the proposed MPSO. Hence, the speed of computation increases and the particles are also not moved to the local solution. The MPSO always provides a global solution to the proposed ELD and EELD problems.

This paper's remaining sections are structured as follows: the second part demonstrates the works published by the researchers. Here, we considered the last 20 years' papers for the study. The third part of the article presents the mathematical formulation of the economic load dispatch and economic emission dispatch. The fourth section of the article presents the mathematical model and algorithm of the new PSO. The fifth section shows the different case studies and the results of the new PSO compared with other optimization techniques. In the last section, the conclusion of the work is provided.

2. Literature Review

The economic load dispatch is formulated and optimized with various constraints using different optimization techniques to find out the minimum generation cost and fulfill the load demand. This section discusses the various optimization techniques used for finding the optimum solution to the ELD problem.

To address the ELD issues, a biogeography-based optimization technique was proposed. The recommended approach primarily uses the two processes of migration and mutation to obtain the global optimum [1]. A new evolutionary technique is suggested for the optimization of multi-objective ELD problems [2].

The linear programming method is used to obtain the real and reactive power of the electrical generation system; however, such methods take a long computation time and are sometimes unable to provide a global solution for large data sets [3].

The pattern search method was proposed for finding the optimum solution to the ELD problem and the valve loading effects were also considered. The proposed algorithm was tested on various test data for validation of the results and compared with other optimization techniques [4]. Quadratic programming was used for the solution of the ELD problem; this consists of a DC load flow and network security constraints [5]. The PSO techniques used the ELD problem along with transmission losses, dynamic operation limits, and restricted operating zones [6].

Discrete and continuous ELD problem solutions are obtained by using a new variant of the PSO (EPSO). In this article, the ELD problem is formulated with penalties and constraints [7].

Article [8] solved the ELD problem, including the ramp rate limits and the transient stability, by using a novel particle swarm optimization called the chaotic quantum-behaved PSO algorithm.

The authors of [9] considered class-topping optimization techniques that are based on human intelligence. They solve the ELD problem as well as the CEED using four different case studies.

Article [10] proposes QPSO and HQPSO to solve the ELD problem. They solve a case ELD problem consisting of data from 13 generating unit systems along with the valve loading effect, and the results are compared to classical PSO.

To resolve the pollution and economic dispatch issues, a new combined genetic-tabu search technique is provided. The suggested technique is designed such that a basic GA serves as the first search to guide the search towards the ideal region [11].

Article [12] optimized the ELD problem along with the valve loading using the EPSO. The research also includes constraints like the prohibited operating zone.

The QPSO technique was used to find the optimum solution to the ELD problem. The suggested PSO particles move in the search area with good speed and explore the solution quickly [13]. Two test cases of 10 and 15 generating units were taken and optimized for the ELD problem using the PPSO [14]. Article [15] used a combination of differential evolution and a PSO called quantum particle swarm optimization (QPSO) as a solution for economic load dispatch optimization.

An artificial bee colony approach is discussed in the article to resolve the economic dispatch problem [16]. The suggested technique is used to solve the economic dispatch problem along with the power balance and network loss constraints.

The BAT method is demonstrated for the optimization of multi-objective problems. This work considered the economic emission dispatch as a multi-objective problem and found the overall generation cost of the plant [17]. The Chameleon Swarm Algorithm is proposed for the minimization of emissions as well as the generation cost of the power plant [18].

The ELD problem with a valve-point effect is solved using a hybrid method [19]. A novel evolutionary optimization approach is proposed to resolve the economic load dispatch issue. The standard harmony search random selection process is replaced with a

mutation process based on wavelet theory to increase the performance of the suggested strategy [20].

An optimization technique that is based on the teaching-learning approach is used to solve ELD problems without taking transmission losses into account. The suggested solution can handle an ELD while taking a nonlinearity, such as valve point loading, into account [21]. A single objective ELD problem along with a prohibited zone and ramp rate and a multi-objective ELD problem are optimized using C andGPSO [22].

An effective evolutionary technique is using the novel adaptive particle swarm optimization for a limited ED issue [23]. The differential evolution algorithm was investigated for the purpose of resolving power system economic load dispatch issues. Five ELD issues with various features were utilized to test the proposed methods [24]. A contemporary search and rescue optimization approach that is motivated by the behavior of humans during search and rescue operations was used to solve the combined emission and economic dispatch [25].

To overcome the ELD difficulties, an enhanced arithmetic optimization is suggested. Two crucial variables in the original AOA are math optimizer acceleration and math optimizer probability [26]. To optimize multi-objective ELDs, data mining technology is used. The proposed techniques provide the best decision for the sample test data [27].

The "Grey Wolf" approach is taken to solve the challenging nonconvex ELD optimization problems effectively and reliably. The grey wolf optimizer algorithm's search agents are helped by the sine and cosine functions in such a way that the solution cannot move to the local optima [28].

Harris Hawks' techniques are used to address the issues of economic load dispatch. The Harris Hawks Optimizer is used to find the number of possible solutions in the search space; each of these regions can be thoroughly searched for the best local solution via adaptive hill climbing [29].

An optimization algorithm based on the theory of demand and supply was used to optimize the ELD model. The proposed algorithm efficiently moves the particles in the search space between the local and global searches [30].

To address the complex economic load dispatch issue, a new hybrid grey wolf optimization method with a strong learning mechanism has been developed [31]. The foraging optimization method is based on the Spiral Foraging approach given for the solution of the ELD problem. Spiral foraging strategies improve global search capability and convergence velocity [32]. A multi-objective ELD problem was formulated using a wind energy system and a distributed generation system [33].

A hybrid generation system can help reduce the cost of power generation as well as carbon emissions [34]. An adaptive multi-population-based differential evolutionary technique is proposed that improves ELD global solutions [35].

A diffusion model with heterogeneous coefficients and a generic nonlinear incidence rate for brucellosis was used for the solution of economic load dispatch [36]. For the solution of economic load dispatch with emissions subject to power balance and generation limit constraints, a new particle swarm optimization technique was proposed [37]. The model proposed is a nonlinear distributed delayed periodic AG-ecosystem with competition on the time scales. Our approach integrates and generalizes the discrete and continuous situations in terms of the time scale [38].

The Bumble Bee Mating Optimization algorithm is used for economic load dispatch optimization. The proposed BBMO works in three different modes: the queen, the workers, and the drones (males) [39]. A multi-objective optimization method is used in this article for the optimal planning of the distributed generators in electric distribution networks. Reducing the annual cost and network loss, along with improving the reliability of the network, are the main objectives of a multi-objective algorithm [40].

3. Formulation of ELD Problem

The mathematical model for minimizing the cost of generation is given as

$$F_{cT} = \text{Minimize} \sum_{i=1}^{N} FC_i(P_i) \tag{1}$$

$$FC_i(P_i) = a_i P_i^2 + b_i P_i + c_i \tag{2}$$

3.1. Formulation of Economic Dispatch along with Valve Point

When using a multi-valve steam turbine system, the fuel cost function of the generating units may vary [4]. The cost of generation increases with the use of multi-valve steam turbines. The generator heat rate curve is the result of the multi-valve steam turbine valve opening operation. The impact of valve-point loading is shown in Figure 1 [22]. In Figure 1, A, B, C, D, and E are the points where the valve can be opened to control the speed of the generator if the load suddenly increases. Due to the opening of the valve, the normal fuel ignition characteristic of the generating plant changes.

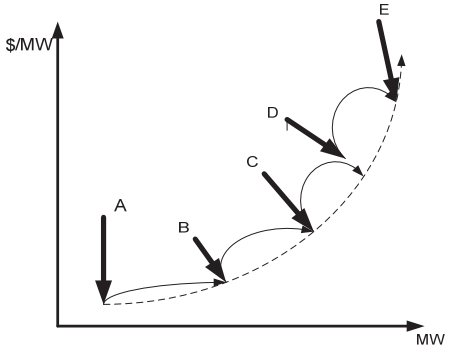

Figure 1. Effect of the valves' loading on generation cost function.

The importance of this impact lies in the fact that the huge steam-producing cost curve's function is, in reality, nonlinear rather than continuous. In reality, the input–output curves for generating units are not a smooth cost function when considering a multi-valve steam operating system. The representation of the cost functions of the generating units is changed by the inclusion of the valve-point loading. Hence, the economic load dispatch cost function is modified when considering the valve point effects [22]; it is mathematically formulated as given in Equation (3).

$$C_{iv}(P_i) = a_i P_i^2 + b_i P_i + c_i + \left| E_i * \sin(F_i \left(P_i^{min} - P_i \right) \right| \tag{3}$$

3.2. Formulation of the ELD with a Ramp Rate Limit

When generating units are operated online, the actual operating ranges depend on the ramp rate limits [14]. The operation of the generating units at the different intervals is shown in Figure 2. The steady-state condition of generation is shown in Figure 2a; when generation increases, it is represented in Figure 2b; Figure 2c shown when generation decreases.

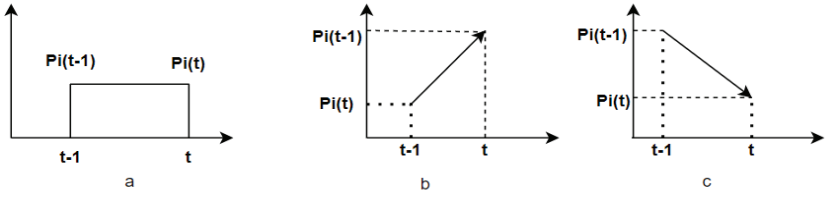

Figure 2. Power generation limits due to ramp rate limits.

When power generation increases, as shown in Figure 2b, it is represented as

$$P_i(t) + P_i(t-1) \leq UR_i \tag{4}$$

and when power generation decreases, as shown in Figure 2c, it is given as

$$P_i(t-1) - P_i(t) \geq DR_i \tag{5}$$

Now the economic load dispatch, with an up rate and down rate of power, is defined as

$$P_{min} = \text{Max}\left[\left(P_i^{min},\ P_i(t-1) - DR_i\right)\right] \tag{6}$$

$$P_{max} = \text{Min}\left[(P_i^{max}, P_i(t-1) - UR_i)\right] \tag{7}$$

$$P_{i,min} \leq P_i \leq P_{i,max} \tag{8}$$

where UR_i and DR_i are the upper and down ramp rate limits, respectively.

3.3. Formulation of the EELD Multi-Objective Problem

When generating power in a thermal power plant, coal is used as fuel; due to the burning of coal, toxic gases like COx, NOx, and SOx are emitted. Such toxic gases not only pollute the environment but also affect human health. So, reducing the emission of gases is a great achievement of the ELD solution. So, when considering the minimization of generation costs and environmental emissions, it is formulated as a multi-objective EELD (economic emission load dispatch) problem [2].

The first objective is the minimization of the cost function already discussed, given in Equations (1) and (2); the minimization of the environmental emission considered as the second objective is given as

$$EC_T = \text{Minimize} \sum_{i=1}^{N} FE_i(P_i) \tag{9}$$

$$FE_i(P_i) = f_i + e_i P_i + d_i P_i^2 \tag{10}$$

To obtain the economic emission dispatch, both objectives are combined using the penalty factor given in Equation (11). The ratio of the power produced by the plant to the actual power requirement of the load being satisfied after line loss is known as the penalty factor (h_i)

$$\frac{Fc_i(P_{i.max})}{FE_i(P_{i.max})} = h_i \tag{11}$$

where

$$FC_i(P_{i.max}) = a_i P_{i.max}^2 + b_i P_{i.max} + c_i \text{ and} \tag{12}$$

$$FE_i(P_{i.max}) = f_i + e_i P_{i.max} + d_i P_{i.max}^2 \tag{13}$$

$$E_T = FC_T + h_i * FE_i \tag{14}$$

where E_T is the total economic emission cost.

3.4. Constraints

When optimized, the ELD problem is required to follow some restrictions or limitations, called constraints. During the formulation of the ELD mathematical model, keep in mind that the constraints should be inserted and then optimized. This work included the following constraints.

3.4.1. Power Balance

The power balancing restrictions make sure that the total amount of power generated by all the different kinds of generating unit is sufficient to satisfy the power load in each time period.

$$\sum_{i=1}^{n} P_i - P_L = P_D \tag{15}$$

3.4.2. Power Limits

The generator's output power must not exceed its nominal value and must not fall below the level required for the boiler to operate steadily. As a result, the production is capped at a certain minimum and maximum range. The following equation may be used to represent each productivity unit with an expected production in the circuit.

$$P_{min} \leq P_i \leq P_{max} \tag{16}$$

4. Heuristic Optimization Technique

The ELD problem is nonlinear in nature because of the presence of different constraints. For the optimization of such nonlinear ELD problems, classical methods were found to be inefficient, and hence, new heuristic optimization techniques were required. The PSO was first introduced in 1995 [1]. After that, many new variants of PSO were investigated and implemented in optimization problems. The PSO is used for the optimization of various nonlinear problems; however, it has some disadvantages, such as difficulties in premature convergence, lagging performance for large test data, diversity in the local solutions, and the appropriate tuning of its parameters.

This work is considered a modified particle swarm optimization technique. A modified PSO is an effective variant of a PSO and can easily optimize single and multi-objective ELD problems. In the MPSO, we are using an attraction factor as shown in Equation (25) that has the following features:

- It controls the movements of the particles in such a way that they cannot move away from the search area;
- It continuously changes the particles' positions so the particles cannot stop during the iteration process until the final results are obtained; therefore, there is no need to update the velocity of the particles after every iteration;
- It also attracts the particles so they cannot move to the local solution.

4.1. Initialization of the Swarm

To optimize the proposed technique, the swarm is required to be initialized randomly within the effective real power minimum and maximum limits of the power generated (P_{min} and P_{max}) using the generating units, as given in Equation (17), and the velocity of the initialized particles, as given in Equation (18).

$$S_i^k = P_{min} + \text{rand}(P_{max} - P_{min}) \tag{17}$$

$$V_i^k = V_{min} + \text{rand}(V_{max} - V_{min}) \tag{18}$$

where $P_{initial}$ and $V_{initial}$ are the initial values of the swarm's position and its velocities are randomly generated using a random positive number (rand) between zero and one using MATLAB software when the algorithm is executed.

Now, initialize the limits of the velocity of the particles using Equations (19) and (20).

$$V_{max} = (P_{max} - P_{min})/10 \tag{19}$$

$$V_{min} = -V_{max} \tag{20}$$

4.2. Updating the Velocity of the Particle

The velocity of the particle is updated using the personal best and the global best value of the swarm is given as

$$V_{inew}^{(K+1)} = WV_i^K + \text{rand} * c_1\left(P_{best,i} - S_i^K\right) + \text{rand} * c_2\left(g_{best,i} - S_i^K\right) \tag{21}$$

Inertia weight helps to accelerate the particles in the search space and is given as

$$W = W_{max} - \frac{W_{max} - W_{min}}{iter_{max}} \times \text{iteration} \tag{22}$$

During the considered optimization, there were 100 iterations: W_{max} and W_{min} were considered 0.9 and 0.4, respectively, and c_1 and c_2 were 2.05.

4.3. Updating the Particles' Positions

This PSO used one attraction factor (S_d) that can attract the particles in the search area and find the global solution to the problem. N is the number of generating units. It is represented as follows.

$$S_d = P_{best} * \text{rand} + g_{i,best} * (1 - \text{rand}) \tag{23}$$

where rand is a random variable generated using MATLAB between 0 and 1, P_{best} is the best value of the particle, and $g_{i,best}$ is the global value.

The positions of the particles are updated by using the best global position of the particles and an attraction factor, as follows.

$$n_{i,best} = \sum_{i=1}^{N} \frac{P_{i,best}}{N} \tag{24}$$

$$\sigma = \frac{R_1 - R_2}{R_3} \tag{25}$$

where R_1 and R_2 are random variables within [0, 1] and R_3 within [−1, 1].

$$S_i^{K+1} = S_d + \alpha * \sigma\left(n_{i,best} - S_i^K\right) \tag{26}$$

4.4. Algorithm of the Proposed MPSO

- Consider the number of particles;
- Define the number of iterations;
- Initialize the swarm using the minimum and maximum values of the generated power, as given in Equations (17) and (18);
- Initialize the velocity of the particles, as shown in Equations (19) and (20);
- Define the objective function of the ELD;

- Define the constraints;
- Initialize the pbest;
- Select the best global values;
- Update the velocity of the particles;
- Insert an attraction factor;
- Update the position of the particles;
- After completing the iteration, collect the best global values;
- Terminate the algorithm if the objective is fulfilled; otherwise, repeat the process again.

A pseudo code of the new modified PSO is given in Figure 3. The conversance characteristic of the modified PSO (MPSO) is shown in Figure 4. It was obtained between the objective functions (ELD and EELD) and the number of iterations taken. In the entire test case, 100 iterations were considered.

Pseudo code of NPSO

K=Number of generating units
Iter=1+itermax
Itermax=100
P=no. of the swarm (population size)
P_i^{Min} =minimum value of generated power
P_i^{max} = maximum value of generated power
For i=K ,j=K
Initialize the position of the particles randomly ($S_i^T = P_i^{Min} + rand * P_i^{Max)}$
Initialized the velocity of the particle randomly ($V_i^k = V_i^{Min} + rand * V_i^{Max}$)
End
End
Check whether the particle positions are under the limits of maximum and minimum limits of power generated
Check whether the speed of the particles between maximum and minimum limits of velocity
If $P_i^{Min} \leq S_i^K \geq P_i^{Max}$
$S_i^K = P_i^{Max}$
End
Formulate the objective function and insert the constant values
For i=1:P
Determine the attraction factor using equation (23)
Update the position of the particles using equation (26)
if
$S_i^{k+1} \geq S_i^K$
Pbest= S_i^{k+1}

Figure 3. Pseudo code for the NPSO.

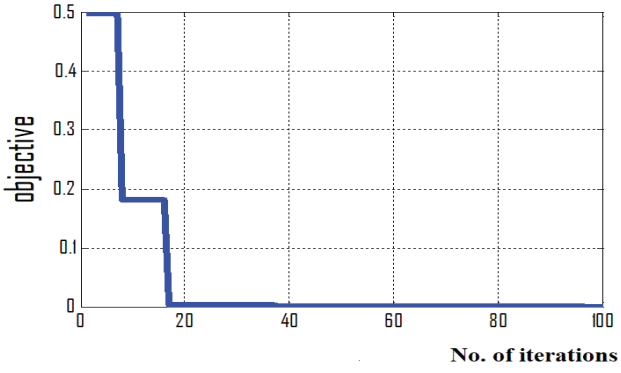

Figure 4. Convergence characteristic of the MPSO plotted between the objective functions and the iteration.

5. Case Study and Result Analysis

All the case studies were run in MATLAB 2022 using a personal laptop, HP P5 8th generation, for the 100 iterations. For each case, 50 trials were considered because after 50 iterations the results were repeated; therefore, only 100 iterations were considered.

5.1. Case 1

For this case study, the test data from 13 generating systems were considered, as shown in Table 1. This case was analyzed with the valve loading effect (E_i and F_i), for the load demand of 1800 MW, included [10,19–22]. Here, a_i, b_i, and c_i are the cost coefficients.

Table 1. Test data for case 1 of 13 generating units for the load demand of 1800 MW.

Gen. Units	P_i^{min}	P_i^{Max}	c_i	b_i	a_i	E_i	F_i
1	0	680	550	8.10	0.00028	300	0.035
2	0	360	309	8.10	0.00056	200	0.042
3	0	360	307	8.10	0.00056	150	0.042
4	60	180	240	7.74	0.00324	150	0.063
5	60	180	240	7.74	0.00324	150	0.063
6	60	180	240	7.74	0.00324	150	0.063
7	60	180	240	7.74	0.00324	150	0.063
8	60	180	240	7.74	0.00324	150	0.063
9	60	180	240	7.74	0.00324	150	0.063
10	40	120	126	8.60	0.00284	100	0.084
11	40	120	126	8.60	0.00284	100	0.084
12	55	120	126	8.60	0.00284	100	0.084
13	55	120	126	8.60	0.00284	100	0.084

The optimum results obtained with the proposed modified PSO are shown in Table 2. The obtained results are compared with other techniques for the validation of the results and show the effectiveness of the proposed algorithm. The results obtained using the MPSO are compared with the HQPSO [10], DE [19], harmony search HS [20], TLBO [21], QPGPSO [22], GPSO-w [22], HHO [29], and ESCSDO [30]. The proposed MPSO has a minimum generation cost of USD 17,962.72/h and a very low computation time of 0.8921 s.

Table 2. Comparative results of 13 generating unit systems.

Power Output	HS [20]	DE [19]	HQPSO [10]	TLBO [21]	GPSO-w [22]	QPGPSO [22]	HHO [29]	ESCSDO [30]	PSO [36]	MPSO
P1(MW)	628.318	628.317	628.318	364.99	628.3185	628.3185		538.5587		628.29
P2(MW)	149.59	149.24	149.109	227.95	224.3707	223.3356		75.6427		149.68
P3(MW)	222.74	223.168	223.322	217.46	148.7126	298.6696		224.3995		222.76
P4(MW)	109.86	109.85	109.865	95.225	60	109.8547		109.8666		109.88
P5(MW)	60	109.86	109.862	106.67	109.865	60		109.8666		60
P6(MW)	109.87	109.866	109.866	123.54	109.6557	60		109.8666		109.85
P7(MW)	109.87	109.82	109.791	112.53	60	60		109.8666		109.854
P8(MW)	109.86	109.82	60.000	144.22	159.73	109.866		109.8666		109.785
P9(MW)	109.686	60	109.866	126.07	109.5848	60		109.8666		109.899
P10(MW)	40	40	40	60.236	40	40		40		40
P11(MW)	40	40	40	48.475	40	40		77.39996		40
P12(MW)	55	55	55	91.364	55	55		92.39991		55
P13(MW)	55	55	55	81.239	55	55		92.39991		55
Power output (MW)	1800	1800	1800	1800	1800	1800		1800	1800	1800
Total fuel cost (USD/h)	17,963.83	17,963.94	17,963.95	18,141.02	17,978.62	19,971.85	17,986.03	18,028.19	18,205.78	17,962.72
CPU time (s)	13.7	5.42	7.58	31.6	38.4	40	5.7	3.82	77.37	1.8921

5.2. Case 2

In this case study, the test data from 15 generating unit systems are considered. This test data system was analyzed with ramp-rate limits. The test data was tested for a load of 2650 MW [14,22]. This system's test data are shown in Table 3.

Table 3. Fuel cost coefficients, ramp rate limits and the generation limits of 15 generating unit systems for a load demand of 2650 MW.

No. Unit	c_i	b_i	a_i	P_i^{min}	P_i^{max}	P_i	UR_i	DR_i
1	671	10.1	0.000299	150	455	400	80	120
2	574	10.2	0.000183	150	455	300	80	120
3	374	8.8	0.001126	20	130	105	130	130
4	374	8.8	0.001126	20	130	100	130	130
5	461	10.4	0.000205	150	470	90	80	120
6	630	10.1	0.000301	135	460	400	80	120
7	548	9.8	0.000364	135	465	350	80	120
8	227	11.2	0.000338	60	300	95	65	100
9	173	11.2	0.000807	25	162	105	60	100
10	175	10.7	0.001203	25	160	110	60	100
11	186	10.2	0.003586	20	80	60	80	80
12	230	9.9	0.005513	20	80	40	80	80
13	225	13.1	0.000371	25	85	30	80	80
14	309	12.1	0.001929	15	55	20	55	55
15	323	12.4	0.004447	15	55	20	55	55

The optimum results obtained with the proposed MPSO are listed in Table 4. The results obtained with the proposed algorithm are compared for validation with recently

developed optimization algorithms like the PPSO [14], Fuzzy and APSO [23], GPSO-w [22], GA [24], G-SCNHGWO [28], and ESCSDO [30]. Results shown in the table clearly show the effectiveness of the modified PSO; it performs better and has a minimum generation cost. The minimum fuel cost given by the MPSO is USD 32,465.69/h and the computation time is 0.824 s.

Table 4. Test results of case 2 for 15 generating unit systems.

Power Output (MW)	PPSO [14]	Fuzzy and APSO [23]	GPSO-w [22]	GA [24]	G-SCNHGWO [28]	ESCSDO [30]	PSO [23]	MPSO
P1	455	455	-	-	455	455	454.9999	421.4
P2	455	455	-	-	380	379.9996	454.9999	455
P3	130	130	-	-	130	129.9999	130	130.6
P4	130	130	-	-	130	130	130	131.6
P5	231.05	271.78	-	-	170	170	234.2005	341
P6	460	460	-	-	460	460	460	460
P7	465	465	-	-	430	430	464.9999	465
P8	60	60	-	-	67.9593	70.257	60	70
P9	25	25	-	-	58.0137	59.332	25	21.6
P10	35.5224	25	-	-	159.99	159.9	30.9939	20
P11	74.29	43.41	-	-	80	80	76.7014	20
P12	80	55	-	-	80	80	79.9999	63.2
P13	25	25	-	-	25	25	25	22
P14	15	15	-	-	17.9118	15	15	13.6
P15	15	15	-	-	15	15	15	15
Total Power (MW)	2650	2650	2650	2650	2650	2650	2650	2650
Fuel Cost (USD/h)	32,543.289	32,548.06	32,548.6	33,063.5	32,687.10	32,692.401	32,858.01	32,465.69
CPU time (s)	3.47	8.7	40	33.5	14.92	2.90	11.3	1.87

5.3. Case 3

This case study is considered multi-objective test data. In this case, we evaluated the economic load dispatch and environmental emissions. Then, both objectives are combined to find the overall economic emissions dispatch. The test data for this case study are shown in Table 5. The case data are tested for a load demand of 900 MW for six generating units along with the emission and fuel cost coefficients.

Table 5. Test data for case 3 for a load demand of 900 MW.

Gen. Unit	a_i	b_i	c_i	d_i	e_i	f_i	P_i^{min}	P_i^{max}
1	0.1525	38.54	756.8	0.0042	0.33	13.86	10	125
2	0.106	46.2	451.4	0.004	0.33	13.9	10	150
3	0.02083	40.159	1049.99	0.00683	−0.55	40.27	35	225
4	0.0356	38.31	1234.5	0.0068	−0.55	40.27	35	210
5	0.0211	36.33	1658.6	0.0046	−0.52	42.7	130	325
6	0.0179	38.27	1356.7	0.0042	−0.52	42.7	125	315

Now, the six generating units' data are analyzed for the load demand of 900 MW. The case data are tested with environmental emissions. The results obtained with the proposed modified PSO technique are shown in Table 6. The MSPO results were compared, for validation, with the BAT [17], ABC [16], RGA [17], and ACB [18] and the proposed algorithm was found to gives the best results compared to the other techniques, as shown in Table 6. The MPSO gives a minimum generation cost of USD 47,889.45/h, a minimum emission discharge of 669.3217 T/h, and a total economic emission dispatch cost of 81,489.12 for a load demand of 900 MW.

Table 6. Results of the six generating units for the economic emission dispatch for a demand of 900 MW.

Output Power	BAT [17]	ABC [16]	RGA [17]	ACB [18]	MPSO
P1(MW)	92.3288	92.3297		92.315	79.4
P2(MW)	98.3910	98.3912		98.3707	99.98
P3(MW)	150.1132	150.1948		150.1997	154.4
P4(MW)	148.586	148.5588		148.5549	145.84
P5(MW)	220.4007	220.4043		220.4051	223.26
P6(MW)	218.1267	218.1307		218.115	224.14
Losses(MW)	28.008975	28.009673	29.725	28.004	27.26
Power output (MW)	928	928	929.725	928.004	927.26
Fuel cost (USD/h)	48,350.163	48,350.683	48,567.7	48,108	47,889.45
Emission (Ton/h)	693.772	693.788	694.19	693.791	669.3217
Total cost(USD/h)	81,527.739	81,529	81,764	81,527	81,489.12
Computation time(s)	11.47	5.28	2.94	3.81	1.72

Before combining the fuel cost and emission required values of the penalty factor shown in Equation (11) using the Equations (12) and (13), the penalty factor (hi) is calculated for six generating units, as given in Table 7.

Table 7. Penalty factor h values.

Generating Units	hi
1	65.9
2	61.6
3	42.4
4	47.89
5	43.64
6	51.3

6. Conclusions

Policies are required for the generation of power in such a way that it fulfils load demands, generates the power at a low cost, and emits fewer toxic gases into the environment. ELD is one of the best optimization approaches that can help generate power with a minimum fuel cost. This work proposes a new PSO for the optimization of economic load dispatch as a single objective for thirteen generating units with valve loading effects and for fifteen generating units with ramp rate limits. The performance of the proposed PSO is important in terms of the minimum generation cost and the computation time taken. According to the results shown for both single objective cases, the performance of the proposed new PSO is better than the other optimization techniques; it also has a

minimum generation cost and takes less computation time (the results are tabulated in Tables 2 and 4). Similarly, the proposed new PSO algorithm was tested for a multi-objective economic emission dispatch problem with line losses. In this case, the performance of the proposed algorithm was the best in comparison with the other techniques (the results are tabulated in Table 6). The proposed algorithm was able to provide the minimum generation cost, the minimum emission, and the minimum total cost, with less computation time (generation +emission). Overall, the proposed technique's performance was the best and it was effective for single as well as multi-objective problems.

Author Contributions: N.S. and T.C. developed the MATLAB coding; S.P.P. and A.G. found the data for optimization; M.M., S.P.P. and S.B.K. formulated the mathematical model for the different objectives; N.S. and B.U. found the best results of the data set after optimization. T.C. and A.G. investigated the reviews of the different articles. S.P.P. and S.B.K. calculated the validation of the results. N.S., S.P.P. and P.C. were responsible for the writing and the original draught preparation. All authors have read and agreed to the published version of the manuscript.

Funding: This research received no external funding.

Data Availability Statement: The data are contained within the article.

Acknowledgments: This is our original work, submitted for review.

Conflicts of Interest: The authors declare no conflict of interest.

Abbreviations

FC_T	Total generation cost
FC_i	Power generation cost function of the ith units
N	Total number of generating units
P_i	Power of the ith generating unit
a_i, b_i, and c_i	Fuel cost coefficients [a_i(USD/MW^{2}h), b_i(USD/MWh), c_i(USD/h)
$FC_{iv}(P_i)$	ELD cost function with valve loading effect
E_i and F_i	Valve loading coefficients of the ith generators [E_i(USD/h), F_i(1/MW)].
Ei(Pi))	Environmental emission function
d_i, e_i, and f_i,	Environmental emission coefficients[d_i(Ton/MW^{2}h), e_i(Ton/MWh), f_i(Ton/h)]
P_{min} and P_{max}	Minimum and maximum generation of the power limits (MW).
pbesti	Best previous position yielding for the ith particle
gbest	Best position discovered by the whole population
c_1 and c_2	Acceleration coefficients
$rand_1$ and $rand_2$	Random numbers generated between zero and one
S_i^k	Initial position of the randomly generated particle
S_i^{K+1}	New position of the particles
$n_{i,best}$	Best global position of the particles; N is the population size
P_D	Demand of power (load demand)
P_L	Line losses
V_i^k	Initial velocity of the particles
S_d	Attraction factor

References

1. Bhattacharya, A.; Chattopadhyay, P.K. Biogeography-Based Optimization for Different Economic Load Dispatch Problems. *IEEE Trans. Power Syst.* **2009**, *25*, 1064–1077. [CrossRef]
2. Abido, M. A novel multiobjective evolutionary algorithm for environmental/economic power dispatch. *Electr. Power Syst. Res.* **2003**, *65*, 71–81. [CrossRef]
3. Farag, A.; Al-Baiyat, S.; Cheng, T. Economic load dispatch multiobjective optimization procedures using linear programming techniques. *IEEE Trans. Power Syst.* **1995**, *10*, 731–738. [CrossRef]
4. Al-Sumait, J.S.; Al-Othman, A.K.; Sykulski, J.K. Application of pattern search method to power system valve point economic load dispatch. *Electr. Power Energy Syst.* **2007**, *29*, 720–730. [CrossRef]
5. Aoki, K.; Satoh, T. Economic dispatch with network security constraints using parametric quadratic programming. *IEEE Trans. Power Appar. Syst.* **1982**, *101*, 4548–4556. [CrossRef]

6. Panigrahi, B.; Pandi, V.R.; Das, S. Adaptive particle swarm optimization approach for static and dynamic economic load dispatch. *Energy Convers. Manag.* **2008**, *49*, 1407–1415. [CrossRef]
7. AlRashidi, M.R.; AlHajri, M.F.; El-Hawary, M.E. Enhanced particle swarm optimization approach for solving the non-convex optimal power flow. *World Acad. Sci. Eng. Technol.* **2010**, *62*, 651–655.
8. Wang, X.; Zhang, Y. Chaotic quantum-behaved PSO algorithm for power system economic load dispatch. *Int. J. Digit. Content Technol. Its Appl.* **2011**, *5*, 290–297.
9. Shrivastava, A.; Kumar, D. A New Aggrandized Class Topper Optimization Algorithm to Solve Economic Load Dispatch Problem in a Power System. *Cybernetics* **2020**, *52*, 4187–4197.
10. Santos, C.L.; Cocco, M.V. Particle swarm approach based on quantum mechanics and harmonic oscillator potential well for economic load dispatch with valve-point effects. *Gen. Energy Convers. Manag.* **2008**, *49*, 3080–3085. [CrossRef]
11. Sudhakaran, M.; Slochanal, S.M.R. Integrating Genetic Algorithm and Tabu Search for Emission and Economic Dispatch Problem. *J. Inst. Eng.* **2005**, *86*, 22–27.
12. Pandian, S.; Muthu, V.; Thanushkodi, K. An evolutionary programming based efficient particle swarm optimization for economic dispatch problem with valve-point loading. *Eur. J. Sci. Res.* **2011**, *52*, 385–397.
13. Chakraborty, S.; Senjyu, T.; Yona, A.; Saber, A.Y.; Funabashi, T. Solving economic load dispatch problem with valve-point effects using a hybrid quantum mechanics inspired particle swarm optimization. *IET Gener. Transm. Distrib.* **2011**, *5*, 1042–1052. [CrossRef]
14. Gholamghasemi, M.; Akbari, E.; Asadpoor, M.B.; Ghasemi, M. A new solution to the non-convex economic load dispatch problems using phasor particle swarm optimization. *Appl. Soft Comput.* **2019**, *79*, 111–124. [CrossRef]
15. Santos, C.L.; Chu-Sheng, L. Solving economic load dispatch problems in power systems using chaotic and Gaussian particle swarm optimization approaches. *J. Electr. Power Energy Syst.* **2008**, *30*, 297–307.
16. Dixit, G.P.; Dubey, H.M.; Pandit, M.; Panigrahi, B.K. Economic load dispatch using artificial bee colony optimization. *Int. J. Adv. Electron. Eng.* **2011**, *11*, 620–625.
17. Reddy, M.S.; Subramanyam, P.S. A Meta-Heuristic Approach of Bat Algorithm to Evaluate the Combined EED Problem. *Int. J. Eng. Res. Technol.* **2014**, *3*, 35–44.
18. Said, M.; El-Rifaie, A.M.; Tolba, M.A.; Houssein, E.H.; Deb, S. An Efficient Chameleon Swarm Algorithm for Economic Load Dispatch Problem. *Mathematics* **2021**, *9*, 2770. [CrossRef]
19. Dos Santos Coelho, L.; de Almeida AD, V.; Mariani, V.C. Cultural differential evolution approach to optimize the economic dispatch of electrical energy using thermal generators. In Proceedings of the 2008 IEEE International Conference on Emerging Technologies and Factory Automation, Hamburg, Germany, 15–18 September 2008; pp. 1378–1384.
20. Pandi, V.R.; Panigrahi, B.K.; Mohapatra, A.; Mallick, M.K. Economic load dispatch solution by improved harmony search with wavelet mutation. *Int. J. Comput. Sci. Eng.* **2011**, *6*, 122–131. [CrossRef]
21. Banerjee, S.; Maity, D.; Chanda, C.K. Teaching learning based optimization for economic load dispatch problem considering valve point loading effect. *Electr. Power Energy Syst.* **2015**, *73*, 456–464. [CrossRef]
22. Salaria, U.A.; Menhas, M.I.; Manzoor, S. Quasi oppositional population based global particle swarm optimizer with inertial weights (qpgpso-w) for solving economic load dispatch problem. *IEEE Access* **2021**, *9*, 134081–134095. [CrossRef]
23. Niknam, T.; Mojarrad, H.D.; Meymand, H.Z. Non-smooth economic dispatch computation by fuzzy and self adaptive particle swarm optimization. *Appl. Soft Comput.* **2011**, *11*, 2805–2817. [CrossRef]
24. Noman, N.; Iba, H. Differential evolution for economic load dispatch problems. *Electr. Power Syst.* **2008**, *78*, 1322–1331. [CrossRef]
25. Said, M.; Houssein, E.H.; Deb, S.; Ghoniem, R.M.; Elsayed, A.G. Economic Load Dispatch Problem Based on Search and Rescue Optimization Algorithm. *IEEE Access* **2022**, *10*, 47109–47123. [CrossRef]
26. Hao, W.; Wang, J.; Li, X.; Wang, M.; Zhang, M. Arithmetic optimization algorithm based on elementary function disturbance for solving economic load dispatch problem in power system. *Appl. Intell.* **2022**, *52*, 11846–11872. [CrossRef]
27. Dai, B.; Wang, F.; Chang, Y. Multi-objective economic load dispatch method based on data mining technology for large coal-fired power plants. *Control Eng. Pract.* **2022**, *121*, 105018. [CrossRef]
28. Alghamdi, A.S. Greedy Sine-Cosine Non-Hierarchical Grey Wolf Optimizer for Solving Non-Convex Economic Load Dispatch Problems. *Energies* **2022**, *15*, 3904. [CrossRef]
29. Al-Betar, M.A.; Awadallah, M.A.; Makhadmeh, S.N.; Abu Doush, I.; Abu Zitar, R.; Alshathri, S.; Elaziz, M.A. A hybrid Harris Hawks optimizer for economic load dispatch problems. *Alex. Eng. J.* **2023**, *64*, 365–389. [CrossRef]
30. Hassan, M.H.; Kamel, S.; Eid, A.; Nasrat, L.; Jurado, F.; Elnaggar, M.F. A developed eagle-strategy supply-demand optimizer for solving economic load dispatch problems. *Ain Shams Eng. J.* **2023**, *14*, 32–46. [CrossRef]
31. Tai, T.-C.; Lee, C.-C.; Kuo, C.-C. A Hybrid Grey Wolf Optimization Algorithm Using Robust Learning Mechanism for Large Scale Economic Load Dispatch with Vale-Point Effect. *Appl. Sci.* **2023**, *13*, 2727. [CrossRef]
32. Zhang, X.-Y.; Hao, W.-K.; Wang, J.-S.; Zhu, J.-H.; Zhao, X.-R.; Zheng, Y. Manta ray foraging optimization algorithm with mathematical spiral foraging strategies for solving economic load dispatching problems in power systems. *Alex. Eng. J.* **2023**, *70*, 613–640. [CrossRef]
33. Wang, R.; Xu, T.; Xu, H. Robust multi-objective load dispatch in microgrid involving unstable renewable generation. *Int. J. Electr. Power Energy Syst.* **2023**, *148*, 137–149. [CrossRef]

34. Lu, X.; Li, H.; Zhou, K.; Yang, S. Optimal load dispatch of energy hub considering uncertainties of renewable energy and demand response. *Energy* **2023**, *262*, 285–307. [CrossRef]
35. Fu, L.; Ouyang, H. A constrained cooperative adaptive multi-population differential evolutionary algorithm for economic load dispatch problems. *Appl. Soft Comput.* **2022**, *121*, 15–26. [CrossRef]
36. Victoire, T.A.A.; Jeyakumar, A.E. Hybrid PSO–SQP for economic dispatch with valve-point effect. *Electr. Power Syst. Res.* **2004**, *71*, 51–59. [CrossRef]
37. Singh, N.; Kumar, Y. Multiobjective Economic Load Dispatch Problem Solved by New PSO. *Adv. Electr. Eng.* **2015**, *2015*, 1–6. [CrossRef]
38. Tawhid, M.A.; Savsani, V. Multi-objective sine-cosine algorithm (MO-SCA) for multi-objective engineering design problems. *Neural Comput. Appl.* **2019**, *31*, 915–929. [CrossRef]
39. Singh, N.; Nighoskar, A.; Ram Krishna, S. Economic Load Dispatch with Valve Loading Effects Optimize By BBMO. *Int. J. Innov. Technol. Explor. Eng.* **2019**, *8*, 104–107.
40. Ahmadi, B.; Ceylan, O.; Ozdemir, A.; Fotuhi-Firuzabad, M. A multi-objective frame work for distributed energy resources planning and storage management. *Appl. Energy* **2022**, *314*, 127–142. [CrossRef]

electronics

MDPI

Article

Impact Mechanisms of Commutation Failure Caused by a Sending-End AC Fault and Its Recovery Speed on Transient Stability

Yifeng Lin [1], Jiawei Hu [2], Tong Wang [1,*] and Zengping Wang [1]

[1] State Key Laboratory of Alternate Electrical Power System with Renewable Energy Sources, North China Electric Power University, Beijing 102206, China; lyf3172@ncepu.edu.cn (Y.L.); wangzp@ncepu.edu.cn (Z.W.)
[2] Central China Subsection of State Grid Corporation of China, Wuhan 430077, China; hjwjh12@gmail.com
* Correspondence: hdwangtong@ncepu.edu.cn

Abstract: A sending-end AC fault may lead to commutation failure (CF) in a line-commutated converter high-voltage direct current (LCC-HVDC) system. In this paper, a theoretical analysis of the impact mechanisms of a CF and its recovery speed on the transient stability of a sending-end power system (TSSPS) is performed. Firstly, the models of the sending-end power system and DC power of CF are established; the ramp function is utilized to characterize the DC power recovery process. Secondly, the swing direction of the relative rotor angle caused by a sending-end AC fault is discussed, and the DC power flow method is employed to theoretically analyze the impacts of CF and its recovery speed on TSSPS. Next, the mathematic relations between parameters of the voltage-dependent current order limiter (VDCOL) and DC power recovery speed are further derived. It is concluded that the impacts of CF and its recovery speed on transient stability are related to the swing direction caused by a sending-end AC fault, the inertia of generators, and the location of the rectifier station. Finally, the theoretical analysis is validated by Kundur's two-area system and IEEE 68-bus-based AC/DC asynchronous interconnection test power systems, respectively.

Keywords: commutation failure; DC power recovery speed; transient stability; mechanism analysis

Citation: Lin, Y.; Hu, J.; Wang, T.; Wang, Z. Impact Mechanisms of Commutation Failure Caused by a Sending-End AC Fault and Its Recovery Speed on Transient Stability. *Electronics* **2023**, *12*, 3439. https://doi.org/10.3390/electronics12163439

Academic Editor: Jen-Hao Teng

Received: 6 July 2023
Revised: 3 August 2023
Accepted: 11 August 2023
Published: 14 August 2023

1. Introduction

Line-commutated converter high-voltage direct current (LCC-HVDC)-based transmission technology is widely utilized in long-distance bulk power transmission and regional power grid interconnection [1–3]. Currently, several regional power grids in China are interconnected asynchronously by LCC-HVDC-based transmission lines, with a rated DC voltage of up to ±1100 kV and transmission power of up to 12,000 MW [4,5]. On the one hand, the improvement in the voltage level and transmission capacity intensifies the threat of a single transmission line fault affecting the transient stability of the power system [6]. On the other hand, due to the complex coupling characteristics between AC and DC systems, the risk of a local isolated fault developing into systemic cascading failure increases [7].

Commutation failure (CF) caused by AC faults is unavoidable, according to the working principle of thyristors adopted by LCC-HVDC-based transmission technology [8], and has become a typical cascading failure. CF will cause overcurrent issues in the thyristors and severe DC power fluctuations in a short time [9,10]. From the power system perspective, severe DC power fluctuations caused by the CF and the following recovery process will significantly deteriorate the operation conditions of the synchronous generator in the power system [11,12], which is a key factor leading to the destruction of the transient stability of the sending-end power system (TSSPS). Therefore, improving the safe and stable operation level of the sending-end power system is of important practical significance.

Typically, the CF is caused by a receiving-end AC fault near the inverter station [13], whose mechanism has been intensely investigated. Researchers have concluded that CF is mainly caused by AC voltage disturbances such as AC voltage reduction [14], phase angle offset [15], and the harmonic caused by single-phase or three-phase faults [16]. Regarding the impact of CF caused by a receiving-end AC fault on the TSSPS, the sending-end power system is first equivalent to a two-machine and then a single-machine infinite-bus power system. The impact of CF on the TSSPS was analyzed by adopting the extended equal area criterion (EEAC) [17,18]. It was determined that CF will affect the TSSPS, and the crucial factors are the equivalent decreased value of DC transmission power and equivalent CF time. In [19], a linearized model for AC tie-line power oscillation was established, and the DC power fluctuation caused by the CF was regarded as the impulse response of the second-order linear system. Hence, the power oscillation peak value on AC tie-lines between two areas after the occurrence of the CF can be calculated quickly and subsequently employed as a power system stability assessment index. Next, the security and stability control measures for the sending-end power system were proposed in [20]. After the occurrence of CF, properly shortening the action time of the tripping generator at the sending-end power system and extending the reclosing time of the receiving-end power system will benefit the TSSPS. Furthermore, the DC power recovery process was considered in [21]. Based on the established power–angle relationship of the equivalent single-machine infinite-bus power system, it was determined that a faster DC power recovery speed will benefit the TSSPS.

However, the sending-end AC fault near the rectifier station might also cause CF during the recovery process after clearing the sending-end AC fault [22], and this mechanism is complex. Based on the quasi-steady-state analytical model of the inverter, it was concluded that the adverse activation of the current error controller (CEC) in the inverter is the inherent cause of CF [23]. In [24], time-varying immunity to this new CF phenomenon is obtained via experimental findings and theoretical explanations. Notably, the mechanisms of CF occurring under different fault levels are not the same [25]. The sudden increase in DC current is directly associated with CF resulting from nonserious faults, and controller interaction is the main factor of the CF occurring under serious faults. Furthermore, the characteristic difference between the CF caused by the sending-end and the receiving-end AC faults was analyzed in [26], and the rapid recovery of active power leading to the forward phase of the receiving-end bus voltage was determined to be the main cause of CF. After CF caused by a sending-end AC fault, the sending-end power system experiences two severe active power shocks. In this situation, the impacts of the CF caused by the sending-end AC fault and its power recovery process on the TSSPS are considerably different from those of the CF caused by a receiving-end AC fault, which is rarely discussed. Hence, the impact mechanisms of CF caused by a sending-end AC fault and its power recovery speed on the TSSPS are first revealed in this paper. Then, the mathematical relations between the parameters of the VDCOL and the DC power recovery speed are obtained. Hence, the TSSPS could be improved by modifying the VDCOL parameters correctly according to the revealed impact mechanisms.

The remainder of this paper is organized as follows. The models of the sending-end power system and DC power of CF are established in Section 2. In Section 3, the DC power flow method is employed to theoretically analyze the impacts of CF and its recovery speed on the TSSPS. Meanwhile, the mathematical relations between the parameters of the VDCOL and DC power recovery speed are derived in Section 4. Finally, the impact mechanisms are verified by Kundur's two-area system and IEEE 68-bus-based AC/DC asynchronous interconnection test power systems in Section 5. Section 6 concludes this paper.

2. System Model

2.1. Model of a Sending-End Power System

For asynchronously interconnected power systems via LCC-HVDC-based transmission lines, the model of the sending-end power system is given in Figure 1 [18].

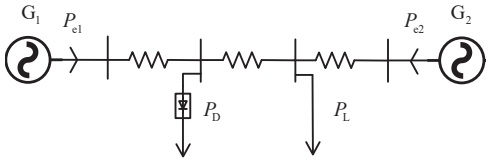

Figure 1. Equivalent model of sending-end power system.

Next, the single-machine infinite-bus power system model is derived [27] as shown below.

$$M_{\mathrm{eq}}\frac{\mathrm{d}^2\delta}{\mathrm{d}t^2} = P_{\mathrm{M}} - P_{\mathrm{E}} \tag{1}$$

$$M_{\mathrm{eq}} = \frac{M_1 M_2}{M_1 + M_2} \tag{2}$$

$$P_{\mathrm{M}} = \frac{1}{M_1 + M_2}(M_2 P_{\mathrm{m1}} - M_1 P_{\mathrm{m2}}) \tag{3}$$

$$P_{\mathrm{E}} = \frac{1}{M_1 + M_2}(M_2 P_{\mathrm{e1}} - M_1 P_{\mathrm{e2}}) \tag{4}$$

where P_{m1} and P_{m2} are the mechanical power, P_{e1} and P_{e2} are the electromagnetic power, M_1 and M_2 are the inertia constant, and δ is the relative rotor angle between G_1 and G_2.

2.2. DC Power Model of CF

Taking the inverter station as an example [28], its mathematical model can be represented by

$$P_{\mathrm{di}} = U_{\mathrm{di}} I_{\mathrm{di}} = \left(\frac{3\sqrt{2}}{\pi} k_{\mathrm{ti}} U_{\mathrm{li}} \cos\gamma - \frac{3}{\pi} x_{\mathrm{i}} I_{\mathrm{di}}\right) I_{\mathrm{di}} \tag{5}$$

where I_{di} and U_{di} are the DC current and DC voltage, x_{i} and k_{ti} are the equivalent commutation reactance and ratio of the inverter transformer, and U_{li} and γ are the inverter bus voltage and extinction angle.

When CF occurs, the primary concern is that the large-capacity active power transmission is blocked, resulting in the swing of relative rotor angles between generators, and sometimes leading to instability [17,21]. In order to mathematically analyze the impacts of the CF and its power recovery process on the TSSPS, the following assumptions are made:

(1) The rectifier station of LCC-HVDC is regarded as the dynamic load on the corresponding bus [29].
(2) The DC power flow method is employed, meaning that only the relationship between the active power and the rotor angle is considered, while the impacts of the reactive power and voltage on the rotor angle and active power are disregarded [30,31].

Next, the benchmark model of LCC-HVDC is built to simulate the CF and its recovery process, as shown in Figure 2. The blue solid line represents the transmitted DC power. The CF occurs and lasts for 20 ms, causing the transmitted DC power to decrease to zero. Then, it takes approximately 100 ms to recover from zero to the rated value, which is mainly affected by the inner DC controllers and the outer AC system [32,33].

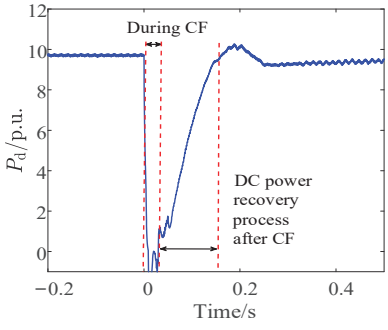

Figure 2. Simulation results of CF.

Then, a DC power model of the CF is established based on the DC power variation characteristics during and after CF. Equation (6) shows the details of this process, in which the ramp function is utilized to characterize the DC power recovery process.

$$P_d = \begin{cases} P_D & t < t_1 \\ P_{D1} & t_1 \le t < t_2 \\ P_{D1} + P_{D2} ramp(k_d, t - t_2) & t_2 \le t \end{cases} \tag{6}$$

where t_1 and t_2 are the start and end times of the CF, P_D is the rated DC power, P_{D1} is the DC power transmitted during the CF, and k_d is the DC power recovery speed; a larger k_d represents a faster DC power recovery speed.

In order to mathematically analyze the impact mechanisms of CF and its power recovery speed on the TSSPS, the DC power flow method is employed to establish the mathematical relationship between the relative rotor angle δ of the sending-end power system and the DC power P_D transmitted on the LCC-HVDC [31,34], as follows:

$$\begin{bmatrix} P_G \\ -P_L \end{bmatrix} = \begin{bmatrix} B_{GG} & B_{GL} \\ B_{LG} & B_{LL} \end{bmatrix} \begin{bmatrix} \delta_G \\ \delta_L \end{bmatrix} \tag{7}$$

where P_G is the set of generator nodes, P_L is the set of load nodes for which the rectifier nodes are regarded as parts of load nodes, B_{GG}, B_{GL}, B_{LG}, and B_{LL} are susceptance matrices, and δ_G and δ_L are rotor angles of generator nodes and phase angles of load nodes.

Finally, we obtain

$$P_G = B_{GG}\delta_G - B_{GL}\left(B_{LL}{}^{-1}(P_L + B_{LG}\delta_G)\right) \tag{8}$$

3. Theoretical Analysis

Based on the established models in Section 2, the theoretical derivation process is divided into three parts according to the chain of fault events [22,23], as shown in Figure 3.

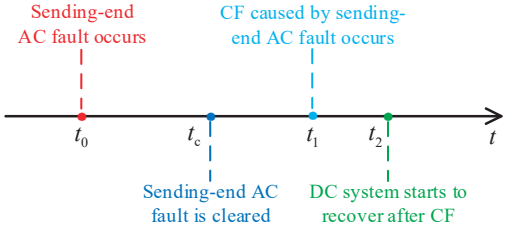

Figure 3. Chain of fault events.

3.1. Sending-End AC Fault

Assuming that the electromagnetic power of G_1 decreases by ΔP_{e1} and the electromagnetic power of G_2 decreases by ΔP_{e2} when the sending-end AC fault occurs, we can determine that

$$\begin{aligned} M_{eq}\frac{d^2\delta}{dt^2} &= \frac{M_2P_{m1}-M_1P_{m2}}{M_1+M_2} - \frac{M_2(P_{e1}-\Delta P_{e1})-M_1(P_{e2}-\Delta P_{e2})}{M_1+M_2} \\ &= \frac{M_2\Delta P_{e1}-M_1\Delta P_{e2}}{M_1+M_2} \end{aligned} \tag{9}$$

Equation (9) shows the relative rotor angle will swing forward when $\Delta P_{e1}/\Delta P_{e2} > M_1/M_2$, and it will swing backward when $\Delta P_{e1}/\Delta P_{e2} < M_1/M_2$, as shown in Figure 4.

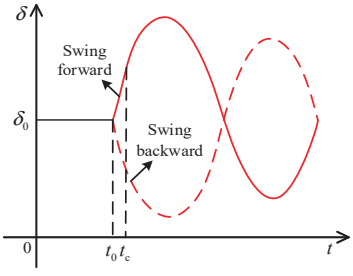

Figure 4. Swing direction of relative rotor angle when the sending-end fault occurs.

Hence, the impact mechanisms of the CF and its power recovery speed on the TSSPS are discussed for scenarios in which the relative rotor angle swings forward or backward. Furthermore, the equivalent reactance diagram of Figure 1 is presented in Figure 5.

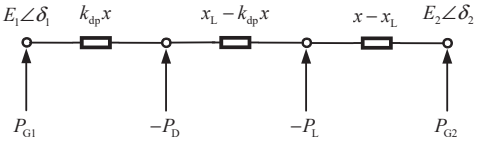

Figure 5. Equivalent reactance diagram of the sending-end power system.

Here, x is the reactance between the inner nodes of G_1 and G_2, $k_{dp}x$ is the reactance between the inner node of G_1 and the location of rectifier station, and x_L is the reactance between the inner node of G_1 and the node of AC load.

Next, the electromagnetic power P_{e1} of G_1 in a short period can be derived based on Equation (8).

$$P_{e1} = \frac{\delta}{x} + \frac{P_L(x-x_L)}{x} + P_D\left(1-k_{dp}\right) \tag{10}$$

where $\delta = \delta_1 - \delta_2$.

According to the power balance, the electromagnetic power of G_2 is obtained.

$$P_{e2} = P_L + P_D - P_{e1} \tag{11}$$

Therefore, Equation (4) can be expressed as

$$\begin{aligned} P_{Ee} &= \frac{M_2}{M_1+M_2}P_{e1} - \frac{M_1}{M_1+M_2}(P_L+P_D-P_{e1}) \\ &= \frac{\delta}{x} + \frac{P_L(x-x_L)}{x} + P_D\left(1-k_{dp}\right) - m(P_L+P_D) \end{aligned} \tag{12}$$

We define that $m = M_1/(M_1+M_2)$, then Equation (3) can be rewritten as

$$P_M = \frac{M_2}{M_1+M_2}P_{m1} - \frac{M_1}{M_1+M_2}(P_D+P_L-P_{m1}) = P_{m1} - m(P_D+P_L) \tag{13}$$

Finally, it can be deduced from Equations (10) and (13) that

$$M_{\mathrm{eq}}\frac{\mathrm{d}^2\delta}{\mathrm{d}t^2} = P_{\mathrm{M}} - P_{\mathrm{Ee}} = P_{\mathrm{m1}} - \frac{\delta}{x} - \frac{P_{\mathrm{L}}(x - x_{\mathrm{L}})}{x} - P_{\mathrm{D}}\left(1 - k_{\mathrm{dp}}\right) \tag{14}$$

3.2. During CF

CF may occur during recovery after the clearance of the sending-end AC fault [23], resulting in severe DC power fluctuations and further affecting the TSSPS. When a CF occurs at $t = t_1$, assuming that the DC power instantaneously decreases to zero, and δ_{d} is denoted as the relative rotor angle of the power system, the mathematical relation between δ_{d} and the electromagnetic power P_{e1d1} of G_1 is derived according to the DC power flow method.

$$P_{\mathrm{e1d1}} = \frac{\delta_{\mathrm{d}}}{x} + \frac{P_{\mathrm{L}}(x - x_{\mathrm{L}})}{x} \tag{15}$$

Similarly, the electromagnetic power of G_2 is

$$P_{\mathrm{e2d1}} = P_{\mathrm{L}} - P_{\mathrm{e1d1}} \tag{16}$$

Then,

$$P_{\mathrm{Md1}} = P_{\mathrm{M}} = P_{\mathrm{m1}} - m(P_{\mathrm{D}} + P_{\mathrm{L}}) \tag{17}$$

$$P_{\mathrm{Ed1}} = \frac{M_2}{M_1 + M_2}P_{\mathrm{e1d1}} - \frac{M_1}{M_1 + M_2}(P_{\mathrm{L}} - P_{\mathrm{e1d1}}) = \frac{\delta_{\mathrm{d}}}{x} + \frac{P_{\mathrm{L}}(x - x_{\mathrm{L}})}{x} - mP_{\mathrm{L}} \tag{18}$$

Finally,

$$M_{\mathrm{eq}}\frac{\mathrm{d}^2\delta_{\mathrm{d}}}{\mathrm{d}t^2} = P_{\mathrm{Md1}} - P_{\mathrm{Ed1}} = P_{\mathrm{m1}} - \frac{\delta_{\mathrm{d}}}{x} - \frac{P_{\mathrm{L}}(x - x_{\mathrm{L}})}{x} - mP_{\mathrm{D}} \tag{19}$$

Defining $\Delta\delta = \delta_{\mathrm{d}} - \delta$, and based on Equations (14) and (19), we find that

$$M_{\mathrm{eq}}\frac{\mathrm{d}^2\Delta\delta}{\mathrm{d}t^2} = P_{\mathrm{Md1}} - P_{\mathrm{Ed1}} - (P_{\mathrm{M}} - P_{\mathrm{Ee}}) = -\frac{\Delta\delta}{x} + P_{\mathrm{D}}\left(1 - k_{\mathrm{dp}} - m\right) \tag{20}$$

The solution structure of Equation (20) is composed of the special solution of Equation (20) ($\Delta\delta_{\mathrm{p1}}(t - t_1)$) and the general solution of the corresponding homogeneous equation of Equation (20) ($\Delta\delta_{\mathrm{g1}}(t - t_1)$), as shown by Equation (21).

$$\Delta\delta(t - t_1) = \Delta\delta_{\mathrm{p1}}(t - t_1) + \Delta\delta_{\mathrm{g1}}(t - t_1) \tag{21}$$

A special solution of Equation (21) and the general solution of its corresponding homogeneous equation are

$$\begin{cases} \Delta\delta_{\mathrm{p1}}(t - t_1) = xP_{\mathrm{D}}\left(1 - k_{\mathrm{dp}} - m\right) \\ \Delta\delta_{\mathrm{g1}}(t - t_1) = c_1\cos\left(\sqrt{\frac{1}{M_{\mathrm{eq}}x}}(t - t_1)\right) + c_2\sin\left(\sqrt{\frac{1}{M_{\mathrm{eq}}x}}(t - t_1)\right) \end{cases} \tag{22}$$

Since $\Delta\delta|_{t=t_1} = \Delta\delta_{10} = 0$, $\dot{\Delta\delta}|_{t=t_1} = \dot{\Delta\delta}_{10} = 0$, we find that

$$\begin{aligned} \Delta\delta(t - t_1) &= \Delta\delta_{\mathrm{p1}}(t - t_1) + \Delta\delta_{\mathrm{g1}}(t - t_1) \\ &= xP_{\mathrm{D}}\left(1 - k_{\mathrm{dp}} - m\right)\left(1 - \cos\left(\sqrt{\frac{1}{M_{\mathrm{eq}}x}}(t - t_1)\right)\right) \end{aligned} \tag{23}$$

According to the swing direction of the relative rotor angle caused by the sending-end AC fault, it can be concluded based on Equation (23) that

(a) If the relative rotor angle swings forward:

(i) If $1 - k_{\mathrm{dp}} > m$, $\Delta\delta > 0$, representing that the CF negatively affects the TSSPS.

(ii) If $1-k_{dp}=m$, $\Delta\delta=0$, representing that the CF does not affect the TSSPS.
(iii) If $1-k_{dp}<m$, $\Delta\delta<0$, representing that the CF positively affects the TSSPS.

(b) If the relative rotor angle swings backward:

(iv) If $1-k_{dp}>m$, $\Delta\delta>0$, representing that the CF positively affects the TSSPS.
(v) If $1-k_{dp}=m$, $\Delta\delta=0$, representing that the CF does not affect the TSSPS.
(vi) If $1-k_{dp}<m$, $\Delta\delta<0$, representing that the CF negatively affects the TSSPS.

Furthermore, the impacts of the CF on the TSSPS with different system parameters are presented in Figure 6.

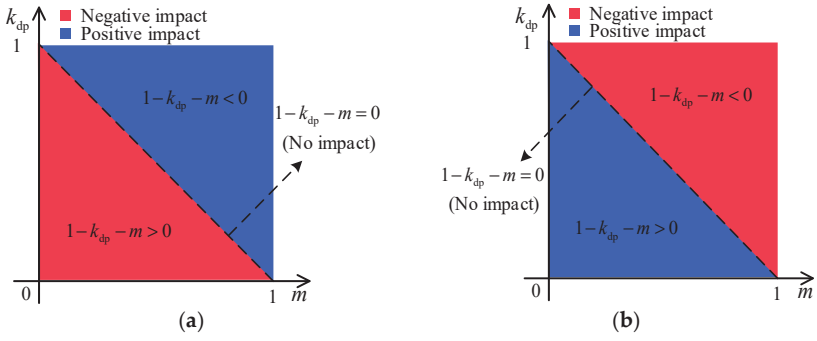

Figure 6. Impact of CF on the TSSPS: (**a**) swing forward; (**b**) swing backward.

3.3. Recovery Process after CF

After CF, the DC system begins to recover to the rated operation state at $t=t_2$. Based on the recovery model shown in Figure 2 and the DC power flow method, the mathematical relation between the relative rotor angle δ_d and the electromagnetic power P_{e1d2} of G_1 during the DC power recovery process is derived as follows.

$$P_{e1d2}=\frac{\delta_d}{x}+\frac{x-x_L}{x}P_L+(1-k_{dp})P_D ramp(k_d,t-t_2) \tag{24}$$

Similarly, the electromagnetic power of G_2 is

$$P_{e2d2}=P_D ramp(k_d,t-t_2)+P_L-P_{e1d2} \tag{25}$$

Then,

$$P_{Md2}=P_M=P_{m1}-m(P_D+P_L) \tag{26}$$

$$\begin{aligned} P_{Ed2} &= \frac{M_2}{M_1+M_2}P_{e1d2}-\frac{M_1}{M_1+M_2}(P_D ramp(k_d,t-t_2)+P_L-P_{e1d2}) \\ &= \frac{\delta_d}{x}+\frac{P_L(x-x_L)}{x}-m(P_D ramp(k_d,t-t_2)+P_L)+(1-k_{dp})P_D ramp(k_d,t-t_2) \end{aligned} \tag{27}$$

Finally,

$$\begin{aligned} M_{eq}\frac{d^2\delta_d}{dt^2} &= P_{Md2}-P_{Ed2} \\ &= P_{m1}-\frac{\delta_d}{x}-\frac{x-x_L}{x}P_L+P_D\Big(-m-(1-k_{dp}-m)ramp(k_d,t-t_2)\Big) \end{aligned} \tag{28}$$

Based on Equations (14) and (28), we obtain

$$\begin{aligned} M_{eq}\frac{d^2\Delta\delta}{dt^2} &= P_{Md2}-P_{Ed2}-(P_M-P_{Ee}) \\ &= -\frac{\Delta\delta}{x}+P_D\Big(1-k_{dp}-m\Big)(1-ramp(k_d,t-t_2)) \end{aligned} \tag{29}$$

The solution structure of Equation (29) is composed of the special solution of Equation (29) ($\Delta\delta_{p2}(t-t_2)$) and the general solution of the corresponding homogeneous equation of Equation (30) ($\Delta\delta_{g2}(t-t_2)$), as given in Equation (30).

$$\Delta\delta(t-t_2) = \Delta\delta_{p2}(t-t_2) + \Delta\delta_{g2}(t-t_2) \tag{30}$$

A special solution of Equation (29) and the general solution of its corresponding homogeneous equation are

$$\begin{cases} \Delta\delta_{p2}(t-t_2) = xP_D\left(1-k_{dp}-m\right)(1-ramp(k_d, t-t_2)) \\ \Delta\delta_{g2}(t-t_2) = c_3\cos\left(\sqrt{\frac{1}{M_{eq}x}}(t-t_2)\right) + c_4\sin\left(\sqrt{\frac{1}{M_{eq}x}}(t-t_2)\right) \end{cases} \tag{31}$$

Since $\Delta\delta|_{t=t_2} = \Delta\delta_{20}$, $\dot{\Delta\delta}|_{t=t_2} = \dot{\Delta\delta}_{20}$, based on Equation (23), we can obtain

$$\Delta\delta_{20} = xP_D\left(1-k_{dp}-m\right)\left(1-\cos\left(\sqrt{\frac{1}{M_{eq}x}}(t_2-t_1)\right)\right) \tag{32}$$

$$\frac{d\Delta\delta_{20}}{dt} = xP_D\left(1-k_{dp}-m\right)\sqrt{\frac{1}{M_{eq}x}}\sin\left(\sqrt{\frac{1}{M_{eq}x}}(t_2-t_1)\right) \tag{33}$$

Substituting Equations (32) and (33) into Equation (30), we can solve

$$c_3 = -xP_D\left(1-k_{dp}-m\right)\cos\left(\sqrt{\frac{1}{M_{eq}x}}(t_2-t_1)\right) \tag{34}$$

$$c_4 = xP_D\left(1-k_{dp}-m\right)\left(\sqrt{M_{eq}x}k_d - \sin\left(\sqrt{\frac{1}{M_{eq}x}}(t_2-t_1)\right)\right) \tag{35}$$

Therefore,

$$\begin{aligned} \Delta\delta(t-t_2) &= \Delta\delta_{p2}(t-t_2) + \Delta\delta_{g2}(t-t_2) \\ &= xP_D\left(1-k_{dp}-m\right)(1-ramp(k_d, t-t_2)) \\ &+c_3\cos\left(\sqrt{\tfrac{1}{M_{eq}x}}(t-t_2)\right) + c_4\sin\left(\sqrt{\tfrac{1}{M_{eq}x}}(t-t_2)\right) \end{aligned} \tag{36}$$

Next, the partial derivative of $\Delta\delta$ with respect to k_d is

$$\frac{\partial\Delta\delta}{\partial k_d} = xP_D\left(1-k_{dp}-m\right)\left(\sqrt{M_{eq}x}\sin\left(\sqrt{\frac{1}{M_{eq}x}}(t-t_2)\right) - (t-t_2)\right) \tag{37}$$

According to the Taylor expansion of trigonometric functions, we find that

$$\begin{aligned} \sqrt{M_{eq}x}\sin\left(\sqrt{\tfrac{1}{M_{eq}x}}(t-t_2)\right) &= \sqrt{M_{eq}x}\left(\sqrt{\tfrac{1}{M_{eq}x}}(t-t_2)\right) \\ &-\tfrac{1}{3!}\left(\sqrt{\tfrac{1}{M_{eq}x}}(t-t_2)\right)^3 + o\left(\sqrt{\tfrac{1}{M_{eq}x}}(t-t_2)\right)^3 \\ &\le \sqrt{M_{eq}x}\left(\sqrt{\tfrac{1}{M_{eq}x}}(t-t_2)\right) = (t-t_2) \end{aligned} \tag{38}$$

Finally, the following conclusions can be drawn based on Equations (36)–(38):

(a) If $1-k_{dp} > m$, $\partial\Delta\delta/\partial k_d < 0$, demonstrating that the greater k_d is, the smaller $\Delta\delta$ will be.

(b) If $1-k_{dp} = m$, $\partial\Delta\delta/\partial k_d = 0$, demonstrating that a greater k_d does not affect the TSSPS.

(c) If $1-k_{dp} < m$, $\partial\Delta\delta/\partial k_d > 0$, demonstrating that the greater k_d is, the greater $\Delta\delta$ will be.

Therefore, the impacts of improving the DC power recovery speed on the TSSPS with different system parameters are given in Figure 7.

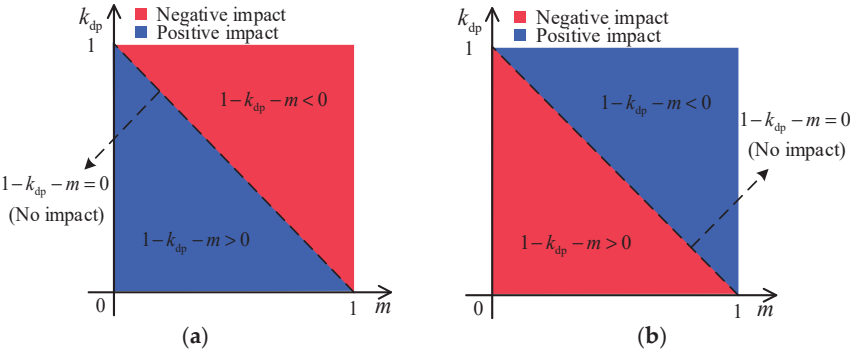

Figure 7. Impact of improving the DC power recovery speed on the TSSPS: (**a**) swing forward; (**b**) swing backward.

Based on the theoretical analysis given in Section 3, we can conclude that:

(a) If the relative rotor angle swings forward:
  (i) If $1-k_{dp}>m$, the CF will negatively affect the TSSPS, and increasing k_d will benefit the TSSPS.
  (ii) If $1-k_{dp}=m$, the CF and increasing k_d will have no impact on the TSSPS.
  (iii) If $1-k_{dp}<m$, the CF will positively affect the TSSPS, and decreasing k_d will benefit the TSSPS.

(b) If the relative rotor angle swings backward:
  (i) If $1-k_{dp}>m$, the CF will positively affect the TSSPS, and decreasing k_d will benefit the TSSPS.
  (ii) If $1-k_{dp}=m$, the CF and increasing k_d will have no impact on the TSSPS.
  (iii) If $1-k_{dp}<m$, the CF will negatively affect the TSSPS, and increasing k_d will benefit the TSSPS.

It should be noted that the analytical solutions, such as those shown in Equations (23) and (36), cannot be derived when the sending-end power system is a multi-machine power system because multivariate second-order differential equations are generally solved using numerical methods. However, the conclusions obtained in this section are still applicable. Equation (8) can be rewritten as

$$P_{ei}=\sum_{j=1}^{n_g}a_{ij}\delta_j+\sum_{j=n_g+1}^{n}b_{ij}P_{Lj} \tag{39}$$

where n is the number of total nodes and n_g is the number of generator nodes.

Next, the sending-end power system could be equivalent to a two-machine power system, dividing generators into A and B clusters according to the CCCOI-RM [35]. Assuming that the rectifier bus is the k-th node, we can obtain that

$$\begin{cases} m=\sum\limits_{i\in A}M_i/\sum\limits_{i\in n_g}M_i \\ 1-k_{dp}=\sum\limits_{i\in A}b_{ik} \end{cases} \tag{40}$$

4. Impact of DC Control on Recovery Speed

The DC recovery process after the CF is affected by DC inverter controllers. Here, the VDCOL is discussed, and its mathematical model is provided in Figure 8 [36,37]. The dynamic characteristic of the VDCOL is represented by

$$U_{\mathrm{d}} = U_{\mathrm{di}}(1 - e^{-\frac{t}{T_v}}) \tag{41}$$

$$I_{\mathrm{olim}} = \begin{cases} I_{\mathrm{o1}} & U_{\mathrm{d}} < U_{\mathrm{d1}} \\ I_{\mathrm{o1}} + \frac{I_{\mathrm{o2}} - I_{\mathrm{o1}}}{U_{\mathrm{d2}} - U_{\mathrm{d1}}}(U_{\mathrm{d}} - U_{\mathrm{d1}}) & U_{\mathrm{d1}} < U_{\mathrm{d}} < U_{\mathrm{d2}} \\ I_{\mathrm{o2}} & U_{\mathrm{d2}} < U_{\mathrm{d}} \end{cases} \tag{42}$$

where T_{v} is the time constant of the filter loop, U_{d1} and U_{d2} are the interpolation module's upper and lower bounds of DC voltage, I_{o1} and I_{o2} are the interpolation module's upper and lower bounds of DC current, and I_{olim} is the output order of the VDCOL.

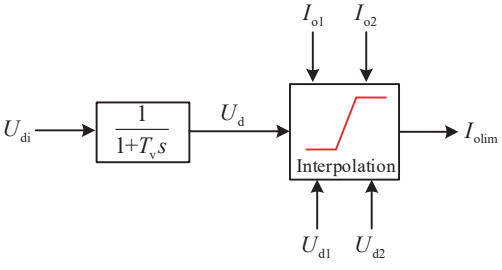

Figure 8. Mathematical model of VDCOL.

It is assumed that the commutation and transmission losses are ignored and the VDCOL is ideal, i.e., $I_{\mathrm{di}} = I_{\mathrm{olim}}$. Then, the DC power P_{dr} transmitted by the rectifier station can be represented as

$$P_{\mathrm{dr}} = P_{\mathrm{di}} = U_{\mathrm{di}} \cdot I_{\mathrm{olim}} = U_{\mathrm{di}}(I_{\mathrm{o1}} + \frac{I_{\mathrm{o2}} - I_{\mathrm{o1}}}{U_{\mathrm{d2}} - U_{\mathrm{d1}}}(U_{\mathrm{d}} - U_{\mathrm{d1}})) \tag{43}$$

Next, k_{d} is obtained by deriving Equation (43) with respect to time t.

$$k_{\mathrm{d}} = U'_{\mathrm{di}}(I_{\mathrm{o1}} + \frac{I_{\mathrm{o2}} - I_{\mathrm{o1}}}{U_{\mathrm{d2}} - U_{\mathrm{d1}}}(2U_{\mathrm{d}} - U_{\mathrm{d1}})) + \frac{(I_{\mathrm{o2}} - I_{\mathrm{o1}})U_{\mathrm{di}}^2}{(U_{\mathrm{d2}} - U_{\mathrm{d1}})T_{\mathrm{v}}} e^{-\frac{t}{T_{\mathrm{v}}}} \tag{44}$$

Finally, the partial derivatives of k_{d} with respect to the main parameters of the VDCOL are stated as follows.

$$\frac{\partial k_{\mathrm{d}}}{\partial I_{\mathrm{o2}}} = U'_{\mathrm{di}} \frac{2U_{\mathrm{d}} - U_{\mathrm{d1}}}{U_{\mathrm{d2}} - U_{\mathrm{d1}}} + \frac{U_{\mathrm{di}}^2}{(U_{\mathrm{d2}} - U_{\mathrm{d1}})T_{\mathrm{v}}} e^{-\frac{t}{T_{\mathrm{v}}}} \tag{45}$$

$$\frac{\partial k_{\mathrm{d}}}{\partial U_{\mathrm{d2}}} = -U'_{\mathrm{di}} \frac{(I_{\mathrm{o2}} - I_{\mathrm{o1}})(2U_{\mathrm{d}} - U_{\mathrm{d1}})}{(U_{\mathrm{d2}} - U_{\mathrm{d1}})^2} - \frac{U_{\mathrm{di}}^2 (I_{\mathrm{o2}} - I_{\mathrm{o1}})}{(U_{\mathrm{d2}} - U_{\mathrm{d1}})^2 T_{\mathrm{v}}} e^{-\frac{t}{T_{\mathrm{v}}}} \tag{46}$$

Equations (45) and (46) show that $\partial k_{\mathrm{d}}/\partial I_{\mathrm{o2}} > 0$ and $\partial k_{\mathrm{d}}/\partial U_{\mathrm{d2}} < 0$, which indicates that the DC power recovery speed could be improved by increasing I_{o2} or decreasing U_{d2}. In addition, the correctness of Equations (45) and (46) are validated by the simulation results shown in Figure 9. The green, blue and red solid lines represent the transmitted DC power when $U_{\mathrm{d2}} = 0.90$ p.u., 0.85 p.u. and 0.80 p.u. or $I_{\mathrm{o2}} = 1.00$ p.u., 1.05 p.u. and 1.10 p.u.

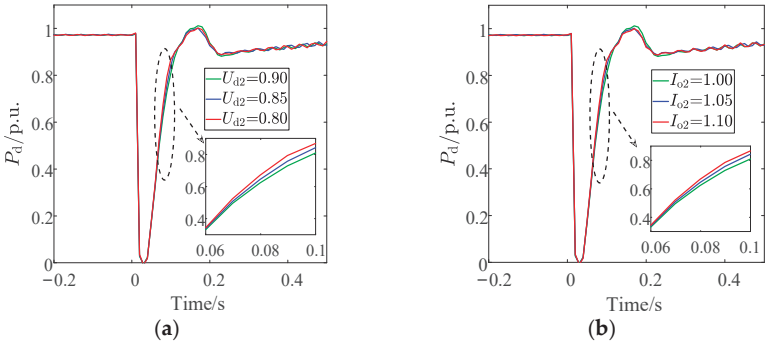

Figure 9. Parameters of VDCOL: (**a**) U_{d2} changes; (**b**) I_{o2} changes.

5. Results and Analysis

5.1. Test Power System A

To verify the accuracy of the impact mechanisms presented in Sections 3 and 4, the test power system based on Kundur's two-area system was built on ADPSS [12]. The network topology is shown in Figure 10.

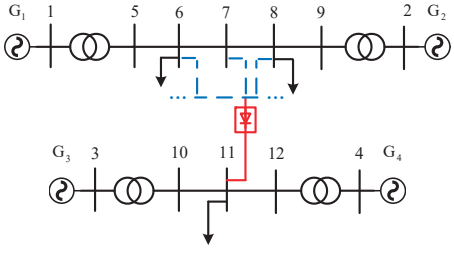

Figure 10. Kundur's two-area-based test power system.

Based on the above theoretical analysis, the expression of m in test power system A is

$$m = {}^{m_1}/_{(m_1+m_2)} \tag{47}$$

where m_1 and m_2 represent the inertia constants of G_1 and G_2.

Meanwhile, x_{1d} represents the reactance between G_1 and the rectifier station; the repression of k_{dp} is

$$k_{dp} = {}^{x_{1d}}/_{x} \tag{48}$$

where $x = x'_{d1} + x_{15} + x_{56} + x_{67} + x_{78} + x_{89} + x_{92} + x'_{d2}$ is the total reactance between G_1 and G_2; x'_{d1} and x'_{d2} represent the transient reactance of G_1 and G_2; and x_{15}, x_{56}, x_{67}, x_{78}, x_{89}, and x_{92} represent the reactance between Bus-1 and Bus-5, Bus-5 and Bus-6, Bus-6 and Bus-7, Bus-7 and Bus-8, Bus-8 and Bus-9, and Bus-9 and Bus-2.

Equations (47) and (48) show that $m \in (0,\ 1)$ and $k_{dp} \in (0,\ 1)$. The value of m could be modified by changing the relative values of m_1 and m_2, also known as the generators' inertia distribution, while the value of k_{dp} could be modified by changing the rectifier station's location as follows, $x_{1d} = x'_{d1} + x_{15} + x_{56}$, when the rectifier station is located at Bus-6.

Next, the sending-end AC fault is set at Bus-5/Bus-9, causing the relative rotor angle to swing forward/backward, and the CF caused by the sending-end AC fault is simulated. The maximum/minimum relative rotor angle of the sending-end power system during the first swing is employed as the assessment index of the TSSPS, which is noted as $\delta_{max}/\delta_{min}$. The simulation results are shown in Figure 11 with different parameters of k_{dp} and m, where $k_{dp} \in [0.2,\ 0.8]$ and $m \in [0.4,\ 0.8]$.

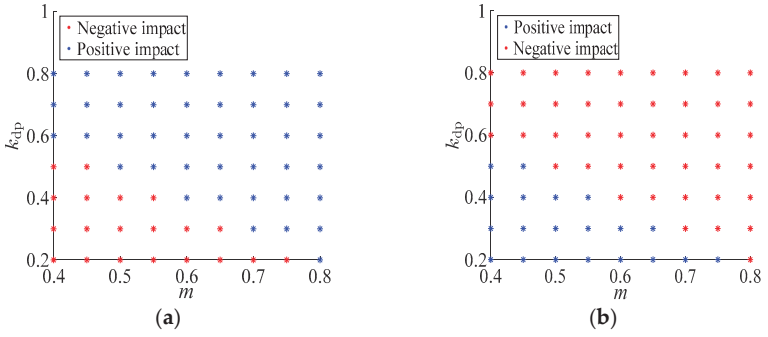

Figure 11. Impact of CF on the TSSPS: (**a**) swing forward; (**b**) swing backward.

In addition, the parameter U_{d2} of the VDCOL is modified from 0.90 p.u. to 0.70 p.u. to increase k_d. The simulation results are shown in Figure 12.

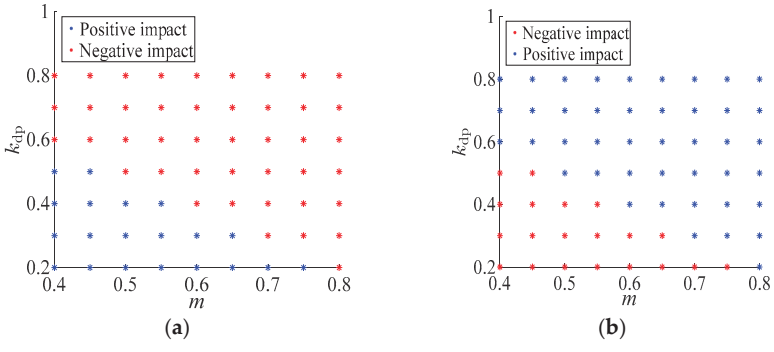

Figure 12. Impact of increasing k_d on the TSSPS: (**a**) swing forward; (**b**) swing backward.

The simulation results shown in Figures 11 and 12 reveal that the impacts of CF and its power recovery speed on the TSSPS are related to the swing direction caused by the sending-end AC fault, the inertia distribution of generators, and the location of the rectifier station, which further verify the accuracy of the impact mechanisms presented in Sections 3 and 4. It should be noted that the conclusions in Section 3 are drawn under certain simplifications. Therefore, the boundary condition that the CF caused by the sending-end AC fault and its recovery speed have no impact on the TSSPS is not strictly $1 - k_{dp} = m$, but near $1 - k_{dp} = m$.

5.2. Test Power System B

To verify the applicability of the proposed approach when the sending-end power system is a multi-machine power system, the IEEE 68-bus-based test power system was built on ADPSS; the network topology is presented in Figure 13. The New England power system (sending-end) is connected to the New York power system (receiving-end) by an LCC-HVDC-based transmission line, and the rectifier station is located at Bus-21/Bus-56. In addition, G_4, G_5, G_6, and G_7 with advanced rotor angles are divided into Cluster-A, and G_1, G_2, G_3, G_8, and G_9 are divided into Cluster-B. Next, we determine that $M_A = 231.6$ s, $M_B = 253.6$ s, and $m = M_A/(M_A + M_B)$ =0.48. The sending-end AC fault is set near the rectifier station, and the CF caused by the sending-end AC fault is simulated. Here, the fault type is a three-phase short circuit fault, and the fault duration is 0.1 s.

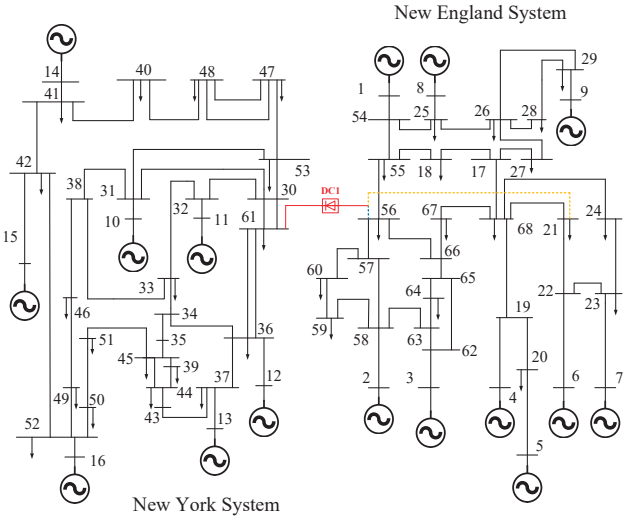

Figure 13. IEEE 68-bus-based test power system.

Scenario I: The rectifier station is located at Bus-21, and it is calculated based on Equation (40). in which $k_{dp} = 0.32$, which is much smaller than $m = 0.48$. Meanwhile, the sending-end AC fault is set at Bus-21.

Scenario II: The rectifier station is located at Bus-21 and $k_{dp} = 0.32 < m = 0.48$. Meanwhile, the sending-end AC fault is set at Bus-56.

In fault scenarios I and II, $1 - k_{dp} > m$, based on $m = 0.48$ and $k_{dp} = 0.32$. As indicated by the blue, green, and red solid lines in Figures 14b and 15b, k_d increases as U_{d2} of the VDCOL decreases. As shown by the black and blue solid lines in Figure 14a,b, the relative rotor angle swings forward due to the sending-end AC fault, and δ_{max} is much bigger when the CF occurs, indicating that the CF negatively affects the TSSPS. Meanwhile, the δ_{max} is smaller when the power recovery speed increases, indicating that the faster power recovery speed positively affects the TSSPS. Similarly, as shown by the black and blue solid lines in Figure 15a,b, the relative rotor angle swings backward due to the sending-end AC fault. δ_{min} is much smaller when the CF occurs, indicating that the CF positively affects the TSSPS. As indicated by the blue, green, and red solid lines given in Figure 15a,b, δ_{min} is greater when the power recovery speed increases, indicating that a faster power recovery speed negatively affects the TSSPS. The simulation results verify the correctness of the impact mechanisms presented in Sections 3 and 4.

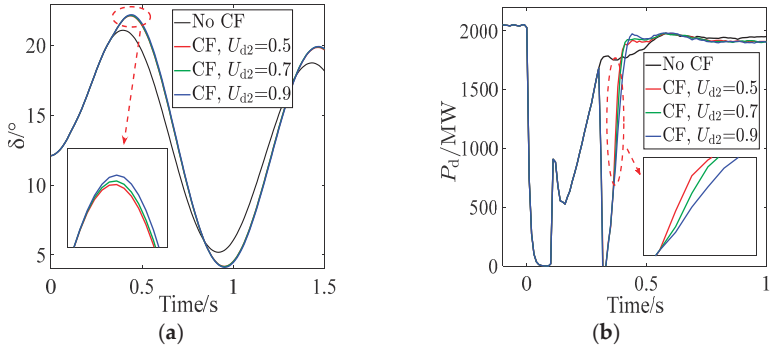

Figure 14. Scenario I: (**a**) relative rotor angle; (**b**) DC power.

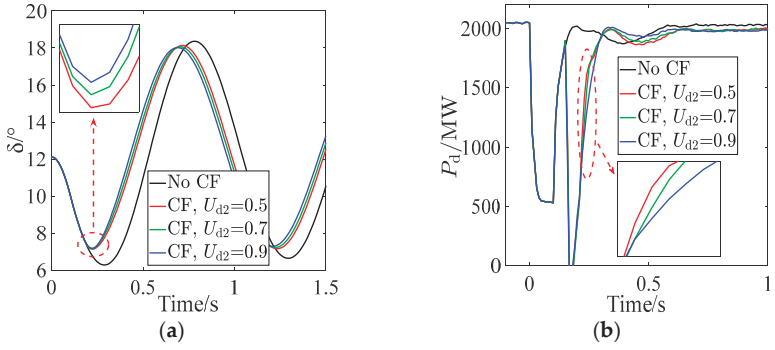

Figure 15. Scenario II: (**a**) relative rotor angle; (**b**) DC power.

Scenario III: The rectifier station is located at Bus-56, and based on Equation (40), it is determined that $k_{dp} = 0.60$, which is much greater than $m = 0.48$. Meanwhile, the sending-end AC fault is set at Bus-21.

Scenario IV: The rectifier station is located at Bus-56, and $k_{dp} = 0.60 > m = 0.48$. Meanwhile, the sending-end AC fault is set at Bus-56.

In fault scenarios III and IV, $1 - k_{dp} < m$, based on $m = 0.48$ and $k_{dp} = 0.60$. As shown by the blue, green, and red solid lines in Figures 16b and 17b, k_d increases as U_{d2} of the VDCOL decreases. As indicated by the black and blue solid lines in Figure 16a,b, the relative rotor angle swings forward due to the sending-end AC fault, and δ_{max} is much smaller when CF occurs, indicating that the CF positively affects the TSSPS. Meanwhile, δ_{max} is greater when the power recovery speed increases, indicating that a faster power recovery speed negatively affects the TSSPS. Similarly, as shown by the black and blue solid lines given in Figure 17a,b, the relative rotor angle swings backward due to the sending-end AC fault, and δ_{min} is much bigger when the CF occurs, indicating that the CF negatively affects the TSSPS. As shown by the blue, green, and red solid lines in Figure 18a,b, δ_{min} is smaller when the power recovery speed increases, indicating that a faster power recovery speed positively affects the TSSPS. The simulation results verify the accuracy of the impact mechanisms presented in Sections 3 and 4.

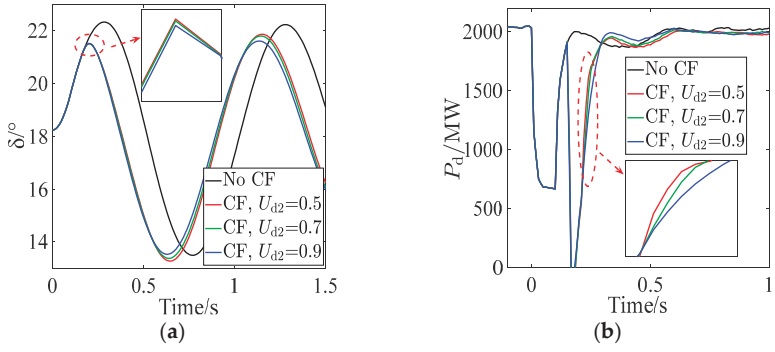

Figure 16. Scenario III: (**a**) relative rotor angle; (**b**) DC power.

Furthermore, the sending-end AC fault is set at different buses when the rectifier station is located at Bus-21 or Bus-56. The sending-end AC fault will cause the relative rotor angle of generators to swing forward or backward. The impacts of the CF and increasing power recovery speed on the TSSPS are given in Figure 18.

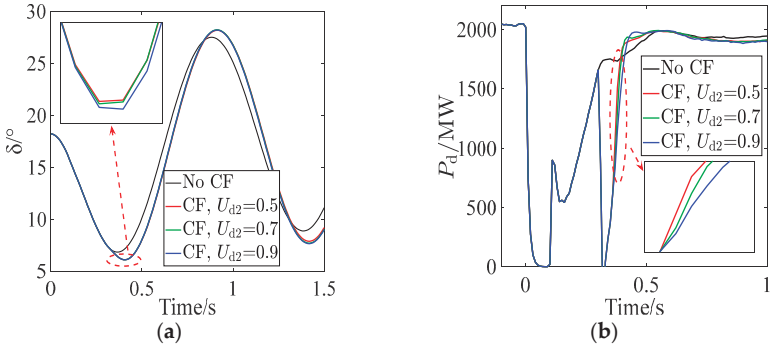

Figure 17. Scenario IV: (**a**) relative rotor angle; (**b**) DC power.

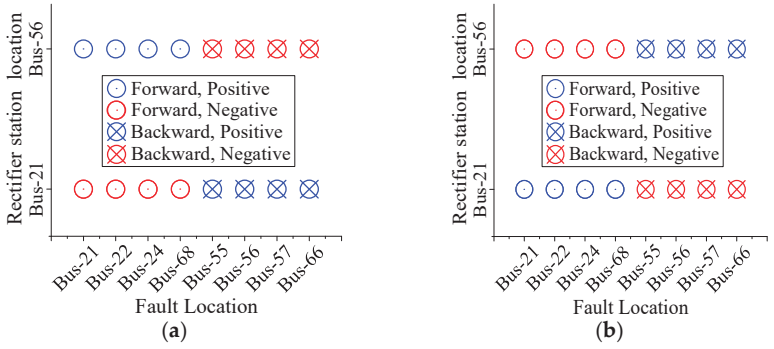

Figure 18. Simulation results of different fault locations: (**a**) impact of CF on TSSPS; (**b**) impact of increasing k_d on TSSPS.

In Figure 18a,b, the CF caused by the sending-end AC fault has a negative/positive impact on the TSSPS when the relative rotor angle swings forward/backward on the condition that the rectifier station is located at Bus-21. Meanwhile, the TSSPS is improved by increasing/decreasing the DC power recovery speed. On the contrary, the CF has a positive/negative impact on the TSSPS when the relative rotor angle swings forward/backward on the condition that the rectifier station is located at Bus-56. Meanwhile, the TSSPS is improved by decreasing/increasing the DC power recovery speed. The simulation results validate the accuracy of the presented impact mechanisms.

Furthermore, the impacts of the CF and its power recovery speed on the TSSPS are related to the swing direction influenced by the sending-end AC fault, the inertia distribution of generators, and the location of the rectifier station, and the TSSPS could be improved by correctly modifying the VDCOL parameters according to the presented impact mechanisms.

6. Conclusions

In this paper, the impact mechanisms of a CF caused by a sending-end AC fault and its DC power recovery speed on the TSSPS are revealed, and the mathematical relations between the parameters of the VDCOL and the DC power recovery speed are derived. The following conclusions are drawn:

(1) The impacts of the CF and its DC power recovery speed on the TSSPS are related to the swing direction of the relative rotor angle, the inertia distribution of generators, and the location of the rectifier station.

(2) The DC power recovery speed is positively correlated with I_o and U_{d2} of the VDCOL, which indicates that the TSSPS could be improved by modifying the VDCOL parameters according to the theoretical analysis.

Regarding the concern about the TSSPS after a CF, the revealed impact mechanisms could provide a reference for improvement. For early power grid planning, the impact of a CF on the TSSPS could be reduced by reducing the difference between $1 - k_{dp}$ and m. For a certain power system, as the values of k_{dp} and m are fixed, the DC power recovery speed could be changed by modifying the parameters of the VDCOL according to its impact mechanism to improve the TSSPS.

In the future, the mathematical relations between the DC power recovery speed and the parameters of other DC controllers, as well as the electrical quantities of the receiving-end AC system, will be discussed, so that the most sensitive and cost-effective method of modifying the DC power recovery speed can be determined.

Author Contributions: Conceptualization, Z.W.; methodology, Y.L.; software, Y.L.; validation, Y.L.; formal analysis, Y.L.; investigation, J.H.; resources, Z.W.; data curation, T.W.; writing—original draft preparation, Y.L.; writing—review and editing, J.H. and T.W.; visualization, T.W.; supervision, Z.W.; project administration, Z.W.; funding acquisition, Z.W. All authors have read and agreed to the published version of the manuscript.

Funding: This work was supported by the National Nature Science Foundation of China (52277096).

Data Availability Statement: The data that support the findings of this study are available on request from the corresponding author. The data are not publicly available due to privacy or ethical restrictions.

Conflicts of Interest: The authors declare no conflict of interest.

References

1. ABB. Special Report 60 Years of HVDC. 2014. Available online: https://library.e.abb.com/public/aff841e25d8986b5c1257d380045703f/140818%20ABB%20SR%2060%20years%20of%20HVDC_72dpi.pdf (accessed on 1 July 2014).
2. Zhang, F.; Xin, H.; Wu, D.; Wang, Z.; Gan, D. Assessing Strength of Multi-Infeed LCC-HVDC Systems Using Generalized Short-Circuit Ratio. *IEEE Trans. Power Syst.* **2019**, *34*, 467–480. [CrossRef]
3. Xiao, H.; Li, Y.; Gole, A.M.; Duan, X. Computationally efficient and accurate approach for commutation failure risk areas identification in multi-infeed LCC-HVDC systems. *IEEE Trans. Power Electron.* **2020**, *35*, 5238–5253. [CrossRef]
4. Shu, Y.; Chen, G.; Yu, Z.; Zhang, J.; Wang, C.; Zheng, C. Characteristic analysis of UHVAC/DC hybrid power grids and construction of power system protection. *CSEE J. Power Energy Syst.* **2017**, *3*, 325–333. [CrossRef]
5. Hu, J.; Wang, T.; Wang, Z.; Liu, J.; Bi, J. Switching System's MLE Based Transient Stability Assessment of AC/DC Hybrid System Considering Continuous Commutation Failure. *IEEE Trans. Power Syst.* **2021**, *36*, 757–768. [CrossRef]
6. Hong, L.; Zhou, X.; Liu, Y.; Xia, H.; Yin, H.; Chen, Y.; Zhou, L.; Xu, Q. Analysis and Improvement of the Multiple Controller Interaction in LCC-HVDC for Mitigating Repetitive Commutation Failure. *IEEE Trans. Power Del.* **2021**, *36*, 1982–1991. [CrossRef]
7. Mirsaeidi, S.; Dong, X. An Integrated Control and Protection Scheme to Inhibit Blackouts Caused by Cascading Fault in Large-Scale Hybrid AC/DC Power Grids. *IEEE Trans. Power Electron.* **2019**, *34*, 7278–7291. [CrossRef]
8. Mirsaeidi, S.; Tzelepis, D.; He, J.; Dong, X.; Mat Said, D.; Booth, C. A Controllable Thyristor-Based Commutation Failure Inhibitor for LCC-HVDC Transmission Systems. *IEEE Trans. Power Electron.* **2021**, *36*, 3781–3792. [CrossRef]
9. Guo, C.; Liu, Y.; Zhao, C.; Wei, X.; Xu, W. Power Component Fault Detection Method and Improved Current Order Limiter Control for Commutation Failure Mitigation in HVDC. *IEEE Trans. Power Deliv.* **2015**, *30*, 1585–1593. [CrossRef]
10. Mirsaeidi, S.; Dong, X. An Enhanced Strategy to Inhibit Commutation Failure in Line-Commutated Converters. *IEEE Trans. Ind. Electron.* **2020**, *67*, 340–349. [CrossRef]
11. Xue, Y.; Zhang, X.; Yang, C. AC Filterless Flexible LCC HVDC With Reduced Voltage Rating of Controllable Capacitors. *IEEE Trans. Power Syst.* **2018**, *33*, 5507–5518. [CrossRef]
12. Hu, J.; Wang, T.; Wang, Z. Transient stability margin assessment of AC/DC hybrid system with commutation failure involved. *Int. J. Electr. Power Energy Syst.* **2021**, *131*, 107056. [CrossRef]
13. Thio, C.V.; Davies, J.B.; Kent, K.L. Commutation failures in HVDC transmission systems. *IEEE Trans. Power Del.* **1996**, *11*, 946–957. [CrossRef]
14. Xiao, H.; Li, Y.; Zhu, J.; Duan, X. Efficient approach to quantify commutation failure immunity levels in multi-infeed HVDC systems. *IET Gener. Transm. Dis.* **2016**, *10*, 1032–1038. [CrossRef]
15. Zhu, R.; Zhou, X.; Xia, H.; Hong, L.; Yin, H.; Deng, L.; Liu, Y. Commutation Failure Mitigation Method Based on Imaginary Commutation Process. *J. Mod. Power Syst. Clean Energy* **2022**, *10*, 1413–1422. [CrossRef]

16. Xiao, H.; Li, Y.; Duan, X. Enhanced commutation failure predictive detection method and control strategy in multi-infeed LCC-HVDC systems considering voltage harmonics. *IEEE Trans. Power Syst.* **2021**, *36*, 81–96. [CrossRef]
17. Tu, J.; Pan, Y.; Zhang, J.; Jia, J.; Qin, X.; Yi, J. Study on the stability mechanism of the sending-side three-machine-group system after multiple HVDC commutation failure. *J. Eng.* **2017**, *2017*, 1140–1145. [CrossRef]
18. Tu, J.; Zhang, J.; Bu, G.; Yi, J.; Yin, Y.; Jia, J. Analysis of the sending-side system instability caused by multiple HVDC commutation failure. *CSEE J. Power Energy Syst.* **2015**, *1*, 37–44. [CrossRef]
19. He, J.; Tang, Y.; Zhang, J.; Guo, Q.; Yi, J.; Bu, G. Fast Calculation of Power Oscillation Peak Value on AC Tie-Line After HVDC Commutation Failure. *IEEE Trans. Power Syst.* **2015**, *30*, 2194–2195. [CrossRef]
20. Jia, J.; Zhang, J.; Zhong, W.; Tu, J.; Yu, Q.; Yi, J. Research on the Security and Stability Control Measures of the Sending Side System Coping with Multiple Parallel-operation HVDCs Simultaneous Commutation Failure. *Proc. CSEE* **2017**, *37*, 6320–6327.
21. Wang, W.; Xiong, X.; Li, M.; Yu, R. A Flexible Control Strategy to Prevent Sending-End Power System from Transient Instability Under HVDC Repetitive Commutation Failures. *IEEE Trans. Power Syst.* **2020**, *35*, 4445–4458. [CrossRef]
22. Liang, W.; Shen, C.; Sun, H.; Xu, S. Overvoltage mechanism and suppression method for LCC-HVDC rectifier station caused by sending end AC faults. *IEEE Trans. Power Del.* **2022**. [CrossRef]
23. Xiao, H.; Li, Y.; Lan, T. Sending End AC Faults can Cause Commutation Failure in LCC-HVDC Inverters. *IEEE Trans. Power Deliv.* **2020**, *35*, 2554–2557. [CrossRef]
24. Xiao, H.; Lan, T.; Li, B.; Su, S. Experimental Findings and Theoretical Explanations on Time-Varying Immunity of LCC-HVdc Inverters to Commutation Failure Caused by Sending End AC Faults. *IEEE Ind. Electron.* **2023**, *70*, 10180–10194. [CrossRef]
25. Hong, L.; Zhou, X.; Xia, H.; Liu, Y.; Luo, A. Mechanism and Prevention of Commutation Failure in LCC-HVDC Caused by Sending End AC Faults. *IEEE Trans. Power Deliv.* **2021**, *36*, 473–476. [CrossRef]
26. Zhu, H.; Hao, L.; Huang, F.; Chen, Z.; He, J. Research on the Suppression Strategy of Commutation Failure Caused by AC Fault at the Sending End. *IEEE Trans. Power Del.* **2023**. [CrossRef]
27. Xue, Y.; Van Custem, T.; Ribbens-Pavella, M. Extended equal area criterion justifications, generalizations, applications. *IEEE Trans. Power Syst.* **1989**, *4*, 44–52. [CrossRef] [PubMed]
28. Szechtman, M.; Wess, T.; Thio, C. A benchmark model for HVDC system studies. In Proceedings of the International Conference on AC and DC Power Transmission, London, UK, 17–20 September 1991; pp. 374–378.
29. Jiang, N.; Chiang, H. Energy function for power system with detailed DC model: Construction and analysis. *IEEE Trans. Power Syst.* **2013**, *28*, 3756–3764. [CrossRef]
30. Yin, C.; Li, F. Reactive Power Control Strategy for Inhibiting Transient Overvoltage Caused by Commutation Failure. *IEEE Trans. Power Syst.* **2021**, *36*, 4764–4777. [CrossRef]
31. Yan, J.; Tang, Y.; He, H.; Sun, Y. Cascading Failure Analysis with DC Power Flow Model and Transient Stability Analysis. *IEEE Trans. Power Syst.* **2015**, *30*, 285–297. [CrossRef]
32. Wang, J.; Huang, M.; Fu, C.; Li, H.; Xu, S.; Li, X. A New Recovery Strategy of HVDC System During AC Faults. *IEEE Trans. Power Deliv.* **2019**, *34*, 486–495. [CrossRef]
33. Zheng, B.; Hu, J.; Wang, T.; Wang, Z. Mechanism Analysis of a Subsequent Commutation Failure and a DC Power Recovery Speed Control Strategy. *Electronics* **2022**, *11*, 998. [CrossRef]
34. Stott, B.; Jardim, J.; Alsac, O. DC Power Flow Revisited. *IEEE Trans. Power Syst.* **2009**, *24*, 1290–1300. [CrossRef]
35. Xu, Y.; Dong, Z.Y.; Zhao, J.; Xue, Y.; Hill, D.J. Trajectory sensitivity analysis on the equivalent one-machine-infinite-bus of multi-machine systems for preventive transient stability control. *IET Gener. Transm. Distrib.* **2015**, *9*, 276–286. [CrossRef]
36. Li, Y.; Wang, J.; Li, Z.; Fu, C. VDCOL parameters setting influenced by reactive power characteristics of HVDC system. In Proceedings of the 2016 International Conference on Smart Grid and Clean Energy Technologies (ICSGCE), Chengdu, China, 19–22 October 2016.
37. Daryabak, M.; Filizadeh, S.; Jatskevich, J.; Davoudi, A.; Saeedifard, M.; Sood, V.K.; Martinez, J.A.; Aliprantis, D.; Cano, J.; Mehrizi-Sani, A. Modeling of LCC-HVDC Systems Using Dynamic Phasors. *IEEE Trans. Power Deliv.* **2014**, *29*, 1989–1998. [CrossRef]

processes

MDPI

Article

New Technology and Method for Monitoring the Status of Power Systems to Improve Power Quality—A Case Study

Rahim Ildarabadi [1,*] and Mahmoud Zadehbagheri [2,*]

[1] Department of Electrical Engineering, Hakim Sabzevari University, Sabzevar 9617976487, Iran
[2] Department of Electrical Engineering, Yasuj Branch, Islamic Azad University, Yasuj 7591493686, Iran
* Correspondence: r.ildar@hsu.ac.ir (R.I.); ma.zadehbagheri@iau.ac.ir (M.Z.)

Abstract: The identification and analysis of harmonics, frequency, and transient events are essential today. It is necessary to have available data relating to harmonics, frequency, and transient events to understand power systems and their proper control and analysis. Power quality monitoring is the first step in identifying power quality disturbances and reducing them and, as a result, improving the performance of the power system. In this paper, while presenting different methods for measuring these quantities, we have made some corrections to them. These reforms have been obtained through the analysis of power network signals. Finally, we introduce a new monitoring system capable of measuring harmonics, frequency, and transient events in the network. In addition, these values are provided for online and offline calculations of harmonics, frequency, and transient events. In this paper, two new and practical methods of the "algebraic method" are used to calculate network harmonics and wavelet transform to calculate transient modes in the network. Furthermore, the proposed monitoring system is able to reduce the amount of data-storage memory. The results of the simulations performed in this article show the superiority of using the new method presented for online and offline monitoring of power quality in electric power systems.

Keywords: power quality; Fourier transform; wavelet transforms (WTs); monitoring; data compression; transient analysis; steady-state analysis; harmonics

Citation: Ildarabadi, R.; Zadehbagheri, M. New Technology and Method for Monitoring the Status of Power Systems to Improve Power Quality—A Case Study. *Processes* **2023**, *11*, 2468. https://doi.org/10.3390/pr11082468

Academic Editors: Da Xie, Yanchi Zhang, Dongdong Li, Chenghong Gu, Ignacio Hernando-Gil and Nan Zhao

Received: 22 July 2023
Revised: 9 August 2023
Accepted: 10 August 2023
Published: 16 August 2023

1. Introduction

The complexity of power grids has increased rapidly in recent decades. To know the different conditions governing the power grid, we must have the ability to measure its electrical quantities [1]. For this purpose, many measurement methods have been provided. The important point, in this case, is to provide the possibility of fast and online analysis of network quantities and harmonics in the power grid [2]. Accurately determining the frequency of the power grid today has become more difficult because of the presence of harmonics and other noises. Because it is difficult to maintain the dynamic balance of power systems in the current conditions that are expanding day by day, the frequency fluctuates around the nominal frequency. In addition, these frequency fluctuations are closely related to the dynamic states of the power grid. Therefore, real-time monitoring and measurement of the power grid frequency is also very important. This importance increases especially with the addition of harmonics to the power grid [3,4]. One of the main issues for industrial factories is how to deal with power grid disturbances. Power quality problems determine the degree of sensitivity of measurement equipment and provide valuable results.. This importance is due to the fact that some disturbances (such as a voltage drop of more than 30% in a short period of time) cause an interruption in the operation of controllers and relays, which makes the importance of qualitative analysis of power systems clearer [5]. In order to improve power quality, sources of error and disturbance should be identified and controlled. This action can be completed by sequentially performing error detection, recording the location and time of error occurrence, and classifying the errors. For this

purpose, it is necessary to place suitable sensors on the network lines and identify the data received from them using suitable tools in real time [6]. In order to achieve this purpose, a powerful mathematical analysis tool is needed to simultaneously provide different analyses of the quality issues of the power system both in the time domain and in the frequency domain.

Among the factors that increase the importance of studying harmonics in the power network are the following: increasing the application of power electronics devices that have voltage and currents with non-linear characteristics and cause harmonics in the power network; increasing the shunt capacitor banks to correct the power factor and regulate the voltage range also increases the level of harmonics; and reducing the equipment design margin, which means that the equipment becomes more sensitive to voltage and current harmonics, harmonics have adverse effects on power network equipment and loads.

Harmonic disturbances usually appear in frequencies other than the main frequency of the network (but not always), and they often result from the non-linear operation of the mentioned factors in a permanent state and cause the collapse of the network. Here, the collapse of the network means the creation of unacceptable conditions for its network voltages and currents [7]. This definition is able to include all the errors and wrong operations and unwanted torques created in the shaft of electric machines. Except in very exceptional cases, common measuring devices and methods are not able to detect the number of harmonics or their different effects on the power system [8].

In this research, after reviewing the previous articles in this field, we present the statement of the proposed strategy.

This paper, considering the problems of power quality monitoring, especially in the online field, presents a new plan to solve these problems using the new algebraic method and wavelet transform.

Two methods are provided to identify transient states: One is performed using the derivative of the signal, and the other is conducted with the help of a new signal-processing technique called wavelet transform (which has been "used recently"). Finally, a monitoring system is proposed that is capable of identifying harmonics, frequency, and transient modes for real-time and offline analysis.

In order to be able to analyze the signal information offline, it is necessary to provide the possibility of storing this information in the memory. In this case, it is necessary to compress this information before saving. Some methods for compressing transients and steady states are mentioned. By applying these methods, information is compressed more than 40 times. In this system, with the new compression technique, the amount of memory needed to store the monitored data (for offline analysis) has been greatly reduced.

1.1. Background

In [9], the authors presented the frequency by calculating the phase voltage in quasi-steady and rotating frames with the DFT technique and regression relations. Because of the use of the DFT technique, this algorithm is inherently insensitive to network harmonics but is vulnerable to noise. Moreover, in this method, a wide measurement window is needed when measuring small frequency changes.

In [10], they used the Kalman filter to measure the frequency, and the method they used was able to remove the noise well, but it could not adequately consider the performance of harmonics.

In [11], the authors calculated the power grid frequency using the least-squares technique. However, their method was sensitive to both noise and network harmonics.

In [12], the frequency was measured using DSP and quadratic sampling data. In this paper, the authors removed the harmonics and the DC component of the grid voltage using a median filter.

In [13], the author defined the instantaneous frequency as the angular velocity of the spatial phasor of the voltage. He obtained good results, but the technique he used was very complicated.

In [14], the description of power quality monitoring (PQM) and the examination of the four main methods of PQM placement, which include monitor access area, coverage and packaging, graph theory, and multivariate regression, were discussed. In addition, the concepts, advantages, and disadvantages of each method were discussed.

Various methods have been presented in this field, including discrete Fourier transform (DFT) and fast Fourier transform (FFT). One of the main reasons for paying special attention to the FFT technique is its lesser need for computing devices. This feature is obtained by removing the additional coefficients of the differential equation of the signal under analysis. However, there are limitations in this method. One of is causing disruptions in the proper selection of data windows. One of these limitations is leakage. Leakage occurs when the data window used for the technique FFT does not contain a precise interval of integers of frequency cycles. Because this method depends on the information windows of the signal under monitoring, due to the inevitable changes in the signal frequency, the problem of leakage will therefore always exist in this method [15].

In addition, the FFT technique has inherent limitations in terms of resolution. Today, improvements have been made to the FFT technique that have improved the mentioned issues to a great extent. Among them, it is possible to mention the selection of information windows based on the detection of crossing the zero level of the signal. Although the use of zero-level detection methods is simple and completely reliable (even for low-level noise pollution conditions), if the range of high-order harmonics of the signal is significant, the accuracy of this method is significantly reduced. Another way to evaluate the monitored signal is to use Taylor series techniques. This method also suffers from the same limitations that existed in detecting the crossing of the zero level [16,17].

There are also some methods that use the FFT technique as a starting point to estimate the phase of the main harmonic, and then the frequency of the main harmonic is calculated based on the change in phase angle shifting. This method is successful only when the changes in the main frequency are insignificant. Otherwise, as mentioned earlier, the leakage problem causes a gross error in the initial values of the central harmonic phase obtained from the technique FFT. These methods have also been improved by the least squares algorithm or using the Kalman filter. In most common methods, the main harmonic is the primary basis. Therefore, if there are many other harmonics in the signal under analysis, these harmonics can affect the results of these methods [18].

The latest method of monitoring electrical quantities uses non-linear methods to follow the signal under monitoring. Using the Newton iteration method and combining it with the least square method is one of these non-linear methods. Nevertheless, this method is computationally intensive, and therefore, several processors must be used in parallel to perform real-time analysis. Artificial neural networks can be used to increase the speed of calculations. It should be remembered that the use of neural networks in monitoring harmonics is not a new concept. This method can provide accurate results of the conditions of network quantities, even if complete information about these quantities is not available [19].

But the new method presented in this article is the algebraic method which will be explained below. While this method is straightforward, it also solves many of the disadvantages of the standard DFT method. Also, in this article, the DFT method and the algebraic method mentioned, have been turned into reversible methods. Hence, their calculation speed is equal to the speed of the minimum gradient method solved with the help of Hopfield neural network.

To analyze transient states, Riberio was one of the first to use WT. He realized that the WT is easily able to separate the transient states and the primary states of the power network signals from each other, with the most minor parameters and the most accuracy, and he identifies them [20]. Later, people like Galli, Heydt, etc., used different types of WT for different cases of power network analysis. Even today, there are many articles about the different use cases of WT in the power network.

1.2. The Weaknesses of Previous Research and the Importance and Necessity of Research

In this section, the weaknesses of the proposed methods in previous many articles are explained. Classical artificial intelligence in previous articles in this field does not give importance to the aspects of system development (how knowledge structures are created and their changes over time). Through monitoring power quality disturbances, it is possible to examine the details of the disturbances and determine solutions to overcome the system's power quality problems. The main part of power quality monitoring, which is very important and effective, is the identification and classification of power disturbance signals and requires signal processing techniques and machine learning tools (intelligent tools) [21,22]. Today, many studies have been published to classify power quality disorders. Each article has achieved different accuracies by using a particular diagnosis structure. The reality is that each diagnosis structure may have the desired answer for specific conditions and data. Therefore, comprehensive and efficient monitoring needs an automatic and intelligent framework to make the best decision among the candidate structures when necessary, according to the set goal [23]. The main problem in this field is the lack of comprehensiveness of the diagnosis system and not making a proper and timely decision in determining the structure of the optimal diagnosis. In the systems presented in the reference articles, the need for adaptability and flexibility to changing environmental conditions and changing the characteristics of the data in the database has not been considered. In many previous studies, there is no feature selection section (data mining) to improve the operation of the detection system. The performance of classification tools depends on several internal parameters, which have been set by trial and error in many previous articles. In many practical applications in this field, the accuracy and efficiency of existing methods are not suitable against different noise conditions and should be improved. In some articles, attempts have been made to improve the performance of these systems by using noise removal methods and adding new steps in the structure of the noise detection system, but these methods have not been well received due to their complexity and large number of calculations. And this research has led to new and advanced signal processing algorithms that are inherently robust to noise. In general, it can be said that in many previous studies, only the performance of an offline monitoring system has been investigated [24,25].

2. Frequency Monitoring Methods

In this section, several methods for measuring frequency are presented.

2.1. The Modified Technique of Crossing the Zero Level

The sampled voltage waveform can be formulated as follows [26,27]:

$$v(k) = v(kT) = \sum_{n=1}^{\infty} V_n \cos(n\omega_0 kT + \delta_n(kT)) \quad (1)$$

The data window $V[k]$ for M consecutive sample is defined as follows:

$$V[k] = [v(k+1), v(k+2), \cdots, v(k+M),]^T \quad (2)$$

The time to open the informational window is optional. The polynomial of degree Lth of $p_l(t)$ is assumed as follows [28]:

$$p_l(t) = a_0 + a_1 t + a_2 t^2 + \cdots + a_l t^l = \sum_{j=1}^{l} a_j t^j \quad (3)$$

If each of the mentioned sentences is equal to the voltage at the moment t, and it can be written as:

$$\begin{bmatrix} 1(k+1)T(k+1)^2T^2 \cdots (k+1)^lT^l \\ 1(k+2)T(k+2)^2T^2 \cdots (k+2)^lT^l \\ \cdots \\ 1(k+M)T(k+M)^2T^2 \cdots (k+M)^lT^l \end{bmatrix} \begin{bmatrix} a_0 \\ a_1 \\ \vdots \\ a_l \end{bmatrix} = V[k] \quad (4)$$

or as:

$$K \cdot a = V[k] \Rightarrow a = \left(K^TK\right)^{-1}K^TV[k] \quad (5)$$

In this way, the voltage waveform can be calculated as a polynomial of degree l, in terms of the time variable and in the distance k to $k + M$. This means that:

$$v(t) = a_0 + a_1t + a_2t^2 + \cdots + a_lt^l \quad for\ k \le t \le k + M \quad (6)$$

Usually, "l" is considered to be at most 3. In this case, for each $M + 1$ sample, $V(t)$ is approximated by a new third-order function. The moment of crossing the zero level is between two sequences in which the sign changes. If these sequences are denoted by m and $m + 1$, then the relation (6) can be written as follows:

$$\begin{gathered} v(t) = a_0 + a_1t + a_2t^2 + \cdots + a_lt^l; \\ for\ m - \left[\tfrac{M+1}{2}\right] \le t \le \left(m - \left[\tfrac{M+1}{2}\right]\right) + M - 1 \end{gathered} \quad (7)$$

Now, if $V(t) = 0$ is solved for Equation (7), the time the curve crosses the zero level is calculated. In the same way, we calculate all the points crossing the zero level of the signal and call them in $\cdots, t_{j_2}, t_{j_1}$ in order, as in Figure 1:

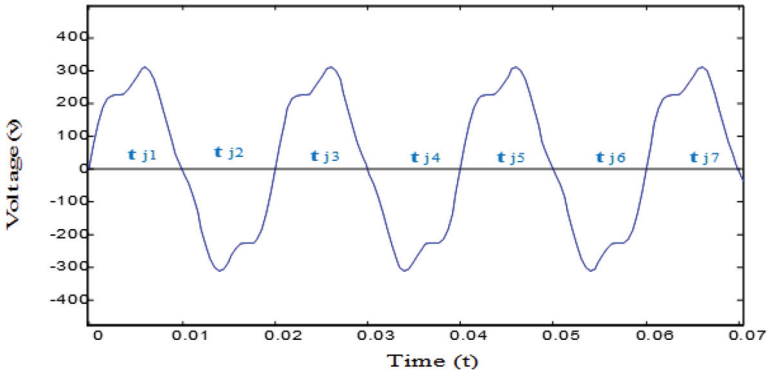

Figure 1. System voltage waveform.

Therefore, the period of the sampled signal in the Jth cycle is:

$$T_j = t_j - t_{j-2}\ for\ j \ge 3 \quad (8)$$

Also, the frequency of this signal in the Jth cycle is calculated from the following equation:

$$f_j = \frac{1}{t_j - t_{j-2}}\ for\ j \ge 3 \quad (9)$$

As seen in the above figure, it can be proved that the calculated frequency for almost "periodic" signals depends on the value of the DC level. Furthermore, if the waveform of the signal has a significant difference from one period to another, before calculating the crossing point of the zero level, the value of the DC level calculated in the previous period

should be subtracted from the relation of the primary wave, and then the crossing point of the level zero measured the resulting signal, which is free of DC component.

2.2. DFT Method with Polynomial Approximation

The sampled voltage waveform can be formulated as follows [29]:

$$v(k) = v(kT) = \sum_{n=1}^{\infty} V_n \cos(n\omega_0 kT + \delta_n(kT)) \tag{10}$$

The data window $V[k]$ for M consecutive sample is defined as follows:

$$V[k] = [v(k+1), v(k+2), \cdots, v(k+M),]^T \tag{11}$$

The real and imaginary parts of the voltage phasor from the discrete Fourier transform relation are as follows:

$$\begin{aligned} &\Re\left\{\widetilde{V}_1[k]\right\} = V_1 \cos\delta_1 = \tfrac{2}{N}\sum_{j=1}^{N} v[k+j]\cos\left(\tfrac{2(k+1)\pi}{N}\right) \\ &\Im\left\{\widetilde{V}_1[k]\right\} = V_1 \cos\delta_1 = \tfrac{2}{N}\sum_{j=1}^{N} v[k+j]\sin\left(\tfrac{2(k+1)\pi}{N}\right) \\ &\Rightarrow \widetilde{V}_1 = V_1 e^{j\delta_1} \end{aligned} \tag{12}$$

The mentioned method can be considered as a harmonic filter. If the phasor voltages of all three phases are available, the positive sequence phasor can be calculated from them follows:

$$\widetilde{V}_1[k] = \widetilde{V}_{1a}[k] + \alpha\widetilde{V}_{1b}[k] + \alpha^2\widetilde{V}_{1c}[k], \left(\alpha = e^{j2\pi/3}\right) \tag{13}$$

To calculate, $\delta[k]$, we consider it as the argument of $\widetilde{V}_1[k]$ and consider a sliding data window as follows:

$$D[k] = [\delta[k+1]\delta[k+2]\cdots\delta[k+M]]^T \tag{14}$$

Now, inside this window, the positive sequence phasor argument function of the voltage is approximated by a polynomial of the Lth degree.

$$\delta(t) = a_0 + a_1 t + \cdots + a_l t^l = \sum_{j=1}^{l} a_j t^j \tag{15}$$

In this way, the instantaneous frequency of the voltage, which is the instantaneous derivative of its argument, can be calculated:

$$f(t) = \frac{1}{2\pi}\frac{d\delta(t)}{dt} = \frac{1}{2\pi}\left(a_1 + 2a_2 t + \cdots + a_l t^{l-1}\right) \tag{16}$$

The discrete form of the relation (16) can also be written as follows:

$$f(k) = f(k\Delta t) = \frac{1}{2\pi}\sum_{j=0}^{l-1} j a_j (k\Delta t)^{j-1} \tag{17}$$

The frequency at the end of each data window should be calculated consecutively.

$$f[k+M] = \frac{1}{2\pi}\sum_{j=0}^{l-1} j a_j ([k+M]\Delta t)^{j-1} \tag{18}$$

It can be seen that the realization of the mentioned method in real time is straightforward. In this method, the DFT technique protects against harmonics, and the least square technique protects the system against noise. Therefore, noise and harmonics can-

not have a great effect on the calculated frequency value. Nevertheless, it has a complex calculation method.

3. Power System Monitoring

In this section, a new method for online and offline monitoring is presented using the mentioned methods for identifying transient states and harmonics. The basis of work in the aforementioned monitoring above system is as follows: First, the signal is passed through a low-pass filter with a cut-off frequency of 10 kHz to solve the aliasing problem. Then, it is sampled with a sampling frequency of 24 kHz (ensuring compliance with Nyquist's theorem). Later, a wavelet stage is taken from the resulting discrete signal. The harmonics of the power network (in steady state) are always limited to less than the 20th order, and therefore, only samples of the signal are used to calculate the harmonics, and the distance between them is equal to 0.02/41 s [30]. In this system, the harmonics and the primary harmonic frequency are calculated in real time via the reversible algebraic method. Also, to identify transient states, two methods are presented here. Depending on the accuracy and sensitivity of the system, any of them can be used. For offline analysis, the monitoring system can compress and store the harmonics and transient states of the signal with a new technique (which will be explained below). The presented method in signal compression, in addition to being highly accurate, can significantly compress any original signal. The block diagram of the mentioned monitoring system is shown in Figure 2 and consists of the following components:

a. Aliasing filter for removing aliasing problem.
b. Sampler; with 24 kHz sampling, for sure of observing the Nyquist theorem.
c. Subsystem WT with one level.
d. Subsystem computation frequency and harmonic with zero crossing method and algebraic method.
e. Frequency and harmonic compressor with the new method.
f. Transient values (wavelet factor) compressor.
g. Memory to store compressed variables (frequency, harmonic and transient values).
h. A subsystem that includes recovery frequency and harmonic and transient values, with new methods and remarking signal monitoring.

3.1. Description of the System Scaling

3.1.1. Signal Analysis by Wavelet

The sampled signal is analyzed via the wavelet transform into the wavelet factor of the first level (d_1) and the scale factor of the first level (c_1).

3.1.2. Harmonic Calculation

The scaling factor of the first level is the parts of the low-frequency spectrum of the monitored signal. In other words, this coefficient includes the steady state of the waveform. Assuming that the harmonics of the signals are limited to the 20th order, it is possible to obtain the DC value and the amplitude and phase of the monitored signals with 41 samples of it in one period using the algebraic method.

Figure 3 shows sampled voltage signal, scaling factor (c_1), and wavelet factor (d_1), respectively. Let us suppose the signal $v(t)$ is calculated as shown below:

$$\begin{array}{l} v(t) = 60 + 40\sin(2\pi(3 \times 50)\, t) \\ +200p(t)\sin(2\pi(50 \times 50)\, t) \end{array} \quad (19)$$

where: $p(t) = u(t - 0.01) - u(t - 0.011)$, and $u(t)$ is a unit function.

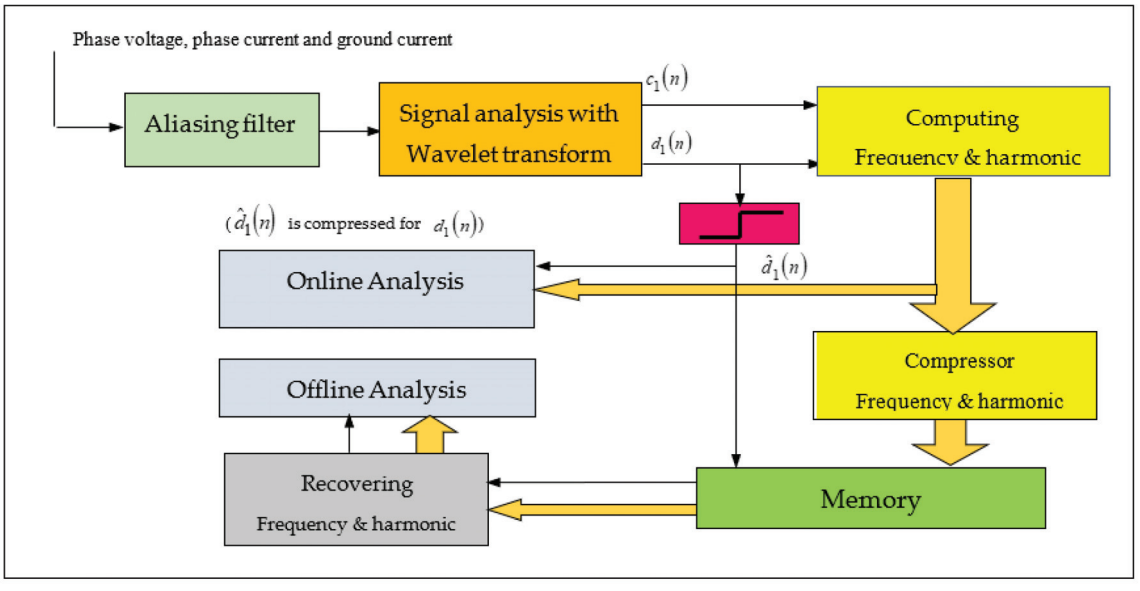

(a)

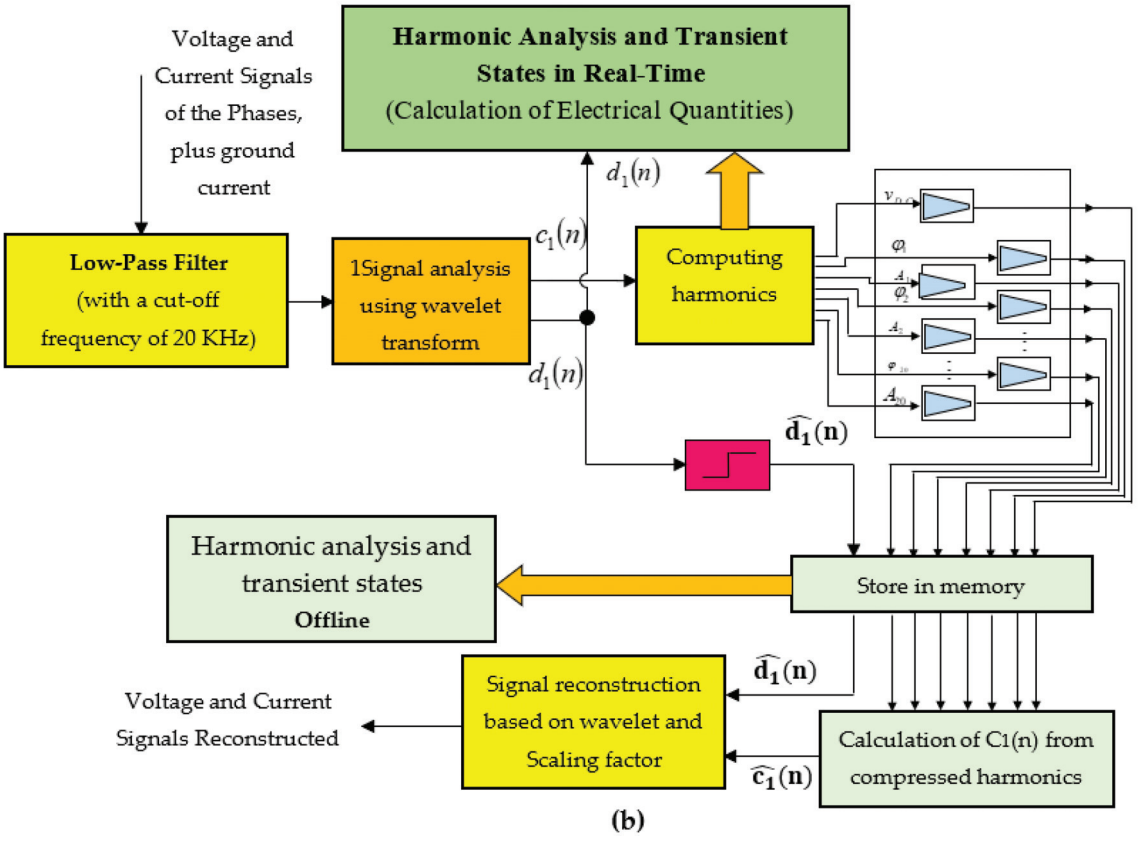

(b)

Figure 2. Monitoring system: (**a**) simplified block diagram; (**b**) simulated structure.

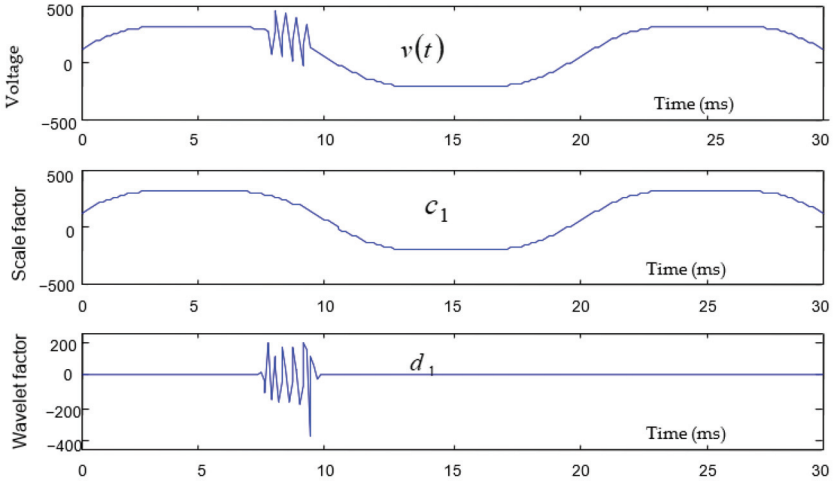

Figure 3. Voltage signal, scaling factor, and wavelet factor for voltage signal.

3.1.3. Algebraic Method for Calculation of Harmonic

The scaling factor (c_1) shows a low-frequency spectrum of the monitoring signal. In other words, this coefficient shows the steady state of the monitoring signal. In this case, we can calculate the DC magnitude and phase harmonics of the monitoring signal with 41 samplings in one period. First, the momentary frequency is calculated by detected the zero crossing of c_1, and then the DC value, magnitude, and phase of harmonics are calculated via the algebraic method. The algebraic method, which has been presented for the time first in this paper, is confirmed based on solving of the algebraic equations obtained through the sampling of c_1 (when that rating frequency is constant) [30]. Thus, for this reason, we have called it the algebraic method, and we describe it in the following section. The waveform of the power network voltage in the presence of network harmonics can be written as follows:

$$v(k) = v_0 + \sum_{n=1}^{N} [a_n \cos(2\,\pi\,n\,f\,T_S\,k) + b_n \sin(2\,\pi\,n\,f\,T_S\,k)] \tag{20}$$

In this equation, f, k, $v(k)$ are known. Thus, $\cos(2\,\pi\,n\,f\,T_S\,k)$, $\sin(2\,\pi\,n\,f\,T_S\,k)$ are also known. We want calculate a_n, b_n *and* v_{DC} [31]. It is observed that number of unknowns is $2N+1$ and that N is the number of harmonics (or the last order harmonic in voltage). Because $\cos(2\,\pi\,n\,f\,T_S\,k)$ and $\sin(2\,\pi\,n\,f\,T_S\,k)$ are known, thus, Equation (21) can be classed as a linear equation on the basis of a_n, b_n *and* v_{DC} variables. Thus, we can write the algebraic equation system with $2N+1$ unknowns and $2N+1$ linear equations for $2N+1$ samples of $v(t)$, in the form below:

$$V = A\,X \tag{21}$$

where

$$V = \begin{bmatrix} v(1) \\ v(2) \\ \vdots \\ v(M) \end{bmatrix}, X = \begin{bmatrix} v_{DC} \\ a_1 \\ \vdots \\ a_n \\ b_1 \\ \vdots \\ b_n \end{bmatrix}, \begin{array}{l} v(k) = v(T_S k)\ , (for\, k = 1, \ldots, M) \\ and \quad M = 2N+1 \end{array} \tag{22}$$

$$A_1 = \begin{bmatrix} 1\ \cos(2\pi f(1T_S)) & \cdots & \cos(2\pi f(1T_S)) \\ 1\ \cos(2\pi f(2T_S)) & \cdots & \cos(2\pi f(2T_S)) \\ & \vdots & \\ 1\ \cos(2\pi f(MT_S)) & \cdots & \cos(2\pi f(MT_S)) \end{bmatrix} \tag{23}$$

and

$$A_2 = \begin{bmatrix} \sin(2\pi f(1T_S)) & \cdots & \sin(2\pi f(1T_S)) \\ \sin(2\pi f(2T_S)) & \cdots & \sin(2\pi f(2T_S)) \\ & \vdots & \\ \sin(2\pi f(MT_S)) & \cdots & \sin(2\pi f(MT_S)) \end{bmatrix} \tag{24}$$

$$A = [A_1\ ,\ A_2]$$

Because A is constant, A^{-1} is also constant. Thus, it is enough to just calculate A one time and then A^{-1}, for solving Equation (1) [32,33].

$$\begin{bmatrix} v_{DC} \\ a_1 \\ \vdots \\ a_n \\ b_1 \\ \vdots \\ b_n \end{bmatrix} = A^{-1} \begin{bmatrix} v(1) \\ v(2) \\ \vdots \\ \vdots \\ \vdots \\ \vdots \\ v(M) \end{bmatrix} \tag{25}$$

3.1.4. Recursive Algebraic Method

If A^{-1} is written in the form below:

$$A^{-1} = \left[c_{i,j}\right]_{2N+1,2N+1}\ ,\ (i,j = 1,\cdots,2N+1) \tag{26}$$

then from Equations (25) and (26), we have:

$$v_{DC} = \sum_{j=1}^{2N+1} c_{1,j}\, v(j) \tag{27}$$

$$a_n = \sum_{j=1}^{2N+1} c_{n+1,j}\, v(j) \tag{28}$$

$$b_n = \sum_{j=1}^{2N+1} c_{N+n+1,j}\, v(j) \tag{29}$$

It is observed that for calculating a_n, b_n, and v_{DC}, it is required that we have completed one period of signal monitoring, and then it is necessary to perform a high volume of calculating for a_n, b_n, and v_{DC}. The reason for this is because for each variable, it is necessary to perform $2N+1$ sum operations and $2N+1$ multiple operations, and also, the number of variables is $2N+1$. In total, $(2N+1)^2$ operations of multiplication and addition should be performed. A method is presented here that divides these calculations among samplings. The method of performing the work is as follows: if the period we calculate the harmonics is the kth period, we can write [34]:

$$v_{DC}^{k}(j+1) = v_{DC}^{k}(j) + c_{1,j}\, v(j) \tag{30}$$

$$a_n^{k}(j+1) = a_n^{k}(j) + c_{n+1,j}\, v(j) \tag{31}$$

$$b_n^k(j+1) = b_n^k(j) + c_{N+n+1,j}\, v(j) \tag{32}$$

In the above relationships, k is the period number, i is the sample number in the kth period, n is the harmonics number, and N is the total number of harmonics. The number of samples in each period starts from one, and the initial values of the variables are one at the beginning of each period; this means that $v_{DC}^k(1) = a_n^k(1) = b_n^k(1) = 0$.

It can be seen that after the 2N + 1 sample or after going through a period, the harmonics and the DC value of the signal are calculated [35]. Then, the sampling number i is equal to zero, and one is added to the value of k (period number) so that the amount of harmonics in the next period is calculated in the same way. In this method, because the value of the variables in each sampling stage (in any period) depends on the value of the variable in the previous sampling stage (of the same period), it is called the recursive method.

3.1.5. Simulation of Algebraic Method

To show the ability of the algebraic method, we consider the voltage of the power system in the form below [36]:

$$\begin{array}{l} v(t) = 60 + 300e^{-2t}\sin(2\pi 50\, t) + 40\sin(2\pi(3\times 50)\, t) \\ +200p(t)\sin(2\pi(50\times 50)\, t) \end{array} \tag{33}$$

where $p(t) = u(t-0.01) - u(t-0.011)$. Moreover, $u(t)$ is a unit function.

The following figures show the simulation of voltage variables with the above relationship. The algorithm of the algebraic method is shown in Figure 4.

Figure 5 show the frequency of the first harmonic, the blue waveform is the actual frequency of the first harmonic, and the waveform of the frequency calculated by the algebraic method.

Figure 6 shows the voltage waveform simulated by algebraic method and its actual value. Figure 7a and 7b show the amplitude and phase of the first harmonics, respectively. Figure 8a and 8b also show the range of the third and fifteenth harmonics, respectively. The algorithm of the DFT method for calculating harmonics is shown in Figure 9.

3.1.6. Simulation for DFT Method

In order to demonstrate the capability of the DFT method, the voltage of the power network is considered as follows [37]:

$$v(t) = v_{DC} + \sum_{n\,=\,1}^{20} A_n\, \sin(2\pi\, nf\, t + \phi_n) \tag{34}$$

where

$$A_n = \begin{cases} 300\, e^{-2\,t}\ ,\ n=1 \\ 40 \quad ,\ n=3 \\ u(t)+u(t-0.25) \quad ,\ n=15 \\ 0 \quad ,\ Otherwise \end{cases} \qquad v_{,\,DC} = 60 \quad ,\ f=50$$

$$\phi_n = \begin{cases} -2\,\cos(2\pi\, 2\, t) \quad ,\ n=1 \\ \\ 0 \qquad\qquad ,\ n\neq 1 \end{cases}$$

The variability of the first harmonic phase (fundamental) causes the variability of the first frequency of the signal. In this case, the first harmonic frequency is:

$$f_1 = \frac{1}{2\pi}\frac{d}{d\, t}(2\pi\, f\, t + \phi_1) = f\ + 4\,\sin(2\pi\, 2\, t) \tag{35}$$

Figure 10 shows the frequency of the first harmonic, the blue waveform is the actual frequency of the first harmonic, and the waveform of the frequency calculated by the DFT method. Figure 11 shows the voltage waveform simulated by DFT method and its actual value. Figure 12a,b show the amplitude and phase of the first harmonics, respectively. Figure 13a,b also show the amplitude of third and fifteenth harmonics, respectively.

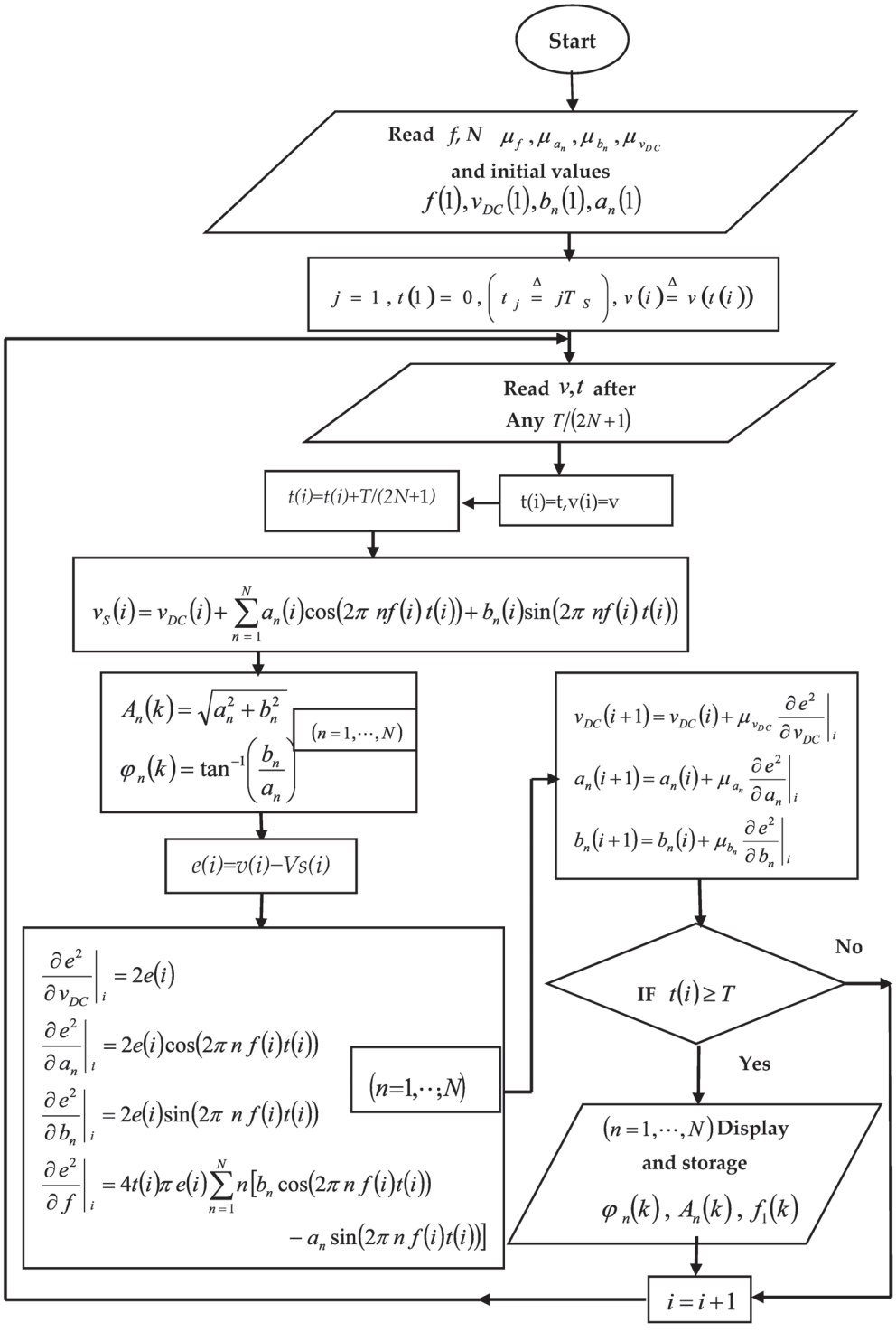

Figure 4. Algorithm of the algebraic method.

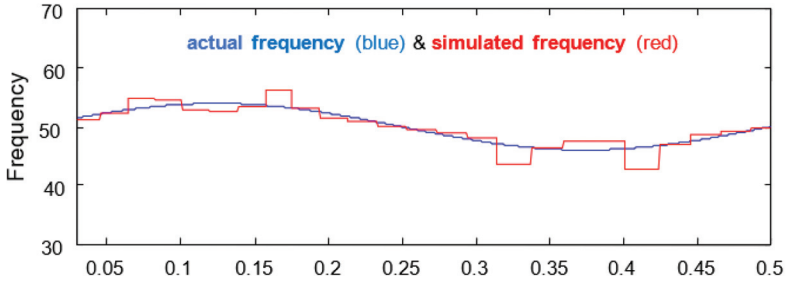

Figure 5. Simulation of the first harmonic frequency (actual and simulated signals).

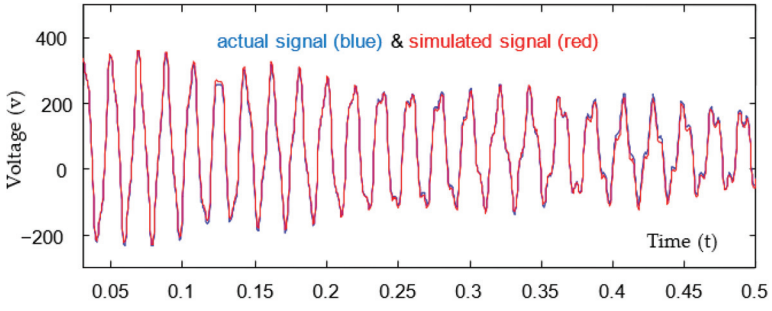

Figure 6. Simulation of voltage V(t) (algebraic method).

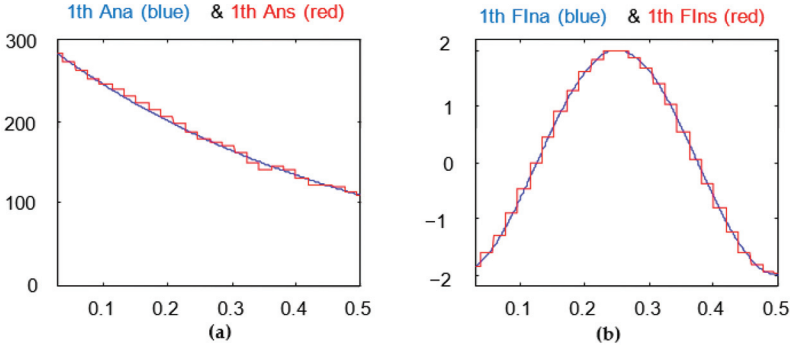

Figure 7. (**a**) First harmonic amplitude; (**b**) first harmonic phase in rad/(blue curves are actual, and red curves are simulated).

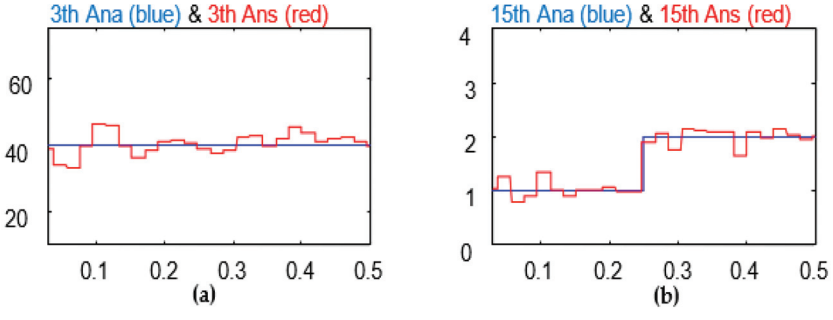

Figure 8. (**a**) 3rd harmonic amplitude; (**b**) 15th harmonic amplitude (blue curves are actual, and red curves are simulated) (algebraic method).

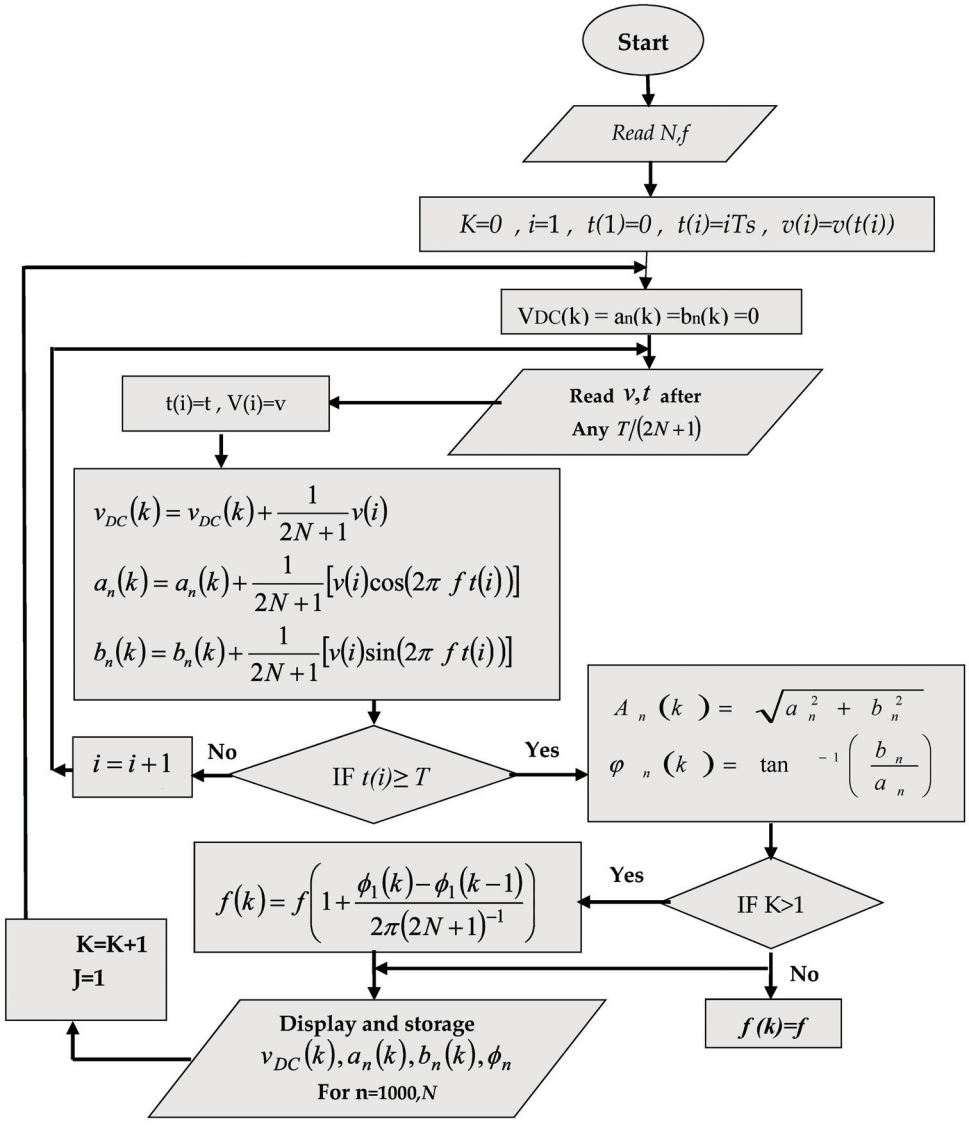

Figure 9. Algorithm of DFT method for calculating harmonics.

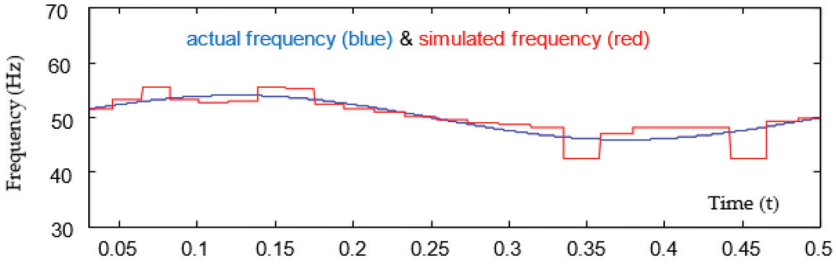

Figure 10. Simulation of the frequency of the first harmonic (DFT Method).

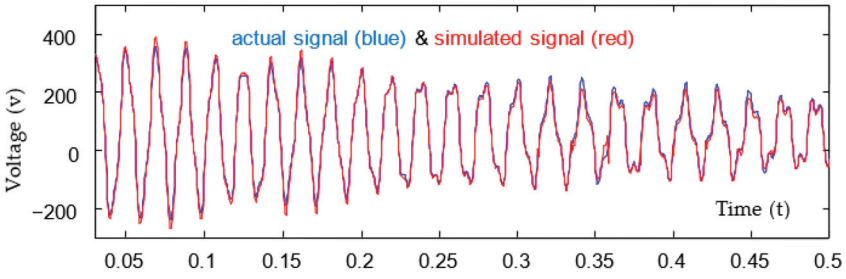

Figure 11. The actual value (blue) and the simulated value (red) of the voltage waveform.

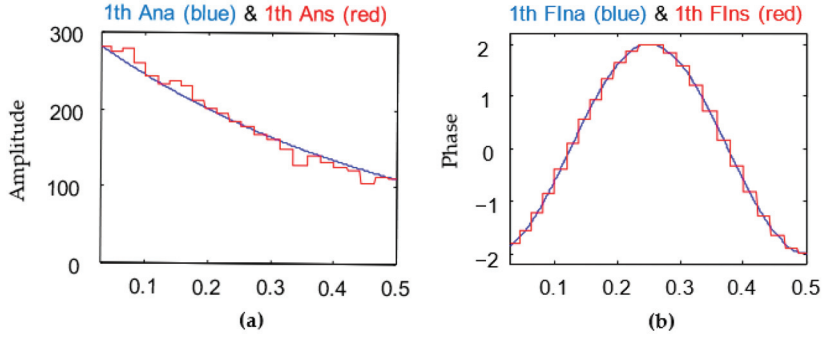

Figure 12. (**a**) Amplitude of the first harmonic (**b**) Phase of the first harmonic in terms of radians (the blue curves are actual, and the red curves are simulated).

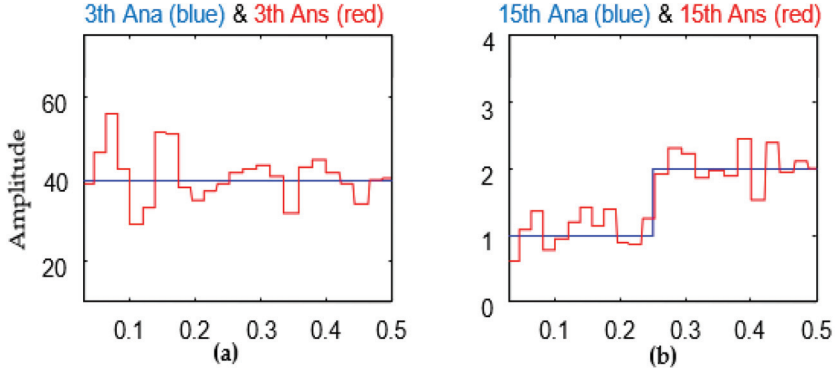

Figure 13. (**a**) 3rd harmonic amplitude; (**b**) 15th harmonic amplitude (blue curves are actual, and red curves are simulated).

One of the drawbacks of the DFT method is the leakage in the spectrum. This effect occurs due to the windowing of the signal under analysis in the time domain and corresponds to the Fourier transform of that window. Figure 14 shows the windowing of the signal in the time domain. As we know, convolutional in the frequency domain means integration over all components of the frequency spectrum. Furthermore, this means the influence of adjacent spectra in the harmonics to be calculated. In other words, spectral energy leaks from one frequency to another due to windowing. The following can be mentioned as ways to reduce this effect: (1) increasing the window's width by increasing the number of DFT points inside this window; (2) using appropriate window functions; (3) removing large intermittent components before windowing [38].

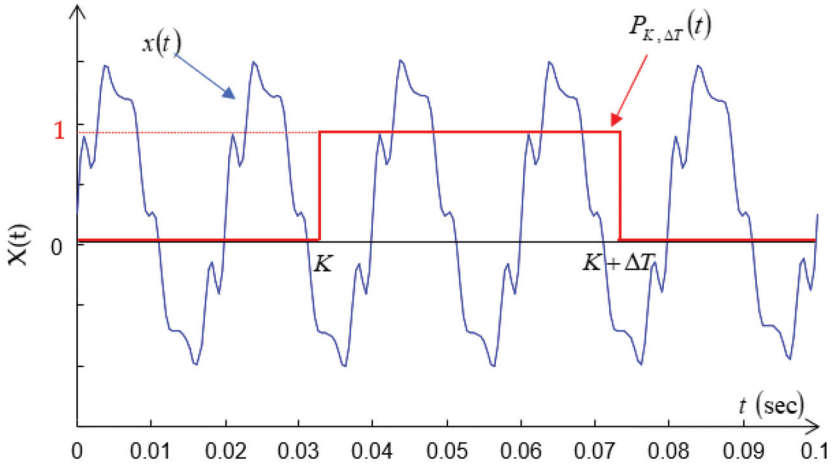

Figure 14. Windowing of $x(t)$ by $P_{K,\Delta T}(t)$ in the time.

3.1.7. Comparison of the Algebraic Method with the Dynamic Gradient Method

In the algebraic method, for 2N + 1 samples during a period, N harmonics and the DC value of the waveform can be obtained entirely (analytically). However, this possibility does not exist in the least squares method; in other words, to increase the accuracy in this method, the number of samples should be increased [39]. In terms of speed, it can be seen that if we convert these methods into reversibility, their speeds will ultimately be the same. It should be noted that it is possible to calculate the instantaneous frequency for the least squares method. However, this possibility is not directly possible for the algebraic method [40].

3.2. Compression Monitored Variables

For making offline analysis available, we must be able to store the frequency, v_{DC} magnitude, harmonics (steady values), and transient modes, and for the maximum decreasing of memory values, we must compress them. For this proposal, we present a method for compressing transient values and a new method for compressing steady values [41].

3.2.1. Compression of Transient Modes

Transient modes are characterized by the first level of wavelet factor ($d_1(n)$). To save this level, we pass it through a limiter. If we show the limiting output in terms of input (d_1) as ($\hat{d_1}$) (according to Figure 15), then we will have:

$$\hat{d_1}(n) = \begin{cases} d_1(n) & , |d_1(n)| \geq \eta \\ 0 & , |d_1(n)| < \eta \end{cases} \quad (36)$$

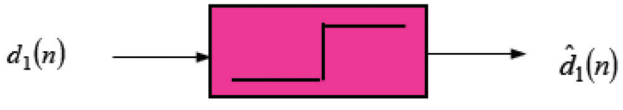

Figure 15. Limiter for wavelet factor ($d_1(n)$).

Thus when the amount of d_1 is smaller than specific values, $\hat{d_1}$ will be zero, and otherwise $\hat{d_1} = d_1$. In this manner, in additionally performed compression, the disturbance of d_1, which has a high-frequency spectrum, is also omitted [42].

3.2.2. Compression of DC Value and Amplitude and Phase of Signal Harmonics

DC value, amplitude, and phase of signal harmonics are steady-state parts of the signal, and usually, its changes are smooth and predictable. The consecutive values for these variables are the values obtained for them in their corresponding consecutive periods. Because the changes in these signals are slow, we therefore approximate the signal with a third-degree function. In order for this approximation to be more accurate, the coefficients of this function (third-order function) are recalculated based on the restrictions mentioned later. The least square technique is used to approximate the signal. That technique is also solved via the reversible algebraic method [43].

Assume $a(k)$ (in Figure 16) is the magnitude of any harmonics that we intend to compact. For this purpose, first, we divide it into different areas. Then, we approximate each of these areas using the third-degree function. To specify these time ranges, we apply the following restrictions [43]. These constraints are considered so that, while minimizing the third-order function with the waveform, the amount of compression is also maximized. It should be noted that the more extensive the selected spatial range, the more significant the amount of compression, which will be discussed in detail in the next section.

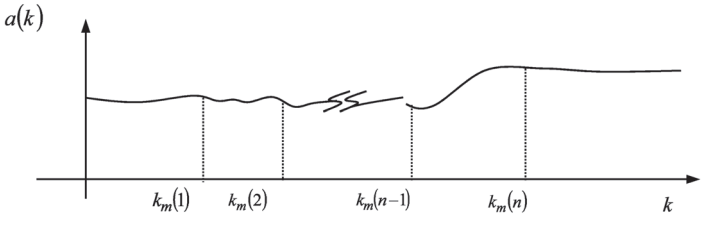

Figure 16. Waveform under compressing.

The constraints based on which the coefficients of the third-degree function change are as follows:

(a) One of the other places where the coefficients of the third-order function should change is the place where, firstly, the derivative of the signal changes its sign, and secondly, the absolute value of the difference in the signal value at that place is greater than a particular value, i.e., [44]:

$$\begin{array}{l} if\ \ \dot{a}(k) = \frac{a(k)-a(k-1)}{\Delta k} \\ then\ \begin{cases} 1:\ \dot{a}(k)\cdot\dot{a}(k-1) < 0 \\ 2:\ a(k) - a(k_m(m-1)) > \eta \end{cases} \end{array} \tag{37}$$

In Equation (37), m, k_m are the number of internal approximations and the end of the previous range, in m intervals, respectively.

(b) The interval of the period, from the end of previous interval $(m-1)$, is more significant than another specific amount L; namely:

$$l = k - k_m(m-1) \geq L \tag{38}$$

3.3. Approximation of the Signal under Compression

As said before, to calculate the coefficients in each period (m = 1000), we try to minimize the square of the error of the third-degree function and the signal under compression. For this purpose, we use an analytical method and make it reversible so that the calculations are divided between the periods. Suppose the signal under compression is $a(k)$ in period m. This signal is approximated by the following third-degree function in the mentioned range [45].

$$p(l) = a_3\, l^3 + a_2\, l^2 + a_1\, l + a_0 \tag{39}$$

In this case, the squared error of the signal under compression and the third-degree function in this range is:

$$E(l) = a(l - km(m-1)) - p(l) \quad \Rightarrow \quad e^2 = \sum_l E(l) \tag{40}$$

For simplicity, in the following, we consider $a(l - km(m-1))$ to be equal to $y(l)$. In order for $p(l)$ to be closer to $a(k)$, the function e^2 should be minimized.

Reversible Algebraic Method

To minimize e^2, its derivatives in terms of variables a_0 , a_1 , a_2 , a_3 can be set equal to zero. We have in this order [46]:

$$\begin{array}{llll} \frac{\partial e^2}{\partial a_3} = 0 & \Rightarrow 2\,E\,l^3 = 0 & \Rightarrow a_3 \sum_l l^6 + a_2 \sum_l l^5 + a_1 \sum_l l^4 + a_0 \sum_l l^3 = \sum_l y(l)\, l^3 \\ \frac{\partial e^2}{\partial a_2} = 0 & \Rightarrow 2\,E\,l^2 = 0 & \Rightarrow a_3 \sum_l l^5 + a_2 \sum_l l^4 + a_1 \sum_l l^3 + a_0 \sum_l l^2 = \sum_l y(l)\, l^2 \\ \frac{\partial e^2}{\partial a_1} = 0 & \Rightarrow 2\,E\,l = 0 & \Rightarrow a_3 \sum_l l^4 + a_2 \sum_l l^3 + a_1 \sum_l l^2 + a_0 \sum_l l = \sum_l y(l)\, l \\ \frac{\partial e^2}{\partial a_0} = 0 & \Rightarrow 2\,E = 0 & \Rightarrow a_3 \sum_l l^3 + a_2 \sum_l l^2 + a_1 \sum_l l + a_0 \sum_l 1 = \sum_l y(l) \end{array} \tag{41}$$

In this way, the following algebraic equation is obtained from Equation (6).

$$\begin{bmatrix} a_3 \\ a_2 \\ a_1 \\ a_0 \end{bmatrix} = \begin{bmatrix} A_6 & A_5 & A_4 & A_3 \\ A_5 & A_4 & A_3 & A_2 \\ A_4 & A_3 & A_2 & A_1 \\ A_3 & A_2 & A_1 & A_0 \end{bmatrix}^{-1} \begin{bmatrix} Y_3 \\ Y_2 \\ Y_1 \\ Y_0 \end{bmatrix} \tag{42}$$

The values of A_j, which is $(j = 0, \cdots, 6)$, and Y_i, which is $(i = 0, \cdots, 3)$, can be reversibly calculated [47]:

$$\begin{array}{l} A_j(l) = A_j(l-1) + l^j \\ Y_i(l) = Y_i(l-1) + y(l)\, l^i \end{array} \tag{43}$$

Thus, at the end of each range, we have:

$$\begin{array}{l} A_j = A_j(l) \\ Y_i = Y_i(l) \end{array} \tag{44}$$

This means that all the matrix elements of coefficients $(A_{4\times4})$ and vector $Y_{4\times1}$ are calculated until the end of each range. Moreover, in the end, it becomes possible to calculate the variables a_0 , a_1 , a_2 , a_3 in much less time. In order to better understand the harmonics compression method, the process of compressing the harmonics permanent part is presented as an algorithm. The algorithm of the compression of steady-state harmonics is shown in Figure 17. In this algorithm, $a(k)$ is simulated by $a_0(m) + a_1(m)l + a_2(m)l^2 + a_3(m)l^3$, and y is $a(k - k_m(m-1))$.

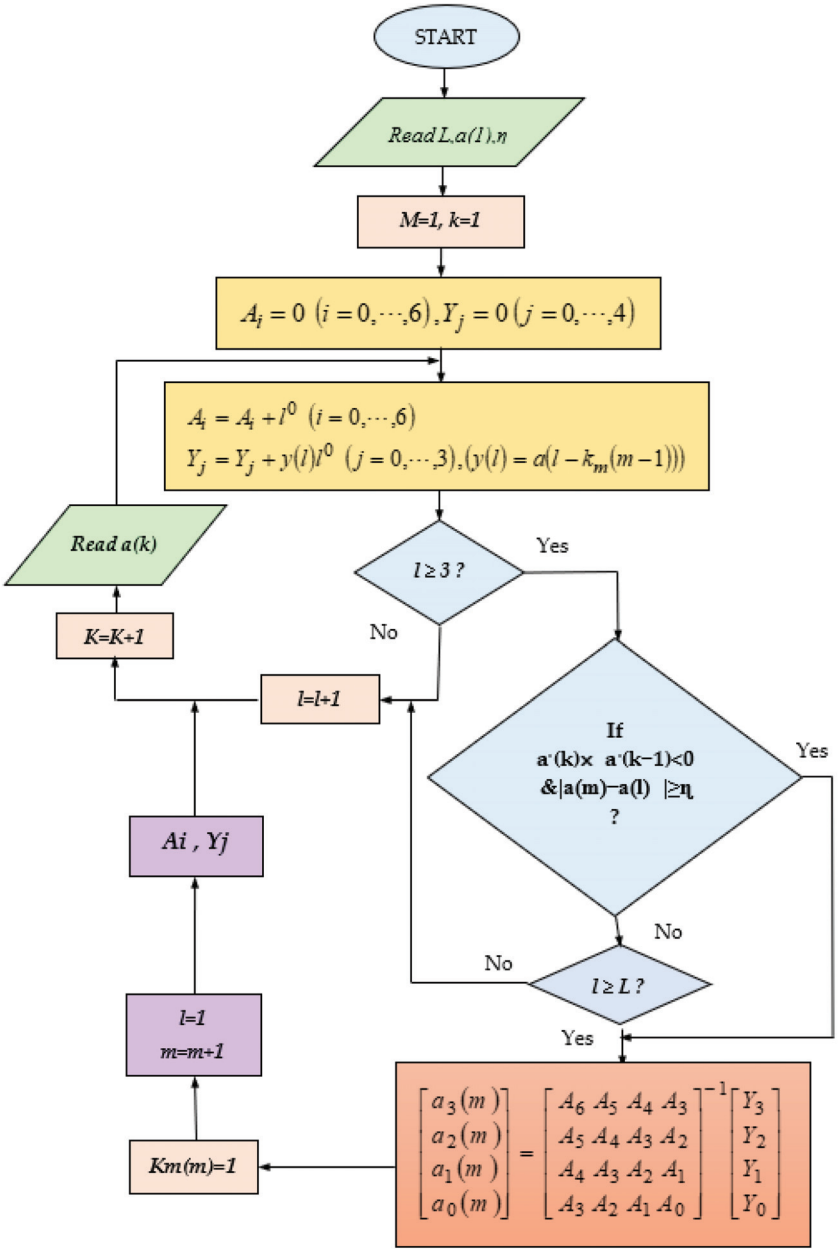

Figure 17. Algorithm of recursive algebraic method for steady-state approximation.

3.4. Amount of Compression

In this part, we want to examine the amount of compression via the mentioned system. The number of samples of the main signal is 24 thousand samples per second. This signal is divided into two parts, one of which represents the transient state (wavelet factor), and the other represents the steady state (scaling factor). Because we have assumed that the frequency spectrum (harmonics order) of the steady state of the power network signal is limited to the 20th harmonic, it is therefore necessary to take 41 × 50 = 2050 samples from the harmonic part of the signal to calculate the harmonics and the DC value. Alternatively, in other words, we use only samples 41 × 50 = 2050 s apart (in this case, the signal frequency is 50 Hz). But after calculating the harmonics, for each period of the signal, 41 values (20 harmonics size values, 20 harmonics phase values, and one for the DC value) are calculated. Therefore, there is no change in the amount of data before and after the harmonics measurement. So far, assuming that the length of transient states that have occurred is 1% on average for each second, then furthermore, the remaining 99% can be considered deleted after passing through the limiter; the number of data have been halved.

However, from the harmonics, the wavelet is taken first. Furthermore, its steady part is passed through the compression system explained in the previous section. If we consider the number of periods in each range to be 50 periods on average, we will have the following: the number of compression values in each range is 5. While the number of data in each limit is considered to be 50, it can be seen that the amount of compression is [48]:

$$\begin{aligned} COM &\triangleq \frac{X_{Actual}}{X_{Compression}} \\ &= \frac{(24000/50) \times 50}{(41 \times 5) + 0.02 \times (12000/50) \times 50} \approx 54 \end{aligned} \tag{45}$$

where X_{Actual}, $X_{Compression}$ are the amount of original signal data in a range and the amount of compressed signal data, respectively.

3.5. Harmonic Recovery

In this part, the values of harmonics are retrieved for different values. After receiving the time when the values of the harmonics are required for that moment, the order of the period in which this time is located is calculated.

$$k = [f \times t] + 1 \tag{46}$$

In the above relation, k is the order of the period, and $[f \times t]$ is the absolute value of the signal frequency and the time for which the harmonics are to be calculated. Then, the range of compression in which k is located is determined, namely [49]:

$$k_m(m-1) < k \leq k_m(m) \tag{47}$$

$$m = 1\,,\ k = [f \times t] + 1 \tag{48}$$

$$l = k - k_m(m-1) \tag{49}$$

$$a(k) = a_0(m) + a_1(m)l + a_2(m)l^2 + a_3(m)l^3 \tag{50}$$

In this relation, m, k_m are the number of the compression interval and the number of the last period that exist this interval, respectively. Harmonics in any interval are specified through calculation of m, k_m. The harmonics recovery algorithm is shows in Figure 18.

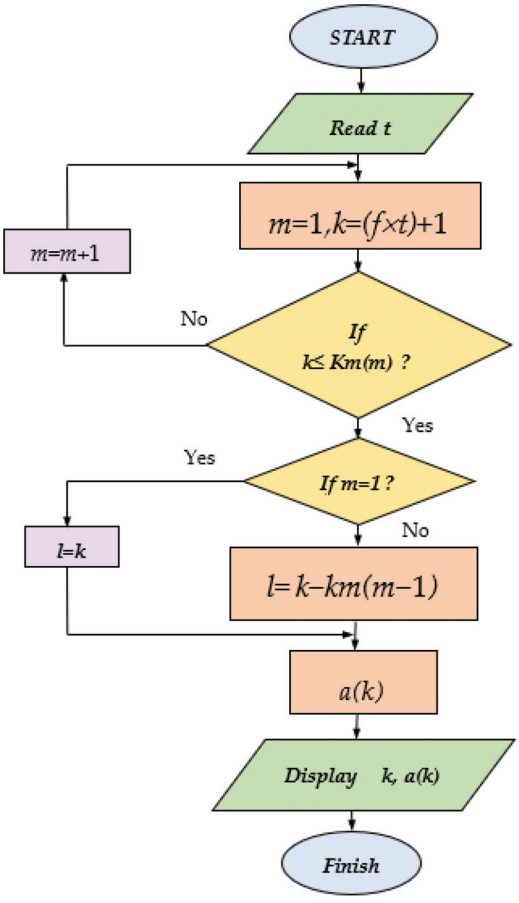

Figure 18. Harmonics recovery algorithm.

4. Simulation and Results

4.1. Real-Time and Offline Analysis of Power System

By obtaining the transient states and harmonics of the voltage and current of the power network phases, the quality of the power network can be analyzed, and necessary electrical quantities can be obtained. These quantities are as follows: the practical values of the voltage and currents of the power network, and the real and imaginary components of the apparent power of the network and also positive, negative, and neutral sequences in real time.

4.1.1. Finding the Location of the Fault by Derivation

Occurred faults are of high importance when they have significant effects on the main component of the power grid voltage. In this case, the fault occurrence time can be obtained by deriving the waveform of the main component of the signal. This is because if we represent this time with t_{fault}, then the difference between two samples before and after the error will be more significant than the difference between consecutive samples in typical moments. Therefore, the derivative will be significant at this moment. This means that:

$$\dot{x}\left(t_{fault}\right) \approx \frac{x\left(t_{fault}^{+}\right) - x\left(t_{fault}^{-}\right)}{\Delta t} \tag{51}$$

In this relation, t^{+}_{fault} , t^{-}_{fault} are, respectively, the sampling times before and after the occurrence of the fault.

However, the derivative of the sinusoidal signal (the main component of the voltage waveform) cannot always be determined when the fault occurs.

In Figure 19, the derivative of the signal at the fault location does not differ much from the derivative of the signal at ordinary moments. Therefore, the derivative of the signal cannot determine the occurrence of the fault.

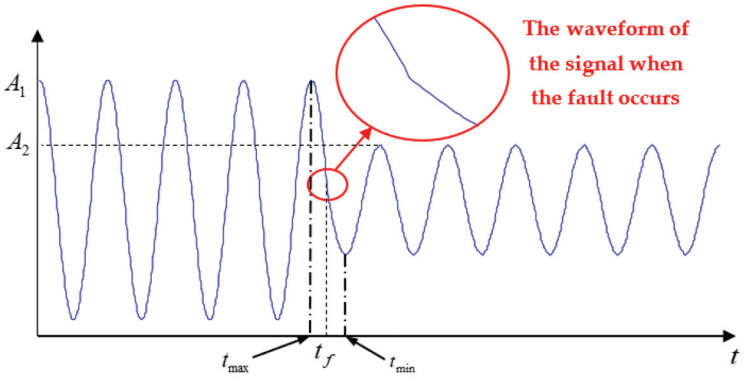

Figure 19. The waveform of the signal when the fault.

However, in Figure 20, the derivative of the signal at the moment of the fault is significantly different from the derivative of the signal at normal moments. So, it is possible to determine the occurrence of the fault from the derivative of the signal.

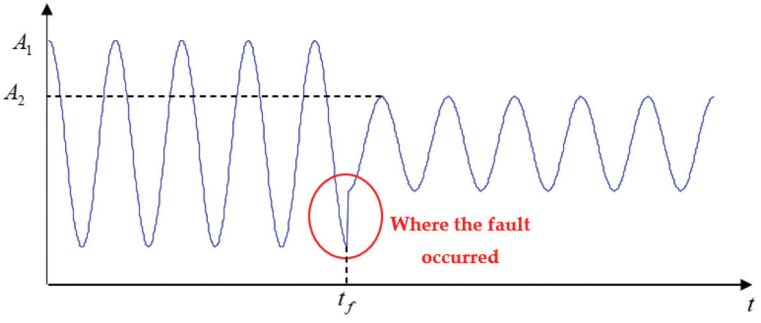

Figure 20. The waveform of the signal when the fault occurs.

It can be seen from the above figure that it is possible to determine the half period of the signal in which the fault occurred. In other words, this time is enclosed between two times in which the signal has the maximum value before the fault and the minimum value after the fault or vice versa (minimum before the fault and maximum after the fault).

It can be seen that in Figure 21, the fault occurred when the value of the sine function is close to zero. Therefore, the derivative of the function will be insignificant at this point.

However, in Figure 22, a fault has occurred in a place where the value of the sinusoidal function is close to one, regardless of its sign. Therefore, the value of the derivative of the signal at this moment is substantial.

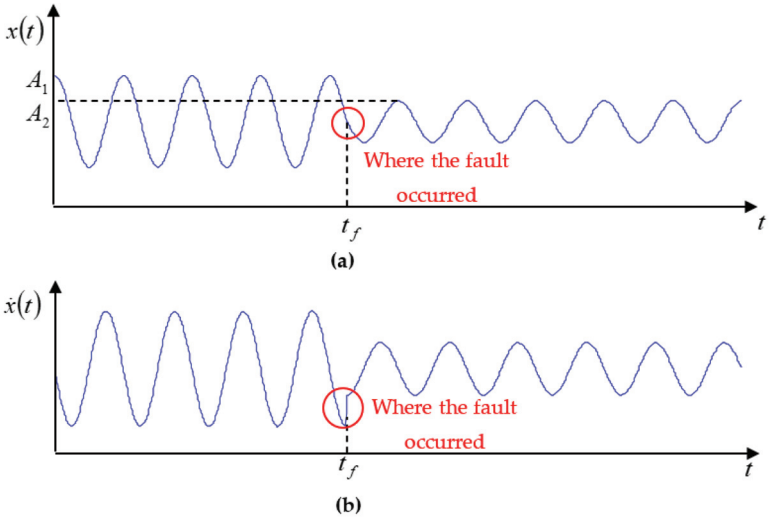

Figure 21. The fault occurred when the size of the derivative of the signal is minimum at that moment. (**a**) The signal itself; (**b**) the derivative of the signal.

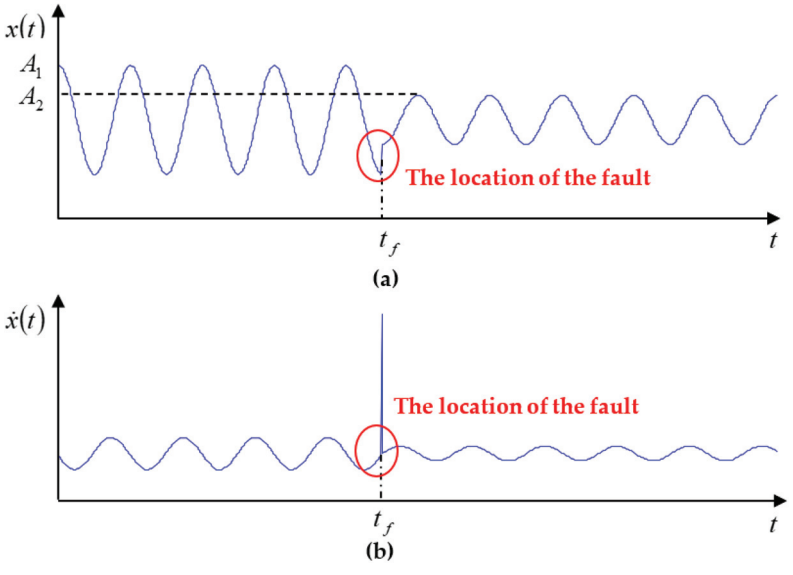

Figure 22. The fault occurred when the size of the derivative of the signal at that moment is maximum. (**a**) The signal itself; (**b**) the derivative of the signal.

4.1.2. Accurate Determination of the Fault Occurrence Time Using Wavelet Transform

As was said before, the first wavelet level of any signal can show the location of the fault in time and frequency.

After taking the wavelet transform (as shown in Figure 23), the wavelet coefficient represents the transient modes. Next, for Figures 24 and 25, the wavelet coefficient and scale coefficient are shown.

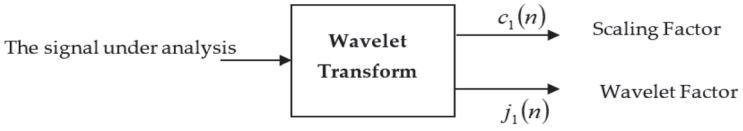

Figure 23. Wavelet transform of the signal under analysis.

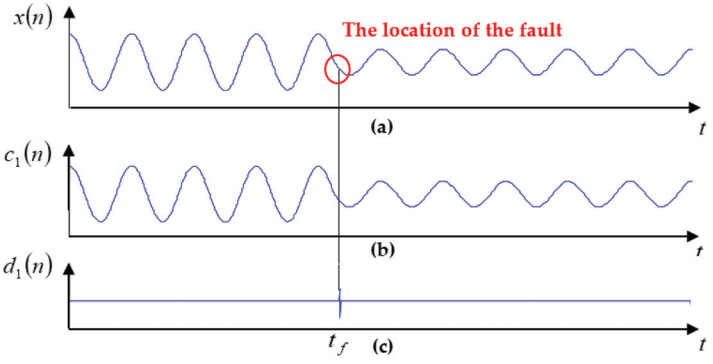

Figure 24. The fault occurred when the size of the derivative of the signal is minimum at that moment. (**a**) Signal itself; (**b**) scaling factor; (**c**) wavelet factor.

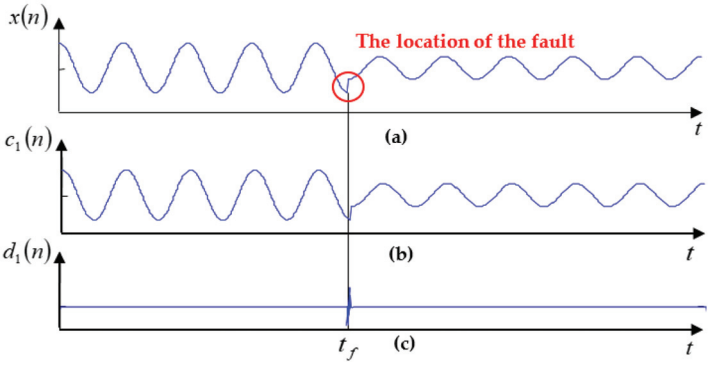

Figure 25. The fault occurred when the size of the derivative of the signal is maximum at that moment. (**a**) Signal itself; (**b**) scaling factor; (**c**) wavelet factor.

For this case, it was observed that we could not obtain the location of the change in the monitored signal through derivation. Nevertheless, in part (c) of the above figure, it can be seen that the location of the change in the signal under study can be easily found. This part actually shows the waveform of wavelet's factor.

4.2. Offline Analysis of the Power Network

Considering that the provided monitoring system is able to store harmonics and transient states, they can therefore be used for offline analysis such as statistical harmonics analysis.

4.3. Simulation of Compression Steady Values

Normally, the waveform of the harmonics and DC value is sinuous or exponential. Thus, we use the presented algorithm for steady compression over these waveforms.

(a) Exponential waveform: If $a(k)$ is considered as follows:

$$a(k) = 200e^{-0.02k} \tag{52}$$

then for $k = 1, \cdots, 100$, we can show $a(k)$, and the simulation is as shown in Figure 26.

(b) Sinuous waveform: If $a(k)$ is considered as follows:

$$a(k) = \sin(0.02\pi k) \tag{53}$$

then for $k = 1, \cdots, 100$, we can show $a(k)$, and the simulation is as shown in Figure 27.

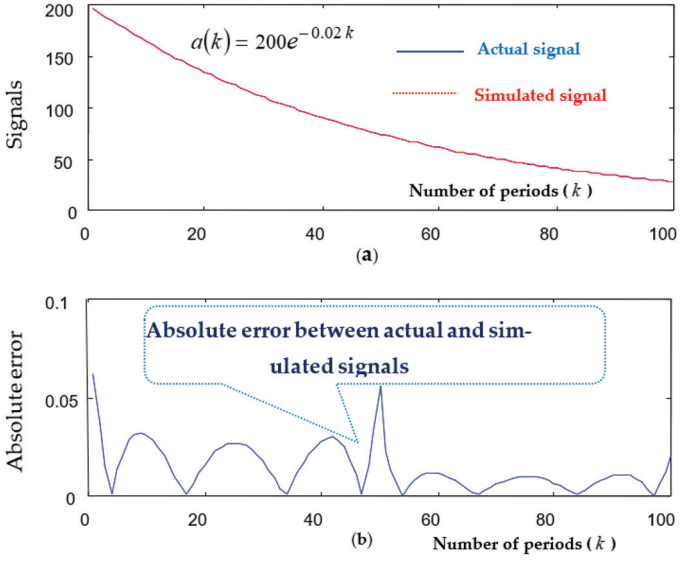

Figure 26. (**a**) Actual and simulated signals. (**b**) Absolute error between actual and simulated signals.

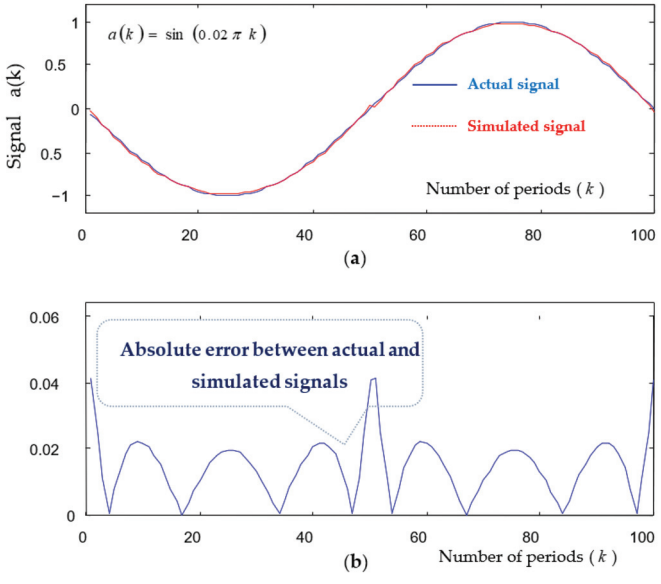

Figure 27. (**a**) Actual and simulated signals. (**b**) Absolute error between actual and simulated signals.

5. Comparison Results with Other Papers

In order to check the quality of the proposed method, a comparison has been made between the results of this study and the results of the articles in Table 1 in terms of

the percentage of classification accuracy and the dimensions of the feature vector. This comparison shows that the classification algorithms presented in this research have high immunity despite the high noise. Also, the overall accuracy in this research is higher than all the mentioned articles. Therefore, the proposed detection structures perform best in noisy conditions without using denoising algorithms, and power quality disturbances can be detected without the complexity of performing noise steps and calculations with an appropriate accuracy.

Table 1. The accuracy results of the proposed method in the classification of power quality disturbances in comparison with previous articles.

Some of the Power Quality Studies		Number of Features	Classification Accuracy (%)				
References			Noiseless	40 dB	30 dB	20 dB	Overall
[5]		7	99.65	99.4	99.2	87	96.62
[8]		17	99.78	--	99.41	97.79	97.93
[11]		8	99.76	99.57	96.98	84.86	96.22
[13]		5	--	99.46	99.11	94	98.08
[18]		12	99.88	94.64	93.85	89.92	91.8
[32]		14	--	92.64	--	93.19	94.16
[38]		16	99.55	99.54	99.21	94.91	98.31
This paper	Online Scheme	6	99.66	99.33	99.33	98.77	99.38
	Offline Scheme	6	99.77	99.44	99.66	99.44	99.66

It should be noted that for the better understanding of the readers and to help the related research in the future, parts of the written computer program are given in Appendix A.

6. Conclusions

In recent times, the non-linear loads in power networks have increased, so the identification of harmonics is critical. Because of this, in order to analyze the network with such loads, the number of harmonics must be known. One of the important parameters in controlling and studying the stability of power systems is the power grid frequency. Therefore, it is necessary to determine its momentary changes; in other words, it should be possible to measure it momentarily.

In this paper, we present a monitoring system that is able to calculate frequency, harmonics, and DC value and transient events. In this research, different methods of frequency and harmonics have been presented and compared to each other. DFT method, algebraic method, and least square method are the three main methods of calculating harmonics and calculating frequency. Techniques to improve these methods have been provided. Based on the comparison, the reversible algebraic method is superior to the others, while being simpler to implement, with high accuracy and speed. Therefore, this method has been used in the monitoring system.

In order to diagnose faults and study their effects on a power network, transient states must be identified. For this purpose, the mathematical technique of signal processing called wavelet transform is used today. We have also used this method to identify the faults that occurred in a power network. In addition to displaying signals in time and frequency domains, a wavelet can display them with the least coefficients. This is because their coefficients rapidly tend to zero with an increase in their levels if the mother wavelet function is selected.

The provided monitoring system provides harmonics and transients for real-time and offline analysis. To perform offline analysis, the measured values must be stored. Obviously, if these measured data are stored directly, they will occupy a significant amount of memory. To reduce the memory usage, it is necessary to compress the measured values

before being stored. The provided monitoring system can multiply the data obtained from the measurement by a new and unique method up to 40 times (while maintaining maximum accuracy).

The simulation results obtained in this article show that this structure and approach are superior to other approaches used in recent years in the discussion of monitoring power quality disturbances.

Due to the introduction of a new processing technique (wavelet transform), which is used to analyze transient states from different points of view that were briefly mentioned, the suggestion that can be made here is to study and complete each of these methods. In particular, these items include the following:

- Studying and improving the exact location of the fault between two parts of the power network, in which it is possible to accurately measure the quantities of the power network (voltage and current).
- Finding the most suitable mother wavelet function, which has maximum compatibility with power network signals.
- The development of methods for finding high-impedance faults by wavelet transform.
- The development and improvement of detecting the location of the short circuit fault and identifying its type with the help of wavelet transform.
- Studying the effects of lightning on the transmission system and power distribution system and their equipment.
- Improving compression methods and the provided monitoring system.
- The use of neural and fuzzy networks and a genetic algorithm in different parts of the techniques used in the monitoring system.

Author Contributions: Conceptualization, M.Z. and R.I.; methodology, M.Z. and R.I.; software, M.Z. and R.I.; validation, M.Z. and R.I.; formal analysis, M.Z.; investigation, M.Z. and R.I.; resources, R.I.; data curation, M.Z.; writing—original draft preparation, M.Z. and R.I.; writing—review and editing, R.I.; visualization, M.Z.; supervision, M.Z. and R.I.; project administration, M.Z.; funding acquisition, M.Z. All authors have read and agreed to the published version of the manuscript.

Funding: This research received no external funding.

Institutional Review Board Statement: This paper does not contain any studies with human participants or animals performed by any of the authors.

Data Availability Statement: The data that support the findings of this study are available from the corresponding author upon reasonable request.

Conflicts of Interest: The authors declare no conflict of interest.

Appendix A. Part of the Programs of the Methods Presented in This Article

A.1. Frequency Measurement via Least Square Method

```
%  calculation of frequency one with six sample in this problem DC values have be added.
%  that v(t) be extended by two first term of tylor series.
t=[0:1/250:4/250]';
a0=100;  % DC value
f0=50;   % rate frequency
f1=40;   % actual frequency
tet=70;  % phase of voltage
v=a0+220*sin(2*pi*f1*t+tet*pi/180);
a=[ones(5,1) , sin(2*pi*f0*t) , 2*pi*t.*cos(2*pi*f0*t) , cos(2*pi*f0*t) ...
     , 2*pi*t.*sin(2*pi*f0*t)];
inva=inv(a);
```

A.2. Program for Calculating Harmonics and Frequency via DFT Method

```
   clear
% detecteted zero crossing for calculating frequency AND
% Discrit time series fourier Transform for calculating amplitude and phase harnmonic
N=20;  % N is number of harmonics
fa=50;% fa is actual constant part of frequency
ml=30;% ml/fa is last time sampled of signal under montoring
nubt=(2*N+1); % nubt is requier rate sampling in every periodic
t=(0:1/(nubt*fa):(ml*nubt-1)/(nubt*fa))'; % 't' is secuence time sampling
% actual valves
for i=1 : ml*nubt;% we have a change pulse to aplitude of 15th harmonic
```

A.3. Program for Calculating Harmonics and Network Frequency via Algebraic Method

```
clear
% detecteted zero crossing for calculating frequency AND algabric
%
% in this method in first 'frequency' be calculated in any half period then for after
% one period, that frequency and series: cos(2*pi*f*k*har) & sin(2*pi*f*k*har)
% {k is sample times & har is harmonic} are known for this period, can calculate
% 'an' & 'bn' diractely by algabric equations.
%
%   |V(k1) |   | 1   cos(2*pi*f*k1) ... cos(2*pi*f*k1*N)  sin(2*pi*f*k1) ... sin(2*pi*f*k1*N)
| |V0 |
%   |V(k2) |   | 1   cos(2*pi*f*k2) ... cos(2*pi*f*k2*N)  sin(2*pi*f*k2) ... sin(2*pi*f*k2*N)
| |a1 |
%   |  :   | = | :       :               :              :                :       |=| : |
%   |  :   |   | :       :               :              :                :       | | : |
```

A.4. Program for Calculating Harmonics and Frequency via Dynamic Gradient Method

```
clear
% 'gradient steepest descent' method for detemaining frequency of singnal with DC level and
harmonics
   N=20;  % N in number of harmonics
   %ml=20;
   nubt=2*N+2;
   m=10000;% number of samples between 0 and 0.5
   %t=(0:1/(nubt*50):(ml*nubt-1)/(nubt*50))'; % 't' is secuence time sampling
t=linspace(0,0.5,m)';
```

References

1. Rao, S.N.V.B.; Kumar, Y.V.P.; Pradeep, D.J.; Reddy, C.P.; Flah, A.; Kraiem, H.; Al-Asad, J.F. Power quality improvement in renewable-energy-based microgrid clusters using fuzzy space vector PWM controlled inverter. *Sustainability* **2022**, *14*, 4663. [CrossRef]
2. Eslami, A.; Negnevitskyet, M.; Franklin, E.; Lyden, S. Review of AI applications in harmonic analysis in power systems. *Renew. Sustain. Energy Rev.* **2022**, *154*, 111897. [CrossRef]

3. Zhang, Y.; Shi, X.; Zhang, H.; Cao, Y.; Terzija, V. Review on deep learning applications in frequency analysis and control of modern power system. *Int. J. Electr. Power Energy Syst.* **2022**, *136*, 107744. [CrossRef]
4. Rahiman, Z.; Dhandapani, L.; Natarajan, R.C.; Vallikannan, P.; Palanisamy, S.; Chenniappan, S. Power Quality Conditioners in Smart Power System. In *Artificial Intelligence-Based Smart Power Systems*; Wiley-IEEE Press: Hoboken, NJ, USA, 2023; pp. 233–258.
5. Sivaraman, P.; Sharmeela, C.; Balaji, S.; Sanjeevikumar, P.; Elango, S. Power Quality Monitoring of Low Voltage Distribution System Toward Smart Distribution Grid Through IoT. In *IoT, Machine Learning and Blockchain Technologies for Renewable Energy and Modern Hybrid Power Systems*; River Publishers: Abingdon, UK, 2023; pp. 61–77.
6. Begovic, M.M.; Djuric, P.M.; Dunlap, S.; Phadke, A.G. Frequency Traking in Power Networks in the Presence of Harmonics. *IEEE Trans. Power Deliv.* **1993**, *8*, 480–486. [CrossRef]
7. Phadke, A.G.; Thorp, J.S.; Adamiak, M.G. A New Measurement for Technique Voltage Phasores, Local System Frequency, and Rate of Change of Frequency. *IEEE Trans. Power Appar. Syst.* **1983**, *PAS-102*, 1025–1038. [CrossRef]
8. George, T.A.; Bone, D. Harmonic Power Flow Determination Using the FFT transform. *IEEE Trans. Power Deliv.* **1991**, *6*, 530–535. [CrossRef]
9. Narasimhulu, N.; Awasthy, M.; de Prado, R.P.; Divakarachari, P.B.; Himabindu, N. Analysis and Impacts of Grid Integrated Photo-Voltaic and Electric Vehicle on Power Quality Issues. *Energies* **2023**, *16*, 714. [CrossRef]
10. Heydet, G.T.; Galli, A.W. Transient Power Quality Analyzed Using wavelets. *IEEE Trans. Power Deliv.* **1997**, *12*, 908–915. [CrossRef]
11. Eristi, H.; Demir, Y. A new algorithm for automatic classification of power quality events based on wavelet transform and SVM. *Expert Syst. Appl.* **2010**, *37*, 4094–4102. [CrossRef]
12. Liang, K.; Xiao, H.; Du, Y.; Lu, C.; Shen, M. A real-time monitoring system for fruit and vegetable cold chain logistics based on Internet of things technology. *Jiangsu J. Agric. Sci.* **2018**, *43*, 519–521.
13. Nanda, P.; Panigrahi, C.K.; Dasgupta, A. Phasor estimation and modelling techniques of PMU-a review. *Energy Procedia* **2017**, *109*, 64–77. [CrossRef]
14. Xu, S.; Leng, X. Design of Real-Time Power Quality Monitoring System for Active Distribution Network Based on Computer Monitoring. *J. Phys. Conf. Ser.* **2021**, *1992*, 032127. [CrossRef]
15. Banuelos-Cabral, E.S.; Nuno-Ayón, J.J.; Sotelo-Castanon, J.; Naredo, J.L. Extended vector fitting for subharmonics, harmonics, interharmonics, and supraharmonics estimation in electrical systems. *Electr. Power Syst. Res.* **2023**, *224*, 109664. [CrossRef]
16. Kirikkaleli, D.; Adebayo, T.S. Do public-private partnerships in energy and renewable energy consumption matter for consumption-based carbon dioxide emissions in India? *Environ. Sci. Pollut. Res.* **2021**, *28*, 30139–30152. [CrossRef] [PubMed]
17. Heydt, G.T.; Fjeld, P.S.; Liu, C.C.; Pierce, D.; Tu, L.; Hensley, G. Application of the Windowed FFT to Electrical Power Quality Assessment. *IEEE Trans. Power Deliv.* **1999**, *144*, 1411–1416. [CrossRef]
18. Mallala, B.; Venkata, P.V.; Palle, K. Analysis of Power Quality Issues and Mitigation Techniques Using HACO Algorithm. In *International Conference on Intelligent Sustainable Systems*; Springer Nature: Singapore, 2023. [CrossRef]
19. Zadehbagheri, M.; Payedar, A. The feasibility study of using space vector modulation inverters in two-level of integrated photovoltaic system. *TELKOMNIKA Indones. J. Electr. Eng.* **2015**, *14*, 205–214. [CrossRef]
20. Huang, S.-J.; Hsieh, C.-T. High-Impedance Fault detection Utilizing a Morlet Wavelet Transform Approach. *IEEE Trans. Power Deliv.* **1999**, *14*, 1401–1410. [CrossRef]
21. Zheng, T.; Makram, E.B.; Girgis, A.A. Power System Transient and Hormonic Studies Using Transform. *IEEE Trans. Power Deliv.* **1999**, *9*, 1461–1468. [CrossRef]
22. Balasubbareddy, M.; Venkata Prasad, P.; Palle, K. Power Quality Conditioner with Fuzzy Logic Controller. In *Information and Communication Technology for Competitive Strategies (ICTCS 2022)*; Kaiser, M.S., Xie, J., Rathore, V.S., Eds.; Lecture Notes in Networks and Systems; Springer: Singapore, 2023; Volume 615. [CrossRef]
23. Abbasi, A.R. Fault detection and diagnosis in power transformers: A comprehensive review and classification of publications and methods. *Electr. Power Syst. Res.* **2022**, *209*, 107990. [CrossRef]
24. Karami, M.; Zadehbagheri, M.; Kiani, M.J.; Nejatian, S. Retailer energy management of electric energy by combining demand response and hydrogen storage systems, renewable sources and electric vehicles. *Int. J. Hydrogen Energy* **2023**, *48*, 18775–18794. [CrossRef]
25. Zahedi, A. A review of drivers, benefits, and challenges in integrating renewable energy sources into electricity grid. *Renew. Sustain. Energy Rev.* **2011**, *15*, 4775–4779. [CrossRef]
26. Gayatri, M.T.L.; Parimi, A.M.; Kumar, A.V.P. Utilization of Unified Power Quality Conditioner for Voltage Sag/Swell Mitigation in Microgrid. In Proceedings of the 2016 Biennial International Conference on Power and Energy Systems: Towards Sustainable Energy (PESTSE), Bengaluru, India, 21–23 January 2016.
27. Chavhan, S.T.; Bhattar, C.; Koli, P.V.; Rathod, V.S. Application of STATCOM for power quality improvement of grid integrated wind mill. In Proceedings of the International Conference on (ISCO) Intelligent Systems and Control, Coimbatore, India, 9–10 January 2015.
28. Wang, L.; Vo, Q.-S.; Prokhorov, A.V. Stability improvement of a multimachine power system connected with a large-scale hybrid windphotovoltaic farm using a supercapacitor. *IEEE Trans. Ind. Appl.* **2018**, *54*, 50–60. [CrossRef]
29. Ashraf, N.; Abbas, G.; Ullah, N.; Al-Ahmadi, A.A.; Raza, A.; Farooq, U.; Jamil, M. Investigation of the Power Quality Concerns of Input Current in SinglePhase Frequency Step-Down Converter. *Appl. Sci.* **2022**, *12*, 3663. [CrossRef]

30. Ravi, T.; Kumar, K.S. Analysis, monitoring, and mitigation of power quality disturbances in a distributed generation system. *Front. Energy Res.* **2022**, *10*, 989474. [CrossRef]
31. Zadehbagheri, M.; Ildarabadi, R.; Nejad, M.B.; Sutikno, T. A new structure of dynamic voltage restorer based on asymmetrical γ-source inverters to compensate voltage disturbances in power distribution networks. *Int. J. Power Electron. Drive Systems* **2017**, *8*, 344–359. [CrossRef]
32. Daneshfar, F.; Bevrani, H. Load– frequency control: A GA-based multiagent reinforcement learning. *IET Gener. Transm. Distrib.* **2010**, *4*, 13–26. [CrossRef]
33. Al-Sharafi, A.; Sahin, A.Z.; Ayar, T.; Yilbas, B.S. Techno-economic analysis and optimization of solar and wind energy systems for power generation and hydrogen production in Saudi Arabia. *Renew. Sustain. Energy Rev.* **2017**, *69*, 33–49. [CrossRef]
34. Zheng, J.; Engelhard, M.H.; Mei, D.; Jiao, S.; Polzin, B.J.; Zhang, J.-G.; Xu, W. Electrolyte additive enabled fast charging and stable cycling lithium metal batteries. *Nat. Energy* **2017**, *2*, 17012. [CrossRef]
35. Hemmati, M.; Mirzaei, M.A.; Abapour, M.; Zare, K.; Mohammadi-ivatloo, B.; Mehrjerdi, H.; Marzband, M. Economic-environmental analysis of combined heat and power-based reconfigurable microgrid integrated with multiple energy storage and demand response program. *Sustain. Cities Soc.* **2021**, *69*, 102790. [CrossRef]
36. Posada, J.O.G.; Rennie, A.J.R.; Villar, S.P.; Martins, V.L.; Marinaccio, J.; Barnes, A.; Glover, C.F.; Worsley, D.A.; Hall, P.J. Aqueous batteries as grid scale energy storage solutions. *Renew. Sustain. Energy Rev.* **2017**, *68*, 1174–1182. [CrossRef]
37. Pena-Alzola, R.; Sebastian, R.; Quesada, J.; Colmenar, A. Review of flywheel based energy storage systems. In Proceedings of the 2011 International Conference on Power Engineering, Energy and Electrical Drives, Malaga, Spain, 11–13 May 2011.
38. Wu, H.; Sun, K.; Li, Y.; Xing, Y. Fixed-Frequency PWM-Controlled Bidirectional Current-Fed Soft-Switching Series-Resonant Converter for Energy Storage Applications. *IEEE Trans. Ind. Electron.* **2017**, *64*, 6190–6201. [CrossRef]
39. Burrus, C.S.; Ramesh; Gopinath, A.; Guo, H. *Introduction to Wavelet and Wavelet Transforms*; Printice Hall: Upper Saddle River, NJ, USA, 1998.
40. Li, Y.; Wang, C.; Li, G.; Wang, J.; Zhao, D.; Chen, C. Improving operational flexibility of integrated energy system with uncertain renewable generations considering thermal inertia of buildings. *Energy Convers. Manag.* **2020**, *207*, 112526. [CrossRef]
41. Guo, Y.; Yang, Z.; Feng, S.; Hu, J. Complex power system status monitoring and evaluation using big data platform and machine learning algorithms: A review and a case study. *Complexity* **2018**, *2018*, 8496187. [CrossRef]
42. Al-Khasawneh, M.A.; Bukhari, A.; Khasawneh, A.M. Effective of Smart Mathematical Model by Machine Learning Classifier on Big Data in Healthcare Fast Response. *Comput. Math. Methods Med.* **2022**, *2022*, 6927170. [CrossRef] [PubMed]
43. Uyar, M.; Yildirim, S.; Gencoglu, M.T. An effective wavelet-based feature extraction method for classification of power quality disturbance signals. *Electr. Power Syst. Res.* **2008**, *78*, 1747–1755. [CrossRef]
44. Rodríguez, A.; Aguado, J.A.; Martín, F.; Lopez, J.J.; Munoz, F.; Ruiz, J.E. Rule-based classification of power quality disturbances using S-transform. *Electr. Power Syst. Res.* **2012**, *86*, 113–121. [CrossRef]
45. Olabi, A.G.; Onumaegbu, C.; Wilberforce, T.; Ramadan, M.; Abdelkareem, M.A.; Al-Alami, A.H. Critical review of energy storage systems. *Energy* **2021**, *214*, 118987. [CrossRef]
46. Wei, P.; Abid, M.; Adun, H.; Awoh, D.K.; Cai, D.; Zaini, J.H.; Bamisile, O. Progress in Energy Storage Technologies and Methods for Renewable Energy Systems Application. *Appl. Sci.* **2023**, *13*, 5626. [CrossRef]
47. Kanakadhurga, D.; Prabaharan, N. Demand side management in microgrid: A critical review of key issues and recent trends. *Renew. Sustain. Energy Rev.* **2022**, *156*, 111915. [CrossRef]
48. Mathiesen, B.V.; Lund, H.; Connolly, D.; Wenzel, H.; Østergaard, P.A.; Möller, B.; Nielsen, S.; Ridjan, I.; Karnøe, P.; Sperling, K.; et al. Smart Energy Systems for coherent 100% renewable energy and transport solutions. *Appl. Energy* **2015**, *145*, 139–154. [CrossRef]
49. Barthelemy, H.; Weber, M.; Barbier, F. Hydrogen storage: Recent improvements and industrial perspectives. *Int. J. Hydrogen Energy* **2017**, *42*, 7254–7262. [CrossRef]

energies

MDPI

Article

Supplementary Control of Conventional Coordinated Control for 1000 MW Ultra-Supercritical Thermal Power Plant Using One-Step Ahead Control

Hyuk Choi [1], Yeongseok Choi [1], Un-Chul Moon [1,*] and Kwang Y. Lee [2,3]

[1] School of Electrical and Electronics Engineering, Chung-Ang University, Seoul 06974, Republic of Korea; chlgur1458@naver.com (H.C.); ys__95@naver.com (Y.C.)
[2] Department of Electrical and Computer Engineering, Baylor University, Waco, TX 76798-7356, USA; kwang_y_lee@baylor.edu
[3] Yonsei Frontier Lab, Yonsei University, Seoul 03722, Republic of Korea
* Correspondence: ucmoon@cau.ac.kr

Abstract: The intermittence of renewable energy sources increases the importance of the effective load-tracking ability of power plants. Coordinated control between boiler and turbine systems is the uppermost layer of a thermal power plant control to follow the load demand. In this paper, a supplementary controller is proposed based on the One-Step Ahead strategy for coordinated control of thermal power plants. After a plant model is developed offline from a step response test, the optimized control of the One-Step Ahead strategy is applied to the boiler feed-forward (BFF) signal to control the electric power output and the main steam pressure simultaneously. Simulation with a 1000 MW ultra-supercritical (USC) once-through type power plant is performed. The results show that the error of Mega-Watt Output (*MWO*) was reduced to 78~95%, and settling time was reduced to 64~79% from conventional coordinated control by adding the proposed supplementary controller.

Keywords: boiler–turbine system; coordinated control; one-step ahead control; power plant control; ultra-supercritical (USC) power plant

Citation: Choi, H.; Choi, Y.; Moon, U.-C.; Lee, K.Y. Supplementary Control of Conventional Coordinated Control for 1000 MW Ultra-Supercritical Thermal Power Plant Using One-Step Ahead Control. *Energies* **2023**, *16*, 6197. https://doi.org/10.3390/en16176197

Academic Editors: Da Xie, Yanchi Zhang, Dongdong Li, Chenghong Gu, Ignacio Hernando-Gil and Nan Zhao

Received: 29 June 2023
Revised: 10 August 2023
Accepted: 15 August 2023
Published: 25 August 2023

1. Introduction

Recently, the energy industry has faced many issues, such as environmental regulation and the need for a transition to energy diversification. As part of a solution, renewable energy sources (RESs) have been participating in power system networks, and their proportion is increasing. Despite the advantages of RESs, their intermittence and variability can cause fluctuation in a power system and thermal power plant output. Typical RESs with intermittence include wind power generation and solar power generation. Both rely on intermittent natural energy sources such as wind and solar and are independent of load demand or grid operator control. This intermittent RESs penetration presents technical challenges in all areas of power systems, including voltage regulation, load-tracking abilities, frequency stability, etc. [1,2]. Therefore, a more advanced control strategy to generate stable energy and regulate the network frequency is needed.

For a stable generation of energy with regulated frequency under a load-changing environment, both boiler and turbine systems should be controlled simultaneously. Therefore, unlike conventional boiler control problems, the controller should include the dynamics of the turbine–generator system to harmonize the slow response of the boiler with the fast response of the turbine–generator to maintain the network frequency in a stable range [3]. That is, for stable network frequency control, the Mega-Watt Output (*MWO*) and the Main Steam Pressure (*MSP*) should be controlled simultaneously under the load-changing situation.

There are two types of conventional control techniques for boiler and turbine systems [4,5]: (1) Boiler Following Type: Electrical power is first controlled by the turbine's

steam pressure, then the boiler is controlled to match the steam pressure demand. This type shows fast power-tracking performance but lacks stability. (2) Turbine Following Type: Electrical power is first controlled by the boiler's fuel flow, then, the turbine is controlled to match the fuel demand. This type shows high stability, but power tracking performance is slow.

Since the boiler and turbine–generator are tightly coupled, an advanced control that controls the boiler and turbine simultaneously may give a better performance than a separated type. This advanced control structure is called the boiler turbine coordinated control (CC). The CC lies in the uppermost control layer of the power plant that controls two control variables, *MWO* and *MSP*, by providing additional control signals. This can match the response of the boiler and turbine during the load-changing environment.

Conventionally, the CC strategy was based on proportional–integral–derivative (PID) multi-loop control [6]. Due to its simple logic and structure, the PID controller is widely used in the industry. However, as the systems become complex, designing the controller with PID is becoming more difficult. Also, using PID control logic for complex nonlinear systems may not provide satisfactory performance. To overcome the limits of the PID controller, several efforts and research to apply an advanced modern control strategy at CC have been made. In [7], intelligent CC based on neural networks for the supercritical boiler has been investigated. More recently, Model Predictive Control (MPC) has been widely used in the modern industry. The MPC is a control theory that predicts the future output for a finite prediction horizon and calculates the optimized control input. In [8], a Generalized Predictive Control (GPC)-based CC is proposed. Dynamic Matrix Control (DMC) is also successfully adopted as a CC [9].

In this paper, we proposed a supplementary controller based on a kind of predictive control called One-Step Ahead control. One-Step Ahead control is a simple discrete control that calculates optimal input for every sampling step. Due to the simple logic, it has been successfully applied in many areas [10–13]. Also, in terms of practicality, the supplementary structure has advantages in application and maintenance. It can be easily implemented in an existing multi-loop control, and in case of an emergency, it can be removed and returned to the conventional control logic. The performance of the supplementary controller is validated by applying it to the ultra-supercritical 1000 MW once-through type power plant system, which is the worldwide mainstream of the electric power industry. The remainder of this paper is as follows: In Section 2, the full scope of the power plant model is introduced. Section 3 describes conventional and proposed boiler combustion control systems. Section 4 presents the development of the discrete prediction model and One-Step Ahead controller. Simulation results are provided in Section 5, and Section 6 presents a discussion. Finally, conclusions are drawn in Section 7.

2. 1000 MW Ultra-Supercritical Once-Through Power Plant

An Ultra-Supercritical (USC) once-through type boiler has been widely used in the global thermal power plant industry for decades [9,14,15]. The USC boiler maintains the steam pressure and temperature above the critical point at a maximum of 30 MPa and 600 °C, respectively. In this extreme condition, water can be directly converted to steam, resulting in the high efficiency of the heat exchange cycle [16]. The advantage of USC boilers is not only high efficiency but also low pollutant emissions.

Figure 1 shows the simplified structure of the conventional 1000 MW USC once-through power plant, the target system of this study [17]. The pulverizers make coal to fine coal dust. Burners attached to the furnace convert the chemical energy in the coal dust into thermal energy. The hot gas produced by combustion travels all over the boiler system. This large thermal energy is absorbed by feedwater in the boiler. This means that heat exchangers such as economizers, water walls, superheaters, and reheaters heat the feed water and convert it into superheated steam. In a turbine system, the thermal energy in the superheated steam turns to mechanical energy. Finally, the mechanical energy is changed to electricity by generators. The USC power plants are a large and complex

system consisting of numerous systems such as a boiler system, turbine–generator system, etc. Controlling the USC power plant is a challenge due to nonlinearity, wide operating range, strong coupling between various control loops, and so on. Among many internal control loops, the uppermost control system is the CC, which controls the boiler system and turbine–generator system simultaneously. In other words, the control variables of CC are *MWO* and *MSP*. The main purpose of CC is to quickly follow the power load demand while maintaining the internal main steam pressure stable, achieving an energy balance between the boiler and turbine [18].

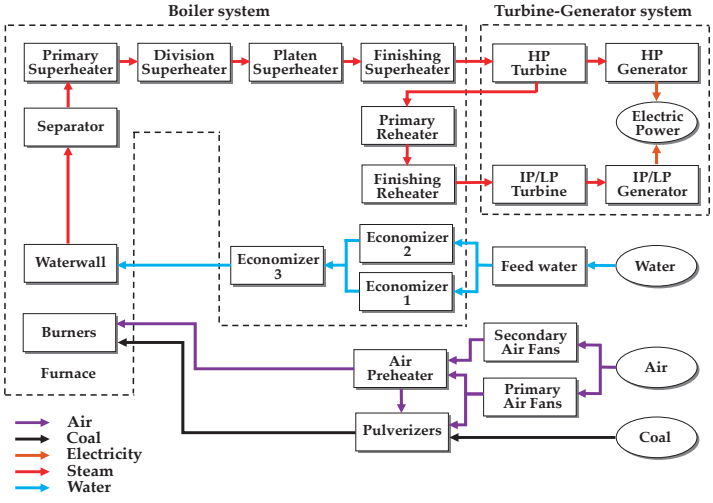

Figure 1. A schematic of a 1000 MW ultra-supercritical once-through type power plant.

3. Conventional and Proposed Boiler Combustion Control System

3.1. Conventional Boiler Combustion System in Coordinated Control

Figure 2 shows the multi-loop control structure of the conventional boiler system in the USC power plant. The red dotted block is the supplementary control proposed in this study, which is added to the existing multi-loop control structure. In the figure, the power load demand is determined by droop control and automatic generation control (AGC) in real time. The Boiler Master Demand (BMD) signal is the master signal for combustion control in the boiler system and is the same unit as the power load demand. In the F_1 block, a suitable BMD signal is generated through the internal PID controller by considering the error between the set points of *MWO* and *MSP* that change according to the power load demand and the current *MWO* and *MSP*. Since the BMD signal is generated not only by *MSP* but also by *MWO*, this structure represents a typical coordinated control.

The F_2–F_5 blocks represent look-up tables or static nonlinear functions for unit conversion. When the BMD signal passes through the F_2 block, it is converted into a boiler feed-forward (BFF) signal with a unit of coal flow, T/H. That is, the output of the F_2 block before the supplementary control is added to the existing multi-loop control is the BFF signal. The BFF signal is compared with the total airflow converted to the same unit of T/H via the F_5 block, and then the lower value becomes coal flow demand. Meanwhile, the F_3 block converts the unit of the BFF signal into an airflow demand. It is also compared with the real coal flow converted into the same unit, and then the airflow demand is determined by a higher value.

The High/Low selector blocks in the figure show the general structure of the "cross-limit algorithm" that prevents fuel-rich conditions in a transient state [19]. When the BFF signal increases due to increased power load demand, the Low-Selector restricts the pass of the BFF signal until Total Air Flow is larger than the BFF signal. On the other hand, since the increased BFF signal is larger than the current Real Coal Flow, the BFF signal

is transferred to the air controller by the High-Selector. This means that Real Coal Flow can increase after the Total Air Flow begins to increase. Conversely, when the power load demand decreases, the decreased BFF signal is passed to the coal controller by the Low-Selector, and the High-Selector limits the pass of the BFF signal until Real Coal Flow starts to decrease. That is, the decrease in Total Air Flow is conducted after the Real Coal Flow starts to decrease. Therefore, this algorithm protects the boiler system by preventing the combustion air shortage and extinguishing boiler firing, whatever the direction changes of power load demand. In conclusion, due to this protection algorithm, there is no problem with the stability of the boiler system, even if the supplementary signal is added to the BFF signal.

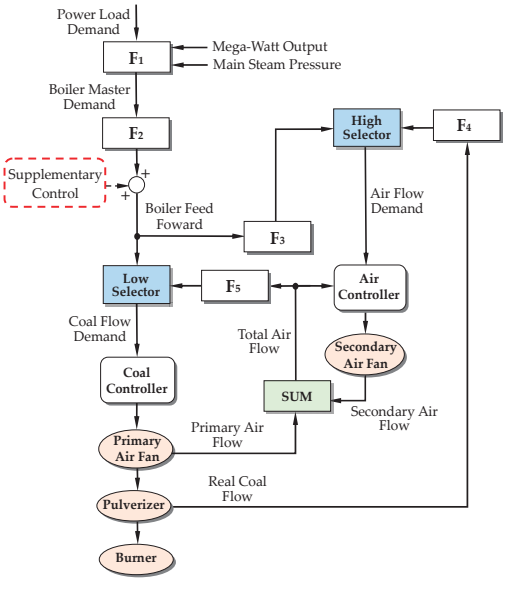

Figure 2. Conventional boiler combustion control system configuration.

3.2. Proposed Supplementary Control Structure

Figure 3 shows the detailed supplementary control structure using the One-Step Ahead controller that is proposed in this study. In Figure 3, the red-dotted block is the same as the red-dotted block in Figure 2. That is, this supplementary controller is added to the existing multi-loop control in the boiler system.

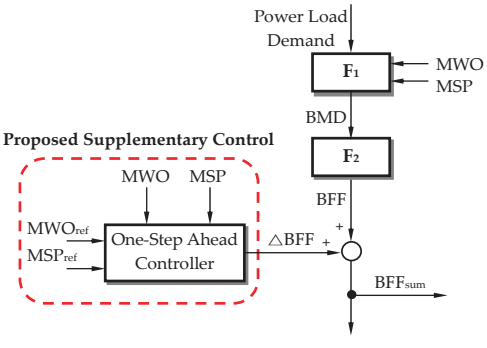

Figure 3. Proposed One-Step Ahead control structure.

In the supplementary controller, the plant output or control variables (CV) are *MWO* and *MSP* because these variables are typical CVs for safe and fast control in thermal power plants. The plant input or manipulated variables (MV) is the ΔBFF signal, which is the supplementary signal for correcting the *BFF* signal of conventional CC. These variables can be expressed as follows:

$$Y = \begin{bmatrix} y_1 & y_2 \end{bmatrix}^T = \begin{bmatrix} y^{MWO} & y^{MSP} \end{bmatrix}^T \tag{1}$$

$$u = \Delta BFF \tag{2}$$

In the figure, the BFF_{sum} signal is newly defined as the sum of two *BFF* signals, which are the output of the F_2 block in the existing boiler system and the ΔBFF signal:

$$BFF_{sum} = BFF + \Delta BFF \tag{3}$$

Therefore, the supplementary control problem of CC is formulated as a Single-Input Multi-Output (SIMO) with two outputs, y^{MWO} and y^{MSP}, and one input in this paper. Two set points of proposed supplementary control are identical to those of conventional CC, which are $y^{MWO,ref}$ and $y^{MSP,ref}$ according to power load demand. This type of supplementary control strategy is simple but efficient and practical. The conventional multi-loop control structure in thermal power plants has been used for a long time in the power plant industry; therefore, plant operators are familiar with this control structure. The proposed supplementary control does not replace existing controllers but adds the supplementary control signal while maintaining the existing multi-loop control system. Therefore, it can be easily implemented and removed without affecting the existing system. In addition, plant operators can quickly return to the existing multi-loop control systems in an emergency.

4. Application to 1000 MW Ultra-Supercritical Once-Through Power Plant

4.1. Obtaining Step Response Data

In this paper, a dynamic boiler simulation model (DBSM) called the Advanced Power and Energy System Simulator (APESS) is used for the simulation. It is an industry-proven simulator [20], and it simulates the realistic behavior of the 1000 MW USC coal-fired once-through type power plant.

The plant model for the proposed One-Step Ahead control is identified using the plant output data of the virtual plant test with DBSM. The step response test is performed at the middle load condition (850 MW), and the size of the step signal is selected as 1.03 (T/H), which is 1% of the operation range of the *BFF* signal.

Figure 4 shows the step responses of two CVs, *MWO* and *MSP*, respectively. In the figure, each response is represented as a normalized variation. When the plant was at a steady state of 850 MW, *BFF* was increased with a step at 0 s. Initially, the step increase of the *BFF* signal increases both coal and airflow. Then, increased mass flow raises the thermal energy of the power plant, resulting in an increase in *MWO* and *MSP*. About 50 s (0.83 min) after the step increase, both outputs started to decrease and settled down to the original value of zero. This is because the existing conventional CC in Figure 2 forces the plant to return to the original steady state corresponding to the load demand. These two-step response data are used for parameter identification to develop discrete prediction models.

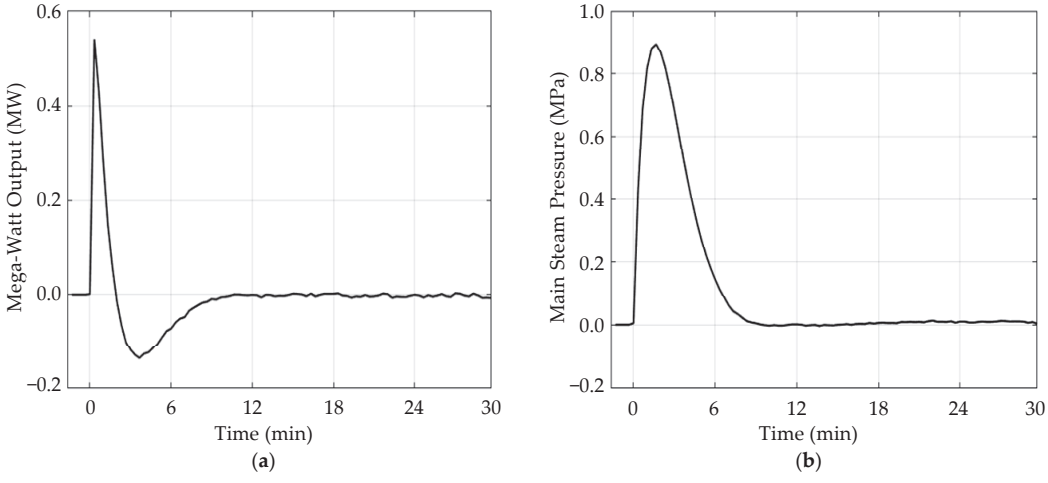

Figure 4. (**a**) Step response data of Mega-Watt Output (*MWO*). (**b**) Step response data of Main Steam Pressure (*MSP*).

4.2. Development of the Discrete Prediction Model

Since the target system is SIMO with two outputs, two output models to describe the dynamics of *MWO* and *MSP* are developed independently. The discrete prediction equation is used as a prediction model of each output as follows [21],

$$\hat{y}_{k+1} = a_1 y_k + a_2 y_{k-1} + \cdots + b_1 u_k + b_2 u_{k-1} + \cdots \tag{4}$$

where the number of output and input history represents the order of the model.

In a discrete prediction equation, a small sampling time gives a more accurate model, but the order of the model also increases, resulting in high complexity and computational cost. Furthermore, a highly accurate model can cause overfitting. On the other hand, a large sampling time gives a simpler model, but its accuracy may become low. Considering the trade-off between model accuracy and complexity, the order of both input and output is chosen as 4, and the sampling time is chosen as 20 s. Thus, the prediction equation for output y^{MWO} or y^{MSP} can be represented as follows [10]:

$$\hat{y}_{k+1} = a_1 y_k + a_2 y_{k-1} + a_3 y_{k-2} + a_4 y_{k-3} + b_1 u_k + b_2 u_{k-1} + b_3 u_{k-2} + b_4 u_{k-3} \tag{5}$$

In this paper, the Least-Squares Method (LSM) is used to identify model parameters [22]. The LSM is a mathematical regression analysis used to determine the best-fit curve for a set of data by minimizing the error between the model output and plant output. For N pairs of step response data, the plant output data can be represented as a form of prediction equations as follows,

$$\begin{cases} \hat{y}_5 = a_1 y_4 + \cdots + a_4 y_1 + b_1 u_4 + \cdots + b_4 u_1 \\ \vdots \\ \hat{y}_{k+4} = a_1 y_{k+3} + \cdots + a_4 y_k + b_1 u_{k+3} + \cdots + b_4 u_k \\ \vdots \\ \hat{y}_N = a_1 y_{N-1} + \cdots + a_4 y_{N-4} + b_1 u_N + \cdots + b_4 u_{N-4} \end{cases} \tag{6}$$

Then, the matrix form of the above equations is represented as

$$\hat{\mathbb{Y}} = \Phi X \tag{7}$$

$$\Phi = \begin{bmatrix} y_4 & \cdots & y_1 & u_4 & \cdots & u_1 \\ y_5 & \cdots & y_2 & u_5 & \cdots & u_2 \\ \vdots & \ddots & \vdots & \vdots & \ddots & \vdots \\ y_{N-2} & \cdots & y_{N-5} & u_{N-2} & \cdots & u_{N-5} \\ y_{N-1} & \cdots & y_{N-4} & u_{N-1} & \cdots & u_{N-4} \end{bmatrix} \tag{8}$$

$$X = \begin{bmatrix} a_1 & a_2 & a_3 & a_4 & b_1 & b_2 & b_3 & b_4 \end{bmatrix}^T \tag{9}$$

$$\hat{\mathbb{Y}} = \begin{bmatrix} \hat{y}_5 & \hat{y}_6 & \ldots & \hat{y}_N \end{bmatrix}^T \tag{10}$$

where $\hat{\mathbb{Y}}$ is a $(N-4) \times 1$ vector representing the predicted output, Φ is a $(N-4) \times 8$ matrix containing input-output data, and X is a 8×1 vector of model parameters to be identified.

Introducing $\varepsilon = \mathbb{Y} - \hat{\mathbb{Y}}$, which is the error between plant output data $\mathbb{Y}$ and predicted data $\hat{\mathbb{Y}}$, the cost function for modeling J^M can be set as follows,

$$J^M(X) = \frac{1}{2}\|\varepsilon\|^2 = \frac{1}{2}\left\|\mathbb{Y} - \hat{\mathbb{Y}}\right\|^2 = \frac{1}{2}\|\mathbb{Y} - \Phi X\|^2 \tag{11}$$

$$= \frac{1}{2}(\mathbb{Y} - \Phi X)^T(\mathbb{Y} - \Phi X) \tag{12}$$

$$= \frac{1}{2}[\mathbb{Y}^T\mathbb{Y} - \mathbb{Y}^T\Phi X - X^T\Phi^T\mathbb{Y} + X^T\Phi^T\Phi X] \tag{13}$$

Then, the solution that minimizes the cost function can be found to make the gradient of J^M to zero.

$$\frac{\partial J^M}{\partial X} = \frac{1}{2}\frac{\partial}{\partial X}[\mathbb{Y}^T\mathbb{Y} - \mathbb{Y}^T\Phi X - X^T\Phi^T\mathbb{Y} + X^T\Phi^T\Phi X] \tag{14}$$

$$= \frac{1}{2}[-(\mathbb{Y}^T\Phi)^T - \Phi^T\mathbb{Y} + \Phi^T\Phi X + (X^T\Phi^T\Phi)^T] \tag{15}$$

$$= \Phi^T\Phi X - \Phi^T\mathbb{Y} = 0 \tag{16}$$

Therefore, the parameter vector X is identified as

$$X = (\Phi^T\Phi)^{-1}\Phi^T\mathbb{Y} \tag{17}$$

This identification process is independently performed for two outputs, y^{MWO} and y^{MSP}, respectively. Table 1 shows the model parameters for two outputs. To evaluate the quality of the model, Figure 5 shows the comparison between the step response data and model output. In the figure, step response data is plotted in a solid black line, and the red dotted line represents the output of the prediction model. It shows that the identified model describes the plant output data successfully. It was reported that this kind of inductive identification model could show better results than a linearized model of the nonlinear physical model [23].

Table 1. Model parameter of SRMs.

Model Parameter	*MWO*	*MSP*
a_1	1.1631	1.1908
a_2	0.2096	−0.0991
a_3	−0.4868	−0.0428
a_4	0.0603	−0.1113
b_1	0.5394	0.4234
b_2	−0.7389	−0.2490
b_3	−0.1363	−0.1308
b_4	0.3356	−0.0434

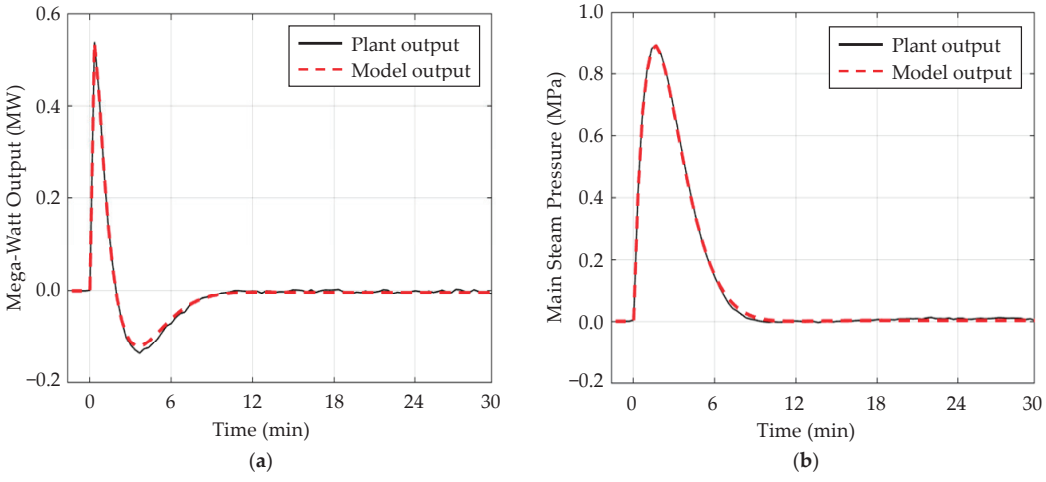

Figure 5. (**a**) Comparison between step response data and model output of *MWO*. (**b**) Comparison between step response data and model output of *MSP*.

4.3. One-Step Ahead Controller Design

One-Step Ahead control is a discrete control that calculates optimal input for every sampling step. In this paper, the control performance of the proposed One-Step Ahead control considers both two output variables y^{MWO} and y^{MSP} simultaneously. Let Y_{k+1} be the integrated prediction equation vector for two outputs which is

$$Y_{k+1} = \begin{bmatrix} y_{k+1}^{MWO} \\ y_{k+1}^{MSP} \end{bmatrix} = \begin{bmatrix} a_1^{MWO} y_k^{MWO} + \cdots + a_4^{MWO} y_{k-3}^{MWO} + b_1^{MWO} u_k + \cdots + b_4^{MWO} u_{k-3} \\ a_1^{MSP} y_k^{MSP} + \cdots + a_4^{MSP} y_{k-3}^{MSP} + b_1^{MSP} u_k + \cdots + b_4^{MSP} u_{k-3} \end{bmatrix} \tag{18}$$

$$= A_1 Y_k + A_2 Y_{k-1} + A_3 Y_{k-2} + A_4 Y_{k-3} + B_1 u_k + B_2 u_{k-1} + B_3 u_{k-2} + B_4 u_{k-3} \tag{19}$$

$$= \sum_{j=1}^{4} \left(A_j Y_{k-(j-1)} + B_j u_{k-(j-1)} \right) \tag{20}$$

where Y_{k+1} is a 2×1 vector representing the predicted future output at the $(k+1)$-th step, $Y_{k-(j-1)}$ is the 2×1 j-th output history vector, and $u_{k-(j-1)}$ is the j-th input history at the k-th step, and

$$A_j = \begin{bmatrix} a_j^{MWO} & 0 \\ 0 & a_j^{MSP} \end{bmatrix} \tag{21}$$

is the 2×2 constant matrix with output parameters,

$$B_j = \begin{bmatrix} b_j^{MWO} \\ b_j^{MSP} \end{bmatrix} \tag{22}$$

is the 2×1 constant vector with input history.

In One-Step Ahead control, optimal control input that minimizes J_{k+1}^C, the control performance at the $(k+1)$-th step is calculated every sampling step. The control performance is set as

$$J_{k+1}^C = (Y_{k+1} - Y_{ref})^T Q (Y_{k+1} - Y_{ref}) + R \Delta u_k^2 \tag{23}$$

where Y_{ref} is a 2×1 vector of the reference value, Q is a 2×2 matrix representing the weight of output error, and R is the weight of input adjustment Δu_k is as follows,

$$\Delta u_k = u_k - u_{k-1} \tag{24}$$

With the control performance, optimized input can be calculated by setting the gradient of J_{k+1}^C with respect to u_k to zero as follows:

$$\frac{\partial J_{k+1}^C}{\partial u_k} = \frac{\partial}{\partial u_k}[(Y_{k+1} - Y_{ref})^T Q(Y_{k+1} - Y_{ref}) + R\Delta u_k^2] \tag{25}$$

Substituting Y_{k+1} with (20) and Δu_k with (24) gives

$$\begin{aligned} \frac{\partial J_{k+1}^C}{\partial u_k} &= \frac{\partial}{\partial u_k}[(\sum_{j=1}^{4}(A_j Y_{k-(j-1)} + B_j u_{k-(j-1)}) - Y_{ref})^T Q(\sum_{j=1}^{4}(A_j Y_{k-(j-1)} + B_j u_{k-(j-1)}) \\ &\quad - Y_{ref}) + R(u_k - u_{k-1})^2] \end{aligned} \tag{26}$$

$$\begin{aligned} &= 2(B_1^T Q B_1 + R)u_k + 2u_k(B_1^T Q A_1 Y_k + B_1^T Q A_2 Y_{k-1} + B_1^T Q A_3 Y_{k-2} + B_1^T Q A_4 Y_{k-3} \\ &\quad + B_1^T Q B_2 u_{k-1} + B_1^T Q B_3 u_{k-2} + B_1^T Q B_4 u_{k-3} - B_1^T Q Y_{ref} - R u_{k-1}) \end{aligned} \tag{27}$$

$$= 0 \tag{28}$$

Arranging (27) and (28) with u_k gives

$$\begin{aligned} u_k = &-(B_1^T Q B_1 + R)^{-1}(B_1^T Q A_1 Y_k + B_1^T Q A_2 Y_{k-1} + B_1^T Q A_3 Y_{k-2} + B_1^T Q A_4 Y_{k-3} \\ &+ B_1^T Q B_2 u_{k-1} + B_1^T Q B_3 u_{k-2} + B_1^T Q B_4 u_{k-3} - B_1^T Q Y_{ref} - R u_{k-1}) \end{aligned} \tag{29}$$

This control law is applied at every sampling step with updated output and input history. Thus, the proposed supplementary BFF signal is applied to the conventional CC at every sampling step.

Figure 6 shows the overall algorithm of the proposed supplementary control in the form of a flow chart. In the figure, the identification process is done offline, while the One-Step Ahead control law is applied in real-time.

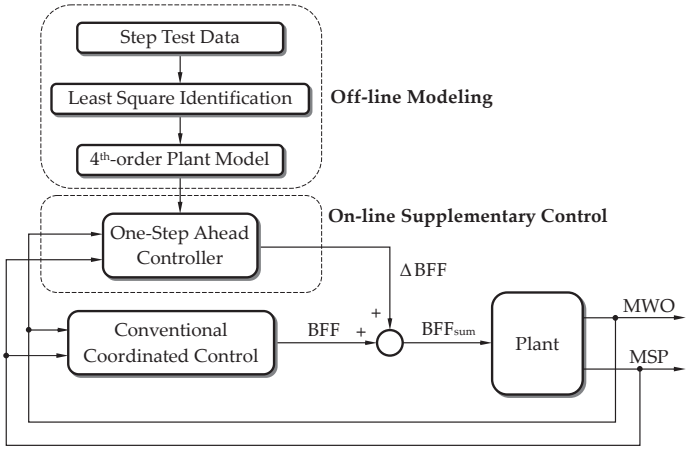

Figure 6. Flow chart of proposed supplementary One-Step Ahead Control.

5. Simulation Results

The performance evaluation of the proposed One-Step Ahead supplementary controller is developed in MATLAB for the DBSM in a personal computer environment. The DBSM has an interface program called DBSM Editor, which can transmit and receive real-time data with MATLAB. Therefore, the supplementary control of the proposed control in MATLAB is sent to the DBSM in real time.

The simulation scenario considers two large-step changes in the power load demand. Figure 7 shows this simulation scenario for a 1000 MW USC power plant. The power load demand is first increased to 950 MW at 0 s from a steady state of 750 MW, and it is decreased to 700 MW from 950 MW at 13,500 s (225 min). To avoid abrupt changes in power load demand, the internal logic of DBSM limits the ramp rate of the power load demand to 60 MW/min, which is 6% of the total load per minute that is basically used in coal power plants [24].

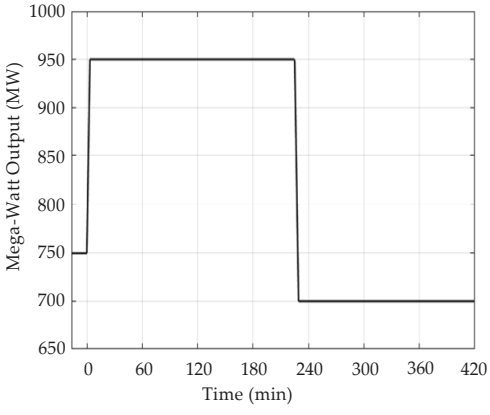

Figure 7. Power load demand scenario of 1000 MW USC power plant.

Table 2 shows set points or steady-state values of two CVs used in the simulation for performance validation. The set points of *MSP* corresponding to each *MWO* are generated automatically by the internal logic of DBSM.

Table 2. Steady-state values of CVs.

MWO **(MW)**	***MSP*** **(MPa)**
750	22.409
950	26.084
700	20.9135

The weight parameters for the One-Step Ahead controller in (23) are as follows:

$$Q = \begin{bmatrix} 6 & 0 \\ 0 & 19 \end{bmatrix}, \; R = 7000. \tag{30}$$

In the cost function (23), a large element in the weight Q makes the output error corresponding to each output more important in performance, while it tends to increase input variation. On the contrary, a large weight R reduces the input variation but increases the output errors. Due to this trade-off, weight parameters are obtained to suitable values by trial and error.

Figure 8 shows the simulation results of *MWO* for two cases, the conventional CC without supplementary control and the conventional CC with the addition of proposed supplementary control. In the figure, the black dotted line indicates set points, the blue

solid line represents the response of the existing conventional CC, and the red solid line represents the response of the CC with proposed supplementary control. Figure 8b,c show the step-up and step-down responses, respectively. In the figure, the *MWO* with proposed supplementary control shows a shorter rising time and settling time in both load changes.

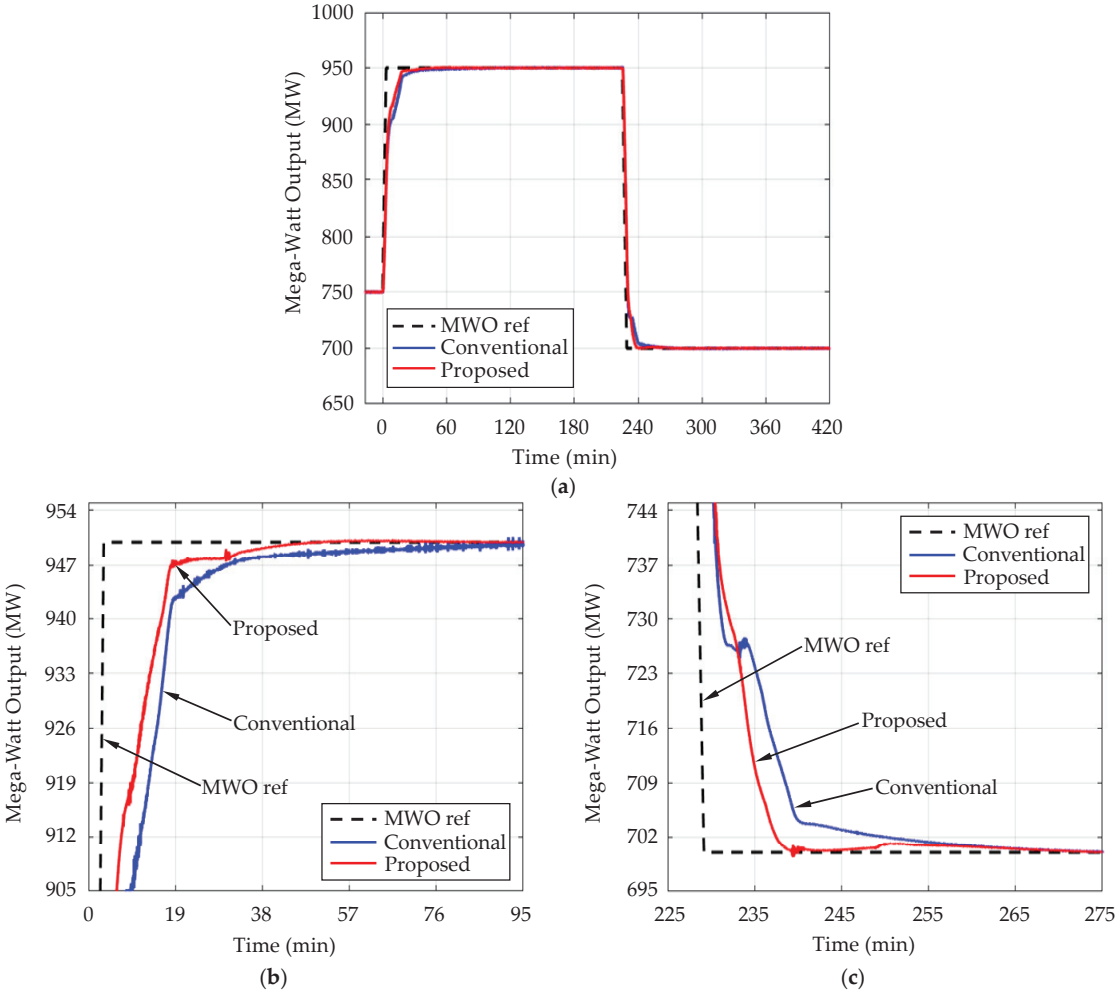

Figure 8. (**a**) Comparison of the *MWO* with the conventional CC and the CC with proposed supplementary control. (**b**) Zoom of the step-up response. (**c**) Zoom of the step-down response.

Figure 9 shows the simulation results of *MSP* for two cases, the conventional CC and the CC with proposed supplementary control. Figure 9b,c show in detail the comparison of step-up and step-down responses, respectively. In the figure, the settling time of *MSP* is greatly reduced by adding the proposed supplementary control.

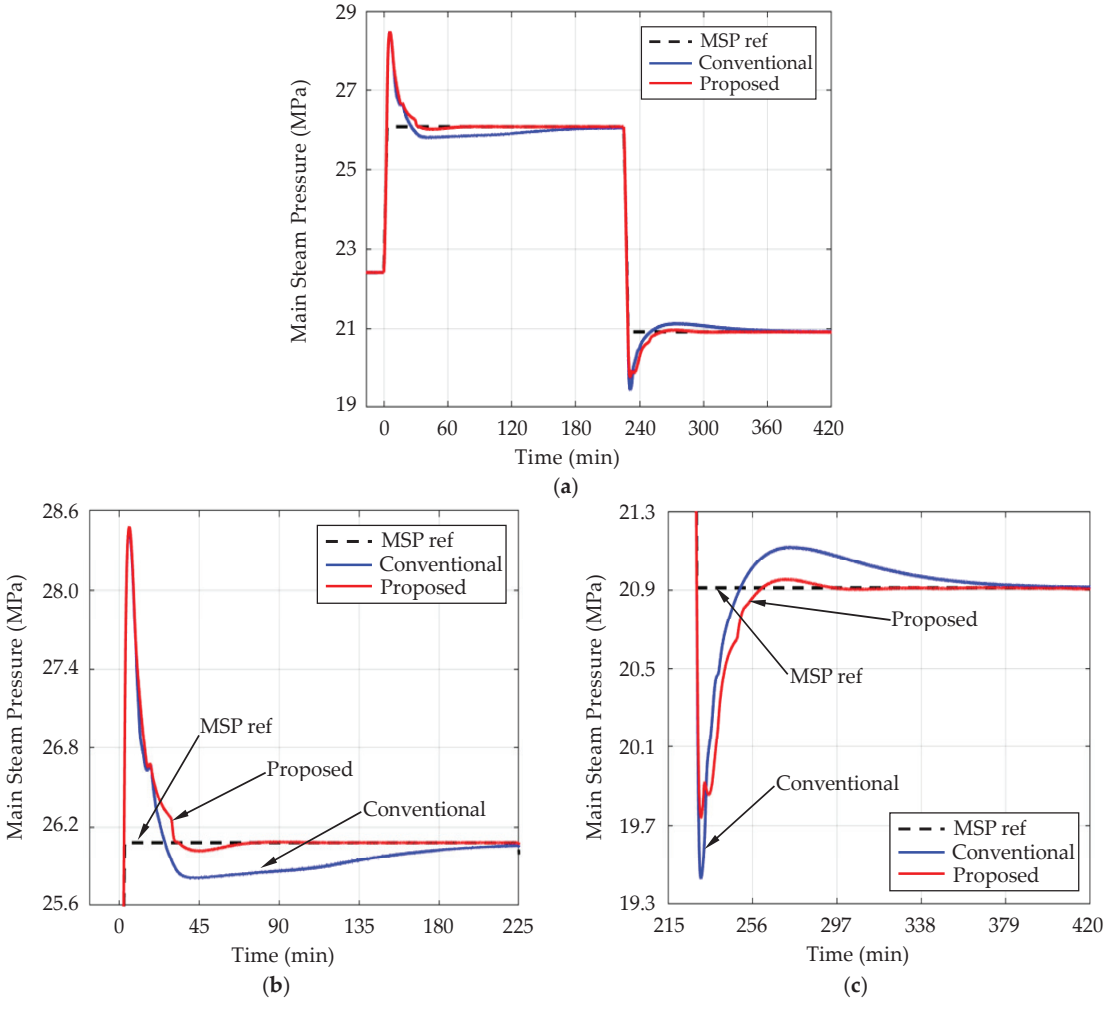

Figure 9. (**a**) Comparison of the *MSP* with the conventional CC and the CC with proposed supplementary control. (**b**) Zoom of the step-up response. (**c**) Zoom of the step-down response.

The quantitative comparison between the conventional CC with and without the proposed supplementary control is calculated. The percentage of the sum of squared errors is calculated as follows,

$$\text{Percentage of sum of squared error} = \frac{\int_{t_s}^{t_e} (y - y_{ref})^2 dt}{\int_{t_s}^{t_e} (y_{cc} - y_{ref})^2 dt} \times 100 \tag{31}$$

where t_s is the start time of load change, t_e is the end time of the transient state, y_{ref} is the set point of output, y_{cc} is the response of conventional CC without supplementary control, and y is the response of CC with the proposed supplementary control. In the first step, t_s is 0 s, and t_e is 13,499 s (224.98 min), and in the second step, t_s is 13,500 s (225 min), and t_e is 25,200 s (420 min). The settling time is also compared to which output reaches within 2% of the final value. The percent ratio, which is the settling time of conventional CC with proposed supplementary control over the settling time of conventional CC, is calculated.

The percentages of error and settling time for *MWO* and *MSP* are listed, respectively, in Tables 3 and 4. In Table 3, the error of *MWO* was reduced to 78~95%, and the settling time was reduced to 64~79% from those of conventional coordinated control by adding the proposed supplementary controller. In Table 4, the settling time of *MSP* was significantly reduced to 18~29% by the supplementary control.

Table 3. Percentages of proposed CC/conventional CC performance for *MWO*.

Performance	First Step Change	Second Step Change
Sum of squared error	78.23%	94.89%
Settling time	64.09%	79.15%

Table 4. Percentages of proposed CC/conventional CC performance for *MSP*.

Performance	First Step Change	Second Step Change
Sum of squared error	93.37%	94.66%
Settling time	17.59%	29.39%

Figure 10 shows the variation of the ΔBFF signal in the simulations. When the power load demand increases from 750 MW to 950 MW in the first step, the ΔBFF supplementary controller increases positively, while ΔBFF is negative in the second step. This additional correction of conventional CC resulted in performance correction for both *MWO* and *MSP*.

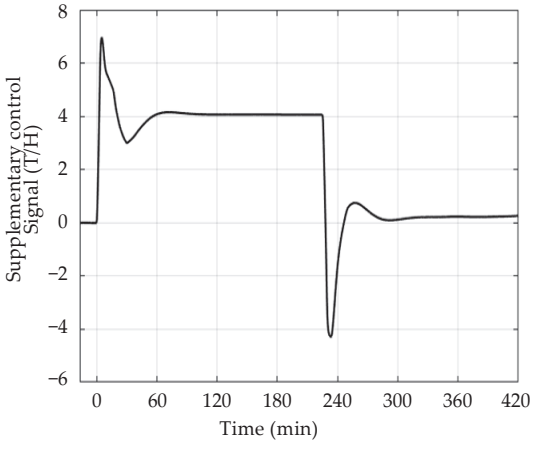

Figure 10. Variation of the supplementary BFF signal of the proposed controller.

6. Discussion

The proposed supplementary control strategy is very simple but has shown effective performance improvements over conventional control. It has the advantage of being able to be simply implemented in the Distributed Control System (DCS) of the actual thermal power plant because it has a relatively small amount of computations compared to other advanced control strategies. In the process of calculating the optimal control input, proper tuning may be required because the performance improvement may vary somewhat due to the weight parameters of the cost function, Q and R.

Although the controller's input and output structure is different, a similar approach using Dynamic Matrix Control (DMC) has been preceded [9]. However, this control strategy requires a large amount of computation, which can be burdensome to apply in practice. That is, it may be difficult to implement in the DCS of the existing thermal power plant,

and an additional computer server may be required. Therefore, in terms of cost, the control strategy proposed in this paper is considered a relatively more practical strategy.

7. Conclusions

In this paper, to update the performance of the coordinated control (CC) of the USC thermal power plant, a supplementary control using One-Step Ahead control was proposed. The controlled variables are selected with the Mega-Watt Output (*MWO*) and the main steam pressure (*MSP*), and the manipulated variable of the supplementary controller is selected with an additional signal of the boiler feed-forward signal. The model of the supplementary controller is identified by the plant output data obtained through the offline step response test. Based on the identified model, online optimization is performed in the One-Step Ahead control algorithm. The simulation results with the 1000 MW USC power plant show that the squared error and settling time of *MWO* and *MSP* are reduced in load demand changes by adding the proposed supplementary controller. Therefore, more fast load-tracking abilities can be expected.

The proposed supplementary control structure is very practical and can be applied immediately to the currently operating thermal power plants because it adds supplementary controllers to the existing control structure. In emergency situations, because it can be easily removed, power plant operators return to familiar conventional control. In addition, the One-Step Ahead algorithm used in the supplementary controller does not require much computation compared to several previously proposed advanced controls, which need additional computer servers for complex computing. Therefore, it can be implemented directly in existing DCS of thermal power plants, which has a large cost advantage in implementation.

Nowadays, intermittent Renewable Energy Sources (RESs) penetration presents technical challenges in all areas of power systems. Proposed supplementary One-Step Ahead control to conventional coordinated control can be one of the effective strategies to prepare for the unexpected load-changing environment of power systems.

Author Contributions: U.-C.M. and H.C. designed the basic idea and the principles of the overall work. H.C. and Y.C. realized simulations. U.-C.M. prepared the initial draft of the paper, and K.Y.L. proposed some technical comments and edited the final draft of the paper. All authors have read and agreed to the published version of the manuscript.

Funding: This research was supported by the Chung-Ang University Graduate Research Scholarship in 2022 and the Korea Electric Power Corporation (Grant number: R20XO02-27).

Data Availability Statement: The data presented in this study are available on request from first author (Hyuk Choi). The data are not publicly available due to future works.

Conflicts of Interest: The authors declare no conflict of interest.

References

1. Mlilo, N.; Brown, J.; Ahfock, T. Impact of intermittent renewable energy generation penetration on the power system networks—A review. *Technol. Econ. Smart G.* **2021**, *6*, 25. [CrossRef]
2. Mokeke, S.; Thamae, L.Z. The impact of intermittent renewable energy generators on Lesotho national electricity grid. *Electr. Pow. Syst. Res.* **2021**, *196*, 107196. [CrossRef]
3. Flynn, D.; Institution of Electrical Engineers. *Thermal Power Plant Simulation and Control*; Institution of Electrical Engineers: London, UK, 2003.
4. Tan, W.; Liu, J.; Fang, F.; Chen, Y. Tuning of PID controllers for boiler-turbine units. *ISA Trans.* **2004**, *43*, 571–583. [CrossRef] [PubMed]
5. Arastou, A.; Rabieyan, H.; Karrari, M. Inclusive modelling and parameter estimation of a steam power plant using an LMI-based unknown input reconstruction algorithm. *IET Gener. Transm. Distrib.* **2022**, *16*, 1425–1437. [CrossRef]
6. Sayed, M.; Gharghory, S.M.; Kamal, H.A. Gain tuning PI controllers for boiler turbine unit using a new hybrid jump PSO. *J. Electr. Syst. Inf. Technol.* **2015**, *2*, 99–110. [CrossRef]
7. Ma, L.; Lee, K.Y.; Wang, Z. Intelligent coordinated controller design for a 600 MW supercritical boiler unit based on expanded-structure neural network inverse models. *Control Eng. Pract.* **2016**, *53*, 194–201. [CrossRef]

8. Gao, Y.; Zeng, D.; Ping, B.; Zhang, L.; Liu, J. Research on coordinated control system of drum boiler units considering energy demand decoupling. *Control Eng. Pract.* **2020**, *102*, 104562. [CrossRef]
9. Lee, Y.; Yoo, E.; Lee, T.; Moon, U.C. Supplementary Control of Conventional Coordinated Control for 1000 MW Ultra-supercritical Thermal Power Plant using Dynamic Matrix Control. *J. Electr. Eng. Technol.* **2018**, *13*, 97–104.
10. Fadali, M.S.; Visioli, A. *Digital Control Engineering: Analysis and Design*, 2nd ed.; Academic Press: Waltham, MA, USA, 2013.
11. Xi, C.; Liuping, W. Discrete-time one-step ahead prediction control (DOPC) of a Quadcopter UAV with constraints. In Proceedings of the 2016 Australian Control Conference (AuCC), Newcastle, Australia, 3–4 November 2016.
12. Xiao, Z.; Meng, S.; Lu, N.; Malik, O.P. One-Step-Ahead Predictive Control for Hydroturbine Governor. *Math. Probl. Eng.* **2015**, *2015*, 382954. [CrossRef]
13. Dadone, A.; Dambrosio, L.; Fortunato, B. One step ahead adaptive control technique for wind systems. *Energy Conv. Manag.* **1998**, *39*, 399–413. [CrossRef]
14. Somova, E.V.; Tugov, A.N.; Tumanovskii, A.G. Modern Coal-Fired Power Units for Ultra-Supercritical Steam Conditions (Review). *Therm. Eng.* **2023**, *70*, 81–96. [CrossRef]
15. Cheng, C.; Peng, C.; Zeng, D.; Gang, Y.; Mi, H. An Improved Neuro-fuzzy Generalized Predictive Control of Ultra-supercritical Power Plant. *Cogn. Comput.* **2021**, *13*, 1556–1563. [CrossRef]
16. Rocha, D.H.D.; Silva, R.J. Exergoenvironmental analysis of a ultra-supercritical coal-fired power plant. *J. Clean. Prod.* **2019**, *231*, 671–682. [CrossRef]
17. Liu, X.J.; Kong, X.B.; Hou, G.L.; Wang, J.H. Modeling of a 1000 MW power plant ultra super-critical boiler system using fuzzy-neural network methods. *Energy Convers. Manag.* **2013**, *65*, 518–527. [CrossRef]
18. Zhu, H.; Tan, P.; He, Z.; Zhang, C.; Fang, Q.; Chen, G. Nonlinear model predictive control of USC boiler-turbine power units in flexible operations via input convex neural network. *Energy* **2022**, *255*, 124486. [CrossRef]
19. Dukelow, S.G.; Instrument Society of America. *The Control of Boilers*; Instrument Society of America: Research Triangle Park, NC, USA, 1986.
20. Lee, K.; Jeong, K.; Jeon, W.; Bae, Y.; Lee, D. Development of APESS software for power plant simulation. In Proceedings of the ASME 2010 Pressure Vessels and Piping Conference, Washington, DC, USA, 18–22 July 2010.
21. Zambrano, J.; Sanchis, J.; Herrero, J.M.; Martínez, M. WH-MOEA: A Multi-Objective Evolutionary Algorithm for Wiener-Hammerstein System Identification. A Novel Approach for Trade-Off Analysis Between Complexity and Accuracy. *IEEE Access* **2020**, *8*, 228655–228674. [CrossRef]
22. Aström, K.J.; Wittenmark, B.R. *Computer-Controlled Systems: Theory and Design*, 3rd ed.; Dover Publications: Mineola, NY, USA, 2011.
23. Moon, U.C.; Lee, K.Y. Step-Response Model Development for Dynamic Matrix Control of a Drum-Type Boiler–Turbine System. *IEEE Trans. Energy Convers.* **2009**, *24*, 423–430. [CrossRef]
24. Gonzalez-Salazar, M.A.; Kirsten, T.; Prchlik, L. Review of the operational flexibility and emissions of gas- and coal-fired power plants in a future with growing renewables. *Renew. Sust. Energ. Rev.* **2018**, *82*, 1497–1513. [CrossRef]

electricity

MDPI

Article

Effect of a Large Proton Exchange Membrane Electrolyser on Power System Small-Signal Angular Stability

Guy Wanlongo Ndiwulu *, Eduardo Vasquez Mayen * and Emmanuel De Jaeger

Mechatronic, Electrical Energy, and Dynamic Systems, UCLouvain, 1348 Louvain-la-Neuve, Belgium; emmanuel.dejaeger@uclouvain.be

* Correspondence: guy.wanlongo@uclouvain.be (G.W.N.); eduardo.vasquez@uclouvain.be (E.V.M.)

Abstract: The dynamics of electrical systems have changed significantly with the increasing penetration of non-conventional loads such as hydrogen electrolysers. As a result, detailed investigations are required to quantify and characterize these loads' effects on the dynamic response of interconnected synchronous machines after being subjected to a disturbance. Many studies have focused on the effects of conventional static and dynamic loads. However, the impact of hydrogen electrolysers on the stability of power systems' rotor angles is rarely studied. This paper assesses the effect of proton exchange membrane (PEM) electrolysers on small-disturbance rotor-angle stability. Dynamic modelling and the control of a PEM electrolyser as a load are first studied to achieve this. Then, the proposed electrolyser model is tested in the Amercoeur plant, which is part of the Belgian power system, to study its effect on the small-signal rotor-angle stability. Two approaches are considered to examine this impact: an analytical approach and time-domain simulations. The analytical approach consists of establishing a state-space model of the Belgian test system through linearisation around an operating point of the non-linear differential and the algebraic equations of the synchronous generators, the PEM electrolyser, the loads, and the network. The obtained state-space model allows for the determination of the eigenvalues, which are useful to evaluate the effect of the PEM electrolyser on the small-signal rotor-angle stability. This impact is investigated by examining the movement of the eigenvalues in the left complex half-plane. The obtained results show that the PEM electrolyser affects the electromechanical modes of synchronous machines by increasing their oscillation frequencies. The results also show that the effect of the electrolyser on these modes can be improved by adjusting the inertial constant and the damping coefficient of the synchronous machines. These results are consolidated through time-domain simulations using the software Matlab/Simscape from the version MatlabR2022a-academic use from Mathworks.

Keywords: PEM electrolyser; small-signal modelling; thyristor rectifier; rotor-angle stability

Citation: Wanlongo Ndiwulu, G.; Vasquez Mayen, E.; De Jaeger, E. Effect of a Large Proton Exchange Membrane Electrolyser on Power System Small-Signal Angular Stability. *Electricity* **2023**, *4*, 381–409. https://doi.org/10.3390/electricity4040021

Academic Editors: Da Xie, Yanchi Zhang, Dongdong Li, Chenghong Gu, Ignacio Hernando-Gil and Nan Zhao

Received: 5 October 2023
Revised: 3 November 2023
Accepted: 13 November 2023
Published: 1 December 2023

1. Introduction

Nowadays, hydrogen demand and production in a multitude of sectors are constantly increasing. As a result, the number of hydrogen electrolysers connected to transmission power systems is increasing. Hydrogen electrolysers are electrochemical devices used to separate water molecules into hydrogen and oxygen by passing a DC current through them [1]. This DC current is proportional to the hydrogen production. There are different hydrogen electrolyser technologies, which range from small systems (kilowatts) to large-scale systems (multiple megawatts) [1]. The most well-known technologies in industrial projects under development are alkaline electrolysers and proton exchange membrane (PEM) electrolysers [2]. Alkaline electrolyser technology, which is widely used today, is considered a mature technology in the industrial sector. Due to their advantages over alkaline electrolysers, such as high power density and cell efficiency, as well as fast dynamics, PEM electrolysers are in a period of great expansion and development for integration into power systems, including renewable energy production systems [1–5]. For this reason,

PEM electrolyser technology is dealt with within this paper. Hydrogen electrolysers can be viewed as flexible loads that can facilitate the large-scale integration of intermittent renewable sources into future power systems and provide power grid services [6,7]. As loads, hydrogen electrolysers can have an impact on the dynamics and stability of power systems. The use of power electronic converters as an interface for their integration into the grid can also affect the power quality and dynamics of power systems [8,9]. In addition, the dynamic response of the required electrolyser current to produce hydrogen can influence the dynamics of power systems. Detailed investigations of the impact of hydrogen electrolysers are required to characterize the dynamic response of the rotor-angle stability, frequency stability, and voltage stability. However, the majority of studies have focused mainly on frequency stability [3,5,6,10] and technoeconomical aspects [10]. Few articles have dealt with the effect of hydrogen electrolysers on voltage stability [10], and the impact of electrolysers on rotor-angle stability has rarely been studied.

This paper focuses on the impact of a large-scale PEM electrolyser on a power system's small-signal rotor-angle stability. The small-disturbance rotor-angle stability can be defined as the capacity of a set of interconnected synchronous machines to maintain synchronism after being subjected to a small disturbance [11]. The dynamic responses of the set of interconnected synchronous machines are quantified and characterized to assess the influence of the PEM electrolyser on the power system dynamics. To this end, a large-scale PEM electrolyser project within the Belgian power system around Amercoeur is considered as a test system. Before investigating the effect of a hydrogen PEM electrolyser on the small-signal rotor-angle stability, we first identify the nature of PEM electrolysers when they are considered as loads within the power system, that is, whether a hydrogen PEM electrolyser can be regarded as a constant impedance load, a constant current load, or a constant power load. To achieve this, it is necessary to first model a hydrogen PEM electrolyser, then model the power electronic converter, and, finally, to develop a control structure for the power electronic converter to adjust the electrolyser current.

Concerning the dynamic modelling of PEM electrolysers, various electrochemical models are proposed in the literature [2,12–14]. The authors of reference [2] developed a dynamic electrical model of a PEM electrolyser, taking into account the dynamic behaviour of the PEM electrolyser during sudden variations in the input current. An equivalent electrical model of the PEM electrolyser with adaptive parameters for both static and dynamic operating conditions was proposed in [12]. The study reported in [12] focused on modelling cell voltage as a function of static and dynamic operations. In [14], an analytical–dynamic analysis model for a PEM electrolyser deduced from physical laws and electrochemical equations was proposed. The dynamic modelling of PEM electrolysers, as described in the literature, can be categorized into four groups based on various physical aspects, such as the required voltage (reversible voltage) for the electrolysis [15,16], activation overpotential, ohmic resistance, and the diffusion aspects at both the anode and the cathode. The activation overpotential represents the electrochemical kinetic behaviour [17]. It is therefore a representation of the speed of the reactions taking place on the electrode surface [17]. In contrast, ohmic overpotential is caused by the ohmic resistance of the electronic materials, such as current collectors, bipolar plates, and electrode surfaces [17]. It includes electron and proton conduction through the PEM. The electrochemical model of the PEM electrolyser investigated in [2,4,12,14,17] is referred to as the first model (*Model* 1) in this paper. *Model* 1 is composed of the activation overpotential at the anode and cathode, membrane overpotential, and reversible potential. The activation overpotential at both the anode and cathode is modelled by two capacitor-resistance branches. Furthermore, the membrane overpotential is modelled by the ohmic overpotential. *Model* 1 is one of the most studied models in dynamic modelling analysis of electrolysers. Nevertheless, its dynamic behaviour is often not studied. The second model (*Model* 2) considered in this paper includes a Warburg impedance at both the anode and the cathode, as proposed in [10]. The Warburg impedance is related to the concentration losses in the PEM electrolyser and is more important at low frequency and high current density [18,19]. However,

dynamic modelling of the electrochemical model related to *Model* 2 is not proposed in the literature. Other authors have neglected the activation overpotential at the cathode, as in [3,4,8,10]. This is because the contribution of this overpotential is considered small compared to the contributions of the activation overpotential at the anode, the ohmic overpotential, and the reversible voltage. As a result, the electrochemical model without the activation overpotential of the cathode can be classified as either a model with a Warburg impedance (*Model* 3) or a model without a Warburg impedance (*Model* 4). The electrochemical model with Warburg impedance is often modelled by a Rangdles–Warburg cell, as depicted in [10,20]. *Model* 3 includes a frequency-dependent Warburg element, which is parallel to a conventional capacitor, and a conventional resistor, which is in series with the Warburg element. The Warburg model brings the frequency-dependent characterizations of the resistor and capacitor, which modify the dynamic response of the cell voltage. *Model* 4, which does not consider the Warburg impedance, is described in [3,4,8]. As with the first two electrochemical models presented previously, the dynamic behaviour of the last two electrochemical models is also not examined in the literature. The dynamic responses of four models proposed in the literature are studied in this article in order to choose which one can be used in load modelling and small signal modelling. This choice is dictated by the time constant that characterizes the dynamic response of each model. For the model of the hydrogen PEM electrolyser, the temperature and pressure are considered to be constant, and the degradation of the catalyst and the membrane is not taken into account.

A 12-pulse thyristor rectifier is often used as interface to integrate hydrogen electrolysers into the grid. Because this technology is one of the most mature and important solutions in high-power rectification applications [8], a current control structure is proposed to adjust the appropriate firing angle to achieve the desired electrolyser current. The proposed current control structure is established based on a dynamic model of the average model of the thyristor rectifier and of the proposed hydrogen PEM electrolyser model.

Finally, the effect of the PEM electrolyser model on the small-signal rotor-angle stability is studied using a state-space model and time-domain simulations of the test transmission system. The proposed state-space model is based on linearisation around an operating point of the non-linear differential and algebraic equations of the synchronous generators, the distribution network, the conventional loads, and the PEM electrolyser. In this approach, the synchronous generators and the network are modelled in the $dq-$synchronous reference frame. Then, all the components within the transmission network are translated into the common synchronous reference frame, rotating at a common frequency, as described in [21]. As well as consolidating the analytical results, time-domain simulations are also employed in this paper to study the impact of the proposed modelling of the electrolyser as a load. The contributions of this study can be summarized as follows:

- A dynamic model and a state-space model of a system formed by a PEM electrolyser and a 12-pulse thyristor rectifier is proposed.
- A control structure for the electrolyser current from the dynamic model of the PEM electrolyser and for the average model of the 12-pulse thyristor rectifier is proposed.
- A model of the PEM electrolyser as a load is proposed to identify whether it can be considered a constant impedance load, a constant current load, or a constant power load.
- We study the effects of the PEM electrolyser on the stability of the small-signal rotor-angle using analytical and time-domain simulation approaches.

The remainder of this paper is organized as follows: Section 2 presents the details of the proposed dynamic model for the PEM electrolyser, the thyristor rectifier, the proposed control structure of electrolyser current, and the modelling of the electrolyser as a load. Section 3 presents the details of the proposed small-signal model of the Belgian test system, while the stability analysis results are presented in Section 4. Finally, Section 5 concludes the paper.

2. Power System Architecture and Integration of Hydrogen PEM Electrolyser

Figure 1 describes the used test system, in which 100 MW of PEM electrolysers are connected to the 150 kV busbar. It is the topology corresponding to the Belgian power system around the Amercoeur power plant. It consists of three synchronous generators (*SGs*) connected to the transmission grid through main *Busbar* 4, 6, and 11. The *SGs* are round rotor machines with static exciters. The three *SGs* are coupled with the thermal power plants. The dynamic of the primary source coupled with the *SG* is not studied in this article. It is assumed that the three *SGs* operate with constant power generated by the primary source. They are modelled as nodes with fixed active power (*P*) and reactive power (*Q*) (*PQ node*). The 270 MW synchronous generator (*SG* 1) is connected to *Busbar* 4, to which the PEM electrolyser is connected. The 150 MW generator (*SG* 2) is connected to the electrolyser via *Busbar* 6 and *Busbar* 5, while the 410 MW synchronous generator *SG* 3) is connected to the electrolyser through *Busbar* 11, *Busbar* 10, and *Busbar* 5. A large 100 WM PEM electrolyser is connected to *Busbar* 4. The large-scale PEM electrolyser is assumed to be viewed as a large load by the power system, consuming only active power.

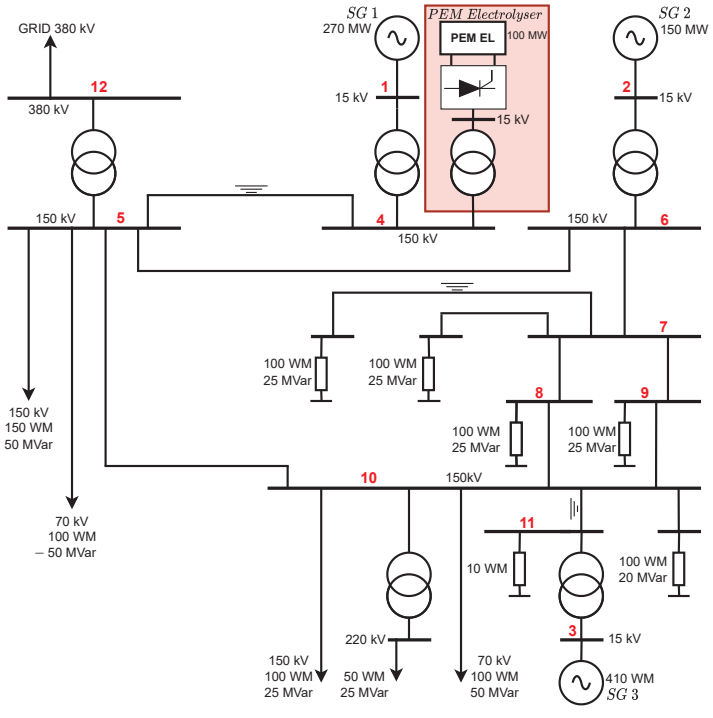

Figure 1. Test grid around the Belgian Amercoeur plant, in which 100 MW of PEM electrolysers are connected to the grid through a 12-pulse thyristor rectifier. The number of each busbar is given in red.

2.1. Dynamic Modelling of the PEM Electrolyser

In order to model an electrolyser as a whole, it is necessary to look at each of its constituent aspects, such as electrochemical, electrical, thermal, mass transfer, and fluid [22] components. This paper focuses only on the electrochemical and electrical models.

Various electrochemical models of PEM electrolysers have been proposed in the literature [2,3,8,10,12–14,20], which can be categorized into four groups, as discussed in the introduction: *Model* 1, *Model* 2, *Model* 3, and *Model* 4. The performance of each model can be quantified by evaluating the dynamic response of the cell voltage for a fixed cell

current. The dynamic behaviour of these four electrochemical models is obtained by the following equations:

- *Model* 1: Classical electrochemical model without Warburg impedance.

This model is described in [2,4,12,13,15,16], and the cell voltage across a PEM stack is given by

$$V_{cell} = V_{act,c} + V_{act,a} + R_m i_{cell} + V_{rev} \tag{1}$$

where $V_{act,a}$ and $V_{act,c}$ are the activation overpotential at the anode and at the cathode, respectively; i_{cell} represents the input current of the cell; and R_m and V_{rev} are the ohmic resistance and reverse voltage potential (reversible potential), respectively, during the water-splitting reaction. The dynamic behaviour of this classical electrochemical model is imposed by $V_{act,i}$, and it is modelled by:

$$\frac{dV_{act,c}}{dt} = \frac{i_{cell}}{C_{dl,c}} - \frac{V_{act,c}}{R_{ct,c}C_{dl,c}} \tag{2}$$

$$\frac{dV_{act,a}}{dt} = \frac{i_{cell}}{C_{dl,a}} - \frac{V_{act,a}}{R_{ct,a}C_{dl,a}} \tag{3}$$

where C_{dl_i} represents the double layer capacity, and $R_{ct,a}$ and $R_{ct,c}$ are the charge transfer resistances at the anode and cathode, respectively, which are temperature-dependent.

- *Model* 2: Classical electrochemical model with a Randles–Warburg cell.

This electrochemical model is presented in [10]. Its dynamic model is given by:

$$\frac{dV_{act,c}}{dt} = \frac{i_{cell}}{C_{dl,c}} - \frac{V_{act,c}}{(R_{ct,c} + Z_w)C_{dl,c}} \tag{4}$$

$$\frac{dV_{act,a}}{dt} = \frac{i_{cell}}{C_{dl,a}} - \frac{V_{act,a}}{(R_{ct,a} + Z_w)C_{dl,a}} \tag{5}$$

where Z_w denotes the Warburg impedance, which is frequency-dependent. Its mathematical expression is given as follows [19]:

$$Z_w = \frac{R_{d_1}}{1 + R_{d_1}C_{d_1}s} + \frac{R_{d_2}}{1 + R_{d_2}C_{d_2}s} \tag{6}$$

where $R_{d_i} = R_i R_d$, R_d, and R_i are the diffusion resistance and charge transfer resistance, respectively, and $C_{d_i} = C_{dli}\tau_d / R_d$, τ_d and C_{dli} represent the diffusion time constant and double layer capacitance, respectively.

- *Model* 3: Electrochemical model without the activation overpotential of the cathode and with Randles–Warburg impedance.

This model is presented in [10,20]. Without the activation overpotential at the cathode, the cell voltage across the PEM stack is modelled as follows:

$$V_{cell} = V_{act,a} + R_m i_{cell} + V_{rev} \tag{7}$$

The dynamic model of activation overpotential at the anode is modelled as in Equation (5).

- *Model* 4: Electrochemical model without activation overpotential at the cathode or a Warburg cell.

This model is depicted in [4,8]. The dynamic model of the cell voltage across the PEM electrolyser as a function of the activation overpotential at the anode is given by Equations (5) and (7). For a cell current set to 5 A, the dynamic responses of the cell voltages of *Model* l, *Model* 2, *Model* 3, and *Model* 4 from Equations (1)–(7) are described in Figure 2. The used cell parameters and Randles–Warburg cell parameters of those models are given in [10,18].

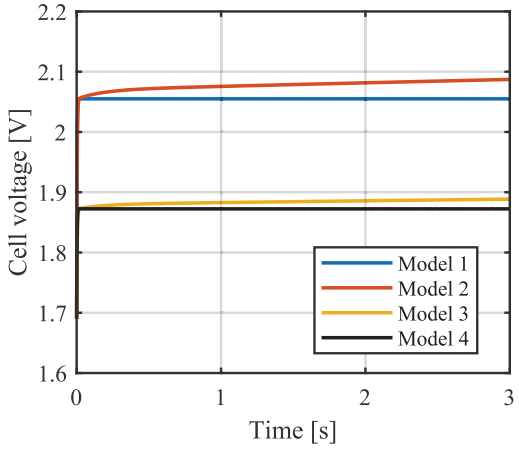

Figure 2. Dynamic response of the cell voltage of each of the four electrochemical models proposed in the literature as a function of the cell current. The cell input current is set to 5 A.

Figure 2 shows that the four electrochemical models can be identified in two groups: models without activation overpotential of the cathode (*Model* 3 and *Model* 4) and complete models (*Model* 1 and *Model* 2). For each group, we can identify models with Warburg impedance (*Model* 2 and *Model* 3) and those without Warburg impedance (*Model* 1 and *Model* 4). The impact of Warburg impedance on the cell voltage is also observed through the voltage deviation between *Model* 2 and *Model* 1 and that between *Model* 3 and *Model* 4. Furthermore, the difference in voltage between the two groups is around 0.182 V, which represents the cathode activation overpotential. This overpotential is smaller than the total cell voltage, which is close to 2.055 V for *Model* 1 and *Model* 2 and around 1.872 V for *Model* 3 and *Model* 4 under steady-state conditions. This may be the reason why some authors neglected this cathode activation overpotential in their models [10].

Additionally, Figure 3 shows that the cell voltage responses of electrochemical models with Warburg impedance (*Model* 2 and *Model* 3) are close to those without Warburg impedance (*Model* 1 and *Model* 4). However, their transient response is higher than that of *Model* 1 and *Model* 4. This is illustrated by the time constant, which is higher for *Model* 2 and *Model* 3 than for *Model* 1 and *Model* 4.

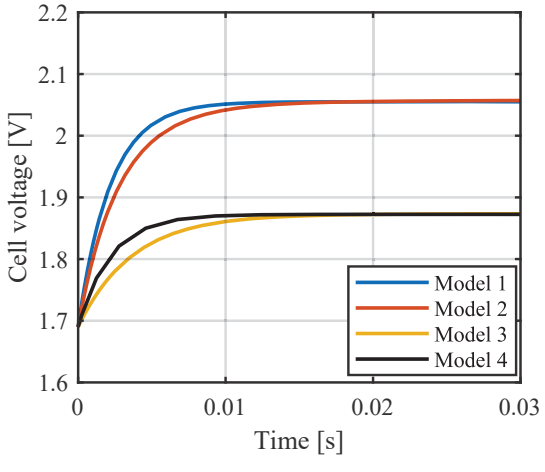

Figure 3. Transient response of the cell voltage of each of the four electrochemical models proposed in the literature as a function of the cell current. The cell input current is set to 5 A.

From these results, it can be concluded that the dynamic response of electrochemical models with a Warburg impedance (or a Randles–Warburg cell) is close to that of those without a Warburg impedance. Nevertheless, Warburg impedance can introduce a larger time constant in the transient response, and it can make the dynamic modelling of the electrochemical model more complex. Therefore, *Model* 4 is used for the rest of this paper. *Model* 4 offers a better transient response compared to the other models (see Figure 3).

2.2. Modelling of the 12-Pulse Thyristor Rectifier and the Electrolyser Current Controller

Figure 4 shows a hydrogen PEM electrolyser model connected to the grid through a 12-pulse thyristor rectifier and a three-winding wye-wye-delta transformer. The PEM electrolyser is modelled by the electrochemical model as described in the previous subsection. The three-winding transformer has the ability to eliminate the 5th-and 7th-order harmonic currents [8]. The electrolyser model is connected to the rectifier bridge via a filter inductance (L_f) and interphase inductances (L_{int}). The two 6-pulse thyristor rectifiers connected in parallel are used to form a 12-pulse thyristor rectifier. This configuration is often considered to be one of the most mature solutions for high-current rectification applications [8]. The operation of each six-pulse rectifier is ensured by a firing angle (α) that is either specified or generated by a controller, depending on the desired response of the rectifier DC side. Figure 4 also highlights that the transfer of active power (P_{AC}) from the AC side to the DC side (P_{DC}) is ensured by an appropriate firing-angle signal. The DC voltage and DC current are also related to the firing angle generated by the current controller from the current set point and the measurements of the DC current signal (i_{dc0}) and the AC voltage signal (V_{abc}). V_{abc} can be measured at the primary or secondary end of the three-winding transformer. It is used by the phase-locked loop (PLL) to synchronize the electrolyser with the grid frequency.

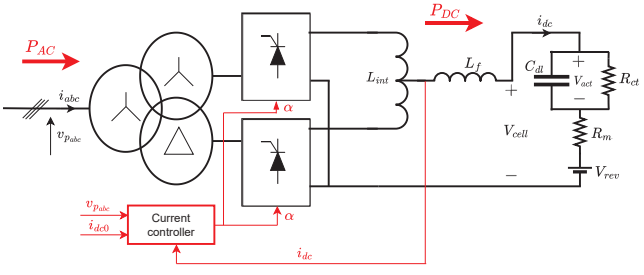

Figure 4. Hydrogen PEM electrolyser model connected to the grid through a 12-pulse thyristor rectifier.

2.2.1. Electrical Model of the 12-Pulse Thyristor Rectifier

Establishing the dynamic model shown in Figure 4 requires that all the parameters and variables on the AC side of the rectifier be brought back to the DC side. To do this, the average model of a 12-pulse thyristor rectifier can be considered. Additionally, the transformer is modelled by the primary and secondary leakage inductances.

Considering that the primary end of the transformer is supplied by U_p, this voltage can be seen by the electrolyser through the DC voltage using the following expression:

$$V_{dc} = 1.4\, k\, U_p\, cos\alpha \tag{8}$$

where U_p is the RMS phase-to-phase voltage at the primary end of the transformer, and k represents the ratio between the RMS phase-to-phase voltage at the secondary end of the transformer (U_s) and that at the primary voltage (U_p). Finally, α corresponds to the firing angle.

Equation (8) shows that the DC voltage is a function of the firing angle. It shows that the maximum voltage can be obtained when the firing angle is equal to zero. We assume that the transfer of current between two consecutive thyristors in a commutation

group takes a finite amount of time (overlap time). This overlap time depends on the phase-to-phase voltage between the thyristors participating in the commutation process, as well as the leakage inductance between the thyristor rectifier and the AC grid [23]. During the overlap time, the voltage and the current on the DC side are given by [23]:

$$V_{dc} = 1.4\,k\;\; U_p\;[cos\alpha + cos(\alpha + \mu)] \tag{9}$$

$$I_{dc} = \frac{1.4\,k}{\omega\; L_T}\; U_p\;[cos\alpha - cos(\alpha + \mu)] \tag{10}$$

where L_T is the leakage inductance of the transformer, and μ is the overlap angle. Equations (9) and (10) allow for the establishment of an equivalent circuit of the thyristor rectifier converter, as shown in Figure 5. The converter is modelled by a voltage source in series with a virtual resistance, whereas the overlap time phenomenon is modelled through the equivalent resistance given by $1.5\omega L_T/\pi$. Note that this resistance is not real (virtual resistance) because it does not dissipate power [23].

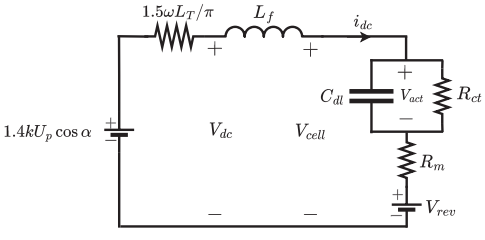

Figure 5. Electrical model of a PEM electrolyser and 12-pulse thyristor rectifier.

The dynamic model of the 12-pulse thyristor rectifier associated with the PEM electrolyser can be obtained from Figure 5 by applying Kirchhoff's law. The resulting model is defined as:

$$V_{cell} = 1.4\;k\;U_p cos\alpha - \frac{1.5\omega L_T}{\pi}\; i_{dc} - L_f\;\frac{i_{dc}}{dt} \tag{11}$$

$$V_{cell} = V_{rev} + R_m i_{dc} + V_{act} \tag{12}$$

$$C_{dl}\frac{dV_{act}}{dt} = i_{dc} - \frac{V_{act}}{R_{ct}} \tag{13}$$

2.2.2. Control Structure Model for the Electrolyser Current

The current control structure can be obtained from the dynamic model that is described by Equations (11) to (13). By applying Laplace transform to these equations and setting the initial conditions of current ($I_{dc}(0)$) and activation voltage ($V_{act}(0)$) to zero, the following is obtained:

$$V_{cell}(s) = 1.4\;k\;U_p cos\alpha - \frac{1.5\omega L_T}{\pi}\; I_{dc}(s) - s\;L_f I_{dc}(s) \tag{14}$$

$$V_{cell}(s) = V_{rev} + R_m I_{dc}(s) + V_{act}(s) \tag{15}$$

$$s\;C_{dl} V_{act}(s) = I_{dc}(s) - \frac{V_{act}(s)}{R_{ct}} \tag{16}$$

A block diagram of the system based on Equations (14) to (16) is shown in Figure 6. It describes the dynamic model of the PEM electrolyser associated with the 12-pulse thyristor rectifier in the s domain. This model is composed of two subloops of current and voltage, as well as signals of reverse voltage (V_{rev}) and DC input voltage ($1.4\;U_s cos(\alpha)$).

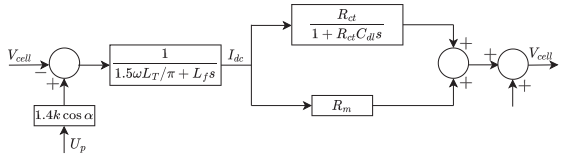

Figure 6. Physical system of the 12-pulse thyristor rectifier associated with the electrolyser model in the s domain.

The proposed cell voltage control structure from the physical system model (Figure 6) is depicted in Figure 7. It consists of an internal current control loop and an external voltage control loop. The feed-forward terms (1.4 $kU_p cos(\alpha)$ and V_{rev}) are added at the output of the DC current control loop to compensate for the opposite signals of physical signals of 1.4 $kU_p cos(\alpha)$ and V_{rev}.

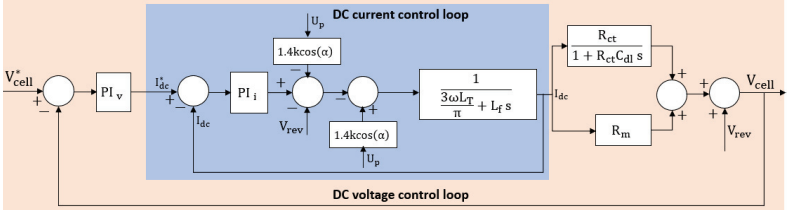

Figure 7. Complete control structure composed of an internal current control loop and an external voltage control loop.

The proposed control structure (Figure 7) is general. It can be used to control both cell voltage and cell current. To control the DC current, the DC current control loop structure is used (light blue), whereas the DC voltage loop control structure including the blue part is used to control the cell voltage.

The implementation of the current control structure given in Figure 7 requires a phase-locked loop (PLL) to synchronize the electrolyser with the grid frequency. The main function of the PLL is to track the phase (θ) of the *Busbar* 4 voltage, which is the voltage node to which the electrolyser is connected (see Figure 1). This phase can be expressed by $\theta = \omega_0 t + \theta_0$ under steady-state conditions, where ω_0 is the pulsation corresponding to the reference frequency of the grid. The control structure of the PLL is described in [24].

The steady-state conditions of 100 MW of PEM electrolysers connected to *Busbar* 4 (see Figure 1) are given in Figure 8. We consider the proposed current control structure and parameter values of the test grid and interpolate parameter values of the PEM electrolyser from [10,18] to those of the 100 MW PEM electrolyser. The DC electrolyser current is given in Figure 8a. The firing angle is depicted in Figure 8b. The DC voltage is presented in Figure 8c. The computed steady-state conditions are 21,790 A, 4588 V, and 19°. The results were obtained using the parameters shown in Table 1 [10,18] and the current control structure illustrated in Figure 8. Figure 8 also shows that the proposed controller is also able to reach another steady-state operating point after changing the electrolyser current set point, for example, by changing the electrolyser current set point by 1% at 6 s, i.e., from 21,790 A to 21,576 A. The controller maintains the DC current at the desired value (see Figure 8a). The firing angle increases (Figure 8b) to decrease the DC voltage (Figure 8c).

Table 1. Electrochemical model and PI controller parameters.

Electrochemical Model	PI Controller
R_m = 0.3818 Ω; R_{ct} = 0.3318 Ω; C_{dl} = 0.9091 F ; V_{rev} = 700 V; L_{int} = 48 µH	Kp_i = 0.06; K_{i_i} = 0.12; L_f = 40 mH; L_T = 119 µH; $\alpha = 30°$

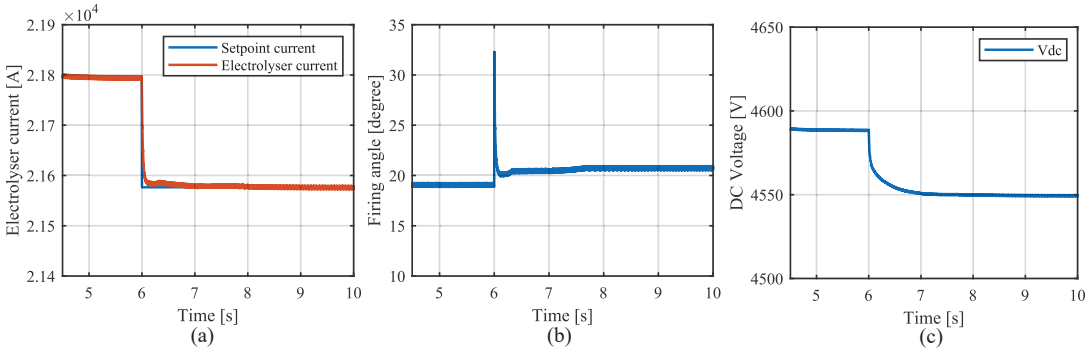

Figure 8. Steady-state conditions of the PEM electrolyser connected to *Busbar* 4: (**a**) DC electrolyser current; (**b**) firing angle; (**c**) DC voltage.

2.3. Modelling of the PEM Electrolyser as a Load

Consider the PEM electrolyser modelled in Figure 4, which is detailed in Figure 5. If one considers just the electrolyser part in Figure 5, the cell voltage of the stack is given by Equation (12). The activation voltage (V_{act}) is essentially caused by the voltage associated with the transfer resistance (R_{ct}) because the current on the capacitance is equal to zero. Therefore, one obtains:

$$V_{cell} = (R_m + R_{ct})\, i_{dc} + V_{rev} \tag{17}$$

If it is assumed that there are no power losses between the grid and the electrolyser—that is to say that the active AC power P_{AC} supplied by the grid is equal to the DC power P_{DC} consumed by the hydrogen electrolyser—the power consumed by the electrolyser can be calculated as:

$$P_{AC} = P_{DC} = R_{eq}\, i_{dc}^2 + V_{rev} i_{dc}\,, \quad with \quad R_{eq} = R_m + R_{ct} \tag{18}$$

Equation (18) shows that equivalent resistance (R_{eq}) and reversible potential (V_{rev}) are constant. This yields the active power (P_{AC}) as a function of the DC current (i_{dc}). P_{AC} is constituted by two active power terms ($R_{eq}\, i_{dc}^2$ and $V_{rev} i_{dc}$). The first element varies directly with the square of the current, while the latter varies with the current. In contrast to traditional static load modelling, the whole active power is modelled as a function of voltage magnitude. Since it is assumed that the DC voltage is fixed by the grid voltage to which the electrolyser is connected, the proposed modelling of the PEM electrolyser as load can be based on the controlled DC current. Thus, the PEM electrolyser can be modelled as a function of the cell current. According to Equation (18) and Figure 4, the PEM electrolyser can be modelled as a fraction of a constant impedance load combined with a fraction of a constant current load. The proposed model is expressed by Equation (19). In contrast to the conventional exponential ZIP model [25,26], the proposed model is modelled as a function of the current ratio instead of the voltage ratio. This makes the proposed load model of the electrolyser different from that of conventional constant impedance and constant current loads.

$$P = P_{El0}\left[a_1\left(\frac{i_{dc}}{i_{dc0}}\right)^2 + a_2\left(\frac{i_{dc}}{i_{dc0}}\right)\right] \tag{19}$$

where P_{El0} is the rated active power of the electrolyser, i_{dc0} represents the nominal DC electrolyser current related to the nominal active power of the electrolyser, i_{dc} is the controlled current of the electrolyser, a_1 represents the fraction of constant impedance load, and a_2 is the fraction of the constant current load.

Note that the modelling of the electrolyser as a load may depend on the model of the electrolyser, the technology of the power electronic converter, and the way in which the

electrolyser is connected to the grid. For a technology based on a single 12-pulse thyristor rectifier with n electrolysers connected in parallel on the DC side, as illustrated in Figure 9, the a_1 factor decreases with an increase in the number of parallel connected electrolyser models. Consequently, the PEM electrolyser behaves as a constant-current dominant load. Otherwise, it behaves as a constant-impedance dominant load.

Equations (18) and (19) and Figures 9 and 10 illustrate an example of the variation of fractions of a constant impedance load (a_1) and constant current load (a_2) depending on the number of electrolysers connected in parallel to the DC rectifier side. Four possibilities of connecting a 100 MW PEM electrolyser to the DC side of the 12-pulse thyristor rectifier are proposed. When one 100 MW PEM electrolyser model is connected to the DC side, Figure 10 shows that the fraction of constant impedance load (a_1) is higher than that of the constant current load (a_2). Therefore, the PEM electrolyser model can be seen by the grid as a dominant constant impedance load,whereas when two 50 MW PEM electrolysers are connected in parallel, this can be considered a dominant constant current load. For four models of 25 MW each connected in parallel, the fraction of constant impedance load (a_2) is higher than that of the constant current load (a_1). The PEM electrolyser can be assimilated to a dominant constant current load.

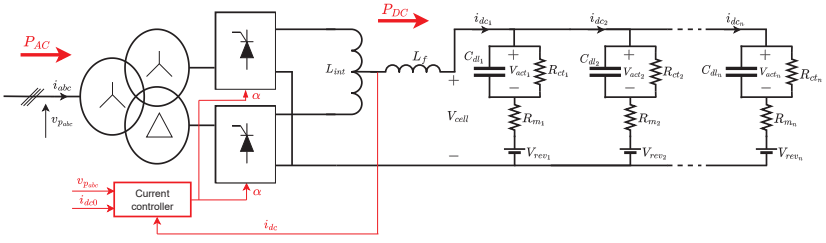

Figure 9. n PEM electrolyser models connected to the grid through a 12-pulse thyristor rectifier.

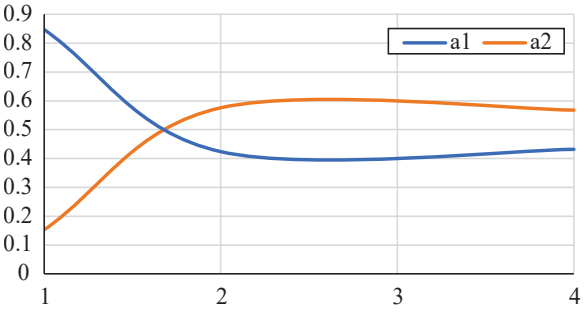

Figure 10. Fractions of constant impedance load and constant current load dependent on the number of electrolysers connected in parallel on the DC rectifier side.

3. Small-Signal Modelling of the Test System

Small-signal analysis was used as a tool to investigate the effects of the PEM electrolyser on the small-signal angular stability, i.e., to investigate the impact of the PEM electrolyser on the capacity of a set of interconnected synchronous machines to maintain synchronism after being subjected to a small disturbance. To do this, the power system shown in Figure 1 can be described by a system of non-linear differential and algebraic equations. Then, it is linearised around the operating point to obtain the state-space model of the grid. Hence, the state-space model of the grid shown in Figure 1 has to be established. It is composed of small-signal submodels of synchronous machines (270 MW, 150 MW, and 410 MW), static exciters, the PEM electrolyser, the network, and loads. Such equations can be written as follows.

3.1. State-Space Model of Synchronous Generators

The state-space model was obtained by the linearisation of non-linear differential and algebraic equations of the synchronous machines around an operational point. The rotor and stator equations are established in the dq reference frame (via Park transformation) [11,21]. The differential equations in the $dq-$synchronous reference frame of each synchronous machine connected to the grid are described by [21]:

$$\frac{d\delta_i}{dt} = \omega_i - \omega_s \tag{20}$$

$$\frac{d\omega_i}{dt} = \omega_s \frac{T_{M_i}}{2H_i} - \omega_s \frac{\left(E'_{q_i} - X'_{d_i} I_{d_i}\right)}{2H_i} I_{q_i} - \omega_s \frac{\left(E'_{d_i} + X'_{q_i} I_{q_i}\right)}{2H_i} I_{d_i} - \omega_s D_i \frac{\omega_i - \omega_s}{2H_i} \tag{21}$$

$$\frac{dE'_{q_i}}{dt} = -\frac{E'_{q_i}}{T'_{do_i}} - \frac{\left(X_{d_i} - X'_{d_i}\right)}{T'_{do_i}} I_{d_i} + \frac{E_{fd_i}}{T'_{do_i}} \quad with \quad E'_{q_i} = \frac{X_{md_i}}{X_{fd_i}} \psi_{fd_i} \tag{22}$$

$$\frac{dE'_{d_i}}{dt} = -\frac{E'_{d_i}}{T'_{qo_i}} + \frac{I_{q_i}}{T'_{qo_i}} \left(X_{q_i} - X'_{q_i}\right) \quad with \quad E'_{d_i} = -\frac{X_{mq_i}}{X_{1q_i}} \psi_{1q_i} \tag{23}$$

where i = 1, 2, and 3 correspond to the number of the synchronous generator (SG 1, SG 2, and SG 3, respectively) connected to the test system; ω_s is the synchronous angular speed of the rotor; and ω_i and $\delta_i = \theta_i - \theta_s$ are the rotor speed and relative rotor angle, respectively. The rotor angle (θ_i) is measured with respect to the synchronously rotating frame of the constant base frequency (ω_b) and satisfies $d\theta_i/dt = \omega_b \omega_i$ [27]. T_{M_i} is the mechanical torque. D_i is the damping torque coefficient. H_i represents the inertial constant. I_{d_i} and I_{q_i} are the current components along the direct axis (d axis) and quadrature axis (q-axis), respectively. X_{d_i} and X_{q_i} are the synchronous reactances along the d axis and q axis, respectively. T'_{do_i} and T'_{qo_i} are the transient time constants along the d axis and q axis, respectively. X'_{d_i} and X'_{q_i} represent the transient reactances along the d axis and q axis, respectively. E_{fd_i} is the field voltage. ψ_{1q_i} represents damper-winding ($1q$) flux linkages. X_{1q_i} is the damper-winding ($1q$) reactance. X_{md_i} and X_{mq_i} are the magnetizing reactances in d-axis and q-axis, respectively. X_{fd_i} is the field d-axis reactance. E'_{d_i} is proportional to the rotor field flux along the d axis, while E'_{d_i} is proportional to the damper-winding flux along the q axis.

Each synchronous machine of the test system is composed of a static exciter to maintain a constant terminal voltage. The dynamic model of the static exciter is expressed according to the following equation [21]:

$$\frac{dE_{fd_i}}{dt} = -\frac{1}{T_{A_i}} E_{fd_i} + \frac{K_{A_i}}{T_{A_i}} \left(V_{ref_i} - V_i\right) \tag{24}$$

The real parts of the equations of the stator for each synchronous generator (SG, $i = 1$, 2, and 3) are given by [21]:

$$E'_{d_i} - V_i \, sin(\delta_i - \theta_i) - R_{s_i} I_{d_i} + X'_{q_i} I_{q_i} = 0 \tag{25}$$

$$E'_{q_i} - V_i \, cos(\delta_i - \theta_i) - R_{s_i} I_{q_i} + X'_{d_i} I_{d_i} = 0 \tag{26}$$

To obtain a linearised model for Equations (20)–(26), a small perturbation around the operating point is superimposed on the state variables δ_i, ω_i, E'_{d_i}, E'_{q_i}, E_{fd_i}, I_{q_i}, I_{d_i}, V_i, V_{ref_i}, T_{M_i}, and θ_i, such as:

$\delta_i = \delta_{0_i} + \Delta\delta_i$; $\omega_i = \omega_{0_i} + \Delta\omega_i$; $E'_{q_i} = E'_{q0_i} + \Delta E'_{q_i}$; $E'_{d_i} = E'_{d0_i} + \Delta E'_{d_i}$; $E_{fd_i} = E_{fd0_i} + \Delta E_{fd_i}$; $I_{q_i} = I_{q0_i} + \Delta I_{q_i}$; $I_{d_i} = I_{d0_i} + \Delta I_{d_i}$; $V_i = V_{0_i} + \Delta V_i$; $V_{ref_i} = V_{ref0_i} + \Delta V_{ref_i}$; $T_{M_i} = T_{M0_i} + \Delta T_{M_i}$; and $\theta_i = \theta_{0_i} + \Delta\theta_i$.

where δ_{0_i}, ω_{0_i}, E'_{d0_i}, E'_{q0_i}, E_{fd0_i}, I_{q0_i}, I_{d0_i}, V_{0_i}, V_{ref0_i}, T_{M0_i}, and θ_{0_i} represent the nominal values of the rotor angle, rotor speed, damper winding flux, rotor field flux, field voltage, q-axis current, d-axis current, terminal voltage of the SG, reference voltage of the exciter, mechanical torque, and voltage angle at bus i, respectively. $\Delta\delta_i$, $\Delta\omega_i$, $\Delta E'_{d_i}$, $\Delta E'_{q_i}$, ΔE_{fd_i}, ΔI_{q_i}, ΔI_{d_i}, ΔV_i, ΔV_{ref_i}, ΔT_{M_i}, and $\Delta\theta_i$ are the small disturbances of the state variables mentioned above.

By substituting the small disturbances defined above around the operating point in Equations (20) to (26) and neglecting the second and higher-order powers of the small perturbation and of the input vector in the Taylor-series expression, the state-space model of three synchronous machines was defined according to the following equations:

$$\Delta\dot{X} = A_{SG}\Delta X + B_{SG1}\Delta I_g + B_{SG2}\Delta V_g + B_{SG3}\Delta U \tag{27}$$

$$0 = C_{SG1}\Delta X + D_{SG1}\Delta I_g + D_{SG2}\Delta V_g \tag{28}$$

where $\Delta X = [\Delta X_1\ \Delta X_2\ \Delta X_3]^T$ represents the state vector composed of the state subvector of each synchronous generator connected to the test system. They are defined by $\Delta X_i = \left[\Delta\delta_i\ \Delta\omega_i\ \Delta E'_{q_i}\ \Delta E'_{d_i}\ \Delta E_{fd_i}\right]^T$. ΔI_g is the vector matrix of current components of the SG i along the d axis and q axis. It is expressed by $\Delta I_g = \left[\Delta I_{d_1}\ \Delta I_{d_2}\ \Delta I_{d_3}\ \Delta I_{q_1}\ \Delta I_{q_2}\ \Delta I_{q_3}\right]^T$. ΔV_g represents the vector matrix of voltage magnitude and the angle of the synchronous generator bus. It is defined by $\Delta V_g = \left[\Delta\theta^T\ \Delta V^T\right]^T$, where $\Delta\theta = [\Delta\theta_1\ \Delta\theta_2\ \Delta\theta_3]^T$ and $\Delta V = [\Delta V_1\ \Delta V_2\ \Delta V_3]^T$. $\Delta U = \left[\Delta T_M^T\ \Delta V_{ref}^T\right]^T$ is the input matrix of SG i, where $\Delta T_M = \left[\Delta T_{M_1}\ \Delta T_{M_2}\ \Delta T_{M_3}\right]^T$ and $\Delta V_{ref} = \left[\Delta V_{ref_1}\ \Delta V_{ref_2}\ \Delta V_{ref_3}\right]^T$. Matrices A_{SG}, B_{SG1}, B_{SG2}, B_{SG3}, C_{SG1}, D_{SG1}, and D_{SG2} are expressed as:

$$A_{SG} = \begin{bmatrix} A_{SG1} & 0 & 0 \\ 0 & A_{SG1} & 0 \\ 0 & 0 & A_{SG1} \end{bmatrix}_{15\times15}, \text{where } A_{SG_i} = \begin{bmatrix} 0 & 1 & 0 & 0 & 0 \\ 0 & -\frac{D_i\omega_s}{2H_i} & -\frac{I_{q_i}\omega_s}{2H_i} & -\frac{I_{d_i}\omega_s}{2H_i} & 0 \\ 0 & 0 & -\frac{1}{T'_{d0_i}} & 0 & \frac{1}{T'_{d0_i}} \\ 0 & 0 & 0 & -\frac{1}{T'_{q0_i}} & 0 \\ 0 & 0 & 0 & 0 & -\frac{1}{T_{A_i}} \end{bmatrix};$$

$$B_{SG1} = \begin{bmatrix} B_{SG1_1} & 0 & 0 \\ 0 & B_{SG1_2} & 0 \\ 0 & 0 & B_{SG1_3} \end{bmatrix}_{15\times6} B_{SG1_i} = \begin{bmatrix} 0 & 0 \\ \frac{X'_{d_i}I_{q_i} - E'_{d_i} - X'_{q_i}I_{q_i}}{2H_i}\omega_s & \frac{-E'_{q_i} + X'_{d_i}I_{d_i} - X'_{q_i}I_{d_i}}{2H_i}\omega_s \\ -\frac{X_{d_i} - X'_{d_i}}{T'_{d0_i}} & 0 \\ 0 & -\frac{X_{q_i} - X'_{q_i}}{T'_{q0_i}} \\ 0 & 0 \end{bmatrix};$$

$$B_{SG2} = \begin{bmatrix} B_{SG2_1} & 0 & 0 \\ 0 & B_{SG2_2} & 0 \\ 0 & 0 & B_{SG2_3} \end{bmatrix}_{15\times6}, \text{where } B_{SG2_i} = \begin{bmatrix} 0 & 0 & 0 & 0 & -\frac{K_{A_i}}{T_{A_i}} \\ 0 & 0 & 0 & 0 & 0 \end{bmatrix}^T;$$

$$B_{SG3} = \begin{bmatrix} B_{SG3_1} & 0 & 0 \\ 0 & B_{SG3_2} & 0 \\ 0 & 0 & B_{SG3_3} \end{bmatrix}_{15\times6}, \text{where } B_{SG3_i} = \begin{bmatrix} 0 & 0 & 0 & 0 & -\frac{K_{A_i}}{T_{A_i}} \\ 0 & \frac{\omega_s}{2H_i} & 0 & 0 & 0 \end{bmatrix}^T;$$

$$C_{SG1} = \begin{bmatrix} C_{SG1_1} & 0 & 0 \\ 0 & C_{SG1_2} & 0 \\ 0 & 0 & C_{SG1_3} \end{bmatrix}_{6\times15}, \text{where } C_{SG1_i} = \begin{bmatrix} -V_i cos(\delta_i - \theta_i) & 0 & 0 & 1 & 0 \\ V_i sin(\delta_i - \theta_i) & 0 & 1 & 0 & 0 \end{bmatrix};$$

$$D_{SG1} = \begin{bmatrix} D_{SG1_1} & 0 & 0 \\ 0 & D_{SG1_2} & 0 \\ 0 & 0 & D_{SG1_3} \end{bmatrix}_{6\times6}, \text{where } D_{SG1_i} = \begin{bmatrix} -R_{s_i} & X'_{q_i} \\ -X'_{d_i} & -R_{s_i} \end{bmatrix}; \text{and}$$

$$D_{SG2} = \begin{bmatrix} D_{SG2_1} & 0 & 0 \\ 0 & D_{SG2_2} & 0 \\ 0 & 0 & D_{SG2_3} \end{bmatrix}_{6\times6}, \text{where } D_{SG2_i} = \begin{bmatrix} V_i cos(\delta_i - \theta_i) & -sin(\delta_i - \theta_i) \\ -V_i sin(\delta_i - \theta_i) & -cos(\delta_i - \theta_i) \end{bmatrix}.$$

3.2. State-Space Model of the Electrolyser (EL)

According to Figure 4, the small-signal model of a set of electrolysers and the average model of a 12-pulse thyristor rectifier can be built around the state variable of current (i_{dc}) and the required firing angle (α) of the thyristor rectifier. By linearising Equation (18) around the operating point and by neglecting the second-order term of Δi_{dc}, one obtains:

$$\Delta P_{EL} = \left(2R_{eq} i_{dc0} + V_{rev}\right)\Delta i_{dc} \tag{29}$$

Considering the current control structure around the proportional–integral (PI) controller as described in Figure 11, the firing angle can be written as a function of the parameters of the PI controller as:

$$\alpha = K_p(i_{dc0} - i_{dc}) + K_i(i_{dc0} - i_{dc}) \tag{30}$$

where K_p, K_i, and i_{dc0} represent the gain of the proportional controller, the gain of the integral controller, and the nominal current of hydrogen electrolyser, respectively.

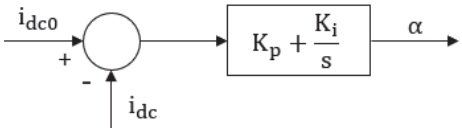

Figure 11. Firing angle associated with the parameters of the proportional-integral controller.

Linearisation of Equation (30) around the operating point, considering a nominal firing angle (α_0) of zero, yields:

$$\Delta\alpha = -\left(K_p + K_i\right)\Delta i_{dc} \tag{31}$$

The state-space model of the active and reactive power consumed by the PEM electrolyser can be expressed as:

$$\begin{bmatrix} \Delta P_{EL} \\ \Delta Q_{EL} \end{bmatrix} = \begin{bmatrix} 2R_{eq} i_{dc0} + V_{rev} & 0 \\ 0 & 0 \end{bmatrix} \begin{bmatrix} \Delta i_{dc} \\ \Delta\alpha \end{bmatrix} \tag{32}$$

According to Equations (11)–(13) and Figure 4, the voltage across the capacitance (C_{dl}) is equal to zero. Because it is seen as smoothing capacitance by the charge transfer resistance (R_{ct}), by substituting Equations (12) and (13) into Equation (11), one obtains:

$$\frac{di_{dc}}{dt} = -\left(R_m + R_{ct} + \frac{1.5\omega L_T}{\pi}\right)\frac{i_{dc}}{L_f} + \frac{1.4U_s cos\alpha}{L_f} - \frac{V_{rev}}{L_f} \tag{33}$$

Thus, linearisation of Equation (33) around the operating point yields:

$$\Delta\dot{i}_{dc} = A_{EL}\Delta i_{dc} + B_{EL}\Delta\alpha \tag{34}$$

where $A_{EL} = -\frac{1}{L_f}\left(R_m + R_{ct} + \frac{1.5\omega L_T}{\pi}\right)$ and $B_{EL} = -\frac{1.4U_s sin\alpha_0}{L_f}$. Meanwhile, α_0 is the firing angle related to steady-state conditions. Equations (31) and (34) describe the state-space model of the PEM electrolyser as a function of the gains of the controller, the parameters of the electrochemical model, and the grid voltage magnitude.

3.3. State-Space Model of the Network and Conventional Loads

The network equations for an $n-$bus system can be expressed in complex form as described in [21]. They are defined in two groups, namely equations associated with the generator buses and those associated with the load buses. It is assumed in this paper that the PEM electrolyser is connected to the generator bus. The constant power loads are connected to the load buses and to the generator buses. The network equations for the three generator buses (1, 2, and 3; see Figure 1) are defined as:

$$P_{G_i} + jQ_{G_i} + P_{L_i}(V_i) + jQ_{L_i}(V_i) + P_{EL}(i_{cell}) = \sum_{k=1}^{n} V_i V_k Y_{ik}[cos(\theta_i - \theta_k - \beta_{ik}) + jsin(\theta_i - \theta_k - \beta_{ik})] \quad (35)$$

with $P_{G_i} = I_{d_i} V_i sin(\delta_i - \theta_i) + I_{q_i} V_i cos(\delta_i - \theta_i)$ and $Q_{G_i} = I_{d_i} V_i cos(\delta_i - \theta_i) - I_{q_i} V_i sin(\delta_i - \theta_i)$, where P_{G_i} and Q_{G_i} are the active power and reactive power injected into bus i due to generator i ($i = 1, 2,$ and 3), respectively. Equation (35) shows that for the generator buses, the active (P_{L_i}) and reactive (Q_{L_i}) powers of the constant power loads depend on the voltage magnitudes of the buses, while the active power of the electrolyser (P_{EL}) depends on the cell current. The power-balance form of Equation (35) is expressed as:

$$I_{d_i} V_i sin(\delta_i - \theta_i) + I_{q_i} V_i cos(\delta_i - \theta_i) + P_{L_i}(V_i) + P_{EL}(i_{cell}) - \sum_{k=1}^{n} V_i V_k Y_{ik} cos(\theta_i - \theta_k - \beta_{ik}) = 0 \quad (36)$$

$$I_{d_i} V_i cos(\delta_i - \theta_i) - I_{q_i} V_i sin(\delta_i - \theta_i) + Q_{L_i}(V_i) - \sum_{k=1}^{n} V_i V_k Y_{ik} sin(\theta_i - \theta_k - \beta_{ik}) = 0 \quad (37)$$

The network equations for the $n-$ load buses (see Figure 1) are expressed in Equation (38). As assumed, only constant power loads are connected to the load buses. These are modelled by considering only the active power ($P_{L_i}(V_i)$) and reactive power ($Q_{L_i}(V_i)$).

$$P_{L_i}(V_i) + jQ_{L_i}(V_i) = \sum_{k=1}^{n} V_i V_k Y_{ik}[cos(\theta_i - \theta_k - \alpha_{ik}) + jsin(\theta_i - \theta_k - \beta_{ik})] \quad (38)$$

The power-balance form of Equation (38) is expressed as

$$P_{L_i}(V_i) - \sum_{k=1}^{n} V_i V_k Y_{ik} cos(\theta_i - \theta_k - \beta_{ik}) = 0 \quad (39)$$

$$Q_{L_i}(V_i) - \sum_{k=1}^{n} V_i V_k Y_{ik} sin(\theta_i - \theta_k - \beta_{ik}) = 0 \quad (40)$$

The state-space model of the generator buses is given by Equation (41). It is obtained by linearising Equations (36) and (37) around the operating point and by neglecting all the second-order terms associated with the small variations.

$$0 = C_{SGEL} \Delta X_{SGEL} + D_{SG3} \Delta I_g + D_{SG4} \Delta V_g + D_{NET1} \Delta V_{NET1} \quad (41)$$

where $\Delta X_{SGEL} = [\Delta X_1 \; \Delta X_2 \; \Delta X_3 \; \Delta X_{EL}]^T$ is the state vector of generators and of the electrolyser connected to the generator buses, $\Delta X_{EL} = \Delta i_{dc}$ represents the state variable of the electrolyser, and $\Delta V_{NET} = \left[\Delta\theta^T \; \Delta V^T\right]^T$ is the vector matrix formed by the voltage magnitude and angle submatrices of the network buses, where $\Delta\theta = [\Delta\theta_1 \; \Delta\theta_2 \; \cdots \; \Delta\theta_m]^T$ represents the angle submatrix of the network buses, and $\Delta V = [\Delta V_1 \; \Delta V_2 \; \cdots \; \Delta V_m]^T$ is the voltage magnitude submatrix of the network buses. m represents the non-generator buses, C_{SGEL} is the observation matrix, as expressed by:

$$C_{SGEL} = \begin{bmatrix} C_{SGEL_1} & 0 & 0 \\ 0 & C_{SGEL_2} & 0 \\ 0 & 0 & C_{SGEL_3} \end{bmatrix}_{6 \times 16}$$

where C_{SGEL_1} is the matrix associated with the generator *Busbar* 4 and the PEM electrolyser, and C_{SGEL_2} and C_{SGEL_3} are the matrices associated with the generator (*Busbar* 6) and *Busbar* 11 without PEM electrolyser, respectively. Matrices C_{SGEL_2} and C_{SGEL_3} have dimensions of 2×5 because they are part of the busbars without an electrolyser.

$$C_{SGEL_1} = \begin{bmatrix} I_{d_i}V_i cos(\delta_i - \theta_i) - I_{q_i}V_i sin(\delta_i - \theta_i) & 0 & 0 & 0 & 0 & 2R_{eq}i_{dc0} + V_{rev} \\ -I_{d_i}V_i sin(\delta_i - \theta_i) - I_{q_i}V_i cos(\delta_i - \theta_i) & 0 & 0 & 0 & 0 & 0 \end{bmatrix}$$

Matrices D_{SG3}, D_{SG4}, and D_{NET1} are the direct transmission matrices and are defined as:

$$D_{SG3} = \begin{bmatrix} D_{SG3_1} & 0 & 0 \\ 0 & D_{SG3_2} & 0 \\ 0 & 0 & D_{SG3_3} \end{bmatrix}_{6\times 6} \text{ with } D_{SG3_i} = \begin{bmatrix} V_i sin(\delta_i - \theta_i) & -V_i cos(\delta_i - \theta_i) \\ V_i cos(\delta_i - \theta_i) & -V_i sin(\delta_i - \theta_i) \end{bmatrix};$$

$$D_{SG4} = \begin{bmatrix} D_{SG4_{11}} & D_{SG4_{12}} & D_{SG4_{13}} \\ D_{SG4_{21}} & D_{SG4_{22}} & D_{SG4_{23}} \\ D_{SG4_{31}} & D_{SG4_{32}} & D_{SG4_{33}} \end{bmatrix}_{6\times 6}$$

where $D_{SG4_{ik}}$ is the submatrix associated with synchronous generator i ($i = 1$, 2, and 3 *SGs*) and with the generator buses (k, where k = 1, 2, and 3 generator buses). They are defined by:

$$D_{SG4_{11}} = \begin{bmatrix} A_{SG4_1} & B_{SG4_1} \\ C_{SG4_1} & D_{SG4_1} \end{bmatrix}, \text{ with}$$

$$A_{SG4_1} = -I_{d_1}V_1 cos(\delta_1 - \theta_1) + I_{q_1}V_1 sin(\delta_1 - \theta_1) + V_1 \sum_{k=1}^{3} V_k Y_{1k} sin(\theta_1 - \theta_k - \beta_{1k})$$

$$B_{SG4_1} = I_{d_1} sin(\delta_1 - \theta_1) + I_{q_1} cos(\delta_1 - \theta_1) - \sum_{k=1}^{3} V_k Y_{1k} sin(\theta_1 - \theta_k - \beta_{1k}) - V_1 Y_{1k} cos(\theta_1 - \theta_k - \beta_{1k}) + \frac{\partial P_{L_1}(V_1)}{\partial V_1}$$

$$C_{SG4_1} = -I_{d_1}V_1 sin(\delta_1 - \theta_1) + I_{q_1}V_1 cos(\delta_1 - \theta_1) - V_1 \sum_{k=1}^{3} V_k Y_{1k} cos(\theta_1 - \theta_k - \beta_{1k})$$

$$D_{SG4_1} = I_{d_1} cos(\delta_1 - \theta_1) - I_{q_1} sin(\delta_1 - \theta_1) - \sum_{k=1}^{3} V_k Y_{1k} sin(\theta_1 - \theta_k - \beta_{1k}) - V_1 Y_{1k} sin(\theta_1 - \theta_k - \beta_{1k}) + \frac{\partial Q_{L_1}(V_1)}{\partial V_1}$$

$$D_{SG4_{12}} = \begin{bmatrix} -V_1 V_2 Y_{12} sin(\theta_1 - \theta_2 - \beta_{12}) & -V_1 Y_{12} cos(\theta_1 - \theta_2 - \beta_{12}) \\ V_1 V_2 Y_{12} cos(\theta_1 - \theta_2 - \beta_{12}) & -V_1 Y_{12} sin(\theta_1 - \theta_2 - \beta_{12}) \end{bmatrix}$$

$$D_{SG4_{13}} = \begin{bmatrix} -V_1 V_3 Y_{13} sin(\theta_1 - \theta_3 - \alpha_{13}) & -V_1 Y_{13} cos(\theta_1 - \theta_3 - \beta_{13}) \\ V_1 V_3 Y_{13} cos(\theta_1 - \theta_3 - \beta_{13}) & -V_1 Y_{13} sin(\theta_1 - \theta_3 - \beta_{13}) \end{bmatrix}$$

$$D_{SG4_{21}} = D_{SG4_{12}}$$

$$D_{SG4_{22}} = \begin{bmatrix} A_{SG4_2} & B_{SG4_2} \\ xC_{SG4_2} & D_{SG4_2} \end{bmatrix}, \text{ with}$$

$$A_{SG4_2} = -I_{d_2}V_2 cos(\delta_2 - \theta_2) + I_{q_2}V_2 sin(\delta_2 - \theta_2) + V_2 \sum_{k=2}^{3} V_k Y_{2k} sin(\theta_2 - \theta_k - \beta_{2k})$$

$$B_{SG4_2} = I_{d_2} sin(\delta_2 - \theta_2) + I_{q_2} cos(\delta_2 - \theta_2) - \sum_{k=2}^{3} V_k Y_{2k} sin(\theta_2 - \theta_k - \beta_{2k}) - V_2 Y_{2k} cos(\theta_2 - \theta_k - \beta_{2k}) + \frac{\partial P_{L_2}(V_2)}{\partial V_2}$$

$$C_{SG4_2} = -I_{d_2}V_2 sin(\delta_2 - \theta_2) + I_{q_2}V_2 cos(\delta_2 - \theta_2) - V_2 \sum_{k=2}^{3} V_k Y_{2k} cos(\theta_2 - \theta_k - \beta_{2k})$$

$$D_{SG4_2} = I_{d_2} cos(\delta_2 - \theta_2) - I_{q_2} sin(\delta_2 - \theta_2) - \sum_{k=2}^{3} V_k Y_{2k} sin(\theta_2 - \theta_k - \beta_{2k}) - V_2 Y_{2k} sin(\theta_2 - \theta_k - \beta_{2k}) + \frac{\partial Q_{L_2}(V_2)}{\partial V_2}$$

$$D_{SG4_{23}} = \begin{bmatrix} -V_2 V_3 Y_{23} sin(\theta_2 - \theta_3 - \beta_{23}) & -V_2 Y_{23} cos(\theta_2 - \theta_3 - \beta_{23}) \\ V_2 V_3 Y_{23} cos(\theta_2 - \theta_3 - \beta_{23}) & -V_2 Y_{23} sin(\theta_2 - \theta_3 - \beta_{23}) \end{bmatrix}$$

$$D_{SG4_{31}} = D_{SG4_{13}}$$

$$D_{SG4_{32}} = D_{SG4_{23}}$$

$$D_{SG4_{33}} = \begin{bmatrix} A_{SG4_3} & B_{SG4_3} \\ C_{SG4_3} & D_{SG4_3} \end{bmatrix}, \text{ with}$$

$$A_{SG4_3} = -I_{d_3}V_3cos(\delta_3-\theta_3) + I_{q_3}V_3sin(\delta_3-\theta_3) + V_3V_3Y_{33}sin(\theta_2-\theta_3-\beta_{33})$$
$$B_{SG4_3} = I_{d_3}sin(\delta_3-\theta_3) + I_{q_3}cos(\delta_3-\theta_3) - V_3Y_{33}sin(\theta_3-\theta_3-\beta_{33}) - V_3Y_{33}cos(\theta_3-\theta_3-\beta_{33}) + \frac{\partial P_{L_3}(V_3)}{\partial V_3}$$
$$C_{SG4_3} = -I_{d_3}V_3sin(\delta_3-\theta_3) + I_{q_3}V_3cos(\delta_3-\theta_3) - V_3V_3Y_{33}cos(\theta_3-\theta_3-\beta_{33})$$
$$D_{SG4_3} = I_{d_3}cos(\delta_3-\theta_3) - I_{q_3}sin(\delta_3-\theta_3) - V_3Y_{33}sin(\theta_3-\theta_3-\beta_{33}) - V_3Y_{33}sin(\theta_3-\theta_3-\beta_{33}) + \frac{\partial Q_{L_3}(V_3)}{\partial V_3}$$

$$D_{NET1} = \begin{bmatrix} D_{NET1_{14}} & D_{NET1_{15}} & \cdots & D_{NET1_{1k}} \\ \vdots & \vdots & \cdots & \vdots \\ D_{NET1_{i4}} & \cdots & \cdots & D_{NET1_{ik}} \end{bmatrix}_{6\times 18}, \text{with}$$
$$D_{NET1_{ik}} = \begin{bmatrix} -V_iV_kY_{ik}sin(\theta_i-\theta_i-\beta_{ik}) & -V_iY_{ik}cos(\theta_i-\theta_i-\beta_{ik}) \\ V_iV_kY_{ik}cos(\theta_i-\theta_i-\beta_{ik}) & -V_iY_{ik}sin(\theta_i-\theta_i-\beta_{ik}) \end{bmatrix}$$

The state-space model of the load buses is given by Equation (42). It is obtained by linearising Equations (39) and (40) around the operating point and by neglecting all the second-order terms associated with the small variations. In addition, $\partial P_{L_i}(V_i)/\partial V_i$ and $\partial Q_{L_i}(V_i)/\partial V_i$ are assumed to be zero because conventional loads are considered to be constant power loads.

$$0 = D_{SG5}\Delta V_g + D_{NET2}\Delta V_{NET} \tag{42}$$

Matrices D_{SG5} and D_{NET2} are given by:

$$D_{SG5} = \begin{bmatrix} D_{SG5_{41}} & \cdots & D_{SG5_{4i}} \\ \vdots & \vdots & \vdots \\ D_{SG5_{k1}} & \cdots & D_{SG5_{ki}} \end{bmatrix}_{18\times 6}, \text{with}$$
$$D_{SG5_{ki}} = \begin{bmatrix} -V_iV_kY_{ik}sin(\theta_i-\theta_k-\beta_{ik}) & V_iY_{ik}cos(\theta_i-\theta_k-\beta_{ik}) \\ -V_iV_kY_{ik}cos(\theta_i-\theta_k-\beta_{ik}) & V_iY_{ik}sin(\theta_i-\theta_k-\beta_{ik}) \end{bmatrix}$$

$$D_{NET2} = \begin{bmatrix} D_{NET2_{44}} & \cdots & D_{NET2_{4k}} \\ \vdots & \vdots & \vdots \\ D_{NET2_{i4}} & \cdots & D_{NET2_{ik}} \end{bmatrix}_{18\times 18}, \text{with}$$
$$D_{NET2_{ik_{i\neq k}}} = \begin{bmatrix} -V_iV_kY_{ik}sin(\theta_i-\theta_k-\beta_{ik}) & -V_iY_{ik}cos(\theta_i-\theta_k-\beta_{ik}) \\ V_iV_kY_{ik}cos(\theta_i-\theta_k-\beta_{ik}) & -V_iY_{ik}sin(\theta_i-\theta_k-\beta_{ik}) \end{bmatrix}$$

$$D_{NET2_{ik_{i=k}}} = \begin{bmatrix} \sum_{k=4}^{12} V_iV_kY_{ik}sin(\theta_i-\theta_k-\beta_{ik}) & \frac{\partial P_{L_i}(V_i)}{\partial V_i} - \sum_{k=4}^{12} V_kY_{ik}cos(\theta_i-\theta_k-\beta_{ik}) - V_iY_{ik}cos(\theta_i-\theta_k-\beta_{ik}) \\ -\sum_{k=4}^{12} V_iV_kY_{ik}cos(\theta_i-\theta_k-\beta_{ik}) & \frac{\partial Q_{L_i}(V_i)}{\partial V_i} - \sum_{k=4}^{12} V_kY_{ik}sin(\theta_i-\theta_k-\beta_{ik}) - V_iY_{ik}sin(\theta_i-\theta_k-\beta_{ik}) \end{bmatrix}$$

In D_{SG3_i}, $D_{NET1_{ik}}$, and $D_{SG5_{ki}}$, i and k represent the generator buses ($i = 1$, 2, and 3) and the non-generator buses ($k = 4$ to 12), respectively, whereas in $D_{NET2_{ik_{i\neq k}}}$ and $D_{NET2_{ik_{i=k}}}$, i and k are the load buses ($i = 4$ to 12) and the non-generator buses ($k = 4$ to 12), respectively.

3.4. Complete Small-Signal State-Space Model of the Test System

The complete state-space model of the test system (Figure 1) is represented by Equations (43)–(46). It is obtained from the developed individual submodels given by Equations (27)–(29), (34), (41), and (42).

$$\Delta\dot{X}_{SGEL} = A_{SGEL}\Delta X_{SGEL} + B_{SG1}\Delta I_g + B_{SG2}\Delta V_g + B_{SGEL}\Delta U_{SGEL} \tag{43}$$

$$0 = C_{SGEL1}\Delta X_{SGEL} + D_{SG1}\Delta I_g + D_{SG2}\Delta V_g \tag{44}$$

$$0 = C_{SGEL2}\Delta X_{SGEL} + D_{SG3}\Delta I_g + D_{SG4}\Delta V_g + D_{NET1}\Delta V_{NET} \tag{45}$$

$$0 = D_{SG5}\Delta V_g + D_{NET2}\Delta V_{NET} \tag{46}$$

with $A_{SGEL} = \begin{bmatrix} A_{SG} & 0 \\ 0 & A_{EL} \end{bmatrix}_{16\times16}$; $\Delta X_{SGEL} = \begin{bmatrix} \Delta X^T & \Delta i_{dc} \end{bmatrix}^T_{16x1}$; $B_{SGEL} = \begin{bmatrix} B_{SG3} & 0 \\ 0 & B_{EL} \end{bmatrix}_{16\times7}$; $\Delta U_{SGEL} = \begin{bmatrix} \Delta U^T & \Delta\alpha \end{bmatrix}^T_{7\times1}$; $C_{SGEL1} = \begin{bmatrix} C_{SG1} & 0 \\ 0 & 0 \end{bmatrix}_{7\times16}$ and $C_{SGEL2} = C_{SGEL}$.

By eliminating ΔI_g from Equations (43)–(46), the complete model is rewritten as:

$$\begin{bmatrix} \Delta\dot{X} \\ 0 \\ 0 \end{bmatrix} = \begin{bmatrix} A_{SGEL} - B_{SG1}D_{SG1}^{-1}C_{SGEL1} & B_{SG2} - B_{SG1}D_{SG1}^{-1}D_{SG2} & 0 \\ C_{SGEL2} - D_{SG3}D_{SG1}^{-1}C_{SGEL1} & D_{SG4} - D_{SG3}D_{SG1}^{-1}D_{SG2} & D_{NET1} \\ 0 & D_{SG5} & D_{NET1} \end{bmatrix} \begin{bmatrix} \Delta X_{SGEL} \\ \Delta V_g \\ \Delta V_{NET} \end{bmatrix} + \begin{bmatrix} B_{SGEL} \\ 0 \\ 0 \end{bmatrix} \Delta U_{SGEL} \tag{47}$$

According to Equation (47), the complete state-space model of the test system can be expressed as:

$$\Delta\dot{X} = A_{grid}\Delta X + B_{grid}\Delta U \tag{48}$$

where A_{grid} is the dynamic matrix of the grid, and B_{grid} represents the input matrix. The effect of the PEM electrolyser on the small-signal angular stability is examined through the movement of the eigenvalues from the dynamic matrix in the complex plane. The complete form of the dynamic matrix is expressed by:

$$\begin{aligned} [A_{grid}] = {} & [A_{SGEL} - B_{SG1}D_{SG1}^{-1}C_{SGEL1}] \\ & - [B_{SG2} - B_{SG1}D_{SG1}^{-1}D_{SG2} \quad 0] \begin{bmatrix} D_{SG4} - D_{SG3}D_{SG1}^{-1}D_{SG2} & D_{NET1} \\ D_{SG5} & D_{NET1} \end{bmatrix}^{-1} \begin{bmatrix} C_{SGEL2} - D_{SG3}D_{SG1}^{-1}C_{SGEL1} \\ 0 \end{bmatrix} \end{aligned}$$

4. Stability Analysis Results

The impact of 100 MW of PEM electrolysers on the stability of the small-signal rotor angle was assessed by analyzing the state-space models associated with the synchronous generators, the PEM electrolyser, and the network as described in the test system (Figure 1). The calculation of the test system's eigenvalues was performed using Matlab. The obtained results were then verified through time-domain simulations. Table 2 lists the parameter values of the synchronous generators and of the static exciters.

Table 2. Parameter values for test-system components.

Machine 1	Machine 2	Machine 3
P_{G1} = 270 MW	P_{G2} = 150 MW	P_{G3} = 410 MW
Q_{G1} = 81 MVar	Q_{G2} = 45 MVar	Q_{G3} = 123 MVar
R_{s1} = 0.089 pu, X_{d1} = 1.5 pu	R_{s2} = 0.089 pu, X_{d2} = 1.5 pu	R_{s3} = 0.089 pu, X_{d3} = 1.5 pu
X'_{d1} = 0.18 pu, T'_{d1} = 5 s	X'_{d2} = 0.18 pu, T'_{d2} = 5 s	X'_{d3} = 0.18 pu, T'_{d3} = 6 s
X'_{q1} = 1.26 pu, T'_{q1} = 0.31 s	X'_{q2} = 1.26 pu, T'_{q2} = 0.31 s	X'_{q3} = 1.26 pu, T'_{q3} = 0.53 s
X_{q1} = 1.26 pu, H_1 = 3.4 s	X_{q2} = 1.26 pu, H_2 = 2.6 s	X_{q3} = 1.26 pu, H_3 = 3.7 s
D_1 = 0.5	D_2 = 0.5	D_3 = 0.6
Static exciter 1	**Static exciter 2**	**Static exciter 3**
K_{A1} = 20, T_{A1} = 0.02 s	K_{A2} = 20, T_{A2} = 0.02 s	K_{A3} = 20, T_{A3} = 0.02 s
K_{F1} = 0.063, T_{F1} = 0.35 s	K_{F1} = 0.063, T_{F2} = 0.35 s	K_{F1} = 0.063, T_{F3} = 0.35 s
K_{E1} = 1, T_{E1} = 0.314 s	K_{E2} = 1, T_{E1} = 0.314 s	K_{E3} = 1, T_{E1} = 0.314 s

4.1. Dominant Modes in Steady State

4.1.1. Without Connecting the PEM Electrolyser to the Test System

Figure 12a shows the modelling results obtained without connecting the PEM electrolyser to *Busbar* 4. The obtained dominant modes of synchronous generators coupled with the test system under steady-state conditions are located in the left half-complex plane. The obtained dominant modes are described in Table 3. Fifteen modes were clearly identified. Conjugate complexes $\lambda_{1,2}$, $\lambda_{3,4}$, and $\lambda_{5,6}$ are identified in Table 3. λ_1 and λ_2

are the electromechanical modes associated with the rotor angle deviation ($\Delta\delta_1$) and rotor speed deviation ($\Delta\omega_1$) of SG 1. λ_3 and λ_4 are the electromechanical modes coupled with SG 2, and λ_5 and λ_6 are the electromechanical modes related to SG 3.

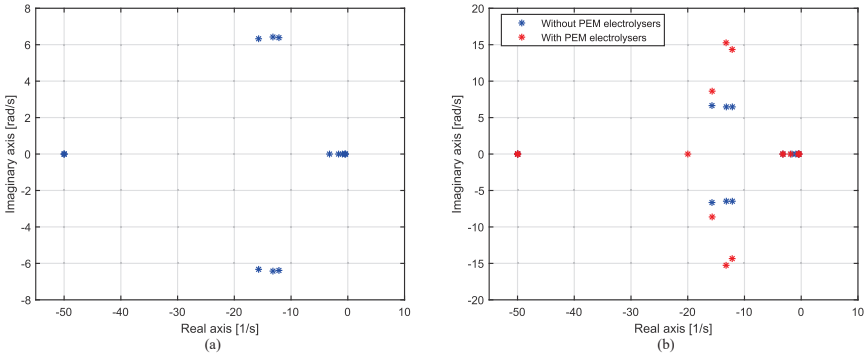

Figure 12. The modelled system's modes in the complex plane: (**a**) without connecting the PEM electrolyser to test system; (**b**) with 100 MW of PEM electrolysers connected to the grid. The modes in the absence of the electrolyzer are depicted in blue, while those incorporating the electrolyzer are illustrated in red.

One can note that the oscillation frequency of these electromechanical modes is close to 1 Hz (63,862 rad/s). This illustrates that the interconnected synchronous machines maintain their synchronism around 50 Hz after being subjected to a small disturbance. The values of these modes are close because the used parameter values of the synchronous generators are close (see Table 2). The effects of the PEM electrolyser on the angular stability must be investigated with respect to these modes.

Modes λ_{13}, λ_{14}, and λ_{15} are associated with the field voltage variations (ΔE_{fd_i}) of static exciters. Modes λ_{10}, λ_{11}, and λ_{12} are related to the magnetic flux variations of damper winding (ΔE_{d_i}) of synchronous machines, whereas modes λ_7, λ_8, and λ_9 are coupled with the magnetic flux variations of field winding (ΔE_{q_i}) of synchronous machines. Figure 12a and Table 3 show that the modes associated with ΔE_{fd_i} are identical to the three exciters using the same parameter values.

Table 3. Identification of modes with respect to the state variables of synchronous generators in the case in which the PEM electrolyser is not connected to the test system.

Mode Values	Identification of Modes
λ_1, λ_2: $-12.1368 \pm j6.3862$	$\Delta\delta_1$ *and* $\Delta\omega_1$
λ_3, λ_4: $-15.7177 \pm j6.3269$	$\Delta\delta_2$ *and* $\Delta\omega_2$
λ_5, λ_6: $-13.1985 \pm j6.4232$	$\Delta\delta_3$ *and* $\Delta\omega_3$
λ_7, λ_8, λ_9: -1.6326, -0.9495 and -0.4654	$\Delta E'_{q_1}$, $\Delta E'_{q_2}$ *and* $\Delta E'_{q_3}$
λ_{10}, λ_{11}, λ_{12}: -0.5125, -0.3880, -0.4654	$\Delta E'_{d_1}$, $\Delta E'_{d_2}$ *and* $\Delta E'_{d_3}$
λ_{13}, λ_{14}, λ_{15}: -49.9982, -49.9928, -49.9992	ΔE_{fd_1}, ΔE_{fd_2} *and* ΔE_{fd_3}

4.1.2. With the PEM Electrolyser Connected to the Test System

Figure 12b shows the modelling results obtained when 100 MW of PEM electrolysers were connected to *Busbar* 4. The results show that the electrolyser model adds an additional negative real mode ($\lambda_{16} = -19.9835$). This mode is associated with the DC electrolyser current variation (Δi_{dc}). In addition, the modes related to the static exciters and the magnetic flux of field winding and the damper winding are not significantly influenced by the PEM electrolyser, as shown in Figure 12b and in Table 4. This is because the dynamic response of the electrolyser current is more related to the voltage angle of the system than to the voltage amplitude. For this reason, the damping and oscillation frequency of the

electromechanical modes ($\lambda_{1,2}$, $\lambda_{3,4}$, and$\lambda_{5,6}$) are significantly affected. In terms of the damping of the electromechanical modes, the effect of the PEM electrolyser is less profound than for the oscillation frequency of these modes. As observed in Figure 12b, there is a large increase in the oscillation frequency of the electromechanical conjugate modes associated with SG 1 ($\lambda_{1,2}$) and SG 3 ($\lambda_{5,6}$) than in the electromechanical modes of SG 2 ($\lambda_{3,4}$). This is caused by the electrical distance between the generator buses and the electrolyser bus. On the other hand, the PEM electrolyser increases the damping of the electromechanical modes associated with the synchronous machine connected to the same busbar ($\lambda_{1,2}$).

Table 4. Identification of modes with respect to the state variables of synchronous generators in the case in which 100 MW of PEM electrolysers are connected to the test system (*Busbar* 4).

Mode Values	Identification of Modes
λ_1, λ_2: $-12.1649 \pm j14.3415$	$\Delta\delta_1$ *and* $\Delta\omega_1$
λ_3, λ_4: $-15.6977 \pm j8.6270$	$\Delta\delta_2$ *and* $\Delta\omega_2$
λ_5, λ_6: $-13.2407 \pm j15.2628$	$\Delta\delta_3$ *and* $\Delta\omega_3$
λ_7, λ_8, λ_9: -3.2258, -3.2258 and -1.8868	$\Delta E'_{q_1}$, $\Delta E'_{q_2}$ *and* $\Delta E'_{q_3}$
λ_{10}, λ_{11}, λ_{12}: -0.4113, -0.4836, -0.3505	$\Delta E'_{d_1}$, $\Delta E'_{d_2}$ *and* $\Delta E'_{d_3}$
λ_{13}, λ_{14}, λ_{15}: -49.9760, -49.9431, -49.9873	ΔE_{fd_1}, ΔE_{fd_2} *and* ΔE_{fd_3}
λ_{16} : -19.9835	Δi_{dc}

4.1.3. Impact of the Synchronous Generator Parameters on the Movement of Electromechanical Modes

- Impact of the inertial constant:

Figures 13–15 show the impact of a change in the inertial constant on the trajectories of the electromechanical modes. With respect to changes in the inertial constant (H_1) from 3 s to 7 s, Figure 13 shows that larger values of H_1 decrease the damping and the oscillation frequency of the system modes (λ_1 and λ_2) associated with SG 1. On the other hand, the modes related to SG 2 and SG 3 are not affected by this variation. This shows that the choice of H_1 values becomes a critical factor in the dynamic response of the machine if the electrolyser is connected to the same busbar with the synchronous generator. Note that to reach the initial oscillation frequency (≈1 Hz), the inertial constant has to be increased but at the risk of reducing the stability margin.

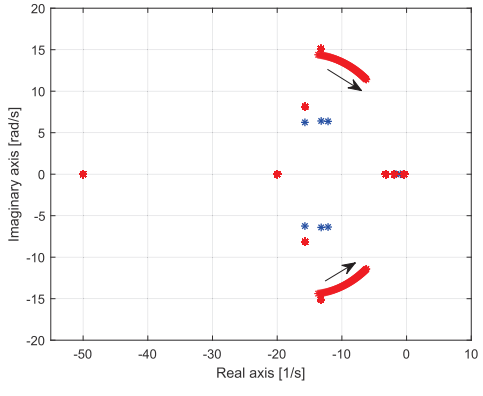

Figure 13. Movement of modes λ_1 and λ_2 caused by changes in the inertial constant value of the synchronous generator connected to *Busbar* 4: H_1 = 3 to 7 s. The modes in the absence of the electrolyzer are depicted in blue, while those incorporating the electrolyzer are illustrated in red.

Figure 14 depicts the movement of modes λ_3 and λ_4 caused by changes in the inertial constant (H_2) from 2.6 s to 7 s. As in the previous case, only the electromechanical modes of SG 2 are affected. The oscillation frequencies of these modes are less affected than

those of *SG* 1 and *SG* 3. However, it is observed that the larger values of H_2 decrease the damping of the modes. On the other hand, larger values of H_2 have no significant impact on the oscillation frequency of the λ_3 and λ_4 modes. This can be attributed to the electrical distance between *Busbar* 6 of *SG* 2 and *Busbar* 4 of the electrolyser. The capacity of this synchronous machine can also have an influence on the observed trajectories of the modes.

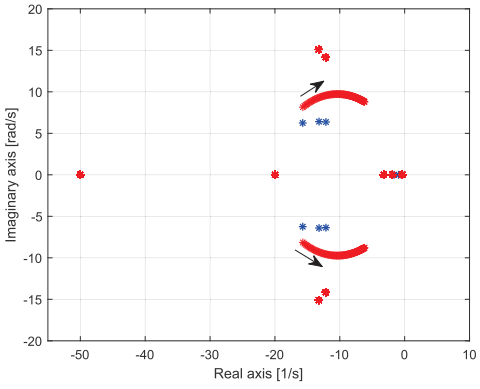

Figure 14. Movement of- the λ_3 and λ_4 modes caused by changes in the inertial constant value of the synchronous generator connected to *Busbar* 6: H_2 = 2.6 to 7 s. The modes in the absence of the electrolyzer are depicted in blue, while those incorporating the electrolyzer are illustrated in red.

Finally, Figure 15 shows the impact of changes in the inertial (constant) H_3 on the trajectories of the λ_5 and λ_6 modes. Note that the oscillation frequencies of these modes decrease with an increase in H_3, and larger values of H_3 lead to decreases in the damping of these modes. As in the previous cases, to reach the initial oscillation frequency (≈1 Hz), the inertial constant must be increased, but the technical limits cannot be exceeded.

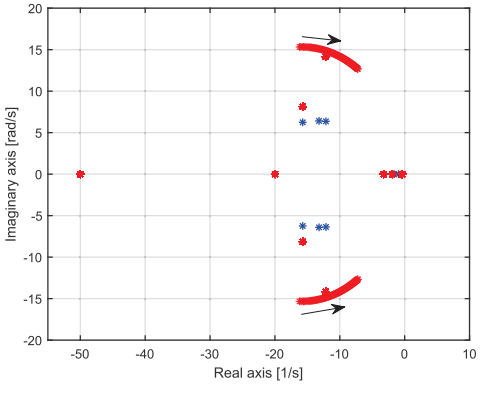

Figure 15. Movement of the λ_5 and λ_6 modes caused by changes in the inertial constant value of the synchronous generator connected to *Busbar* 11: H_3 = 3 to 7 s. The modes in the absence of the electrolyzer are depicted in blue, while those incorporating the electrolyzer are illustrated in red.

- Impact of the damping torque coefficient

The impacts of the damping torque coefficient on the movement of the electromechanical modes are illustrated from Figures 16–18. These results indicate that the damping torque coefficient has a significant impact on the damping and oscillation frequency of the electromechanical modes. Figure 16 reveals that the oscillation frequencies of the λ_1 and λ_2 modes decrease with increases in the value of the damping torque coefficient (D_1) *SG* 1. In contrast, the damping of these modes is increased. The effect of this coefficient

on the modes is opposite to that of the inertial constant in terms of oscillation frequency and damping of the electromechanical modes. As observed in Figure 16, the oscillation frequency of the affected modes can return to the initial condition value (≈1 Hz).

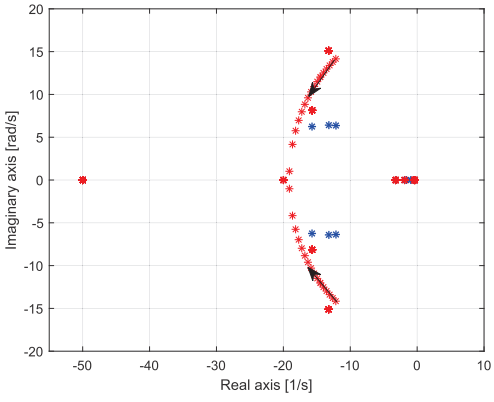

Figure 16. Movement of the λ_1 and λ_2 modes caused by changes in the damping torque coefficient value of the synchronous generator connected to *Busbar* 4: D_1 = 0.5 to 0.8. The modes in the absence of the electrolyzer are depicted in blue, while those incorporating the electrolyzer are illustrated in red.

Figure 17 shows that higher values of the damping torque coefficient (D_2) of SG 2 have a significant impact on the oscillation frequency of the λ_3 and λ_4 modes. These oscillation frequencies reach zero for certain values of D_2. Note that the damping of the λ_3 mode increases when that of the λ_4 mode decreases. The observed trajectories of the λ_3 and λ_4 modes may be due to their small capacity compared to that of the other two generators. The electrical distance between SG 2 and the electrolyser can also be a cause of this phenomenon.

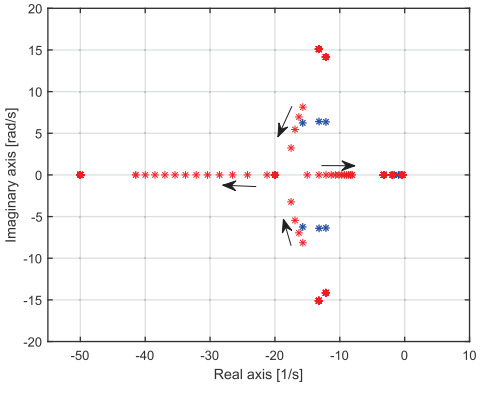

Figure 17. Movement of the λ_3 and λ_4 modes caused by changes in the damping torque coefficient value of the synchronous generator connected to *Busbar* 4: D_2 = 0.5 to 0.8. The modes in the absence of the electrolyzer are depicted in blue, while those incorporating the electrolyzer are illustrated in red.

Figure 18 shows the effect of increasing the value of D_3 associated with SG 3 on the λ_5 and λ_6 modes. These results are close to those obtained for SG 1 (Figure 16). Note that the oscillation frequency of modes decreases with an increasing damping torque coefficient. The trajectories of the two groups of modes are different. These trajectories illustrate that the modes coupled to SG 1 are more affected than those associated with SG 2 and SG 3.

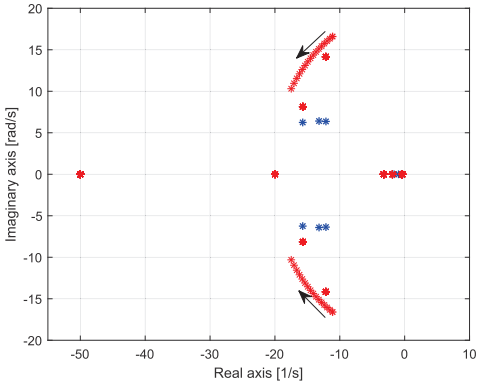

Figure 18. Movement of the λ_5 and λ_6 modes caused by changes in the damping torque coefficient value of a synchronous generator connected to *Busbar* 4: D_3 = 0.5 to 0.8. The modes in the absence of the electrolyzer are depicted in blue, while those incorporating the electrolyzer are illustrated in red.

4.2. Time-Domain Simulations

The obtained eigenvalue analysis results were consolidated through time-domain simulations implemented in the Matlab/Simulink/Simscape environment. The test power system depicted in Figure 1 was implemented with the same parameter values as those listed in Table 2. Two small disturbances were considered. The first one is the connection of the 100 MW of PEM electrolysers to the test system. The second disturbance consists of a decrease in the electrolyser current set point of 1%, from 21.794 kA to 21.576 kA. The dynamic response of the rotor angle deviation and rotor speed deviation were investigated to examine the small-signal angular stability. The impact of the proposed electrolyser model as a load on the rotor-angle stability was also examined.

Dynamic Response of Electromechanical State Variables

- Connecting the electrolyser to the test system:

The first scenario consists of connecting the 100 MW of PEM electrolysers to *Busbar* 4 at $t = 15$ s. The obtained results are illustrated in Figures 19–22. It is observed that the interconnected synchronous machines maintain synchronism. This is shown by the rotor speed deviations ($\Delta\omega_1$, $\Delta\omega_2$, and $\Delta\omega_3$) of *SG* 1, *SG* 2, and *SG* 3, which are zero before and after connecting the electrolyser (Figure 19a). Figure 19 also illustrates the influence of the line impedance between the electrolyser busbar and the synchronous generator busbars. For example, the dynamic response of the rotor speed deviation ($\Delta\delta_1$) of *SG* 1 is different than that of $\Delta\delta_2$ and $\Delta\delta_3$, as shown in Figure 19a. Because *SG* 1 is connected to *Busbar* 4, the connection of the 100 MW of PEM electrolysers to *Busbar* 4 is perceived by *SG* 1 as an increase in electrical power in an attempt to reduce the frequency and, therefore, the rotor angle deviation. It is observed that the connection of the electrolyser is regarded by *SG* 2 and *SG* 3 as an increase in frequency and, therefore, an increase in the rotor angle deviation. Note that the variation of *SG* 1 is higher than that of *SG* 2 and *SG* 3. In contrast, the settling time for *SG* 1 is shorter than for *SG* 2 and *SG* 3. Figure 19b shows that the PEM improves the oscillation magnitudes of the rotor speed deviation of the synchronous machine connected to the same busbar. The oscillation amplitudes of *SG* 1 are smaller than those of *SG* 2 and *SG* 3. The electrolyser provides a damping effect on the synchronous machine connected to the same busbar.

The influence of the proposed model of the electrolyser as a load is also shown in Figures 20–22. Three ways of connecting PEM electrolysers were considered, as described in Figure 9. The first consists of using two electrochemical submodels, i.e., 2 × 50 MW in parallel on the DC side of the 12-pulse thyristor rectifier. The second is to use four electrochemical submodels in parallel, i.e., 4 × 25 MW. The last one is to use one electrochemical

model, i.e., 1 × 100 MW. These three ways affect the dynamic response of the rotor angle deviation and of the rotor speed deviation, as illustrated in Figures 20–22. Note that the dynamic responses associated with the 2 × 50 MW and 4 × 25 MW cases are close. This is due to the electrolyser being seen by the system as a dominant constant current load. Figures 20b, 21b, and 22b show that the 2 × 50 MW connection mode allows the PEM electrolyser to act as constant current loads. This supports the modelling result presented in Section 2.3.

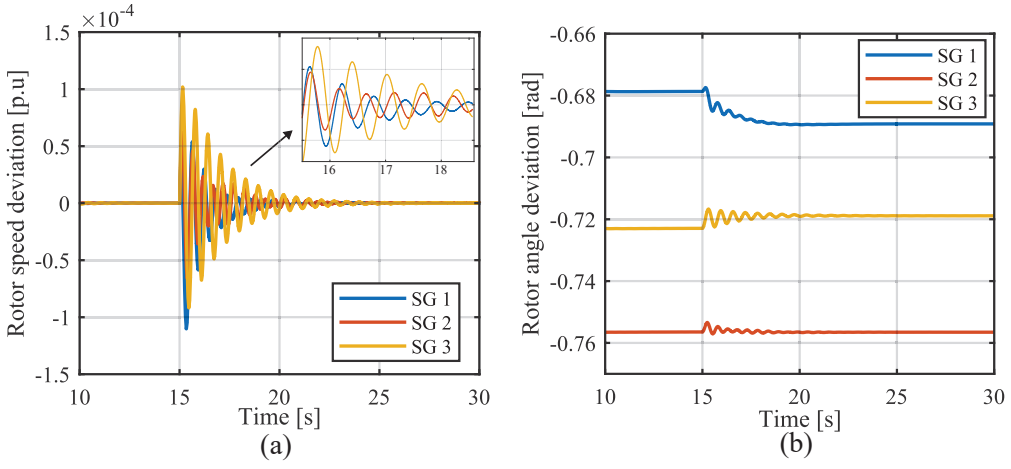

Figure 19. (**a**) Dynamic response of the rotor speed deviations ($\Delta\omega_i$) and (**b**) the dynamic response of the rotor angle deviations ($\Delta\theta_i$).

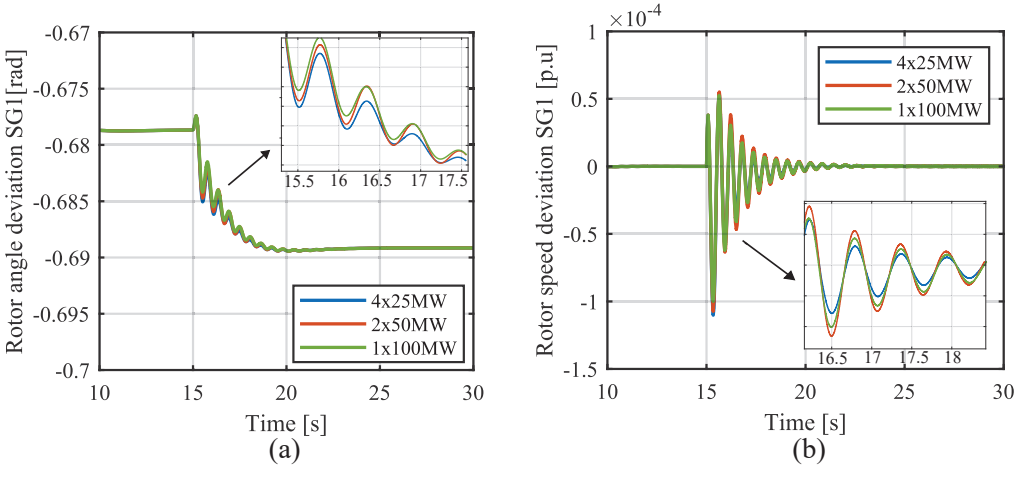

Figure 20. Dynamic response of electromechanical state variables of *SG* 1 when 100 MW of PEM electrolysers are connected to the grid at 15 s: (**a**) rotor angle deviation and (**b**) rotor speed deviation with the impact of modelling the electrolyser as a load.

The obtained results show that the effect of modelling the electrolyser as a load is more significant on the rotor angle variation and the rotor speed variation of the generator that shares the same busbar with the electrolyser.

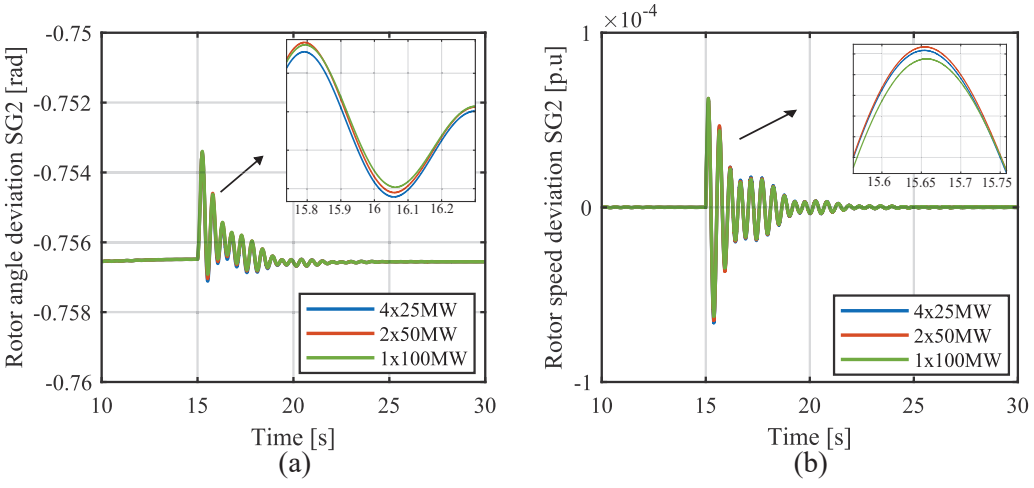

Figure 21. Dynamic response of electromechanical state variables of *SG* 2 when 100 MW of PEM electrolysers are connected to the grid at 15 s: (**a**) rotor angle deviation and (**b**) rotor speed deviation with the impact of modelling the electrolyser as a load.

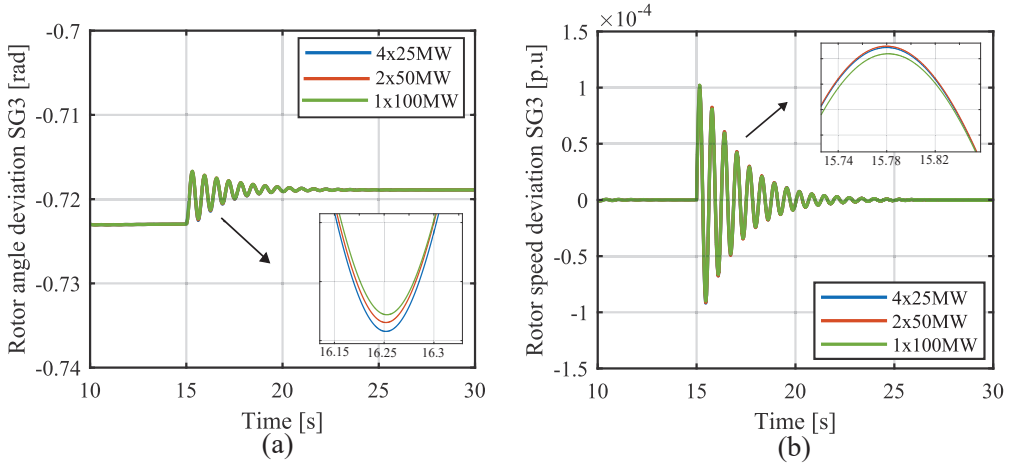

Figure 22. Dynamic response of electromechanical state variables of *SG* 3 when 100 MW of PEM electrolysers are connected to the grid at 15 s: (**a**) rotor angle deviation and (**b**) rotor speed deviation with the impact of modelling the electrolyser as a load.

- Decrease in the electrolyser current set point:

Figure 23 shows the results obtained by changing the electrolyser current set point from 21.797 kA to 21.577 kA (i.e., a 1% reduction). Figure 23a illustrates that the proposed current controller maintains the electrolyser current at the desired value. Figure 23b shows that the synchronism of the interconnected synchronous machines is maintained. The observed settling time is close to that of the first scenario.

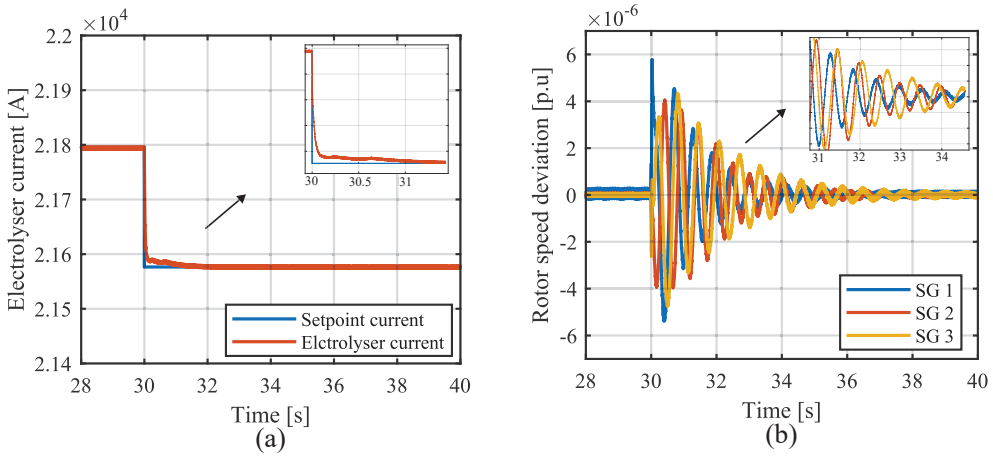

Figure 23. Dynamic responses of electromechanical state variables of *SG i* of electrolyser current: (**a**) DC electrolyser current and (**b**) rotor speed deviations $\Delta\omega_i$.

5. Conclusions

The effect of a large PEM electrolyser on the small-disturbance rotor angle stability was analyzed in this paper. First, the dynamic modelling of the PEM electrolyser and the control structure of the electrolyser current was proposed. Since several electrochemical PEM electrolyser models have been proposed in the literature, in this paper, we proposed a comparative analysis of the cell voltage dynamic response of these models to identify which model presents a better dynamic response. The time constant was considered as the metric for comparison and selection. The dynamic model of the selected PEM electrolyser was then used to propose a control structure to adjust the electrolyser current via the firing angle of a 12-pulse thyristor rectifier. Afterwards, we showed that as a load, the PEM electrolyser can be modelled as a combination of a constant impedance load fraction and a constant current load fraction. We showed that the percentage of the load modelled as either a constant impedance or a constant current load depends on the connection of the PEM electrolyser model to the DC side of the 12-pulse thyristor rectifier. Finally, the influence of the electrolyser on the rotor angle stability was assessed using an analytical analysis and time-domain simulations. The first method used a state-space model to evaluate the trajectories of the eigenvalues in the left-half complex plane. The obtained results show that the PEM electrolyser affects the electromechanical modes of synchronous machines. This effect consists of an increase in the oscillation frequencies of the modes and a decrease in the damping of the electromechanical modes. In contrast, it increases the damping of the electromechanical modes associated with the synchronous machine connected to the same busbar. The results show that to mitigate this effect, either the inertial constant or the damping torque coefficient can be adjusted. However, this can lead to a tradeoff between the two parameters when high values have to be set. The analytical results were validated through time-domain simulations. The results show the efficiency of the proposed control structure of the electrolyser current and the proposed model of the electrolyser when viewed as a load. In future work, the effect of a large PEM electrolyser on transient rotor angle stability will be addressed.

Author Contributions: Conceptualization, G.W.N., E.V.M., and E.D.J.; methodology, G.W.N., E.V.M., and E.D.J.; validation, G.W.N. and E.D.J.; investigation, G.W.N., E.V.M., and E.D.J.; writing—original draft preparation, G.W.N. and E.V.M.; writing—review and editing, G.W.N., E.V.M., and E.D.J. All authors have read and agreed to the published version of the manuscript.

Funding: This research is supported by the Energy Transition Funds project "BEST" organized by the Belgian FPS economy.

Institutional Review Board Statement: Not applicable.

Informed Consent Statement: Not applicable.

Data Availability Statement: Data are contained within the article.

Conflicts of Interest: The authors declare no conflict of interest.

Abbreviations

The following abbreviations and symbols are used in this manuscript:

PEM	Proton exchange membrane
SGs	Synchronous generators
PLL	Phase-locked loops
PI	Proportional–integral
EL	Electrolyser

Nomenclature

α	Rectifier firing angle
α_0	Nominal rectifier firing angle
a_1	Fraction of the load represented as a constant impedance load
a_2	Fraction of the load represented as a constant current load
A_{grid}	Dynamic matrix of the grid for the complete state-space model of the test system
B_{grid}	Input matrix for the complete state-space model of the test system
C_{dli}	Double layer capacity
C_{SGEL}	Observation matrix associated with the synchronous generators and electrolyser
δ_i	Relative rotor angle
ΔI_g	Vector matrix of current components of the synchronous generator
ΔU_g	Input matrix of the synchronous generator
$\Delta\theta$	Phase-angle submatrix of the network buses
ΔV	Voltage magnitude submatrix of the network buses
ΔV_g	Vector matrix of voltage magnitude and angle of the synchronous generator bus
ΔV_{NET}	Vector matrix formed by the voltage magnitude and angle submatrices of the network buses
ΔX	State vector composed of the state subvector of each synchronous generator
ΔX_{EL}	State variable of the electrolyser
ΔX_{SGEL}	State vector of generators and the electrolyser connected to the generator buses
D_i	Damping torque coefficient
D_{SGi}	Direct transmission matrices
$D_{SGi_{ik}}$	Submatrix associated with the synchronous generator
E_{fd_i}	Field voltage
H_i	Inertial constant
i_{cell}	Input current of the cell
i_{dc}	DC current of the electrolyser
i_{dc0}	Nominal electrolyser DC current at nominal active power
k	Ratio between the secondary and primary RMS phase-to-phase voltage of the transformer
k_i	Gain of the integral controller
k_p	Gain of the proportional controller
λ_i	Modes
L_f	Filter inductance
L_{int}	Interphase inductances
L_T	Leakage inductance of the transformer
μ	Overlap angle
ψ_{1q_i}	Damper winding 1q flux linkages
P_{El0}	Rated active power of the electrolyser
P_{El}	Active power of the electrolyser
P_{G_i}	Active power injected into bus i
P_{L_i}	Active power of the constant power load
Q_{G_i}	Reactive power injected into bus i

Q_{L_i}	Reactive power of the constant power load
R_{ct}	Charge transfer resistance
$R_{ct,a}$	Charge transfer resistance at the anode
$R_{ct,c}$	Charge transfer resistance at the cathode
R_d	Diffusion resistance
R_i	Charge transfer resistance
R_m	Ohmic resistance during the water-splitting reaction
τ_d	Diffusion time constant
θ_i	Rotor angle
T'_{dqo_i}	Transient time constants along the d axis and q axis
T_{M_i}	Mechanical torque
U_p	RMS phase-to-phase voltage at the primary end of the transformer
U_s	RMS phase-to-phase voltage at the secondary end of the transformer
V_{act}	Activation overpotential
$V_{act,a}$	Activation overpotential at the anode
$V_{act,c}$	Activation overpotential at the cathode
V_{cell}	Cell voltage across the proton exchange membrane stack
V_{rev}	Reverse voltage potential during the water-splitting reaction
ω_i	Speed of the rotor
ω_s	Synchronous angular speed of the rotor
X_{dq}	Synchronous reactances along the d axis and q axis
X_{1q_i}	Damper winding $1q$ reactance
X_{fd_i}	Field d-axis reactance
X_{mdq_i}	Magnetizing reactances along the d axis and q axis
X'_{dq_i}	Transient synchronous reactances along the d axis and q axis
Z_w	Warburg impedance

References

1. Tavakoli, S.D.; Dozein, M.G.; Lacerda, V.A.; Mañe, M.C.; Prieto-Araujo, E.; Mancarella, P.; Gomis-Bellmunt, O. Grid-Forming Services From Hydrogen Electrolyzers. *IEEE Trans. Sustain. Energy* **2023**, *14*, 2205–2219. [CrossRef]
2. Guilbert, D.; Vitale, G. Dynamic Emulation of a PEM Electrolyzer by Time Constant Based Exponential Model. *Energies* **2019**, *12*, 750. [CrossRef]
3. Tuinema, B.W.; Adabi, E.; Ayivor, P.K.; García Suárez, V.; Liu, L.; Perilla, A.; Ahmad, Z.; Rueda Torres, J.L.; van der Meijden, M.A.; Palensky, P. Modelling of large-sized electrolysers for real-time simulation and study of the possibility of frequency support by electrolysers. *IET Gener. Transm. Distrib.* **2020**, *14*, 1985–1992. [CrossRef]
4. Guilbert, D.; Vitale, G. Improved Hydrogen-Production-Based Power Management Control of a Wind Turbine Conversion System Coupled with Multistack Proton Exchange Membrane Electrolyzers. *Energies* **2020**, *13*, 1239. [CrossRef]
5. Ghazavi Dozein, M.; Maria De Corato, A.; Mancarella, P. Fast Frequency Response Provision from Large-Scale Hydrogen Electrolyzers Considering Stack Voltage-Current Nonlinearity. In Proceedings of the 2021 IEEE Madrid PowerTech, Madrid, Spain, 28 June–2 July 2021; pp. 1–6. [CrossRef]
6. Dozein, M.G.; Jalali, A.; Mancarella, P. Fast Frequency Response From Utility-Scale Hydrogen Electrolyzers. *IEEE Trans. Sustain. Energy* **2021**, *12*, 1707–1717. [CrossRef]
7. Dozein, M.G.; De Corato, A.M.; Mancarella, P. Virtual Inertia Response and Frequency Control Ancillary Services From Hydrogen Electrolyzers. *IEEE Trans. Power Syst.* **2023**, *38*, 2447–2459. [CrossRef]
8. Chen, M.; Chou, S.F.; Blaabjerg, F.; Davari, P. Overview of Power Electronic Converter Topologies Enabling Large-Scale Hydrogen Production via Water Electrolysis. *Appl. Sci.* **2022**, *12*, 1906. [CrossRef]
9. Solanki, J.; Fröhleke, N.; Böcker, J. Implementation of Hybrid Filter for 12-Pulse Thyristor Rectifier Supplying High-Current Variable-Voltage DC Load. *IEEE Trans. Ind. Electron.* **2015**, *62*, 4691–4701. [CrossRef]
10. Samani, A.E.; D'Amicis, A.; De Kooning, J.D.; Bozalakov, D.; Silva, P.; Vandevelde, L. Grid balancing with a large-scale electrolyser providing primary reserve. *IET Renew. Power Gener.* **2020**, *14*, 3070–3078. [CrossRef]
11. Kundur, P. *Power System Stability and Control*; McGraw Hill: New York, NY, USA,1994.
12. Hernández-Gómez, A.; Ramirez, V.; Guilbert, D.; Saldivar. Cell voltage static-dynamic modeling of a PEM electrolyzer based on adaptive parameters: Development and experimental validation. *Renew. Energy* **2021**, *163*, 1508–1522. [CrossRef]
13. Olivier, P.; Bourasseau, C.; Bouamama, P.B. Low-temperature electrolysis system modelling: A review. *Renew. Sustain. Energy Rev.* **2017**, *78*, 280–300. [CrossRef]
14. Lebbal, M.; Lecœuche, S. Identification and monitoring of a PEM electrolyser based on dynamical modelling. *Int. J. Hydrogen Energy* **2009**, *34*, 5992–5999. [CrossRef]

15. Hernández-Gómez, A.; Ramirez, V.; Guilbert, D. Investigation of PEM electrolyzer modeling: Electrical domain, efficiency, and specific energy consumption. *Int. J. Hydrogen Energy* **2020**, *45*, 14625–14639. [CrossRef]
16. Hernández-Gómez, A.; Ramirez, V.; Guilbert, D.; Saldivar, B. Development of an adaptive static-dynamic electrical model based on input electrical energy for PEM water electrolysis. *Int. J. Hydrogen Energy* **2020**, *45*, 18817–18830. [CrossRef]
17. Abdin, Z.; Webb, C.; Gray, E. Modelling and simulation of a proton exchange membrane (PEM) electrolyser cell. *Int. J. Hydrogen Energy* **2015**, *40*, 13243–13257. [CrossRef]
18. Martinson, C.; van Schoor, G.; Uren, K.; Bessarabov, D. Characterisation of a PEM electrolyser using the current interrupt method. *Int. J. Hydrogen Energy* **2014**, *39*, 20865–20878. [CrossRef]
19. Rubio, M.; Urquia, A.; Dormido, S. Diagnosis of PEM fuel cells through current interruption. *J. Power Sources* **2007**, *171*, 670–677. [CrossRef]
20. Garcia-Navarro, J.; Schulze, M.; Friedrich, K. Measuring and modeling mass transport losses in proton exchange membrane water electrolyzers using electrochemical impedance spectroscopy. *J. Power Sources* **2019**, *431*, 189–204. [CrossRef]
21. Mondal, D.; Chakrabarti, A.; Sengupta, A. *Power System Small Signal Stability Analysis and Control*; Elsevier: Amsterdam, The Netherlands, 2020.
22. Olivier, P. Modélisation et Analyse du Comportement Dynamique d'un Système d'Électrolyse PEM Soumis à des Sollicitations Intermittentes: Approche Bond Graph. Ph.D. Thesis, Université Lille 1, Villeneuve d'Ascq, France, 2016.
23. Rashid, M.H. *Power Electronics Handbook Devices, Circuits, and Applications*; Elsevier: Amsterdam, The Netherlands, 2011.
24. Ndiwulu, G.W.; Matalatala, M.; Lusala, A.K.; Bokoro, P.N. Distributed Hybrid Power-Sharing Control Strategy within Islanded Microgrids. In Proceedings of the 2023 31st Southern African Universities Power Engineering Conference (SAUPEC), Johannesburg, South Africa, 24–26 January 2023; pp. 1–6. [CrossRef]
25. Zacharia, L.; Asprou, M.; Kyriakides, E.; Polycarpou, M. Effect of dynamic load models on WAC operation and demand-side control under real-time conditions. *Int. J. Electr. Power Energy Syst.* **2021**, *126*, 106589. [CrossRef]
26. Pasiopoulou, I.; Kontis, E.; Papadopoulos, T.; Papagiannis, G. Effect of load modeling on power system stability studies. *Electr. Power Syst. Res.* **2022**, *207*, 107846. [CrossRef]
27. Villegas Pico, H.N.; Aliprantis, D.C.; Lin, X. *Transient Stability Assessment of Power Systems with Uncertain Renewable Generation*; Technical Report; National Renewable Energy Lab. (NREL): Golden, CO, USA, 2017.

electronics

MDPI

Article

Analysis of Phase-Locked Loop Filter Delay on Transient Stability of Grid-Following Converters

Chenglin Zhang *, Junru Chen and Wenjia Si

The College of Electrical Engineering, Xinjiang University, Urumqi 830046, China; junru.chen@xju.edu.cn (J.C.); wenjia_si@stu.xju.edu.cn (W.S.)
* Correspondence: 107552104082@stu.xju.edu.cn

Abstract: To ensure precise phase estimation within the q-axis of the phase-locked loop (PLL), integrating a filter into the q-axis loop is essential to mitigate grid-voltage harmonics. Nevertheless, the intrinsic delay characteristics of this filter impede PLL synchronization during significant grid disturbances. This study begins by developing mathematical models for three types of filters—moving-average filter (MAF) for eliminating odd harmonic components, dq-frame cascaded delayed signal cancellation (dqCDSC) filter, and notch filter (NF). Following the reduction in filter orders, a third-order nonlinear large-signal model of the PLL, incorporating an additional q-axis internal filter, is formulated. Using phase plane analysis, this study investigates the transient synchronism of the grid-following converter (GFL) and explores the influence of delay time constants from the three PLL filters on its behavior while delineating the boundaries of their basins of attraction. Theoretical findings indicate that, relative to the traditional SRF-PLL, incorporating an internal filter into the PLL compromises the transient synchronous stability of GFL. Specifically, greater filter delay time constants exacerbate the GFL's vulnerability to transient instability amid substantial grid disturbances. Hence, careful consideration is essential when using MAF-PLL and NF-PLL in situations demanding high synchronization stability. The theoretical analyses are validated using Matlab/Simulink to verify their accuracy.

Keywords: PLL; filter; grid-following converter; synchronous stability; phase plane; attraction domain

Citation: Zhang, C.; Chen, J.; Si, W. Analysis of Phase-Locked Loop Filter Delay on Transient Stability of Grid-Following Converters. *Electronics* **2024**, *13*, 986. https://doi.org/10.3390/electronics13050986

Academic Editor: Jen-Hao Teng

Received: 10 February 2024
Revised: 28 February 2024
Accepted: 2 March 2024
Published: 5 March 2024

1. Introduction

To fulfill the strategic goal of establishing a new power system primarily reliant on renewable energy sources [1,2], grid-connected converters have emerged as a pivotal interface, enabling the swift advancement of renewable energy generation [3]. Consequently, it has progressively supplanted synchronous generator power as the primary energy source within the power grid. This transformative shift has ushered in a "double high" trend within the power system, characterized by a significant presence of both renewable energy sources and power electronic equipment [4]. The reliable and secure operation of such "double high" systems critically hinges on the effective performance of grid-connected converters. In recent years, stability concerns surrounding grid-connected converters have garnered significant attention, notably in the aftermath of incidents such as the UK's 8.9 blackout and the 2021 Texas blackout [5,6].

At present, the predominant synchronization control strategies for grid-connected converters involve proportional-resonant (PR) control in the $\alpha\beta$ coordinate system [7–9] and proportional-integral (PI) control with phase-locked loops (PLLs) synchronization in the dq coordinate system, attributed to the enhanced robustness of PI control. As a result, the PLL synchronization control strategy is uniformly applied across wind and photovoltaic grid-connected converters. Grid-connected converters employing PLL synchronization are also known as grid-following converters (GFLs). The current implementation of GFL heavily relies on PLL to monitor the grid-voltage phase at the point of connection (POC)

for grid synchronization [10]. The voltage present at the POC is equivalent to the voltage output by the GFL. Consequently, the dynamic characteristics of the PLL significantly influence the grid-tied stability of the GFL [11]. References [12,13] advocate for integrating a filter into the PLL's q-axis control loop to enhance the GFL's stability, under minor disturbances in high harmonic grid environments. Moreover, the literature [14] suggests the incorporation of a notch filter (NF) or multiple NFs into the PLL control loop to eliminate harmonic components selectively. Reference [15] explores the use of a moving-average filter (MAF) within the PLL control loop, functioning as both a linear phase filter and, under certain conditions, an ideal low-pass filter. Additionally, in reference [16], the investigation into repetitive regulators (RRs) within the PLL control loop demonstrates their efficacy in attenuating harmonic components and providing rapid dynamic responses to disturbances. Proposing delayed signal cancellation, reference [17,18] introduces the dq-frame cascaded delayed signal cancellation (dqCDSC) to enhance PLL's phase-locking performance under high harmonic grid conditions. Additionally, in addressing approaches to attenuate grid harmonics, references [19,20] focus on leveraging the inherent control strategies of GFL. They introduce a cooperative control framework based on a hybrid algorithm, aimed at mitigating the adverse effects of grid harmonics on GFL performance. However, the studies mentioned above overlook the impact of inherent filter delay characteristics on GFL's synchronization during significant disturbances.

The synchronization stability of a converter is defined by its ability to sustain synchronization with the grid despite significant disturbances [21]. The extensive transmission distances associated with renewable energy sources and the substantial grid impedance at the POC contribute to positive feedback in the synchronization loop, amplifying synchronization instability. Reference [22] introduced the quasi-static large signal (QSLS) model to elucidate this phenomenon, leveraging phase plane analysis, the equal-area criterion, and the energy function method to dissect the synchronization stability mechanism of the GFL. In a related study, reference [23] applied the equal-area criterion, based on principles of kinetic and potential energy conservation, to assess whether the operational state during a fault could revert to stability, thereby evaluating the transient synchronization stability of the GFL. Additionally, reference [24] visually depicted transient instability phenomena without analytical tools, utilizing numerical solutions of first and second-order nonlinear system equations to graph phase trajectories. Moreover, reference [25] formulated an analytical Lyapunov energy function, deriving a more conservative stability region. Furthermore, reference [26] investigated the interaction between the current control and the PLL loop, devising a more intricate QSLS model to scrutinize transient synchronization stability. Additionally, taking into account the synergistic impact of active filters at the GFL output, current regulation, and the PLL feedback mechanism, the literature [27–29] introduces an advanced PLL parameterization strategy aimed at improving the synchronizing stability of GFL amidst weak grid scenarios. The modeling and analysis of transient stability in GFL typically assume an environment devoid of grid harmonics. However, real-world scenarios necessitate the integration of filters within the PLL control loop to eliminate these harmonics. During grid faults, the delay characteristics inherent in these filters can significantly influence the synchronization of GFL with the grid.

1.1. Novelty and Contribution

In this research, the impact of grid harmonics on the transient stability of GFL is included in the modeling and analysis. Diverging from the traditional presumption of a harmonics-free grid environment, this manuscript highlights the critical necessity of implementing filters within the PLL control scheme to eliminate harmonics, as well as to address the consequential effects of filter delays on the synchronizing stability of GFL systems. By exploiting the higher-order nonlinear characteristics inherent in filters, a third-order nonlinear large-signal model that integrates the filter's PLL is developed herein. This model facilitates an investigation into the influence of varying filter delay time constants

on the synchronizing stability of GFL, guiding the strategic selection of PLL filters for scenarios where enhanced synchronizing stability is imperative.

1.2. Chapter Organization

The ensuing segments of this manuscript scrutinize the ramifications of filter delays on the transient stability of GFL, structured as follows. Section 2 presents the mathematical modeling of GFL, develops mathematical models for three distinct inner-loop filters, and realizes filter model order reduction, laying the foundation for the large-signal analysis in Section 3. Section 3 investigates the mechanism underlying the effect of filter delays on the transient stability of GFL. The simulation results presented in Section 4 are used to validate the theoretical analysis provided in Sections 2 and 3. Section 5 succinctly concludes the discourse.

2. Modeling of Synchronization Stability

2.1. GFL Modeling

The system structure of the GFL is illustrated in Figure 1. Here, $\boldsymbol{V}_{\mathbf{POC}}$ and $\boldsymbol{V}_{\mathbf{g}}$ denote the voltages at the POC and the grid, respectively. The injected current into the grid is represented by $\boldsymbol{I}$, while l_f refers to the filter located at the converter's output port. Additionally, r_g and l_g denote the resistance and inductance on the grid side. The DC voltage source is represented as U_{dc}, typically maintained at a constant value. The synchronization between the GFL and the grid is achieved using the synchronous reference frame phase-locked loop (SRF-PLL), with θ_{pll} and ω_{pll} representing its output phase angle and frequency, respectively. Current control is effected through a PI regulator, wherein k_{pc} and k_{ic} delineate the proportional and integral coefficients of the controller, correspondingly.

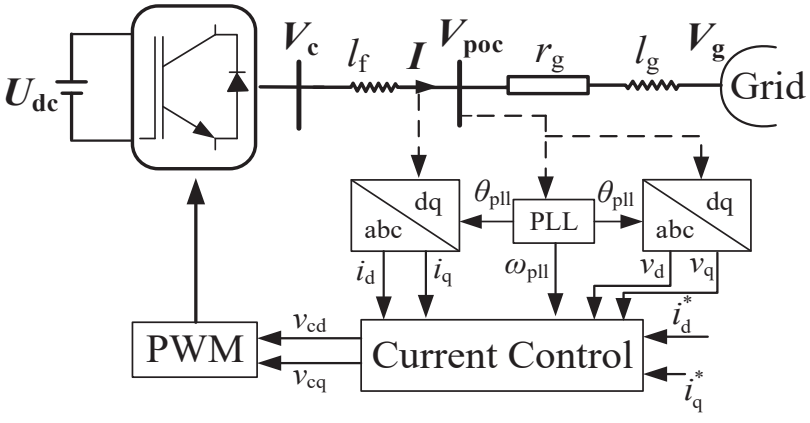

Figure 1. Grid-following converter system structure.

The voltage at the POC can be obtained from Figure 1:

$$\boldsymbol{V}_{\mathrm{POC}} = \boldsymbol{V}_g + \boldsymbol{I}(Z_g) \tag{1}$$

where Z_g represents the grid impedance, given by $Z_g = r_g + j\omega_{pll} l_g$. The q-axis voltage component can be obtained by performing a Park transformation on $\boldsymbol{V}_{\mathbf{POC}}$:

$$V_{pocq} = r_g i_q^* + \omega_{pll} l_g i_d^* - V_g \sin\delta \tag{2}$$

In (2), $\delta = \theta_{pll} - \theta_g$, where θ_g denotes the grid phase, the output current of the GFL maintains a constant reference current value i_d^* owing to the significantly shorter time scale of the current loop control compared to the PLL. The PLL, through the application of a PI

regulator, achieves grid synchronization by ensuring $V_{\mathrm{pocq}} = 0$, as specified in its governing dynamic equation.

$$\begin{cases} \frac{d\theta_{\mathrm{pll}}}{dt} = \omega_{\mathrm{pll}} = \omega_{\mathrm{g}} + \Delta\omega_{\mathrm{pll}} \\ \frac{d\omega_{\mathrm{pll}}}{dt} = k_{\mathrm{p,pll}} V_{\mathrm{pocq}} + k_{\mathrm{i,pll}} \int V_{\mathrm{pocq}} dt \end{cases} \tag{3}$$

where ω_{g} signifies the nominal angular frequency of the grid. If V_{pocq} consists solely of fundamental frequency components, the PLL can accurately estimate the grid phase by setting $V_{\mathrm{pocq}} = 0$. Yet, if there are harmonic components in V_{pocq}, incorporating filters into the PLL control loop becomes essential to eliminate these components and ensure precise grid phase estimation.

2.2. Filter Modeling

In practical scenarios, the main grid-voltage harmonic components typically include the −5th, +7th, −11th, and +13th harmonics. Even-order harmonics and the DC component are ignored due to their notably lower amplitudes, in comparison to the odd-order harmonics. Consequently, the mathematical model of the internal loop filter is primarily tailored to eliminate these specified harmonic components. Figure 2 illustrates the PLL configuration incorporating the additional internal loop filter. Given our focus on fundamental frequency synchronization, the filter exhibits delay characteristics when projected onto the low-frequency range. Therefore, subsequent discussions treat the three filters as first-order inertial elements in modeling synchronization stability.

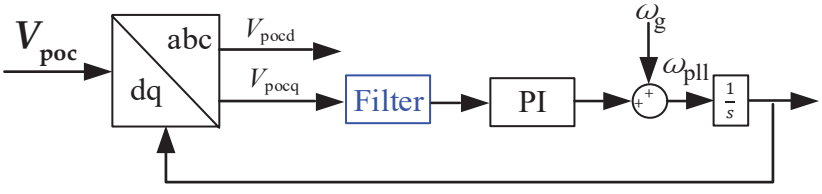

Figure 2. The PLL schematic diagram of the q-axis inner loop filter.

2.2.1. MAF

The MAF, alternatively referred to as a rectangular window filter, is characterized by its transfer function in the Laplace domain, given as:

$$G_{\mathrm{MAF}}(s) = \frac{1 - e^{-T_{\mathrm{w}}s}}{T_{\mathrm{w}}s} \tag{4}$$

The equation defines T_{w} as the window length of the MAF. MAF can eliminate DC components and frequency components that are integer multiples of $1/T_{\mathrm{w}}$ (in Hz). When the grid voltage consists solely of odd-order harmonic components, the standard configuration for MAF's window length is $T_{\mathrm{w}} = T/2$, where T represents the fundamental period of the grid voltage.

When G_{MAF}(s) is integrated into the q-axis loop of the PLL, its $e^{-T_{\mathrm{w}}s}$ term becomes a non-rational function, which is not conducive to subsequent analysis of transient stability. Utilizing the first-order Pade approximation, we derive the following:

$$e^{-T_{\mathrm{w}}s} \approx \frac{1 - T_{\mathrm{w}}s/2}{1 + T_{\mathrm{w}}s/2} \qquad G_{\mathrm{MAF}}(s) \approx \frac{1}{T_{\mathrm{w}}s/2 + 1} \tag{5}$$

The approximated transfer function yields a first-order inertial component. By defining $T_{\mathrm{w}}/2 = T_{\mathrm{MAF}}$ as the time delay constant of the MAF, Figure 3a is utilized to assess the accuracy of this approximation through a comparison of the Bode plot between G_{MAF}(s) and its approximated transfer function. It is evident that the approximation effectively represents the dynamic behavior of G_{MAF}(s).

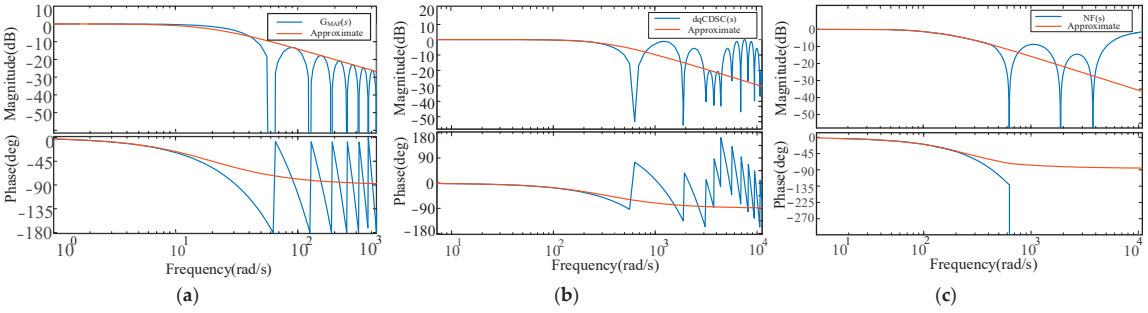

Figure 3. Bode plots of the filter transfer function and its first-order counterpart. (**a**) Comparison of $G_{MAF}(s)$ with approximate. (**b**) Comparison of $dqCDSC_{n1,n2}(s)$ with approximate. (**c**) Comparison of NF(s) with approximate.

2.2.2. dqCDSC

In the dq coordinate system, harmonic components demonstrate "half-wave symmetry", allowing for the summation of delayed harmonic components to eliminate those injected into the q-axis loop. This process maintains the DC component in the dq coordinate system unchanged. It is referred to as dqDSC [18]. Its transfer function is as follows:

$$\mathrm{dqDSC}_n(s) = \frac{1}{2}(1 + e^{-\frac{T}{n}s}) \tag{6}$$

In (6), n represents the delay factor, where its selection can prevent certain characteristic harmonic components. In most scenarios, a single dqDSC operator might be insufficient to counteract associated harmonic components. Depending on the harmonic type in the grid and existing applications, multiple dqDSC operators with specific delay factors are usually cascaded. Equation (7) describes dqCDSC in the Laplace domain, where m represents the quantity of cascaded dqDSC operators. Figure 4 illustrates the time-domain implementation of $\mathrm{dqCDSC}_{n1,n2,\ldots,n_m}$.

$$\begin{aligned}\mathrm{CDSC}_{n_1,n_2,\ldots,n_m}(s) = dq\mathrm{DSC}_{n_1}(s) \times dq\mathrm{DSC}_{n_2}(s) \\ \times \cdots \times dq\mathrm{DSC}n_m(s)\end{aligned} \tag{7}$$

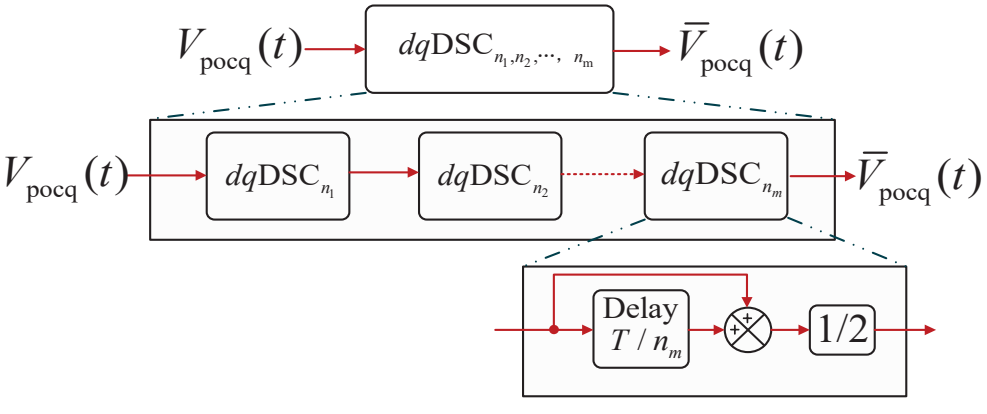

Figure 4. Time-Domain implementation of dqCDSC operator.

The presence of odd-order harmonic components alone in the grid necessitates the cascading of two dqDSC operators with delay factors of $n_1 = 4$ and $n_2 = 24$. Consequently, the transfer function is formulated as:

$$\mathrm{dqCDSC}_{n_1,n_2}(s) = \frac{1}{2}(1 + e^{-(T/n_{1)}s}) \times \frac{1}{2}(1 + e^{-(T/n_2)s}) \tag{8}$$

Similarly, based on the first-order Pade approximation, substitute $e^{-(T/n)s} \approx \frac{1-(\frac{T}{2n})s}{1+(\frac{T}{2n})s}$ yields the following:

$$\mathrm{dqCDSC}_{n1,n2}(s) \approx \frac{1}{\frac{T^2}{4n_1n_2}s^2 + (\frac{T}{2n_1} + \frac{T}{2n_2})s + 1} \tag{9}$$

In the low-frequency range, the s^2 term can be neglected, further yielding the following:

$$\mathrm{dqCDSC}_{n1,n2}(s) \approx \frac{1}{\frac{T}{2}(1/n_1 + 1/n_2)s + 1} \tag{10}$$

The time delay constant of the dqCDSC filter is defined as $T_{\mathrm{dq}CDSC} = T \times (1/n_1 + 1/n_2)/2$. Based on Figure 3b, the approximated outcome still predicts the dynamic behavior of its original transfer function.

2.2.3. NF

The NF is a band-stop filter designed to substantially reduce harmonic components within a defined frequency band while maintaining minimal impact on other frequency components. The transfer function representing NF [30] is:

$$\mathrm{NF}(s) = \frac{s^2 + \omega_{\mathrm{nf}}^2}{s^2 + (\omega_{\mathrm{nf}}/Q)s + \omega_{\mathrm{nf}}^2} \tag{11}$$

where ω_{nf} represents the notch frequency and Q denotes the quality factor. To eliminate odd-order harmonic components in the phase-locked loop's q-axis loop, cascading three NFs is necessary. Each NF has notch frequencies set, respectively, at $2\pi(2 \times 50)$, $2\pi(6 \times 50)$, and $2\pi(12 \times 50)$rad/s. The selection of the quality factor Q depends on the expected range of variation in the grid frequency. Reference [24] proposes that when Q is chosen as $Q = \sqrt{2}$, NF effectively suppresses odd-order harmonic components even under significant variations in the grid frequency.

When three NFs are cascaded, the equation representing their transfer function is as follows:

$$\mathrm{NFs}(s) = \mathrm{NF}_{\omega_{\mathrm{nf}_1}}(s) \times \mathrm{NF}_{\omega_{\mathrm{nf}_2}}(s) \times \mathrm{NF}_{\omega_{\mathrm{nf}_3}}(s) \tag{12}$$

Equation (12) presents an 8th-order transfer function, which challenges mathematical simplification. Therefore, this study employs system identification techniques to fit the frequency, magnitude, and phase data obtained from the frequency domain response model in (12). Consequently, a first-order transfer function is derived through this identification process.

$$\mathrm{NFs}(s) \approx \frac{125}{125 + s} \tag{13}$$

A comparison between the transfer functions of (12) and (13) is conducted using a Bode plot. Figure 3c illustrates that, especially in the low-frequency range, the output magnitude of the identified transfer function closely aligns with that of the original transfer function. The accuracy of the fitted results in this low-frequency spectrum indicates a close correspondence between the identified and original transfer functions.

Based on the aforementioned, the transfer functions of these three filters can be consistently represented as first-order inertial elements. Their individual time constants correspond to the delay time constants of the filters, as illustrated in Table 1.

Table 1. The time constants of three filters.

PLL	MAF-PLL	dqCDSC-PLL	NFs-PLL
Time constant	5×10^{-3} s	2.9×10^{-3} s	8×10^{-3} s

3. Synchronization Stability Analysis

3.1. 3rd PLL QSLS Model

Derived from the reduced-order filter transfer functions in the preceding section, they can all be equivalently represented as first-order inertial elements. This section initially establishes the large-signal model of the PLL incorporating a first-order inertial element [31]. The introduction of this inertial element transforms the PLL from a second-order system to a third-order system, as illustrated in Figure 5.

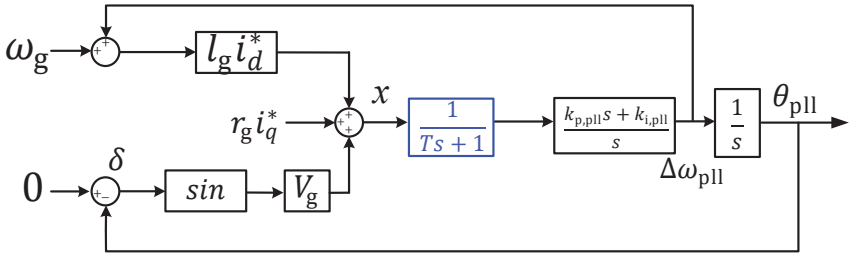

Figure 5. The QSLS model of 3rd PLL.

The output from the inertial element depicted in Figure 5 is considered the state variable x, and δ, and $\Delta\omega_{pll}$ represent the outputs of the remaining two integrators. These three state variables collectively portray the system's time-domain behavior. The state variables $(\delta, \Delta\omega_{\mathrm{pll}}, x) = (x_1, x_2, x_3)$ are defined, facilitating the formulation of the state-space equations for the third-order PLL as depicted in (14).

$$\begin{cases} \dot{x}_1 = x_2 = f_1 \\ \dot{x}_2 = k_{\mathrm{p,pll}}(r_g i_q^* + (x_2 + \omega_g) l_g i_d^* - V_g \sin x_1 - x_3)/T \\ \qquad\qquad + k_{\mathrm{i,pll}} x_3 = f_2 \\ \dot{x}_3 = (r_g i_q^* + (x_2 + \omega_g) l_g i_d^* - V_g \sin x_1 - x_3)/T = f_3 \end{cases} \tag{14}$$

Due to the nonlinear characteristics of the third-order PLL system integrating inertial elements, this study utilizes phase-plane analysis for numerical solutions [32]. This method, employing the ode45 algorithm, illustrates the trajectory of the numerical solution of the nonlinear system under specific initial conditions. Thus, it visually captures the system's dynamics, stability, equilibrium points, and the influence of initial states of the system behavior.

Before analyzing transient stability, it is crucial to evaluate the existence and stability of equilibrium points during transients. Setting the state equations (14) to zero—$f_1 = 0, f_2 = 0$, $f_3 = 0$—facilitates the determination of the system's two equilibrium points: $\delta_0(x_{10}, x_{20}, x_{30})$ and $\delta_u(\pi - x_{10}, x_{20}, x_{30})$

$$x_{10} = \arcsin\left(\frac{r_g i_q^* + \omega_g l_g i_d^*}{V_g}\right), x_{20} = 0, x_{30} = 0 \tag{15}$$

Under the condition of $V_g > r_g i_q^* + \omega_g l_g i_d^*$, δ_u is always unstable. Therefore, we primarily study the stability of the equilibrium points of δ_0 and regard them as the equilibrium points for normal operation.

3.2. Transient Stability Analysis Due to Time Constant of the Inertial Element

In the absence of an inertial element in the q-axis loop of the PLL, when the grid-voltage amplitude drops to $V_{g,f}$, the proportional component of the PI controller responds instantaneously, leading to a non-zero initial velocity $\Delta\omega_{pll}(t_0^+)$ and an input error $V_{pocq}(t_0^+)$ at time t_0^+.

$$\Delta\omega_{pll}(t_0^+) = \frac{k_{p,pll}(V_{g,0} - V_{g,f})\sin\delta_0}{1 - k_{p,pll} l_g i_d^*} \tag{16}$$

$$V_{pocq}(t_0^+) = l_g i_d^* \Delta\omega_{pll}(t_0^+) + (V_{g,0} - V_{g,f})\sin\delta_0 \tag{17}$$

In (16) and (17), $V_{g,0}$ denotes the initial grid-voltage value, while $\Delta\omega_{pll}(t_0^+)$ and $V_{pocq}(t_0^+)$ are both positive values. During a sustained fault, the dynamic response of GFL is as follows:

$$V_{pocq}(t) = l_g i_d^* \Delta\omega_{pll}(t) + V_{g,0}\sin\delta_0 - V_{g,f}\sin(\delta_0 + \int_0^{t_1} \Delta\omega_{pll}(t)dt) \tag{18}$$

$$\Delta\omega_{pll}(t) = k_{p,pll} V_{pocq}(t) + k_{i,pll}\int_0^{t_1} V_{pocq}(t)dt \tag{19}$$

where t_1 represents the time required for the PI controller to attain a steady state without the presence of an inertial element. When incorporating an inertial element into the q-axis loop of the PLL, the integrator within the inertial element mitigates sudden fluctuations in the state variable x_3, leading to the following expression:

$$\Delta\widetilde{\omega}_{pll}(t_0^+) = 0 \tag{20}$$

$$\widetilde{V}_{pocq}(t_0^+) = (V_{g,0} - V_{g,f})\sin\delta_0 \tag{21}$$

Hence, it follows that $\Delta\omega_{pll}(t_0^+) > \Delta\widetilde{\omega}_{pll}(t_0^+)$, $V_{pocq}(t_0^+) > \widetilde{V}_{pocq}(t_0^+)$. The behavior of the inertial element and the PI controller throughout the fault duration is as follows:

$$\widetilde{V}_{pocq}(t) = \int_0^{t_2} \frac{1}{T}(V_{pocq}(t) - \widetilde{V}_{pocq}(t))dt + V_{pocq}(t_0^+) \tag{22}$$

$$\Delta\widetilde{\omega}_{pll}(t) = k_{p,pll}\widetilde{V}_{pocq}(t) + k_{i,pll}\int_0^{t_3} \widetilde{V}_{pocq}(t)dt \tag{23}$$

where t_2 and t_3 denote the time needed for the inertial element and the PI controller output response to attain steady-state, respectively. Owing to the delayed response of the inertial element, t_1 the time required for the PI controller to rectify the same error is shorter than t_3. Furthermore, as the time constant T of the inertial element increases, the output voltage $\widetilde{V}_{pocq}$ decreases, leading to an increase in integration accumulation and an elongation of the time t_2 required to reach a steady state. Consequently, this results in a larger transient peak phase of the PLL. Therefore, the inclusion of the inertial element exacerbates synchronization stability.

The analysis conducted previously suggested that incorporating an inertial element led to an increase in the transient peak phase of the PLL, consequently undermining the transient synchronization stability of the GFL. To formulate comprehensive conclusions, this study incorporates the parameters outlined in Section 4 into the transient stability analysis model. Subsequently, numerical techniques are employed to calculate the transient peak phase of the PLL, varying V_g and T, as depicted in Figure 6. The surface plot demonstrates

that, as the magnitude of the voltage drop rises, the transient peak phase similarly increases, particularly with larger time constants associated with the inertial element.

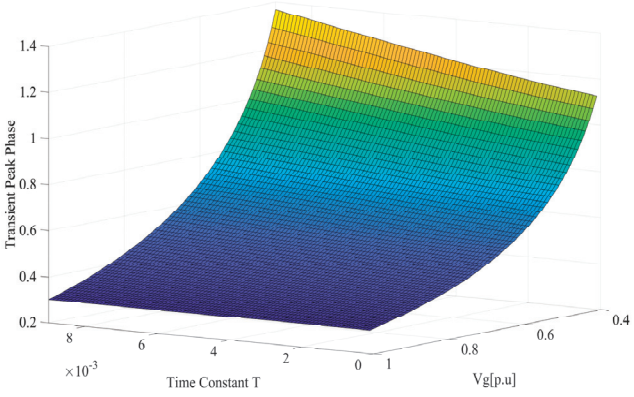

Figure 6. Surface plot of transient peak phase variation with V_g and T.

3.3. Estimation of Attraction Domains

In the domain of large-signal systems, the detection of equilibrium points amidst transient conditions does not guarantee stability during such periods. It is critical to delineate the extent of 'attraction' for these points, defined as the domain of attraction. If the initial state and trajectory of the system deviate from this domain, the risk of transient instability becomes imminent. Therefore, the domain of attraction underscores the system's capability to counteract disturbances, serving as an indispensable index for evaluating system stability [25,33]. Depicted in Figure 7 are the basins of attraction for the SRF-PLL and three additional filters within the PLL, calculated using the ode45 algorithm and parameters specified in Section 4. The order of the basin areas, ranked from largest to smallest, is $S_{\text{SRF-PLL}} > S_{\text{dqCDSC-PLL}} > S_{\text{MAF-PLL}} > S_{\text{NFs-PLL}}$. This observation implies that as the filter delay time constants increase, the basin area decreases. Larger filter delay time constants exacerbate transient synchronization stability issues.

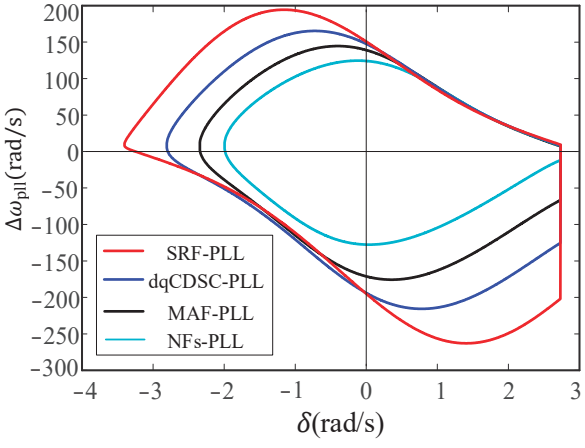

Figure 7. The attraction domain of the SRF-PLL and PLLs with additional filters.

To validate the accuracy of the attraction domain delineated, we consider the NFs-PLL as an exemplar. When the grid voltage plummets to 0.05 p.u, the absence of equilibrium points in the system signifies instability. The trajectory during the fault event is

depicted [34,35] as curve *l* in Figure 8. Subsequently, upon reaching point A after 37.62 ms, coinciding with the fault clearance, the system follows trajectory a, ultimately reverting to the equilibrium point. However, upon reaching point B after 45.2 ms, although the fault is rectified, the post-fault trajectory deviates along path b, resulting in transient instability. The attraction domain illustrated in this study exhibits a degree of conservatism. However, this conservative approach provides a safety buffer in fault detection and clearance, mitigating the risk of undetected GFL instability resulting from grid faults. This, in turn, helps prevent situations where protective devices fail to trigger, thereby averting the escalation of faults.

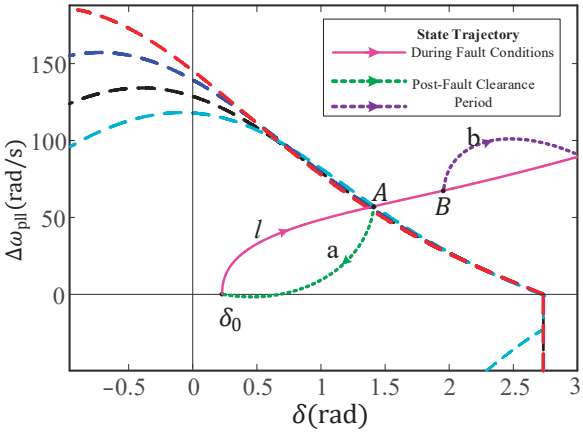

Figure 8. Validation of the attraction domain.

Figure 9 juxtaposes the phase trajectory plots of the SRF-PLL with three additional filter-based PLLs. When subjected to identical fault voltages, the SRF-PLL and dqCDSC-PLL, featuring smaller filter time delay constants, converge towards the post-fault equilibrium point. Conversely, the MAF-PLL and NFs-PLL, equipped with larger filter time delay constants, exhibit transient instability under the same fault scenario. The maximum phase value of the trajectory and the maximum deviation from the equilibrium point denote the transient peak phase. It is evident that during grid faults, the incorporation of additional filters leads to an escalation in the transient peak phase of the PLL. A heightened transient peak phase signifies an increased likelihood of the GFL transitioning to an unstable equilibrium point δ_u. Consequently, the integration of filters exacerbates the transient synchronization stability of the GFL [36,37].

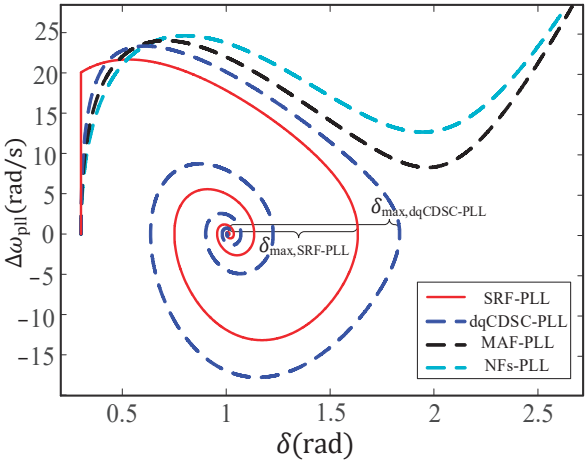

Figure 9. Phase trajectory plots of SRF-PLL and PLL with additional filters under fault conditions.

4. Simulation Validation

Electromagnetic transient models (EMTs)of the GFL are individually developed in Matlab/Simulink to enhance the verification of the theoretical analysis. The parameters required for the simulation model are as detailed in Table 2.

Table 2. Main parameters of GFL.

Parameter	Value	Parameter	Value
Grid voltage V_g	220 V	Converter capacity	5000 W
Grid inductance l_g	0.025 H	Grid resistance r_g	0.1 Ω
Active current reference value i_d^*	11.72 A	Reactive current reference value i_q^*	0 A
Proportional coefficients of PLL $k_{p,pll}$	0.3	Integral coefficients of PLL $k_{i,pll}$	14
Converter DC side voltage U_{dc}	1200 V	Proportional gain of current loop k_{pc}	214.5
Integral gain of current loop k_{ic}	1347.7	Inductance of converter output inductor l_f	0.032 H

4.1. Validity Assessment of the 3rd-PLL QSLS Model

To enhance the validation of the reduced-order [38] models of the PLL incorporating three additional filters, a series of simulation experiments mimicking extreme grid faults is designed as follows: Scenario (1) entails a +3 Hz step change in the grid frequency at 2 s, whereas Scenario (2) involves an abrupt phase jump of +40° in the grid at 2 s. Subsequently, the reduced-order models are juxtaposed with the simulation outcomes of the third-order PLL QSLS model. The transient responses of the PLL frequency and the grid-phase error with the three additional filters are depicted in Figure 10 for further analysis.

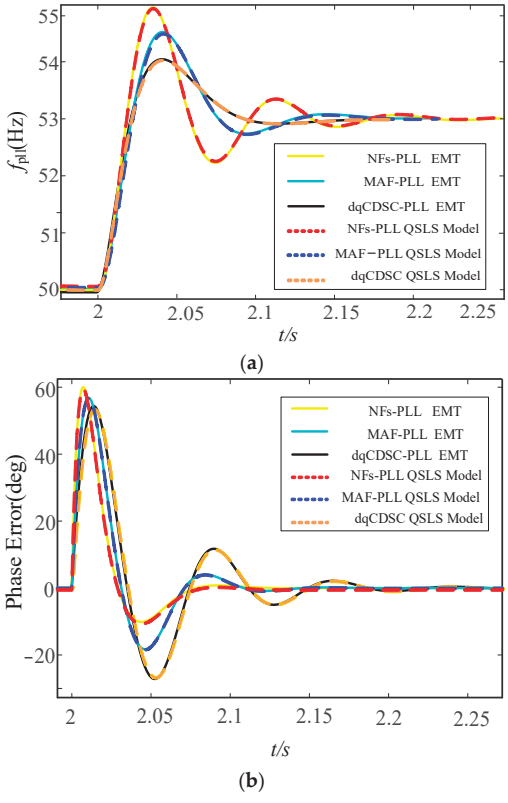

Figure 10. The response curves of different filters for PLL with grid step of +3Hz and phase jump of +40 degrees. (**a**) f_{pll} (Hz). (**b**) Phase Error.

As depicted in Figure 10, following a grid-frequency step change of +3Hz and a phase jump of +40°, the transient response curves closely align with those of the approximated inertial element. This alignment underscores the capability of the approximate results presented in this paper to precisely forecast the dynamic behavior of the full-order filtered PLL.

4.2. Impact of Inertial Element on Transient Synchronization Stability of GFL

In this section, we conduct a detailed analysis to ascertain and validate the influence of the inertial element on the transient stability of the GFL. Leveraging the system parameters delineated in Section 4 and the formulated QSLS model of the 3rd PLL, we proceed to explore this impact. Specifically, we initiate the examination by orchestrating a scenario where the grid voltage plummets to 0.4 p.u. at t = 2 s. Subsequently, we juxtapose the phase deviation δ and the frequency deviation $\Delta\omega_{\text{pll}}$ responses of the SRF-PLL with those of the PLL augmented by the additional inertial element, as illustrated in the accompanying figure.

From Figure 11, it is apparent that the introduction of an inertial element into the PLL control loop enhances the transient phase peak of the system. Moreover, as the time constant T of the inertial element increases, the transient peak grows larger. Conversely, analyzing the response curve of the frequency deviation $\Delta\omega_{\text{pll}}$ versus time t it is evident that upon an instantaneous fault occurrence, the incorporation of an inertial element in the PLL control loop prevents $\Delta\omega_{\text{pll}}$ from undergoing abrupt changes. Consequently, it mitigates the same error magnitude. The PLL lacking the inertial element swiftly converges to a stable value, and as T escalates, the time taken by the PLL to attain a steady state response also extends. Hence, a greater time constant T of the inertial element exacerbates the synchronization stability of the GFL.

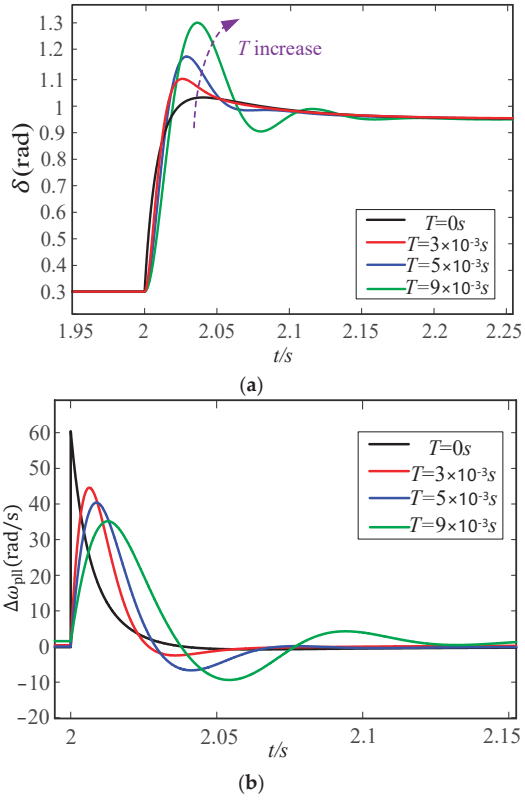

Figure 11. GFL under fault conditions with PLL response curves for different inertia time constants. (**a**) Phase output. (**b**) Frequency deviation.

4.3. Validation of the Effectiveness of the Attraction Domain

Figure 12 illustrates the simulation validation results derived from the theoretical analysis presented in Section 3.3. At 2 s, a simulated grid fault causes the voltage to decrease to 0.05 p.u. By 37.62 milliseconds, the fault is rectified, resulting in the resynchronization of the NFs-PLL with the grid. The NFs-PLL navigates within the basin of attraction, reconverging to the equilibrium point. However, by 45.2 milliseconds, following the clearance of the grid fault, the NFs-PLL exhibits instability, with its trajectory failing to stabilize outside the basin of attraction.

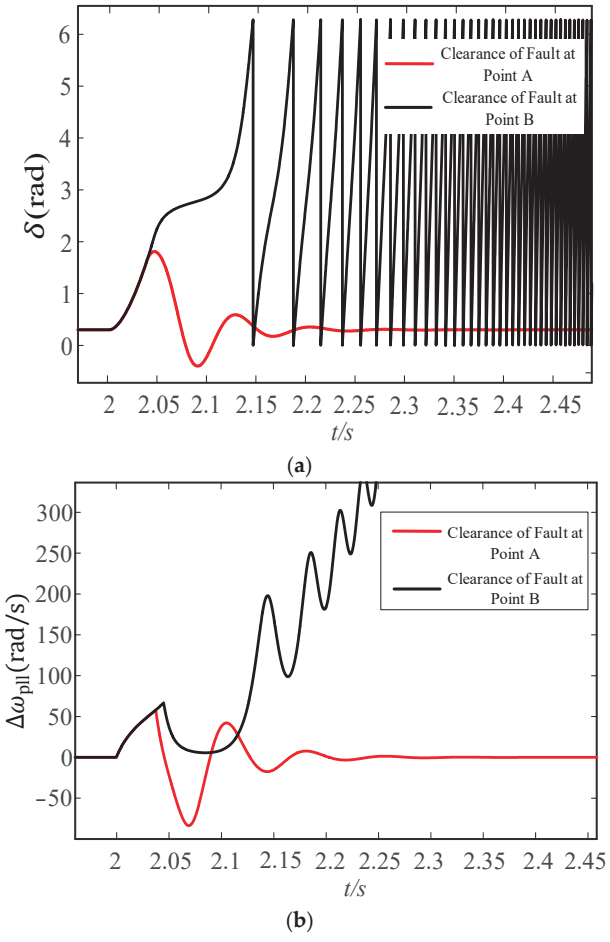

Figure 12. Validation of the attraction domain. (**a**) Phase output. (**b**) Frequency deviation.

4.4. Verification of the Impact of Filter Time Constants on Transient Synchronization Stability

Figure 13 presents a comparative analysis of the phase responses between the SRF-PLL and PLLs augmented with three additional filters, with the grid voltage dropping to 0.35 p.u. While the SRF-PLL and the dqCDSC-PLL featuring smaller filter time constants maintain synchronization with the grid during this fault scenario, the incorporation of dqCDSC filters exacerbates the synchronization stability issues of the GFL. Conversely, the MAF-PLL and NF-PLL, characterized by larger filter time constants, exhibit transient instability under similar fault conditions. Consequently, caution is advised when deploying MAF-PLL and NF-PLL configurations during severe grid faults.

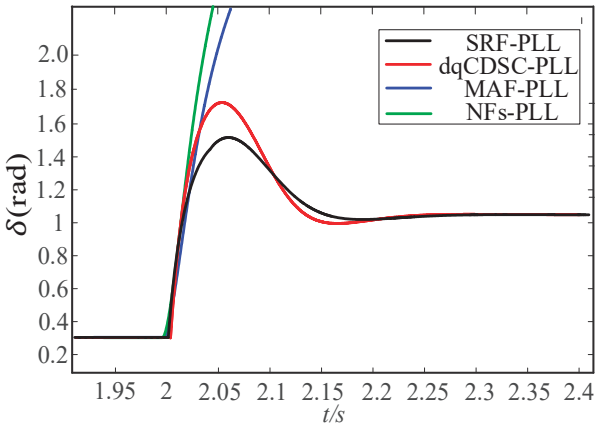

Figure 13. Phase response of SRF-PLL and Additional Filter PLL at V_g = 0.35 p.u.

5. Conclusions

Reference [28] explores the challenge of voltage oscillations at the POC across differing grid strengths, proposing modifications to filter gains to mitigate voltage oscillations at grid interconnection points for GFL. While this method effectively boosts GFL's small-signal synchronizing stability, its influence on GFL's transient dynamics remains uncharted territory. This work aims to bridge this knowledge gap, focusing on the repercussions of integrating a filter into the q-axis control loop of the PLL on the transient synchronizing stability of GFL systems; this study formulates third-order state-space equations tailored for analyzing this issue post-reduction in the filter mathematical model. Leveraging this model, we employ phase-plane analysis to explore transient stability concerns associated with three supplemental filter PLLs: MAF-PLL, dqCDSC-PLL, and NFs-PLL. This investigation unveils the impact mechanisms of varied PLL filter time constants on the transient synchronization stability of the GFL. Subsequently, simulation experiments are executed to corroborate the insights, culminating in the following conclusions:

(1) In juxtaposition with the traditional SRF-PLL, integrating a filter within the q-axis control loop of the PLL has been observed to compromise the transient stability of GFL. This phenomenon is characterized by amplified peak phase deviations during transient episodes and protracted durations for the GFL to re-establish a stable equilibrium state in the aftermath of substantial grid perturbations. Notably, the severity of these impacts escalates concomitantly with the increment in the filter's delay time constant.

(2) In power grids containing a significant amount of odd-order harmonics, to improve the accuracy of phase locking in the PLL while avoiding transient instability of the GFL, it is recommended to use the dqCDSC-PLL with smaller delay time constants in practice.

The conclusions drawn are rigorously validated via MATLAB/Simulink simulations, with the outcomes affirming the accuracy of the mathematical models and theoretical analyses outlined earlier.

Author Contributions: Conceptualization, C.Z. and J.C.; methodology, C.Z., J.C. and W.S.; validation, C.Z. and J.C.; data curation, C.Z. and W.S.; writing—original draft preparation, C.Z.; writing—review and editing, C.Z., J.C. and W.S.; supervision, J.C. and W.S. All authors have read and agreed to the published version of the manuscript.

Funding: The Major Science and Technology Project of the Xinjiang Uygur Autonomous Region provided funding for this study under project number 2022A01004-1. This project was also funded by the Department of Science and Technology of the Xinjiang Uygur Autonomous Region, China.

Data Availability Statement: Data are contained within the article.

Acknowledgments: The authors express their gratitude for the support provided by the Xinjiang Uyghur Autonomous Region's major science and technology special program.

Conflicts of Interest: The authors declare no conflict of interest.

References

1. Kroposki, B.; Johnson, B.; Zhang, Y.; Gevorgian, V.; Denholm, P.; Hodge, B.-M.; Hannegan, B. Achieving a 100% renewable grid: Operating electric Power systems with extremely high levels of variable renewable energy. *IEEE Power Energy Mag.* **2017**, *15*, 61–73. [CrossRef]
2. Paul, S.; Dey, T.; Saha, P.; Dey, S.; Sen, R. Review on the development scenario of renewable energy in different country. In Proceedings of the 2021 Innovations in Energy Management and Renewable Resources (52042), Kolkata, India, 5–7 February 2021; pp. 1–2.
3. Zhao, J.T.; Huang, M.; Yan, H.; Tse, C.K.; Zha, X.M. Nonlinear and Transient Stability Analysis of Phase-Locked Loops in Grid-Connected Converters. *IEEE Trans. Power Electron.* **2021**, *36*, 1018–1029. [CrossRef]
4. He, X.Q.; Geng, H. PLL Synchronization Stability of Grid-Connected Multiconverter Systems. *IEEE Trans. Ind. Appl.* **2022**, *58*, 830–842. [CrossRef]
5. North American Electric Reliability Corporation. *1200 MW Fault Induced Solar Photovoltaic Resource Interruption Disturbance Report*; North American Electric Reliability Corporation: Atlanta, GA, USA, 2016.
6. Bialek, J. What does the GB power outage on 9 August 2019 tell us about the current state of decarbonised power systems? *Energy Policy* **2020**, *146*, 111821. [CrossRef]
7. Haro-Larrode, M.; Bergna-Diaz, G.; Eguia, P.; Santos-Mugica, M. On the Tuning of Fractional Order Resonant Controllers for a Voltage Source Converter in a Weak AC Grid Context. *IEEE Access* **2021**, *9*, 52741–52758. [CrossRef]
8. de Bosio, F.; Pastorelli, M.; Ribeiro, L.A.; Lima, M.S.; Freijedo, F.; Guerrero, J.M. Current control loop design and analysis based on resonant regulators for microgrid applications. In Proceedings of the 41st Annual Conference of the IEEE Industrial Electronics Society (IECON), Yokohama, Japan, 9–12 November 2015; pp. 5322–5327.
9. Heredero-Peris, D.; Chillón-Antón, C.; Sanchez-Sanchez, E.; MontesinosMiracle, D. Fractional proportional-resonant current controllers for voltage source converters. *Electr. Power Syst. Res.* **2019**, *168*, 20–45. [CrossRef]
10. Wang, X.F.; Taul, M.G.; Wu, H.; Liao, Y.C.; Blaabjerg, F.; Harnefors, L. Grid-synchronization stability of converter-based resources—An overview. *IEEE Trans. Ind. Appl.* **2020**, *1*, 115–134. [CrossRef]
11. Zhang, Y.; Cai, X.; Zhang, C.; Lv, J.; Li, Y. Transient synchronization stability analysis of voltage source converters: A review. *Proc. CSEE* **2021**, *41*, 1687–1702.
12. Chen, Q.; Lyu, J.; Li, R.; Cai, X. Impedance modeling of modular multilevel converter based on harmonic state space. In Proceedings of the 2016 IEEE 17th Workshop on Control and Modeling for Power Electronics (COMPEL), Trondheim, Norway, 27–30 June 2016; pp. 1–5.
13. Golestan, S.; Guerrero, J.M.; Vasquez, J.C. Three-Phase PLL: A review of recent advances. *IEEE Trans. Power Electron.* **2017**, *32*, 1894–1907. [CrossRef]
14. Zhu, X.L.; Wen, C. Notch Filter Design based on Linear Quadratic Regulation Method. In Proceedings of the 2022 41st Chinese Control Conference (CCC), Hefei, China, 25–27 July 2022; pp. 1779–1784.
15. Mellouli, M.; Hamouda, M.; Slama, J.B.H.; Al-Haddad, K. A Third-Order MAF Based QT1-PLL That is Robust Against Harmonically Distorted Grid Voltage with Frequency Deviation. *IEEE Trans. Energy Convers.* **2021**, *36*, 1600–1613. [CrossRef]
16. Wang, L.P.; Freeman, C.T.; Rogers, E.; Young, P.C. Disturbance Observer-Based Repetitive Control System with Nonminimal State-Space Realization and Experimental Evaluation. *IEEE Trans. Control Syst. Technol.* **2023**, *31*, 961–968. [CrossRef]
17. Gude, S.; Chu, C.-C. Three-Phase PLLs by Using Frequency Adaptive Multiple Delayed Signal Cancellation Prefilters under Adverse Grid Conditions. *IEEE Trans. Ind. Appl.* **2018**, *54*, 3832–3844. [CrossRef]
18. Golestan, S.; Ramezani, M.; Guerrero, J.M.; Monfared, M. dq-frame cascaded delayed signal cancellation-based PLL: Analysis, design, and comparison with moving average filter-based PLL. *IEEE Trans. Power Electron.* **2014**, *30*, 1618–1632. [CrossRef]
19. Çelik, Ö.; Teke, A. A Hybrid MPPT method for grid connected photovoltaic systems under rapidly changing atmospheric conditions. *Electr. Power Syst. Res.* **2017**, *152*, 194–210. [CrossRef]
20. Haro-Larrode, M.; Bayod-Rújula, A. A coordinated control hybrid MPPT algorithm for a grid-tied PV system considering a VDCIQ control structure. *Electr. Power Syst. Res.* **2023**, *221*, 109426. [CrossRef]
21. Geng, H.; He, C.J.; Liu, Y.S.; He, X.Q.; Li, M. Overview on Transient Synchronization Stability of Renewable-rich Power Systems. *High Volt. Eng.* **2022**, *48*, 3367–3383.
22. Dong, D.; Wen, B.; Boroyevich, D.; Mattavelli, P.; Xue, Y.S. Analysis of phase-locked loop low-frequency stability in three-phase grid-connected power converters considering impedance interactions. *IEEE Trans. Ind. Electron.* **2015**, *62*, 310–321. [CrossRef]
23. Taul, M.G.; Wang, X.F.; Davari, P.; Blaabjerg, F. An Overview of Assessment Methods for Synchronization Stability of Grid-Connected Converters Under Severe Symmetrical Grid Faults. *IEEE Trans. Power Electron.* **2019**, *34*, 9655–9670. [CrossRef]
24. Wu, H.; Wang, X.F. Design-oriented transient stability analysis of PLL-synchronized voltage-source converters. *IEEE Trans. Power Electron.* **2019**, *35*, 3573–3589. [CrossRef]

25. Zhang, Y.; Zhang, C.; Cai, X.; Qiu, W.; Zhao, X.B. Transient Grid-synchronization Stability Analysis of Grid-tied Voltage Source Converters: Stability Region Estimation and Stabilization Control. *Proc. CSEE* **2022**, *42*, 7871–7884.
26. Chen, J.R.; Liu, M.Y.; O'Donnell, T.; Milano, F. Impact of current transients on the synchronization stability assessment of grid-feeding converters. *IEEE Trans. Power Syst.* **2020**, *35*, 4131–4134. [CrossRef]
27. Zhu, D.H.; Zhou, S.Y.; Zou, X.D.; Kang, Y. Improved design of PLL controller for LCL-type grid connected converter in weak grid. *IEEE Trans. Power Electron.* **2020**, *35*, 4715–4727. [CrossRef]
28. Haro-Larrode, M.; Eguia, P.; Santos-Mugica, M. Analysis of voltage dynamics within current control time-scale in a VSC connected to a weak AC grid via series compensated AC line. *Electr. Power Syst. Res.* **2024**, *229*, 110189. [CrossRef]
29. Zhou, D.H.; Zhou, S.Y.; Zou, X.D.; Kang, Y. An improved design of current controller for LCL -type grid connected converter to reduce negative effect of PLL in weak grid. *IEEE J. Emerg. Sel. Top. Power Electron.* **2018**, *6*, 648–663. [CrossRef]
30. Golestan, S.; Guerrero, J.M.; Gharehpetian, G.B. Five approaches to deal with problem of DC offset in phase-locked loop algorithms: Design considerations and performance evaluations. *IEEE Trans. Power Electron.* **2015**, *31*, 648–661. [CrossRef]
31. Liu, Y.; Yao, J.; Pei, J.X.; Zhao, Y.; Sun, P.; Zeng, D.Y.; Chen, S.Y. Transient stability enhancement control strategy based on improved PLL for grid connected VSC during severe grid fault. *IEEE Trans. Energy Convers.* **2020**, *36*, 218–229. [CrossRef]
32. Zou, Z.-X.; Liserre, M. Modeling phase-locked loop-based synchronization in grid-interfaced converters. *IEEE Trans. Energy Convers.* **2019**, *35*, 394–404. [CrossRef]
33. Dai, Z.Y.; Li, G.Q.; Fan, M.D.; Huang, J.; Yang, Y.; Hang, W. Global stability analysis for synchronous reference frame phase-locked loops. *IEEE Trans. Ind. Electron.* **2021**, *69*, 10182–10191. [CrossRef]
34. Wu, C.; Xiong, X.L.; Taul, M.G.; Blaabjerg, F.J. Enhancing transient stability of PLL-synchronized converters by introducing voltage normalization control. *IEEE J. Emerg. Sel. Top. Power Electron.* **2020**, *11*, 69–78. [CrossRef]
35. Fu, X.K.; Sun, J.J.; Huang, M.; Tian, Z.; Yan, H.; Iu, H.H.-C.; Hu, P.; Zha, X.M. Large-signal stability of grid-forming and grid-following controls in voltage source converter: A comparative study. *IEEE Trans. Power Electron.* **2020**, *36*, 7832–7840. [CrossRef]
36. Geng, H.; Liu, L.; Li, R.Q. Synchronization and reactive current support of PMSG-based wind farm during severe grid fault. *IEEE Trans. Sustain. Energy* **2018**, *9*, 1596–1604. [CrossRef]
37. Wu, Q.H.; Lin, Y.Q.; Hong, C.; Su, Y.S.; Wen, T.H.; Liu, Y. Transient stability analysis of large-scale power systems: A survey. *CSEE J. Power Energy Syst.* **2023**, *9*, 1284–1300.
38. Hu, P.F.; Chen, Z.; Yu, Y.X.; Jiang, D.Z. On Transient Instability Mechanism of PLL-Based VSC Connected to a Weak Grid. *IEEE Trans. Ind. Electron.* **2022**, *70*, 3836–3846. [CrossRef]

electronics

MDPI

Article

Research on Torque Characteristics of Vehicle Motor under Multisource Excitation

Mingliang Yang [1,2], Yangyang Bao [1], Haibo Huang [1,2], Yalei Liu [1], Honglin Zhu [1] and Weiping Ding [1,2,*]

[1] School of Mechanical Engineering, Southwest Jiaotong University, Chengdu 610031, China; mingliangyang01@swjtu.edu.cn (M.Y.); baoyangyang@swjtu.edu.cn (Y.B.); huanghaibo214@my.swjtu.edu.cn (H.H.); yaleiliu@swjtu.edu.cn (Y.L.); honglingzhu@swjtu.edu.cn (H.Z.)
[2] Institute of Automotive, Energy and Power Engineering, Chengdu 610031, China
* Correspondence: dwp@swjtu.edu.cn

Abstract: A hub motor is integrated into an electric wheel. The external excitation is complex and the heat dissipation conditions are poor. The working temperature of the hub motor easily becomes too high, resulting in large fluctuations in the output torque, which affect its service life. Taking a four-wheel hub-driven electric vehicle as the research object and aiming to resolve the issue of inaccurate prediction of the output torque of the hub motor in the real operating environment of the vehicle, a method for analyzing the temperature rise and torque characteristics of the hub motor considering multisource excitation and magnetic–thermal bidirectional coupling is proposed. First, the multisource excitation transmission path of the hub motor and the coupling principle of the road-electric wheel-vehicle body suspension system are analyzed from three aspects: the electromagnetic effect of the hub motor itself, the tire-ground effect, and the interaction between suspension (body) and electric wheel. We concluded that the load torque and air gap change in the motor are the key factors of its torque characteristics. On this basis, a dynamic model of the road-electric wheel-suspension-vehicle body system, an electromagnetic field model of the hub motor, and a temperature field model are established, and the influence of load torque and air gap change on the loss of in-wheel motor under multisource excitation is analyzed. Furthermore, based on the magnetic–thermal bidirectional coupling method, the motor loss under the combined action of load torque and air gap change is introduced into the temperature field model, and combined with the electromagnetic field model of the hub motor, the temperature distribution law and torque characteristics of the hub motor are accurately predicted. Finally, the accuracy and effectiveness of the calculation results of the temperature and torque characteristics of the hub motor are verified via an electric wheel bench test.

Keywords: hub motor; multisource excitation; magnetic–thermal bidirectional coupling; temperature distribution; torque characteristics

Citation: Yang, M.; Bao, Y.; Huang, H.; Liu, Y.; Zhu, H.; Ding, W. Research on Torque Characteristics of Vehicle Motor under Multisource Excitation. *Electronics* **2024**, *13*, 2019. https://doi.org/10.3390/electronics13112019

Academic Editor: Sonia Leva

Received: 15 March 2024
Revised: 7 May 2024
Accepted: 15 May 2024
Published: 22 May 2024

1. Introduction

Distributed drives, especially hub drives, are regarded as some of the most promising drive carriers for the next generation of new energy vehicles, intelligent driving vehicles, and driverless vehicles due to their high degree of electrification, controllability, and intelligence. As the core component of distributed drive vehicles, hub motors must have a high power density, a large starting torque, and a strong overload capacity [1,2]. Under complex road conditions and variable operating conditions, and due to the narrow space of the hub motor of the distributed drive vehicle, circulation of the surrounding air is difficult, making the working temperature of the hub motor too high and aggravating the magnetic loss [3,4]. This will not only greatly affect the working life of the hub motor but also cause output torque fluctuations in such a way that the vehicle power output is unstable and uncontrollable, which can easily lead to safety accidents [5–8]. Therefore, it is

very important to study the coupling mechanism of the multisource excitation of the hub motor and its influence on the temperature rise and torque output characteristics of the hub motor under the actual operating conditions of distributed drive vehicles.

Domestic and foreign scholars have performed much research on the temperature rise characteristics and torque characteristics of hub motors [9]. In [10], the thermal conductivity of the winding, stator core, and air gap of the direct drive hub motor and the heat dissipation coefficient of the inner and outer surfaces of the casing were studied. The authors in [11–13] studied the distribution of and variation in the electromagnetic loss and temperature characteristics of hub motors under different load conditions. The authors in [14] studied the loss and temperature rise distribution characteristics of each component of the hub motor under different air gap lengths. The authors in [15–17] studied the temperature rise characteristics caused by heat loss due to internal factors such as the iron core, winding, and permanent magnet in the hub motor. The authors in [18] noted that under the influence of external factors such as ambient temperature, altitude, and road excitation, the temperature of the iron core, winding, and permanent magnet inside the hub motor will further increase. The authors in [19] proposed a transient thermal model of the in-wheel motor, ignoring the influence of the leakage magnetic field and the leakage electric field. The internal temperature is constantly changing, the winding resistance value is also changing, and the ohmic loss increases. The work in [20] is based on the Bertotti theory; the iron loss is divided into hysteresis loss, eddy current loss, and additional loss according to the thermal mechanism. The time-stepping finite element analysis of each component is carried out to obtain the variation law of magnetic flux density. The classical eddy current loss is only related to the change rate of magnetic flux density. The authors in [21] analyzed the iron loss of the motor by combining the harmonic analysis method and the finite element method. Despite the machining accuracy and magnetic flux density difference of the yoke teeth, the magnetic flux density wave at any given point of the in-wheel motor was decomposed into a series of elliptical harmonic magnetic flux density vectors, and the voltage harmonic frequency that maximizes the stator iron loss was obtained. According to [22], through the JMAG built-in function block, the eddy current loss of the iron core is calculated by the fast Fourier transform (FFT), and the hysteresis loss is calculated by the loop analysis method. The authors in [23] show that due to the rotating magnetic field generated by the energization of the stator excitation winding, eddy current-like electromotive force and current will be induced in the permanent magnet. The magnitude is inversely proportional to the axial length and resistivity of the permanent magnet and is proportional to the volume of the permanent magnet, the alternating frequency of the magnetic field, the proportional constant of the electromotive force, and the maximum magnetic flux density. The eddy current loss and hysteresis loss are generated by the time-varying magnetic field at the working point of the magnet. The slot effect of the motor leads to a change in the air gap reluctance and causes additional changes in the magnetic field of the magnet, even under no-load conditions. Most of the above scholars' research on the temperature rise characteristics of in-wheel motors analyze the variation law of the temperature rise of in-wheel motors from the internal factors such as material properties and structural parameters that affect the temperature rise of the motor and rarely consider the external complex factors that affect the temperature characteristics of the motor.

Moreover, when considering external factors, the existing research usually assumes external conditions and often ignores the various excitation effects of the hub motor in the actual operating environment of the vehicle. The authors in [24] reported that the hub motor will be excited by the vibration of the road through the tire and the vibration of the body through the suspension, indicating that the air gap between the stator and rotor of the hub motor will change under various excitations, and then, the magnetic pull of the motor will change. The authors in [25,26] studied the variation in the unbalanced magnetic pull under the influence of road excitation and motor torque fluctuation excitation. The authors in [27] characterized the force between the stator and rotor (that is, unbalanced magnetic pull) by simulating the radial magnetic pull of the hub motor under different

air gap spacings and studied the relative offset of the stator and rotor of the hub motor in the actual operating environment of the vehicle with the help of a dynamic model of the hub drive suspension. The authors in [28,29] explained that when the vehicle is traveling at a constant speed on the road, it must overcome the rolling resistance from the ground, the air resistance from the air, and the slope resistance. At the same time, the vehicle speed changes, and the rolling resistance is also different. This is an essential factor for studying the actual power and cruising range of a vehicle. An increase in the temperature of the motor is unavoidable, and this temperature rise will lead to changes in the thermally sensitive materials in the motor, such as in the winding resistance and permanent magnet properties; that is, an increase in the temperature will increase the winding resistance, weaken the magnetic properties of the permanent magnet and even cause demagnetization, which will affect the actual output torque of the motor. In [30], a dynamic loss model of the electric drive system considering the change in the temperature rise characteristics of the motor was established; combined with the dynamic characteristics of the battery voltage, a torque distribution strategy with minimum loss of the electric drive system was proposed, but the influence of temperature on the torque was not considered. The authors in [31,32] studied the influence of motor temperature changes on the output torque of the hub motor through finite element simulation. When the motor temperature rises, the back EMF, air gap flux density, and output torque of the motor decrease, but these studies all ignored the various excitations experienced by the hub motor in the actual operating environment of the vehicle also affect its actual output torque. The authors in [33] studied the influence of road excitation, extracted the vibration velocity response curves of the stator and rotor from a vehicle dynamics model, loaded them into a thermal–fluid coupling analysis model of the hub motor as the excitation load, and analyzed the temperature change but did not consider the influence of the unbalanced magnetic pull of the motor on its vibration, the influence of the actual load torque of the vehicle on the temperature rise of the motor, or the relationship between the output torque and the temperature rise.

According to the research literature that has been consulted at present, most scholars' research on the temperature rise characteristics of hub motors mainly focuses on various electromagnetic characteristics and temperature changes under steady-state conditions. Regarding the internal temperature change in the motor caused by 'magnetic–thermal coupling' under transient conditions, they do not consider the influence from the external environment. At the same time, the research on the torque of the hub motor focuses on the influence of temperature rise caused by its internal factors, and the influence of external excitation on the torque characteristics of the in-wheel motor under temperature rise during the actual operation of the vehicle remains to be further studied.

In view of the shortcomings of the above research on the temperature rise characteristics and torque characteristics of hub motors, this paper proposes a method for analyzing the temperature rise and torque characteristics of hub motors, given multisource excitation and magnetic–thermal bidirectional coupling. This method considers the excitation of the radial electromagnetic force generated by the rotor eccentricity of the hub motor transmitted to the suspension system, the excitation of the road surface and the body transmitted to the hub motor stator and rotor, and the rolling resistance torque excitation with the change in vehicle speed. The load torque changes in the hub motor caused by the rolling resistance torque at different motor speeds, and the air gap changes caused by the excitation of the road surface transmitted to the hub motor stator and rotor through the tire and of the body transmitted through the suspension, are studied. The two change results are fed back into the electromagnetic field model of the hub motor to analyze the loss distribution law of each component of the motor. The magnetic–thermal bidirectional coupling method is used to introduce the motor loss into the temperature field model to analyze the spatial distribution of the temperature rise characteristics in the magnetic–thermal coupling of the hub motor, and the output torque variation law caused by the temperature rise of the hub motor is obtained. The accuracy and effectiveness of the temperature rise characteristics of

the hub motor calculated by the proposed method are verified by a temperature rise test of a prototype.

This article is arranged as follows: The second section presents an analysis of the multisource excitation of the hub motor. The purpose is to explain the sources of multisource excitation and the influencing factors (output torque change and air gap deformation) that affect the temperature rise of the motor and the torque change caused by the temperature rise. The third section introduces the model. The purpose is to analyze the temperature rise of the motor and the torque change caused by the temperature rise. The fourth section presents the result analysis. The purpose is to analyze the influence of the output torque and air gap deformation on the motor loss, the law of the motor temperature rise, and the law of the torque change caused by a temperature rise. The fifth section describes the experimental verification, and the simulation results are verified and compared. The sixth section presents the conclusion, which summarizes the full text.

2. Multisource Excitation Analysis of the Hub Motor

The hub motor is highly integrated with the tire and complements and interacts with the vehicle suspension system. In the process of uniform flat motion of the vehicle, the hub motor is subjected to multisource excitation from itself and from the outside world (mainly from four aspects: first, the electromagnetic force excitation caused by the relative eccentricity of the internal stator and rotor; second, the excitation of transverse and longitudinal forces of the road surface (uneven road excitation) acting on the rotor of the hub motor; third, the excitation of the body transmitted through the suspension acting on the hub motor stator; and fourth, the excitation of the rolling resistance moment transmitted to the rotor of the hub motor with the change in the vehicle speed), as shown in Figure 1. From the multisource transmission path diagram, it can be seen that the road excitation will be transmitted to the hub motor rotor through the tire, the body excitation will be transmitted to the hub motor stator through the suspension, the radial electromagnetic force generated by the eccentricity of the hub motor rotor will act on the stator and rotor, and the rolling resistance torque excitation under the influence of different speeds will act on the hub motor rotor through the tire. Under the combined action of various excitations, the vibration will affect the ride comfort of the vehicle through the suspension. Additionally, it will cause vibration of the hub motor itself and accelerate the damage of the hub motor; due to the change in the rolling resistance torque, the torque control of the motor will be unstable, which will affect the dynamic performance of the vehicle. The influence of various excitations on the hub motor is mainly reflected in the change in the air gap deformation and load torque. Through the above analysis, the coupling principle of the road surface-electric wheel-suspension system is obtained, as shown in Figure 2. To obtain the changes in the air gap deformation and load torque of the stator and rotor during motor operation, the rolling resistance torque T_p of the vehicle in the actual operating environment must be calculated, and then the load torque T_i of the motor can be determined. Then, the component F_y of the unbalanced magnetic pull force in the Y direction under different eccentricity e values of the stator and rotor of the hub motor must be calculated. The relationship between the eccentricity e and the component F_y of the unbalanced magnetic pull force in the Y direction is obtained, that is, the air gap magnetic field stiffness K_{UMP_y}. Finally, the air gap deformation e_d of the hub motor and the influence of the air gap magnetic field stiffness K_{UMP_y} are calculated. Through the above method, the important factors affecting the temperature rise of the hub motor (the change in the air gap deformation of the stator and rotor and the change in the output torque) can be obtained, and the temperature rise law of the motor can be obtained under the combined action of the two influencing factors. With increasing motor temperature, the variation law of the output torque T_a of the motor can be found.

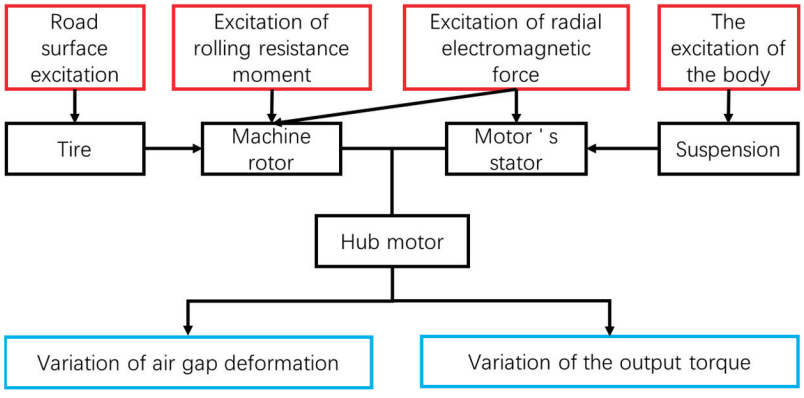

Figure 1. Multisource excitation transmission path of a hub-drive vehicle.

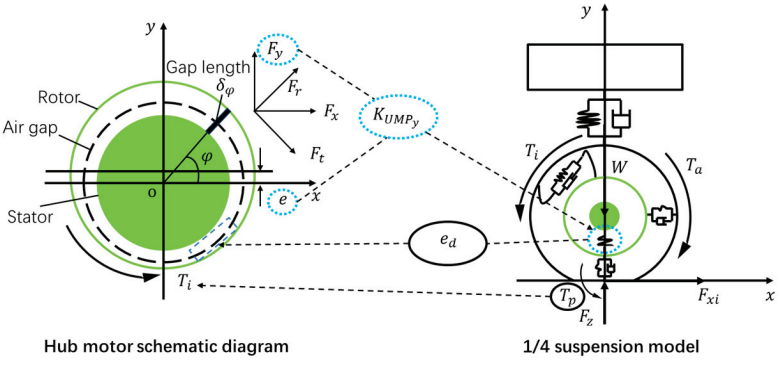

Figure 2. Coupling principle of the road-electric wheel-suspension system.

In Figure 2, T_p is the rolling resistance moment of the vehicle, T_i is the load torque of the hub motor, T_a is the output torsion of the hub motor, W is the vertical load of the tire, e is the eccentricity of the stator and rotor, e_d is the air gap deformation, F_x and F_y are the components of the radial magnetic pull in the X and Y directions, F_r and F_t are the radial magnetic pull and tangential magnetic pull, φ is the mechanical rotation angle, K_{UMP_y} is the stiffness of the air gap magnetic field in the Y direction, F_Z is the normal reaction force of the ground on the tire, and F_{xi} is the tangential reaction force of the ground on the tire (the value is the driving force minus the rolling resistance of the wheel).

The vehicle must overcome the rolling resistance from the ground, the air resistance from the air, and the gravity component along the ramp (slope resistance). If the air resistance and slope resistance are not considered, then only the rolling resistance from the ground needs to be calculated. When the vehicle is running at a constant speed, the rolling resistance torque T_p received by the tire will act as the load torque T_i on the hub motor, and the rolling resistance torque is related to the vertical load W received by the tire. As shown in Figure 3, the rolling resistance is equal to the product of the rolling resistance coefficient and the vertical load W [34], i.e.,

$$F_f = Wf \tag{1}$$

It can also be expressed as follows:

$$F_f = (W_s + W_d)f \tag{2}$$

where F_f is the rolling resistance; f is the rolling resistance coefficient; W_s is the vehicle static load; and W_d is the tire dynamic load.

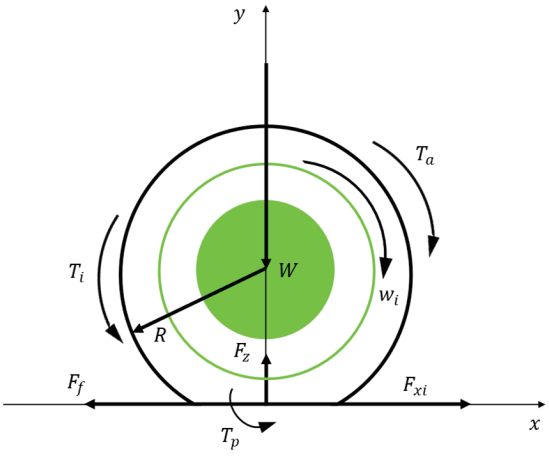

Figure 3. Force analysis of the electric wheel during rolling.

The rolling resistance moment is the following:

$$T_p = F_f R \tag{3}$$

where R is the rolling radius of the tire.

The following empirical formula is used to calculate the tire rolling resistance coefficient f:

$$f = f_0 + f_1\left(\frac{u_a}{100}\right) + f_3\left(\frac{u_a}{100}\right)^4 \tag{4}$$

where u_a is the vehicle speed, km/h, and f_0, f_1, and f_3 are fitting parameters; in this paper, $f_0 = 0.012$, $f_1 = 0.0034$, and $f_3 = 0.001$.

From Figure 3, the wheel rotation dynamics equation can be obtained [35] as follows:

$$T_a - F_f R = F_{xi} R = J_{wi}\frac{dw_i}{dt} \tag{5}$$

where J_{wi} is the moment of inertia of the wheel around the wheel center and w_i is the wheel angular velocity.

The tangential reaction torque $F_{xi}R$ of the ground acting on the tire is the combined torque that truly drives the vehicle, and its value equals the motor output torque T_a minus the rolling resistance torque $F_f R$. When the vehicle is traveling at a constant speed, the wheel angular acceleration $\frac{dw_i}{dt}$ is zero, and the combined torque driving the vehicle is zero; that is, the motor output torque is completely used to overcome the rolling resistance torque with $T_a = F_f R = T_p$. Therefore, the actual output torque of the hub motor is related to the rolling resistance torque, and the rolling resistance torque acts on the hub motor in the form of a load torque, that is, $T_p = T_i$.

To determine the actual load torque of the hub motor, the component F_y of the unbalanced magnetic pull force in the Y direction under different air gap spacing, e values of the hub motor are calculated. Usually, the air gap magnetic field distribution is uniform, and the rotor does not bear an unbalanced magnetic pull. However, when the rotor static eccentricity leads to distortion of the radial air gap magnetic field, an unbalanced magnetic pull will be generated, which makes the rotor force uneven. After the finite element model of the hub motor is established and solved, the air gap flux density can be extracted, and

then the component F_y of the unbalanced magnetic pull in the Y direction is obtained from the following formula [36–39]:

$$F_y = \frac{lr_p}{2\mu_0}\int_0^{2\pi}\left[(B_{rp}^2 - B_{tp}^2)\sin\varphi + 2B_{rp}B_{tp}\cos\varphi\right]d\varphi \tag{6}$$

$$B_{rp} = B_x\cos\varphi + B_y\sin\varphi \tag{7}$$

$$B_{tp} = B_y\cos\varphi - B_x\sin\varphi \tag{8}$$

where l is the axial length of the silicon steel sheet of the rotor; r_p is the integral radius of the unbalanced magnetic pull; B_{rp} and B_{tp} are the radial magnetic density and tangential magnetic density, respectively; and B_x and B_y are the X and Y components of the magnetic induction intensity, respectively.

Through the relationship between the air gap spacing e and the component F_y of the unbalanced magnetic pull in the Y direction, the force between the stator and the rotor is obtained, that is, the air gap magnetic field stiffness K_{UMP_y}, and K_{UMP_y} is added to the hub-driven suspension dynamics model. The force and relative offset between the stator and the rotor during actual operation are simulated, and the relative offset e_d of the stator and the rotor is extracted. By setting the maximum dynamic eccentricity e_{dmax} of the rotor, the displacement changes in the rotor of the hub motor relative to the stator in the Y direction (as shown in Figure 4) are used to simulate the displacement change law of the motor under the influence of various excitations in the actual operation process. From Equation (9), the maximum dynamic eccentricity e_{dmax} and the relative offset e_d of the stator and rotor can be obtained.

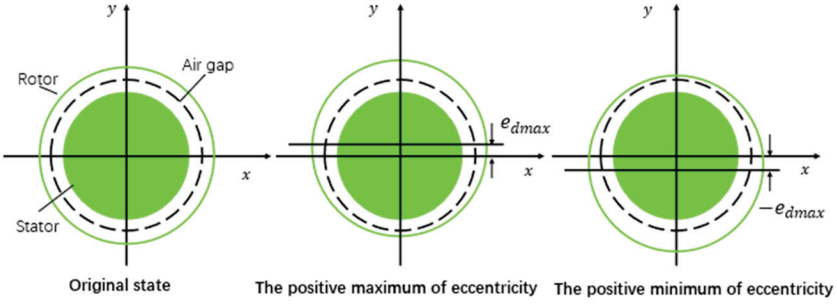

Figure 4. Change rule of dynamic eccentricity e_d.

$$e_d = e_{dmax}\sin\left(2\pi\frac{n}{60}t\right) \tag{9}$$

where e_{dmax} is the maximum displacement of the relative offset e_d, mm; n is the hub motor speed, rpm; and t is time, s.

3. Model Introduction

To obtain the temperature rise characteristics and output torque characteristics of the hub motor under the magnetic–thermal coupling, it is necessary to establish a suspension dynamics model under the action of the road surface and the hub motor and calculate the driving resistance torque in the vehicle operating environment, that is, the load torque of the motor. An electromagnetic field model of the hub motor is established, the variation law of the unbalanced magnetic pull is analyzed, and the stiffness of the air gap magnetic field is then obtained. The air gap deformation of the hub motor and the loss of each component of the motor are analyzed by combining the electromagnetic field model and the suspension dynamics model. On this basis, a temperature field model of the hub motor is established, and the temperature rise variation law under changes in the air gap and

load torque is analyzed. Finally, the temperature calculated by the temperature field model is fed back into the electromagnetic field model to further analyze the change law of the output torque caused by the temperature rise of the motor, as shown in Figure 5.

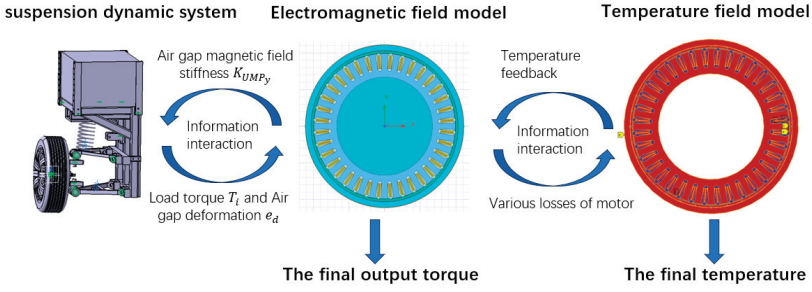

Figure 5. Relationships between various models.

3.1. Suspension Dynamics Model Considering the Hub Motor

The hub motor is installed in the wheel, and the radial force generated by the hub motor directly acts on the stator and rotor. At the same time, the road excitation directly acts on the rotor of the hub motor through the wheel, and the body vibration excitation also acts on the stator through the suspension, making the air gap change. During the operation of the hub motor, the driving resistance torque of the vehicle is used as the load input of the hub motor and affects the output torque of the motor. Therefore, the suspension dynamics model under the action of the road surface and hub motor must be analyzed.

As shown in the 1/4 suspension model principle of the hub-driven suspension in Figure 6a, the tire and the hub motor rotor are connected by the sidewall, and the sidewall is equivalent to the torsional stiffness, longitudinal translation stiffness, and vertical stiffness. The stator and rotor of the hub motor are connected by bearing m_2, where the stiffness K_2 is the bearing stiffness; body m_1 is connected to unsprung masses m_2 and m_3 through springs and shock absorbers.

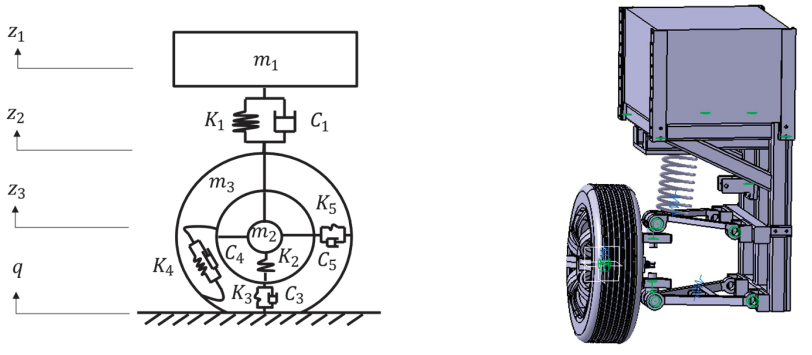

(**a**) (**b**)

Figure 6. (**a**) 1/4 suspension model principle. (**b**) 1/4 suspension dynamics model.

According to the dynamic model established in Figure 6, the following vertical dynamic equation is obtained:

$$m_1\ddot{Z}_1 = -K_1(Z_1 - Z_2) - C_1\left(\dot{Z}_1 - \dot{Z}_2\right) \tag{10}$$

$$m_2\ddot{Z}_2 = -K_1(Z_2 - Z_1) - C_1\left(\dot{Z}_2 - \dot{Z}_1\right) - K_2(Z_2 - Z_3) \tag{11}$$

$$m_3\ddot{Z}_3 = -K_2(Z_3 - Z_2) - K_3(Z_3 - q) - C_3\left(\dot{Z}_3 - \dot{q}\right) \quad (12)$$

where m_1 is the body mass; m_2 is the mass of the stator, bearing, and swing arm of the hub motor; m_3 is the mass of the hub motor rotor and tire carcass; K_1, K_2 and K_3 are the spring stiffness, bearing stiffness, and tire vertical stiffness, respectively; and C_1 and C_3 are the shock absorber damping coefficient and tire vertical damping coefficient, respectively.

Based on the above analysis, a multibody dynamics model is established, as shown in Figure 6b, and the parameters are shown in Table 1.

Table 1. Wheel drive suspension parameters.

Parameter	Value	Parameter	Value
Body mass m_1 (kg)	181.90	Tire longitudinal stiffness K_1 $(\mathrm{N{\cdot}m^{-1}})$	371,800
Bearing, swing arm and other mass m_2 (kg)	28.37	Tire torsional stiffness K_1 $(\mathrm{N{\cdot}rad^{-1}})$	55,634
Hub motor rotor and tire carcass mass m_3 (kg)	73.16	Tire vertical stiffness K_3 $(\mathrm{N{\cdot}m^{-1}})$	220,000
Tire rolling radius (m)	0.35	Shock absorber damping coefficient $(\mathrm{N{\cdot}m{\cdot}s^{-1}})$	4000
Spring stiffness K_1 $(\mathrm{N{\cdot}m^{-1}})$	33,700	Tire vertical damping coefficient $(\mathrm{N{\cdot}m{\cdot}s^{-1}})$	50
Bearing stiffness K_2 $(\mathrm{N{\cdot}m^{-1}})$	6.2×10^6	Tire longitudinal damping coefficient $(\mathrm{N{\cdot}m{\cdot}s^{-1}})$	50

3.2. Finite Element Model of the Electromagnetic Field of the Hub Motor

In this paper, a 3 kW hub motor for pure electric vehicles is taken as the research object, and its structure consists of an outer rotor permanent magnet synchronous motor. Table 2 shows the main parameters of the hub motor. Figure 7 shows the finite element model of the hub motor established by Ansys/Maxwell, in which the total grid number is 89,300, the box is the grid detail at the air gap.

Table 2. Main parameters of the hub motor.

Parameter	Value	Parameter	Value
Motors' rated speed	600 rpm	Coil diameter	0.04 mm
Motor rated power	3000 W	Permanent magnet thickness	3.1 mm
Motor rated voltage	72 V	Motor length	60.5 mm
Rotor inner diameter	200 mm	Ferrite magnetic materials	NdFe35
Rotor outer diameter	222 mm	Rotor and stator materials	DW310
Stator inner diameter	134 mm	Winding material	Copper
Stator outer diameter	198.4 mm		Hs0: 0.7 mm
Average air gap length of motor	0.8 mm		Hs2: 3.25 mm
Number of pole-pairs	16	Groove parameter	Bs0: 3.25 mm
Number of stator slots	36		Bs1: 8 mm
Number of turns per phase coil	280		Bs2: 5 mm

On the basis of the above, the relationship between the speed and the output torque is obtained by setting the voltage to 72 V and setting different speeds. The electromagnetic field model of the hub motor is verified. As shown in Figure 8, when the speed is low, the hub motor can provide a larger output torque. In contrast, when the speed is high, the output torque it can provide rapidly decreases. The simulation and test have errors to a certain extent, and the maximum error does not exceed 10.9%. The trends of the two are the same, which indicates the applicability of the theory for trend research. This paper will focus on the research and analysis of the hub motor under the three speed conditions of 200 rpm, 400 rpm, and 600 rpm (that is, speeds of 26 km/h, 52 km/h, and 78 km/h).

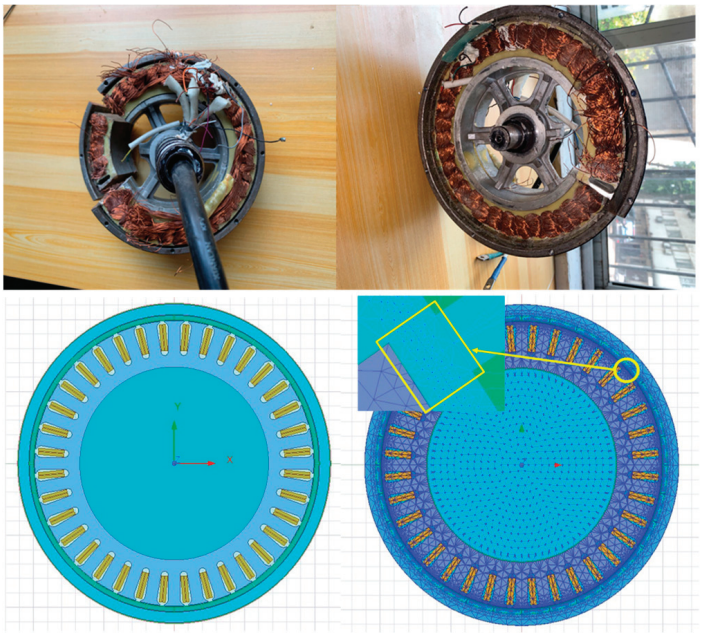

Figure 7. Finite element model of the hub motor electromagnetic field.

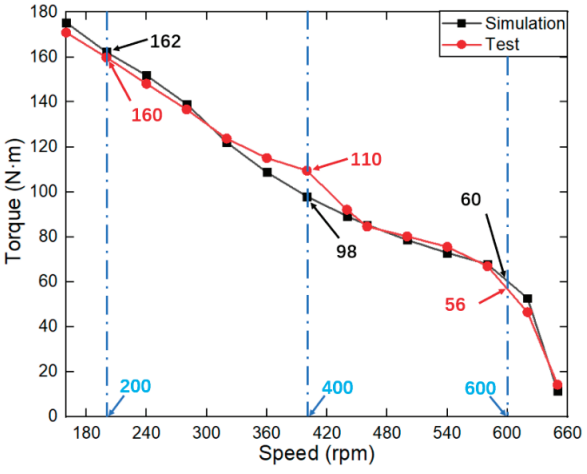

Figure 8. Relationship between the speed and output torque of the hub motor.

The finite element model of the electromagnetic field is established mainly to analyze the loss of each component of the motor, and the temperature rise of the motor is caused by various internal losses. The internal losses of the motor mainly include the core loss, winding loss, and permanent magnet loss. The loss calculation of the electromagnetic field is input into the finite element analysis of the temperature field in the form of a thermal load or input into the thermal network analysis of the temperature field in the form of a heat source.

The hub motor losses [40] can be expressed as follows:

$$P = P_{Fe} + P_{Cu} + P_e \tag{13}$$

They can also be written as follows:

$$P = K_b \tau B_m^2 + K_e \tau^2 B_m^2 + K_{ex} (\tau B_m)^{\frac{3}{2}} + 3I^2 R + \int V_m \frac{|J|^2}{2\sigma} \tag{14}$$

where P is the total loss of the motor; P_{Fe} is the core loss of the hub motor; K_b, K_e, and K_{ex} are the core hysteresis loss coefficient, the core eddy current loss coefficient, and the core additional loss coefficient, respectively; τ is the alternating frequency; B_m is the magnetic flux density; P_{Cu} is the winding loss; I is the phase current of the motor winding; R is the motor winding resistance; P_e is the eddy current loss of the permanent magnet of the hub motor; V_m is the volume of the permanent magnet; J is the current density; and σ is the conductivity of the permanent magnet.

3.3. Finite Element Model of the Hub Motor Temperature Field

Due to the need for thermal analysis of the loss calculated by the finite element model of the electromagnetic field as a heat source, a finite element model of the temperature field of the hub motor must be established to determine its temperature rise characteristics. According to the basic law of heat conduction, in the rectangular coordinate system, the transient temperature field in a certain calculation area of the motor is solved as follows [41]:

$$\begin{cases} c\gamma \frac{\partial T}{\partial t} = \lambda \left(\frac{\partial^2 T}{\partial x^2} + \frac{\partial^2 T}{\partial y^2} + \frac{\partial^2 T}{\partial z^2} \right) + p \\ T|_{s_1} = T_0 \\ \lambda \left(\frac{\partial T}{\partial x} n_x + \frac{\partial T}{\partial y} n_y + \frac{\partial T}{\partial z} n_z \right) \Big|_{s_2} = -q \\ \lambda \left(\frac{\partial T}{\partial x} n_x + \frac{\partial T}{\partial y} n_y + \frac{\partial T}{\partial z} n_z \right) \Big|_{s_3} = -a(T - T_0) \end{cases} \tag{15}$$

where c is the specific heat capacity; γ is the density; t is the time; T is the temperature that changes with time; λ is the thermal conductivity; p is the heat source density; T_0 is the known temperature distribution on the boundary; q is the boundary heat dissipation caused by heat conduction; a is the heat dissipation coefficient; n_x, n_y, and n_z are the cosines of the angle between the normal direction of the boundary and the x, y, and z axes, respectively; and s_1, s_2 and s_3 are the first to third types of heat transfer boundary surfaces.

The essence of solving the temperature field by the finite element method is to transform the temperature problem into the extreme value problem of the universal function. According to the variational principle, Equation (15) is transformed into energy functional I, as shown below [42,43]:

$$\begin{cases} I(T) = \iint\limits_{\Omega} \left\{ \frac{\lambda}{2} \left[\left(\frac{\partial T}{\partial x} \right)^2 + \left(\frac{\partial T}{\partial y} \right)^2 + \left(\frac{\partial T}{\partial z} \right)^2 \right] + \frac{c\gamma}{2} T \frac{\partial T}{\partial t} - pT \right\} d\Omega - \int\limits_{s_2} qT ds_2 - \int\limits_{s_3} \left(\frac{a}{2} T^2 - aT_0 T \right) ds_3 \\ T|_{s_1} = T_0 \end{cases} \tag{16}$$

Equation (16) can be discretized into algebraic equations, and the temperature distribution problem is transformed into a problem involving a finite number of node temperatures. The temperature at each node can be obtained via this equation. After the overall synthesis, the transient temperature field in the solution domain Ω is obtained.

The loss generated by the motor in actual operation will become heat, which will increase the temperature of each part of the motor. The heat transfer process is a comprehensive process of heat conduction and heat convection, which is related to the thermal conductivity and heat dissipation coefficient of the dielectric surface. The equivalent thermal conductivity of stator, rotor, and winding, and the heat dissipation coefficient of the stator end face, outer surface of rotor yoke, and winding end are very important to the calculation accuracy of motor temperature rise.

When establishing the magnetic–thermal coupling model of the hub motor, the stator winding model is simplified as follows: the winding copper wire is equivalent to a conduc-

tor with the same volume, and the wire insulation layer and the coating between the wires are equivalent to a heat conduction layer evenly distributed around the equivalent winding. The equivalent thermal conductivity of the stator, rotor, and winding [44] is as follows:

$$\alpha_r = \frac{\delta_k + \delta_0 + \delta_x}{\frac{\delta_k}{\alpha_k} + \frac{\delta_0}{\alpha_0} + \frac{\delta_x}{\alpha_x}} \tag{17}$$

where δ_k and α_k are the thickness and thermal conductivity of the conductor insulation in the direction of heat flow, respectively; δ_0 and α_0 are the thickness and thermal conductivity of air and the insulating paint between wires, respectively; and δ_x and α_x are the thickness and thermal conductivity of the conductor insulation layer, respectively.

The heat dissipation coefficient of the stator end face is [45] the following:

$$h_{sh} = 15 + v_r^{0.7} \tag{18}$$

where v_r is the linear velocity of the rotor surface, m/s.

The heat dissipation coefficient of the outer surface of the rotor yoke is [46] the following:

$$h_k = 7.68\omega_{air}^{0.78} \tag{19}$$

where ω_{air} is the air velocity of the rotor accessory, which can be taken as 75% of the speed.

The winding end heat dissipation coefficient is [47] the following:

$$h_{ci} = \frac{N_{uc}\lambda_{air}}{d_{et}} \tag{20}$$

$$N_{uc} = 0.103Re_c^{0.66} \tag{21}$$

$$Re_c = \frac{\rho\pi R_r n d_{et}}{30\mu} \tag{22}$$

$$d_{et} = \frac{(R_{sR} + R_r)}{2} \tag{23}$$

where N_{uc} is the Nusselt number at the end of the stator winding; d_{et} is the equivalent diameter of the winding end, m; λ_{air} is the thermal conductivity of air, $W\cdot(m\cdot K)^{-1}$; Re_c is the air gap Reynolds number at the end of the winding; R_{sR} and R_r are the diameter of the groove bottom and the inner diameter of the rotor, m; n is the motor speed, r/s; ρ is the air density, kg/m^3; and μ is the dynamic viscosity of air, Pa·s.

The air gap heat dissipation coefficient is [48] the following:

$$h_{airgap} = \frac{\left(0.386Re_c^{0.5}P_r^{0.27}\right)\lambda_{air}}{g} \tag{24}$$

$$P_r = \frac{\mu c_p}{\lambda_{air}} \tag{25}$$

where P_r is the Prandtl number and c_p is the specific heat at constant pressure.

Through the above empirical formula and experience, the thermal parameters of the materials in the model are obtained, as shown in Table 3.

Based on the above analysis results and the parameters required for modeling, a finite element model of the temperature field of a prototype, including the stator core, the stator winding, the rotor, and the air gap, is established. As shown in Figure 9, the model does not have any special cooling devices and relies on the natural circulation of the surrounding air to dissipate heat, ignoring axial heat transfer.

Table 3. Thermal parameters of the hub motor materials.

Unit	Material	Density (kg/m^3)	Specific Heat Capacity (J/kg · °C)	Thermal Conductivity (W/m · °C)	Coefficient of Heat Emission (W/m^2 · °C)
Stator	Silicon steel	7700	426	40	17.72
Rotor	10# steel	7800	448	49.8	25.55
Winding	Copper	8954	383.1	386	69.67
Permanent magnet	Nd-Fe-Boron	7500	420	9	26
Equivalent air gap	Air	1.164	1008	0.027	76.52

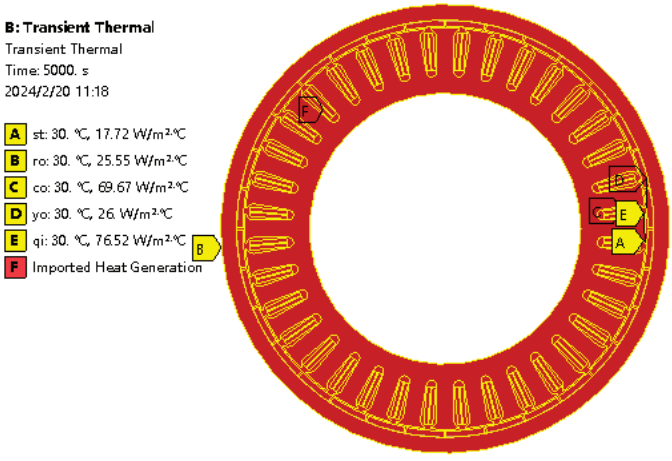

Figure 9. Finite element model of the hub motor temperature field.

4. Results

According to the analysis of multisource excitation of the hub motor in Section 2, the influence of the load torque and air gap changes on the motor loss must be analyzed. The loss calculation results are imported into the motor temperature field model for temperature field analysis. Finally, the variation law of the motor output torque caused by the temperature rise is analyzed. A simulation comparison analysis is carried out under a working environment of 30 °C, a simulation time of 3000 s, natural air cooling, and uniform speeds of 200 rpm, 400 rpm, and 600 rpm. Two-way coupling simulations of the two-dimensional electromagnetic field and temperature field are carried out, and the temperature rise of the hub motor and the torque output changes in the hub motor are simulated and analyzed, as shown in Figure 10.

4.1. Analysis of Influencing Factors of the Motor Loss

4.1.1. Relationship between the Load Torque and Motor Loss

To obtain the load torque of the hub motor, it is necessary to calculate the rolling resistance torque during the actual operation of the vehicle, obtain the relationship between the load torque of the hub motor and its output torque, and then analyze the influence of the load torque on the motor loss. In the case of road grade A, in the simulation, the output torque of the hub motor is loaded at the wheel center through the suspension dynamics model to make the wheel speed reach 200 rpm, 400 rpm, or 600 rpm and then remain at the left and right of the wheel speed. The relationship between the output torque of the hub motor and the wheel speed is shown in Figure 11a, and the dynamic load W_d of the tire is obtained via suspension dynamics calculations, as shown in Figure 11b. The rolling resistance moment of the vehicle at a uniform speed is calculated by theoretical Formula (3) and compared with the output torque of the hub motor loaded at the center of the

wheel. As shown in Table 4, the rolling resistance moment calculated by the formula is compared with the output torque loaded at the center of the wheel obtained by simulation. The accuracy is above 87%, indicating that the output torque of the hub motor loaded at the center of the wheel under the support of the theoretical formula is correct.

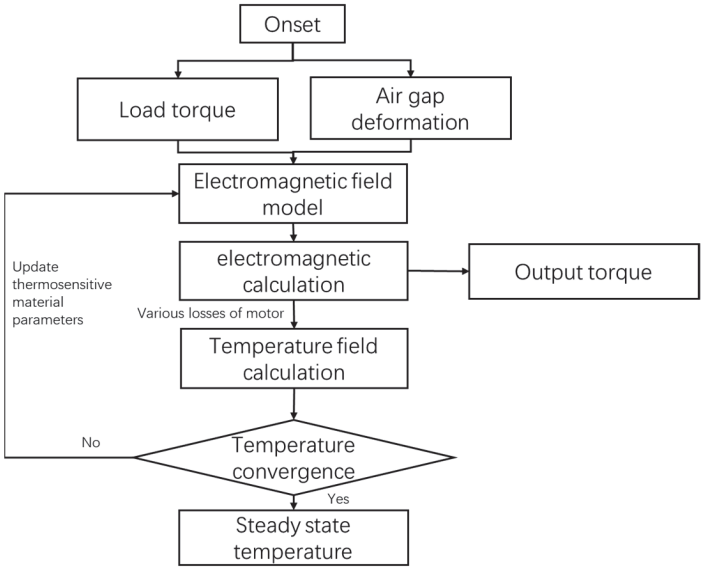

Figure 10. Magnetic–thermal two-way coupling process.

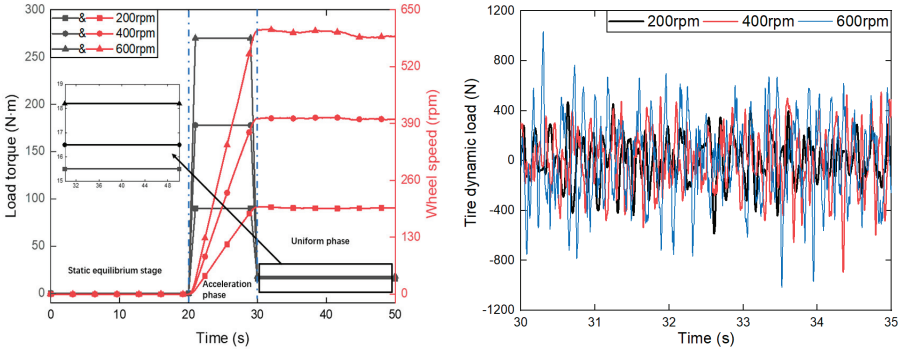

(**a**) (**b**)

Figure 11. (**a**) Relationship between the output torque of the hub motor and the wheel speed under different working conditions. (**b**) Tire dynamic load under different working conditions.

Table 4. Comparison of the rolling resistance torque theoretical and simulation values under different working conditions.

Motor Speed/rpm	Tire Dynamic Load/N	Rolling Resistance Torque (Theoretical Calculation)/N · m	Rolling Resistance Torque (Simulation Calculation)/N · m	Precision
200	165.59	13.54	15.50	87.35%
400	238.08	14.92	16.50	90.42%
600	313.40	16.64	18.10	91.93%

After the rolling resistance moment in the actual running process of the vehicle is calculated with the suspension dynamics model, it is input into the electromagnetic field model of the hub motor as the load torque to obtain the output torque of the motor and the loss of each component without considering the temperature rise. Figure 11a shows that when obtaining the output torque of the hub motor in the actual operating environment, the actual operating conditions of the vehicle need to be considered. It is not necessarily how much torque is output according to the corresponding speed shown in Figure 8 that is of interest but how much torque is output according to the actual load torque of the vehicle.

Figure 12 shows the calculation results of the loss and output torque of the hub motor under different working conditions. Table 5 shows that when the rolling resistance torque at different speeds is applied to the electromagnetic field finite element model of the hub motor, the calculated output torque is greater than the rolling resistance torque. This may be due to the reluctance torque and cogging torque of the motor. With increasing speed, the rolling resistance torque of the car increases; that is, the load torque of the hub motor increases, the corresponding output torque also increases, and the loss of its components accordingly increases. Therefore, the variation in the loss of the hub motor in combination with the load torque of the car must be analyzed.

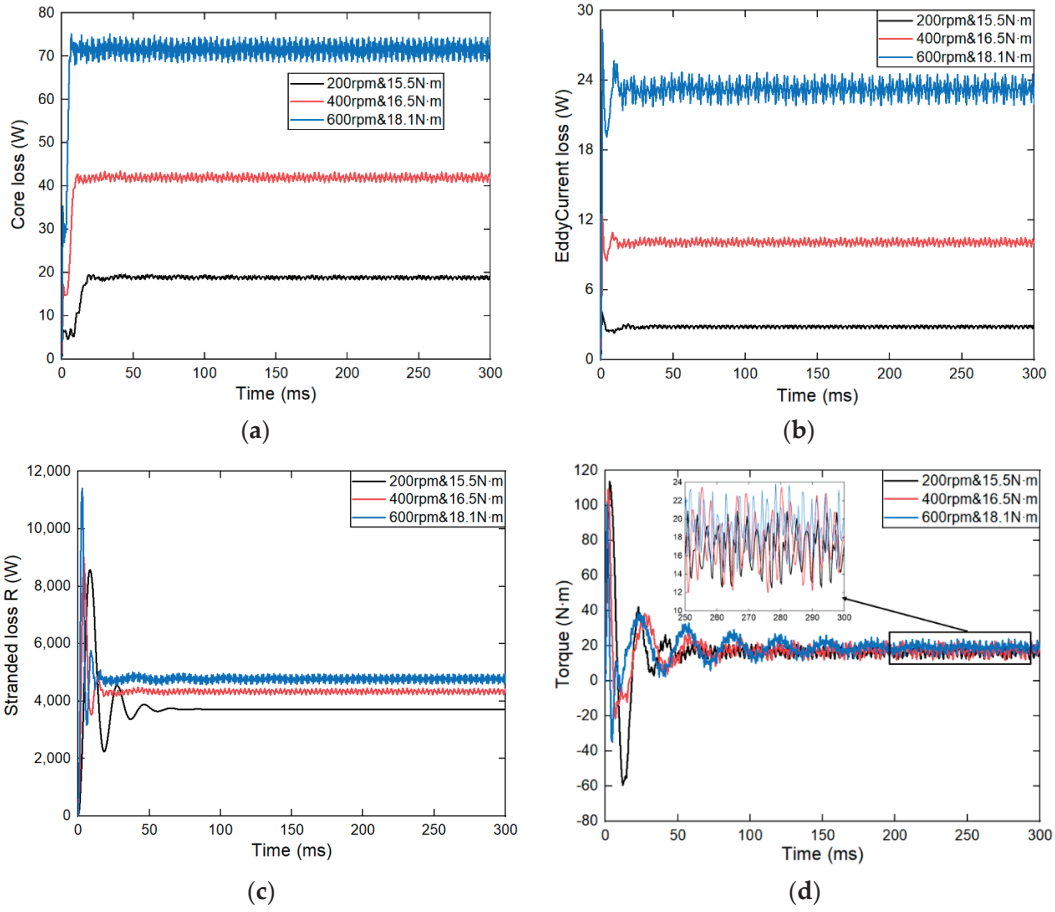

Figure 12. (**a**) Core loss of the hub motor; (**b**) eddy current loss of the hub motor; (**c**) winding loss of the hub motor; (**d**) output torque of the hub motors.

Table 5. The loss and output torque of the hub motor under various working conditions.

Parameter	200 rpm and 15.5 N · m	400 rpm and 16.5 N · m	600 rpm and 18.1 N · m
Output torque/N · m	16.94	17.89	19.48
Core loss/W	18.88	41.97	71.58
Eddy current loss/W	2.84	10.09	23.26
Winding loss/W	3719.25	4335.94	4777.27

4.1.2. Relationship between the Air Gap and Motor Loss

To obtain the air gap variation law of the hub motor, it is necessary to calculate the variation law of the unbalanced magnetic pull F_y under different air gap spacings in the electromagnetic field model, obtain the air gap magnetic field stiffness K_{UMP_y} between the stator and the rotor, and then add it to the suspension dynamics model to simulate the relative offset of the stator and the rotor under the influence of various excitations in the actual operation process, which is the air gap deformation. Finally, the influence of air gap changes on the motor loss is analyzed. According to the analysis results of the load torque in Section 4.1.1, the rolling resistance torque at different speeds is added to the hub motor as the load torque, and the corresponding speed is set. With a non-eccentricity value of 0 mm and a dynamic eccentricity of 0.6 mm as examples, the radial air gap flux density is extracted, as shown in Figure 13a (see Figures A1a and A2a for the 200 rpm and 400 rpm conditions). With increasing speed, the radial air gap flux density does not significantly change, but with increasing dynamic eccentricity, the radial air gap flux density gradually increases, which also indicates that the unbalanced magnetic pull has a similar change rule. Therefore, the unbalanced magnetic pull under different air gaps must be studied and analyzed.

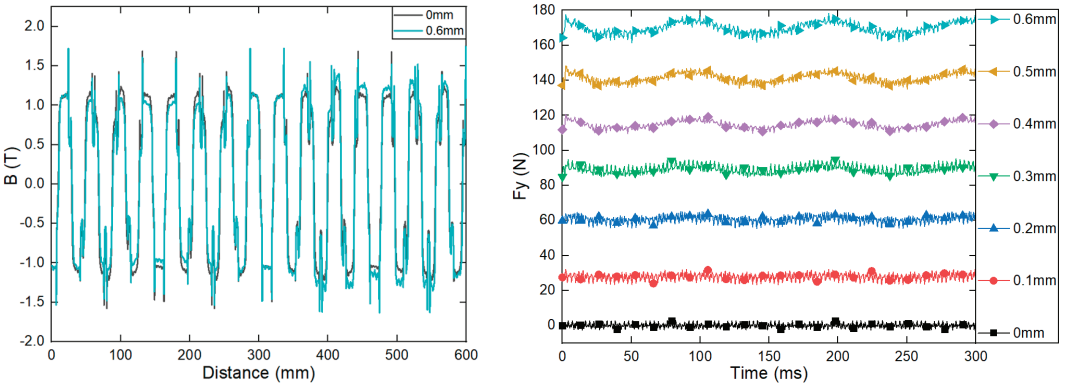

Figure 13. (**a**) Change in the radial magnetic density at 600 rpm; (**b**) Change in the unbalanced magnetic pull F_y at 600 rpm.

Using Equation (4), the radial magnetic density is calculated to obtain the component of the unbalanced magnetic pull force in the *Y* direction, and the relationship between the unbalanced magnetic pull force F_y and time at different speeds is obtained, as shown in Figure 13b; see Figures A1b and A2b for the 200 rpm and 400 rpm conditions. As shown in Table 6, there is a common change rule: when there is no eccentricity, F_y fluctuates around zero; however, as the degree of dynamic eccentricity increases, F_y also increases. Through the relationship between the eccentricity e and unbalanced magnetic pull force F_y, the air gap magnetic field stiffness K_{UMP_y}, which is used to characterize the unbalanced magnetic pull force in the *Y* direction, can be obtained. As shown in Figure 14, the air gap magnetic field stiffness K_{UMP_y} curves of the motor at different speeds show that K_{UMP_y} has a certain linearity, and then the K_{UMP_y} of the motor at different speeds can be obtained. As shown

in Table 7, as the motor speed exponentially increases, K_{UMP_y} increases by no more than 1%. It can be considered that the motor speed is independent of K_{UMP_y} when the other working conditions are constant, so the same air gap magnetic field stiffness can be used at any speed.

Table 6. Relationship between the unbalanced magnetic pull F_y and dynamic eccentricity under different working conditions.

Eccentricity *e*/mm	200 rpm	400 rpm	600 rpm
	Unbalanced Magnetic Pull F_y/N	Unbalanced Magnetic Pull F_y/N	Unbalanced Magnetic Pull F_y/N
0	0.09	0.08	0.08
0.1	27.36	27.64	27.90
0.2	59.50	60.14	60.74
0.3	87.44	88.42	89.26
0.4	112.53	113.79	114.88
0.5	138.59	140.10	141.42
0.6	166.58	168.43	169.96

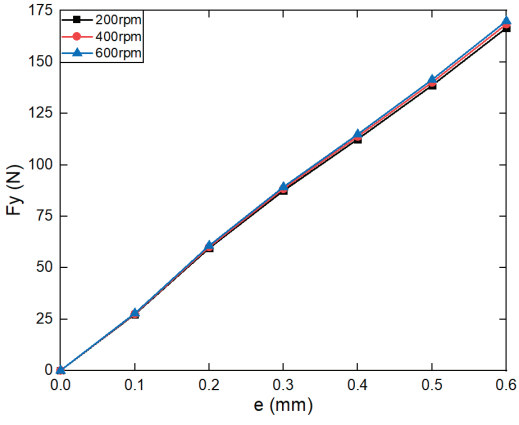

Figure 14. Equivalent stiffness K_{UMP_y} curves of the motor at different speeds.

Table 7. Equivalent stiffness K_{UMP_y} of the motor at different speeds.

Parameter	200 rpm	400 rpm	600 rpm
Linear K_{UMP_y} value (N/m)	277,633.33	280,716.67	283,266.67

According to Table 7, the average value of the air gap magnetic field stiffness K_{UMP_y} under the three motor speed conditions is set in the hub-driven suspension dynamics model. Through simulation analysis, the force between the stator and rotor F_s and the relative offset of the stator and rotor e_d (Figure 15a,b) are obtained. The root mean square values are shown in Table 8, which are used to characterize the air gap deformation of the hub motor under the coupling of the suspension and the hub motor.

Table 8. Air gap deformation simulation values.

Motor Speed/rpm	Rms F_s/N	Rms e_d/mm	e_{dmax}/mm
200	2231.824	0.023	0.033
400	2265.646	0.028	0.040
600	2296.414	0.033	0.047

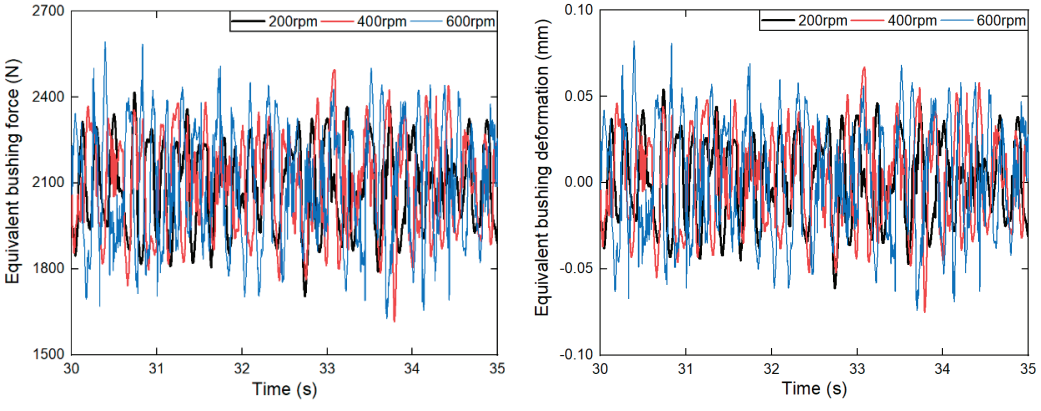

(**a**) (**b**)

Figure 15. (**a**) Force between the stator and rotor; (**b**) relative offset of the stator and rotor.

Through Equation (9), the rms value of the relative offset e_d of the stator and rotor can be obtained as $\frac{1}{\sqrt{2}}e_{dmax}$ mm; thus, the maximum displacement of the dynamic eccentricity $e_{dmax} = \sqrt{2}e_d$ mm, and the maximum dynamic eccentricity e_{dmax} at different speeds is calculated, as shown in Table 8. Under the load torque corresponding to different speeds, the influence of the air gap deformation of the hub motor on the output torque and loss of the hub motor is studied by setting the eccentricity in the finite element model of the electromagnetic field to the non-eccentricity value and the maximum dynamic eccentricity of the motor rotor at the corresponding speed, as shown in Figure 16 (see Figures A3 and A4 for the 200 rpm and 400 rpm conditions).

Table 9 shows that during vehicle operation, as the motor speed increases, the loss of each component of the hub motor also increases, and the output torque also increases. At the same speed, based on a comparison of the results when considering the air gap deformation and not considering the air gap deformation, this deformation has little effect on the output torque of the hub motor, but it has a great influence on the loss of each component of the hub motor, among which the strongest influence is on the winding loss, whereas the other losses are slightly increased. From the above analysis results, it can be concluded that at different speeds, the deformation of the air gap differs, which greatly influences the change in the loss of each component. Therefore, the temperature characteristics of the hub motor must be analyzed in combination with the deformation of the air gap.

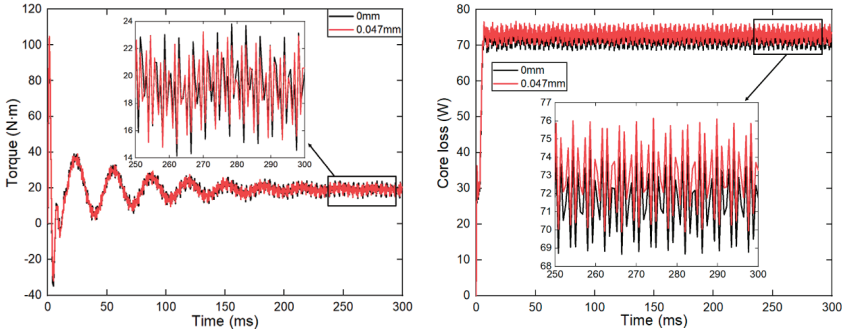

(**a**) (**b**)

Figure 16. *Cont.*

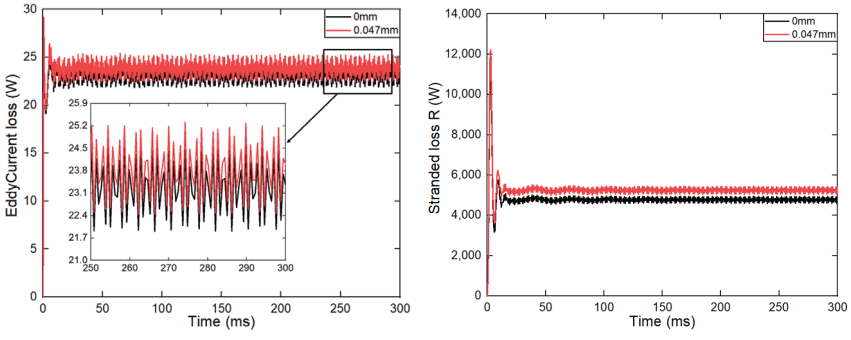

Figure 16. (**a**) Output torque of the hub motor caused by changes in the air gap at 600 rpm; (**b**) core loss of the hub motor caused by air gap changes at 600 rpm; (**c**) eddy current loss of the hub motor caused by air gap changes at 600 rpm; (**d**) winding loss of the hub motor caused by air gap changes at 600 rpm.

Table 9. Changes in the torque and loss of the hub motor caused by changes in the air gap under different working conditions.

Parameter	200 rpm			400 rpm			600 rpm		
	0 mm	0.033 mm	Rate of Change	0 mm	0.040 mm	Rate of Change	0 mm	0.047 mm	Rate of Change
Output torque/N·m	16.71	16.75	0.24%	17.66	17.62	−0.23%	19.16	19.17	0.05%
Core loss/w	18.88	19.16	1.48%	41.30	42.71	3.41%	71.58	73.00	1.98%
Eddy current loss/w	2.84	2.90	2.11%	10.05	10.32	2.69%	23.26	23.83	2.45%
Winding loss/w	3719.25	3890.49	4.60%	4353.00	4665.00	7.17%	4777.27	5248.85	9.87%

4.2. Temperature Field Analysis of the Hub Motor

According to the actual operating environment of the vehicle, the rolling resistance torque in the actual operation of the vehicle under different motor speeds and the influence of the air gap deformation of the hub motor caused by various excitations on the temperature characteristics of the hub motor are considered. By comparing the temperature cloud diagrams of the magnetic–thermal coupling of the hub motor at different speeds, as shown in Figure 17, the high-temperature area inside the hub motor is found to be mainly concentrated on the stator and winding, and the lowest temperature appears in the permanent magnet and rotor. With increasing motor speed, the corresponding temperature also accordingly increases. The high-temperature area is mainly concentrated in the stator and winding, and the highest temperature of the stator appears in the stator yoke. This is mainly due to the small heat dissipation area of the stator yoke, which results in a poor heat dissipation capacity. In the radial direction of the stator, from the stator yoke to the tooth, the temperature gradually decreases, and the temperature in the stator air gap suddenly decreases. This is mainly because only the permanent magnet in the air gap area produces a small amount of heat, while the winding and stator of the stator yoke tooth produce more heat. The low-temperature area is mainly concentrated on the permanent magnet and the rotor. The reason for this phenomenon is that the outermost heat dissipation condition of the rotor is better, so the temperatures of the rotor and the permanent magnet are relatively low, and the lowest temperature of the motor only appears on the outer side of the rotor.

Figure 18 and Table 10 show that the temperature of each component of the hub motor gradually increases with time during vehicle operation. The temperature rises faster before 1000 s. Between 1000 s and 2000 s, the temperature rise trend of the motor gradually decreases. At different speeds, the temperature of the motor winding gradually stabilizes at 85.43 °C, 95.67 °C and 101.56 °C. After running for 2000 s, the temperature curve of each component of the hub motor gradually stabilizes, the temperatures of the motor winding

and the stator gradually approach each other, and the temperatures of the permanent magnet and the rotor gradually approach each other.

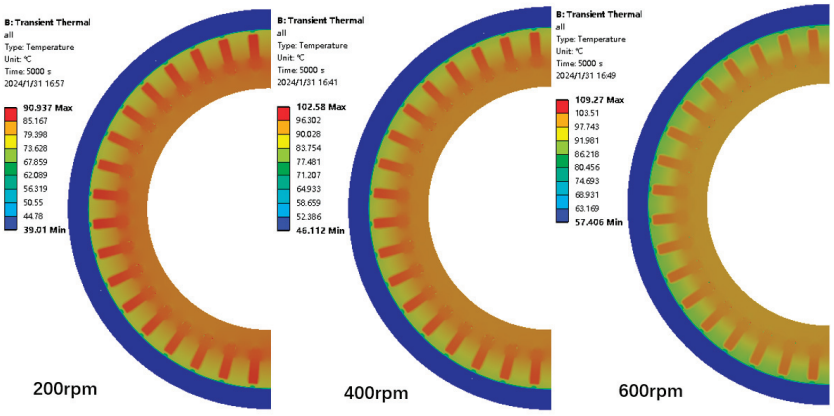

Figure 17. Overall temperature cloud diagrams of the hub motor at 200 rpm, 400 rpm, and 600 rpm.

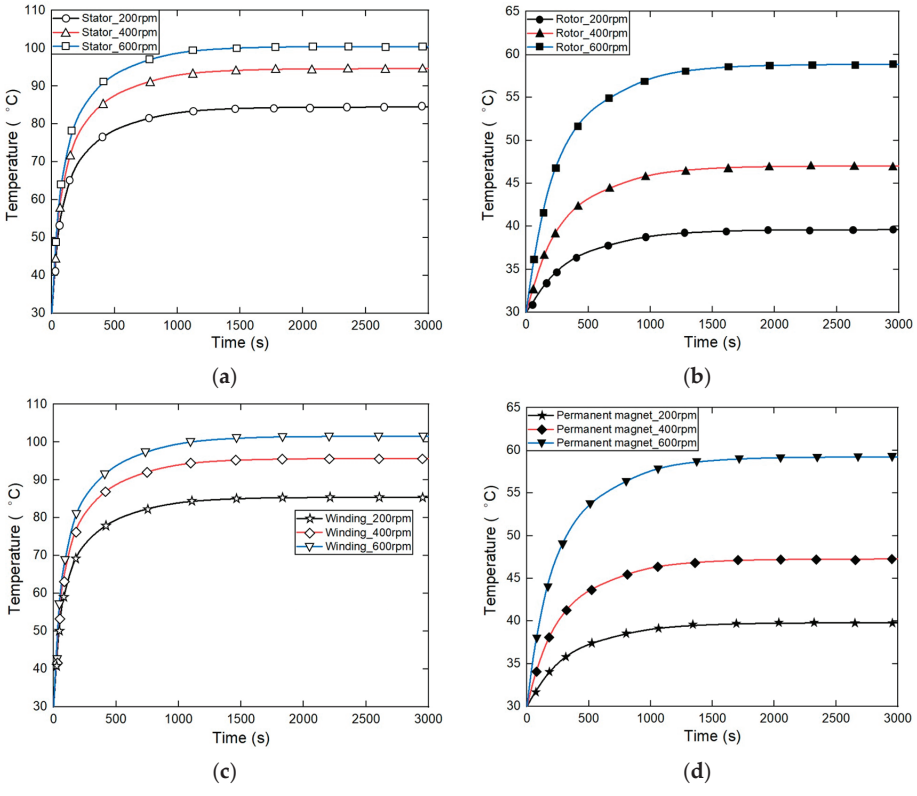

Figure 18. (**a**) Temperature variation curves of the hub motor stator. (**b**) Temperature variation curves of the hub motor rotor. (**c**) Temperature variation curves of the hub motor winding. (**d**) Temperature variation curves of the hub motor permanent magnet.

Table 10. Temperature of each component of the hub motor under different working conditions.

Working Condition	Maximum Stator Temperature/°C	Rotor Maximum Temperature/°C	Maximum Winding Temperature/°C	Maximum Temperature of Permanent Magnet/°C
200 rpm	84.48	39.61	85.43	39.79
400 rpm	94.61	47.02	95.67	47.26
600 rpm	100.47	58.84	101.56	59.23

4.3. Torque Output Analysis of Hub Motor

According to the actual operating environment of the vehicle, the influences of the actual operating load torque of the vehicle at different motor speeds and the air gap deformation of the hub motor caused by various excitations on the temperature characteristics of the hub motor are considered. By comparing the output torque of the hub motor at different speeds under the influence of the motor temperature rise (the maximum temperature of the motor winding), as shown in Figure 19 (see Figure A5 for the 200 rpm and 400 rpm conditions) and Table 11, as the internal temperature rise of the hub motor reaches a steady state, its output torque is found to be reduced to a certain extent, by 4–8% compared with the output torque at room temperature. This phenomenon occurs because, with increasing temperature, the copper wire resistance of the winding also increases, which affects the magnetic field strength inside the hub motor and consequently affects the actual output capacity of the motor. Due to the decrease in the output torque caused by the increase in the internal temperature of the hub motor, there may be problems such as insufficient power and weakness during the operation of the vehicle, and the accuracy of motor torque control will also be reduced. Therefore, the influence of the temperature rise on the output torque of the hub motor should be considered in the actual analysis process.

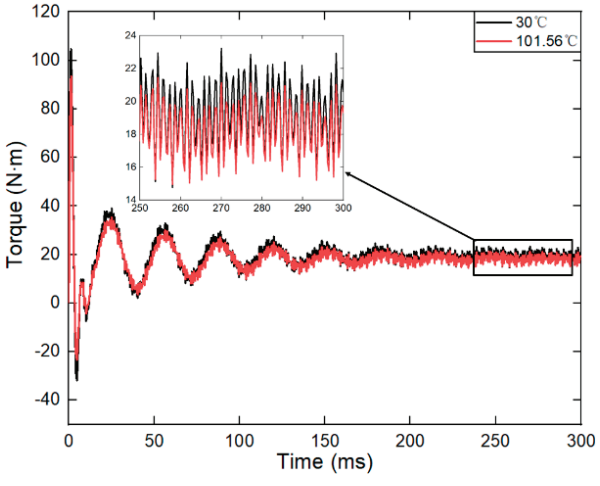

Figure 19. Changes in the output torque of the hub motor at 600 rpm.

Table 11. Changes in the output torque of the hub motor under different working conditions.

Working Condition	Output Torque at Room Temperature/N · m	Output Torque under Temperature Rise/N · m	Rate of Change
200 rpm	16.75	15.91	5.01%
400 rpm	17.62	16.19	8.12%
600 rpm	19.17	18.22	4.96%

5. Experimental Verification

A temperature rise test of the hub motor is carried out, and the results are compared with the temperature rise simulation results. As shown in Figure 20, the temperature rise test system of the hub motor of the 1/4 suspension driven by the hub mainly includes the 1/4 suspension, a torque sensor, an infrared thermometer, and a temperature sensor. The torque sensor is used to measure the torque applied by the hub motor on the drum (i.e., the output torque of the hub motor). The temperature sensor is installed in the motor winding to measure the temperature of the internal winding of the motor, and the infrared thermometer is used to measure the surface temperature of the rotor. In the temperature rise test of the hub motor, the temperature of the measuring point is read by the temperature sensor and the infrared thermometer, as shown in Figure 21 (see Figure A6 for the 200 rpm and 400 rpm conditions) and Table 12. The calculated temperature and test temperature change curves of the winding and rotor shell can be well fitted, indicating the accuracy of the calculation results, but there are some differences. The maximum error of the winding and rotor temperatures is not more than 2%. The reasons for the discrepancy may be that, on the one hand, the motor model system is simplified to a certain extent, and the calculated thermal conductivity and heat dissipation coefficient deviate from the actual values. On the other hand, there are errors in the accuracy of the test methods, means, and sensors, but the results are within a controllable range.

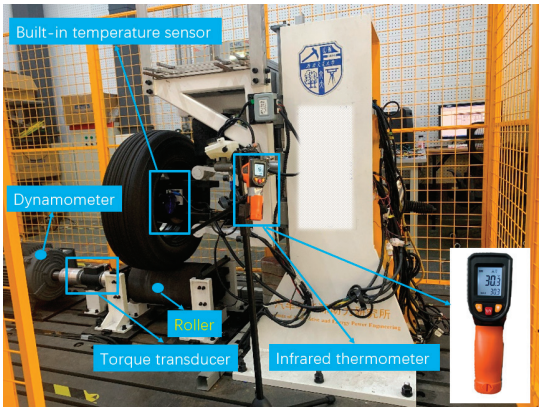

Figure 20. Temperature rise test system of the 1/4 suspension hub motor driven by the hub.

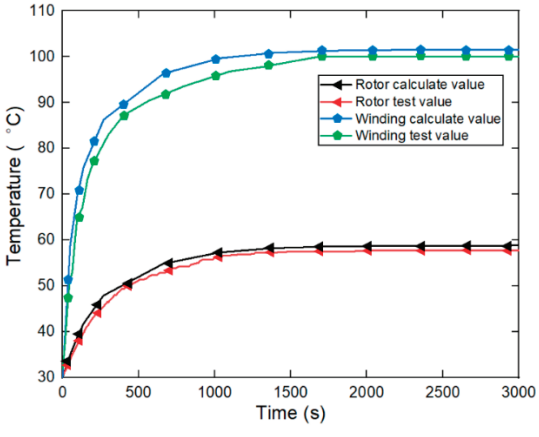

Figure 21. Rotor and winding test temperature and calculated temperature curves at 600 rpm.

Table 12. Comparison of the test temperatures and calculated temperatures of the rotor and winding under different working conditions.

Working Condition	Rotor			Winding		
	Simulated Temperature/°C	Measured Temperature/°C	Error	Simulated Temperature/°C	Measured Temperature/°C	Error
200 rpm	39.61	39.96	0.88%	85.43	86.50	1.24%
400 rpm	47.02	46.50	1.12%	95.67	94.00	1.78%
600 rpm	58.84	57.80	1.80%	101.56	99.80	1.76%

The curve of the motor test torque with time at 600 rpm is shown in Figure 22 (Figures A7 and A8 for the 200 rpm and 400 rpm conditions.). The two yellow dotted lines in the figure represent the motor output torque at room temperature and the steady-state temperature, respectively. The output torque of the motor gradually increases with increasing motor speed. Over time, the output torque decreases with the increase in temperature, and the amplitude of the decrease is in the range of 0.82~1.25 N·m. As shown in Table 13, by comparing the variations in the simulation and test output torques at room temperature and under a temperature rise, it can be seen that at the same speed, the test output torque values of the hub motor at room temperature and under the temperature rise are greater than the simulated values. A possible reason is that there is a bearing friction resistance inside the motor, dynamometer, and drum in practice, which increases the output torque of the hub motor. The variation trends of the simulation and test output torques of the motor are similar, and the change rate can be well matched. By comparing the temperatures and output torques from the simulation and test, it is proven that the research method for determining the temperature rise characteristics of a hub motor under multisource excitation coupling proposed in this paper is reasonable and effective.

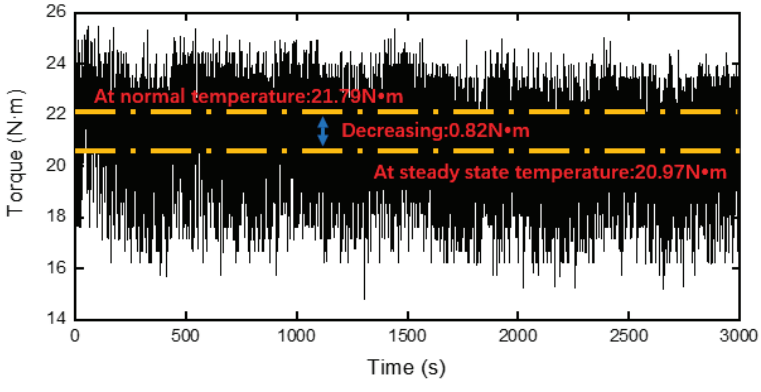

Figure 22. Motor test torque with time at 600 rpm.

Table 13. Comparison of simulated and tested motor torques under different working conditions.

Working Condition	Simulation			Test		
	Output Torque at Room Temperature/N · m	Output Torque under a Temperature Rise/N · m	Rate of Change	Output Torque at Room Temperature/N · m	Output Torque under a Temperature Rise/N · m	Rate of Change
200 rpm	16.75	15.91	5.01%	17.28	16.03	7.23%
400 rpm	17.62	16.19	8.12%	19.88	18.71	5.89%
600 rpm	19.17	18.22	4.96%	21.79	20.97	3.76%

6. Conclusions

In this paper, the hub motor of an electric vehicle is taken as the research object, and the change in the load torque of the hub motor caused by the rolling resistance torque in the actual operating environment of the vehicle and the change in the air gap deformation caused by the excitation of the hub motor stator and rotor transmitted from the road surface through the tire and by the excitation of the body transmitted through the suspension are considered. The temperature rise characteristics and output torque characteristics of the hub motor under the combined action of the two changes at different motor speeds are studied and analyzed. First, with the support of theoretical calculations, the rolling resistance torque in the actual operating environment of the vehicle is obtained through simulation analysis of the dynamic model of the hub drive suspension, which is added to the electromagnetic field model of the hub motor as the actual load torque to analyze its influence on the loss of each component of the motor. Then, on the basis of the actual load torque of the hub motor, the change in the unbalanced magnetic pull under different air gap spacings is simulated and analyzed by the electromagnetic field model. Second, the relationship between the unbalanced magnetic pull and the air gap spacing is input into the dynamic model of the hub-driven suspension as the air gap magnetic field stiffness. The air gap change caused by the vibration excitation of the road surface transmitted to the stator and rotor of the hub motor through the tire and by the excitation of the body transmitted through the suspension in the actual operating environment is simulated, and the influence of air gap deformation on the loss of each component of the motor is analyzed. Next, through the magnetic–thermal two-way coupling method, the variation law of the temperature rise characteristics of the hub motor and the variation law of the motor output torque caused by the temperature rise under the combined action of the two factors of the load torque change and air gap change are analyzed. The validity and accuracy of the method adopted in this paper are verified by the temperature rise test of a prototype. The method for analyzing the temperature rise and torque characteristics of a hub motor, considering multisource excitation magnetic–thermal bidirectional coupling proposed in this paper, is reasonable and effective. It provides a theoretical basis for the precise control of the output torque of the distributed drive vehicle hub drive motor and produces greater economic benefits.

Due to the limitation of research conditions, the comprehensiveness of vehicle driving cycle selection, model simplification methods, and principles need to be further studied in this paper. Specifically, further improvement and in-depth research can be carried out from the following aspects:

1. The influence of load torque and air gap changes in the hub motor on the temperature rise characteristics and torque characteristics of hub motor under multiple driving conditions (turning, braking, acceleration, different road grades, different body mass, and composite conditions) is carried out.
2. The finite element model of the electromagnetic field and temperature field of the hub motor is improved, and the 3D finite element model is established to improve the accuracy of the simulation.
3. Through the research of this paper, it is found that the load torque and air gap change in the hub motor will have a certain impact on its temperature rise characteristics and torque characteristics. On the basis of this research, the rolling resistance torque and vertical vibration of the vehicle can be reduced from the suspension control so as to reduce the load torque and air gap change in the motor, reduce the temperature rise and output torque fluctuation of the motor; at the same time, it also provides some research support for the torque control of the hub motor.
4. The calculation method proposed in this paper has a certain reliability. However, due to the combination of dynamics and finite element analysis methods, the calculation process of the temperature rise and torque of in-wheel motors may be more complicated than in conventional methods. However, as long as the analysis steps are

correct, the torque change characteristics caused by the temperature rise of the hub motor under actual operating conditions can still be calculated efficiently.

Author Contributions: Methodology and writing-original draft: M.Y.; writing-original draft: Y.B.; methodology: H.H.; writing—review and editing: Y.L.; experiments and records: H.Z.; supervision, funding acquisition: W.D. All authors have read and agreed to the published version of the manuscript.

Funding: This research was funded by the Natural Science Foundation of Sichuan Province (2023NSFSC0395) and the Sichuan Science and Technology Program (2022ZHCG0061).

Data Availability Statement: The data used to support the findings of this study are available from the corresponding author upon request.

Acknowledgments: The authors would like to acknowledge the support from the Sichuan Provincial Natural Science Foundation and the facilities provided by the Institute of Energy and Power Research at Southwest Jiaotong University for the experimental research.

Conflicts of Interest: The authors declare no conflict of interest.

Appendix A

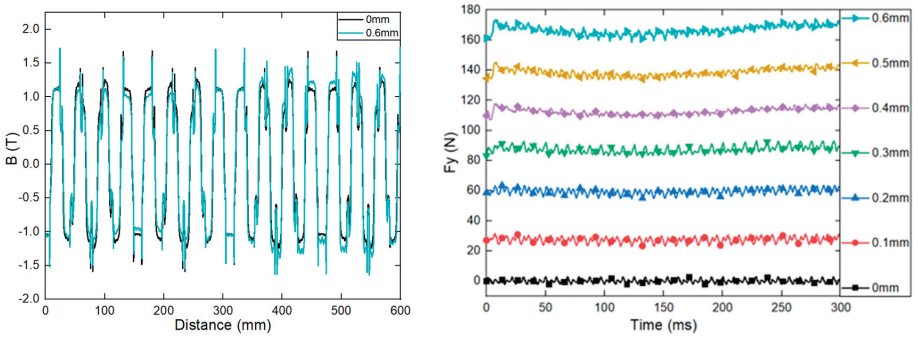

(**a**) (**b**)

Figure A1. (**a**) Change in the radial magnetic density at 200 rpm. (**b**) Change in unbalanced magnetic pull F_y at 200 rpm.

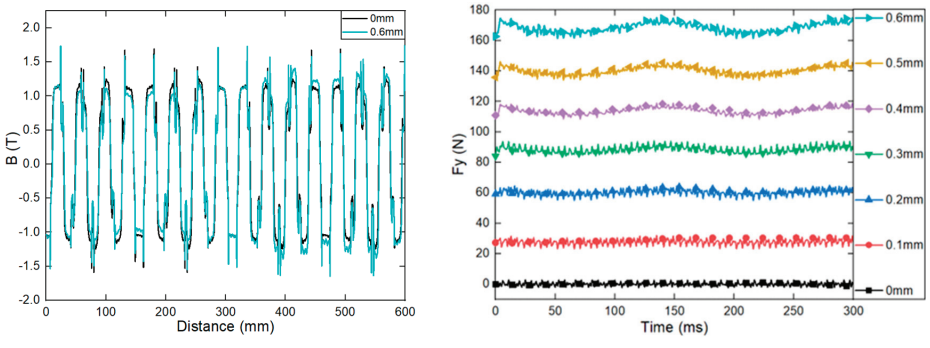

(**a**) (**b**)

Figure A2. (**a**) Change in the radial magnetic density at 200 rpm. (**b**) Change in unbalanced magnetic pull F_y at 400 rpm.

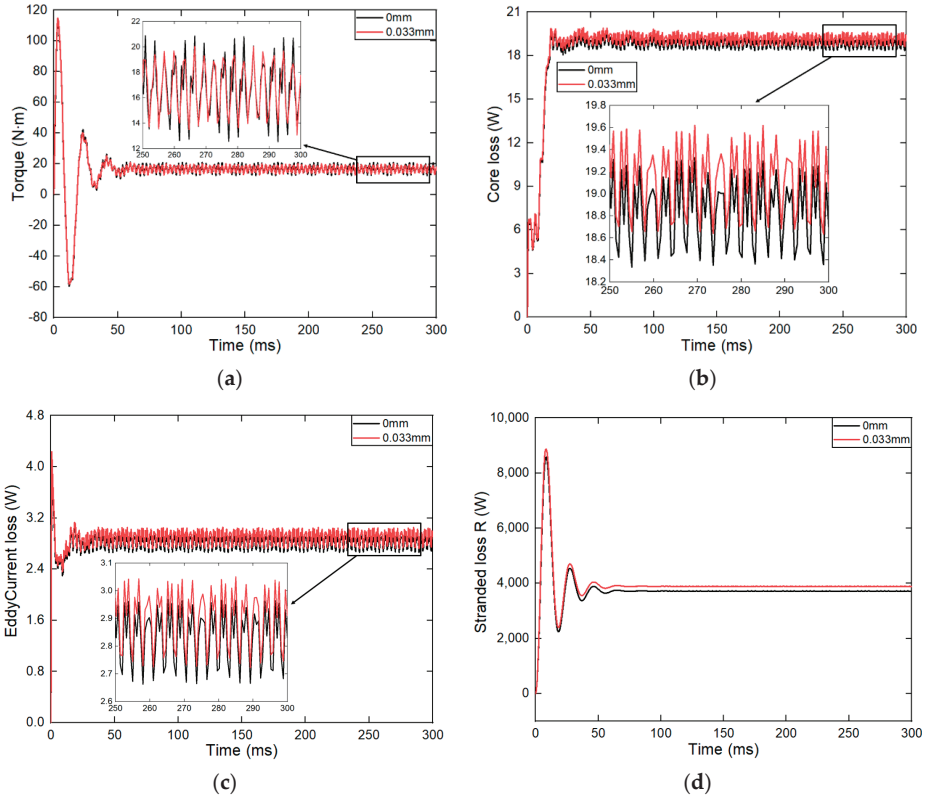

Figure A3. (**a**) Output torque of the hub motor caused by changes in the air gap at 200 rpm. (**b**) Core loss of the hub motor caused by air gap changes at 200 rpm. (**c**) Eddy current loss of the hub motor caused by air gap changes at 200 rpm. (**d**) Winding loss of the hub motor caused by air gap changes at 200 rpm.

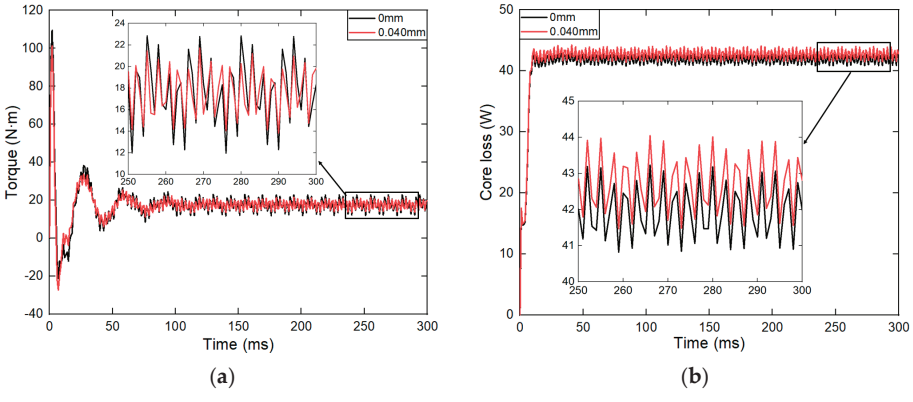

Figure A4. *Cont.*

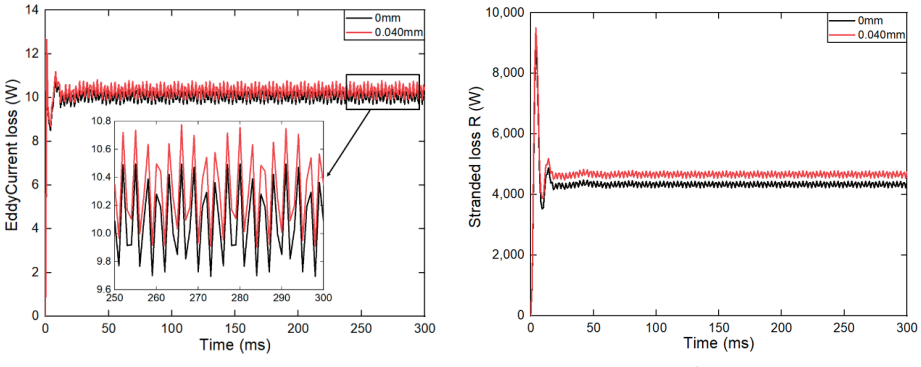

(**c**) (**d**)

Figure A4. (**a**) Output torque of the hub motor caused by changes in the air gap at 400 rpm. (**b**) Core loss of the hub motor caused by air gap changes at 400 rpm. (**c**) Eddy current loss of the hub motor caused by air gap changes at 400 rpm. (**d**) Winding loss of the hub motor caused by air gap changes at 400 rpm.

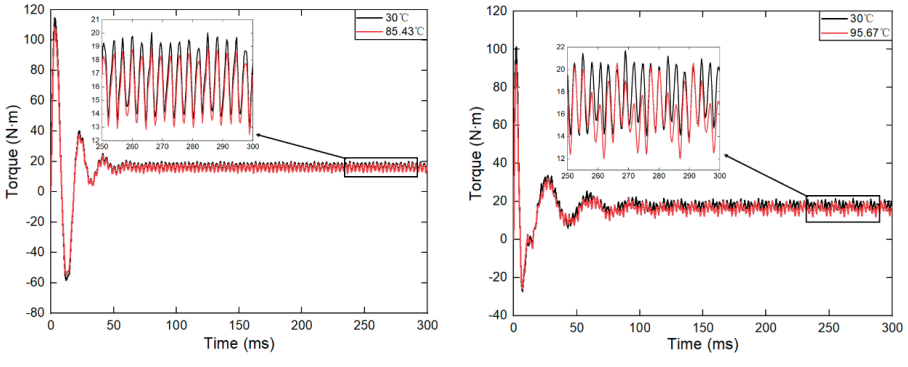

(**a**) (**b**)

Figure A5. (**a**) Output torque change in the hub motor at 200 rpm. (**b**) Output torque change in the hub motor at 400 rpm.

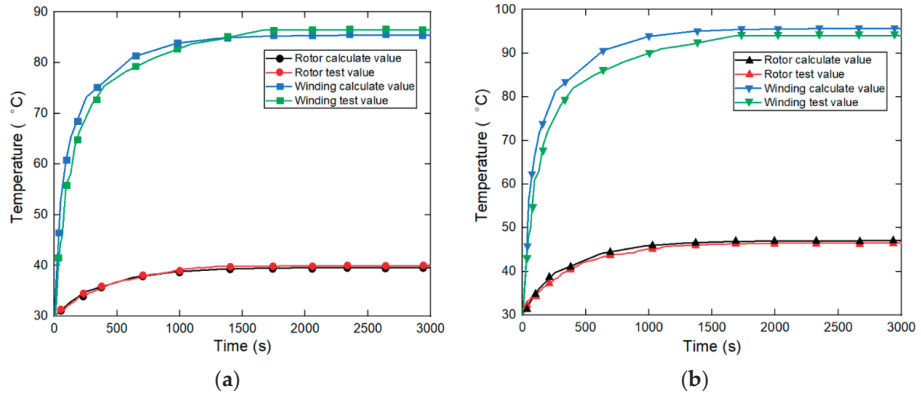

(**a**) (**b**)

Figure A6. (**a**) Rotor and winding test temperature and calculated temperature curves at 200 rpm. (**b**) Rotor and winding test temperature and calculated temperature curves at 400 rpm.

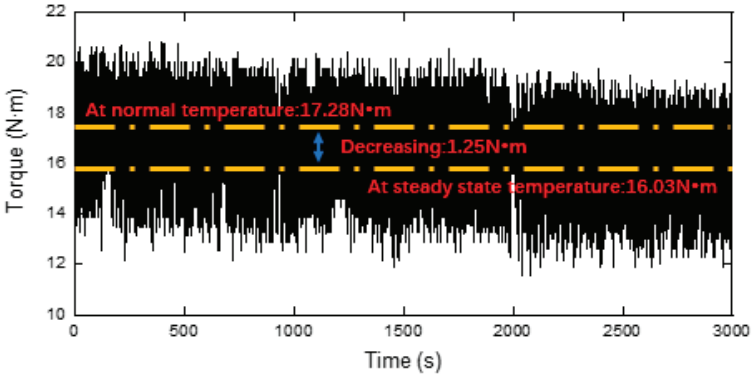

Figure A7. Motor test torque curve with time at 200 rpm.

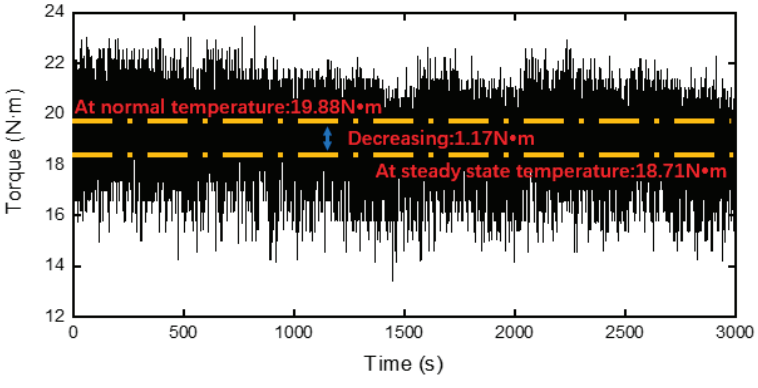

Figure A8. Motor test torque curve with time at 400 rpm.

References

1. Ma, J.; Liu, X.; Chen, Y. China's new energy automobile industry and technology development status and countermeasures. *China J. Highw. Transp.* **2018**, *31*, 1–19. [CrossRef]
2. Huang, H.; Lim, T.C.; Wu, J.; Ding, W.; Pang, J. Multitarget prediction and optimization of pure electric vehicle tire/road airborne noise sound quality based on a knowledge-and data-driven method. *Mech. Syst. Signal Process.* **2023**, *197*, 110361. [CrossRef]
3. Chan, C.C.; Chau, K.T. *Modern Electric Vehicle Technology*; Oxford University Press: Oxford, UK, 2001. [CrossRef]
4. Huang, H.; Huang, X.; Ding, W.; Zhang, S.; Pang, J. Optimization of electric vehicle sound package based on LSTM with an adaptive learning rate forest and multiple-level multiple-object method. *Mech. Syst. Signal Process.* **2023**, *187*, 109932. [CrossRef]
5. Chen, S.; Zhang, Q.; He, B.; Huang, S.; Hui, D.D. Thermal Analysis of High Density Permanent Magnet Synchronous Motor Based on Multi Physical Domain Coupling Simulation. *J. Electr. Eng. Technol.* **2017**, *12*, 91–99. [CrossRef]
6. Glass, L. An Input-to-State Stable Virtual Sensor for Electric Motor Rotor Temperature. *IFAC-Pap.* **2023**, *56*, 240–245. [CrossRef]
7. Yang, W.; Zhou, Z.; Li, Z. Study on the temperature field of hub motor by oil cooling temperature and flow rate. *Micromotors* **2020**, *53*, 31–34+42. [CrossRef]
8. Huang, H.; Huang, X.; Ding, W.; Yang, M.; Yu, X.; Pang, J. Vehicle vibro-acoustical comfort optimization using a multi-objective interval analysis method. *Expert Syst. Appl.* **2023**, *213*, 119001. [CrossRef]
9. Zhang, L.; Yan, Y.; Ma, Q. Magnetic-thermal bidirectional coupling of in-wheel motor for electric vehicle. *J. Mech. Electr. Eng.* **2019**, *36*, 407–412. [CrossRef]
10. Li, X.; Ding, B.; Jia, T. Three-dimensional temperature field analysis of direct-drive permanent magnet in-wheel motor for electric vehicles. *Micromotors* **2017**, *45*, 45–48+58. [CrossRef]
11. Wang, S.; Liu, M.; Zhu, B. Analysis on Temperature Field of Permanent Magnet Synchronous Motor in P2 Hybrid Electric Vehicle. *Micromotors* **2016**, *44*, 33–36.
12. Wu, Y.; Fang, X. Calculation of Motor Temperature Field under Different Loads. *Micromotors* **2020**, *48*, 27–31. [CrossRef]
13. Zhang, Q.; Lei, L.; Liu, G. Analysis of Electromagnetic Loss Characteristics of Electric Vehicle In-Wheel Motor Based on Maxwell. *Electr. Mach. Control Appl.* **2019**, *46*, 59–64.
14. Wei, Y.; Meng, D.; Wen, J. *Internal Heat Exchange of Motor*; Mechanical Industry Press: Beijing, China, August 1998.

15. Ma, J.; Pan, Y.; Luo, X.; Xiao, H.; Yang, J.; Simpson, N.; Mellor, P. Design of a 10 kW Superconducting Homopolar Inductor Machine Based on HTS REBCO Magnet. *IEEE Trans. Appl. Supercond.* **2024**, *34*, 5200407. [CrossRef]
16. Zhu, S.; Cheng, M.; Dong, J.; Du, J. Core Loss Analysis and Calculation of Stator Permanent-Magnet Machine Considering DC-Biased Magnetic Induction. *IEEE Trans. Ind. Electron.* **2014**, *61*, 5203–5212. [CrossRef]
17. Zhai, L. Losses estimation, thermal-structure coupled simulation analysis of a magnetic-bearing reaction wheel. *Int. J. Appl. Electromagn. Mech.* **2019**, *60*, 33–53. [CrossRef]
18. Han, Y.; Chen, T.; Li, G. Vibration Characteristics and Unbalanced Electromagnetic Force Analysis of a Rotor for a Hub Motor with Air Gap Eccentricity. *Sci. Technol. Eng.* **2019**, *19*, 140–145. [CrossRef]
19. Chen, Q.P. Study on temperature influence factors and electromagnetic heat coupling of in-wheel motor for micro-electric vehicle. *Mechanika* **2014**, *20*, 80–86. [CrossRef]
20. Xue, S.; Zhu, Z.Q.; Wang, Y.; Feng, J.; Guo, S.; Li, Y.; Chen, Z.; Peng, J. Thermal-Loss Coupling Analysis of an Electrical Machine Using the Improved Temperature-Dependent Iron Loss Model. *IEEE Trans. Magn.* **2018**, *54*, 18105005. [CrossRef]
21. Yang, C.; Zhang, Y.; Qiu, H. Influence of Output Voltage Harmonic of Inverter on Loss and Temperature Field of Permanent Magnet Synchronous Motor. *IEEE Trans. Magn.* **2019**, *55*, 8201605. [CrossRef]
22. Jiang, W.; Jahns, T.M. Coupled Electromagnetic–Thermal Analysis of Electric Machines Including Transient Operation Based on Finite-Element Techniques. *IEEE Trans. Ind. Appl.* **2015**, *51*, 1880–1889. [CrossRef]
23. Chang, H.Y.H.; Yang, Y.P.; Lin, F.K.T. Thermal-fluid and electromagnetic coupling analysis and test of a traction motor for electric vehicles. *J. Chin. Inst. Eng.* **2018**, *41*, 51–60. [CrossRef]
24. Tan, D.; Lu, C. The Influence of the Magnetic Force Generated by the In-Wheel Motor on the Vertical and Lateral Coupling Dynamics of Electric Vehicles. *IEEE Trans. Veh. Technol.* **2016**, *65*, 4655–4668. [CrossRef]
25. Li, D. *Longitudinal Vibration Analysis and Optimization of in-Wheel Motor Drive Electric Wheel System Considering Unbalanced Magnetic Pull*; Tongji University: Shanghai, China, 2019.
26. Wu, L.; Yu, S.; Yu, Y. Electromechanical coupling rotor dynamics analysis of permanent magnet synchronous motorized spindle. *Modul. Mach. Tool Autom. Manuf. Tech.* **2021**, *11*, 10–14. [CrossRef]
27. Hu, Z. *Research on In-Wheel Motorvibration Control of Distributed Drive Vehicle*; Southwest Jiaotong University: Chengdu, China, 2022.
28. Zeng, X.; Han, B.; Ling, X. Study on Vehicle Road Resistance Considering Incoming Flow Yaw Angle. *Automot. Eng.* **2022**, *12*, 170–179. [CrossRef]
29. Chen, S.; Hu, M.; Zhao, J. Real-time 'Torque Distribution Strategy for Dual-motor Pure Electric Vehicle with Minimum System Loss. *J. Mech. Eng.* **2024**, *59*, 411–423. [CrossRef]
30. Shi, L. *Research on Precise Torque Control Method of PMSM for Vehicles Considering Motor Temperature Variation*; Chongqing University: Chong Qing, China, 2022. [CrossRef]
31. Sun, Z. *Research on Performance and Temperature Rise of Permanentmagnet Synchronous Motor in High Temperature Environment*; Harbin Institute of Technology: Harbin, China, 2017.
32. Kim, Y.-S.; Sul, S.-K. Torque Control Strategy of an IPMSM Considering the Flux Variation of the Permanent Magnet. In Proceedings of the IEEE Industry Applications Annual Meeting, New Orleans, LA, USA, 23–27 September 2007; pp. 1301–1307. [CrossRef]
33. Feng, J. *Research on Temperature Field Characteristics of Water-Cooled in-Wheel Motor under Road Excitation*; Shandong University of Technology: Zibo, China, 2021. [CrossRef]
34. Yu, Z. *Automobile Theory*, 6th ed.; Mechanical Industry Press: Beijing, China, 2018.
35. Fu, X.; Liu, Z.; Liu, D. Pivot Steering Control of Off-road Vehicles Driven by In-wheel Motors. *China Mech. Eng.* **2023**, *34*, 1251–1259. [CrossRef]
36. Wang, Y.; Li, P.; Ren, G. Electric vehicles with in-wheel switched reluctance motors: Coupling effects between road excitation and the unbalanced radial force. *J. Sound Vib.* **2016**, *372*, 69–81. [CrossRef]
37. Ma, J.; Wu, L.; Zhu, Z.Q. Effect of magnet thickness on electromagnetic performance of high-speed permanent magnet machines. In Proceedings of the 2017 IEEE International Electric Machines and Drives Conference (IEMDC), Miami, FL, USA, 21–24 May 2017; pp. 1–7. [CrossRef]
38. Huang, H.B.; Li, R.X.; Yang, M.L.; Lim, T.C.; Ding, W.P. Evaluation of vehicle interior sound quality using a continuous restricted Boltzmann machine-based DBN. *Mech. Syst. Signal Process.* **2017**, *84*, 245–267. [CrossRef]
39. Rezaee-Alam, F.; Rezaeealam, B.; Faiz, J. Unbalanced Magnetic Force Analysis in Eccentric Surface Permanent-Magnet Motors Using an Improved Conformal Mapping Method. *IEEE Trans. Energy Convers.* **2017**, *32*, 146–154. [CrossRef]
40. Zhou, Z.; Yang, W.; Meng, X. Research on Temperature Field of In-wheel Motors with Different Cold Sources in Multi-mode Switching. *J. Hunan Univ. Nat. Sci.* **2021**, *48*, 51–58.
41. Zhang, H.; Xu, J.; Deng, Z. Temperature Field of in-Wheel Motor Using Coupled Multi-physics Domain Solution. *J. Southwest Jiaotong Univ.* **2020**, *55*, 76–83. [CrossRef]
42. Wang, Z.; Meng, Q.; Yan, W. Finite element method for calculating three-dimensional temperature field in electrical apparatus. *Low Volt. Appar.* **1987**, *4*, 19–23. [CrossRef]
43. Chen, X. *Analysis of Temperature Process of Rockfill Concrete Arch Dam Pouring through Warehouse*; Guizhou University: Guiyang, China, 2023. [CrossRef]

44. Hao, S. *Research on Vibration and Temperature Rise of In-Wheel Motor for Electric Vehicle*; East China Jiaotong University: Nanchang, China, 2021. [CrossRef]
45. Zhu, G.; Zhu, Y.; Tong, W. Analysis and enhancement of cooling system of high-speed permanent magnet motor based on computational fluid dynamics. *Adv. Technol. Electr. Eng. Energy* **2017**, *36*, 1–7. [CrossRef]
46. Wang, X.; Gao, P. Analysis of 3-D temperature field of in-wheel motor with inner-oil cooling for electric vehicle. *Electric Mach. Control* **2016**, *20*, 36–42.
47. Alatalo, M. Evaluation of Three Cooling Concepts for an Electric Vehicle Motor—3D Models. In Proceedings of the 2020 International Conference on Electrical Machines (ICEM), Gothenburg, Sweden, 23–26 August 2020; pp. 867–873. [CrossRef]
48. Karnavas, Y.L.; Chasiotis, I.D.; Peponakis, E.L. Cooling system design and thermal analysis of an electric vehicle's in-wheel PMSM. In Proceedings of the 2016 XXII International Conference on Electrical Machines (ICEM), Lausanne, Switzerland, 4–7 September 2016; pp. 1439–1445. [CrossRef]

energies

MDPI

Article

A Contoured Controller Bode-Based Iterative Tuning Method for Multi-Band Power System Stabilizers

Hao Xu [1], Chongxi Jiang [2] and Deqiang Gan [1,*]

[1] School of Electrical Engineering, Zhejiang University, Hangzhou 310027, China; eexuhao@zju.edu.cn
[2] Hangzhou Power Supply Company, State Grid Zhejiang Electric Power Co., Ltd., Hangzhou 310027, China; jiangchongxi@outlook.com
* Correspondence: dgan@zju.edu.cn

Abstract: An iterative tuning method for multi-band power system stabilizers is proposed, which utilizes the contoured controller Bode (CCBode) plot. The typical multi-band power system stabilizer, PSS4B, is conceptualized as a series connection of two filters: a band-pass filter and a phase compensator. The tuning process involves a space searching approach for the phase compensator to ensure its phase–frequency response remains within acceptable bounds. Subsequently, the CCBode plot is employed to adjust the magnitude–frequency response of the band-pass filter, thereby enhancing stability performance across a broad frequency range. The method proposed can be applied to the parameter design of the multi-band power system stabilizer PSS4B in the power system to suppress the low-frequency oscillations of the local mode and inter-regional mode in the system. The effectiveness of this proposed method is demonstrated through case studies of the four -machine/two-area system and the North China Power Grid.

Keywords: contoured controller Bode (CCBode) plot; low-frequency oscillation; multi-band power system stabilizer; space searching approach

Citation: Xu, H.; Jiang, C.; Gan, D. A Contoured Controller Bode-Based Iterative Tuning Method for Multi-Band Power System Stabilizers. *Energies* **2024**, *17*, 3243. https://doi.org/10.3390/en17133243

Academic Editors: Ignacio Hernando-Gil, Da Xie, Yanchi Zhang, Dongdong Li, Chenghong Gu and Nan Zhao

Received: 23 May 2024
Revised: 16 June 2024
Accepted: 28 June 2024
Published: 1 July 2024

1. Introduction

The mechanism of low-frequency oscillation in power systems involves the system oscillating near the steady-state operating point after a disturbance due to the inertial response of synchronous generators. This can lead to increased amplitude oscillations and a potential loss of synchronization. Low-frequency oscillation is an inherent issue in synchronous generator operation and has caused numerous incidents globally. For example, in 1996, a severe blackout in the western United States was attributed to low-frequency oscillation. Similarly, interconnected power grids in North China, Central China, and Northeast China have experienced low-frequency oscillations [1–3]. Particularly in the North China Power Grid, the damping ratio of regional oscillations has been declining since 2009, frequently triggering low-frequency oscillations after accidents, thereby constraining inter-provincial power transmission [4]. Power system stabilizers (PSSs) are recognized as one of the most effective methods to suppress low-frequency oscillations, among which the multi-band power system stabilizer PSS4B is more flexible thus has gained attention as a potential solution [5,6].

Compared to the widely used single-band power system stabilizer PSS2B, PSS4B incorporates three frequency bands that can, respectively, compensate the phase lag of different modes. Previous studies [7,8] indicate that the PSS4B outperforms the PSS2B in damping multiple modes due to its higher degrees of freedom, which, however, bring challenges to the parameter tuning of PSS4B.

The tuning process for PSS parameters remains an unsolved fixed-order controller design challenge within the control filed [9,10], and numerous heuristic approaches have been proposed. Many approaches rely on first-order approximations of the dominant

eigenvalues [2,8,11–13]. Frequently, eigenvalue-based results are incorporated into an optimization model to yield more systematic solutions [3,14,15].

The most famous PSS tuning method is the so-called ideal phase curve method, which is an approach that is widely used in industry [16–20]. The shortcoming of this method is obvious, as it does not take the PSS magnitude–frequency characteristic into account and thus causes difficulties in PSS gain tuning. It is well recognized that one PSS has a critical gain, above which the instability of the so-called "exciter mode" occurs. As a rule of thumb, PSS gains are often set to one-third of the critical gain [21]. The existing method has a significant shortcoming: it separates the amplitude–frequency characteristic and phase–frequency characteristic of the PSS during the setting process. This separation makes it impossible to accurately measure the PSS's contribution to the stability margin and to ensure that the designed PSS parameters provide maximum damping for the oscillation mode. To address this issue, a contoured controller Bode-based iterative tuning method is proposed for the parameter tuning of PSS4Bs.

This paper first reviews the symmetrical approach to PSS4B parameter tuning, which promotes the practical application of PSS4B at the expense of reducing control freedom and does not discuss how to optimize the amplitude–frequency characteristics. Therefore, it has inadequacy in providing enough damping for local modes. To solve this problem, this paper proposes a revised PSS4B model with enhanced phase compensation, and an iterative design method is introduced based on this model, leveraging the contour controller Bode (CCBode) plot, which offers clear stability margins and considers the damping ratio. This method is based on two tuning tools: the space searching approach for tuning the appended phase compensation blocks, and the CCBode plot for tuning the band-pass filters to design PSS4B in an iterative manner. The advantage of the method is that both inter-area and local modes avoid the instability of the exciter mode, ensuring that the system can provide sufficient damping in the full frequency band of low-frequency oscillations, and has good engineering application prospects. The effectiveness of the proposed method is verified by the classic four-machine/two-area system and the North China Power Grid.

2. Revised Model of PSS4B

2.1. The Limitation of the Symmetrical Approach

The general structure of the PSS4B is shown in Figure 1. The widely used symmetrical approach uses only the first block in each branch and synthesize the pairs of lead–lag blocks into three symmetrical band-pass filters with center frequencies F_L, F_I, and F_H and gains K_L, K_I, and K_H [6].

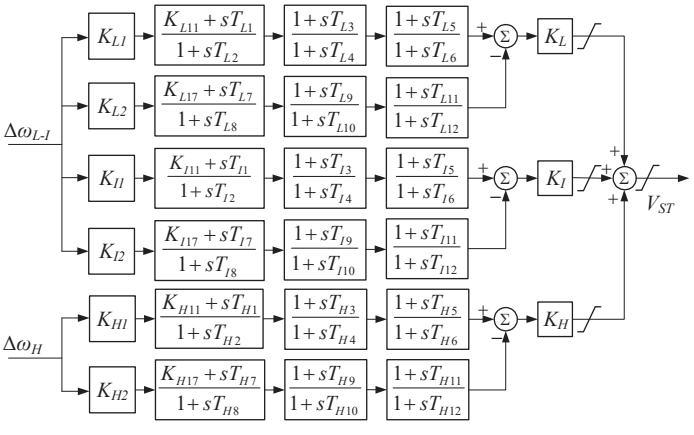

Figure 1. Standard IEEE model of PSS4B.

In Figure 1, s is the Laplace operator; $\Delta\omega_{L-I}$ is the input of the low- and medium-frequency branch, which is often the speed of generator; $\Delta\omega_H$ is the input of high frequency branch, which is often the active power of the generator; V_{ST} is the output signal of PSS4B, where each T represents a time constant.

The parameters are derived from the following equations when taking the high-frequency band as an example:

$$\begin{cases} K_{H11} = K_{H17} = 1 \text{ (lead} - \text{lag blocks)} \\ T_{H2} = T_{H7} = 1/(2\pi F_H\sqrt{R}) \\ T_{H1} = T_{H2}/R \\ T_{H8} = T_{H7} \times R \\ K_{H1} = K_{H2} = (R^2 + R)/(R^2 - 2R + 1) \end{cases}. \tag{1}$$

In Equation (1), R is the constant ratio, which is often set to 1.2.

Therefore, the transfer function of the high band $G_{Hn}(s)$ is given:

$$G_{Hn}(s) = K_H \cdot \frac{(R^2 + R)s}{R(2\pi F_H \cdot \sqrt{R} + s)(2\pi F_H + \sqrt{R} \cdot s)}. \tag{2}$$

The transfer function given in (2) can be viewed as a band-pass filter with a center frequency F_H. Compared with the complex combination of the original lead–lag blocks, the simplified PSS4B model has a clear physical meaning.

As the gains K_L, K_I, and K_H for the three band-pass filters are tuned independently, the PSS4B stabilizer enjoys many more degrees of freedom than the PSS2B stabilizer, which has only one gain parameter. This feature allows for the PSS4B to produce a flexible magnitude–frequency characteristic that not only offers sufficient damping to electromechanical oscillation modes, but also prevents the stabilizer gain from reaching too high in the high frequency range.

However, a PSS4B stabilizer designed using the above symmetrical parameter approach cannot provide enough phase compensation. To explain it, substitute $s = j\omega$ in (2) and then notice the following:

$$\angle G_{Hn}(j\omega) = 90^\circ - \tan^{-1}\left(\frac{\omega \cdot (1 + R)}{\sqrt{R}(2\pi F_H - \omega^2/2\pi F_H)}\right), \tag{3}$$

which is a monotonically decreasing function with a maximum value of 90° at ω = 0. Therefore, the total phase compensation provided by a PSS4B is limited:

$$\begin{aligned} &\angle G_{PSS4Bn}(j\omega) = \angle(G_{Ln}(j\omega) + G_{In}(j\omega) + G_{Hn}(j\omega)) \\ &\leq \max(\angle G_{Ln}(j\omega), \angle G_{In}(j\omega), \angle G_{Hn}(j\omega)) = 90^\circ, \end{aligned} \tag{4}$$

which is no greater than each of its frequency band can supply. The experience in the North China system shows that a PSS is sometimes required to provide a phase compensation over 100° to damp the local modes. Therefore, the PSS4B tuned using the symmetrical setting approach does not meet this requirement.

2.2. The Revised Model of PSS4B

Such a lack of enough phase compensation can be overcome by appending two additional lead–lag blocks to each band, as shown in Figure 2.

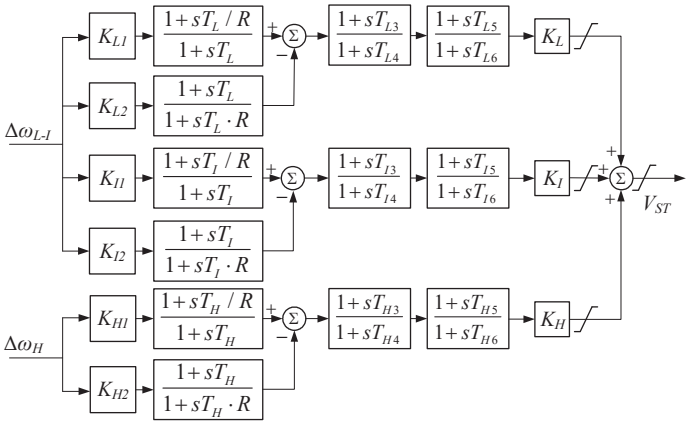

Figure 2. Revised model of PSS4B.

Here, we recommend a parameter setting principle for these additional blocks so that they fit in with the symmetrical setting approach. Take the high-frequency band as an example; we set the parameters as follows:

$$T_{H3} = T_{H9}, T_{H4} = T_{H10}, T_{H5} = T_{H11}, T_{H6} = T_{H12}, \tag{5}$$

then, the transfer function for the high band $G_H(s)$ becomes as follows:

$$G_H(s) = G_{Hn}(s) \cdot \frac{1+sT_{H3}}{1+sT_{H4}} \cdot \frac{1+sT_{H5}}{1+sT_{H6}}. \tag{6}$$

For each lead–lag block, e.g., $G(j\omega) = (1 + j\omega T_{H3})/(1 + j\omega T_{H4})$, it can be easily proved that the maximum phase $\angle G(j\omega_m)$ is 90° at $\omega_m = 1/\sqrt{T_{H3}T_{H4}}$. Thus, the two lead–lag blocks in (6) provide a phase lead up to 180°, and so do the ones in the other two bands. With this approach, the PSS4B stabilizer enjoys more degrees of freedom in achieving a precise phase–frequency characteristic that covers a wide spectrum of frequencies.

3. Iterative Design of PSS4B Stabilizer

The revised model of PSS4B in Section 2 raises the upper limit of the phase compensation while preserving the original advantages of the symmetrical approach. However, compared with conventional PSSs, the PSS4B stabilizer has a large number of parameters, which compounds the tuning process. In this section, we first introduce two tuning tools: the space searching approach for tuning the appended phase compensation blocks, and the CCBode plot for tuning the band-pass filters. We then show how to use these tools to design PSS4B in an iterative manner.

3.1. Space Searching Approach

Suppose a fixed-structure controller is given:

$$C(s,\ \mathbf{d}) = \frac{\sum_{l=0}^{n} \beta_l s^l}{\sum_{i=0}^{m} \alpha_i s^i}, \tag{7}$$

where α_i and β_l (for $i = 0,\ldots, m$ and $l = 0,\ldots, n$) are the parameters of the controller. Let $\mathbf{d} = [\alpha_0,\ldots, \alpha_m, \beta_0,\ldots, \beta_n]$ be the parameter vector. The task is to find a vector $\mathbf{d}$ such that the closed-loop system meets various engineering requirements.

The idea of the suggested iterative design is illustrated in Figure 3, where $C(s, \mathbf{d})$ is the controller of which the parameters are to be sought, and $C_r(s)$ is the desired reference controller. For now, let us suppose the frequency response of the reference controller $C_r(s)$

is known. Given a parameter space, which is a hyper-rectangular domain, for the controller $\mathbb{D} = \{\mathbf{d} \mid \alpha_i \in [\alpha_i^-, \alpha_i^+], i = 0,\ldots, m, \beta_l \in [\beta_l^-, \beta_l^+], l = 0,\ldots, n\}$, where α_i^- and α_i^+ are the upper and lower bounds for parameter α_i, and β_l^- and β_l^+ are the upper and lower bounds for parameter β_l, our goal is to find a feasible $\mathbf{d} \in \mathbb{D}$ so that the frequency response error $e = C(j\omega, \mathbf{d}) - C_r(j\omega)$ is acceptable.

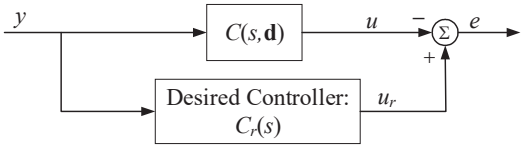

Figure 3. Controller $C(s, \mathbf{d})$ matches a reference model $C_r(s)$.

In Figure 3, y is the input of the controller, u is the output of the controller, u_r is the desired output of the controller, and e is the error of the output.

Consider a set of distinct frequencies $[\omega_1, \omega_2,\ldots, \omega_N]$, where ω_1 is the lowest frequency, and ω_N is the highest. The desired controller can be defined as follows:

$$C_r(j\omega_\Omega) = |C_r(j\omega_\Omega)|\angle C_r(j\omega_\Omega),\ \Omega = 1,\ldots, N \tag{8}$$

where $|C_r(j\omega_\Omega)|$ and $\angle C_r(j\omega_\Omega)$ are the desired magnitude and phase–frequency responses of the controller $C_r(s)$ at frequency ω_Ω, $\Omega = 1,\ldots, N$. Note that the desired reference controller $C_r(s)$ need not have a closed-form expression—it can be a set of measured frequency-dependent data points, that is, this method is data-driven.

Similarly, the actual controller $C(s, \mathbf{d})$ is expressed as

$$C(j\omega_\Omega, \mathbf{d}) = |C_r(j\omega_\Omega, \mathbf{d})|\angle C(j\omega_\Omega, \mathbf{d}), \Omega = 1,\ldots, N \tag{9}$$

where $|C(j\omega_\Omega, \mathbf{d})|$ and $\angle C(j\omega_\Omega, \mathbf{d})$ are the magnitude and phase–frequency responses of $C(s)$ at frequency ω_Ω, $\Omega = 1,\ldots, N$.

The error between the actual frequency response $C(j\omega, \mathbf{d})$ and the desired frequency response $C_r(j\omega)$ is defined as follows:

$$|e(\omega_\Omega, \mathbf{d})| = |C_r(\omega_\Omega)| - |C(\omega_\Omega, \mathbf{d})|, \Omega = 1,\ldots, N \tag{10}$$

and

$$\angle e(\omega_\Omega, \mathbf{d}) = \angle C_r(\omega_\Omega) - \angle C(\omega_\Omega, \mathbf{d}), \Omega = 1,\ldots, N \tag{11}$$

where $|e(\omega_\Omega, \mathbf{d})|$ is the magnitude error and $\angle e(\omega_\Omega, \mathbf{d})$ is the phase error at frequency ω_Ω, $\Omega = 1,\ldots, N$.

Now, the control design problem is formulated as a frequency domain curve-fitting problem as follows: find a feasible parameter vector $\mathbf{d} \in \mathbb{D}$ so that for each of the frequencies of concern ω_Ω, $\Omega = 1,\ldots, N$, both the magnitude and phase errors remain bounded within their respective limits.

$$\begin{cases} A_l(\omega_\Omega) \le |e(\omega_\Omega, d)| \le A_u(\omega_\Omega) \\ \theta_l(\omega_\Omega) \le \angle e(\omega_\Omega, d) \le \theta_u(\omega_\Omega) \end{cases} \tag{12}$$

The upper and lower bounds for the magnitude and phase errors, $A_l(\omega_\Omega)$, $A_u(\omega_\Omega)$, $\theta_l(\omega_\Omega)$, and $\theta_u(\omega_\Omega)$, $\Omega = 1,\ldots, N$, are chosen small enough to ensure that the actual frequency response $C(j\omega_\Omega, \mathbf{d})$ is close enough to the desired response $C_r(j\omega_\Omega)$ at any of the frequencies ω_Ω, $\Omega = 1,\ldots, N$.

The above curve-fitting problem can be solved using several algorithms. In this work, we tested three methods: a grid search algorithm recently presented in [22], a Monte Carlo algorithm we developed in [23], and a global optimization method described in [24]; all three methods worked well.

It remains to determine the reference controller response $C_r(j\omega)$. There are basically two approaches. In the first approach, specify the desired reference controller response $|C_r(j\omega)|$, $\angle C_r(j\omega)$ using a CCBode, and solve (12) for the parameters of the controller.

To describe the second approach, let us define a complex matrix $\mathbf{H}_{EX}$:

$$\mathbf{H}_{EX} = \mathbf{K}_2\left[\mathbf{K}_6 + \mathbf{K}_A^{-1}(j\omega \cdot \mathbf{T}_A + \mathbf{I}) \cdot (j\omega \cdot \mathbf{T}'_{d0} + \mathbf{K}_3)\right]^{-1}, \tag{13}$$

where $\mathbf{K}_2$, $\mathbf{K}_3$, and $\mathbf{K}_6$ are system coefficient matrices [2]; $\mathbf{I}$ is an identity matrix; $\mathbf{T}_A$ is a diagonal matrix of exciter time constants; and $\mathbf{T}'_{d0}$ is a diagonal matrix with machine constants. Notice that the phase lag of the excitation system of the k-th generator is equal to $\angle\mathbf{H}_{EX}(k,k)$ [8]. This phase lag can be either computed [19] or measured onsite [21].

In the second approach, first determine the parameters of the band-pass filters using the CCBode plot, then let the reference phase response $\angle C_r(j\omega)$ be equal to the phase lag of the excitation system. To find the parameters of the phase compensation filters, let $\mathbf{d} = [T_{i3}, T_{i4}, T_{i5}, T_{i6}]$, $i \in \{L, I, H\}$. Solve problem (12), obtaining all the parameters of a PSS4B.

The second approach is adopted in this work, as it is most consistent with the practice widely accepted in the industry. In what follows, we will illustrate how to determine the parameters of the band-pass filters using the CCBode plots.

3.2. Contoured Controller Bode Plot

Compared with the classic Bode plot, a CCBode plot [25,26] gives the frequency characteristic of the controller despite the system. The advantage of the CCBode is that it illustrates the contours of the performance index $\Gamma(\omega)$. The values of $\Gamma(\omega)$ indicate the stability margin of the system, a weighted average of stability margin, or other desired performance indices, say, output energy [27]. In this work, only stability margin is considered.

3.2.1. Performance Index

Figure 4 shows a PSS installed at the k-th generator of a multi-machine power system, where $C(j\omega)$ is the controller, and ω_k and V_{refk} are the frequency and the voltage reference of the generator, respectively. The output signal V_{STk} of the controller is applied to the reference voltage of the excitation. The multi-machine system is described by its frequency response $G(j\omega)$. The open-loop transfer function can be defined $L_o(s)$ as follows:

$$L_o(s) = -C(s) \cdot G(s), \tag{14}$$

Then, the characteristic equation of the closed-loop system is as follows:

$$1 + L_o(s) = 0. \tag{15}$$

According to Nyquist stability criterion, the distance $|1 + L_o(j\omega)|$ between $L_o(j\omega)$ and the critical point $(-1, j0)$ can be viewed as a stability margin of the system.

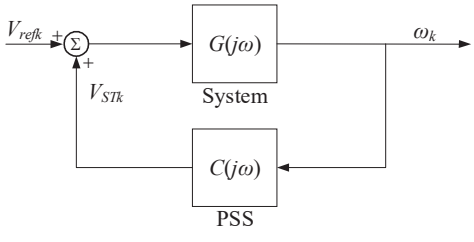

Figure 4. Block diagram representing installing a PSS to the k-th generator of a multi-machine system.

From a control point of view, the objective of a PSS is to shift the dominant eigenvalues to the left. Let the order of the open-loop system be n; then, $G(s)$ be can expressed by the following partial fraction expansion:

$$G(s) = \frac{R_1}{s-\lambda_1} + \ldots + \frac{R_n}{s-\lambda_n}, \tag{16}$$

where R_1,. . ., R_n are the residues. Consider $\lambda_p = \sigma_p + j\omega_p$ as an eigenvalue of the open-loop system; it follows that the eigenvalue shift introduced by a PSS has the following first-order approximation formula [10]:

$$\Delta\lambda_p \approx -R_p C(s)|_{s=\lambda_p} = -R_p \frac{L_o(s)|_{s=\lambda_p}}{G(s)|_{s=\lambda_p}} \approx -R_p \frac{L_o(j\omega_p)}{G(j\omega_p)}. \tag{17}$$

Since residue R_p and open-loop frequency response $G(j\omega_p)$ are fixed, the magnitude of $1 + L_o(j\omega_p)$ is therefore a clear measure of stability margin. In particular, if λ_p is purely imaginary, then $\sigma_p = 0$ and $|1 + L_o(j\omega)| = 0$. When λ_p is shifted to the left, $|1 + L_o(j\omega)|$ varies in a pattern determined by λ_p's point of departure. If λ_p is initially stable, the distance $|1 + L_o(j\omega)|$ will increase at frequencies around ω_p; if λ_p is initially unstable, then $|1 + L_o(j\omega)|$ will decrease at first, until it reaches 0; then, it will increase.

Therefore, define the performance index $\Gamma(\omega)$ as the reciprocal of the distance between $L_o(j\omega)$ and $(-1, j0)$:

$$\Gamma(\omega) := \frac{1}{|1 + L_o(j\omega)|}. \tag{18}$$

Thus, the values of $\Gamma(\omega)$ at frequencies around ω_p indicate the relative stability of λ_p: if λ_p is initially stable, then the lower values of $\Gamma(\omega)$ at frequencies around ω_p indicate a more stable λ_p; if λ_p is initially unstable, then a more stable λ_p requires that $\Gamma(\omega)$ increases at first, until $\Gamma(\omega_p)$ reaches $+\infty$ and then decreases.

3.2.2. CCBode Plot

To construct a CCBode plot, it is first required to obtain the frequency responses of the open-loop system and the controller, $G(j\omega)$ and $C(j\omega)$. The structure of a controller like a PSS is often not complicated, so the magnitude–frequency response $|C(j\omega)|$ and phase–frequency response $\angle C(j\omega)$ can be easily calculated by a sweep over ω.

Two methods can be used to obtain the frequency response $G(j\omega)$: from a field measurement, or from the data of an operating condition. As for the latter option, it is usually derived from the state-space model of the system.

$$G(j\omega) = \mathbf{c}^T \cdot (j\omega\mathbf{I} - \mathbf{A})^{-1} \cdot \mathbf{b}. \tag{19}$$

where $\mathbf{A}$ is the state-space matrix, and $\mathbf{b}$ and $\mathbf{c}$ are input and output vectors. However, the order of a large-scale power system model can be very high. If we tried to derive $G(j\omega)$ by a sweep over ω using its state-space model, the computational cost would be huge. To compute $G(j\omega)$ efficiently, we apply the sparsity method described in [28]. Consider a power system given by its differential algebraic equation (DAE) model:

$$\begin{pmatrix} \dot{\mathbf{x}} \\ \hline \mathbf{0} \end{pmatrix} = \underbrace{\left(\begin{array}{c:c} \mathbf{J_1} & \mathbf{J_2} \\ \hdashline \mathbf{J_3} & \mathbf{J_4} \end{array}\right)}_{\mathbf{J}_{nx+nv}} \begin{pmatrix} \mathbf{x} \\ \hline \mathbf{v} \end{pmatrix} + \mathbf{b}u, \; y = \mathbf{c}^T \begin{pmatrix} \mathbf{x} \\ \hline \mathbf{v} \end{pmatrix}, \tag{20}$$

where **x** is the *nx*-dimensional state-variable vector, **v** is the *nv*-dimensional algebraic-variable vector, u is the algebraic variable representing the input, and y is the algebraic variable representing the output. Then, we have

$$G(j\omega) = \mathbf{c}^T \left[j\omega \begin{pmatrix} \mathbf{I}_{nx} & \\ & \mathbf{0}_{nv} \end{pmatrix} - \mathbf{J} \right]^{-1} \mathbf{b}. \tag{21}$$

This method makes use of the sparsity of the Jacobian matrix **J**, therefore producing solutions of the magnitude–frequency response $|G(j\omega)|$ and phase–frequency response $\angle G(j\omega)$ at a low computational cost.

Now we are in a position to derive the CCBode plot. When designing a controller for a plant, notice that the plant frequency response $G(j\omega)$ is given:

$$\begin{aligned} \Gamma(\omega) &= \tfrac{1}{|1+L_o(j\omega)|} = \tfrac{1}{\sqrt{[1+L_o(j\omega)]\cdot[1+L^*{}_o(j\omega)]}} \\ &= \tfrac{1}{\sqrt{1-2|G(j\omega)||C(j\omega)|\cdot\cos[\angle G(j\omega)+\angle C(j\omega)]+|G(j\omega)|^2|C(j\omega)|^2}}. \end{aligned} \tag{22}$$

When determining the CCBode magnitude plot, the controller phase $\angle C(j\omega)$ needs to be fixed. Now, the magnitude index Γ_{mag} is a function of frequency ω and controller gain K:

$$\Gamma_{mag}(\omega, K) = \frac{1}{\sqrt{1-2|G(j\omega)|K\cos[\angle G(j\omega)+\angle C(j\omega)]+|G(j\omega)|^2K^2}}. \tag{23}$$

The contours of the magnitude function $\Gamma_{mag}(\omega, K)$ can now be easily constructed using graphical tools. To build a CCBode phase plot, fix the controller magnitude $|C(j\omega)|$. The phase performance index Γ_{phase} becomes a function of frequency ω and controller phase φ:

$$\Gamma_{phase}(\omega, \varphi) = \frac{1}{\sqrt{1-2|G(j\omega)||C(j\omega)|\cdot\cos(\angle G(j\omega)+\varphi)+|G(j\omega)|^2|C(j\omega)|^2}}. \tag{24}$$

Again, the contours of the phase function $\Gamma_{phase}(\omega, \varphi)$ can be easily obtained. With the CCBode plot, we can adjust $|C(\omega)|$ and $\angle C(\omega)$ by tuning the parameters of the PSS so that $\Gamma(\omega)$ decreases at the frequencies of concern, thus improving the damping of the corresponding modes.

3.2.3. CCBode Plot Using Generalized Frequency

The afore-described CCBode plot is based on the classic Nyquist stability criterion, which states the condition that a controller shall satisfy in order to keep eigenvalues from crossing the imaginary axis. This is known as Hurwitz stability. In practice, however, regulations often require that the minimum damping ratio should not fall less than 3% [19]. This is the so-called D-stability. In this section, we extend the previous solution to deal with this practical issue.

An analogous Nyquist-type stability criterion exists for D-stability [29]: to determine the number of poles/zeros inside an arbitrary, bounded, symmetrical region in the complex plane, we only need to replace $s = j\omega$ in the classic Nyquist theorem with the so-called generalized frequency $s = \sigma + j\omega$ when plotting the Nyquist diagram (see Figure 5).

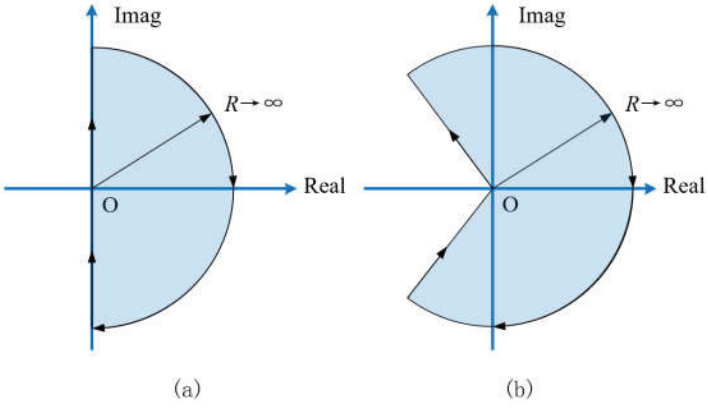

Figure 5. The Nyquist contour for: (**a**) Hurwitz stability; (**b**) D-stability.

Let ζ be the desired damping ratio; the definition of the generalized frequency $s = \sigma + j\omega$ is as follows:

$$s(\omega, \zeta) = \sigma(\omega, \zeta) + j\omega = (\frac{-\zeta}{\sqrt{1-\zeta^2}} + j)\omega, \ \omega \in [0, \infty). \tag{25}$$

In (25), $\sigma(\omega, \zeta)$ is the real part of $s(\omega, \zeta)$ determined by the frequency ω of concern and the damping ratio ζ of this mode.

To construct a CCBode plot with a given damping ratio ζ, we follow the same process described in the previous subsection, except that this time, generalized frequency $s(\omega, \zeta)$ is used in the calculation of frequency responses $G(s(\omega, \zeta))$ and $C(s(\omega, \zeta))$. Obviously, if $1 + L_o(s(\omega, \zeta)) = 0$, an eigenvalue passes through the stability boundary. Therefore, the performance index $\Gamma(\omega, \zeta)$ using generalized frequency is also a useful indication of stability margin:

$$\Gamma(\omega, \zeta) := \frac{1}{|1 + L_o(s(\omega, \zeta))|}. \tag{26}$$

Compared with the classic Bode plot, the CCBode plot directly shows the frequency response of the controller, which simplifies the controller tuning process.

3.3. Iterative Design Approach

We first assign typical values to the band-pass filter parameters K_L, K_I, K_H, F_L, F_I, F_H, and R, and calculate the parameters of the appended phase compensation blocks T_{i3}, T_{i4}, T_{i5}, and T_{i6}, $i \in \{L, I, H\}$, by the space searching approach.

Then, we calculate the concerned eigenvalues of the closed-loop system and check whether the system has adequate damping ratio. If so, we terminate the process; otherwise, the iterative design procedure for the PSS4B stabilizer, illustrated in Figure 6, is followed.

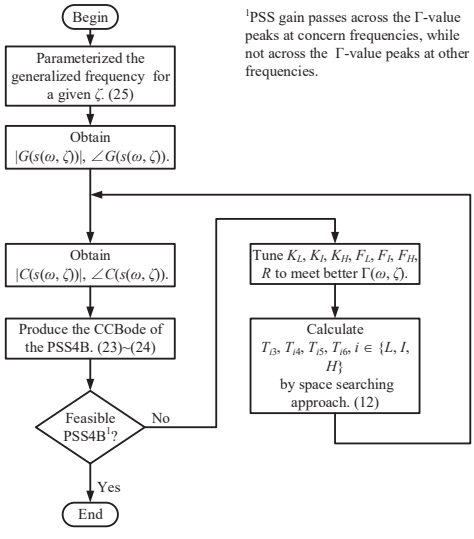

Figure 6. Iterative design process of PSS4B.

4. Case Study

In this section, we apply the proposed iterative design approach to both the classic four-machine/two-area system and the actual North China Power Grid.

4.1. Results of the Four-Machine/Two-Area Test System

Figure 7 depicts Kundur's four-machine/two-area system, the details of which are available in [30].

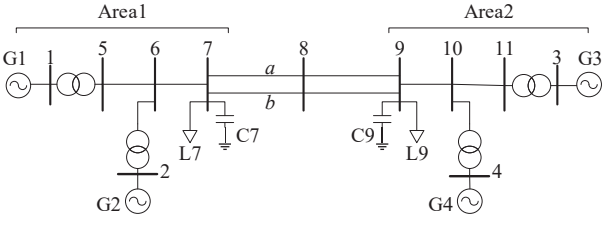

Figure 7. Four-machine/two-area system.

There are three oscillation modes in the original system: one unstable inter-area mode (0.54 Hz) and two stable local modes in each area (around 1 Hz). Generator G1 is selected to install PSS4B, the parameters of which are tuned by the method proposed in order to achieve the following:

- Stabilize the unstable inter-area mode;
- Improve the damping of the local mode;
- Avoid the exciter instability (around 5.5 Hz).

First, the plant transfer function (21) and desired phase–frequency response given by (13) is calculated. Then the typical parameters recommended in IEEE Standard 421.5 [31] are assigned to the three band-pass filters. Subsequently, the space searching approach is utilized to determine the parameters for the phase compensation blocks. The resulting stabilizer is designated as PSS4B(1). Figure 8 illustrates the corresponding CCBode plot with a damping ratio $\zeta = 0$. The magnitude plot reveals two performance peaks: peak 1, which corresponds to the inter-area mode, and peak 2, which corresponds to the exciter mode. By

increasing the controller gain while maintaining a fixed phase–frequency response so that the magnitude plot aligns with either peak, an eigenvalue at the corresponding frequency is positioned on the imaginary axis.

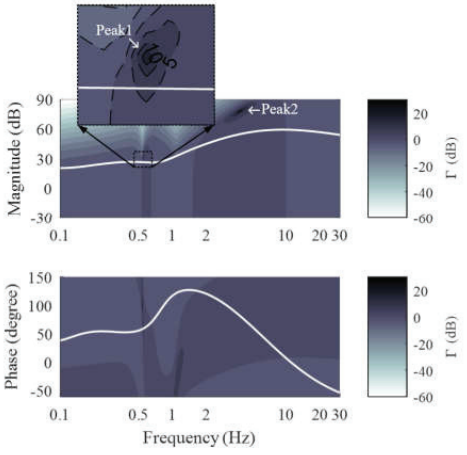

Figure 8. CCBode plots with $\zeta = 0$: PSS4B(1).

After the installation of the PSS4B(1), both the local mode and the inter-area mode move to the left, yet the inter-area mode is still unstable. The magnitude plot suggests that, to shift the inter-area mode across the imaginary axis, we should raise the controller gain so that its magnitude response curve pass through peak 1 at 0.5 Hz. Since the system has no unstable eigenvalue around 5.5 Hz, the performance index $\Gamma(\omega)$ around 5.5 Hz should not be raised to $+\infty$, which means the controller gain around 5.5 Hz should be limited. This is a loop shaping situation, typical in the control community, but not quite usual PSS practice.

To raise the low-frequency gain of the controller while limiting its high-frequency gain, we reset the parameters of the three band-pass filters, and use the space searching approach to tune the phase compensation blocks. Figure 9 shows the CCBode plot of the new PSS4B (designated as PSS4B(2)). It indicates that peak 1 is now beneath the controller magnitude curve while peak 2 is still on top of it. Hence, the new PSS4B is able to stabilize the inter-area mode, which is further confirmed by the eigenvalue calculation result.

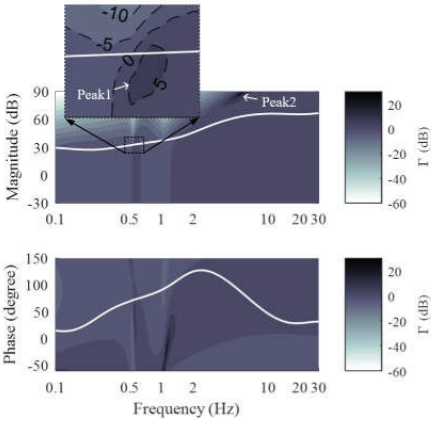

Figure 9. CCBode plots with $\zeta = 0$: PSS4B(2).

To see the results of D-stability, we constructed the CCBode plot with ζ = 3%. By doubling the gain of each branch of PSS4B(2), we can obtain PSS4B(3). Figures 10 and 11 show the corresponding CCBode plots of PSS4B(2) and PSS4B(3), indicating that PSS4B(3) warrants D-stability as well.

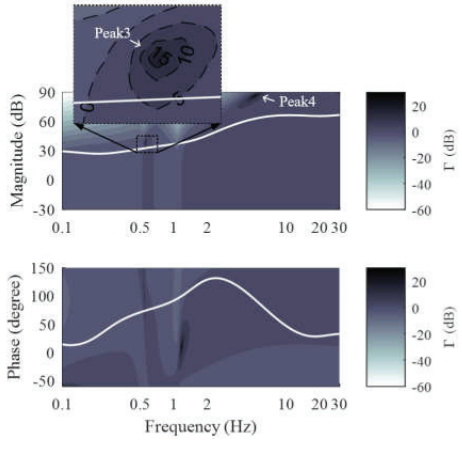

Figure 10. CCBode plots with ζ = 3%: PSS4B(2).

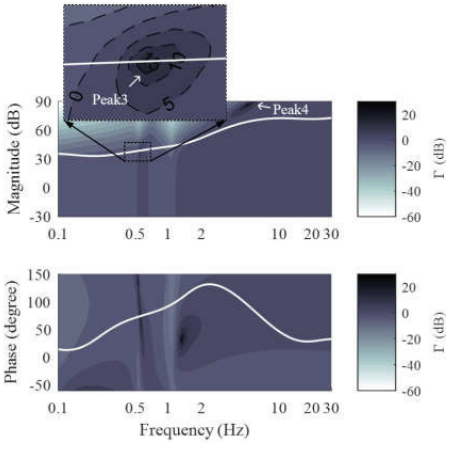

Figure 11. CCBode plots with ζ = 3%: PSS4B(3).

Figure 12 shows the simulation results of the test system with different PSS4Bs installed after a three-phase short-circuit on line 7-8-b (cleared after 0.1 s). Table 1 shows the eigenvalues of interest with different PSSs installed at G1. Table 2 lists the parameters of the PSSs.

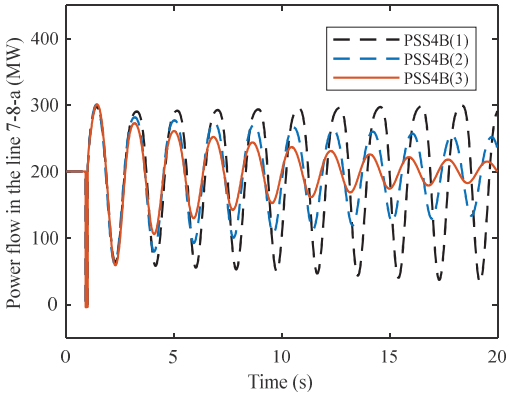

Figure 12. Simulation results of four-machine/two-area system.

Table 1. Changes in damping ratios in the four-machine/two-area system with and without PSS.

	Oscillation Mode	Eigenvalue	Frequency (Hz)	Damping Ratio (%)
None	Inter-area	$0.055 \pm j3.39$	0.54	−1.62%
	Local	$-0.591 \pm j6.68$	1.06	8.81%
PSS4B(1)	Inter-area	$0.020 \pm j3.42$	0.55	−0.59%
	Local	$-0.912 \pm j6.56$	1.04	13.8%
PSS4B(2)	Inter-area	$-0.028 \pm j3.44$	0.55	0.83%
	Local	$-1.224 \pm j6.93$	1.10	17.4%
PSS4B(3)	Inter-area	$-0.104 \pm j3.47$	0.55	3.00%
	Local	$-1.956 \pm j7.13$	1.14	26.4%

Table 2. Parameters of the PSS4B installed at G1.

G1-PSS	Low-Frequency Band		Intermediate-Frequency Band		High-Frequency Band	
PSS4B(1)	K_L	7.5	K_I	30	K_H	120
	F_L	0.07	F_I	0.7	F_H	8
	T_{L3}	0.0531	T_{I3}	0.3876	T_{H3}	0.1652
	T_{L4}	0.2447	T_{I4}	0.4723	T_{H4}	0.0555
	T_{L5}	0.0531	T_{I5}	0.3876	T_{H5}	0.1652
	T_{L6}	0.2447	T_{I6}	0.4723	T_{H6}	0.0555
PSS4B(2)	K_L	30	K_I	30	K_H	10
	F_L	0.07	F_I	0.7	F_H	8
	T_{L3}	0.3489	T_{I3}	0.2212	T_{H3}	0.4836
	T_{L4}	0.0902	T_{I4}	0.0017	T_{H4}	0.0362
	T_{L5}	0.3489	T_{I5}	0.2212	T_{H5}	0.4836
	T_{L6}	0.0902	T_{I6}	0.0017	T_{H6}	0.0362
PSS4B(3)	K_L	60	K_I	60	K_H	20
	Other parameters are the same as for PSS4B(2)					

It can be seen from Figure 12 and Table 1 that PSS4B(2) and PSS4B(3) with the optimized parameters of the three band-pass filters perform better than PSS4B(1), which uses the typical filter parameters. Specifically, the PSS4B(3), with greater gains in each frequency branch, provides more damping for both inter-area mode and local mode, and the increase in gain does not cause the instability of the exciter mode, which verifies the efficiency of the proposed method.

4.2. Results of the North China Power Grid

In recent years, the North China Power Grid has experienced decreased damping ratios, posing a significant limitation for inter-area power transmission. Details of the system analyzed in this study can be found in [4]. This system is characterized by a dominant inter-area mode (between Inner Mongolia and Shandong) at 0.35 Hz. Despite the existing installation of numerous PSS2B stabilizers, the damping ratio of this mode remains below 3%.

For this study, a thermal power plant (Mengxilai 250 MVA) with high participation in the inter-area mode was selected. The desired frequency response was derived from field measurements. Following the methodology outlined in Section 4.1, two stabilizers were designed: PSS4B(4), with typical filter parameters, and PSS4B(5), with optimized filter parameters. Figures 13 and 14 present the CCBode plots (with ζ = 3%) for both PSS4Bs, demonstrating that the installation of PSS4B(5) achieves an inter-area mode damping ratio of no less than 3%. Comparatively, the PSS2B currently in operation at Mengxilai, with a gain K_{s1} = 3, would require a gain ten times larger to match the performance of PSS4B(5) in the inter-area mode, which could cause exciter mode instability.

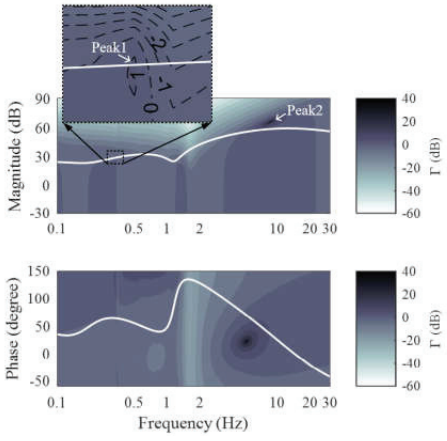

Figure 13. CCBode plots with ζ = 3%: PSS4B(4).

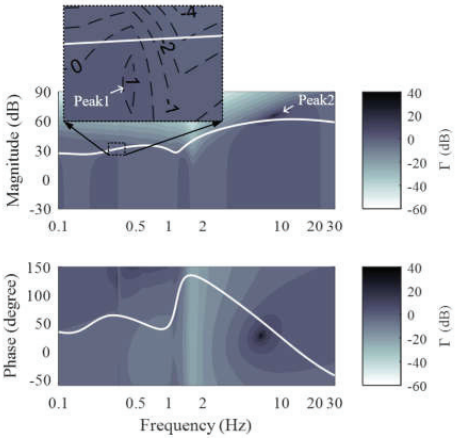

Figure 14. CCBode plots with ζ = 3%: PSS4B(5).

The following conclusions can be drawn from Table 3. First, the currently used PSS2B is very effective in suppressing local oscillation modes, but it cannot provide sufficient damping for inter-area modes. However, due to its higher degree of freedom, PSS4B can provide damping for both local and inter-area modes. Specifically, PSS4B(5) with optimized filter parameters is better than PSS4B(4) with typical filter parameters in suppressing both modes of oscillation without causing exciter mode instability in the system. Table 4 lists the parameters of the PSSs.

Table 3. Changes in damping ratios in the North China Power Grid with and without PSS.

	Oscillation Mode	Eigenvalue	Frequency (Hz)	Damping Ratio (%)
None	Inter-area [1]	$-0.053 \pm j2.18$	0.35	2.44%
	Local [2]	$-0.950 \pm j9.92$	1.58	9.53%
PSS2B	Inter-area	$-0.055 \pm j2.18$	0.35	2.52%
	Local	$-2.626 \pm j10.03$	1.60	25.31%
PSS4B(4)	Inter-area	$-0.063 \pm j2.18$	0.35	2.92%
	Local	$-5.962 \pm j10.03$	1.60	50.87%
PSS4B(5)	Inter-area	$-0.068 \pm j2.18$	0.35	3.13%
	Local	$-8.049 \pm j10.05$	1.60	62.51%

[1] Inter-area: Inner Mongolia vs. Shandong. [2] Local: Inner Mongolia.

Table 4. Parameters of the PSS4B installed at Mengxilai.

Mengxilai PSS	Low-Frequency Band		Intermediate-Frequency Band		High-Frequency Band	
PSS4B(4)	K_L	12.6	K_I	21.7	K_H	47.6
	F_L	0.116	F_I	0.506	F_H	12.1
	T_{L3}	0.3047	T_{I3}	0.3984	T_{H3}	0.4125
	T_{L4}	0.4620	T_{I4}	0.1812	T_{H4}	0.0965
	T_{L5}	0.3047	T_{I5}	0.3984	T_{H5}	0.4125
	T_{L6}	0.4620	T_{I6}	0.1812	T_{H6}	0.0965
PSS4B(5)	K_L	18	K_I	31	K_H	68
	Other parameters are the same as PSS4B(4)					

5. Conclusions

This paper introduces an iterative design methodology for tuning the parameters of the multi-band power system stabilizer PSS4B using the contoured controller Bode (CCBode) plot. This method combines the benefits of traditional Nyquist and Bode plots, offering vivid and accessible stability margins for the system. Based on the damping index required by the engineering, the corresponding stability margins at the oscillation frequencies of the local mode and the inter-area mode can be obtained. By maximizing the stability margin, the method can flexibly adjust the parameters of the phase compensation block and the band-pass filter to provide greater damping for the corresponding weakly damped modes. The proposed method ensures sufficient damping in the full frequency band of low-frequency oscillations and has good engineering application prospects. It is a valuable enhancement to PSS4B parameter setting techniques in engineering applications. The practicality and effectiveness of the proposed method are demonstrated through case studies involving a four-machine/two-area system and the North China Power Grid.

Author Contributions: Methodology, H.X. and C.J.; Writing—original draft, H.X. and C.J.; Writing—review & editing, H.X. and D.G.; Supervision, C.J. All authors have read and agreed to the published version of the manuscript.

Funding: This research received no external funding.

Data Availability Statement: The original contributions presented in the study are included in the article, further inquiries can be directed to the corresponding author.

Conflicts of Interest: Author Chongxi Jiang was employed by the company Hangzhou Power Supply Company, State Grid Zhejiang Electric Power Co., Ltd. The remaining authors declare that the research was conducted in the absence of any commercial or financial relationships that could be construed as a potential conflict of interest. The authors declare no conflicts of interest.

References

1. Kundur, P. *Power System Stability and Control*; McGraw-Hill: New York, NY, USA, 1994.
2. Wang, H.; Du, W. *Analysis and Damping Control of Power System Low-Frequency Oscillations*; Springer: New York, NY, USA, 2016.
3. Wang, G.; Xin, H.; Gan, D.; Li, N. A probability-one homotopy method for stabilizer parameter tuning. *IEEE Trans. Power Syst.* **2013**, *28*, 4624–4633. [CrossRef]
4. Zhou, J.; Shi, P.; Gan, D.; Xu, Y.; Xin, H.; Jiang, C.; Xie, H.; Wu, T. Large-Scale Power System Robust Stability Analysis Based on Value Set Approach. *IEEE Trans. Power Syst.* **2017**, *32*, 4012–4023. [CrossRef]
5. Grondin, R.; Kamwa, I.; Trudel, G.; Taborda, J.; Lenstroem, R.; Gerin-Lajoie, L.; Gingras, J.P.; Racine, M.; Baumberger, H. The multi-band PSS: A flexible technology designed to meet opening markets. In *Cigré General Session 2000*; CIGRE: Paris, France, 2000; pp. 39–201.
6. Grondin, R.; Kamwa, I.; Trudel, G.; Gerin-Lajoie, L.; Taborda, J. Modeling and closed-loop validation of a new PSS concept, the multi-band PSS. In Proceedings of the 2003 IEEE Power Engineering Society General Meeting (IEEE Cat. No.03CH37491), Toronto, ON, Canada, 13–17 July 2003; pp. 1804–1809.
7. Kamwa, I.; Grondin, R.; Trudel, G. IEEE PSS2B versus PSS4B: The limits of performance of modern power system stabilizers. *IEEE Trans. Power Syst.* **2005**, *20*, 903–915. [CrossRef]
8. Jia, L.; Gao, X.; Xu, Y.; Xie, H.; Wu, T.; Su, W.; Zhou, J.; Gan, D.; Xin, H. Application of PSS4B stabilizers in suppressing low frequency oscillations: A case study. In Proceedings of the 2015 IEEE Power & Energy Society General Meeting, Denver, CO, USA, 26–30 July 2015; pp. 1–5.
9. Blondel, V.; Gevers, M.; Lindquist, A. Survey on the state of systems and control. *Eur. J. Control* **1995**, *1*, 5–23. [CrossRef]
10. Hilhorst, G.; Pipeleers, G.; Michiels, W.; Swevers, J. Sufficient LMI conditions for reduced-order multi-objective H_2/H_∞ control of LTI systems. *Eur. J. Control* **2015**, *23*, 17–25. [CrossRef]
11. Pagola, F.L.; Perez-Arriaga, I.J.; Verghese, G.C. On sensitivities, residues and participations: Applications to oscillatory stability analysis and control. *IEEE Trans. Power Syst.* **1989**, *4*, 278–285. [CrossRef] [PubMed]
12. Rouco, L.F.; Pagola, F.L. An eigenvalue sensitivity approach to location and controller design of controllable series capacitors for damping power system oscillations. *IEEE Trans. Power Syst.* **1997**, *12*, 1660–1666. [CrossRef] [PubMed]
13. Rouco, L.; Pagola, F.L. Eigenvalue sensitivities for design of power system damping controllers. In Proceedings of the 40th IEEE Conference on Decision and Control (Cat. No.01CH37228), Orlando, FL, USA, 4–7 December 2001; pp. 3051–3055.
14. Rimorov, D.; Kamwa, I.; Joós, G. Model-based tuning approach for multi-band power system stabilisers PSS4B using an improved modal performance index. *IET Gener. Transm. Distrib.* **2015**, *9*, 2135–2143. [CrossRef]
15. Wang, Z.; Chung, C.Y.; Wong, K.P.; Tse, C.T. Robust power system stabiliser design under multi-operating conditions using differential evolution. *IET Gener. Transm. Distrib.* **2008**, *2*, 690–700. [CrossRef]
16. Kundur, P.; Lee, D.C.; El-Din, H.Z. Power system stabilizers for thermal units: Analytical techniques and on-site validation. *IEEE Trans. Power Appar. Syst.* **1981**, *1*, 81–95. [CrossRef]
17. Kundur, P.; Klein, M.; Rogers, G.J.; Zywno, M.S. Application of power system stabilizers for enhancement of overall system stability. *IEEE Trans. Power Syst.* **1989**, *4*, 614–626. [CrossRef]
18. Gibbard, M.J.; Vowles, D.J. Reconciliation of methods of compensation for PSSs in multimachine systems. *IEEE Trans. Power Syst.* **2004**, *19*, 463–472. [CrossRef]
19. Rogers, G. *Power System Oscillations*; Kluwer: Norwell, MA, USA, 2000.
20. Kundur, P.; Berube, G.R.; Hajagos, L.M.; Beaulieu, R. Practical utility experience with and effective use of power system stabilizers. In Proceedings of the 2003 IEEE Power Engineering Society General Meeting (IEEE Cat. No.03CH37491), Toronto, ON, Canada, 13–17 July 2003; Volume 3, pp. 1777–1785.
21. Larsen, E.V.; Swann, D.A. Applying power system stabilizers Part III: Practical considerations. *IEEE Trans. Power Appar. Syst.* **1981**, *6*, 3034–3046. [CrossRef]
22. Khadraoui, S.; Nounou, H.N.; Nounou, M.N.; Datta, A.; Bhattacharyya, S.P. A measurement-based approach for designing reduced-order controllers with guaranteed bounded error. *Int. J. Control* **2013**, *86*, 1586–1596. [CrossRef]
23. Xin, H.; Gan, D.; Huang, Z.; Zhuang, K.; Cao, L. Applications of stability-constrained optimal power flow in the East China system. *IEEE Trans. Power Syst.* **2010**, *25*, 1423–1433.
24. Moiseev, S. Universal derivative-free optimization method with quadratic convergence. *arXiv* **2011**, arXiv:1102.1347.
25. Taylor, J.D.; Messner, W. Controller design for nonlinear systems using the Contoured Robust Controller Bode plot. *Int. J. Robust Nonlinear Control* **2014**, *24*, 3196–3213. [CrossRef]

26. Taylor, J.D.; Messner, W. Controller Design for Nonlinear Multi-Input/Multi-Output Systems Using the Contoured Robust Controller Bode Plot. In Proceedings of the ASME 2013 Dynamic Systems and Control Conference, Palo Alto, CA, USA, 21–23 October 2013.
27. Ke, D.P.; Chung, C.Y. An inter-area mode oriented pole-shifting method with coordination of control efforts for robust tuning of power oscillation damping controllers. *IEEE Trans. Power Syst.* **2012**, *27*, 1422–1432. [CrossRef]
28. Martins, N. Efficient eigenvalue and frequency response methods applied to power system small-signal stability studies. *IEEE Trans. Power Syst.* **1986**, *1*, 217–224. [CrossRef]
29. Nakhmani, A.; Lichtsinder, M.; Zeheb, E. Generalized Bode envelopes and generalized Nyquist theorem for analysis of uncertain systems. *Int. J. Robust Nonlinear Control* **2011**, *21*, 752–767. [CrossRef]
30. Kamwa, I.; Performance of Three PSS for Interarea Oscillations. Sym-PowerSystems Toolbox. Available online: https://www.mathworks.com/examples/simpower/ (accessed on 1 April 2024).
31. IEEE Std 421.5-2016 (Revision of IEEE Std 421.5-2005); IEEE Recommended Practice for Excitation System Models for Power System Stability Studies. IEEE: Piscataway, NJ, USA, 2016; pp. 1–207.

energies

MDPI

Article

Identifying Weak Transmission Lines in Power Systems with Intermittent Energy Resources and DC Integration

Anqi He [1], Jijing Cao [2], Shangwen Li [3], Lianlian Gong [1,*], Mingming Yang [1] and Jiawei Hu [4]

[1] College of Railway Locomotive and Rolling Stock, Wuhan Railway Vocational College of Technology, Wuhan 430205, China; 20180001@wru.edu.cn (A.H.); 20140004@wru.edu.cn (M.Y.)
[2] Wuhan EMU Depot of China Railway Wuhan Group Co., Ltd., Wuhan 430061, China; 15871742719@163.com
[3] State Grid Hubei Electric Power Co., Ltd., Wuhan Power Supply Company, Wuhan 430013, China; lsw_0128@163.com
[4] Central China Branch of State Grid Corporation of China, Wuhan 430072, China; hjw_ncepu@163.com
* Correspondence: m18138160122@163.com

Abstract: Nowadays, intermittent energy resources, such as wind turbines, and direct current (DC) transmission have been extensively integrated into power systems. This paper proposes an identifying method for weak lines of novel power systems with intermittent energy resources and DC lines integration, which aims to provide decision making for control strategies of novel power systems and prevent system blackouts. First, from the perspective of power system safety and stability, a series of risk indicators for the risk assessment of vulnerable lines is proposed. Then, lines in the system are tripped one by one. The calculation method for the proposed risk indicators is introduced. The impact of each line outage on system safety and stability can be fairly evaluated by these proposed risk indicators. On this basis, each risk assessment indicator is weighted to obtain a comprehensive risk assessment indicator, and then the risk caused by each line outage on the system can be quantified efficiently. Finally, the test system of a modified IEEE-39 bus system with wind farms and DC lines integration is used to verify the applicability of the proposed method, and the effectiveness of the proposed method is also demonstrated by comparing with existing methods.

Keywords: weak line identification; intermittent energy resources; Gaussian mixture model; novel power systems

Citation: He, A.; Cao, J.; Li, S.; Gong, L.; Yang, M.; Hu, J. Identifying Weak Transmission Lines in Power Systems with Intermittent Energy Resources and DC Integration. *Energies* **2024**, *17*, 3918. https://doi.org/10.3390/en17163918

Academic Editor: Frede Blaabjerg

Received: 15 July 2024
Revised: 2 August 2024
Accepted: 6 August 2024
Published: 8 August 2024

1. Introduction

Recently, power system blackouts have occurred frequently around the world, causing huge economic losses and serious social impact [1–3]. Research shows that catastrophic blackouts are usually initiated by failure of one or several components [4–6]. These components can be called weak components or vulnerable components [7], including transmission lines, transformers, etc. Meanwhile, intermittent energy resources, such as wind turbines, and DC transmission have been extensively integrated into power systems, which makes the dynamic characteristics and operation mode of power systems more complex [8,9]. The safe and stable operation of novel power systems is facing severe challenges due to their own development [10]. In this case, once weak components of a novel power system fail, blackout accidents could be further exacerbated, and the system may face higher operation risk. To this end, identifying weak components of the novel power system with intermittent energy resources and DC integration is of great significance, which contributes to maintaining secure system operation and preventing system blackout.

Much research has been conducted on identifying the weak components of power systems. There are mainly two types of methods in the research field. The first type of research is based on complex network theory. This type of method uses the concept of degree and betweenness and combines with electrical characteristics to identify the weak components of power systems. The authors in [11] indicated that degree centrality methods

inherently only take into account the local information of a power network, and the analysis results are not fully reliable. The concept of line electrical betweenness based on the physical characteristics of a power grid was proposed in [12] to identify weak components. The concept of extended betweenness based on the power transfer distribution factors was proposed in [13], which can consider the contribution of each transmission line. A maximum flow-based complex network approach was proposed in [14] to identify weak lines in power systems. The network is modeled as a graph. Then, an improved maximum flow-based complex network approach was used for topology analysis. The complex network theory for modern smart grid applications was investigated in [15], including structural vulnerability assessment, cascading blackouts, etc. A weak transmission lines identification method based on the depth of the K-shell decomposition was proposed in [16], which fully considers the dynamic characteristics of the power transfer and transmission capability after the power grid fault. The hybrid flow betweenness is defined in [17] to identify weak lines, which covers the direction of power flow and the maximum transmission capacity of lines with a more comprehensible physical background. An electrical betweenness method that can better balance the accuracy and efficiency of identifying vulnerable lines was proposed in [18]. The power percentage of the generator load is used as an indicator to evaluate the stability of a power grid, and the dynamic influence of generator and load node removal on a power grid is considered in the literature. A holomorphic embedding method was proposed in [19] to assess the vulnerable bus of power systems. The concept of an interaction graph was applied to model cascading outages in [20–22], and then vulnerable lines of power systems can be efficiently determined.

The second type of research method is based on power system operation condition, which aims to define several indexes reflecting system operation state. In [23], a reactive power loss index (RPLI) is proposed to identify the weak components of power systems. Then, this index is further used for determining the optimal locations for placement of reactive compensation devices. In [24,25], several security indexes, such as generator output capacity, line reactance, maximum line transfer capacity value, and power transfer characteristics of the power system were defined to identify the weak components of the system. Then, these indexes were weighted to form a comprehensive index. In [26], several indexes were proposed by jointly considering the topology structural vulnerability and the power flow transmission vulnerability, and then a clustering algorithm was proposed and employed to divide the lines to identify the vulnerable lines in the systems. A vulnerable lines identification method based on a weighted H-index was proposed in [27], which mainly reflected the correlation of the transmission branches on the active power transmission and constructed the correlation network. The authors in [28,29] used the concept of entropy to identify vulnerable components. Specifically, power flow entropy and improved power flow entropy were defined to discriminate line vulnerability in terms of system power flow calculation. In [30], several indexes concerning complex network and electrical characteristics of a power system were defined to identify the weak components of power systems, where the electrical characteristics are mainly based on the power transfer distribution factor. Then, an intercriteria correlation-based multi-index decision-making method was proposed to comprehensively identify the importance of components. The authors in [31] converted the power flow computation challenge into an optimization problem with constraints, wherein crucial components were discerned through a dynamic interplay between attackers and defenders. The authors in [32] introduced a vulnerability assessment method for transmission lines in power system incorporating network topology and system operational states, where the improved power transfer distribution factor and line outage distribution factor are used to build the line operational state vulnerability indices. In [33], a series of line vulnerability indexes were defined for vulnerable line identification, where these indexes incorporate line load rate, power flow fluctuation index, line failure probability, etc. Then, the combination weighting method was used to obtain a comprehensive vulnerability index.

The above research can fairly identify the vulnerable components of power systems but mainly focuses on traditional power systems. Nowadays, intermittent energy resources and DC transmission have been extensively integrated into novel power systems. The stochastic characteristic induced by intermittent energy output and the operational characteristic of DC transmission change the system operation mode overwhelmingly. The above vulnerable component identification method is not well applicable to novel power systems. Therefore, the integration of intermittent energy resources and their impact on vulnerable component identification has gradually become a hot topic. In [34], an electrical LeaderRank method is proposed to identify the important nodes in power grids, considering the renewable energy uncertainties and transmission power flow. In [35], a method for identifying vulnerable lines based on the theory of topological potential is proposed, which can consider wind power uncertainty. The proposed index comprehensively considers the in-degree and out-degree topological potentials of nodes and uses the entropy weight method for weight allocation.

In summary, the current weak component identification research of novel power systems with renewable energy and DC integration is relatively lacking. Moreover, rarely has the literature considered the impacts of renewable energy and DC on power system vulnerable component identification simultaneously. The stochastic characteristic of renewable energy output and the operational characteristic of DC transmission need to be considered synchronously. Furthermore, the current research method based on power system operation condition mainly uses the tool of power flow calculation to identify vulnerable components, which focuses on the steady state of the system. The dynamic characteristic of the system is less considered, which makes it hard to reflect the impacts of vulnerable components on power systems comprehensively.

Therefore, a novel identifying method for weak components of novel power systems with intermittent energy sources and DC integration is proposed in this paper, which aims to prevent novel power system blackouts. It is worth mentioning that references to vulnerable components in this paper mainly refer to vulnerable lines. Firstly, a series of risk assessment indexes consisting of power system security and stability is proposed, which can quantify the system risk due to vulnerable line outage in a comprehensive fashion. Then, a comprehensive weight method based on game theory is adopted. A comprehensive risk assessment indicator can be obtained by weighting each risk assessment indicator, which can determine the vulnerability of each line in power systems. Finally, the proposed method is tested in an improved IEEE 39 bus system with wind farms and AC/DC interconnection.

The rest of this paper is organized in the following manner. Section 2 proposes an overall risk assessment index system for the vulnerable lines. Section 3 details the calculation process of the proposed risk assessment index system. In Section 4, a comprehensive risk assessment index of vulnerable lines is proposed based on game theory. In Section 5, a modified IEEE 39 bus system which is integrated into wind farms and DC is used to test the proposed method. The software Matlab 2020b is used to test the proposed method. Section 6 concludes the whole paper.

2. Risk Assessment Index System of Vulnerable Lines

The security and stability of power systems are always the important indexes to evaluate the operation state of the system. Therefore, this paper proposes six risk indicators to evaluate the vulnerability of each line from the perspective of safety and stability of system operation for a novel power system. Among them, the safety indicators include the bus voltage violation index (VVI), line overload index (LOI), and static security index (SSI). The stability indexes consist of static frequency stability (SFS), static rotor angle stability (SRAS), and static voltage stability (SVS). These risk indexes are shown in Figure 1.

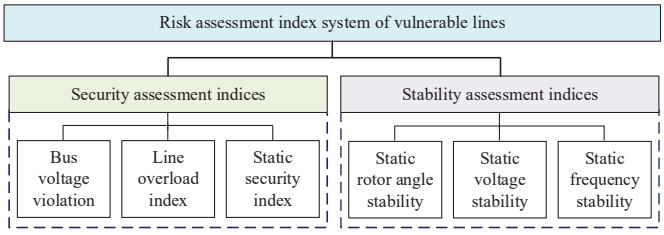

Figure 1. Risk assessment index system.

The security indicators defined in this paper are mainly used to evaluate whether the bus voltage and line transmission power of the system are within the security constraints after each line outage. If these security indicators exceed their security constraints, the system will be at high risk. Therefore, it is necessary to define such indicators to evaluate the impact of each line outage on system security. The stability indexes defined in this paper mainly focus on the static stability of the system, that is, the stable operation ability of the system under small disturbance after each line outage. The power system is constantly suffering from small disturbances. Therefore, ensuring the stable operation of the system under small disturbances is the most basic operating premise that the system should meet at all times. Once the system cannot achieve stable operation under small disturbances, the system will collapse and be difficult to recover. As for the stable operation ability under a large disturbance, it is not considered in this paper. The reason is that the system has basic stable operation ability when it meets stable operation under a small disturbance. If a large disturbance occurs, it can also be dealt with in time by stability control measures, such as generator/load shedding control [36] and DC modulation [37]. Therefore, although it is very meaningful to check the stable operation ability under a large disturbance, it is not an index that must be checked compared with the stability under a small disturbance. In order to comprehensively evaluate the influence of each line outage on the system stability, this paper establishes three small disturbance stability indexes, i.e., frequency stability, rotor angle stability, and voltage stability. With the access to a high proportion of renewable energy and DC, these three stability problems are more prominent. If any stability index does not meet stability constraints, the system will have a high risk of losing stability. Therefore, it is necessary to verify these three stability indexes at the same time to better apply them to the risk assessment of vulnerable lines for the novel power system.

3. Calculation Method for Risk Assessment Index

3.1. Bus Voltage Violation and Line Overload Index

The bus voltage violation and line overload risk of the novel power system with renewable energy and DC injection after a line outage can be obtained by power flow calculation. Therefore, it is necessary to study the power flow calculation method for the novel power system with renewable energy and DC access. The power flow equation of the AC/DC interconnected system needs to be augmented on the basis of the traditional power flow equation of the AC system [38]:

$$\begin{bmatrix} \Delta \mathbf{S} \\ \Delta \mathbf{d} \end{bmatrix} = \mathbf{J}_D \begin{bmatrix} \Delta \mathbf{X} \\ \Delta \mathbf{D} \end{bmatrix} = \begin{bmatrix} \mathbf{J} & \mathbf{A} \\ \mathbf{C} & \mathbf{F} \end{bmatrix} \begin{bmatrix} \Delta \mathbf{X} \\ \Delta \mathbf{D} \end{bmatrix} \tag{1}$$

where **S** is the power injection vector of each bus including the active and reactive power injection of each bus; **X** is the bus state vector, including the phase angle and voltage amplitude of each bus; **d** is the DC converter equation, DC network equation, and DC control equation; $\mathbf{D} = [\mathbf{V}_d, \mathbf{I}_d, \mathbf{K}_T, \cos\boldsymbol{\theta}_d, \boldsymbol{\varphi}_d]^{\mathrm{T}}$ is the relevant parameters of the DC side, including DC voltage, DC current, control angle, converter transformer ratio, and converter power factor angle; $\mathbf{J}_D$ is the Jacobian matrix of the AC/DC interconnected system; **J** is the Jacobian matrix of the traditional AC system; **A**, **C**, and **F** are the corresponding augmented

Jacobian matrix elements after increasing the DC related variables. The calculation process of specific parameters in (1) is detailed in [38].

Then, the probabilistic AC/DC power flow calculation with renewable energy is studied. The most direct probabilistic power flow calculation method is the Monte Carlo method (MCS). This method has high accuracy, but the calculation is time-consuming [39]. The risk assessment method of vulnerable lines proposed in this paper aims to provide decision making for preventive control. The vulnerability of all lines in the system needs to be evaluated before the risk really occurs. Although the time required is relatively abundant, it still needs to ensure a certain rapidity in calculation efficiency. Therefore, this paper proposes an analytical-method-based probabilistic AC/DC power flow calculation method, which can greatly improve the computational efficiency of risk assessment while satisfying the calculation accuracy. One of the difficulties in probabilistic power flow calculation based on an analytical method is how to establish a probabilistic model that can accurately describe the randomness of renewable energy. In this paper, the Gaussian mixture model (GMM) is used to establish the probability model of renewable energy injection. GMM can accurately model the probability distribution of random variables through the convex combination of multiple Gaussian distributions:

$$f(\mathbf{W}) = \sum_{m=1}^{M} \omega_m N_m(\mathbf{W}), \quad \sum_{m=1}^{M} \omega_m = 1 \tag{2}$$

$$N_m(\mathbf{W}) = \frac{1}{(2\pi)^{w/2} \det(\sum_m)^{1/2}} e^{-\frac{1}{2}(\mathbf{W}-\boldsymbol{\mu}_m)^{\mathrm{T}} \sum_m^{-1} (\mathbf{W}-\boldsymbol{\mu}_m)} \tag{3}$$

where $\mathbf{W}$ is the vector composed of the output power of w wind farms; f ($\mathbf{W}$) is the probability density function of $\mathbf{W}$; N_m ($\mathbf{W}$) is the probability density function of the mth Gaussian component; M is the number of Gaussian components; ω_m, $\boldsymbol{\mu}_m$, and $\boldsymbol{\Sigma}_m$ are the weight coefficient, mean vector, and covariance matrix of each Gaussian component, respectively, which are usually solved by the maximum expectation algorithm [40].

By linearizing the line power flow equation at the reference operating point, the linear expression between the line transmission power and the injected power of each bus can be obtained:

$$\mathbf{Z} = \mathbf{Z}_0 + \Delta\mathbf{Z} = \mathbf{Z}_0 + (\partial\mathbf{Z}/\partial\mathbf{X})|_{\mathbf{X}=\mathbf{X}_0} \ \mathbf{J}_D^{-1}\Delta\mathbf{S} \tag{4}$$

where $\mathbf{Z}$ is the line power flow column vector, including the active and reactive power of a transmission line; the subscript 0 represents the base operating point. Equations (1) and (4) are linear expressions between bus state variables, line transmission power variables, and bus injection power, respectively. For ease of the following description, the two equations are simplified to a general linear expression:

$$\mathbf{Y} = \mathbf{K}_1\mathbf{S} + \mathbf{B}_1 \tag{5}$$

where the element in $\mathbf{Y}$ represents the bus state variable and branch power flow variable, which contains y variables; $\mathbf{K}_1$ and $\mathbf{B}_1$ represent the corresponding coefficient matrices. The output of wind farms in $\mathbf{S}$ has been modeled by GMM, which is weighted by multiple Gaussian distributions with a mean of $\boldsymbol{\mu}_m$ and a variance of $\boldsymbol{\Sigma}_m$. The random variables that obey the Gaussian distribution still obey the Gaussian distribution after linear transformation [40]. Thus, it can be obtained from linear Equation (5) that each Gaussian component of the variable $\mathbf{Y}$ obeys the Gaussian distribution with a mean of $\mathbf{K}_1\boldsymbol{\mu}_m + \mathbf{B}_1$ and a variance of $\mathbf{K}_1\boldsymbol{\Sigma}_m{\mathbf{K}_1}^{\mathrm{T}}$. The cumulative distribution function of each Gaussian component of $\mathbf{Y}$ is expressed as follows:

$$F^m(\mathbf{Y}) = \int_{-\infty}^{Y} \frac{e^{-\frac{1}{2}(\mathbf{Y}-\mathbf{K}_1\boldsymbol{\mu}_m-\mathbf{B}_1)^{\mathrm{T}}(\mathbf{K}_1\sum_m\mathbf{K}_1)^{-1}(\mathbf{Y}-\mathbf{K}_1\boldsymbol{\mu}_m-\mathbf{B}_1)}}{(2\pi)^{y/2}\det(\mathbf{K}_1\sum_m\mathbf{K}_1)^{1/2}} d\mathbf{Y} \tag{6}$$

From the total probability in Equation (7), the cumulative probability distribution function of multiple subcomponents is weighted according to the weight calculated by (3). Finally, the probability distribution function of random variables in **Y** is obtained as follows:

$$P(Y) = \sum_{m=1}^{M} P(Y) \times \omega_m \tag{7}$$

$$F(\mathbf{Y}) = \sum_{m=1}^{M} \omega_m F^m(\mathbf{Y}) \tag{8}$$

where $P(Y)$ is the probability of occurrence of the state variable corresponding to the mth subcomponent. For the novel power system with renewable energy and DC access, when there is a line outage, it may cause the bus voltage or line power to exceed their limits. In order to quantify these risks, the probability distribution of wind farm output can be obtained by GMM. Then, through the above process, the probability distribution function of each bus state variable and line power variable of the system after the line outage can be quickly solved. By setting the critical values of voltage violation and line overload, the probability of voltage violation of each bus and overload of each line after there is a line outage can be obtained by (8). Then, the severity of voltage violation and the severity of line overload are defined as follows:

$$Sev(U_i) = \begin{cases} \left(U_i^{\min} - U_i\right)/U_i^{\min} & U_i > U_i^{\max} \\ 0 \quad U_i^{\min} \le U_i \le U_i^{\max} & \\ \left(U_i - U_i^{\max}\right)/U_i^{\max} & U_i > U_i^{\max} \end{cases} \tag{9}$$

$$Sev(L_i) = \left(P_{ij} - P_{ij,\max}\right)/P_{ij,\max} \tag{10}$$

where $U_i^{\max}$ and $U_i^{\min}$ are the upper and lower limits of the voltage amplitude of bus i; U_i is the most serious value of bus i voltage amplitude during the fluctuation of renewable energy which can be calculated by probabilistic AC/DC power flow. $P_{ij,\max}$ is the transmission power limit of line ij. P_{ij} is the maximum value of the transmission power of the line ij with the fluctuation of the renewable energy output, which can also be calculated by the probabilistic AC/DC power flow. Both indicators take the most serious situation when defining the severity. Therefore, the risk of bus voltage violation and line overload caused by a line outage can be obtained as follows:

$$R_{VV} = \sum_{i=1}^{n_1} P(U_i) \times Sev(U_i) \tag{11}$$

$$R_{LO} = \sum_{i=1}^{n_2} P(L_i) \times Sev(L_i) \tag{12}$$

where n_1 is the number of system buses; n_2 is the number of rest lines after a line outage; $P(U_i)$ is the probability of voltage exceeding limits; $P(L_i)$ is the probability of line overload.

3.2. Static Security Index

The static security analysis of power systems refers to the application of the N − 1 principle. Each line needs to be tripped one by one without fault to check whether line overload and voltage violation occur. Then, the structural strength and operation mode of power systems can be checked. In the risk assessment of vulnerable lines in this paper, when there is a line outage, the N − 1 principle is used to trip remaining lines one by one without fault. Equations (11) and (12) are used to solve the bus voltage violation risk and

line overload risk, respectively. Finally, the two risk results are added, as there is a risk of losing the static security of the system after a line outage, shown as follows:

$$R_{SSA} = R_{VV} + R_{LO} \tag{13}$$

3.3. Static Frequency Stability Index

The eigenvalue analysis method based on the power system linearization model and electromechanical transient simulation are two common tools for small signal frequency stability calculation [41]. In order to improve computational efficiency, this paper will use the eigenvalue analysis method and propose a calculation method of static frequency stability eigenvalues based on an analytical method.

There is a certain function between the eigenvalues of the power system and the output of renewable energy. However, the function is generally nonlinear and difficult to clarify. Because it is a small disturbance analysis, a linear expression can be used to approximately characterize the function [42]. It is assumed that there are K eigenvalues in the novel power system, and the kth eigenvalue is $\lambda_k = \xi_k + j\omega_k$. The function between the system eigenvalue and the output power of the wind farm can be linearized at the reference operating point, and then the linear relationship is shown as follows:

$$\begin{aligned} \Delta\lambda_k &= \Delta\xi_k + j\Delta\omega_k = \sum_{i=1}^{w}[(\partial\lambda_k/\partial W_i)\Delta W_i] \\ &= \sum_{i=1}^{w}[\mathrm{Re}(\partial\lambda_k/\partial W_i)]\Delta W_i \\ &+ j\sum_{i=1}^{w}[\mathrm{Im}(\partial\lambda_k/\partial W_i)]\Delta W_i \end{aligned} \tag{14}$$

where W_i denotes the output power of the ith wind farm; $\partial\lambda_k/\partial W_i$ is the sensitivity of the kth eigenvalue of the system to the output power of the ith wind farm, which can be solved by numerical method:

$$\frac{\partial\lambda_k}{\partial W_i} = \frac{\lambda_k(W_i + \Delta W_i) - \lambda_k(W_i)}{\Delta W_i}, i = 1, 2, \cdots w \tag{15}$$

The linear relationship between the eigenvalue of the system and the output power of the wind farms is established by (14) and (15). The probability distribution of the output power of wind farms has been modeled by GMM, which is weighted by multiple Gaussian distributions with a mean value of $\boldsymbol{\mu}_m$ and a variance of $\boldsymbol{\Sigma}_m$. Similar to the derivation in Section 3.1, since the Gaussian distribution still obeys the Gaussian distribution after linear transformation, each Gaussian subcomponent of the eigenvalue probability distribution should obey the Gaussian distribution with a mean value of $\mathbf{K}_2\boldsymbol{\mu}_m + \mathbf{B}_2$ and a variance of $\mathbf{K}_2\boldsymbol{\Sigma}_m\mathbf{K}_2^{\mathrm{T}}$, where $\mathbf{K}_2$ and $\mathbf{B}_2$ are the coefficient matrices of the linear expression obtained by (15), respectively. Thus, the cumulative distribution function of the Gaussian subcomponent is shown in (16). Then, through the total probability in Equation (7), the probability distribution function expression of the novel power system eigenvalue can be obtained as follows:

$$F^m(\boldsymbol{\lambda}) = \int_{-\infty}^{\lambda} \frac{e^{-\frac{1}{2}(\boldsymbol{\lambda}-\mathbf{K}_2\boldsymbol{\mu}_m-\mathbf{B}_2)^{\mathrm{T}}(\mathbf{K}_2\sum_m\mathbf{K}_2)^{-1}(\boldsymbol{\lambda}-\mathbf{K}_2\boldsymbol{\mu}_m-\mathbf{B}_2)}}{(2\pi)^{K/2}\det(\mathbf{K}_2\sum_m\mathbf{K}_2)^{1/2}}\, d\boldsymbol{\lambda} \tag{16}$$

$$F(\boldsymbol{\lambda}) = \sum_{m=1}^{M} \omega_m F^m(\boldsymbol{\lambda}) \tag{17}$$

When the real part of the eigenvalue is greater than 0, the system's static frequency will lose stability. Therefore, the probability P(SFS) of the static frequency instability can be obtained by (17). When static frequency instability occurs, the severity Sev(SFS) is defined

as 1, and then the risk of static frequency instability of the system after a line outage can be defined as follows:

$$R_{SFS} = P(\text{SFS}) \times Sev(\text{SFS}) \tag{18}$$

3.4. Static Rotor Angle Stability Index

Similar to the analysis in Section 3.3, there is also a non-explicit function between the static stability power limit of any generator and the output power of wind farms. Because it is a small disturbance analysis, the function relationship can be linearized at the reference operating point, and the linear expression of the static stability power limit of any generator and the output power of a wind farm can be obtained:

$$\Delta P_{\max,i} = \sum_{k=1}^{w} [(\partial P_{\max,i} / \partial W_k) \Delta W_k] \tag{19}$$

where $P_{\max,i}$ is the static power limit of the ith generator; W_k represents the output power of the kth wind farm; $\partial P_{\max,i} / \partial W_k$ is the sensitivity of the static stability power limit of the ith generator to the output power of the kth wind farm. Similarly, the sensitivity can be calculated by numerical method:

$$\frac{\partial P_{\max,i}}{\partial W_k} = \frac{P_{\max,i}(W_k + \Delta W_k) - P_{\max,i}(W_k)}{\Delta W_k} \tag{20}$$

The linear relationship between the static stability power limit of generators and the output power of wind farms is established by (19) and (20). Similar to the derivation in Section 3.3, the probability distribution of the output power of wind farms has been modeled by GMM. After the linear transformation of (19), each Gaussian subcomponent of the probability distribution of the static stability power limit of the generator should obey the Gaussian distribution with a mean of $\mathbf{K}_3\boldsymbol{\mu}_m + \mathbf{B}_3$ and a variance of $\mathbf{K}_3\boldsymbol{\Sigma}_m\mathbf{K}_3{}^{\mathrm{T}}$, where $\mathbf{K}_3$ and $\mathbf{B}_3$ are the coefficient matrices of the linear expression obtained by (20). Then, using the total probability in Equation (7), the final probability distribution of the static stability power limit of each generator can be obtained as follows:

$$\begin{aligned} F(\mathbf{P}_{\max}) &= \sum_{m=1}^{M} \omega_m F^m(\mathbf{P}_{\max}) \\ F^m(\mathbf{P}_{\max}) &= \int_{-\infty}^{P_{\max}} \frac{e^{-\frac{1}{2}(\mathbf{P}_{\max} - \mathbf{K}_3\boldsymbol{\mu}_m - \mathbf{B}_3)^{\mathrm{T}} (\mathbf{K}_3 \sum_m \mathbf{K}_3)^{-1} (\mathbf{P}_{\max} - \mathbf{K}_3\boldsymbol{\mu}_m - \mathbf{B}_3)}}{(2\pi)^{p/2} \det(\mathbf{K}_3 \sum_m \mathbf{K}_3)^{1/2}} d\mathbf{P}_{\max} \end{aligned} \tag{21}$$

The Chinese standard [41] stipulates that the static power angle stability reserve coefficient should not be less than 10% after fault. The equation is as follows:

$$K_{P,i} = (P_{\max,i} - P_{0,i}) / P_{0,i} \tag{22}$$

where $P_{0,i}$ is the output power of the ith generator under normal operation; $K_{P,i}$ is the static rotor angle stability reserve coefficient of the ith generator. Through Equation (22), the minimum value of the static stability power limit satisfying the standard can be obtained. Then, through the probability distribution function (21) of the static stability limit power, the probability $P(K_{P,i})$ of the static rotor angle stability reserve coefficient of less than 10% can be obtained. The severity of static rotor angle instability is defined as follows:

$$Sev(K_{P,i}) = (0.1 - K_{P,i,\min}) / 0.1 \tag{23}$$

where $K_{P,i,\min}$ is the minimum value that the static stability limit power of ith generator may reach during the power fluctuation of wind farms, i.e., the most serious situation is considered as the severity of static rotor angle instability. Therefore, when there is a line outage, the static rotor angle instability risk of the system is defined as follows:

$$R_{SRAS} = \sum_{i=1}^{n_3} P(K_{P,i}) \times Sev(K_{P,i}) \tag{24}$$

where n_3 is the number of generators.

3.5. Static Voltage Stability Index

The static voltage stability calculation can be solved by gradually increasing loads to estimate the critical point of voltage instability of the current operating point. The static voltage stability reserve coefficient is shown as follows:

$$K_{U,i} = (U_{0,i} - U_{cr,i})/U_{cr,i} \tag{25}$$

where $K_{U,i}$ is the static voltage stability reserve coefficient of the ith bus; $U_{0,i}$ is the voltage amplitude of the ith bus under normal operation; $U_{cr,i}$ is the critical point of voltage instability at the ith bus.

For the novel power system with renewable energy and DC access, when there is a line outage, this paper will gradually increase the load of each bus and calculate the probability distribution of the critical point of voltage instability of each bus through the probabilistic AC/DC power flow of (6)–(8). The Chinese standard stipulates that the static voltage stability reserve should not be less than 8% at the post-fault operation mode [41]. Through the probability distribution of the critical voltage of each bus and (25), the probability $P(K_{U,i})$ that the static voltage stability reserve coefficient of the system does not meet the operation requirements can be solved. Then, the severity function of static voltage instability is defined as follows:

$$Sev(K_{U,i}) = (0.08 - K_{U,i,\min})/0.08 \tag{26}$$

where $K_{U,i,\min}$ is the minimum value that the static voltage stability reserve coefficient may reach during the fluctuation of renewable energy output, i.e., the most serious situation deviating from the security constraint is used as the severity of the index. Therefore, the risk of static voltage instability caused by a line outage can be defined as follows:

$$R_{SVS} = \sum_{i=1}^{n_1} P(K_{U,i}) \times Sev(K_{U,i}) \tag{27}$$

4. Comprehensive Risk Assessment Index of Vulnerable Lines

In this paper, six risk assessment indexes are defined to identify vulnerable lines from the perspective of system security and stability for the novel power system. When there is a line outage, the vulnerability of the line is evaluated by calculating the six indicators, respectively. On this basis, in order to comprehensively evaluate the vulnerability of each line, it is necessary to integrate these assessment indicators. In this paper, the comprehensive weight method based on game theory is used to weight these risk indicators.

Firstly, the magnitude and dimension of the six indicators need to be unified, and then they need to be weighted. The comprehensive risk evaluation index R_c of vulnerable lines is obtained by weighting each index.

$$\begin{aligned} R_c = \; & \alpha_1 \overline{R}_{VV} + \alpha_2 \overline{R}_{LO} + \alpha_3 \overline{R}_{SSA} \\ & + \alpha_4 \overline{R}_{SFS} + \alpha_5 \overline{R}_{SRAS} + \alpha_6 \overline{R}_{SVS} \end{aligned} \tag{28}$$

Here, α_1 to α_6 are the weights of each risk index; the upper line represents the normalized risk index. The weight calculation process using the comprehensive weighting method based on game theory is as follows [43]:

(1) The subjective weight $\mathbf{B}_1$ of each risk index is obtained based on the analytic hierarchy process, and the objective weight $\mathbf{B}_2$ of each risk index is obtained based on the entropy weight method. The weights of the two methods are linearly combined to obtain the weight $\mathbf{B} = \beta_1\mathbf{B}_1 + \beta_2\mathbf{B}_2$ of the comprehensive weighting method, where β_1 and β_2 are the comprehensive weight combination coefficients.

(2) In order to minimize the deviation between the comprehensive weight and each basic weight, it is necessary to establish the corresponding optimization objective to optimize the coefficient β_1 and β_2.

$$\min \left\| \sum_{i=1}^{2} \beta_i B_i^{\mathrm{T}} - B_j^{\mathrm{T}} \right\|_2 \tag{29}$$

(3) According to the differential properties of matrices, Equation (29) can be transformed into:

$$\begin{bmatrix} \mathbf{B}_1^{\mathrm{T}}\mathbf{B}_1 & \mathbf{B}_1^{\mathrm{T}}\mathbf{B}_2 \\ \mathbf{B}_2^{\mathrm{T}}\mathbf{B}_1 & \mathbf{B}_2^{\mathrm{T}}\mathbf{B}_2 \end{bmatrix} \begin{bmatrix} \beta_1 \\ \beta_2 \end{bmatrix} = \begin{bmatrix} \mathbf{B}_1^{\mathrm{T}}\mathbf{B}_1 \\ \mathbf{B}_2^{\mathrm{T}}\mathbf{B}_2 \end{bmatrix} \tag{30}$$

The comprehensive weights β_1 and β_2 can be obtained by substituting the solved weights $\mathbf{B}_1$ and $\mathbf{B}_2$ into (30), and then the comprehensive weight $\mathbf{B}$ obtained by the comprehensive weighting method based on game theory can be solved by the linear combination in step (1).

Based on the above analysis, for the novel power system, each line in the system is tripped one by one, and each risk assessment index defined is calculated separately. All risk indicators are weighted by the comprehensive weighting method to obtain a comprehensive risk assessment index. The vulnerability of each line is assessed according to the level of the comprehensive risk assessment index. When there is a line outage, the higher the comprehensive risk assessment index, the greater the system risk caused by the line outage, the more important the line in the system, and the more vulnerable the line.

5. Simulation Tests

An improved IEEE 39 bus system with wind farms and DC access was used as a test system to verify the applicability of the method proposed in this paper. The system structure is shown in Figure 2. The original synchronous generators of busses 32, 34, and 38 are replaced by wind farms. It is assumed that the installed capacity of each wind farm is 650 MW, 500 MW, and 450 MW, respectively, and the total permeability of renewable energy is about 33%. The original AC line L3–18 is replaced by the LCC-HVDC line, in which bus 3 is the rectifier station and bus 18 is the inverter station. The constant ratio and constant current control are used for rectifiers, and the constant ratio and constant control angle are used as inverters. The constant power model is used in the simulation test, and the total load power of the system is 6150 MW. The wind turbine is regarded as a power source. All synchronous generators apply the classical model with a first-order governor model.

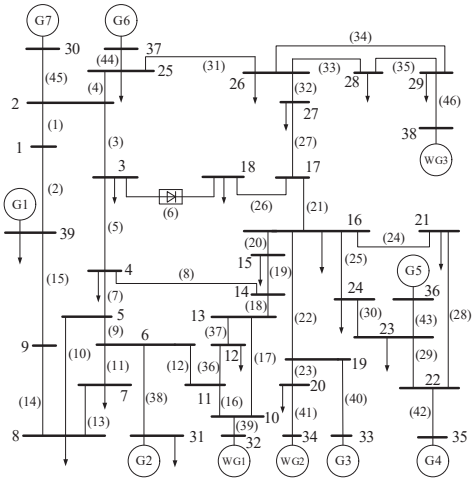

Figure 2. Improved IEEE 39 bus system.

Firstly, the probabilistic AC/DC power flow calculation method based on the analytical method proposed in this paper is used to calculate the bus voltage violation and line overload risk after each line outage. Taking line L1–2 as an example, when it is tripped, the probability distribution of each bus voltage and each line power can be determined by using the probabilistic AC/DC power flow calculation method proposed in this paper. The probability distribution of the bus voltage amplitude of bus 22 and the probability distribution of the active power on line L16–19 are shown in Figure 3. At the same time, the probabilistic AC/DC power flow is also calculated by MCS to verify the accuracy of the proposed probabilistic power flow method.

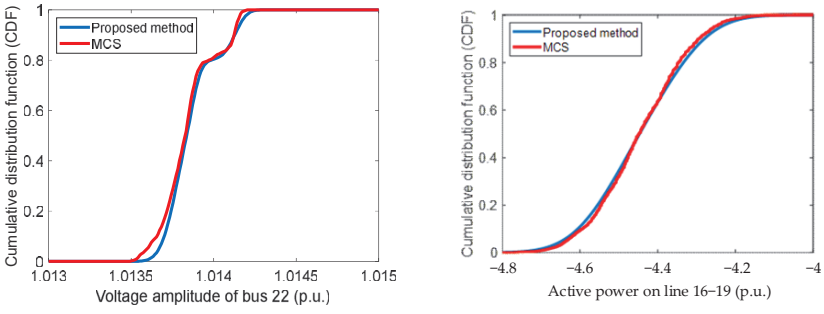

Figure 3. Probability AC/DC power flow results: (**a**) bus voltage; (**b**) line transmission power.

In Figure 3, the red curve is the result obtained by MCS, and the blue curve is the result obtained by the analytical method proposed in this paper. It can be seen that the results obtained by the two methods are very close. In terms of calculation time, the proposed method takes 0.43 s and MCS takes 97 s, indicating that the proposed method greatly improves the calculation efficiency while satisfying the calculation accuracy.

Based on the probability distribution of the bus voltage and line power, the risk of system voltage violation and line overload after each line outage can be obtained by (9) to (12), as shown in Figures 4 and 5.

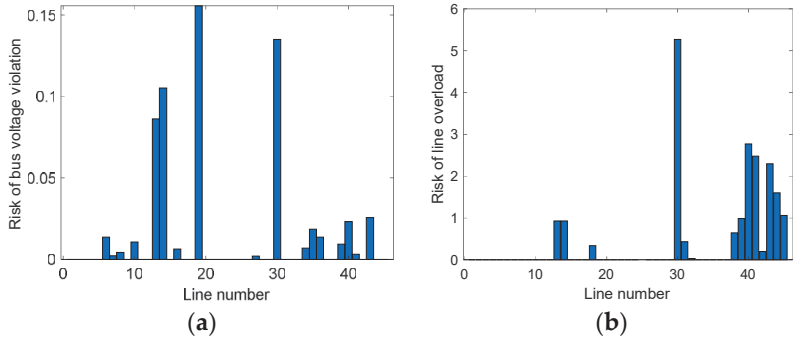

Figure 4. Risk of voltage violation and line overload after each line outage: (**a**) bus voltage violation risk; (**b**) line overload risk.

In Figure 4, the risk of bus voltage violation and line overload occur after some lines are tripped. According to the risk level, the top 10 lines that cause voltage violation risk and line overload risk are selected, respectively, as shown in Table 1.

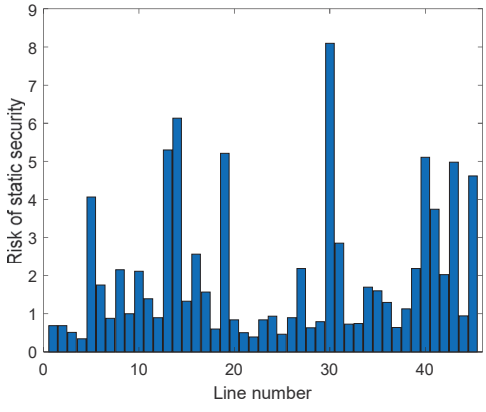

Figure 5. Static security after each line outage.

Table 1. Risk sorting for voltage violation and line overload.

Rank	Voltage Violation Risk		Line Overload Risk	
	Line Number	**Risk Value**	**Line Number**	**Risk Value**
1	L15–16	0.1556	L25–26	5.2697
2	L25–26	0.1371	L20–34	2.7717
3	L9–39	0.1046	L22–35	2.4761
4	L8–9	0.0860	L25–37	2.2993
5	L25–37	0.0254	L2–30	1.5992
6	L20–34	0.0232	L29–38	1.0576
7	L12–11	0.0189	L19–33	0.9878
8	L4–5	0.0139	L9–39	0.9322
9	L12–13	0.0137	L8–9	0.9322
10	L6–7	0.0106	L10–32	0.6455

In Table 1, the risk of voltage violation caused by the outage of L15–16, L25–26, and L9–39 is 0.1556, 0.1371, and 0.1046, respectively, ranking the top three in all lines. If these lines are attacked and tripped, the system will have a high risk of voltage violation. In the line overload risk index, the outage of L25–26 and L20–34 is more likely to cause an overload of other lines in the system, indicating that these lines are more important and vulnerable in the line overload risk index. After there is an outage in some lines, such as L1–2 and L16–24, the risk of bus voltage violation and line overload is zero, indicating that these lines are not important lines in the system under these two indicators. Even if they are attacked, they will not cause the risk of voltage violation and line overload.

The static security of the system after each line outage is assessed. When there is an outage in each line, the remaining lines are tripped one by one by using the $N-1$ principle. The static security risk of the system after each line outage is solved by (13), as shown in Figure 5.

In Figure 5, the outage of each line has impacts on the static security of the system. According to the risk level, the top 10 lines are ranked as shown in Table 2. Among them, L25–26, L9–39, and L8–9 are the top three lines, indicating that these lines have the greatest impact on the static security of the power system once there is an outage. They are the most vulnerable lines in the static security index.

The risk of static frequency instability of the system after each line outage is assessed. Through (14)–(17), the probability distribution of system eigenvalues during the fluctuation of wind farm outputs can be obtained, respectively. Then, the static frequency instability risk of the system after each line outage can be obtained by (18), as shown in Figure 6.

Table 2. Risk sorting for static security.

Rank	Line Number	Risk Value	Rank	Line Number	Risk Value
1	L25–26	7.9996	6	L25–37	5.0127
2	L9–39	6.0973	7	L29–38	4.4849
3	L8–9	5.2484	8	L22–35	3.7451
4	L15–16	5.2099	9	L3–4	3.2632
5	L20–34	5.1403	10	L26–27	2.8230

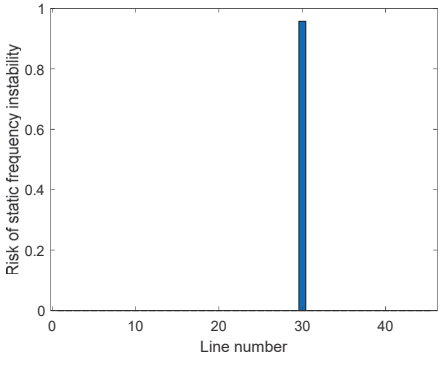

Figure 6. Static frequency stability after each line outage.

From Figure 6, only when there is an outage in L25–26, the system will have the risk of static frequency instability, indicating that L25–26 is the most vulnerable line in the static frequency stability risk index. When the line is attacked, it is prone to causing static frequency instability of the system.

The risk of static rotor angle instability of the system after each line outage is evaluated. Through (19)–(21), the probability distribution of the static stability limit of each generator after each line outage can be obtained, and then through (22)–(24), the risk that the static rotor angle stability reserve coefficient of the system does not meet the operation requirements is determined, as shown in Figure 7.

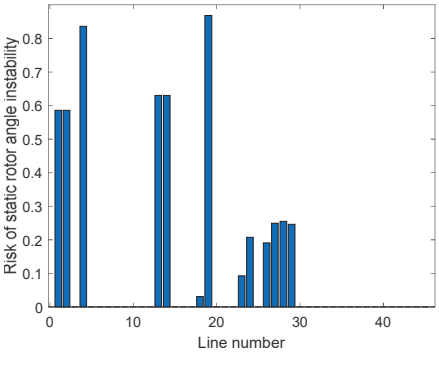

Figure 7. Static rotor angle stability after each line outage.

In Figure 7, the outage of some lines leads to insufficient static rotor angle stability reserve in the system. The top 10 lines are shown in Table 3. Among them, lines such as L15–16, L2–25, and L9–39 are the most vulnerable lines in the static rotor angle stability index. When they are attacked, the system is prone to static rotor angle instability.

Table 3. Risk sorting for static rotor angle stability.

Rank	Line Number	Risk Value	Rank	Line Number	Risk Value
1	L15–16	0.8680	6	L1–2	0.5855
2	L2–25	0.8336	7	L22–23	0.2524
3	L9–39	0.6304	8	L21–22	0.2491
4	L8–9	0.6304	9	L23–24	0.2460
5	L1–39	0.5855	10	L16–24	0.2075

The risk of static voltage instability in the system after each line outage is evaluated. By tripping each line of the system one by one, the probability distribution of the critical value of voltage instability for each bus is assessed by probabilistic power flow. Then, the risk of static voltage instability is calculated by (25)–(27), as shown in Figure 8.

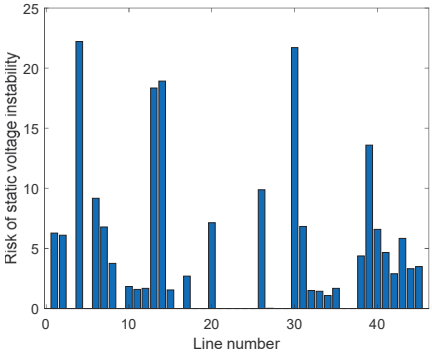

Figure 8. Static voltage stability after each line outage.

From Figure 8, the static voltage stability reserve of the system does not meet the operation requirements due to the outage of some lines, and there is a certain risk of static voltage instability. Taking the top 10 risk lines as shown in Table 4, the outages of L2–25, L25–26, and other lines have the greatest impact on static voltage stability. When they are attacked, they are very likely to cause static voltage instability in the system.

Table 4. Risk sorting for static voltage stability.

Rank	Line Number	Risk Value	Rank	Line Number	Risk Value
1	L2–25	22.22	6	L17–27	9.71
2	L25–26	21.71	7	L4–5	9.18
3	L9–39	18.92	8	L16–17	6.88
4	L8–9	18.22	9	L26–27	6.82
5	L19–33	13.59	10	L4–14	6.78

Through the above simulation results, the influence of line outage on system security and stability is evaluated. The vulnerability of each line under each risk assessment index is obtained. In order to finally obtain the vulnerability of each line, the game-theory-based comprehensive weighting method is used to weight multiple indicators to form a comprehensive risk index to evaluate the vulnerability of each line. Firstly, the results of each index are normalized, and the subjective weight B_1 = [0.0859, 0.0650, 0.1508, 0.2790, 0.2097, 0.2097] of each index is solved by analytic hierarchy process. The objective weight B_2 = [0.1823, 0.1657, 0.0430, 0.3637, 0.1603, 0.0849] of each index is obtained by entropy weight method, and β_1 = 0.2945, β_2 = 0.7597 is obtained by (30). Then, the comprehensive weight of each index is B = [0.1638, 0.1450, 0.0771, 0.3585, 0.1836, 0.1263]. The normalized risk assessment index results are weighted according to the comprehensive

weight B. Finally, the comprehensive risk of each line outage on the system's security and stability can be obtained as shown in Figure 9.

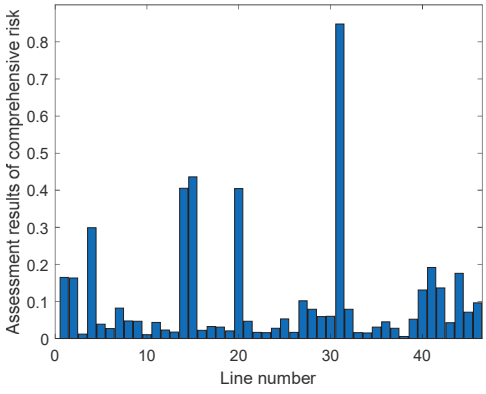

Figure 9. Comprehensive index after each line outage.

In Figure 9, the top 10 risk lines are shown; they are shown in Table 5 according to the risk ranking. From the perspective of system security and stability, L25–26 has the highest importance in the system. When there is an outage, it has the greatest impact on system security and stability, and it is the most important and vulnerable line in the system. Compared with L25–26, the importance of lines such as L9–39, L8–9, L15–16, and L2–25 is second, but they are also relatively vulnerable lines in the system. Once they experience an outage, it will also have a great impact on the security and stability of the system.

Table 5. Sorting for comprehensive assessment index.

Rank	Line Number	Risk Value	Rank	Line Number	Risk Value
1	L25–26	0.8469	6	L20–34	0.1897
2	L9–39	0.4361	7	L25–37	0.1738
3	L8–9	0.4066	8	L1–2	0.1691
4	L15–16	0.3997	9	L1–39	0.1671
5	L2–25	0.3076	10	L22–35	0.1360

By assessing the vulnerable lines in the system, it can provide a decision-making basis for the control strategy that can prevent power systems from blackouts. For example, in the simulation test, the defense of vulnerable lines such as L25–26 and L9–39 can be strengthened. From the perspective of power system operation, corresponding control measures and contingency plans can be formulated and implemented according to these vulnerable lines, so that the system can still maintain safe operation even if these vulnerable lines experience an outage.

In order to further demonstrate the effectiveness of the proposed method, the method proposed in [25] is used to compare with the proposed method in this paper. The authors in [25] also identified the weak lines of the system by defining a variety of vulnerability indicators, such as topology indexes based on network structure and indexes based on power flow calculation. Moreover, these indexes proposed in [25] are also weighted to form a comprehensive index to identify vulnerable lines of power systems. Therefore, [25] could be regarded as representative enough to compare with the proposed method in this paper. The vulnerable lines that rank in the top 10 obtained by the proposed method in this paper and [25] are shown in Table 6.

Table 6. Sorting results comparison.

Rank	The Proposed Method	The Method of [25]
1	L25–26	L25–26
2	L9–39	L2–30
3	L8–9	L22–35
4	L15–16	L10–32
5	L2–25	L20–34
6	L20–34	L29–38
7	L25–37	L15–16
8	L1–2	L25–37
9	L1–39	L19–33
10	L22–35	L6–7

From Table 6, the method in this paper is the same as the method proposed in [25] to identify a total of five lines in the set of vulnerable lines. The most vulnerable line obtained by [25] is L16–19, which is the same as the results obtained by the proposed method. The indexes proposed in [25] contain power transfer characteristics. Thus, lines that are prone to inducing line overload after an outage such as L25–26, L22–35, and L2–30 are more vulnerable than other lines. Meanwhile, the indexes proposed in [25] also contain topology connectivity. Some lines such as L2–30, L22–35, and L10–32 are more vulnerable than other lines since the outage of these lines will make some generators split from the system, which damages the topology connectivity of the system. This paper assumes that the generator on the swing bus has enough capacity. Although these line outages will unbalance the system power, the swing bus will regulate the power to keep the system power balanced. Therefore, in this paper, the outage of these lines does not cause severe problems (such as static rotor angle instability, etc.) other than triggering overloading of the lines connected to the swing bus. These lines are not the most vulnerable lines in this paper. Furthermore, for L9–39, its vulnerability ranks second in this paper but does not rank in the top 10 in [25], indicating that the line is not vulnerable after identification in [25]. However, although the impact of L9–39 outage on line overload is small, its outage will cause static rotor angle instability and static voltage instability in this paper, which will cause severe operation issues for power systems. However, it cannot be well reflected by [25]. In contrast, the indicators proposed in this paper can assess the security and stability of the system simultaneously. These indexes are always the most important indexes for power systems, which can give more comprehensive and effective identification for vulnerable lines than existing methods.

6. Conclusions

This paper proposes an identification method for weak transmission lines of power systems with intermittent energy resources and DC integration, which aims to provide a decision-making basis for control strategies and contingency plans. Firstly, this paper proposes a series of risk assessment index systems from the perspective of the security and stability of the novel power system. In terms of security, the influences of outages in each line on the electrical quantities such as bus voltage and line power are evaluated. In terms of stability, from the perspective of system static stability, three risk indicators of static rotor angle stability, static voltage stability, and static frequency stability are defined, respectively. The proposed risk assessment indicators aim at comprehensively quantifying the impact of each line outage on system stability. Then, the game-theory-based comprehensive weighting method is used to weight the results of each risk index to form a comprehensive risk evaluation index to evaluate the impact of each line outage on the system. Finally, the effectiveness of the proposed method is tested by the improved IEEE-39 bus system with renewable energy and DC lines integration. Meanwhile, the proposed method is compared with the current method. The simulation test results show that vulnerable lines of novel power systems can be evaluated effectively by the proposed method.

Author Contributions: Conceptualization, L.G. and J.H.; methodology, L.G., A.H. and M.Y.; software, A.H.; validation, A.H.; formal analysis, A.H.; investigation, A.H. and S.L.; resources, A.H. and J.C.; data curation, A.H.; writing—original draft preparation, A.H. and L.G.; writing—review and editing, A.H. and L.G.; visualization, J.C.; supervision, L.G., M.Y. and J.H.; project administration, L.G.; funding acquisition, L.G. All authors have read and agreed to the published version of the manuscript.

Funding: This research was supported by Hubei Provincial Natural Science Foundation of China (2022CFB301).

Data Availability Statement: The data that support the findings of this study are available upon request from the corresponding author. The data are not publicly available due to privacy or ethical restrictions.

Conflicts of Interest: Author Jijing Cao was employed by the company Wuhan EMU Depot of China Railway Wuhan Group Co., Ltd., Author Shangwen Li was employed by the Wuhan Power Supply Company, Author Jiawei Hu was employed by the Central China Branch of State Grid Corporation of China. The remaining authors declare that the research was conducted in the absence of any commercial or financial relationships that could be construed as a potential conflict of interest.

References

1. Kumar, S.; Pandey, A.; Goswami, P.; Pentayya, P.; Kazi, F. Analysis of Mumbai Grid Failure Restoration on Oct 12, 2020: Challenges and Lessons Learnt. *IEEE Trans. Power Syst.* **2022**, *37*, 4555–4567. [CrossRef]
2. Xiang, Y.; Wang, T.; Wang, Z. Risk Prediction Based Preventive Islanding Scheme for Power System Under Typhoon Involved with Rainstorm Events. *IEEE Trans. Power Syst.* **2023**, *38*, 4177–4190. [CrossRef]
3. Liu, S.; Chen, C.; Jiang, Y.; Lin, Z.; Wang, H.; Waseem, M.; Wen, F. Bi-Level Coordinated Power System Restoration Model Considering the Support of Multiple Flexible Resources. *IEEE Trans. Power Syst.* **2023**, *38*, 1583–1595. [CrossRef]
4. Dobson, I.; Newman, D.E. Cascading blackout overall structure and some implications for sampling and mitigation. *Int. J. Elect. Power Energy Syst.* **2017**, *86*, 29–32. [CrossRef]
5. Li, M.J.; Tse, C.K.; Liu, D.; Zhang, X. Cascading Failure Propagation and Mitigation Strategies in Power Systems. *IEEE Syst. J.* **2023**, *17*, 3282–3293. [CrossRef]
6. Rajkumar, V.S.; Ştefanov, A.; Torres, J.L.R.; Palensky, P. Dynamical Analysis of Power System Cascading Failures Caused by Cyber Attacks. *IEEE Trans. Ind. Informat.* **2024**, *20*, 8807–8817. [CrossRef]
7. Gao, Q.; Wang, Y.; Cheng, X.; Yu, J.; Chen, X.; Jing, T. Identification of Vulnerable Lines in Smart Grid Systems Based on Affinity Propagation Clustering. *IEEE Internet Things J.* **2019**, *6*, 5163–5171. [CrossRef]
8. Liu, Y.; Lai, X.; Xin, H.; Zhu, J.; Huang, L.; Xia, S. Generalized short-circuit ratio based distributed real-time stability assessment of renewable power systems. *IEEE Trans. Power Syst.* **2023**, *38*, 5953–5956. [CrossRef]
9. Shu, Y.; Tang, Y. Analysis and recommendations for the adaptability of China's power system security and stability relevant standards. *CSEE J. Power Energy Syst.* **2017**, *3*, 334–339. [CrossRef]
10. Zhu, Y.; Zhou, Y.; Wei, W.; Zhang, L. Real-time cascading failure risk evaluation with high penetration of renewable energy based on a graph convolutional network. *IEEE Trans. Power Syst.* **2023**, *38*, 4122–4133. [CrossRef]
11. Kitsak, M.; Gallos, L.K.; Havlin, S.; Liljeros, F.; Muchnik, L.; Stanley, H.E.; Makse, H.A. Identification of influential spreaders in complex networks. *Nat. Phys.* **2010**, *6*, 888–893. [CrossRef]
12. Xu, L.; Wang, X.L.; Wang, X.F. Electric betweenness and its application in vulnerable line identification in power system. *Chin. Soc. Electr. Eng.* **2010**, *30*, 33–39.
13. Bompard, E.; Pons, E.; Wu, D. Extended topological metrics for the analysis of power grid vulnerability. *IEEE Syst. J.* **2012**, *6*, 481–487. [CrossRef]
14. Fang, J.; Su, C.; Chen, Z.; Sun, H.; Lund, P. Power system structural vulnerability assessment based on an improved maximum flow approach. *IEEE Trans. Smart Grid* **2018**, *9*, 777–785. [CrossRef]
15. Chu, C.C.; Lu, H.H.C. Complex networks theory for modern smart grid applications: A survey. *IEEE J. Emerg. Sel. Top. Circuits Syst.* **2017**, *7*, 177–191. [CrossRef]
16. Fan, W.; Zhang, X.; Mei, S. Vulnerable transmission line identification considering depth of K-shell decomposition in complex grids. *IET Gener. Trans. Distrib.* **2018**, *12*, 1137–1144. [CrossRef]
17. Bai, H.; Miao, S. Hybrid flow betweenness approach for identification of vulnerable line in power system. *IET Gener. Trans. Distrib.* **2015**, *9*, 1324–1331. [CrossRef]
18. Chen, C.Y.; Zhou, Y.; Wang, Y.; Ding, L.; Huang, T. Vulnerable Line Identification of Cascading Failure in Power Grid Based on New Electrical Betweenness. *IEEE Trans. Circuits Syst. II Express Briefs* **2023**, *70*, 665–669. [CrossRef]
19. Rao, S.; Tylavsky, D.; Vittal, V.; Yi, W.; Shi, D.; Wang, Z. Fast weak-bus and bifurcation point determination using holomorphic embedding method. In Proceedings of the IEEE Power & Energy Society General Meeting (PESGM), Portland, OR, USA, 5–10 August 2018; pp. 1–5.

20. Ma, Z.; Shen, C.; Liu, F.; Mei, S. Fast screening of vulnerable transmission lines in power grids: A pagerank-based approach. *IEEE Trans. Smart Grid* **2019**, *10*, 1982–1991. [CrossRef]
21. Wei, X.; Zhao, J.; Huang, T.; Bompard, E. A novel cascading faults graph based transmission network vulnerability assessment method. *IEEE Trans. Power Syst.* **2018**, *33*, 2995–3000. [CrossRef]
22. Zhang, S.; Yu, M.; Hu, J.; Sun, J.; Wei, J.; Wu, Y. Research on vulnerable line identification based on PMU data and graph theory. In Proceedings of the 2022 Power System and Green Energy Conference (PSGEC), Shanghai, China, 25–27 August 2022; pp. 853–858.
23. Moger, T.; Dhadbanjan, T. A novel index for identification of weak nodes for reactive compensation to improve voltage stability. *IET Gener. Trans. Distrib.* **2015**, *9*, 1826–1834. [CrossRef]
24. Zhu, D.; Wang, R.; Duan, J.; Chen, L.; Xue, B.; Cheng, W. Identification of critical transmission lines considering multiple influencing factors. *Proc. CSEE* **2019**, *39*, 5938–5947.
25. Zhu, D.; Wang, R.; Duan, J.; Cheng, W. Comprehensive weight method based on game theory for identify critical transmission lines in power system. *Int. J. Electr. Power Energy Syst.* **2021**, *124*, 106362. [CrossRef]
26. Yang, L.; Li, C. Identification of vulnerable lines in smart grid systems based on improved agglomerative hierarchical clustering. *IEEE Access* **2023**, *11*, 13554–13563. [CrossRef]
27. Fan, W.; He, X.; Xiao, Y.; Li, Q. Vulnerability analysis of power system by modified H-index method on cascading failure state transition graph. *Electr. Power Syst. Res.* **2022**, *209*, 107986. [CrossRef]
28. Li, Y.; Liu, J.; Liu, X.; Jiang, L.; Wei, Z.; Xu, W. Vulnerability assessment in power grid cascading failures based on entropy of power flow. *Auto. Elect. Power Syst.* **2012**, *36*, 11–16.
29. Liu, W.; Wang, J.; Xie, C.; Wang, W. Brittleness source identification model for cascading failure of complex power grid based on brittle risk entropy. *Pro. CSEE* **2014**, *32*, 142–149.
30. Lin, Z.; Wen, F.; Wang, H.; Lin, G.; Mo, T.; Ye, X. CRITIC-based node importance evaluation in skeleton-network reconfiguration of power grids. *IEEE Trans. Circuits Syst. II Express Briefs* **2018**, *65*, 206–210. [CrossRef]
31. Cheng, M.X.; Crow, M.; Ye, Q. A game theory approach to vulnerability analysis: Integrating power flows with topological analysis. *Int. J. Electr. Power Energy Syst.* **2016**, *82*, 29–36. [CrossRef]
32. Zhu, B.; Zhang, L.; Li, G. Identification of vulnerable transmission lines in power system based on game theory. *IEEE Access* **2024**, *12*, 29607–29616. [CrossRef]
33. Sun, J.; Liu, J.; Li, C.; Zhi, N. An identification method for vulnerable lines based on combination weighting method and GraphSAGE algorithm. *Int. J. Electr. Power Energy Syst.* **2023**, *149*, 109035. [CrossRef]
34. Zhou, B.; Lei, Y.; Li, C.; Fang, B.; Wu, Q.; Li, L.; Li, Z. Electrical LeaderRank method for node importance evaluation of power grids considering uncertainties of renewable energy. *Int. J. Electr. Power Energy Syst.* **2019**, *106*, 45–55. [CrossRef]
35. Zhang, L.; Zhu, B.; Wang, Y. Identification of vulnerable lines in power grids with wind power integration based on topological potential. *Electr. Power Syst. Res.* **2024**, *234*, 110593. [CrossRef]
36. Zhu, S.; Wang, T.; Wang, Z. Bi-level optimized emergency load/generator shedding strategy for AC/DC hybrid system following DC blocking. *IET Gener. Trans. Distrib.* **2020**, *14*, 1491–1499. [CrossRef]
37. Wang, T.; Li, C.; Mi, D.; Wang, Z.; Xiang, Y. Coordinated modulation strategy considering multi-HVDC emergency for enhancing transient stability of hybrid AC/DC power systems. *CSEE J. Power Energy Syst.* **2020**, *6*, 806–815.
38. Kundur, P. *Power System Stability and Control*; McGraw-Hill: New York, NY, USA, 1994.
39. Wang, Z.; Shen, C.; Liu, F.; Gao, F. Analytical expressions for joint distributions in probabilistic load flow. *IEEE Trans. Power Syst.* **2017**, *32*, 2473–2474. [CrossRef]
40. Xiang, Y.; Wang, T.; Wang, Z. Improved Gaussian mixture model based probabilistic power flow of wind integrated power system. In Proceedings of the IEEE Power & Energy Society General Meeting (PESGM), Atlanta, GA, USA, 4–8 August 2019; pp. 1–5.
41. *GB 38755-2019*; Code on Security and Stability for Power System. Standardization Administration of China: Beijing, China, 2019.
42. Bu, S.; Du, W.; Wang, H.; Chen, Z.; Xiao, L.; Li, H. Probabilistic analysis of small-signal stability of large-scale power systems as affected by penetration of wind generation. *IEEE Trans. Power Syst.* **2012**, *27*, 762–770. [CrossRef]
43. Han, X.; Zhao, S.; Wei, Z.; Bai, W. Planning and overall economic evaluation of photovoltaic-energy storage station based on game theory and analytic hierarchy process. *IEEE Access* **2019**, *7*, 110972–110981. [CrossRef]

MDPI AG
Grosspeteranlage 5
4052 Basel
Switzerland
Tel.: +41 61 683 77 34

MDPI Books Editorial Office
E-mail: books@mdpi.com
www.mdpi.com/books

Academic Open
Access Publishing

mdpi.com

ISBN 978-3-7258-2164-8